A Rate-Dependent and Pinching-Sensitive Constitutive Model for Reinforcing Steel

by

Juan F. Velásquez

Final Report

October 2026

Department of Civil Engineering
Universidad Nacional de Colombia
Facultad de Minas

A Rate-Dependent and Pinching-Sensitive Constitutive Model for Reinforcing Steel

by

Juan Fernando Velásquez Bedoya

Department of Civil Engineering

Universidad Nacional de Colombia

Facultad de Minas

October 2026

Acknowledgments

This report is based on the Ph.D. dissertation of the author. I am deeply grateful to Professor John J. Blandón, Facultad de Minas, Universidad Nacional de Colombia, Medellín, for his guidance, support, and encouragement throughout this work, as well as for the opportunity to carry out this research under his supervision. I am equally thankful to Professor José I. Restrepo, University of California San Diego, for his advice, thoughtful discussions, and valuable feedback throughout the development of this research.

I also wish to acknowledge Professors Óscar Echeverri and Freddy Bolaños, Facultad de Minas, Universidad Nacional de Colombia, Medellín, for their support, guidance, encouragement, and valuable contributions to this work. I am particularly grateful to Professor Echeverri for providing the opportunity that made this work possible, and to Professor Bolaños for his willingness to share his knowledge and for his valuable comments on the dissertation.

I am particularly thankful to my family for their patience, understanding, and constant support throughout this process. I also appreciate the support and collaboration of my colleagues and students, as well as everyone who contributed to this work in one way or another.

Last but not least, I gratefully acknowledge the financial support provided through a doctoral fellowship from the Facultad de Minas, Universidad Nacional de Colombia, Sede Medellín.

The opinions and findings presented in this report are my own and do not necessarily reflect the views of the sponsoring institution.

Abstract

Reinforced concrete structures subjected to seismic loading experience strain rates in the longitudinal reinforcement that are orders of magnitude higher than those applied in standard quasi-static material tests, yet most constitutive models used in nonlinear time-history analysis neglect this rate dependence. This dissertation develops SteelDRCV (Dodd-Restrepo-Carreño-Velásquez), a hysteretic constitutive model for reinforcing steel that extends the SteelDRC formulation with two mechanisms: (i) a nonlinear Voigt-type viscous overstress term that captures rate-dependent strengthening beyond initial yield, and (ii) a quadrant-dependent curvature factor that phenomenologically reproduces bond-slip-induced pinching in cyclic response. Both extensions are implemented in OpenSees and formulated to preserve compatibility with large-scale nonlinear structural analysis.

Strain-rate demands are first characterized from two full-scale shake-table specimens tested at the LHPOST facility at UC San Diego: (i) a circular bridge column and (ii) a seven-story structural wall, quantifying the magnitude, distribution, and amplification of strain rates in longitudinal reinforcement under realistic seismic excitation. High-strain-rate tensile tests then characterize the viscous mechanism and support proposing two nonlinear Voigt-type parameters. A phenomenological curvature formulation is proposed to reproduce bond-slip-induced pinching in cyclic response.

Model calibration follows a two-stage strategy. The first stage identifies the cyclic and pinching parameters from the quasi-static structural response under displacement-controlled conditions. The second employs Bayesian inference to refine the remaining strain-rate, damping, and concrete damage parameters using Gaussian-Process surrogates, variance-based sensitivity decomposition, and Transitional Markov Chain Monte Carlo sampling. The posterior distributions quantify parameter uncertainty and identify which parameters are informed by the dynamic response versus the quasi-static stage. The results also show that, for highly nonlinear structural models with interacting parameters, engineering judgment informed by the physical response remains essential when assessing surrogate-based Bayesian solutions. The calibrated model is validated against an independent seismic simulation. Finally, seismic input energy is decomposed into hysteretic, viscous damping, and strain-rate-dependent contributions. Rayleigh viscous damping and strain-rate-dependent dissipation contribute approximately 5.5% and 5.1%, respectively, corresponding to a combined equivalent viscous damping ratio of approximately 0.9%, compared with the ad hoc 2% conventionally adopted in nonlinear analysis to represent additional dissipation sources not explicitly modeled.

Table of Contents

Acknowledgments iii
Abstract xxx
Table of Contents vi
List of Symbols xiii
List of Acronyms xxi
List of Figures xxii
List of Tables xxviii
1 INTRODUCTION 1
1.1 Theoretical and Empirical Foundations of the Research Problem 2
1.1.1 Experimental Evidence and Modeling Limitations of Strain Rate Effects in Reinforcing Steel under Seismic Loading 2
1.1.2 Empirical Gap in Strain Rate Characterization: Underestimation in Conventional Seismic Analysis of Reinforcing Steel 3
1.1.3 Constitutive Modeling Gap: Rate-Dependent Cyclic Viscoplasticity of Reinforcing Steel 3
1.2 Problem Statement 4
1.2.1 Problem Definition 4
1.2.2 General Research Objective 5
1.2.2.1 Specific Research Objectives 5
1.2.3 Scope of the Research 6
1.2.3.1 Conceptual Scope 6
1.2.3.2 Experimental Scope 7
1.2.3.3 Modeling Scope 7
1.2.3.4 Validation Scope 7
1.2.3.5 Explicit Exclusions 7
1.3 Outline 8
2 REVIEW OF PREVIOUS RESEARCH WORK 9
2.1 Research Work on Monotonic Constitutive Models 10
2.1.1 Watstein (1953) 11
2.1.2 Cowper-Symonds (1957) 12
2.1.3 Johnson & Cook (1983) 13
2.1.4 Bertero, Mahin, and Herrera (1978) 14
2.1.5 Mander (1983) 14
2.1.6 Shing & Mahin (1988) 17
2.1.7 Eibl (1988) 18
2.1.8 CEB-FIP Model Code (1993) 19

2.1.9 Ross, Tedesco, and Hughes (1996) 20
2.1.10 Malvar & Crawford (1998) 21
2.1.11 Malvar (1998) 22
2.1.12 Filiatrault & Holleran (2001) 22
2.1.13 Schenker, Anteby, Gal, Kivity, Nizri, Sadot, & Ben-Dor (2008) 24
2.1.14 Dougherty, Cerreta, Gray, Trujillo, López, Vecchio & Kusinski (2009) 24
2.1.15 Asprone, Cadoni & Prota (2009) 25
2.1.16 Cadoni, Fenu & Forni (2012) 26
2.1.17 Ghannoum, Saouma, Haussmann, Polkinghorne, Eck & Kang (2012) 26
2.1.18 Levings, J., & Sritharan, S. (2012) 27
2.1.19 Zhang, Li & Shang (2012) 28
2.1.20 Cadoni & Forni (2015) 30
2.1.21 Cadoni, Dotta, Forni & Tesio (2015) 31
2.1.22 Lin, Dong, Kuang & Lu (2016) 31
2.1.23 Khonsari, England, Shabani & Shsavar (2017) 32
2.1.24 Cadoni, Fontana, Forni & Knobloch (2018) 33
2.1.25 Zeng, Huo, Wang, Wang & Elchalakani (2020) 34
2.1.26 Zeng, Wang & Huo (2020) 35
2.1.27 Cadoni & Forni (2021) 35
2.1.28 Zeng & Huo (2023) 36
2.2 Research Work on Cyclic Constitutive Models 36
2.2.1 Ramberg & Osgood (1943) 37
2.2.2 Kent & Park (1973) 38
2.2.3 Menegotto-Pinto (1973) 40
2.2.4 Mander (1983) 41
2.2.5 Monti & Nuti (1992) 42
2.2.6 Dodd & Restrepo (1995) 44
2.2.7 Balan, Filippou, & Popov (1998) 47
2.2.8 Li & Li (2012) 49
2.2.9 Kim & Koutromanos (2016) 50
2.2.10 Qiu & Gong (2019) 51
2.2.11 Massone, Rosa & Mesa (2023) 52
2.2.12 Tripathi & Dhakal (2023) 53
2.3 Research Work on Microscopic Bond-Slip Models 55
2.3.1 Ciampi, Eligehausen, Bertero, and Popov (1982) 55
2.3.2 Eligehausen, Ciampi, Bertero & Popov (1982) 56

2.3.3 Filippou, Popov & Bertero (1983) 57
2.3.4 Murcia-Delso (2013) 57
2.4 Research Work on Macroscopic Bond-Slip Models 59
2.4.1 Zhao and Sritharan (2007) 59
2.4.2 Rashid, James, and Dunham (2013) 61
2.5 Synthesis and Identified Gaps 63
3 Characterization of the Strain Rates in Steel Reinforcement 65
3.1 Influence of Loading Rate 67
3.2 Description of Specimens 67
3.2.1 7-Story Building Slice 68
3.2.2 Single-Column Bridge Bent 72
3.3 Reinforcing Bar Reversed Cyclic Stress-Strain Response 75
3.4 Evaluation of Bar Strain Rates Using First Principles 78
3.4.1 Average Strain Rates for the Wall-Building Specimen 83
3.4.2 Average Strain Rates for the Bridge Column Specimen 84
3.5 Instantaneous and Average Strain Rates 85
3.6 Strain Signals 88
3.7 Period Definitions 91
3.7.1 Initial Periods, To 91
3.7.2 Predominant Periods, Tp 91
3.7.3 Effective Periods, Te 95
3.8 Signal Processing Workflow 99
3.8.1 Signal Truncation 99
3.8.2 Signal Filtering 103
3.8.3 Signal realignment 106
3.8.4 Strain Rate Signals 111
3.9 Strain Rate Characterization 115
3.9.1 Ratio of peak to average strain rate: κ-ratio 120
3.9.1.1 Effect of Dynamic Dislocations in the Lüders Plateau: κL-ratio 120
3.9.1.2 Effect of "Higher" Modes of Response: κH-ratio 124
3.9.1.3 Ratio of peak to average strain rate: κ-ratio 133
3.9.1.4 Effect of Waveform: κW-ratio 139
3.10 Conclusions 140
4 Rate-Dependent Hysteretic Model for Reinforcing Steel with Bond-Slip-Induced Pinching 142
4.1 Testing Procedure 144
4.1.1 Reinforcing Steel Configuration 144

4.1.2 Mechanical Properties 145
4.1.3 Chemical Composition 148
4.1.4 Cyclic Strain Loading Protocols 149
4.2 Stress-Strain Cyclic Response 151
4.3 Experimental Evidence of Strain-Rate Sensitivity under Cyclic Loading 155
4.4 Time-window-based characterization of strain-rate effects 160
4.4.1 Tension Branch 160
4.4.2 Compression Branch 162
4.4.3 Undulation-Resolved Stress Increments vs. Strain-Rate Excursions 164
4.5 Implications for Constitutive Modeling 166
4.6 Baseline Rate-Independent Constitutive Model 166
4.6.1 Extent of the Unloading Branch 169
4.6.2 Strain-Hardening Branch 170
4.6.3 Closed-Form Bauschinger Curve 171
4.6.4 Implementation of Tangent, Secant, and Initial Moduli 176
4.6.5 SteelDRC Model Calibration and Verification 177
4.7 Strain-Rate-Dependent Extension of the SteelDRC Model 179
4.8 Quadrant-Dependent Bond-Slip Mechanism 186
4.8.1 Definition of the β-factor evolution interval 188
4.8.2 Evolution governed by λ 192
4.8.3 Truncated evolution due to reversal 195
4.8.4 Cyclic Stress-Strain Response with Pinching 196
4.8.5 Structural-level strain histories and material response 198
4.8.5.1 Parametric Study on λ and np 199
4.9 Conclusions 217
5 Two-Stage Calibration, Sensitivity Analysis, and Validation of the SteelDRCV Model 219
5.1 Numerical Modeling Framework 220
5.1.1 Boundary Conditions and Inertial Properties 220
5.1.2 Fixed-End Rotation and Flexural Plasticity 221
5.1.3 Structural Idealization and Element Formulation 222
5.1.4 Coordinate System Definition and Section Orientation 225
5.1.5 Numerical Solution Procedure 226
5.1.6 Geometric and Sectional Discretization 227
5.2 Material Constitutive Modeling 228
5.2.1 Longitudinal reinforcement 229
5.2.1.1 Unloading Modulus 230

5.2.2 Concrete Constitutive Modeling 232
5.2.2.1 Concrete in Column Element 233
5.2.2.1.1 Unconfined Concrete 233
5.2.2.1.2 Confined Concrete 234
5.2.2.2 Concrete in the Fixed-End Rotation Element 237
5.2.3 Tensile in Concrete 239
5.2.3.1 Regularization of the Tensile Response 240
5.3 Calibration and Validation Procedure 242
5.4 Experimental Data Used for Calibration 243
5.5 Two-Stage Constitutive Parameter Identification 247
5.6 Parameter Provenance and Explored Intervals 248
5.7 Stage 1 - Displacement-Controlled Cyclic Calibration 251
5.7.1 Objective Functions 251
5.7.2 First sub-stage: Concrete Tensile Parameters 252
5.7.3 Second Sub-stage: Reinforcing-Steel Parameters 253
5.7.4 Sensitivity of the Response to the Identified Parameters 258
5.7.5 Outcome of Stage 1 261
5.8 Stage 2 - Bayesian Dynamic Calibration 261
5.8.1 Bayesian Formulation of the Inverse Problem 264
5.8.2 Calibration Parameters and Physical Relations 265
5.8.3 Calibration Metrics 266
5.8.4 Design of Experiments and Simulation Campaign 267
5.8.5 Gaussian-Process Surrogate 267
5.8.6 Validation of the Surrogate 269
5.8.6.1 Peak-Displacement Metrics 269
5.8.6.2 Cumulative Hysteretic Energy Metrics 271
5.8.6.3 Overall Assessment of GP Surrogate Accuracy and Uncertainty 273
5.8.7 Global Sensitivity Analysis via Sobol Indices 275
5.8.7.1 Physical Interpretation of the Informative Parameters 280
5.8.7.2 Robustness of the Sensitivity Ranking to the Prior Distribution. 281
5.8.8 Likelihood and Error Model 283
5.8.9 Transitional Markov Chain Monte Carlo Sampler 284
5.8.9.1 TMCMC convergence diagnostics 285
5.8.9.1.1 Tempering Exponent 286
5.8.9.1.2 Metropolis Acceptance 286
5.8.9.1.3 Effective Sample Size 287

5.8.10 Posterior Results 290
5.8.10.1 Robustness of the Posterior Inference to the Prior Distribution 297
5.8.10.2 Choice of Prior Distribution 308
5.8.10.3 Per-Parameter Synthesis of Sensitivity and Posterior Information 309
5.8.11 Identifiability of the Strain-Rate-Dependent Mechanism 311
5.8.12 Model-Experiment Discrepancy 313
5.8.13 Verification and Validation 317
5.8.13.1 Close-the-Loop Verification 317
5.8.14 Held-Out Validation 319
5.8.15 Outcome 321
5.8.16 Model-side Limitation 322
5.8.16.1 Closing Statement 323
5.9 Model Validation against the Held-Out Seismic Simulation (EQ5) 323
5.9.1 Quantities Compared 323
5.9.2 Validation Results 324
5.10 Energy Decomposition Analysis 330
5.10.1 Rayleigh Damping 331
5.10.2 Strain-Rate Dissipation Energy 333
5.10.3 Energy Dissipation Mechanisms and the Role of Strain-Rate Effects 334
5.10.4 Post-Calibration Refinement of Confined Concrete Parameters 337
6 Conclusions And Recommendations 339
6.1 Conclusions 339
6.1.1 Strain-Rate Demands in Reinforcing Steel Under Seismic Loading 339
6.1.2 Development and Assessment of the SteelDRCV Constitutive Model 339
6.1.3 Two-Stage Calibration and Parameter Identifiability 340
6.1.4 Limitations and Domain of Applicability 341
6.1.5 Predictive Validation and Implications for Viscous Damping 341
6.1.6 Post-Calibration Refinement of Confined Concrete Parameters 342
6.2 Scientific and Engineering Contributions 343
6.3 Recommendations for Future Research 344
6.3.1 Additional Energy Dissipation Mechanisms 344
6.3.2 Improved Fixed-End Rotation Formulation 344
6.3.3 Three-Dimensional Solid Finite Element Modeling 344
6.3.4 Extension to a Broader Range of Reinforcement Grades 344
6.3.5 Integration of Inelastic Buckling and Low-Cycle Fatigue 345
6.3.6 Generalization Across RC Structural Typologies 345

6.3.7 Integration with performance-based seismic design. 345
7 References 346

List of Symbols

Latin Symbols

A, B:	First and second independent sample matrices (Nxp).
$A_B^{(i)}$:	Hybrid matrix (A with its i-th column replaced by the i-th column of B).
AR:	Column aspect ratio.
A_b:	Longitudinal reinforcement bar area.
A_g:	Gross cross-sectional area.
A_{sh}:	Area of transverse reinforcement.
a_0, a_1, a_2, a_3:	Polynomial coefficients (cubic).
a:	Absolute translational acceleration at the center of mass.
a_v:	Shear span.
$b_0(t^*)$:	Bernstein basis vector (cubic).
$b_1(t^*)$:	First derivative of the Bernstein basis vector.
c:	Neutral axis depth.
c:	Concrete cover measured to the side of the transverse reinforcement.
D:	Column diameter.
D_c:	Diameter of effectively confined concrete.
D_{cb}:	Diameter through the centroids of the longitudinal reinforcement bars.
D_{fu}:	Unloading-rejoining deformation parameter.
d_0:	Optimal lag corresponding to the maximum correlation coefficient.
d:	Time lag (in time steps).
$\hat{d}$:	Interpolated peak lag.
d^*:	Discrepancy vector.
d_{bl}:	Diameter of the longitudinal reinforcement bars.
d_{bt}:	Diameter of the transverse reinforcement bars.
d_i:	Perpendicular distance to the rotation axis.
$diag(f_p')$:	Diagonalization of control-point stress vector.
$df_s'/d\varepsilon_s'$:	Tangent modulus along the Bauschinger curve.
E_0:	Initial modulus.
E_1-E_4:	Logarithmic ratio of the cumulative hysteretic energy of simulations 1-4.
E_{cC}:	Initial tangent modulus for the confined concrete
E_{cU}:	Initial tangent modulus for the unconfined concrete.
E_{cUFER}:	Initial tangent modulus for the FER element.
E_E:	Cumulative hysteretic energy from the experimental response.
EI_e:	Effective flexural stiffness.
EI_g:	Gross flexural stiffness.
E_{ini}, E_{final}:	Initial and final moduli of elasticity.
E_L:	Logarithmic ratio of the cumulative hysteretic energy.
E_M:	Relative root-mean-square error of the inertial moment.
E_{Input}:	Cumulative input energy.
$E_{Rayleigh}$:	Cumulative Rayleigh viscous-damping energy dissipation.

$E_{Restoring}$: Cumulative hysteretic energy dissipation.
E_{rate}: Cumulative hysteretic energy dissipation attributable to the strain-rate-dependent amplification of the reinforcing-steel yield stress.
E_{Sec}: Secant modulus.
$E_{SteelDRC}$: Cumulative hysteretic energy obtained with the strain-rate-dependent amplification suppressed.
$E_{SteelDRCV}$: Cumulative hysteretic energy obtained using the complete SteelDRCV model.
E_T: Tangent modulus.
$E_{t,eff}$ Effective tangent stiffness.
E_s: Modulus of elasticity of steel.
E_{sim}: Simulated cumulative hysteretic energy.
E_{test}: Simulated cumulative hysteretic energy.
$\mathbb{E}_{\boldsymbol{\theta}_{\sim i}}$: Expectation over the complementary parameters.
E'_a, E'_b: Tangent modulus at the curve start and end points.
E'_s: Modulus of elasticity of steel in natural coordinates.
E'_u: Unloading modulus in natural coordinates.
e_s: Elasticity index.
$F(j\omega)$: Fourier transform.
$\mathcal{F}\{\varepsilon(t)\}$: Fourier transform operator, applied to $\varepsilon(t)$.
f: Surrogate function (GP predictive mean).
$f(A_k)$, $f(B_k)$: Surrogate evaluation at the k-th sample of A and B, respectively.
f_{cc}: Compressive stress.
f_{cu}: Unconfined compressive strength.
$f_{m,i}$: Measured stress at step i.
f_{o1}, f_{o2}: Initial first- and second-mode frequencies.
$f_{p,i}$: Predicted stress at step i.
f_{pl}: Idealized lateral confinement pressure.
f_{ple}: Effective lateral confinement pressure.
f_{plec}: Confinement index.
f_r: Reversal stress in engineering coordinates.
f_s: Engineering steel stress.
fs_{RI}: Rate-independent stress computed from the SteelDRC formulation.
f_{sd}: Viscous stress contribution associated with strain-rate effects.
$f_{sd,ref}$: Viscous overstress at the reference strain rate.
f_{shys}: Hysteretic (rate-independent) stress component.
f_{su}: Ultimate tensile strength.
f_t: Concrete tensile strength.
f_y: Yield strength of the longitudinal reinforcement.
f_{yh}: Yield strength of the transverse reinforcement.
f'_a, f'_b: True stresses at the curve start and end points.
f'_c: Concrete compressive strength.
f'_{cC}: Confined concrete compressive strength.
f'_{cCFER}: Confined concrete compressive strength for the FER element.
f'_{cUFER}: Unconfined concrete compressive strength for the FER element.

f'_{cu}: Peak unconfined concrete compressive strength.
f'_p: Control-point stress vector of the Bézier curve.
f'_r: Reversal stress in natural coordinates.
f'_s: True steel stress.
f'_t: Peak stress in true-stress coordinates.
f''_N: Normalized-transformed stress.
G_e: Effective shear modulus.
G_{ft}: Tensile fracture energy.
G_g: Gross shear modulus.
g: Gravitational acceleration.
g_{ft}: Fracture energy dissipated per unit volume.
H: Column height.
h: Vector of target experimental metrics.
h_{cr}: Elevation from the wall base to the first crack.
$h_{e,i}$: Modal effective height.
h_i: Story height.
h_r: Roof height.
I_e: Effective moment of inertia.
I_g: Gross-section moment of inertia.
I_r: Rotational inertia.
i, j: Imaginary units.
$j\omega$: Complex frequencies.
K: Shear coefficient by Cowper's formulation.
K_N: Training covariance matrix (N×N matrix between training points).
K_{sp}: Strain penetration coefficient.
k: Sample index (k-th row of the sample matrices).
k_*: Vector of covariances between x_* and the N training points,
k_{**}: Cross-covariance vector.
k_a: Anchorage-condition coefficient.
k_e: Geometric efficiency factor.
k_{rate}: Strain-rate sensitivity coefficient.
L_{ch}: Characteristic length associated with the fiber section.
L_p: Plastic-hinge integration-region length.
L_{pFER}: FER plastic-hinge characteristic length.
L_{pc}: Column plastic-hinge characteristic length.
L_{sp}: Reference length for fixed-end rotation.
l_{fs}: Flexure-shear plastic length.
l_i: Length scale of dimension i (one per input parameter, ARD).
l_p: Equivalent plastic hinge length= $l_{fs} + l_{sp}$.
l_{sp}: Bar strain penetration length.
l_w: Wall length.
M: Lateral bending moment at the column base.
M_{DR}: Rayleigh viscous damping bending moment.

M_E: Experimental moment from the measured response during the test.
M_N: Numerical moment obtained from the inertial response.
M_R: Restoring base moment.
M_{rate}: Strain-rate damping bending moment.
m_i: Discrete mass element.
m_t: Equivalent translational mass.
N: Number of samples/Number of training points.
N_{eff}: Effective sample size
n: Number of levels / Parameter governing the ascending branch slope in Tsai's equation.
n_p: Pinching-shape exponent.
n_{rate}: Strain-rate sensitivity coefficient.
P_0, P_1, P_2, P_3: Bézier control points.
P: Strain-hardening exponent.
P_u: Axial load.
p, q, r: Cardano's resolvent coefficients.
$p(d^*)$: Evidence or marginal likelihood.
peak$_{1\text{-}4}$: Logarithmic ratio of the peak displacement of simulations 1-4.
$p(\theta)$: Prior probability density.
$p(\theta)$: Posterior probability density.
$p(\theta|d^*)$: Likelihood function.
R_ξ: Damping correction factor.
r: Shape parameter governing the post-peak (in compression) or post-cracking (in tension) branch, in Tsai's equation.
$r(d)$: Cross-correlation coefficient at lag d.
r_{cC}: Post-peak shape parameter for the confined concrete.
r_{cCFER}: Post-peak shape parameter for the FER confined concrete.
r_{cU}: Post-peak shape parameter for the unconfined concrete.
r_{cUFER}: Post-peak shape parameter for the FER unconfined concrete.
$r_i(\theta)$: Vector of target experimental metrics.
r_t: Tensile post-cracking shape parameter.
r_{tCOL}: Tensile post-cracking shape parameter for the column element.
r_{tFER}: Tensile post-cracking shape parameter for the FER element.
r_x: Scaled distance (weighted Euclidean distance between two input points).
$\hat{S}_{T,i}$: Estimated total-order index (Jansen estimator).
$S_{T,i}$: Total-order sensitivity index (including all interactions).
$S_{T,i}^{max}$: Maximum total-order Sobol index.
S_i: First-order sensitivity index (due to parameter i alone).
$\hat{S}_i$: Estimated first-order index (Saltelli estimator).
s: Center-to-center spacing of the transverse reinforcement.
s_p: Clear spacing between transverse reinforcement legs.
T_e: Effective period.
$T_{e,max}$: The greatest effective period observed in a test.
T_{o1}, T_{o2}: Initial first- and second-mode periods.

T_p: Predominant period.
T_{p1}, T_{p2}: First- and second-mode predominant periods.
t: Time.
t^*: Parametric variable of the Bézier curve.
t_i, t_j: Forward and reversal semi-cycle time.
t_{min}, t_{max}: Lower and upper Arias-intensity bounds.
V: Total output variance (unconditional variance of the response).
$\hat{V}$: Estimated total output variance.
V_{DR}: Rayleigh viscous damping shear force.
V_i: First-order partial variance (contribution from parameter i alone).
V_{ij}: Second-order interaction variance (contribution from the interaction between parameters i and j).
V_{rate}: Strain-rate damping shear force.
W: Weight of the loading block.
W_i: Seismic weight at each floor level.
W_t: Weight of the loading block.
w_0, w_1, w_2, w_3: Weights of Bézier control points.
$w^{(k)}$: Importance weight associated with particle k.
w_p: Weight vector of the Bézier control points.
X: Training input matrix (N input points).
x: Vector of SteelDRC material parameters.
x_*: New input point for GP prediction.
x_{crnC}: Non-dimensional critical strain on the compression envelope for the confined concrete.
$x_{crnCFER}$: Non-dimensional critical strain on the compression envelope for the FER confined concrete.
x_{crnU}: Non-dimensional critical strain on the compression envelope for the unconfined concrete.
$x_{crnUFER}$: Non-dimensional critical strain on the compression envelope for the FER unconfined concrete.
x_{crpt}: Non-dimensional critical strain on the tension envelope.
x_i, x_i': Coordinates of two input points in dimension i.
x_{lo}, x_{hi}: Lower and upper bounds of the admissible parameter interval.
Y: Scalar model output (response of the GP surrogate).
y: Training response vector (N observed responses).

Greek Symbols

$\alpha(AR)$: Aspect-ratio coefficient.
α_M: Mass-proportional Rayleigh damping coefficient.
α_R: Rotational acceleration.
α_u: Unloading-modulus scaling parameter.
β_{K_0}: Initial-stiffness-proportional Rayleigh damping coefficient.
β_j: Tempering level at stage j.

$\beta(\xi)$: Bond-slip curvature factor (β-factor).
Γ_1^*: First-mode contribution factor.
Δ: Cardano's discriminant.
Δf_s: Stress increase.
Δt: Sampling increment.
$\Delta\dot{\varepsilon}$: Strain rate increase.
δ: Lateral displacement measured at the center of mass of the loading block.
δ_e: Elastic displacement.
$\delta_{e,F}$: Flexure contribution to the elastic displacement.
$\delta_{e,FV}$: Flexure-shear contribution to the elastic displacement.
$\delta_{e,sp}$: Fixed-end rotation contribution to the elastic displacement.
δ_p: Plastic displacement.
$\delta_{p,FV}$: Flexure-shear contribution to the plastic displacement.
$\delta_{p,sp}$: Strain penetration.
$\delta_{peak,sim}$: Simulated peak displacement.
$\delta_{peak,test}$: Experimental peak displacement.
δ_{ri}, δ_{rj}: Maximum roof displacements at times t_i and t_j, respectively.
ε_0: Strain amplitude.
ε: Axial strain in the reinforcing steel.
ε_{cc}: Compressive strain.
ε_{ct}: Tensile cracking strain.
ε_{cu}: Unconfined compressive strain.
ε_d: Characteristic strain length of the β-factor interval.
ε_r: Reversal strain in engineering coordinates.
ε_s: Engineering strain.
$\varepsilon_{s,end}$: Effective terminal strain.
ε_{s0}, ε_{s1}: Initial and terminal strain of the β-factor evolution interval.
ε_{sh}: Strain at the onset of strain hardening.
ε_{si}: Strain in the bar "a" at time t_i.
ε_{sj}: Strain in the bar "a" at time t_j.
ε_{su}: Uniform strain.
ε_{tU}: Concrete tensile strain.
ε_u: Strain at ultimate tensile strength.
ε_y: Yield strain.
ε'_0: Plastic strain in natural coordinates.
ε'_a, ε'_b: Natural strains at the curve start and end points.
ε'_{cC}: Strain at the peak confined concrete stress.
ε'_{cCFER}: Strain at the peak FER confined concrete stress.
ε'_{cUFER}: Strain at the peak FER unconfined concrete stress.
ε'_{cu}: Unconfined concrete strain at peak unconfined concrete compressive strength.
ε'_p: Control-point strain vector.
ε'_r: Reversal strain in natural coordinates.
ε'_s: Steel strain in natural coordinates.

ε'_{su}: Strain at ultimate tensile strength in natural coordinates.
ε''_N: Normalized-transformed strain.
$\dot{\varepsilon}$: Steel strain rate.
$\dot{\varepsilon}_{ref}$: Reference strain rate.
$\bar{\dot{\varepsilon}}_{sij}$: Average strain rate.
$\bar{\dot{\varepsilon}}_{sij,max}$: Peak strain rate.
ζ_1: First-mode Rayleigh damping ratio.
ζ_2: Second-mode Rayleigh damping ratio.
η: Unloading-length parameter.
η: Effective-to-initial period ratio.
θ: Vector of model parameters to be identified.
θ_i: i-th input parameter under consideration.
θ^k: Parameter vector associated with particle k.
$\theta_{\sim i}$: Complementary parameter vector (all input parameters except θ_i).
κ: Peak-to-average strain-rate ratio.
κ_H: Higher-mode strain-rate ratio.
κ_L: Dynamic dislocation strain-rate ratio.
κ_W: Waveform amplification strain-rate ratio.
λ: Cross-section coefficient.
λ: Pinching amplitude parameter.
μ: Displacement ductility factor.
μ_ϕ: Curvature ductility factor.
ν: The coefficient that accounts for the location of the centroid of the elastic curvature diagram, $\nu \approx \left({}^{4}/_{3} + n\right)/(3 + 4n)$.
ν: Poisson's ratio.
ξ_1: Maximum longitudinal bar distance to extreme compressive fiber-to-wall length ratio.
ξ: Effective damping.
ξ: Normalized strain variable for β-factor evolution.
ξ_a, ξ_b: Intermediate control-point location parameter at the curve start and end.
ξ_{eq}: Equivalent viscous damping ratio.
ρ_s: Volumetric confinement ratio.
σ Baseline stress.
σ_{eff} Effective stress.
σ_*^2: Predictive variance of the GP emulator.
$\sigma_{err,f(i)}^2$: Error variance assigned to metric family i.
σ_f^2: Marginal variance of the GP prior.
σ_n^2: Noise variance (residual variability not captured by the latent function).
σ_{unload}: Unloading stress.
τ: Temporal shift.
$\phi_{1,i}$: First mode of vibration.
ϕ_e: Elastic curvature at time j.
ϕ_p: Plastic curvature at time j.

ϕ_t: Total curvature at the wall base.

ψ_e, ψ_p: Second-moment area coefficient for the elastic and for the plastic portions of the curvature diagram.

Ω: Partial area under the normalized Bauschinger curve.

Ω_{fac}: Bauschinger-effect shape factor.

Ω_{ws}: Overstrength factor.

ω: Angular frequency.

List of Acronyms

ACI:	American Concrete Institute
AM:	All modes
ARD:	Automatic Relevance Determination
ASTM:	American Society for Testing and Materials
DDBA:	Direct Displacement-Based Assessment
DIC:	Digital Image Correlation
DIF:	Dynamic Increase Factor
DR:	Dodd-Restrepo constitutive model
DRC:	Dodd-Restrepo-Carreño constitutive model
DRCV:	Dodd-Restrepo-Carreño-Velásquez constitutive model
FER:	Fixed-End Rotation
FFT:	Fast Fourier Transform
GP:	Gaussian Process
LHPOST:	Large High-Performance Outdoor Shake Table
LM:	Lower modes
MAP:	Maximum A Posteriori
NEES:	Network for Earthquake Engineering Simulation
NURBS:	Nonuniform rational B-splines
PBEE:	Performance-Based Earthquake Engineering
PDF/CDF:	Probability/Cumulative Distribution Function
PGA:	Peak Ground Acceleration
PGV:	Peak ground velocity
RC:	Reinforced concrete
RMSE:	Root Mean Square Error
RRMSE:	Relative root-mean-square error
SDOF:	Single-degree-of-freedom
TCL:	Tool Command Language
TMCMC:	Transitional Markov Chain Monte Carlo

List of Figures

Figure 1. Monotonic stress-strain curve for reinforcing steel [82]. 16
Figure 2. Assumed effect of strain rate on monotonic loading. 16
Figure 3. Reversals in the reinforcing bar cyclic response. 42
Figure 4. Normalization of the Bauschinger Effect. 45
Figure 5. The geometric idealization of the longitudinal reinforcing steel bar 53
Figure 6. Rebar yield strength factor and pinched hysteresis loop [112]. 62
Figure 7. Southwest view of the 7-story wall-building test specimen (photo by Dr. José Restrepo). 69
Figure 8. Longitudinal and transverse reinforcement layout for the wall-building test specimen. 70
Figure 9. Pseudo-acceleration response spectra (5% damping) of input ground motions for the wall-building specimen. 71
Figure 10. View of the south face of the first floor of the wall-building specimen at maximum displacement during test EQ4 (video-sourced images by J. Restrepo). 72
Figure 11. Southwest view of the bridge column specimen (photo by Dr. José Restrepo). 73
Figure 12. Longitudinal and transverse reinforcement layout for the bridge column specimen. 74
Figure 13. Pseudo-acceleration response spectra (5% damping) of input ground motions for the bridge column specimen. 74
Figure 14. Stress-strain response in a reinforcing bar. 76
Figure 15. Schematic representation of a laterally deformed structural wall responding to earthquake input. 79
Figure 16. Idealized strain profile at the wall elevation at times ti and tj. 80
Figure 17. Harmonic strain-time history. 87
Figure 18. Strain-time signals - Wall-building specimen. 89
Figure 19. Strain-time signals - Bridge column specimen. 90
Figure 20. Variation of the First and Second Mode Periods with Shaking Intensity - Wall-building specimen. 93
Figure 21. Variation of the First and the Second Mode Periods with Shaking Intensity - Bridge column specimen. 93
Figure 22. Period ratio $Tp1To1$ versus PGV for the test specimens. 95
Figure 23. Variable effective periods from the strain gauge A2_5 97
Figure 24. Variable effective periods from the strain gauge WS8 98
Figure 25. Cumulative Arias Intensity for the wall-building specimen. 101
Figure 26. Cumulative Arias Intensity for the bridge column specimen. 102
Figure 27. Pseudo-transfer functions for the wall-building specimen (3 Hz cutoff). 104
Figure 28. Pseudo-transfer functions for the bridge-column specimen (2 Hz cutoff). 105
Figure 29. Sequential filtering stages for the strain gauge A4_3 subjected to EQ4 105
Figure 30. Sequential filtering stages for the strain gauge WS05 subjected to EQ6 106
Figure 31. AM and LM strain signals for the wall-building strain gauge A2-5 under EQ4. 109
Figure 32. AM and LM strain signals for the bridge column strain gauge WS under EQ5. 110
Figure 33. Strain and strain-rate time histories for the wall-building strain gauge A3-4 from EQ4. 113
Figure 34. Strain and strain-rate time histories for the bridge column strain gauge EN5 from EQ3. 114
Figure 35. Peak strain rate versus effective-to-initial first mode period ratio in strain-gauged bars in the plastic hinge region of the wall-building specimen. 117
Figure 36. Peak strain rate versus effective-to-initial first mode period ratio in strain-gauged bars in the plastic hinge region of the bridge column specimen. 117
Figure 37. Evolution of Dislocation Dynamics During Lüders Band Propagation. Modified from [27]. 121

Figure 38. Histogram of strain rate distribution in the Lüders plateau for wall-building and bridge column specimens. 123
Figure 39. κH-ratio variation versus effective-to-initial first mode period for the wall-building specimen. 125
Figure 40. κH-ratio variation versus effective-to-initial first mode period for the wall-building specimen. 126
Figure 41. STFT Spectrograms for the strain gauge A1_4 under EQ4 127
Figure 42. STFT Spectrograms for the strain gauge EN07 under EQ3 128
Figure 43. κH-ratio PDF and CDF for wall-building specimen. 130
Figure 44. κH-ratio PDF and CDF for the bridge column specimen. 131
Figure 45. Cumulative frequency of the κH-ratio for both specimens. 132
Figure 46. κ-ratio variation versus effective-to-initial first mode period ratio for the wall-building specimen. 134
Figure 47. κH-ratio variation versus effective-to-initial first mode period for the bridge column specimen. 134
Figure 48. κ-ratio PDF and CDF for wall-building specimen. 136
Figure 49. κ-ratio PDF and CDF for bridge column specimen. 137
Figure 50. Cumulative frequency of the strain rate κ-ratio for both specimens. 138
Figure 51. Geometry and dimensional configuration of reinforcing steel test coupons [30]. 144
Figure 52. Application of strain gauges to machined coupons [30]. 145
Figure 53. Cyclic loading histories at a strain rate of 0.001 s^{-1}. 150
Figure 54. Cyclic loading histories at a strain rate of 0.02 s^{-1}. 151
Figure 55. Cyclic stress-strain response of machined coupons from Mill A. 152
Figure 56. Cyclic stress-strain response of machined coupons from Mill B. 153
Figure 57. Cyclic stress-strain response of machined coupons from Mill C. 154
Figure 58. Strain-rate sensitivity of reinforcing bars under cyclic loading. 156
Figure 59. Evolution of actuator-induced undulation families during cyclic plastic deformation of reinforcing steel. 157
Figure 60. Extensometer-resolved undulation activity during a tensile branch of cyclic plastic deformation. 158
Figure 61. Tension-dominated actuator-induced rate excursions. 161
Figure 62. Compression-dominated actuator-induced rate excursions. 163
Figure 63. Rate-dependent stress increments extracted from undulation-resolved strain-rate excursions - A615 reinforcing steel. 164
Figure 64. Rate-dependent stress increments extracted from undulation-resolved strain-rate excursions - A706 reinforcing steel. 165
Figure 65. Stress-strain response in engineering and natural coordinates [43]. 167
Figure 66. Backbone curve of the Dodd-Restrepo Model - Monotonic behavior [43]. 168
Figure 67. Length of linear unloading branch [29]. 169
Figure 68. Sensitivity of strain-hardening response to curvature parameter *P* 170
Figure 69. Bauschinger effect representation using Bézier curves [29]. 173
Figure 70. Shape of the Bauschinger effect [43]. 175
Figure 71. Regression Analysis of Bézier Curve [29]. 175
Figure 72. Sample Bauschinger curves [29]. 176
Figure 73. Different options of material modulus [29]. 177
Figure 74. Comparison between the SteelDRC and Menegotto-Pinto (Steel02) constitutive models in OpenSees [29]. 178

Figure 75. Decomposition of rate-dependent stress response: (a) equilibrium hysteretic component; (b) transient viscous overstress; and (c) superposition of mechanisms. 181
Figure 76. Experimental and SteelDRC-predicted cyclic stress-strain response with and without strain-rate dependence - A79. 185
Figure 77. Experimental and SteelDRC-predicted cyclic stress-strain response with and without strain-rate dependence - B78. 185
Figure 78. Steel-concrete interface kinematics - Crack closure. 187
Figure 79. Steel-concrete interface kinematics - Crack opening. 188
Figure 80. Function $\beta\xi$ for different values of the exponent np. 189
Figure 81. Effect of the function $\beta\xi$ on hysteretic response. 192
Figure 82. Influence of the parameter λ on the extent of the pinching zone. 194
Figure 83. Effect of load reversal on the truncation of the β-factor evolution. 195
Figure 84. Comparison of cyclic stress-strain response with and without pinching - A68. 196
Figure 85. Comparison of cyclic stress-strain response with and without pinching - B69. 197
Figure 86. Comparison of cyclic stress-strain response with and without pinching - C79. 197
Figure 87. Comparison of simulated and measured stress-strain response of instrumented reinforcing bars - Wall-building. 198
Figure 88. Comparison of simulated and measured stress-strain response of instrumented reinforcing bar - Bridge column. 199
Figure 89. Cyclic stress-strain hysteretic response for λ=0.5 and varying np values from 0.5 to 4 - EQ5-EN5. 201
Figure 90. Cyclic stress-strain hysteretic response for λ=1 and varying np values from 0.5 to 4 - EQ5-EN5. 202
Figure 91. Cyclic stress-strain hysteretic response for λ=1.5 and varying np values from 0.5 to 4 - EQ5-EN5. 203
Figure 92. Cyclic stress-strain hysteretic response for λ=2 and varying np values from 0.5 to 4 - EQ5-EN5. 204
Figure 93. Cyclic stress-strain hysteretic response for λ=2.5 and varying np values from 0.5 to 4 - EQ5-EN5. 205
Figure 94. Cyclic stress-strain hysteretic response for λ=3 and varying np values from 0.5 to 4 - EQ5-EN5. 206
Figure 95. Cyclic stress-strain hysteretic response for λ=3.5 and varying np values from 0.5 to 4 - EQ5-EN5. 207
Figure 96. Cyclic stress-strain hysteretic response for λ=4 and varying np values from 0.5 to 4 - EQ5-EN5. 208
Figure 97. Cyclic stress-strain hysteretic response for λ=0.5 and varying np values from 0.5 to 4 - B79. 209
Figure 98. Cyclic stress-strain hysteretic response for λ=1 and varying np values from 0.5 to 4 - B79. 210
Figure 99. Cyclic stress-strain hysteretic response for λ=1.5 and varying np values from 0.5 to 4 - B79. 211
Figure 100. Cyclic stress-strain hysteretic response for λ=2 and varying np values from 0.5 to 4 - B79. 212
Figure 101. Cyclic stress-strain hysteretic response for λ=2.5 and varying np values from 0.5 to 4 - B79. 213
Figure 102. Cyclic stress-strain hysteretic response for λ=3 and varying np values from 0.5 to 4 - B79. 214
Figure 103. Cyclic stress-strain hysteretic response for λ=3.5 and varying np values from 0.5 to 4 - B79. 215

Figure 104. Cyclic stress-strain hysteretic response for λ=4 and varying np values from 0.5 to 4 - B79. 216
Figure 105. Bar-slip measurements during Test EQ2 [124]. 222
Figure 106. Structural idealization of the bridge column. 224
Figure 107. Coordinate system. 226
Figure 108. Circular fiber-section discretization for the column element. 228
Figure 109. Circular fiber-section discretization for the FER element. 228
Figure 110. SteelDRCV Monotonic tensile envelope adopted for the reinforcing steel. 229
Figure 111. Normalized unloading modulus as a function of maximum absolute plastic strain for selected values of αu. 231
Figure 112. Influence of αu on the unloading branch. 232
Figure 113. Monotonic compressive envelope adopted in the ConcreteCM for the unconfined cover concrete. 233
Figure 114. Monotonic compressive envelope adopted in the ConcreteCM for the confined cover concrete. 237
Figure 115. Monotonic compressive envelope adopted in the ConcreteCM for the FER element. 238
Figure 116. Influence of the tensile shape parameter rt on the post-cracking tensile response of the ConcreteCM model. 240
Figure 117. Lateral displacement histories of the four seismic simulations concatenated into the continuous loading protocol used for constitutive-parameter calibration. 244
Figure 118. Experimental hysteretic responses vs. drift ratio for the tests. 246
Figure 119. Numerical and experimental normalized moment-drift responses for EQ1. 253
Figure 120. Simulated and measured normalized moment-drift response over the complete loading EQ1-EQ4. 254
Figure 121. Cumulative hysteretic energy per seismic simulation. 256
Figure 122. Normalized moment-drift response per seismic simulation. 257
Figure 123. Distribution of the (a) moment error and (b) energy error over the plane of the pinching parameters λ and np. 259
Figure 124. Dependence of the normalized base-moment error on λ, np, ft and rt. 260
Figure 125. The twelve-step Bayesian calibration pipeline. 263
Figure 126. Ten-fold cross-validation of the peak-displacement GP surrogates. 270
Figure 127. Ten-fold cross-validation of the cumulative hysteretic-energy GP surrogates. 272
Figure 128. Minimum ARD length-scale of the twelve input parameters across the eight GP surrogates. 274
Figure 129. Total-order Sobol index $ST, imax$ for the twelve independently sampled parameters. 279
Figure 130. TMCMC convergence diagnostics during the Bayesian calibration. 289
Figure 131a. Marginal posterior distributions under the uniform prior - Displacement-controlled stage parameters 294
Figure 132. Corner plot of the posterior parameter distribution under the uniform prior. 296
Figure 133a. Marginal posterior distributions under the lognormal prior - Displacement-controlled stage parameters. 299
Figure 134. Corner plot of the posterior parameter distribution under the lognormal prior. 301
Figure 135a. Marginal posterior distributions under the truncated normal prior - Displacement-controlled stage parameters. 305
Figure 136. Corner plot of the posterior parameter distribution under the truncated normal prior. 307
Figure 137. Posterior distribution of the strain-rate sensitivity exponent. 312
Figure 138. Joint posterior distribution of the viscous rate parameters $krate$ and $nrate$, with iso-overstress contours at the reference strain rate. 313

Figure 139. Posterior predictive distributions of the peak-displacement metrics. 315
Figure 140. Posterior predictive distributions of the energy metrics. 316
Figure 141a. Close-the-loop verification of the GP surrogate vs. the true OpenSees simulator for the peak displacements 318
Figure 142. Held-out validation metrics. 320
Figure 143. EQ1 displacement time history. 325
Figure 144. EQ1 normalized moment-drift hysteresis. 325
Figure 145. EQ2 displacement time history. 326
Figure 146. EQ2 normalized moment-drift hysteresis. 326
Figure 147. EQ3 displacement time history. 327
Figure 148. EQ3 normalized moment-drift hysteresis. 327
Figure 149. EQ4 displacement time history. 328
Figure 150. EQ4 normalized moment-drift hysteresis. 328
Figure 151. EQ5 displacement time history. 329
Figure 152. EQ5 normalized moment-drift hysteresis. 329
Figure 153. Energy decomposition flowchart. 331
Figure 154. Cumulative normalized dissipated energy by mechanism for the five shake-table events. 336
Figure 155. Effect of confined concrete post-peak parameters on moment-drift hysteresis for EQ3 and EQ5. 338

List of Tables

Table 1. Seismic Weights (*) and Corresponding Heights. 83
Table 2. Average strain rates at the maximum theoretical displacement - Wall-building specimen. 84
Table 3. Average strain rates at the maximum theoretical displacement - Cridge column test. 85
Table 4. Initial periods for the first two translational modes 91
Table 5. Predominant periods for the first two translational modes 92
Table 6. Predominant periods for the first two translational modes 92
Table 7. Maximum effective periods for both tests. 96
Table 8. Arias intensity bounds for the wall-building specimen. 100
Table 9. Arias intensity bounds for the bridge column specimen. 100
Table 10. Second initial mode periods and frequencies. 103
Table 11. Peak Strain Rates for both specimens. 118
Table 12. Comparison of experimental peak strain rates to the average by DDBA 119
Table 13. Comparison of experimental peak strain rates to the average by DDBA 119
Table 14. Peak strain rates in the Lüders plateau region. 122
Table 15. κH-ratio statistics in the work-hardening regime. 132
Table 16. κ-ratio statistics in the work-hardening and Lüders regimes. 135
Table 17. Baseline mechanical properties of unmachined reinforcing bar segments for pre-machining verification (ASTM A615/A706 compliance) [30]. 145
Table 18. In-house test results for unmachined coupons [30]. 147
Table 19. In-house test results for machined coupons [30]. 147
Table 20. Chemical composition of the coupons [30]. 148
Table 21. Coupon identification [30]. 151
Table 22. SteelDRCV monotonic tensile constitutive parameters determined from the experimental results. 230
Table 23. ConcreteCM compressive constitutive parameters adopted for the unconfined cover concrete. 234
Table 24. ConcreteCM compressive constitutive parameters adopted for confined-core concrete. 236
Table 25. ConcreteCM compressive constitutive parameters adopted for the FER element. 238
Table 26. The fifteen calibration parameters: physical role and identification stage. 247
Table 27. Initial parameter intervals adopted for the parameter exploration. 248
Table 28. Reinforcing-steel cyclic parameters identified in the second sub-stage. 253
Table 29. Normalized base-moment error per seismic simulation. 254
Table 30. Calibration parameters and prior bounds. 265
Table 31. Summary of GP surrogate accuracy and uncertainty calibration. 273
Table 32. Total-order Sobol sensitivity indices for the eight GP surrogates, with bootstrap-based 95% confidence intervals. 278
Table 33. Maximum total-order Sobol index across eight metrics: uniform vs. lognormal prior. 283
Table 34. Posterior parameter estimates and uncertainty - Uniform prior. 291
Table 35. GP-predicted residuals at the MAP estimate - Uniform prior. 292
Table 36. Posterior parameter estimates and uncertainty - Lognormal prior. 297
Table 37. GP-predicted residuals at the MAP estimate - Lognormal prior. 298
Table 38. Posterior parameter estimates and uncertainty - Truncated normal prior. 302
Table 39. GP-predicted residuals at the MAP estimate - Truncated-normal prior. 303
Table 40. Per-parameter synthesis of GP sensitivity, posterior contraction, and identification status. 310

Table 41. Closed-loop verification of the Gaussian-Process surrogate: RMSE, bias, and 2σ predictive coverage for the eight calibration metrics. 317
Table 42. Metrics across EQ1-EQ5 earthquakes 321
Table 43. Evolution of model parameters from initial values to posterior estimates. 322
Table 44. Viscous damping energy contribution for the earthquake sequence. 332
Table 45. Strain-rate energy contribution for the earthquake sequence. 334
Table 46. Viscous damping and strain-rate dissipation ratios. 335

1 INTRODUCTION

The seismic response of reinforced concrete (RC) structures under strong ground motion is governed by highly localized inelastic mechanisms that concentrate in plastic hinge regions. Within these regions, the global response emerges from the interaction between concrete and reinforcing steel; however, reinforcing steel plays a dominant role in controlling strength degradation, cyclic stability, and energy dissipation capacity. This study focuses on the constitutive behavior of reinforcing bars, considering the contribution of concrete only through its interaction effects implicit in the structural response. Despite its central role, the constitutive behavior of reinforcing steel, although extensively characterized under cyclic loading, remains inadequately represented in current modeling approaches when coupled with transient high strain rates and load reversals.

During earthquake excitation, longitudinal reinforcement in plastic hinge zones experiences non-uniform and time-dependent strain fields, with strain rates that may exceed those typically observed under quasi-static laboratory conditions by one to two orders of magnitude. These strain rates are not merely secondary descriptors; they are internal variables that alter the stress-strain response, including yield-strength amplification, changes in strain-hardening characteristics, and shifts in cyclic degradation patterns. Accurately representing strain-rate effects is essential for predictive nonlinear dynamic analysis.

Experimental studies have shown that increasing strain rate increases the yield stress and ultimate tensile strength of reinforcing steel, primarily because dislocation motion is strain-rate sensitive. In contrast, ductility evolution and cyclic hysteretic response are governed by the interaction between rate effects, loading reversals, and microstructural mechanisms such as dislocation accumulation and strain localization, resulting in behavior that simple monotonic scaling laws cannot describe.

A gap persists between observed material behavior and its numerical representation in structural analysis. Current approaches fail to capture the interaction between strain rate effects and cyclic plasticity at the material level. The problem is exacerbated in regions of strain localization, as conventional continuum formulations do not adequately represent the underlying deformation mechanisms.

The present research addresses this gap through an integrated experimental-analytical framework. First, strain rate histories are extracted from two full-scale structural tests conducted on the Large High-Performance Outdoor Shake Table (LHPOST) at the University of California, San Diego. These data provide direct insight into the magnitude, distribution, and temporal evolution of strain rates in reinforcing bars under realistic seismic loading. Second, a cyclic constitutive model for reinforcing steel is developed by extending the SteelDRC (Dodd-Restrepo-Carreño) formulation to explicitly incorporate nonlinear viscous overstress terms, enabling the representation of rate-dependent plasticity under load reversals, with the rate-dependent formulation focused on the strain-hardening regime where continuum viscoplastic modeling is applicable.

Two fundamentally different rate-dependent mechanisms govern the response of reinforcing steel at different spatial and physical scales. Within the Lüders plateau, plastic deformation localizes into inclined bands that propagate along the bar through dislocation unlocking processes associated

with interstitial solute atoms. The propagation of these bands depends on microstructural and geometric factors, including grain size, bar diameter, and measurement gauge length, resulting in inherently heterogeneous strain fields. Under these conditions, locally recorded strain rates represent macroscopic manifestations of underlying dislocation dynamics, whereas conventional continuum plasticity formulations lack the internal structure to resolve these mechanisms explicitly.

In contrast, the strain-hardening regime responds more readily to continuum viscoplastic modeling. At elevated strain rates, experimental evidence indicates the emergence of stress undulation on the hardening branches, attributed to the hydraulic actuator reaching its flow-rate capacity. Unlike Lüders bands, however, these instabilities do not dominate the global deformation field; the macroscopic stress-strain response retains a well-defined envelope that can be represented through rate-dependent overstress formulations. This distinction supports the working hypothesis that rate effects in the strain-hardening regime can be incorporated within a continuum framework using nonlinear viscous overstress models. In contrast, the Lüders plateau requires a separate phenomenological treatment beyond the predictive scope of standard constitutive formulations.

1.1 Theoretical and Empirical Foundations of the Research Problem

1.1.1 Experimental Evidence and Modeling Limitations of Strain Rate Effects in Reinforcing Steel under Seismic Loading

Experimental evidence has consistently demonstrated that the mechanical response of reinforcing steel is sensitive to strain rate over a wide range of loading conditions. Monotonic tensile tests conducted at strain rates spanning several orders of magnitude (10^{-6} s^{-1} to 10^{2} s^{-1}) have shown systematic increases in yield stress, typically on the order of 10-30% for strain rates relevant to seismic loading. These observations have led to dynamic increase factors, commonly expressed as functions of the logarithm of strain rate, and incorporated into empirical relations such as Cowper-Symonds or Johnson-Cook models.

However, directly transferring these results to the seismic response of RC structures is fundamentally limited. Monotonic tests do not capture key cyclic phenomena, including the Bauschinger effect, stiffness degradation, and strength deterioration under load reversals, which govern the hysteretic behavior of reinforcing steel in plastic hinge regions. The geometry and boundary conditions of laboratory specimens (typically straight, unconfined coupons) differ significantly from those of reinforcing bars embedded in concrete, where confinement, bond interaction, and multiaxial stress states influence the material response.

Experimental investigations that explicitly address rate effects under cyclic loading remain comparatively limited. Early studies showed that increasing loading rates modify the shape of hysteretic loops, affecting both energy dissipation per cycle and reversal yield stress. More recent work has explored the combined influence of strain rate and axial demand at the structural level, indicating that rate dependence becomes increasingly significant in elements subjected to high ductility demands. These findings highlight a persistent gap between characterizing rate effects under controlled laboratory conditions and representing them in constitutive models for seismic analysis.

1.1.2 Empirical Gap in Strain Rate Characterization: Underestimation in Conventional Seismic Analysis of Reinforcing Steel

Despite the extensive experimental literature on RC structural systems subjected to seismic excitation, this work is the first to directly characterize strain-rate histories in longitudinal reinforcement at the material level. Most existing studies rely on indirect inference from global response quantities, such as displacement or curvature, from isolated component testing under controlled loading conditions, or on numerical simulations without direct bar-level validation. In contrast, this work directly measures strain-rate histories in reinforcing bars within plastic hinge regions of full-scale specimens subjected to strong ground motions, providing an experimental basis for their characterization under realistic seismic conditions.

Peak strain rates under seismic loading can significantly exceed those predicted by simplified analytical procedures. Test observations from this study indicate that strain rates can reach values on the order of 44%/s during the nucleation and propagation of Lüders bands across instrumented regions, and remain close to 20%/s once these bands are fully developed. These values exceed estimates by a factor of 2 to 3 from displacement-based assessment procedures, showing that conventional approaches systematically underestimate the strain-rate demands on reinforcing steel.

Several mechanisms contribute to this discrepancy. Microstructural processes associated with Lüders band propagation introduce localized deformation dynamics that standard continuum models cannot resolve. Higher-mode effects amplify local strain demands beyond those predicted by single-degree-of-freedom idealizations. The non-harmonic nature of seismic excitation produces peak-to-average amplification of strain rates. These effects are therefore treated separately in the interpretation of the measured strain-rate histories. At the same time, the constitutive formulation focuses on the continuum rate dependence observed in the strain-hardening regime. The combined effect of these contributions can be expressed as a multiplicative amplification factor, denoted as -ratio, which averages about 1.85 in the strain-hardening regime.

Most computational models currently used for seismic assessment neglect the strain-rate dependency of reinforcing steel in their constitutive formulations. Rate-dependent material behavior is therefore not explicitly represented, while additional energy dissipation is commonly introduced through empirically prescribed viscous damping. This omission raises a modeling question that is not only constitutive but also energetic: the relative contributions of material rate dependence and viscous damping to total seismic energy dissipation should be quantified rather than assumed. Explicitly incorporating strain-rate-dependent stress-strain relationships provides a physically grounded framework for evaluating this contribution within nonlinear dynamic analysis.

1.1.3 Constitutive Modeling Gap: Rate-Dependent Cyclic Viscoplasticity of Reinforcing Steel

Constitutive models for reinforcing steel used in the seismic analysis of RC structures have evolved from simple bilinear representations to advanced formulations that capture kinematic hardening, the Bauschinger effect, cyclic degradation, and the coupling between plasticity and damage. Among these, the SteelDRC model, implemented in the OpenSees framework (Open System for Earthquake Engineering Simulation), provides a refined formulation for simulating cyclic behavior under large inelastic deformations and complex loading histories. Despite these advances, current models remain fundamentally rate-independent in their standard implementations.

Incorporating strain-rate effects into cyclic constitutive formulations for reinforcing steel remains largely unresolved in structural engineering applications. Existing approaches are fragmented and limited in scope. Classical viscoplasticity models, originally developed for metal forming processes, provide a theoretical basis for rate dependence but lack validation under large-amplitude cyclic loading with load reversals. Additive viscous overstress formulations have been calibrated primarily for monotonic response and do not account for the evolution of viscous effects under cyclic loading. More physically grounded dislocation-based models offer mechanistic insight into rate-dependent behavior, but their computational cost limits their use in nonlinear structural analysis.

No constitutive framework currently available simultaneously achieves: (1) an accurate representation of cyclic behavior under large reversed plastic deformations, (2) an explicit and consistent incorporation of strain-rate effects within the strain hardening regime, and (3) computational efficiency compatible with nonlinear dynamic analysis of full structural systems. This gap defines the central theoretical problem this research addresses.

Existing formulations also cannot capture the stiffness degradation and pinching observed in the cyclic force-deformation response of RC members. These effects arise from the progressive loss of kinematic compatibility at the steel-concrete interface during crack closure and reopening, as bond deterioration allows localized relative slip to accumulate under repeated load reversals. Conventional constitutive models for reinforcing steel generally assume perfect bond, leading to systematic overestimation of stiffness recovery upon load reversal and, consequently, of the energy dissipated per cycle. Representing pinching within fiber-section frameworks, without introducing additional degrees of freedom to account for interface slip, remains unresolved.

This research develops the SteelDRCV model (Dodd-Restrepo-Carreño-Velásquez), a rate-dependent extension of the SteelDRC formulation implemented in OpenSees. The model incorporates two principal extensions: (1) a nonlinear Voigt-type viscous overstress term, driven by strain-rate excursions, to capture rate-dependent strengthening beyond initial yield; and (2) a quadrant-dependent curvature factor that phenomenologically reproduces bond-slip-induced pinching in cyclic response. Both extensions are formulated to preserve compatibility with large-scale nonlinear structural analysis.

1.2 Problem Statement

1.2.1 Problem Definition

The research problem is structured across three interrelated levels of increasing complexity. At the characterization level, the problem involves quantifying the magnitude and temporal evolution of strain-rate demands in the longitudinal reinforcement of RC structures subjected to seismic excitation, and identifying the governing mechanical and dynamic factors that control their distribution. Particular emphasis is placed on distinguishing the response within the Lüders plateau and the strain-hardening regime, and on establishing their relationships with structural response parameters such as effective periods, modal contributions, and ground motion characteristics.

At the modeling level, the central challenge is to develop a constitutive framework for reinforcing steel that integrates (1) strain-rate effects via nonlinear viscous overstress to capture dynamic

strengthening in the strain-hardening regime, and (2) bond-slip-induced pinching via quadrant-dependent stiffness reduction to reproduce stiffness degradation and energy dissipation loss during load reversals, while preserving predictive fidelity of the hysteretic response under large reversed plastic deformations.

At the application level, the problem is to assess how strain-rate-dependent constitutive behavior affects seismic response predictions for RC structures. It involves quantifying the influence of rate effects and pinching severity on ductility demands, energy dissipation mechanisms, stiffness degradation patterns, and the extent to which physically based constitutive modeling can reduce reliance on empirically calibrated viscous damping formulations.

At the calibration level, the problem is to identify the proposed model's constitutive parameters from full-scale experimental data in a rigorous and reproducible manner. The parameter space is high-dimensional, the forward model is computationally expensive, and several parameters interact strongly. A two-stage calibration strategy is therefore required: a first stage that isolates the cyclic and pinching parameters under displacement-controlled quasi-static conditions, and a second stage that employs Bayesian inference to jointly identify the strain-rate, damping, and remaining parameters from the dynamic shake-table response. The Bayesian framework provides not only point estimates but also posterior distributions that quantify residual uncertainty for each parameter and reveal which are informed by the dynamic data and which are effectively resolved only by the quasi-static stage.

1.2.2 General Research Objective

To experimentally characterize strain-rate histories in longitudinal reinforcement of full-scale RC members subjected to seismic excitation, and to develop a rate-dependent cyclic constitutive model with integrated bond-slip pinching for reinforcing steel that preserves the cyclic plasticity framework, is implemented in OpenSees, and is validated against time-history analyses of a full-scale LHPOST bridge column, thereby improving the prediction of hysteretic response, pinching characteristics, ductility demands, and energy dissipation in nonlinear dynamic structural simulations.

1.2.2.1 Specific Research Objectives

- Establish a detailed experimental characterization of strain-rate distributions in reinforcing steel of full-scale RC shake table specimens, and quantify their magnitudes under strong seismic excitation.

- Decompose the overall strain-rate amplification into contributions from localized microstructural dynamics, higher-mode vibrations, and waveform effects, establishing their probabilistic distributions from full-scale shake table measurements.

- Formulate a mathematical extension of the SteelDRC constitutive model for reinforcing steel that incorporates strain-rate dependence via a nonlinear viscous overstress term and bond-slip-induced pinching via a quadrant-dependent curvature factor, while preserving the underlying cyclic plasticity framework and ensuring compatibility with OpenSees implementation.

- Calibrate the proposed constitutive model (SteelDRCV) using controlled cyclic loading tests conducted at elevated strain rates, capturing the macroscopic consequences of strain-rate-dependent overstress and explicitly incorporating rate-dependent effects in the strain-hardening regime.

- Validate the SteelDRCV model by implementing it as the reinforcing steel material in a numerical OpenSees model of the full-scale bridge column, and compare simulation results with experimental measurements from LHPOST to assess its representation of hysteretic response, pinching-induced stiffness degradation, and energy dissipation relative to the rate-independent formulation.

- Develop and execute a two-stage calibration procedure comprising (1) a deterministic displacement-controlled stage that identifies the cyclic and pinching parameters from the quasi-static structural response, and (2) a Bayesian dynamic stage that jointly refines the remaining parameters (strain-rate, damping, and concrete post-peak parameters) using Transitional Markov Chain Monte Carlo sampling on Gaussian-Process surrogates trained from nonlinear time-history analyses, and quantify the posterior uncertainty and sensitivity of each parameter through variance-based decomposition.

- Quantify the impact of strain-rate effects on structural energy dissipation and the reliance on empirically prescribed viscous damping, isolating the fraction of energy attributable specifically to material rate dependence.

1.2.3 Scope of the Research

This research is defined by four interrelated dimensions (conceptual, experimental, modeling, and validation), which collectively establish the domain of applicability of the proposed SteelDRCV formulation and ensure consistency among physical observations, constitutive modeling, and structural-level assessment.

1.2.3.1 Conceptual Scope

This study focuses on the strain-rate dependence of low-carbon reinforcing steel in RC structures subjected to seismic loading. The investigation explicitly distinguishes between two deformation regimes with fundamentally different governing mechanisms. The strain-hardening regime constitutes the domain in which rate effects are modeled through a continuum viscoplastic formulation. In contrast, the Lüders plateau is treated as a phenomenological regime characterized by localized deformation propagation, whose underlying microstructural dynamics are not represented within the continuum framework. The constitutive model's predictive domain is restricted to the strain-hardening regime, while observed strain-rate magnitudes in the plateau are used solely for empirical characterization. Thermal effects and multiaxial stress-state responses are not considered, restricting the analysis to uniaxial conditions governing flexural response in plastic hinge regions.

The pinching mechanism is introduced as a phenomenological modification of the steel stress-strain response through a quadrant-dependent curvature factor, which reduces the local tangent stiffness: in the second quadrant, during compressive loading following crack closure, where

residual tensile plastic strain and bond degradation induce relative slip before reestablishment of concrete contact; and in the fourth quadrant, during tensile reloading following crack reopening, where residual compressive deformation and degraded bond delay reengagement in tension. This formulation captures the macroscopic effects of steel-concrete interface slip and bond degradation without adding degrees of freedom, preserving compatibility with fiber-section discretizations in beam-column elements. The underlying mechanisms (rib-concrete interaction, confinement loss, and progressive bond deterioration) are not explicitly resolved but are represented through an effective stiffness reduction calibrated against experimental hysteretic loops.

1.2.3.2 Experimental Scope

The study's empirical basis is restricted, first, to full-scale shake table experiments conducted at LHPOST, including a 1219 m-diameter circular bridge column and a seven-story structural wall. This study limits its analysis to direct strain measurements from gauges in plastic hinge regions, ensuring that strain-rate histories match localized inelastic demand. Second, controlled cyclic tests on low-carbon reinforcing steel (Grade 60, ASTM A615/A706) calibrate the constitutive model under elevated strain-rate conditions.

1.2.3.3 Modeling Scope

The SteelDRCV model is a uniaxial, rate-dependent extension of the SteelDRC framework, implemented in OpenSees as a material model. Its application is restricted to fiber-based beam-column elements, ensuring compatibility with nonlinear time-history analysis of structural systems while avoiding the computational complexity of higher-dimensional formulations. The model is calibrated at a strain rate of 0.02 s^{-1}, corresponding to seismic loading conditions in civil engineering structures. Strain-rate regimes beyond this range, including impact and explosive loading, are excluded because they activate additional physical mechanisms not represented in the formulation. The pinching formulation is restricted to uniaxial fiber-section implementations and has not been validated for higher-dimensional continuum or interface-element discretizations.

1.2.3.4 Validation Scope

Validation is performed through numerical simulation of the full-scale bridge column tested at LHPOST, where the SteelDRCV model is implemented as the constitutive representation of reinforcing steel within an OpenSees model of the specimen. Simulated structural response is directly compared with experimental measurements from the first five seismic simulations (EQ1-EQ5), as progressive deterioration of the experimental instrumentation during subsequent tests precluded their use. The first four are used for calibration, and the fifth is reserved for independent validation. This separation provides an independent assessment of the calibrated model without using the EQ5 response during parameter identification. The validation is restricted to this configuration and does not extend to alternative structural typologies, high-strength reinforcement grades, or loading regimes dominated by monotonic or fatigue behavior.

1.2.3.5 Explicit Exclusions

The research does not address microstructural modeling of deformation band propagation, bond-slip degradation under high strain rates, or rate-dependent damage in concrete. These phenomena, while physically relevant, require distinct modeling frameworks and are therefore excluded to maintain a consistent focus on integrating experimentally observed strain-rate effects into a computationally efficient constitutive formulation for structural analysis.

The pinching formulation represents the macroscopic effects of bond-slip degradation through a phenomenological reduction in curvature. It does not explicitly resolve the underlying rib-concrete interaction, confinement loss, or progressive bond deterioration. Its validation is restricted to the global hysteretic response of the calibration specimen and has not been extended to isolated bond-slip tests, interface-element discretizations, or alternative structural typologies.

1.3 Outline

Chapter 1 introduces the research problem, establishes the theoretical and empirical foundations, defines the objectives, and delimits the scope. Chapter 2 surveys the existing literature on strain-rate effects in reinforcing steel, cyclic constitutive modeling, and bond-slip behavior, including microscopic and mechanistic models and macroscopic formulations for representing bond-slip-induced pinching and degradation. Chapter 3 extracts and analyzes strain-rate histories from two full-scale LHPOST specimens, quantifying the magnitude, distribution, and amplification of strain-rate demands in longitudinal reinforcement under seismic excitation. Chapter 4 develops the SteelDRCV hysteretic constitutive model, presents the high-strain-rate tensile test used to characterize the strain-rate mechanism and to propose two nonlinear Voigt-type viscous parameters, and adopts the cyclic and pinching parameters from controlled-loading tests. Chapter 5 describes the two-stage calibration (a deterministic displacement-controlled stage that identifies the cyclic and pinching parameters from the quasi-static response, followed by a Bayesian dynamic stage employing Gaussian-Process surrogates, variance-based sensitivity analysis, and Transitional Markov Chain Monte Carlo sampling) and validates it against an independent seismic simulation, and decomposes the total input energy into its hysteretic, Rayleigh viscous damping, and strain-rate contributions. Chapter 6 summarizes the principal findings, discusses the contributions and limitations, and outlines recommendations for future work.

2 REVIEW OF PREVIOUS RESEARCH WORK

The mechanical response of structural materials under dynamic or transient loading is influenced by the rate at which deformation develops, commonly expressed in terms of strain rate. This dependence has been extensively documented and becomes particularly relevant in applications involving impact, blast, seismic excitation, and other loading conditions involving rapid deformation. As strain rate increases, materials may exhibit changes in strength, stiffness, and energy absorption capacity. Accounting for these rate-dependent effects is therefore an important aspect of constitutive modeling when simulating structural response under dynamic loading.

In RC structures, both the concrete matrix and the embedded reinforcing steel exhibit strain-rate sensitivity, although the magnitude and nature of these effects differ. Reinforcing steel generally exhibits increased yield and ultimate strength with increasing strain rate. In contrast, concrete exhibits a more complex rate-dependent response involving changes in strength, stiffness, cracking, and fracture behavior. Because reinforcing steel plays a central role in the development of inelastic deformation and energy dissipation in RC members, particular attention in this chapter is given to the rate-dependent response of reinforcing steel. Concrete behavior is discussed where necessary to provide the context required for understanding the interaction between reinforcement and the surrounding concrete.

Although extensive research has examined the strain-rate sensitivity of both materials, it has focused particularly on reinforcing steel, given its critical role in ensuring structural integrity and energy dissipation. Experimental studies show that reinforcing bars experience appreciable increases in strength and significant changes in inelastic behavior as strain rates rise, especially within the range typical of seismic loading. The applied strain rate does not solely govern these effects; factors such as steel grade, manufacturing process, bar diameter, and prior deformation history also influence them. In real seismic events, reinforcing bars often experience strain rates far higher than under quasi-static conditions. This strain-rate sensitivity directly affects key mechanical properties-including yield strength, ultimate strength, and ductility-and must be carefully considered in the constitutive modeling of steel components in nonlinear structural analysis.

Although concrete also exhibits strain-rate-dependent behavior, typically manifested as increased strength and stiffness under rapid loading, this chapter focuses primarily on reinforcing steel. References to concrete are included where necessary to provide context within RC systems, but the core discussion centers on the rate-dependent response of steel reinforcement. Temperature can also significantly influence the mechanical behavior of both concrete and steel, affecting properties such as yield strength, ductility, and strain-hardening characteristics, particularly under cold conditions. However, this chapter does not explicitly address temperature effects and mentions them only for context.

Several constitutive models have been developed to represent strain-rate effects in reinforcing steel, with many formulations derived or calibrated primarily from monotonic loading. These approaches commonly introduce rate dependence through empirical relationships, dynamic increase factors (DIFs), or viscoplastic formulations, including rate-sensitive yield criteria and overstress-based descriptions. Their applicability to cyclic loading is less established, particularly when strain-rate

effects must be considered simultaneously with path-dependent phenomena such as the Bauschinger effect, cyclic hardening, stiffness degradation, and hysteretic energy dissipation. This distinction motivates the separate examination of monotonic and cyclic constitutive formulations in the following sections.

The cyclic response of reinforcing steel, however, cannot be considered independently from the interaction between reinforcement and concrete. Bond-slip at the steel-concrete interface can introduce additional deformation and modify the stiffness, strength, hysteretic shape, and energy dissipation of RC members, particularly under load reversals. Different modeling approaches have been developed to represent these effects. Microscopic and mechanistic bond-slip models seek to represent the local mechanisms governing force transfer between reinforcement and concrete, including rib bearing and wedging, friction, concrete damage, confinement, and slip reversal. Macroscopic bond-slip models, in contrast, represent the structural consequences of these mechanisms through equivalent constitutive, interface, or section-level formulations. The distinction between these approaches is relevant for evaluating how bond-related mechanisms can be incorporated into nonlinear structural models and how their effects interact with the constitutive response of reinforcing steel.

This chapter reviews previous research on strain-rate effects in reinforcing steel, cyclic constitutive modeling, and bond-slip behavior in reinforced-concrete structures. Section 2.1 examines monotonic constitutive models, focusing on formulations that incorporate rate dependence through empirical relations, dynamic increase factors, or viscoplastic frameworks, and evaluates their applicability to reinforcing steel. Section 2.2 reviews cyclic constitutive models and their ability to reproduce key hysteretic features, including the Bauschinger effect, cyclic hardening, stiffness degradation, and energy dissipation, with particular attention to the assumptions adopted regarding loading rate. Section 2.3 reviews microscopic and mechanistic bond-slip models, focusing on the local mechanisms governing reinforcement–concrete interaction and their representation of anchorage, confinement, damage, and cyclic interface behavior. Section 2.4 examines macroscopic bond-slip models, focusing on formulations that incorporate the structural consequences of reinforcement–concrete interaction through localized or equivalent constitutive and section-level representations, including additional deformation, stiffness degradation, strength deterioration, and hysteretic pinching. Finally, Section 2.5 synthesizes the experimental evidence and modeling approaches reviewed throughout the chapter to identify their principal limitations and establish the gaps that motivate the developments presented in the subsequent chapters.

2.1 Research Work on Monotonic Constitutive Models

Researchers have widely studied the influence of strain rate on the mechanical behavior of reinforcing steel bars over the past decades. Early experimental research showed that both the yield and ultimate strengths of steel increase under higher strain rates, leading to the development of empirical and analytical models to capture this behavior. These models have evolved to include complex interactions with temperature, strain hardening, and loading history.

Understanding these effects is crucial for designing and analyzing RC structures subjected to dynamic loads, such as seismic events. Numerous authors have expanded the experimental database and refined constitutive formulations. This growing body of work has laid the foundation for strain-rate-dependent models, all based on monotonic tensile tests conducted at different

loading rates. While these tests do not reflect the full complexity of real cyclic or seismic loading, they provide a practical basis for defining dynamic increase factors and other rate-sensitive parameters.

2.1.1 Watstein (1953)

Watstein [139] conducted one of the earliest and most influential studies on the effect of strain rate on the mechanical behavior of reinforcing bars. In this seminal work, the author investigated how strain-rate variations affect the yield stress of steel reinforcement, underscoring the importance of dynamic material behavior in structural design under high-rate loading conditions, such as seismic or impact events. The study was motivated by the recognition that material properties obtained under quasi-static conditions may not reflect the actual behavior of reinforcing steel in dynamic environments.

Watstein conducted a series of tensile tests on reinforcing bars at different strain rates, ranging from quasi-static loading to much faster rates intended to simulate dynamic conditions. By controlling other parameters, the study isolated the effect of strain rate on the steel's yield strength. The results indicated a clear trend: the yield stress increased with increasing strain rate, a phenomenon now recognized as strain-rate sensitivity. In particular, the data demonstrated an approximately logarithmic relationship between yield stress and strain rate. The yield stress (σ_y) could be expressed in terms of strain rate ($\dot{\varepsilon}$) as:

$$\sigma_y(\dot{\varepsilon}) \approx \sigma_{y0} + k.\log\left(\frac{\dot{\varepsilon}}{\dot{\varepsilon}_0}\right) \tag{1}$$

Where,

- k: A material-dependent constant representing the sensitivity of the steel to strain rate.
- $\dot{\varepsilon}$: The applied strain rate.
- $\dot{\varepsilon}_0$: The reference strain rate typically corresponds to standard static testing.
- $\sigma_y(\dot{\varepsilon})$: The yield stress of the steel at a given strain rate ($\dot{\varepsilon}$).
- σ_{y0}: The yield stress under quasi-static conditions (reference value).

Watstein's findings had significant implications. First, they challenged the assumption that steel reinforcement behaves strain-rate-independently under typical loading conditions. Second, they suggested that under seismic loading, where strain rates may be an order of magnitude higher than those in quasi-static tests, reinforcing bars can exhibit enhanced strength. This effect, now commonly referred to as the DIF, is central to modern dynamic material models.

Although the study was conducted on isolated steel bars (without interaction with concrete or consideration of bond-slip behavior), it was groundbreaking for highlighting the need to incorporate strain-rate effects into the modeling and design of RC structures. Subsequent experimental and theoretical studies throughout the second half of the 20th century confirmed and expanded upon Watstein's conclusions, leading to the widespread adoption of strain-rate-sensitive constitutive laws in advanced structural analysis, especially in earthquake engineering.

2.1.2 Cowper-Symonds (1957)

Cowper and Symonds [40] conducted a comprehensive investigation into the combined influence of strain hardening and strain-rate sensitivity on the plastic deformation of cantilever beams subjected to dynamic loading. The primary objective was to understand how mild steel responds to high-rate deformation and to develop a model that accurately predicts this behavior under impact conditions.

To conduct this investigation, the authors performed a series of controlled-impact tests on cantilever beams. The experimental setup consisted of a drop-weight system in which a known mass was released from various heights to produce different impact velocities. These tests induced a range of strain rates in the beams, allowing the researchers to record data on deflection, strain, and strain rate during plastic deformation. The study emphasized that metals' plastic flow behavior under dynamic loading differs significantly from that under quasi-static conditions, with yield stress increasing noticeably as strain rate increases.

They introduced a material model that captures elasto-plastic behavior, strain hardening, and strain-rate sensitivity using the empirical Ludwik formulation [79]. This model accounts for strain-rate effects, making it suitable for high-rate loading scenarios, such as impacts. However, it cannot capture the complex hardening behavior required for cyclic loading applications.

$$\sigma_y(\varepsilon, \dot{\varepsilon}) = \sigma_y^s(\varepsilon)\left\{1 + \left(\frac{\dot{\varepsilon}}{C}\right)^{\frac{1}{p}}\right\} \tag{2}$$

The constants C and p, are material parameters selected to describe material sensitivity to strain rate. The quasi-static yield stress, σ_y^s is explained by the power law:

$$\sigma_y^s(\varepsilon) = K(\varepsilon + \varepsilon_0)^n \qquad \varepsilon_0 = \left(\frac{E}{K}\right)^{\frac{1}{(n-1)}} \tag{3}$$

The parameter K, is the strength hardening coefficient; the factor n, is the strength hardening exponent; and E, is Young's modulus. Hence,

$$\sigma_y(\varepsilon, \dot{\varepsilon}) = K\left(\varepsilon + \left(\frac{E}{K}\right)^{\frac{1}{(n-1)}}\right)^n \left\{1 + \left(\frac{\dot{\varepsilon}}{C}\right)^{\frac{1}{p}}\right\} \tag{4}$$

The model assumed rigid-plastic behavior with strain hardening, neglecting elastic effects-a simplification consistent with the experimentally observed response under high strain rates. The researchers showed that this approach accurately captured the plastic response of beams under impact loading, making it particularly suitable for engineering applications involving short-duration, high-intensity forces. As a widely used empirical formulation for metals under dynamic loading, the model defines true stress as a function of effective uniaxial plastic strain and strain

rate, incorporating both quasi-static yield and dynamic flow stress. It represents a class of strain-rate-dependent phenomenological models in which strain-rate-sensitive parameters modulate the yield stress.

2.1.3 Johnson & Cook (1983)

Johnson and Cook [63] introduced a constitutive model (JC) and data for metals undergoing large strains, high strain rates, and elevated temperatures. In this model, the material behaves linearly elastically when the equivalent stress remains below the yield stress, then transitions to plastic behavior when it exceeds this threshold. It was demonstrated that the material's response to the interaction between stress, σ, and strain, ε, can be expressed in the following scaling form:

$$\sigma(\varepsilon, \dot{\varepsilon}, T) = f_1(\varepsilon).f_2(\dot{\varepsilon}).f_3(T) \tag{5}$$

Where,

$f_1(\varepsilon)$: Effects of work hardening

$f_2(\dot{\varepsilon})$: Effects of strain rate

$f_3(T)$: Effects of temperature

Eq. (5) is usually determined with true stress and true plastic strain in uniaxial tension or compression tests. It is described as having von Mises flow stress, $\sigma(\varepsilon, \dot{\varepsilon}, T)$, and equivalent plastic strain.

$$\sigma(\varepsilon, \dot{\varepsilon}, T) = [A + B\varepsilon^n]\left[1 + C.\ln\left(\frac{\dot{\varepsilon}}{\dot{\varepsilon}_0}\right)\right]\left[1 - \left(\frac{T - T_0}{T_m - T_0}\right)^m\right] \tag{6}$$

In the JC model, five material constants describe the material's work-hardening behavior, strain rate sensitivity, and thermal softening effects: constants A, B, C, m, and n. Here, A represents the initial yield stress, and B is the hardening constant measured in pressure units. Constants C and m are dimensionless parameters associated with strain rate sensitivity and thermal softening, respectively, while n is a dimensionless hardening exponent. The value of n dictates the material's plastic flow characteristics: (1) when $n = 1$, the material is an ideal linear elastic material; (2) when $n = 0$, the material is nonlinear elastic; (3) when $0 < n < 1$, it indicates elastoplastic behavior.

The expressions in the second and third brackets represent strain rate and temperature effects, respectively. T_0 is the reference temperature and usually refers to room temperature, and T_m, is the melting temperature of the material. ε is the equivalent plastic strain. The strain ratio ($\dot{\varepsilon}/\dot{\varepsilon}_0$) is the dimensionless plastic strain rate for $\dot{\varepsilon}_0 = 1.0\ s^{-1}$.

The JC model was used to simulate the dynamic behavior of reinforcing steel bars under loading conditions characteristic of seismic events and impacts. Experimental evidence confirms that reinforcing steels exhibit significant strain-rate sensitivity, with both yield and ultimate strengths increasing with increasing strain rate. By calibrating the JC model parameters using high-strain-

rate experimental data (typically obtained via Split Hopkinson Pressure Bar (SHPB) tests), researchers have accurately predicted reinforcing steel response under dynamic conditions.

Originally developed to describe metal behavior under high strain rates, elevated temperatures, and large deformations, the JC model captures key aspects of material performance in extreme loading scenarios, such as impacts or explosions. It provides a framework for quantifying how strain rate and temperature influence stress response. However, the model is inherently monotonic and does not capture cyclic phenomena such as load reversals, hysteresis, or the Bauschinger effect, which are critical in modeling seismic or fatigue loading.

2.1.4 Bertero, Mahin, and Herrera (1978)

In their seminal 1978 report, Bertero et al. [13] conducted an in-depth experimental investigation into the seismic behavior of RC structural walls. This work, developed at the Earthquake Engineering Research Center (EERC) at the University of California, Berkeley, examined wall performance under cyclic lateral loading and provided early insights into how strain rate and load history affect the nonlinear response of RC elements.

Although the study primarily focused on global wall behavior, including stiffness degradation, strength deterioration, and energy dissipation, the authors acknowledged the complex interaction between material-level phenomena and structural response. Reinforcing steel, as a critical component in resisting tensile demands during lateral loading, was subjected to varying strain rates throughout the cyclic tests. While not the study's main objective, the steel's response to repeated reversals and rapid strain excursions suggested the relevance of strain-rate-dependent effects, particularly under seismic loading conditions.

The report emphasized that, during strong ground motions, the strain rate in structural elements can vary significantly, potentially altering the mechanical properties of the materials involved. The authors called for future research to quantify how strain rates affect both reinforcing steel and concrete, especially under the cyclic and dynamic demands typical of earthquakes. This work thus contributed conceptually to the growing recognition of strain-rate effects, even if it did not quantify them explicitly through material models.

Although Bertero et al. [13] did not explicitly formulate strain-rate-dependent material models, their large-scale cyclic experiments indirectly highlighted the importance of rate effects in RC walls under dynamic loading conditions.

2.1.5 Mander (1983)

Mander [82] established an analytical formulation to represent the monotonic stress-strain behavior of reinforcing steel, dividing the response into four regions: elastic, yield plateau, strain hardening, and post-ultimate (Figure 1).

The elastic branch is linear up to the yield point, defined by $f_s = E_s \varepsilon_s$, where E_s is the elastic modulus. The yield plateau assumes constant stress, $f_s = f_y$, although later studies, such as Restrepo et al. [115], reported a nonzero tangent modulus in this range. Beyond yielding, strain hardening is represented through a power function calibrated by the strain-hardening modulus, E_{sh},

and the parameter, P, defining the transition to ultimate stress, depending on the slope at the onset of strain hardening. The resulting relations provide continuous stress-strain and tangent modulus expressions, forming a complete analytical curve applicable to both monotonic and cyclic load modeling.

The approach assumes that the dynamic yield stress and tangent modulus scale proportionally to a dynamic magnification factor, D_s, which depends on the applied strain rate, $\dot{\varepsilon}$, relative to a reference rate $\dot{\varepsilon}_s$.

$$\begin{aligned} \left(f_y\right)_d &= D_s\, f_y \\ D_s &= d\left[1 + \left|\frac{\dot{\varepsilon}}{\dot{\varepsilon}_s}\right|^{1/n}\right] \end{aligned} \tag{7}$$

Where,

- d: A material-dependent constant representing the baseline dynamic amplification at quasi-static conditions.
- f_y: The quasi-static coupon test yield strength, for which most tension tests use a strain rate of about 0.00001/s.
- $\left(f_y\right)_d$: The dynamic strength of steel.
- n: An exponent governing the sensitivity of the material to strain rate effects.
- $\dot{\varepsilon}$: The applied strain rate.
- $\dot{\varepsilon}_s$: The reference strain rate at which the yield strength of the material is approximately doubled.

Empirical calibration provided explicit forms for mild and high-strength steels in tension and compression. For mild steel subjected to tension, the parameters are equal $d = 0.953$, $\dot{\varepsilon}_s = 700\ s^{-1}$, and $n = 6$. For high-strength steel under tension, the corresponding values are $d = 0.949$, $\dot{\varepsilon}_s = 5 \times 10^7\ s^{-1}$, and $n = 10$. In the case of mild steel under compression, based on a separate dynamic test program, the parameters are $d = 0.966$, $\dot{\varepsilon}_s = 5000\ s^{-1}$, and $n = 6$. This expression quantifies how strain-rate sensitivity varies with steel grade and loading mode, indicating that mild steel exhibits greater rate dependence and that the exponent, n, remains consistent across tension and compression.

The constitutive extension assumes uniform amplification of both stress and stiffness, as follows:

$$\begin{aligned} (f_s)_d &= D_s\, f_s \\ (E_t)_d &= D_s\, E_t \end{aligned} \tag{8}$$

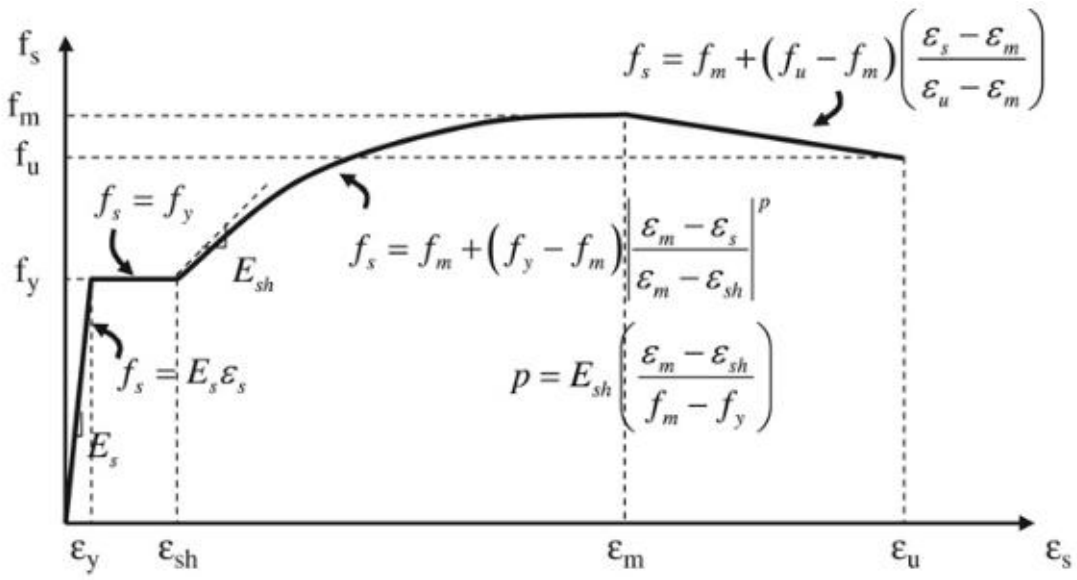


Figure 1. Monotonic stress-strain curve for reinforcing steel [82].

This assumption implies that the dynamic stress-strain curve is a scaled version of the static one, maintaining the same shape but with higher magnitudes. Figure 2 shows the assumed effect of strain rate on the stress-strain curve loaded monotonically at two different rates of strain. Although initially based on monotonic loading, Mander extended this scaling to cyclic conditions, recognizing the limited availability of experimental cyclic data at high strain rates. The model predicts a modest amplification (7-10%) in stress response under reversed loading, consistent with observed Bauschinger-type cyclic behavior.

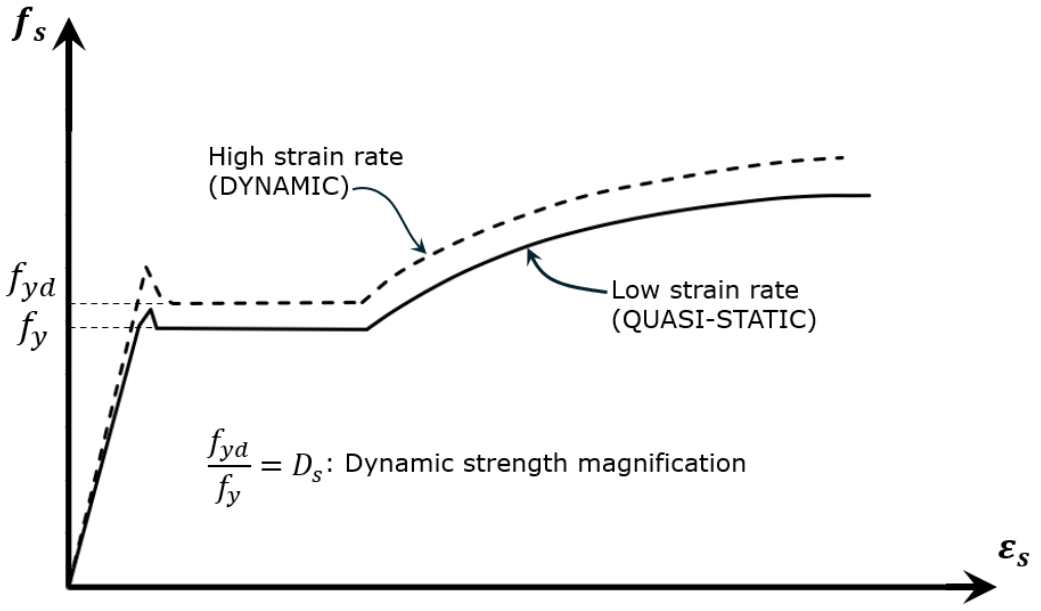


Figure 2. Assumed effect of strain rate on monotonic loading.

By coupling the rate-dependent yield stress and modulus into a single constitutive law, the formulation provides a practical means to incorporate dynamic strength enhancement into nonlinear analyses of RC members.

2.1.6 Shing & Mahin (1988)

Shing and Mahin [125] analyzed the influence of loading rate on the accuracy of pseudo-dynamic testing, which simulates seismic response by computing inertia forces in real time as loads are slowly applied through actuators. Although the method captures overall system dynamics, it neglects the inherent rate sensitivity of structural materials, particularly mild steel, potentially underestimating strength and overestimating ductility under actual earthquake loading conditions.

To quantify these effects, the authors developed a rate-dependent analytical model based on a single-degree-of-freedom elastic-viscoplastic system governed by Perzyna's overstress theory, where the total strain rate equals the sum of the elastic and viscoplastic components.

The elastic strain rate ($\dot{\varepsilon}_e$) is governed by Hooke's law, and the viscoplastic strain rate ($\dot{\varepsilon}_p$) is activated only when the applied stress exceeds the static yield limit and follows a power-law function:

$$\dot{\varepsilon}_p = \gamma \left(\frac{|\sigma|}{\sigma_y} - 1 \right)^{\delta} sign(\sigma) \quad if\ |\sigma| > \sigma_y$$
$$\dot{\varepsilon}_p = 0 \quad if\ |\sigma| \leq \sigma_y \tag{9}$$

Where γ and δ define the material's sensitivity to overstress and rate effects.

Calibrated using tensile test data across varying strain rates, the selected constants ($\gamma = 14, \delta = 5$) reproduce experimental trends for mild steel, predicting a yield strength increase of approximately 40% at a strain rate of 0.1 s^{-1}, consistent with strong-motion conditions during seismic events. The formulation captures the delayed onset of plastic flow under dynamic stress, providing a mechanistic description of rate-induced strengthening within a constitutive law suitable for structural analysis.

Simulations were conducted under harmonic and real earthquake excitations, including the 1940 El Centro record, comparing three scenarios: static (rate-insensitive), pseudo-dynamic (slow loading), and fully dynamic (rate-dependent). Results indicate that rate-induced strengthening substantially reduces plastic strain and ductility demands. For stiff systems (short natural periods), ignoring strain-rate effects can overestimate displacement ductility by up to 25%, whereas for flexible systems (periods> 0.6 s), the discrepancy is below 10%. When pseudo-dynamic conditions were simulated, representing actuator-controlled tests where every 0.01 s of simulated seismic time corresponds to 1-2 s of real loading, the effective strain rates were 50-100 times lower than in real earthquakes. Consequently, the material response exhibited limited dynamic strengthening, resulting in slightly higher plastic deformation. Nevertheless, the peak-strength deviation between pseudo-dynamic and dynamic conditions remained moderate (~13%), and the resulting spectral-response error did not exceed 12%.

The study further examined cyclic behavior by modifying viscoplastic parameters to reflect reduced rate sensitivity during stress reversals. Under such cyclic conditions, dynamic overstrength decreased, aligning more closely with experimental results from reversed-loading tests. Although rate effects persisted, their influence on cyclic strength gain was smaller than under monotonic conditions. This finding supports the notion that pseudo-dynamic tests, which inherently involve cyclic deformation at low loading rates, provide conservative yet reasonably accurate estimates of inelastic demands, particularly for flexible or long-period structures.

The viscoplastic constitutive model developed by Shing and Mahin provides a physically grounded framework for incorporating strain rate effects into structural response simulations. By linking rate-dependent plasticity with pseudo-dynamic testing methodologies, the study clarifies the range of conditions under which simplified quasi-static or pseudo-dynamic procedures remain valid. It demonstrates that while rate effects can meaningfully influence the seismic response of stiff, low-period systems, omitting them has a limited impact on more flexible configurations. This work therefore bridges experimental practice and constitutive modeling, reinforcing the importance of rate-dependent formulations for accurate nonlinear analysis and calibration of seismic testing protocols.

2.1.7 Eibl (1988)

Eibl [45], published in 1988 as a CEB Bulletin, provides a comprehensive analysis of the dynamic behavior of RC structures under impact and impulsive loading, with particular emphasis on the strain-rate sensitivity of reinforcing steel bars. The primary objective is to develop a framework for understanding and modeling the response of RC structures to extreme dynamic events, such as vehicle impacts, missile strikes, or blast loadings, which induce high strain rates in both concrete and reinforcing steel. This outline is critical for designing resilient structures such as nuclear containment systems, bridge piers, and protective shelters, where material dynamic properties significantly influence performance. The study aims to synthesize experimental data and theoretical models to help engineers predict structural behavior under these conditions, focusing on the strain-rate-dependent properties of reinforcing steel to enhance RC design.

The methodology integrates a review of experimental tensile tests on reinforcing steel bars, typically hot-rolled grades with a nominal yield strength of 420 MPa, conducted at strain rates up to 10 s^{-1}. These tests, often using hydraulic machines or early Split Hopkinson Bar setups, measure changes in yield strength, ultimate tensile strength, and ductility. Eibl also employs analytical and numerical methods, including simplified finite-element models, to simulate the response of RC elements to impact and impulsive loads. The bulletin references steel microstructural characteristics, noting differences between hot-rolled and cold-drawn bars, to explain variations in dynamic behavior. The experimental data are used to derive empirical relationships that quantify strain-rate effects, providing a basis for constitutive modeling in structural analysis.

The mathematical formulations are centered on DIFs, which quantify the enhancement of material properties under dynamic loading. For reinforcing steel with a yield strength of 420 MPa, the DIF for yield strength is expressed as a logarithmic function:

$$\frac{f_{y,d}}{f_{y,st}} = 1 + \frac{6}{f_{y,st}} \ln\left(\frac{\dot{\varepsilon}}{5x10^{-5}}\right)$$
$$\frac{f_{u,d}}{f_{u,st}} = 1 + \frac{7}{f_{u,st}} \ln\left(\frac{\dot{\varepsilon}}{5x10^{-5}}\right) \quad (10)$$

Where,

$f_{y,d}, f_{y,st}$: The dynamic and quasi-static yield strengths, respectively.

$f_{u,d}, f_{u,st}$: The dynamic and quasi-static ultimate strengths, respectively.

$\dot{\varepsilon}$: The applied strain rate.

These equations, derived from regression analysis of experimental data, predict strength increases with increasing strain rate, enabling engineers to adjust static material properties for dynamic conditions. For example, at a strain rate of 10 s^{-1}, the yield strength DIF is approximately 1.16-1.20, indicating a 16-20% increase. These formulations are designed for use in numerical simulations, such as finite element analysis, to model RC structures under impact.

The key results demonstrate that reinforcing steel exhibits significant strain-rate sensitivity, with the yield strength increasing by more than the ultimate tensile strength as strain rates rise from quasi-static (10^{-4} s^{-1}) to dynamic (10 s^{-1}) conditions. For 420 MPa steel, the DIF for yield strength reaches 1.16-1.20, while the ultimate strength DIF is around 1.13, indicating a 13% increase. The elastic modulus remains unaffected, consistent with prior research, while ductility trends vary: hot-rolled bars show stable or slightly reduced ultimate strains. These enhancements improve the axial and flexural capacities of RC elements. Still, they may shift failure modes from ductile to brittle, such as shear failure, under high strain rates.

The DIF formulations provided a practical tool for adjusting static design parameters in Eurocode 2, although challenges related to potential brittle failures and bond behavior at high strain rates remained unresolved.

2.1.8 CEB-FIP Model Code (1993)

The Comité Euro-International du Béton (CEB) published a pivotal design guideline, the CEB-FIP Model Code [38], which considered dynamic effects on materials, particularly reinforcing steel. Although the Model Code primarily provided recommendations for structural concrete design, it recognized the importance of strain-rate effects in dynamic and seismic applications.

The CEB-FIB 1993 proposed a simplified approach to account for increased material strength in both concrete and steel under high strain rates. For reinforcing steel, the DIF was introduced as a strain-rate function to adjust yield and ultimate strengths under dynamic conditions relative to their static values. The formulation was derived empirically based on available experimental data and is commonly expressed as:

$$DIF = \left(\frac{\dot{\varepsilon}}{\dot{\varepsilon}_0}\right)^k \quad (11)$$

Where,

k: A material-dependent coefficient.

$\dot{\varepsilon}$: The applied strain rate.

$\dot{\varepsilon}_0$: The reference strain rate (typically 0.001 s^{-1}).

The values of the material-dependent coefficient (k) proposed by CEB depend on the steel type and the strain rate range and were calibrated primarily for monotonic loading conditions.

Importantly, the Model Code provided separate DIF expressions for yield stress and ultimate stress, acknowledging that these may not increase at the same rate with increasing strain rate. The recommendations were largely based on monotonic tensile tests conducted at varying strain rates, consistent with the type of experimental program used to develop most rate-dependent models at the time. At the same time, more sophisticated constitutive models such as Johnson-Cook or Cowper-Symonds exist; the CEB's proposal was meant to be practical and easy to implement in design procedures and simplified dynamic analyses.

2.1.9 Ross, Tedesco, and Hughes (1996)

In their seminal study, Ross et al. [118] conducted a comprehensive experimental and analytical investigation of strain-rate effects in RC beams subjected to dynamic flexural loading. Their work focused on quantifying how both the reinforcing steel and the surrounding concrete respond under high-strain-rate loading, a condition relevant to impact and blast scenarios. The strain rates in these tests ranged from quasi-static conditions to approximately 10^{-1} s^{-1}, representative of intermediate-rate dynamic events such as vehicular collisions or seismic pulses. Reinforcement strains were measured directly using strain gauges, enabling precise evaluation of strain-rate-dependent behavior. The beams exhibited increased load-carrying capacity and modified failure modes compared to their quasi-static counterparts.

A key contribution of this work was the empirical derivation of DIFs, particularly for reinforcing steel. The authors proposed the following general power-law expression:

$$DIF = \left(\frac{\dot{\varepsilon}}{\dot{\varepsilon}_0}\right)^n \tag{12}$$

Where,

n: An experimentally calibrated exponent.

$\dot{\varepsilon}$: The strain rate during loading.

$\dot{\varepsilon}_0$: The reference strain rate.

This DIF expression was embedded into a finite element model of the beams, using rate-dependent constitutive laws for both concrete and steel. The numerical simulations showed significantly improved agreement with the experimental results when strain-rate sensitivity was included, particularly in capturing the peak load and post-peak response.

2.1.10 Malvar & Crawford (1998)

Malvar and Crawford's work [80] focuses on developing empirical DIFs to quantify increases in the yield and ultimate strength of reinforcing steel bars under high-strain-rate loading, such as blast or impact events. They define DIF as the ratio between the dynamic strength (yield or ultimate) and the corresponding static strength.

$$DIF = \frac{f_d}{f_s} \tag{13}$$

Where,

f_d: The dynamic stress (yield or ultimate).

f_s: The static stress.

Their work synthesized data from over 250 tensile tests on ASTM A615 reinforcing bars, spanning a wide range of strain rates from quasi-static (approximately 10-5 s^{-1}) to high dynamic (up to 10^2 s^{-1}). The tests were monotonic, and the authors evaluated increases in yield and ultimate strength due to strain-rate effects. Based on their observations, they proposed a piecewise power-law formulation to define the DIF as a function of the strain rate ($\dot{\varepsilon}$), using a reference static strain rate equal to 10^{-4}. This proposed formulation assumed that the DIF data could be approximated by a straight line when plotting log DIF versus log strain rate. The adopted DIF formulation was, for both yield and ultimate stress:

$$DIF = \left(\frac{\dot{\varepsilon}}{10^{-4}}\right)^{\alpha} \tag{14}$$

The strain rate, $\dot{\varepsilon}$, is in s^{-1} (1/second), and the bar yield strength, f_y, in ksi, if, f_y, is in MPa, replace the 60 ksi denominator with 414 MPa.

For the yield stress, $\alpha = \alpha_{fy}$, was found to be:

$$\alpha_{fy} = 0.074 - 0.040\frac{f_y}{60} \tag{15}$$

and for the ultimate stress, $\alpha = \alpha_{fu}$, was found to be:

$$\alpha_{fu} = 0.019 - 0.009\frac{f_y}{60} \tag{16}$$

This model provides a smooth transition across the full strain-rate spectrum and has become one of the most widely used formulations in dynamic structural analysis. Importantly, the authors emphasized that the rate effects are more significant at the yield point than at ultimate conditions and that the total elongation capacity is only marginally affected by strain rate. The use of

monotonic tests also implies that the model applies primarily to impulsive loading scenarios, where cyclic degradation is not a dominant factor.

Compared to formulations in the CEB-FIP Model Code, the Malvar-Crawford model is purely empirical and derived solely from tensile test data rather than structural member response. While both models adopt power-law forms, the Malvar-Crawford approach allows for explicit variation of the exponent (α) as a function of steel properties, enhancing its adaptability to different grades and applications.

2.1.11 Malvar (1998)

Malvar [81] presents a comprehensive synthesis of the mechanical behavior of reinforcing steel under both quasi-static and dynamic loading conditions. This work remains a foundational reference for engineers and researchers studying reinforcement performance under impulsive loads, particularly in blast-resistant design and other high-strain-rate applications.

The study compiles and critically analyzes results from over 800 individual tensile tests on ASTM A615 reinforcing bars, incorporating variables such as bar diameter, strain rate, steel grade, and testing methodology. It distinguishes between static properties-such as yield strength, ultimate strength, and elongation-and dynamic characteristics, with a particular focus on strain-rate effects on the stress-strain response. A key contribution of the study is quantifying strain-rate sensitivity in reinforcing bars. Malvar demonstrates that yield strength increases significantly with strain rate, while the increase in ultimate strength is comparatively modest. These findings support formulating DIFs as power-law functions to account for strength enhancement under dynamic conditions. Although the paper does not introduce a new constitutive model, it extends and validates the empirical foundation of previously proposed models, including that of Malvar-Crawford [80].

This study also identifies critical limitations in several data sources, emphasizing the impact of inconsistent testing protocols, including strain measurement methods, gage lengths, and grip configurations, on data variability. It advocates using true stress-strain representations rather than over-engineered stress-strain curves in dynamic analysis and highlights the importance of consistent strain definitions. Significantly, Malvar notes that while dynamic loading enhances the apparent strength of reinforcing steel, it may reduce ductility, particularly at high strain rates. Elongation capacity remains relatively stable at moderate strain rates, with reductions primarily observed in the post-peak regime under very rapid loading.

The review confirms that dynamic strength enhancement is primarily governed by strain rate rather than loading mode (e.g., tension versus compression) and that monotonic testing provides a valid basis for characterizing reinforcing steel behavior under impulsive loading. Furthermore, the analysis reveals that cold-worked bars tend to exhibit greater strain-rate sensitivity than hot-rolled bars.

2.1.12 Filiatrault & Holleran (2001)

Filiatrault et al. [49] investigated the uniaxial stress-strain behavior of reinforcing steel and concrete under combined seismic strain rates and low temperatures, addressing a critical gap in understanding the performance of RC bridge structures in cold, seismically active regions. The primary objective is to experimentally quantify how earthquake-type strain rates (from quasi-static

at 80×10^{-6} s^{-1} to 0.1 s^{-1}) and low temperatures (+20°C to -40°C) affect the mechanical properties of reinforcing steel (CSA G30.16, nominal yield strength 400 MPa) and concrete (nominal compressive strength 20 MPa). This study is motivated by the potential for winter earthquakes to impose high strain rates and low temperatures simultaneously, altering material properties and the seismic response of RC structures. The authors aim to provide preliminary data on monotonic stress-strain curves to inform seismic design in cold climates.

The methodology is purely experimental, utilizing a 100-kN servo-hydraulic dynamic testing machine (Instron Model 1350) for both tensile tests on steel and compressive tests on concrete. For reinforcing steel, 30 coupons (12 mm diameter, 20 mm gauge length) were tested, with stress measured via a load cell and strain via clip gauges, ensuring high-precision data capture with a high-speed acquisition system. Concrete tests involved 36 cylinders (38 mm diameter, 76 mm height), with strain measured using LVDTs over a 50 mm gauge length. A temperature-controlled chamber, cooled by liquid nitrogen and monitored with thermocouples in dummy specimens, maintained consistent temperatures (+20°C, -20°C, -40°C). Steel specimens came from a single heat, and concrete cylinders from a single batch, minimizing material variability. The tests covered monotonic loading at seismic-relevant strain rates and involved no numerical or theoretical modeling.

Key results for reinforcing steel indicate moderate increases in mechanical properties under combined high strain rates and low temperatures. Yield strength increased by 22% (from baseline at 80×10^{-6} s^{-1} and +20°C to 0.1 s^{-1} and -40°C), and ultimate tensile strength rose by 12%. However, Young's modulus and ultimate tensile strain remained largely unaffected, suggesting no significant change in stiffness or ductility. For concrete, compressive strength surged by 91% under the same conditions, with Young's modulus increasing significantly at strain rates above 0.02 s^{-1} and temperatures of -20°C or -40°C. Ultimate compressive strain showed negligible variation, indicating sustained deformation capacity. Data were presented with best-fit linear regression lines on a semi-logarithmic plot, though scatter was noted for concrete and attributed to material heterogeneity.

This research does not develop new constitutive models or provide explicit mathematical expressions for stress-strain relationships. Instead, it relies on empirical trends, showing yield strength, tensile strength, compressive strength, and Young's modulus as functions of strain rate and temperature. These relationships are described qualitatively, with strength increases modeled as linear on a semi-logarithmic scale (e.g., increasing with logarithmic strain rate and decreasing with decreasing temperature). The absence of equations like the CS or JC models, common in strain rate studies, limits direct application in computational simulations but provides clear trends for qualitative design considerations.

Filiatrault et al. emphasize the critical role of strain rates in seismic design, particularly at low temperatures. They support the theory that strain-rate sensitivity enhances material strength, with yield strength more sensitive than tensile strength in steel, consistent with prior studies. In conclusion, the authors provide valuable preliminary data on the combined effects of seismic strain rates and low temperatures, demonstrating moderate increases in reinforcing steel strength and substantial gains in concrete strength. Although lacking constitutive models, the study validates strain-rate-sensitivity theories and offers practical insights for seismic design in cold climates.

2.1.13 Schenker, Anteby, Gal, Kivity, Nizri, Sadot, & Ben-Dor (2008)

Schenker et al. [123] investigated the dynamic behavior of high-strength steel reinforcing bars (HSSRBs) under a wide range of strain rates to evaluate their applicability in structures subjected to extreme dynamic loads such as blasts. The study focused on hot-rolled ribbed steel bars with nominal yield strengths above 600 MPa, commonly used in protective and military-grade structural applications. The experimental campaign covered a broad spectrum of strain rates, from quasi-static conditions (around 10^{-4} s^{-1}) to high dynamic rates exceeding 103 s^{-1}, allowing a detailed assessment of the strain-rate sensitivity of the yield and ultimate strength of the tested materials.

Testing used both servo-hydraulic testing machines for quasi-static conditions and a Split Hopkinson Tension Bar (SHTB) apparatus for high-strain-rate conditions. The experimental setup incorporated advanced measurement techniques, including digital image correlation (DIC), to ensure accurate, homogeneous strain tracking during testing. The results showed a clear increase in both yield and ultimate strength as strain rate increased. Specifically, the dynamic yield strength increased by up to 40% at the highest strain rates tested, while the ultimate strength also increased significantly. These increases occurred alongside a slight reduction in elongation at failure, although the residual ductility remained within acceptable bounds for engineering use.

The authors quantified the dynamic increase in strength using strain-rate-dependent expressions of the general form, consistent with prior models in the literature.

$$DIF = \left(\frac{\dot{\varepsilon}}{\dot{\varepsilon}_0}\right)^{\alpha} \tag{17}$$

However, unlike previous works that provide generalized values for the exponent (α), Schenker et al. derived empirical values based on their data for each bar diameter and steel grade. They did not generalize these into a single formulation but presented them graphically, reinforcing the importance of experimental calibration. The study presented dynamic true stress-strain curves and corresponding DIF plots for both yield and ultimate strengths. A comparison with existing models, such as those by Cowper-Symonds [40] and Malvar-Crawford [80], showed that previously established formulations might underestimate the increase in strength in high-strength steels under dynamic loading.

Moreover, the authors highlighted the strain-rate dependence of the tangent modulus, noting a steeper slope in the initial portions of the dynamic curves compared to their static counterparts. These observations confirm the need to adjust constitutive models used in numerical simulations to account for the specific behavior of high-strength rebars under rapid loading conditions. The findings support implementing strain-rate-dependent material models derived from monotonic tests, especially for applications involving blast or impact loads, where accurate modeling of dynamic strength enhancement is critical.

2.1.14 Dougherty, Cerreta, Gray, Trujillo, López, Vecchio & Kusinski (2009)

Dougherty et al. [44] investigate the mechanical behavior and microstructural evolution of low-carbon (LC) and microcomposite (MC) steels under quasi-static and dynamic shear loading, with strain rates ranging from 0.001 s^{-1} to over 5000 s^{-1}. The work focuses on how the initial

microstructure and strain rate influence shear localization and adiabatic shear band (ASB) formation, phenomena directly tied to constitutive behavior at high strain rates.

The MC steel, composed primarily of lath martensite with small retained austenite fractions, exhibited approximately 1.5 times the compressive strength of LC steel due to its microstructural refinement. Under quasi-static loading, both steels showed similar hardening behavior, but MC steel showed broader shear localization zones, indicating greater stability against low-rate shear. With increasing strain rate, both materials displayed pronounced strain-rate sensitivity; however, the MC steel's higher yield stress delayed but intensified shear localization once initiated.

At high strain rates (>1000 s^{-1}), deformation became increasingly localized, leading to ASB formation driven by dynamic recovery and continuous dynamic recrystallization. The study confirmed that ASB evolution followed the progressive subgrain misorientation (PriSM) model, where subgrain rotation and boundary misorientation increase with strain rate until fine equiaxed grains form. In LC steel, these transformations occurred at higher critical rates and over broader transition zones, whereas in MC steel, lower rates produced sharper ASBs with narrower cores.

The research establishes that the constitutive response of both steels depends strongly on the interaction between microstructural stability, defect mobility, and strain rate. The observed continuous transition from distributed shear to localized shear banding demonstrates that both large strains and high strain rates can destabilize the microstructure by limiting dislocation motion, providing a rate-dependent constitutive basis for ductility loss and failure in high-strength steels.

2.1.15 Asprone, Cadoni & Prota (2009)

Asprone et al. [9] explored the tensile behavior of reinforcing steel bars extracted from an existing bridge, focusing on their response under high strain rates. The primary objective was to evaluate the dynamic tensile properties of aged reinforcement steel at elevated strain rates and to assess whether these materials retain sufficient ductility and strength for reliable structural performance under dynamic actions, such as earthquakes or explosions. This study is particularly relevant for retrofitting or evaluating existing infrastructure, where the actual mechanical properties of in-situ materials can deviate significantly from those of modern, nominally equivalent steels.

The experimental program involved direct tension tests on 14 mm diameter ribbed steel bars in service for over 40 years. Strain rates ranged from quasi-static ($\sim 10^{-3}$ s^{-1}) to high-rate loading conditions reaching approximately 10^{2} s^{-1}, using an SHTB setup for the dynamic tests. True stress-strain relationships were obtained for each strain-rate regime, revealing a clear strain-rate sensitivity in both yield and ultimate strength. The aged steel showed a yield-strength increase of up to 35% at high strain rates compared with the quasi-static baseline, while ultimate strength also increased, though to a slightly lesser extent. Importantly, the strength increase was accompanied by reduced ultimate elongation, highlighting the potential trade-off between strength enhancement and ductility under dynamic loading.

The authors adopted a power-law form to describe DIF as a function of strain rate, consistent with prior literature. The general formulation used is:

$$DIF = \left(\frac{\dot{\varepsilon}}{\dot{\varepsilon}_0}\right)^{\alpha} \quad (18)$$

The reference strain rate ($\dot{\varepsilon}_0$) is typically taken as 10^{-3} s^{-1}, and the exponent (α) is a material-dependent factor determined empirically. Although the authors did not propose a universal value for this exponent, they compared their results with existing models, such as those by Cowper-Symonds [40] and Malvar-Crawford [80]. They showed good agreement within the tested strain-rate range. Notably, the experimental DIF values for aged steel were slightly lower than those reported for modern rebars, potentially reflecting microstructural changes due to aging or differences in original manufacturing.

The variability observed across samples, however, underscores the need for material-specific testing in structural assessment projects involving aged reinforcement.

2.1.16 Cadoni, Fenu & Forni (2012)

Cadoni et al. [19] studied the tensile behavior of austenitic stainless steel reinforcing bars under a wide range of strain rates, from quasi-static to dynamic conditions. Their work aimed to understand the mechanical response of these corrosion-resistant steels under high-strain-rate conditions, such as those encountered in impact or blast scenarios. The research is relevant given the increasing interest in using stainless steel reinforcement in structures where durability is critical, especially under extreme loading conditions.

The experimental campaign was carried out on austenitic stainless steel AISI 304, a non-magnetic, low-carbon variant with high corrosion resistance and notable ductility. The tensile tests were performed using three main testing devices to cover a broad strain-rate range: a traditional universal testing machine for quasi-static tests (10^{-3} s^{-1} to 10^{-1} s^{-1}), a servo-hydraulic testing machine for intermediate strain rates (1 s^{-1} to 100 s^{-1}), and a Split Hopkinson Tension Bar (SHTB) apparatus for high strain rates, reaching up to about 10^{3} s^{-1}.

The results show that austenitic stainless steel exhibits significant strain-rate sensitivity in terms of yield strength, ultimate tensile strength, and uniform strain. Both the yield stress (f_y) and the ultimate tensile strength (f_u) increase with increasing strain rate. DIF quantitatively describes this behavior. The DIF increased with strain rate, confirming the strain-rate sensitivity. The increase was more pronounced in yield stress than in ultimate stress.

2.1.17 Ghannoum, Saouma, Haussmann, Polkinghorne, Eck & Kang (2012)

Ghannoum et al. [53] investigated the impact of loading rates on the seismic behavior of RC columns, focusing on strain-rate effects in reinforcing steel and concrete. The study addresses the scarcity of data on loading-rate phenomena. It proposes an alternative to costly shaking-table tests, using high-velocity, multiactuator setups to test individual RC columns under seismically representative conditions. The research was conducted at the University of Colorado, Boulder, using ten identically designed columns to assess variations in loading rates and protocols.

The columns, constructed with eight 10-mm-diameter longitudinal bars and 3.2-mm-diameter ties, were subjected to an axial load ratio of 0.10, equivalent to 75.6 kN, and lateral displacements at

velocities ranging from 0.25 mm/s (pseudo-static) to 1,016 mm/s (fast cyclic). The concrete had a compressive strength of 33.8 MPa, and the reinforcing steel, ASTM A615 Grade 60, had a yield stress of 414 MPa. Three independently controlled actuators applied axial and transverse loads, with advanced control systems (e.g., an MTS 493 controller and Simulink-based models) managing high-velocity tests. The setup evolved from an L-shaped beam rig for pseudo-static tests to a stiffened configuration for high-velocity tests to mitigate vibrations.

The study's numerical model incorporated strain-rate effects into the material constitutive relationships. For reinforcing steel, the dynamic increase in yield strength with strain rate (e.g., 0.35/s in Test 10) is modeled based on prior research reporting an approximately 28% increase (Malvar [81]). The concrete's tensile and compressive strength variations with strain rate (10^{-2} to 1 s^{-1} during earthquakes) are also considered, though compressive strength gains are minimal. The strain rate effects are detailed as follows:

Experimental results showed a flexure-shear failure mode across all tests, with flexural yielding at about 1% drift ratio and shear failure at 1.75% drift. Fast cyclic tests (254-1016 mm/s) increased the maximum shear demand by 27-33% compared to pseudo-static values, attributed to higher longitudinal bar yield strength at higher strain rates. However, failure modes remained consistent, and lateral stiffness was unaffected pre-yield. Strain-gauge data from Test 10 confirmed a strain rate of 0.35/s, consistent with the observed 28% increase in yield strength. The study notes that peak velocities were only briefly sustained, potentially masking further rate effects, and suggests monotonic ramp tests for future validation.

Theoretically, the research advances constitutive models by linking strain-rate effects to reinforcing-steel behavior, thereby improving predictions of seismic performance. In practice, the increased shear demand at higher rates highlights the need to reassess seismic design codes, which may be conservative for short-duration loading but unconservative for long-duration cyclic loading. The multiactuator setup offers a cost-effective alternative to shaking table tests and can refine collapse-hazard mitigation for flexure-shear-critical columns. The authors conclude that further tests are needed to validate these findings across diverse column types, emphasizing the critical role of strain rate effects in seismic assessment.

2.1.18 Levings, J., & Sritharan, S. (2012)

Levings et al. [73] investigated the effects of low temperatures and strain rates on the stress-strain behavior of ASTM A706 Grade 420 (60) mild steel reinforcement, a material increasingly used in seismic regions due to its ductility and weldability. The study aimed to improve the design of structures exposed to seasonal freezing, particularly bridges in seismic zones, by quantifying how temperature and strain rate affect key mechanical properties. This work addresses a critical gap in the literature, as limited prior research has examined this steel grade under the combined influence of cold temperatures and dynamic loading.

The methodology combined experimental and analytical approaches. Monotonic tensile tests were performed on 19 mm and 25 mm diameter bars using an MTS fatigue machine within an environmental chamber set at 20°C, 5°C, -1°C, -20°C, and -40°C. To isolate temperature effects, tests used strain rates of 0.001896/min (up to 1% strain) and 0.275/min thereafter. Additional tests at -1°C and -20°C used strain rates of 0.003, 0.03, and 0.3/min to assess rate dependence.

Specimens were milled to ensure uniform failure within the gauge length, with aluminum sleeves and machined ends mitigating gripping issues. High-frequency data acquisition (over 300 points per minute) enabled detailed stress-strain curves, from which yield strength, ultimate strength, and strain-hardening onset were determined using best-fit techniques. Numerical validation was performed using the Dodd-Restrepo model [43].

The results indicate that both yield and ultimate strengths increase as temperature decreases and strain rate increases. Specifically, yield strength rose by 5.1%, and ultimate strength by 6.3%, as the temperature dropped from 20°C to -40°C. These trends followed quadratic relationships:

$$\begin{aligned} \Delta f_y(\%) &= 0.0009(T)^2 - 0.0674(T) + 0.9880 \quad \text{with } T \text{ in °C} \\ \Delta f_u(\%) &= 0.0007(T)^2 - 0.0912(T) + 1.5440 \quad \text{with } T \text{ in °C} \end{aligned} \tag{19}$$

Where the temperature (T) is in °C; for strain rates between 0.003 and 0.3/min, yield strength increased by 3%, and ultimate strength by 1.67%, with more pronounced effects observed at -20°C. Additionally, the yield plateau shortened by 34.7% (0.00084 strain) at the highest rate and was eliminated at elevated rates, whereas the elastic modulus and ultimate strain remained largely unaffected. Bar diameter exhibited a minor influence, with larger bars showing slightly greater strength enhancements.

The Dodd-Restrepo model effectively captures temperature effects but lacks an explicit formulation of strain-rate sensitivity. The authors indirectly incorporated dynamic effects by adjusting strength values with temperature, resulting in reasonable agreement with experimental data. However, the absence of a strain-rate-dependent term limits the model's applicability to dynamic analyses. The results are interpreted through the lens of viscous-effect theory, suggesting that strength gains at strain rates below 0.3/min are attributable to material viscosity rather than inertia.
Practically, the findings reinforce the value of the Dodd-Restrepo model for predicting reinforcing steel behavior in cold climates, particularly in seismic design applications. However, its current form is insufficient for simulating rapid loading, such as during earthquakes. The authors advocate that future developments explicitly incorporate rate effects to enhance the model's accuracy for dynamic structural analysis.

The observed logarithmic strain-rate dependency and temperature-rate interaction underscore the need to integrate both effects into seismic design provisions for cold-climate bridges, an aspect ACI 318-08 [3] does not address.

2.1.19 Zhang, Li & Shang (2012)

Zhang et al. [148] investigated the seismic response of RC structures, emphasizing strain-rate effects in concrete and reinforcing steel. A 1/5-scale three-story frame-wall specimen was tested on a shaking table, and a finite element model was developed and validated in ABAQUS using fiber beam elements discretized into concrete and steel fibers. Concrete behavior was represented by uniaxial stress-strain relations with damage parameters for degradation, while reinforcing steel was modeled with a bilinear kinematic hardening formulation that reproduced yielding, strain

hardening, and the Bauschinger effect, with a post-yield slope equal to 0.01 times the elastic modulus.

Concrete's uniaxial tensile stress-strain relationship was defined as:

$$\sigma = (1 - d_t)E_c\varepsilon \tag{20}$$

$$d_t = 1 - \rho_t[1.2 - 0.2x^5] \qquad x \leq 1$$

$$d_t = 1 - \frac{\rho_t}{\alpha_t(x-1)^{1.7} + x} \qquad x > 1$$

$$x = \varepsilon/\varepsilon_{t,r} \qquad \rho_t = f_{t,r}/(E_c.\varepsilon_{t,r})$$

Where,

d_t: The tensile damage parameter.
α_t: The parameter of the descending portion.
$f_{t,r}$: The uniaxial compressive strength.
$\varepsilon_{t,r}$: The strain at peak stress.
E_c: The elastic modulus.

Concrete's uniaxial compressive stress-strain relationship was defined as:

$$\sigma = (1 - d_c)E_c\varepsilon$$

$$d_c = 1 - \frac{\rho_c n}{n - 1 + x^n} \qquad x \leq 1$$

$$d_t = 1 - \frac{\rho_c}{\alpha_c(x-1)^2 + x} \qquad x > 1 \tag{21}$$

$$x = \varepsilon/\varepsilon_{c,r} \qquad \rho_c = f_{c,r}/(E_c.\varepsilon_{c,r})$$

$$n = E_c.\varepsilon_{c,r}/(E_c.\varepsilon_{c,r} - f_{c,r})$$

Where,

d_c: The uniaxial compressive damage parameter.
α_c: The parameter of the descending portion of the uniaxial compressive stress-strain curve.
$f_{c,r}$: The uniaxial compressive strength.
$\varepsilon_{c,r}$: The strain at peak stress.
E_c: The elastic modulus.

Strain-rate effects were incorporated as strength increments during dynamic loading. For micro-concrete:

$$\frac{{f_c}^d}{{f_c}^s} = 0.9892 + 0.08607 \log\left(\frac{\dot{\varepsilon}_d}{\dot{\varepsilon}_s}\right) \quad (22)$$

Where,

${f_c}^d$: The dynamic strength.

${f_c}^s$: The static strength.

$\dot{\varepsilon}_d$: The strain rate.

$\dot{\varepsilon}_s$: The quasi-static strain rate is 10^{-5} s^{-1}.

For galvanized wires, the increments of the yield strength (f_{yd}/f_{ys}) and the tensile strength (f_{ud}/f_{us}) are:

$$\frac{f_{yd}}{f_{ys}} = 1 + 0.0456 \log\left(\frac{\dot{\varepsilon}_w}{\dot{\varepsilon}_{w0}}\right)$$
$$\frac{f_{ud}}{f_{us}} = 1 + 0.0212 \log\left(\frac{\dot{\varepsilon}_w}{\dot{\varepsilon}_{w0}}\right) \quad (23)$$

Where,

$\dot{\varepsilon}_w$: The strain rate.

$\dot{\varepsilon}_{w0}$: The quasi-static strain rate is 2.5×10^{-4} s^{-1}.

f_{yd}, f_{ys}: The dynamic and static yield strengths.

f_{ud}, f_{us}: The dynamic and static tensile strengths.

Numerical simulations closely matched the experimental acceleration, displacement, and torsional time histories, with the first natural frequency predicted at 4.407 Hz, compared with the experimental value of 4.425 Hz. The study shows that strain-rate effects substantially affect the stiffness, strength, and ductility of RC structures. Incorporating these effects into constitutive models enhances predictive accuracy for nonlinear time-history analyses, providing a robust framework for seismic design of RC frame-wall systems.

2.1.20 Cadoni & Forni (2015)

Cadoni et al. [20] investigated the strain-rate sensitivity of European reinforcing steels B500A, B500B, and B500C under tensile loading across 10^{-3} to 10^{3} s^{-1}. The study aims to accurately characterize the dynamic mechanical properties of RC structures under seismic, impact, or blast loading, addressing limited existing data. Cylindrical specimens were extracted from rebars using turning (B500A/B) and wire EDM (B500C, accounting for its hardened outer, intermediate, and soft-core layers). Quasi-static tests (10^{-3} s^{-1}) employed a Zwick/Roell-Z50 machine; intermediate rates (5-25 s^{-1}) used a hydro-pneumatic setup; high rates (250-1000 s^{-1}) utilized a split-Hopkinson tension bar. Stress-strain responses, including yield strength, ultimate tensile strength (UTS),

uniform strain, and fracture strain, were determined, weighting B500C results by layer contribution.

Two constitutive models were calibrated: Cowper-Symonds (B500A: D=141917, q=2.816; B500B: D=599, q=0.753), capturing strain-rate-dependent yield stress, and Johnson-Cook (excluding thermal softening; B500A: A=564 MPa, B=946 MPa, n=0.875, C=0.01769; B500B: A=571 MPa, B=643 MPa, n=0.720, C=0.02139), predicting flow stress. Experimental results confirmed strong strain-rate dependence: yield strength and UTS increased with strain rate for all steels. B500A and B500B maintained high ductility dynamically, whereas B500C's ductility decreased at high rates due to its composite microstructure. The core material of B500C exhibited larger increases in fracture strain, consistent with its softer nature. Both constitutive models accurately represented observed behaviors.

The calibrated models enable finite element analyses compatible with EN 10080 and fib Model Code 2010. However, the reduced ductility of B500C at high rates indicates a risk of brittle failure and warrants design adjustments.

2.1.21 Cadoni, Dotta, Forni & Tesio (2015)

Cadoni et al. [21] analyzed the strain-rate sensitivity of cold-drawn B500A reinforcing steel (6-10 mm diameter) under tensile loading up to 1000 s^{-1}, revealing substantial increases in yield, ultimate, and fracture strength with rising strain rate. These enhancements, relevant for seismic ($\approx 10^2$ s^{-1}) and blast design, indicate improved energy dissipation and ductility in RC elements under rapid loading, though reduced ductility in smaller diameters reflects cold-drawing effects.

Dynamic tests using a split-Hopkinson tension bar and high-speed imaging accurately captured the true stress-strain behavior, including necking, and were validated via Bridgman's correction. Results confirmed linear post-necking trends, enabling reliable constitutive calibration.

The study calibrated the CS and JC models. The former, efficient for implementation in finite element codes, captured strain-rate-dependent yielding; the latter, incorporating isotropic hardening and potential thermal effects, described flow behavior across loading regimes. Parameter sets were diameter-specific, linking microstructural strain hardening to geometric scale.

Existing DIF formulations (Malvar, CEB) were inadequate beyond 10 s^{-1}; the authors proposed a reformulation to extend predictive validity for blast rates. Gaps were noted in high-rate shear and bond-slip behavior, which are critical for assessing brittle transitions and anchorage performance.

2.1.22 Lin, Dong, Kuang & Lu (2016)

Lin et al. [75] quantified the strain-rate sensitivity of hot-rolled reinforcing steels HPB235, HRB335, HRB400, and HRB500 at tensile rates ranging from 2 to 75 s^{-1}, establishing empirical models for the dynamic design of RC structures. Dumbbell-shaped specimens were tested quasi-statically ($\leq 3\times10^{-4}$ s^{-1}) and dynamically using a servo-hydraulic system, with a real-time laser extensometer and SEM fracture analysis confirming ductile failure.

Dynamic increases in yield and ultimate strengths reached 13-41% and 9-19%, respectively, without changes in elastic modulus. The lowest-strength grade, HPB235, exhibited the highest rate

sensitivity. Yield DIFs consistently exceeded ultimate DIFs, indicating that strain-rate effects primarily influence yielding.

The study derived empirical logarithmic relations for DIFs:

$$\frac{f_{y,d}}{f_{y,st}} = 1 + \frac{D_1}{f_{y,st}} \ln\left(\frac{\dot{\varepsilon}}{\dot{\varepsilon}_0}\right)$$
$$\frac{f_{u,d}}{f_{u,st}} = 1 + \frac{D_2}{f_{u,st}} \ln\left(\frac{\dot{\varepsilon}}{\dot{\varepsilon}_0}\right) \quad (24)$$

Where,

D_1, D_2 The empirical coefficients (obtained through linear regression).

$f_{y,d}$, $f_{y,st}$: The dynamic and quasi-static yield strengths, respectively.

$f_{u,d}$, $f_{u,st}$: The dynamic and quasi-static ultimate strengths, respectively.

$\dot{\varepsilon}$: The applied strain rate.

$\dot{\varepsilon}_0$: The reference quasi-static strain rate equals $3\text{x}10^{-4}$ s^{-1}

Coefficients D_1: 10.05, 8.73, 8.72, and 9.72 MPa, and D_2: 6.38, 6.54, 6.54, and 7.78 MPa for HPB235-HRB500 were obtained by regression analysis. The Johnson-Cook model, excluding thermal softening, was also calibrated, with parameters that accurately reproduced flow stress up to 75 s^{-1} with ≤21% error.

The results confirm consistent strain-rate hardening across all grades, validating the proposed DIF and the JC formulations for seismic and impact modeling. The data correct overestimations from earlier expressions, such as Malvar's, and extend applicability beyond 10 s^{-1}. Enhanced strength at elevated rates improves the bending and shear capacity of RC elements, supporting performance-based design for bridges, nuclear containments, and protective facilities. The data fill a material-specific gap for Chinese rebar grades, though thermal, shear, and bond-rate effects remain unaddressed.

2.1.23 Khonsari, England, Shabani & Shsavar (2017)

Khonsari et al. [66] quantified the strain-rate sensitivity of A-III (A400) steel rebars under monotonic tensile and compressive loading at 0.002-0.04 s^{-1}. Tensile tests on 20 mm bars showed yield stress increases of 4.5% and ultimate stress increases of 0.9% with strain rate, yield strain rising by 113%, and ductility decreasing by 64%; elastic modulus remained constant. Compressive tests revealed buckling-induced reductions in critical load up to 11% for slender specimens, with negligible effects for short, buckling-resistant specimens.

The DIF for yield stress is expressed as:

$$K_y = 1.12\dot{\varepsilon}^{0.012}$$
$$K_u = 1.077\dot{\varepsilon}^{0.0077} \quad (25)$$

And for flexural moment capacity:

$$DIF_{moment} = \frac{K_y}{K_c}\left\{\frac{\left[\left(2\alpha_{cc}\eta f_{ck,st}\right)/\gamma_c\right] - \rho K_y f_y}{\left[\left(2\alpha_{cc}\eta f_{ck,st}\right)/\gamma_c\right] - \rho f_y}\right\} \tag{26}$$

Where the factor, K_y, is defined in (25), and the factor K_c, as follows:

$$K_c = \left(\frac{\dot{\varepsilon}}{\dot{\varepsilon}_s}\right)^{\alpha} \qquad \text{for } \dot{\varepsilon}_s = 5x10^{-5}\ s^{-1} \le \dot{\varepsilon} \le 50\ s^{-1}$$
$$\alpha = 0.228\left(f_{ck,st}\right)^{-0.7} \tag{27}$$

Where,

$f_{ck,st}$: (static) compressive strength of concrete [18]
f_y: Yield stress of steel bars
α_{cc}: The coefficient accounts for the long-term effects on compressive strength and for unfavorable effects arising from the load application method.
γ_c: Partial safety factor for concrete.
η: Effective strength coefficient.
ρ: Tension reinforcement ratio in members.

Results confirm A-III's limited rate sensitivity relative to ASTM A615, with enhanced rebar strength improving RC flexural and shear capacity under seismic loading. At the same time, ductility loss can shift failure toward brittle modes. DIFs increase with strain rate and reinforcement ratio, and decrease with concrete strength. These calibrated constitutive relations enable accurate finite element analysis (FEA) and performance-based design for earthquake-resistant RC structures, informing retrofitting and seismic code applications.

2.1.24 Cadoni, Fontana, Forni & Knobloch (2018)

Cadoni et al. [22] investigated the coupled effects of high strain rates (250-800 s^{-1}) and elevated temperatures (20-600 °C) on B500B reinforcing steel under tensile loading. Quasi-static tests (33×10^{-6}-167×10^{-6} s^{-1}) and SHTB dynamic tests with water-cooled induction heating were performed, measuring stress, strain, and strain rate via one-dimensional wave propagation.

Results show that strain-rate hardening increases yield and ultimate strength at room temperature (up to 23% at 800 s^{-1}), whereas elevated temperatures reduce strength and ductility, especially above 400 °C. Uniform strain, fracture strain, and reduction of area decrease with temperature, though partial recovery occurs at high strain rates due to thermal activation.

Constitutive calibration employed the JC and CS models. The JC model parameters (strain-hardening n≈0.72, rate sensitivity C≈0.021, thermal softening exponent m=(0.92-1.35) vary significantly with strain rate and temperature, demonstrating that fixed parameters yield inaccurate predictions. The CS model (D, q) similarly requires temperature-dependent calibration. Derived

quantities, including modulus of toughness and strain-hardening rate, decrease with temperature but increase with strain rate during early plastic deformation. Bridgman correction and fractography validated true stress-strain curves to fracture.

The study confirms B500B exhibits nonlinear interactions between strain rate and temperature, necessitating rate- and temperature-dependent constitutive formulations for accurate FEA and design under multi-hazard conditions, such as fire followed by blast or impact. These calibrated models support advanced performance-based design of RC structures exposed to extreme dynamic and thermal loading.

2.1.25 Zeng, Huo, Wang, Wang & Elchalakani (2020)

Zeng et al. [144] evaluated the strain-rate sensitivity of HRB500E reinforcing steel over 0.00025-550 s^{-1}, quantifying dynamic tensile behavior for seismic, impact, and blast-resistant design. Tests on 12 mm bars showed that yield stress increased from 567 MPa to 721 MPa (27.2%) and ultimate strength from 781 MPa to 886 MPa (13.4%) with increasing strain rate; uniform elongation varied non-monotonically, generally decreasing at the highest rates.

Constitutive calibration employed the Cowper-Symonds, Malvar, Mander, and Johnson-Cook models. The proposed rate-dependent model expresses flow stress as:

$$\sigma = A.DIF_y + B\left(\varepsilon_p\right)^n.\overline{f(\dot{\varepsilon}^*)} \tag{28}$$

Parameters (A, B, and n) represent the same meanings as those in the Johnson-Cook (JC) Model [63]. At a certain strain rate, the flow stress at any plastic strain (ε_p), is the summation of yield stress $\left(A.DIF_y\right)$ and plastic part of the stress $\left(\left(\varepsilon_p\right)^n.\overline{f(\dot{\varepsilon}^*)}\right)$. DIF_y can be calculated using the CS model [40] or the Malvar-Crawford model [80]. $f(\dot{\varepsilon}^*)$ is a function of strain rate and represents the average effect of strain rate $\dot{\varepsilon}$. This model is determined by the average of $f(\dot{\varepsilon}^*)$, which denotes the ratio of dynamic flow stress to quasi-static flow stress (the stress excluding $A.DIF_y$) at the same plastic strain, ε_p, under the strain rate of $\dot{\varepsilon}$. $f(\dot{\varepsilon}^*)$.

$$f(\dot{\varepsilon}^*) = \frac{\sigma - A.DIF_y}{B\left(\varepsilon_p\right)^n} \tag{29}$$

Under quasi-static loading, DIF_y and $\overline{f(\dot{\varepsilon}^*)}$ are equal to 1 in Eq. (28); hence, it becomes Eq. (30), which describes the quasi-static curve.

$$\sigma = A + B\left(\varepsilon_p\right)^n \tag{30}$$

Strain-rate dependence of DIF_y is nonlinear over wide ranges, necessitating broad-range dynamic calibration; standard CS and Malvar models are inaccurate outside limited domains. The Mander model with strain-rate-dependent exponent P improves hardening predictions. The calibrated

models accurately capture full stress-strain response and yield behavior, supporting numerical simulations and design of RC elements under extreme dynamic loads.

2.1.26 Zeng, Wang & Huo (2020)

Zeng et al. [145] characterized the strain-rate-dependent tensile behavior of HRB400E reinforcing steel across 0.00025-870 s^{-1}. Yield stress and ultimate strength increased nonlinearly with strain rate, while the strain-hardening onset shifted at higher rates. Standard DIF models (CS [40], Malvar-Crawford [80]) were inadequate across the full range; modified versions, including a logarithmic strain-rate dependence for Malvar's exponent, improved predictive accuracy by up to 3.2%. A rate-dependent Mander model captured the full engineering stress-strain response using a strain-rate-dependent exponent.

$$P = -0.0669 \ln\left(\frac{\dot{\varepsilon}}{\dot{\varepsilon}_s}\right) + 4.0449 \tag{31}$$

True stress-plastic strain behavior was modeled with a new constitutive relation:

$$\sigma = A.DIF_y + \left(A_1\varepsilon_p + B_1\left(1 - \left(-\beta\varepsilon_p\right)\right)\right)\left(1 - f(\dot{\varepsilon}^*)\right) \tag{32}$$

Where,

A: The initial hardening stress.
A_1, B_1: Coefficients controlling linear and exponential hardening.
β: The shape parameter.
$f(\dot{\varepsilon}^*)$: The logarithmic rate function fitted as $f(\dot{\varepsilon}^*) = 0.00473 \ln(\dot{\varepsilon}^*)$.

Calibrated experimental data, combining strain hardening and rate sensitivity. The Johnson-Cook model performed well at low rates but failed at high rates. The modified constitutive models provide accurate inputs for finite element simulations and performance-based seismic design, enabling reliable prediction of dynamic response in RC structures.

Zeng et al. demonstrate that HRB400E reinforcing steel exhibits strong strain-rate sensitivity, with yield and ultimate strengths increasing and the onset of strain hardening shifting at higher rates. Modified constitutive models for engineering and true stress-strain responses accurately capture these effects, enabling implementation in finite element analyses for nonlinear dynamic simulations. The proposed DIFs and rate-dependent formulations provide robust predictive tools for seismic- and impact-resistant RC design, improving the precision of performance-based engineering and enabling reliable assessment of structural behavior under extreme dynamic loading.

2.1.27 Cadoni & Forni (2021)

Cadoni et al. [23] examined the high strain rate and thermal response of cold-worked B500A reinforcing steel to quantify its constitutive behavior under combined fire and blast conditions. Using Split Hopkinson Tensile Bar tests across 20-600 °C and strain rates from 0.001 to 900 s^{-1},

they identified moderate rate sensitivity and pronounced thermal softening. Yield strength rose from 559 MPa to 623 MPa with increasing rate, but dropped sharply above 400 °C, while ductility diminished with increasing temperature. The CS (D=704328 s^{-1}, q=3.6234) and JC (A=564 MPa, B=946 MPa, m=0.859-0.927) models were calibrated to describe rate- and temperature-dependent stress-strain responses. The CS model captured rate effects accurately, whereas JC underestimated strength at 600 °C because it did not account for combined degradation mechanisms. A modified CS formulation incorporating thermal softening factors improved strength-yield prediction.

The results confirm that the quasi-static assumptions of standard design codes are inadequate for high-rate, high-temperature scenarios. The proposed constitutive relations provide reliable parameters for nonlinear finite element simulations, enabling more accurate modeling of RC structures exposed to blast or fire and strengthening the predictive framework for performance-based seismic and protective design.

2.1.28 Zeng & Huo (2023)

Zeng et al. [146] investigated the strain-rate sensitivity of high-strength reinforcing steel HTRB600E under tensile loading over a strain rate range of 0.00025 s^{-1} to 590 s^{-1}. HTRB600E, a heat-treated ribbed steel with nominal yield strength ≥600 MPa, exhibits high ductility and corrosion resistance, making it suitable for dynamic loading conditions. The research aimed to quantify rate-dependent mechanical properties and develop constitutive formulations describing engineering and true stress-strain relationships, including post-necking behavior.

Monotonic tensile tests were conducted from quasi-static to high strain rates in accordance with ISO 26203-2:2011 and ASTM E8/E8M-16a, using digital image correlation (DIC) and high-speed imaging to measure strain. Results confirmed a clear rate dependency: yield strength increased from 636 MPa to 743 MPa and ultimate strength from 865 MPa to 993 MPa (DIF≈1.16 and 1.15, respectively). Ductility remained stable (≈11% uniform elongation), and the yield-to-tensile ratio stayed below 0.8.

Existing DIF models (logarithmic [38], CS [40], and Malvar-Crawford [80]) were recalibrated; only a modified CS model reproduced experimental trends with deviations below 1.5%. Two rate-dependent constitutive models were proposed. The first, based on a bilinear Mander-type formulation, captures the elastic, yield, and strain-hardening phases with strain-rate-dependent transition strain and constant hardening exponent (P≈2.99), effectively reproducing the loss of the yield plateau at high rates. The second describes true stress-plastic strain behavior using a piecewise Voce-type law with strain-rate-sensitive coefficients, achieving predictive errors below 1.5%.

A refined model was further obtained through an inverse calibration procedure in ABAQUS, extending prediction beyond necking via a Voce-type saturation law incorporating a strain-rate function, $\varphi(\dot{\varepsilon})$. This hybrid formulation reproduces the full deformation range and remains consistent with experimental force-displacement curves.

2.2 Research Work on Cyclic Constitutive Models

The development of cyclic constitutive models for reinforcing steel under dynamic loading has become increasingly important in recent years, particularly for seismic design and performance-

based assessment. Unlike monotonic models, which are primarily derived from unidirectional tensile tests, cyclic models aim to capture the complex hysteretic behavior of steel under repeated loading and unloading, including the Bauschinger effect, cyclic hardening or softening, stiffness degradation, and energy dissipation.

Various modeling approaches have been proposed to incorporate these cyclic effects, ranging from phenomenological formulations based on empirical hysteresis rules to more advanced models grounded in plasticity theory and internal state variables. Incorporating strain rate sensitivity into these models remains a significant challenge, as the interaction between loading rate and cyclic behavior is not straightforward. Experimental studies show that strain rate can modify not only strength parameters but also the shape and amplitude of hysteresis loops, affecting overall energy dissipation and structural response.

Despite these complexities, researchers have extended monotonic rate-dependent models to cyclic conditions by introducing rate-sensitive evolution laws or modifying existing hysteresis rules. However, comprehensive experimental data under controlled cyclic loading at different strain rates remain limited, which constrains model calibration and validation. Consequently, many existing cyclic models either neglect strain-rate effects or incorporate them in a simplified manner. Addressing this gap is critical for improving the reliability of numerical simulations and enhancing the seismic resilience of RC structures.

2.2.1 Ramberg & Osgood (1943)

Ramberg and Osgood [111] introduced a phenomenological model to represent the continuous transition from elastic to plastic behavior in metals through a compact analytical expression governed by three physically meaningful parameters. Their formulation addresses the limitations of elastic-perfectly plastic and bilinear laws in capturing the smooth yielding typical of high-strength alloys and structural steels. The model expresses total strain as the sum of elastic and nonlinear components:

$$\frac{\varepsilon}{\sigma} = \frac{1}{E} + K\left(\frac{\sigma}{E}\right)^{n} \tag{33}$$

Where,

- E: The Young's modulus.
- K, n: Material parameters that characterize the nonlinear portion of the stress-strain curve.
- ε: The total strain.
- σ: The stress.

Where E is the Young's modulus, K, a scaling nonlinear strain contribution coefficient, and n, an exponent describing the curvature of the stress-strain response; high n values indicate sharp yielding, while low $n$values describe gradual transitions. The nonlinear term modifies Hooke's law to account for progressive deviation from linearity as stress increases.

The parameters K and n are determined from two secant yield strengths, s_1 and s_2, corresponding to predefined fractions of the elastic modulus (m_1E and m_2E). The exponent n is obtained as:

$$n = 1 + \frac{\log\left(\frac{1-m_1}{1-m_2}\right)}{\log\left(\frac{s_2}{s_1}\right)} \tag{34}$$

This expression defines the curve's curvature directly from measurable data. Once n is known, K follows by substitution, allowing the full nonlinear stress-strain relationship to be reconstructed with minimal experimental input.

The tangent modulus E_t, representing instantaneous stiffness and showing stiffness degradation as yielding progresses, is derived as:

$$\frac{\sigma}{E_t} = \frac{1}{E} + nK\left(\frac{\sigma}{E}\right)^{n-1} \tag{35}$$

A reduced modulus E_r is also introduced to approximate effective stiffness loss for buckling analyses, defined as a function of E_t.

$$E_r = \frac{4EE_r}{E + E_t} \tag{36}$$

Validation against experimental results for carbon steels, aluminum alloys, and stainless steels demonstrated the model's accuracy in both tension and compression up to stresses near 90% of the elastic limit. The smooth transition between elastic and plastic regions enables a more precise representation of metals that exhibit nonlinear hardening, unlike idealized bilinear models.

Its differentiable form and physically interpretable parameters have facilitated widespread implementation in finite element codes and enabled subsequent extensions that incorporate strain-rate and temperature dependence.

2.2.2 Kent & Park (1973)

Kent and Park [65] systematically investigated the cyclic stress-strain behavior of mild reinforcing steel, emphasizing how load reversals affect its mechanical response. Through quasi-static tensile and compressive tests on deformed bars (12.7-22.2 mm), they captured the full hysteretic behavior of the material under alternating tension-compression loading representative of seismic demand.

Their experiments revealed a pronounced Bauschinger effect, evidenced by a marked reduction in yield strength upon stress reversal after plastic deformation. While unloading and reloading in the same direction followed approximately elastic paths, reversed loading produced early yielding and nonlinear reloading paths, invalidating monotonic stress-strain relationships for cyclic conditions. The results showed that the steel's response is path-dependent: under the same-sign loading, the

stress-strain curve returns to the monotonic envelope, but under reversals, the mechanical history determines the subsequent stiffness and strength.

Initially, Kent and Park examined the exponential model of Singh et al., which defines the stress as:

$$f_s = f_y + (f_{su} - f_y)(1 - \alpha^{\varepsilon}) \tag{37}$$

Where α is a fitting constant derived from reversed loading paths, and ε is the strain. This proposal failed to reproduce the effects of prior plastic strain and load history. They therefore reformulated the constitutive law using a Ramberg-Osgood-type expression (section 2.2.1):

$$\frac{\varepsilon_s}{\varepsilon_{ch}} = \frac{f_s}{f_{ch}}\left[1 + \left(\frac{f_s}{f_{ch}}\right)^{r-1}\right] \tag{38}$$

Where,

f_s: The stress.
f_{ch}: The characteristic stress parameter.
r: The shape-controlling Ramberg-Osgood exponent.
ε_s: The total strain.
ε_{ch}: The characteristic strain parameter.

The initial elastic modulus (E_s) is related to the characteristic parameters by:

$$f_{ch} = E_s \varepsilon_{ch} \tag{39}$$

This formulation provides a continuous transition from the elastic to the plastic regime and effectively captures cyclic nonlinearity.

Both key parameters-f_{ch} and r-were modeled as functions of the material's deformation history. The characteristic stress decays exponentially with prior inelastic strain, ε_{ip}:

$$\frac{f_{ch}}{f_y} = 1 - A(1 - e^{-B\varepsilon_{ip}}) \tag{40}$$

While $r$evolves with the number of reversals n, reflecting cyclic hardening effects:

$$r = -0.469 + \frac{3.04}{\log_e(1 + i)} \quad \text{(odd cycles)} \tag{41}$$

$$r = -0.303 + \frac{4.49}{\log_e(1+n)} \quad \text{(even cycles)} \tag{42}$$

Regression constants A and B were calibrated from test data, producing an accurate match to the observed hysteretic loops of 11 specimens. The model achieved significantly lower prediction errors than the Singh et al. expression, particularly in moderate strain ranges.

Validation through moment-curvature analyses of RC sections confirmed the model's ability to reproduce the cyclic hysteresis and energy dissipation governed by the steel's inelastic behavior. The results underscore that the Bauschinger effect and cyclic stiffness evolution control post-yield performance in RC members, directly affecting ductility and energy absorption.

Although the experiments were performed under quasi-static conditions, the authors noted the potential influence of rate- and temperature-dependent mechanisms beyond the formulation's scope.

2.2.3 Menegotto-Pinto (1973)

Menegotto and Pinto [89] developed a phenomenological constitutive model for reinforcing steel under cyclic loading that remains foundational in nonlinear modeling of RC structures. The model addressed limitations of traditional monotonic stress-strain laws by introducing a continuous formulation that reproduces stiffness degradation, cyclic hardening or softening, and the Bauschinger effect. Built on the Ramberg-Osgood framework, it defines a smooth, nonlinear stress-strain relationship that transitions from elastic to plastic behavior while maintaining continuity under load reversals.

A principal innovation is the evolution of the curvature parameter R, which governs the transition sharpness. Instead of being constant, R varies with strain history through a logarithmic law as follows:

$$R = R_0 - a.\ln(1 + b.\zeta) \tag{43}$$

Where,

a, b: The empirically calibrated constants.
R_0: The initial curvature parameter (typically around 20).
ζ: Accumulated plasticity.

This mechanism enables progressive softening of the hysteretic loops, reflecting the material's memory and cyclic degradation. The model defines unloading and reloading paths with elastic slopes that intersect the reloading curve at pivot points derived from the prior loading branch, thereby ensuring path continuity and realistic cyclic hysteresis.

Despite its accuracy in reproducing quasi-static cyclic behavior, the Menegotto-Pinto model omits explicit strain-rate dependence. All parameters are calibrated under low-rate experimental conditions, assuming time-independent plasticity. The absence of rate-sensitive terms limits its

applicability to dynamic regimes with rapid strain variations. However, later formulations have introduced rate-dependent modifications by linking b or R to the strain rate.

The formulation has been widely adopted in finite element and fiber-section analyses of RC components. However, it remains constrained to quasi-static conditions because it lacks rate-sensitive terms.

2.2.4 Mander (1983)

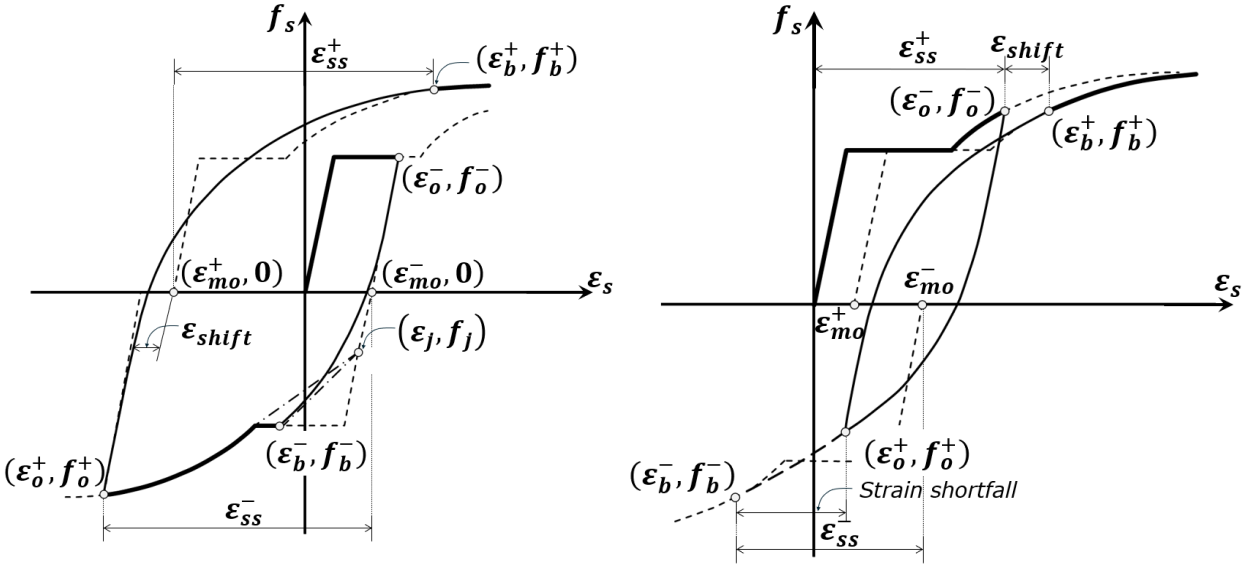
Mander [82] proposed an analytical constitutive model to reproduce the cyclic stress-strain response of reinforcing steel, emphasizing path dependence, stiffness degradation, and the Bauschinger effect. The model extends the Menegotto-Pinto formulation by introducing explicit shift and reattachment mechanisms that describe how load reversals alter the material's effective origin and tangent stiffness. Each reversal generates a new local coordinate system defined by residual stresses and strains, ensuring continuity with the preceding branch and preserving material memory through strain-dependent shift functions.

When a reversal occurs, the origin shift (ε_{shift}) is determined by the strain history, distinguishing between elastic-plastic transitions within the yield plateau and those that extend into the strain-hardening region. For small plastic excursions ($|\ \varepsilon_{max}\ | < |\ \varepsilon_{sh}\ |$), the shift depends linearly on the strain gap between reversal and skeleton points, while for large excursions ($|\ \varepsilon_{max}\ | > |\ \varepsilon_{sh}\ |$). A correction term proportional to the yield stress accounts for strength degradation. These expressions allow geometric and energetic consistency, enabling the reversed branches to reproduce realistic hysteretic loops and cumulative softening.

The reversed branch is governed by a modified Menegotto-Pinto equation [89], introducing parameters Q, R, and f_{ch} to control post-yield stiffness, curvature, and characteristic stress, respectively. The constitutive relation maintains tangency at the junction point, ensuring a smooth transition from the unloading path to the reloading curve. The curvature parameter R determines the degree of nonlinearity, with low values yielding smooth hyperbolic transitions and high values approaching bilinearity. The model explicitly defines the secant and tangent moduli, maintaining thermodynamic admissibility and differentiability throughout the cycle.

Mander's approach formalizes control-parameter computation through an iterative numerical scheme. It begins by identifying the reversal type (from skeleton or softened branch, see Figure 4), computes the tangent modulus based on the yield or hardening region, derives the characteristic stress enforcing tangency, and iteratively adjusts Q, E_m, and R until convergence of the tangent modulus is achieved. This algorithmic process ensures stress-strain continuity and that the cyclic response evolves realistically with successive load reversals. The model integrates stiffness reduction, residual strain accumulation, and strength loss within a consistent phenomenological framework. Unlike purely empirical hysteretic laws, it derives parameter evolution directly from mechanical relations between stress, strain, and plastic history. The softened Menegotto-Pinto form guarantees numerical stability and allows straightforward calibration from monotonic test data. Although the model was formulated under quasi-static conditions and does not include explicit rate sensitivity, its structure can accommodate strain-rate dependence by extending the parameters (E_m, R, or Q) as functions of the strain-rate parameter. Consequently, Mander's formulation serves as a

physically grounded reference for cyclic constitutive modeling of reinforcing steel. It can reproduce stiffness degradation, energy dissipation, and memory effects that dominate under seismic loading.



a) Skeleton branch b) Softened branch

Figure 3. Reversals in the reinforcing bar cyclic response.

2.2.5 Monti & Nuti (1992)

Monti and Nuti [93] formulated a nonlinear constitutive model to describe the cyclic behavior of reinforcing steel bars, explicitly accounting for inelastic buckling. Experimental tests on FeB44 steel under various slenderness ratios (L/D=5, 8, 11) demonstrated that when $L/D > 5$, inelastic buckling induces pronounced post-yield softening in compression, while tension remains largely unaffected. The experimental evidence established a critical slenderness ratio, $(L/D)_{cr} = 5$, marking the onset of instability. Beyond this limit, compressive stiffness and stress capacity degrade according to the empirical laws:

$$b^- = a\left[\left(\frac{L}{D}\right)_{cr} - \frac{L}{D}\right] \qquad for\ \frac{L}{D} > \left(\frac{L}{D}\right)_{cr} \tag{44}$$

And,

$$\sigma_{cr} \approx \frac{6\sigma_y}{L/D} \tag{45}$$

These define the negative post-yield slope and the asymptotic compressive stress, respectively.

To capture the observed cyclic response, characterized by isotropic hardening at low slenderness and isotropic softening with reduced stiffness at higher ratios, the authors proposed a combined hardening framework governed by four interrelated rules: kinematic, isotropic, memory, and saturation. The resulting KIMS model evaluates stress-strain states at reversal points, ensuring

accurate reproduction of path-dependent effects and progressive degradation. The loading branches between reversals are described using a modified Menegotto-Pinto function with normalized stress and strain variables, maintaining continuity and curvature control.

The curvature parameter, R, evolves with accumulated plastic strain and bar slenderness, following an exponential-type law, bounded below by a slenderness-dependent limit, R_1^b.

$$R = R_0 - \frac{A_1 \xi_{max}}{A_2 \xi_{max}} > R_1^b = 2\left[\frac{L}{D} - \left(\frac{L}{D}\right)_{cr}\right] b^+ \tag{46}$$

This adaptive curvature ensures realistic stabilization of compressive branches during repeated cycles. The elastic modulus degrades exponentially with the accumulated plastic strain, where A_5scales with geometric slenderness and A_6controls the sensitivity of stiffness decay to plastic excursions.

$$E = E_0\left[A_5 + (1 + A_5)e^{-A_6 {\xi_p}^n}\right]$$
$$A_5 = 1 + \frac{\left[\left(\frac{L}{D}\right)_{LIM} - \frac{L}{D}\right]}{7.5} \qquad A_6 = 620 \tag{47}$$

The model's incremental logic is structured around half-cycle updates of plastic excursion (ξ_p^n), plastic work (Φ_p^n), and memory variables (γ_p^n). These quantities determine the evolution of the hardening ratio $b$and the yield stress through exponential and mixed linear-exponential functions. Kinematic hardening evolves from cumulative plastic stress paths, while isotropic hardening depends on the absolute plastic work. The memory and saturation components regulate the activation and rate of these mechanisms, preventing unrealistic growth under small reversals. For bars with $L/D > 5$, the softening branch parameters are further modified to incorporate buckling-induced stiffness loss through $b^-$and γ_s.

$$\gamma_s = \frac{11 - L/D}{e^{c(L/D)} - 1} \geq 0 \qquad for\ 5 < \frac{L}{D} \leq 11 \tag{48}$$

Where c=0.5 for the tested bars. Each cycle updates the yield stress and strain via explicit relations that link stress reversals, plastic excursions, and a degraded modulus. The model ensures thermodynamic consistency, continuity at reversals, and convergence of stiffness parameters through iteration. It can operate in either stress-driven or strain-driven formats, making it computationally efficient for numerical implementations in nonlinear dynamic analyses.

The formulation unifies cyclic plasticity with post-yield instability by embedding slenderness-dependent degradation laws, reproducing the transition from stable hysteresis to buckling-induced softening observed experimentally in bars with L/D>5.

2.2.6 Dodd & Restrepo (1995)

Dodd and Restrepo [43] developed a phenomenological model to simulate the cyclic stress-strain response of reinforcing steel using natural coordinates, allowing a geometrically consistent representation of large strains and ensuring symmetry between tension and compression. In this framework, monotonic behavior is defined by eight measurable parameters, E_0, f_y, ε_y, ε_{sh}, f_{sh}, ε_{su}, f_{su}, and an intermediate point ($\varepsilon_{sh1}, f_{sh1}$), which delineate the elastic, yield plateau, and strain-hardening regions. The hardening branch follows a power-law curve passing through the key experimental points, ensuring a smooth transition beyond yield.

Stress and strain transformations between engineering and natural coordinates make the formulation invariant to large deformations and enable near-symmetric monotonic curves up to about 6% strain before buckling. Within the yield plateau, the model treats unloading and reloading as linear transitions to a new yield point, assuming the Lüders strain is constant regardless of the number of reversals. The model's main advancement lies in its treatment of load reversals and the Bauschinger effect (see Figure 4).

$$\begin{aligned} \varepsilon' &= \ln(1+\varepsilon) & \varepsilon &= e^{\varepsilon'} - 1 \\ \sigma' &= \sigma(1+\varepsilon) & \sigma &= \frac{\sigma'}{(1+\varepsilon)} = \frac{\sigma'}{e^{\varepsilon'}} \\ E'_t &= \frac{d\sigma'}{d\varepsilon'} = \left(\frac{d\sigma}{d\varepsilon} + \frac{\sigma}{1+\varepsilon}\right).(1+\varepsilon)^2 & E_t &= \frac{d\sigma}{d\varepsilon} = \left(\frac{d\sigma'}{d\varepsilon'} - \sigma'\right).e^{-2\varepsilon'} \end{aligned} \tag{49}$$

Upon reversal, unloading initiates with a slope E'_u, which depends on the maximum plastic strain, ε'_M:

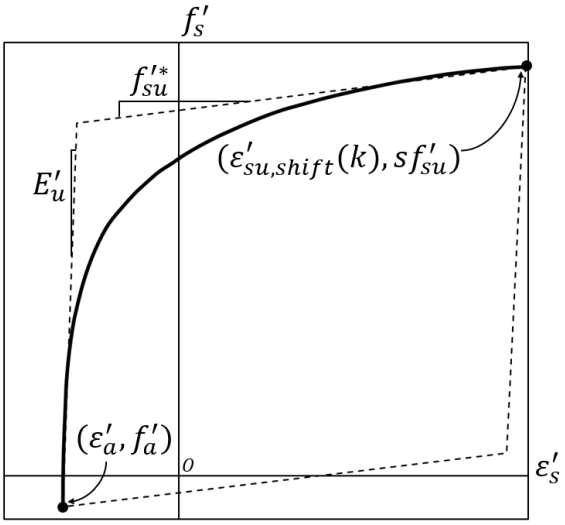
$$\frac{E'_u}{E_s} = 0.82 + \frac{1}{5.55 + 1000\varepsilon'_M} \tag{50}$$

This branch terminates at a point (ε'_a, f'_a), from which reloading occurs along a softened curve that joins a shifted skeleton curve in the opposite direction.

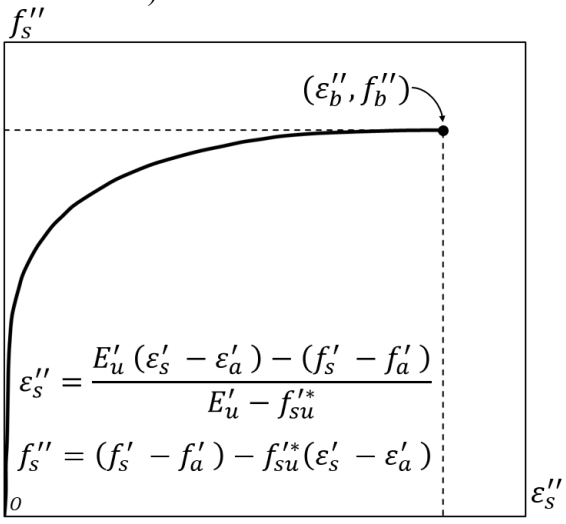
The shift strain, $\varepsilon'_o(k)$, preserves the memory of plastic deformation:

$$\varepsilon'_o(k) = \varepsilon'_r(m) + \frac{sf'_r(m)}{E'_u} \tag{51}$$

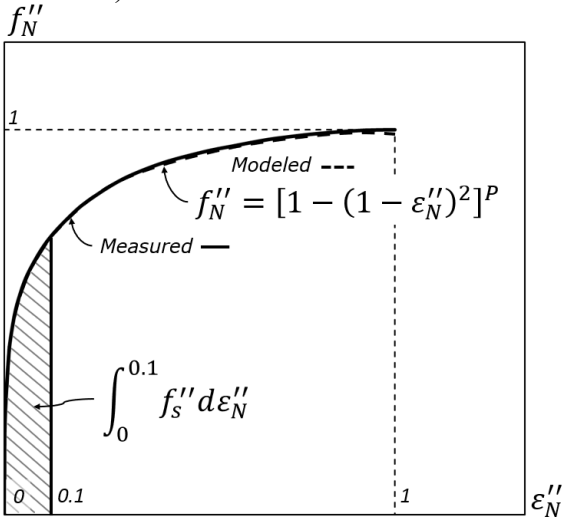
Where $s = \pm 1$, denotes tension or compression, and k and m indicate the directionality of reversals. The softened reloading curve, representing the Bauschinger transition, is expressed in normalized coordinates as:



a) Natural Coordinates.



b) Transformed Coordinates.



c) Normalized Transformed Coordinates

Figure 4. Normalization of the Bauschinger Effect.

$$f_N'' = [1 - (1 - \varepsilon_N'')^2]^P \tag{52}$$

Where the empirical parameter, P, controls curvature and energy dissipation. The curve is derived geometrically from a normalized rigid-plastic parallelogram, ensuring continuity in stress and slope and providing a direct link between hysteretic softness and dissipated energy. P is calibrated via logarithmic relations between stress and strain ratios, guaranteeing that the transition curve accurately reproduces experimental cyclic loops.

$$P = \log\left[\frac{f'_{sh,1} + f'^{*}_{su}\left(\varepsilon'_{su} - \varepsilon'_{sh,1}\right) - f'_{su}}{f'_{sh} + f'^{*}_{su}(\varepsilon'_{su} - \varepsilon'_{sh}) - f'_{su}}\right] \Big/ \log\left(\frac{\varepsilon'_{su} - \varepsilon'_{sh,1}}{\varepsilon'_{su} - \varepsilon'_{sh}}\right) \tag{53}$$

The final form of the softened reloading curve, when expressed in natural coordinates, is:

$$\begin{aligned} f'_s = s[f'_{sh} + f'^{*}_{su}(\varepsilon'_{su} - \varepsilon'_{sh}) - f'_{su}]\left\{\frac{\varepsilon'_{su} - s[\varepsilon'_s - \varepsilon'_o(k)]}{\varepsilon'_{su} - \varepsilon'_{sh}}\right\}^P \\ - f'^{*}_{su}\{s\varepsilon'_{su} - (\varepsilon'_s - \varepsilon'_o(k))\} + sf'_{su} \end{aligned} \tag{54}$$

Eq. (54) describes the stress response (f'_s) as a function of the normalized distance from the reversal point to the ultimate strain, modulated by the curvature parameter P. It ensures that the softened transition curve fits the experimental stress-strain behavior across a range of reversal scenarios, while maintaining energy consistency.

The endpoint of the unloading branch preceding the softened reloading curve is also analytically defined. The stress and strain at this point (ε'_a, f'_a) are given by:

$$\begin{aligned} f'_a &= f'_r + sf_y \\ \varepsilon'_a &= \varepsilon'_r + \frac{sf_y}{E'_u} \end{aligned} \tag{55}$$

These expressions ensure continuity between the unloading and reloading paths and are essential for constructing the complete reversal loop consistently and in a thermodynamically admissible manner.

Energy dissipation during reversals is quantified by the nondimensional area Ω under the softened curve, which is correlated with normalized plastic strain and force ratios. Empirical relationships allow estimation of Ω from measurable parameters, closing the loop between geometric features and constitutive energy.

$$\Omega = \frac{1}{0.18}\left[0.001 + \frac{0.00108}{1.043 - \varepsilon'_p/\varepsilon'_{su}}\right]\left(\frac{f'_p}{f'_t} - 0.69\right) + 0.085 \tag{56}$$

This empirical correlation enables predicting the energy dissipated during a reversal from a few measurable geometric and mechanical parameters, closing the loop between the physical hysteretic behavior and the internal shape parameter P used in the constitutive formulation.

A recursive classification of reversals ensures path dependence and energy consistency:

- Major reversals originate from the skeleton or a previous major branch ($\Delta\sigma > 2f_y$) and produce new softened paths joining the opposite skeleton.

- Minor reversals occur within softened major branches ($\Delta\sigma < 2f_y$) and rejoin the prior major curve.

- Simple reversals arise from minor branches and retrace or reconnect to the last active curve, depending on reversal amplitude.

This hierarchy enables realistic modeling of complex cyclic loading histories, including nested loops and partial reversals. The model maintains smooth transitions and preserves continuity in both stress and tangent stiffness across all branches.
Validation against cyclic tests on Grade 300 and 430 steel bars demonstrated accurate reproduction of stiffness degradation, hysteretic loop shape, and cumulative strain effects. The model predicted a reduction in ultimate tensile strain with increasing compressive plasticity, which is essential for low-cycle fatigue evaluation under seismic demands.

Limitations of the formulation include neglecting buckling and fatigue effects and relying on extensive monotonic calibration data.

2.2.7 Balan, Filippou, & Popov (1998)

Balan et al. [10] developed a macroscopic hysteretic constitutive model to simulate the short-term cyclic response of both ordinary and high-strength reinforcing steels. The formulation operates in natural coordinates, unifying tensile and compressive behavior into a single monotonic envelope, then mapping it into engineering coordinates. This interpretation ensures symmetric material response and accurately represents large-strain effects.

The monotonic law employs a smooth hyperbolic function that transitions from elasticity to the Lüders plateau and then into strain hardening. Key parameters include the elastic modulus (E_s), yield strength (f_y), hardening modulus (E_h), curvature parameter (δ), and ultimate quantities (f_{su}, ε_{su}). The model remains analytically invertible, providing closed-form expressions for both stress-strain and strain-stress relationships, ensuring numerical stability through a nonzero hardening ratio in the plateau region.

Three core components govern cyclic behavior:

(1) Envelope curves derived from the monotonic response and shifted after each load reversal.
(2) Reversal branches, which are represented by softened hyperbolas connecting the unloading and reloading paths.

(3) Loading-unloading detection functions that determine transition points.

Upon reversal from the yield plateau, the unloading modulus equals the elastic modulus ($E_u^k = E_s$), with no degradation and a constant curvature parameter, δ_0. For reversals from the strain-hardening regime, unloading stiffness decreases according to Dodd and Restrepo's empirical relation:

$$E_u^k = E_s \left[0.83 + \frac{0.001}{0.006 + \left(\varepsilon_r^k - \varepsilon_y \right)} \right] \tag{57}$$

And the curvature degradation follows:

$$\delta^k = \frac{\delta_0}{(1-\rho)} \left[1 + a^k \left(\frac{\varepsilon_p^k}{\varepsilon_y^k} \right)^2 \right], (k = 0, 1, \dots, n) \tag{58}$$

Where, ε_p^k is the plastic strain amplitude and a^k is the degradation amplification factor (6 for full reversals, 3 for partial reversals).

Full reversals are defined by stress differentials $\geq 2f_y$, producing new softened branches with reduced stiffness; incomplete reversals ($<2f_y$) follow the same constitutive law but with less curvature degradation. Each reloading branch consists of two asymptotes (initial slope, E_u^k, and final slope, E_h), ensuring a smooth transition to the monotonic envelope.

The formulation remains continuous and differentiable, suitable for finite element implementation. It reproduces essential cyclic features-stiffness degradation, curvature softening, strain hardening, and strength deterioration -using only a few parameters. Validation against experimental data for both conventional and high-strength steels shows accurate hysteresis up to 6-8% strain.

Balan's model integrates the symmetry of natural coordinates, the computational simplicity of hyperbolic functions, and explicit degradation rules driven by plastic strain and reversal amplitude. It achieves high predictive capacity for cyclic steel behavior with minimal calibration effort, making it efficient for seismic and nonlinear structural simulations. Limitations arise mainly from excluding low-cycle fatigue, aging, and buckling effects, restricting applicability beyond the strain range where local instability dominates.

Compared to the Dodd-Restrepo model [43], Balan's model offered a mathematically smoother yet phenomenologically simpler constitutive law. Both rely on natural coordinates and path-dependent softening; however, Dodd and Restrepo emphasized energy consistency and geometric normalization, whereas Balan et al. focused on analytical tractability and reduced parameterization. Together, they form a continuum of constitutive models describing reinforcing steel under cyclic loading and strain-rate-insensitive conditions.

2.2.8 Li & Li (2012)

Li et al. [74] conducted a comprehensive study on the influence of strain rate on the constitutive behavior of RC structures subjected to seismic loading, focusing on the rate-dependent response of both reinforcing steel and concrete. The research addressed limited understanding of material behavior in strain-rate ranges typical of earthquake excitations (10^{-4}-10^{-1} s^{-1}) and proposed constitutive formulations that capture these effects for seismic design and analysis. A combined experimental and numerical program was developed.

Experimentally, reinforcing steel grades HPB235, HRB335, and HRB400 were tested under monotonic, constant-amplitude (±0.02), and variable-amplitude (±0.01-0.04) cyclic loading, using an MTS New 810 servo-hydraulic testing system at controlled strain rates between 2.5×10^{-4}/s and 0.1/s. The results revealed a clear strain-rate sensitivity: yield strength increased by 10.5-22.4% and ultimate strength by 3.7-4.9% as the strain rate increased. The lower-strength steel HPB235 exhibited the greatest sensitivity. Hysteretic curves showed stable cyclic behavior after four to five cycles, confirming consistent energy dissipation and deformation mechanisms.

Based on regression analyses of experimental results, DIFs were formulated for both concrete and steel to quantify rate-dependent strength enhancement. For concrete, the expressions adopted were

$$DIF_{c1} = \frac{f_{cd}}{f_c} = \left(\frac{\dot{\varepsilon}_c}{\dot{\varepsilon}_{c0}}\right)^{1.026a}; \qquad \dot{\varepsilon}_c \le 30s^{-1}$$
$$DIF_{c1} = \frac{f_{cd}}{f_c} = r\dot{\varepsilon}_c{}^{1/3}; \qquad \dot{\varepsilon}_c > 30s^{-1} \tag{59}$$
$$a = (5 + 0.75f_{cu})^{-1} \qquad \log\gamma = 6.156a - 0.492$$

For reinforcing steel, the corresponding relationships were

$$DIF_{sy} = \frac{f_{yd}}{f_{ys}} = 1 + C_f \log\frac{\dot{\varepsilon}_s}{\dot{\varepsilon}_{s0}} \qquad C_f = 0.1709 - 3.289x10^{-4}f_{ys}$$
$$DIF_{su} = \frac{f_{ud}}{f_{us}} = 1 + C_u \log\frac{\dot{\varepsilon}_s}{\dot{\varepsilon}_{s0}} \qquad C_u = 0.02738 - 2.982x10^{-5}f_{ys} \tag{60}$$
$$DIF_{sh} = \frac{\varepsilon_{hd}}{\varepsilon_{hs}} = 1 + C_h\frac{\dot{\varepsilon}_s}{\dot{\varepsilon}_{s0}} \qquad C_h = 0.9324 - 0.00212f_{ys}$$

Where,

$\dot{\varepsilon}_s$: The strain rate of steel.
$\dot{\varepsilon}_{s0}$: The quasi-static strain rate of steel.
f_{ys}, f_{yd}: The quasi-static and dynamic yield strength of steel, in MPa.
f_{us}, f_{ud}: The quasi-static and dynamic ultimate strength of steel, in MPa.
ε_{hs}, ε_{hd}: The quasi-static and dynamic strain at which strain hardening begins.
C_f, C_u, C_h: The parameters are functions of the quasi-static yield strength of steel.

These parameters establish direct correlations between mechanical strength enhancement and loading rate as a function of material strength.

A three-dimensional finite element model of a four-story RC frame was developed in ABAQUS, incorporating Drucker-Prager plasticity for concrete and Mises plasticity for steel, with rate effects implemented via the derived DIF formulations. The frame was subjected to three ground motion records (Northridge, Taft, and El Centro) with peak ground accelerations ranging from 0.22g to 0.62g. The simulations demonstrated that the maximum concrete compressive strain rates at the base increased with excitation intensity, ranging from 0.01/s to 0.084/s. Dynamic effects increased base shear and bending moments by 3-13%, while top displacements decreased by up to 18%, indicating enhanced apparent stiffness at high strain rates.

A key observation was the strong correlation between monotonic and cyclic skeleton curves at identical strain rates, demonstrating that monotonic rate-dependent stress-strain relationships can effectively represent the envelope of cyclic constitutive behavior. This equivalence simplifies developing rate-dependent cyclic models by allowing monotonic data to be extrapolated to cyclic loading conditions. The study further validated the theory of viscous strengthening for strain rates below 1 s^{-1}, confirming that strength enhancement in this regime arises from intrinsic material viscosity rather than inertia.

2.2.9 Kim & Koutromanos (2016)

Kim and Koutromanos [67] formulated an advanced uniaxial phenomenological model for reinforcing steel under cyclic loading, extending the Dodd and Restrepo framework (Section 2.2.6) to include inelastic buckling and low-cycle fatigue rupture. The model introduces three central features: a closed-form, non-iterative stress update; nonuniform rational B-spline (NURBS) interpolation of reversal paths; and physically motivated formulations that model buckling and rupture as energy-driven phenomena. Defined in natural (logarithmic) stress-strain space, the formulation ensures symmetry between tension and compression, avoiding distinct envelope definitions for each regime. The monotonic response is fully characterized by seven parameters (E_s, f_y, ε_{sh}, f_u, ε_u, f_{sh1}, and ε_{sh1}) allowing precise control over hardening and softening.

Cyclic reversals are generated by NURBS segments controlled by three points: the origin, auxiliary, and target, ensuring smooth, thermodynamically consistent stress-strain transitions. Major reversals are split into two NURBS branches joined at a characteristic point, preserving curvature continuity. The curvature of reversal branches is governed by the dimensionless parameter β, derived from Ω through a piecewise relation calibrated via regression, thus enabling accurate reproduction of experimental hysteresis shapes. The tangent stiffness, E_T, is obtained analytically in closed form, first in the natural coordinate system and subsequently transformed to engineering space, ensuring exact stiffness computation without iterative correction-an advantage for Newton-Raphson solvers in nonlinear finite element analysis.

Inelastic buckling is modeled using a physically based beam analogy, in which the bar segment between ties behaves as a pinned-pinned beam under axial compression. Buckling occurs when the incremental stiffness matrix becomes singular, establishing a critical stress criterion dependent only on the slenderness ratio L/D. Post-buckling degradation is captured by scaling the hysteretic stress

with a reduction coefficient, F_b, defined as a NURBS-based function of normalized inelastic strain ε_n. Bayrak et al. [12] calibrate the coefficients from experimental data, providing a continuous, path-independent reduction in compressive strength.

Fracture under low-cycle fatigue is simulated through a continuous internal damage variable that evolves with energy dissipation, allowing a smooth transition to rupture without discrete cycle counting. The resulting model accurately reproduces asymmetry in tension-compression hysteresis, stiffness degradation, and strength loss due to bar instability. Its non-iterative algorithm, closed-form stiffness, and modular structure enable efficient implementation in finite element platforms such as OpenSees.

2.2.10 Qiu & Gong (2019)

Qiu and Gong [107] developed an analytical hysteresis model for reinforcing bars under cyclic loading, integrating two primary degradation mechanisms: stiffness deterioration due to inelastic buckling and progressive failure from low-cycle fatigue. The model extends the Bouc-Wen framework [61] and [140] by introducing degradation functions in both the restoring-force and hysteretic-evolution equations. Axial stress $\sigma_s(\varepsilon, z)$ is expressed as a weighted sum of elastic and hysteretic components, with post-yield stiffness ratio α controlling the partition and evolving according to strain-dependent buckling effects.

$$\sigma_s(\varepsilon, z) = [\alpha\varepsilon + (1-\alpha)z]f_y = \sigma f_y \tag{61}$$

Where,

E_0: The elastic modulus.
f_y: The yield strength $= \varepsilon_y E_0$.
z: The normalized hysteretic strain $= z_s/\varepsilon_y$
z_s: The hysteretic strain.
α: The post-yield stiffness ratio.
ε: The normalized strain $= \varepsilon_s/\varepsilon_y$
ε_s: The strain of the reinforcing bar.
ε_y: The yield strain.
σ: The normalized stress.
$\sigma_s(\varepsilon, z)$: The stress of the reinforcing bar.

Here, $\alpha \in [0,1]$ is a weighting coefficient that partitions the total force between the linear elastic component and the hysteretic component. The variable z, which evolves under loading, captures the irreversible and nonlinear characteristics of the bar's response.

The hysteretic strain, z, evolves via a first-order nonlinear differential equation with shape parameters β, γ, n, and degradation coefficients η and ν, which are functions of accumulated hysteretic energy, w. Degradation parameters capture stiffness (δ_η) and strength (δ_ν) reductions, updated incrementally at each time step using backward Euler discretization and Newton-Raphson iterations. A strain-dependent model asymmetry due to inelastic buckling:

$$\alpha = \alpha_0(\lambda z + 1 - \lambda) \quad (62)$$

Here, α_0 is the post-yield stiffness ratio on the tension side, λ, is a reduction coefficient that controls the extent of softening on the compression side.

Model parameters are classified into post-yield stiffness (α_0, λ), shape (β, γ, n), and degradation (δ_η, δ_ν) groups. Hysteresis loop behavior is controlled by n (smoothness), λ (loop asymmetry), and δ_η/δ_ν (degradation levels). Parameters are identified using genetic algorithms against Monti and Nuti's experimental data [92], achieving errors below 0.7%. Regression-based predictions for α_0, λ, δ_η and δ_ν allow general application without experimental calibration, linking them to reinforcement properties and geometric ratios (L/D, f_y, f_u).

The model captures both compressive softening from inelastic buckling and fatigue-induced strength degradation, providing a single-equation, computationally efficient formulation for finite element platforms such as OpenSees (BWreinforcingsteel). It accurately simulates reinforcing bar cyclic behavior and enables reliable assessment of RC structures under seismic demands, emphasizing strain-rate- and energy-dependent constitutive effects.

2.2.11 Massone, Rosa & Mesa (2023)

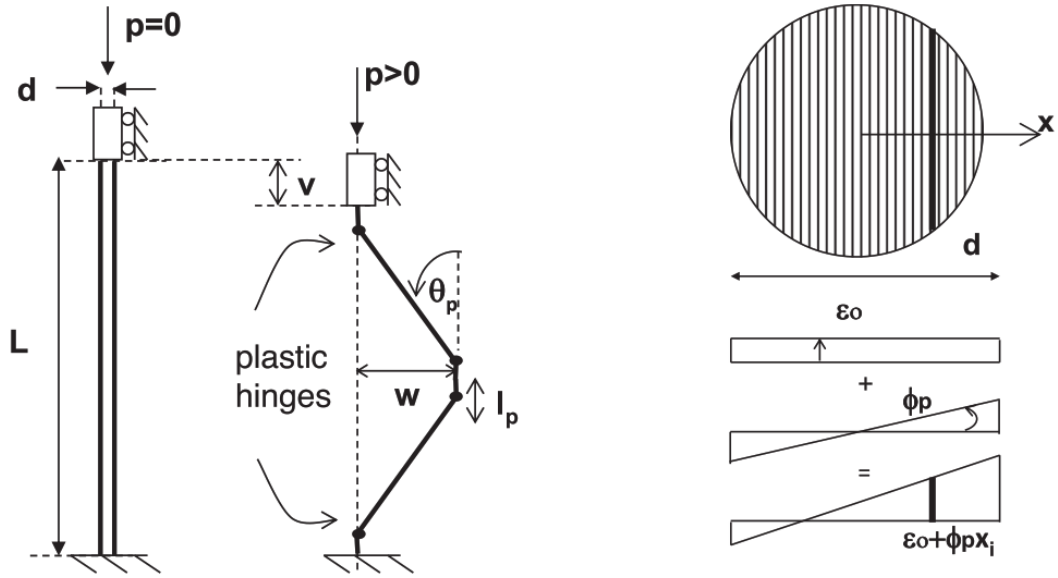
The model proposed by Massone et al. [85] presents a uniaxial hysteretic model for reinforcing bars that integrates all primary degradation mechanisms, including inelastic buckling and cyclic strength reduction, within a computationally efficient framework. The backbone stress-strain envelope is defined by four control points-origin, yield, peak stress, and ultimate strain-and implemented via a rule-based, point-by-point approach that captures pre- and post-yield stiffness, peak strength, softening, and asymmetric responses without continuous constitutive equations or internal state variables.

Cyclic behavior follows rules for unloading, reloading, and strain reversal, reproducing the Bauschinger effect and stiffness degradation. Inelastic buckling is represented by geometric formulations that link bar curvature, axial strain, and plastic hinge rotations. The average bar curvature, ϕ_{lin}, accounts for axial strain and geometry, while the maximum concrete compressive strain, $\varepsilon_{c,max}$, is derived from peak curvature. Total axial shortening, v, and lateral displacement of buckled segments, w, are expressed as functions of plastic hinge rotation, ϕ_p, plastic hinge length, l_p, and uniform axial strain, ε_0, providing a cohesive framework for local deformation effects.

Figure 5 illustrates the idealized geometry of a buckled reinforcing bar confined between two plastic hinges of length L, along with the corresponding strain distribution across its cross-section.

The model uses concentrated plasticity at discrete hinges to simulate post-buckling behavior efficiently, avoiding distributed plasticity along the bar length. The numerical implementation uses iterative curvature adjustments to achieve moment equilibrium and incorporates axial and transverse effects within the sectional analysis. Validation against monotonic and cyclic

experiments demonstrates accurate reproduction of hysteresis shape, strength asymmetry, unloading stiffness, strain accumulation, and progressive degradation.



a) Overall view b) Plastic hinge cross-section

Figure 5. The geometric idealization of the longitudinal reinforcing steel bar represented by a concentrated plasticity model [84].

2.2.12 Tripathi & Dhakal (2023)

Tripathi and Dhakal [132] developed a unified constitutive model for reinforcing bars that simultaneously accounts for inelastic buckling and low-cycle fatigue, providing a continuous, physically grounded representation of cyclic behavior under seismic loading. Unlike earlier models that treat buckling and fatigue independently, their formulation couples both degradation mechanisms through interacting indices within a single stress-strain law.

The framework is founded on extensive experimental testing of Grade 300E and 500E bars under monotonic and cyclic loading in tension and compression. Results revealed that ductility and energy dissipation strongly depend on steel grade and bar slenderness (L/D). Grade 300E exhibited a yield strain capacity of about 180%, while 500E reached about 55%. Increasing slenderness accelerated compressive degradation-L/D=15 specimens lost up to 80% more strength than L/D=6 bars, producing asymmetric hysteresis and earlier softening onset.

These experimental observations were incorporated into analytical expressions that define the tensile and compressive backbones. The tensile branch uses a three-phase elastic-yield-hardening formulation with a continuous transition to ensure stability and grade sensitivity. The compressive branch introduces a buckling parameter, λ,

$$\lambda = \frac{L}{D}\sqrt{\frac{f_y}{100}} \tag{63}$$

Where L is the bar length between end restraints, D is the bar diameter, and f_y is the yield strength (in MPa).

This buckling parameter controls the strain at degradation onset:

$$\frac{\varepsilon_i}{\varepsilon_y} = max\begin{Bmatrix}55 - 2.3\lambda \\ 7\end{Bmatrix} \tag{64}$$

And governs post-peak softening via:

$$\sigma = max\begin{Bmatrix}f_t - 0.02E_s(\varepsilon - \varepsilon_i) \\ 0.2f_y\end{Bmatrix} \tag{65}$$

Where f_t represents the compressive stress at the onset of degradation. The slope $0.02E_s$ reflects the stiffness loss rate calibrated from tests, and the residual plateau at $0.2f_y$ prevents unrealistic negative stresses. This formulation captures slenderness-dependent softening and tension-compression asymmetry.

Cyclic behavior is modeled using a modified Menegotto-Pinto formulation [89] incorporating path-dependent stiffness degradation and a bifurcated reloading stiffness system distinguishing moderate- from severe-buckling regimes

$$\frac{E_u}{E_s} = 0.82 + \frac{1}{5.55 + 1000\varepsilon_p} \tag{66}$$

Here, ε_p is the accumulated plastic strain, which causes a gradual stiffness loss consistent with the test data. Pinching and hysteresis curvature evolve through a buckling damage index that tracks degradation across cycles.

Fatigue is integrated through a strain-life relation linking slenderness to fatigue resistance, expressed as:

$$\varepsilon_a = (350 + 0.2\lambda)\left(2N_f\right)^{-\frac{1}{1200+0.44\lambda}} \tag{67}$$

Here, ε_a is the strain amplitude and N_f, the number of reversals to failure.

Cumulative damage follows Miner's rule, progressively reducing tensile and compressive capacities, expressed as:

$$\Delta D_i = \frac{1}{\varepsilon_a{}^{1/a}} \tag{68}$$

Here, ΔD_i is the incremental damage in the i-th cycle, and a, a material calibration constant.

The resulting model reproduces experimental hysteresis loops with 92% accuracy, correctly predicting degradation rates, pinching severity, and fatigue-life reduction across a range of slendernesses. It eliminates the 30-50 % overprediction of residual capacity typical of prior formulations. The unified fatigue-buckling-hysteresis law offers enhanced realism, numerical stability, and implementation readiness for nonlinear analyses of RC members-especially in plastic hinge regions of seismic structural systems-while maintaining extensibility for future inclusion of corrosion, biaxial stress states, and steel-concrete interaction effects.

2.3 Research Work on Microscopic Bond-Slip Models

Microscopic and mechanistic bond-slip models seek to represent the local mechanisms governing force transfer between reinforcing steel and surrounding concrete, rather than prescribing the complete bond stress-slip response solely from empirical calibration. At this scale, bond behavior is associated with the mechanical interaction between the reinforcing-bar ribs and the surrounding concrete, including rib bearing and wedging, friction, local concrete crushing and cracking, slip reversal, and the development and evolution of confinement. The level of mechanical representation varies among formulations, from local constitutive descriptions of the steel-concrete interface to formulations that explicitly couple tangential slip with radial deformation or represent the surrounding concrete through a discrete numerical framework.

These models are particularly relevant to detailed nonlinear finite-element simulations in which a perfect-bond assumption cannot adequately represent the local behavior of the reinforcement-concrete interface. They have been used to investigate reinforcement anchorage, lap splices, beam-column joints, and other RC connections, where bond deterioration and reinforcement slip can influence force transfer and deformation distribution. Their use is therefore associated with analyses in which local interface behavior, rather than only the global member response, is of interest. The following studies illustrate the development of these formulations from energy-based and hysteretic descriptions of bond deterioration to approaches that incorporate an increasingly explicit representation of the mechanical interaction between the reinforcement and surrounding concrete.

2.3.1 Ciampi, Eligehausen, Bertero, and Popov (1982)

Ciampi et al. [35] developed an analytical constitutive framework for local bond stress-slip behavior under arbitrary cyclic loading and a numerical procedure for solving the boundary-value problem of RC bar anchorages. The formulation represented the progressive deterioration of bond through a damage parameter d, which reduced the characteristic stresses of the monotonic bond-slip envelope according to the accumulated energy dissipated at the interface. The damage variable was defined as

$$d = 1 - \exp\left[-1.2\left(\frac{E}{E_0}\right)^{1.1}\right] \tag{69}$$

where E is the accumulated dissipated bond energy and E_0 is a reference energy. Thus, d=0 represents the undamaged condition, whereas $d \rightarrow 1$ corresponds to the progressive loss of the mechanical interlocking contribution to bond resistance. The formulation also incorporated residual friction and the low-resistance region associated with the gap produced by crushing of the concrete in front of the bar ribs during slip reversal.

The study further developed a nonlinear shooting technique based on transfer matrices to integrate equilibrium, compatibility, steel behavior, and interface constitutive relations along the embedded bar. The model was validated against experimental results from cyclic anchorage tests. The formulation therefore provided a mathematical connection between cyclic loading history, accumulated energy dissipation, interface damage, and the resulting degradation of bond resistance, providing an analytical basis for subsequent hysteretic bond-slip formulations.

2.3.2 Eligehausen, Ciampi, Bertero & Popov (1982)

Eligehausen et al. [46] investigated the local bond stress-slip behavior of deformed reinforcing bars embedded in confined concrete under monotonic and cyclic loading, with particular emphasis on the conditions that develop in the anchorage regions of RC beam-column joints subjected to severe seismic excitations. The experimental program used short embedment lengths of approximately $5d_b$, allowing the local bond behavior to be characterized under controlled confinement conditions. The resulting experimental data were used to develop an analytical bond stress-slip model for generalized loading histories, which was subsequently extended to represent the behavior of longer anchorages and the bond conditions found in RC frame joints.

For the monotonic envelope, the ascending branch was represented by a power-law relationship,

$$\tau(s) = \tau_1\left(\frac{s}{s_1}\right)^{\alpha}, 0 \leq s \leq s_1 \tag{70}$$

where τ_1 is the maximum bond stress, s_1 is the slip corresponding to maximum bond stress, and α controls the shape of the ascending branch. The complete envelope was then defined through the characteristic points s_1, s_2, and s_3, with a maximum-strength plateau, a descending branch, and a residual friction branch. The characteristic parameters were related to the concrete strength, reinforcement characteristics, confinement, bar diameter, clear spacing, transverse pressure, and other bond conditions investigated experimentally.

Under cyclic loading, the formulation introduced the gap effect associated with crushing of the concrete in front of the bar ribs during previous excursions. After load reversal, the bar could undergo a relatively low-resistance slip until the ribs re-established contact with the surrounding concrete. Subsequent reloading followed a hysteretic path toward a degraded envelope. The reduction of the envelope was governed by the accumulated damage, which was related to the total dissipated energy. Thus, the formulation combined an explicit monotonic $\tau - s$ relationship with

rules for unloading, reloading, slip reversal, gap formation and closure, and progressive cyclic degradation. The experimental study considered the influence of loading history, confinement, bar diameter and deformation pattern, concrete compressive strength, clear bar spacing, transverse pressure, and loading rate, and the resulting model was used to predict the response of anchored bars under severe seismic loading.

2.3.3 Filippou, Popov & Bertero (1983)

Filippou et al. [50] developed an analytical model for the hysteretic behavior of RC beam-column joints subjected to random cyclic excitations, explicitly accounting for the deterioration of bond along anchored reinforcing bars. The formulation was derived from the local behavior of a single reinforcing bar embedded in concrete and coupled the steel stress, relative bar slip, bond stress, and equilibrium along the anchorage. The governing relations were expressed as

$$\frac{d\sigma_s}{dx} = \frac{q\,\psi}{A} \qquad \frac{du}{dx} = \varepsilon_s - \varepsilon_c \qquad (71)$$
$$q = f(u) \qquad \varepsilon_s = f(\sigma_s)$$

where σ_s is the reinforcing-steel stress, u is the relative slip between steel and concrete, q is the local bond stress, ψ is the reinforcing-bar perimeter, A is the bar area, and ε_s and ε_c are the steel and concrete strains, respectively. For the large inelastic excursions considered in the study, the contribution of concrete strain to relative slip was neglected, such that $du/dx \approx \varepsilon_s$. The resulting formulation therefore provided the differential framework required to obtain the distribution of steel stress and slip along the anchorage rather than prescribing bond-slip only at a single interface point.

For the hysteretic bond-slip relation itself, Filippou et al. adopted the bond model developed from the preceding experimental work of Eligehausen et al. They introduced a structural implementation suited to cyclic joint analysis. During each half-cycle after unloading, the monotonic bond envelope was reduced according to the total energy dissipated during the preceding loading history. The frictional bond resistance was related to the previous maximum slip, u_{max}, and to the ultimate bond resistance of the corresponding degraded envelope. A modification was introduced for reloading: instead of following the original polynomial reloading branch, the formulation used a linear branch connecting the zero-slip point on the friction branch with the intersection between the unloading curve and the reduced envelope. The resulting hysteretic bond-slip formulation was incorporated into the analysis of beam-column joints, where cyclic deterioration of the steel-concrete interface produced bar slip and concentrated rotations at the beam-column interfaces.

2.3.4 Murcia-Delso (2013)

Murcia-Delso [94] investigated the bond-slip behavior of large-diameter longitudinal reinforcing bars used in non-contact lap splices between bridge columns and enlarged pile shafts, with particular emphasis on cyclic bond deterioration under seismic loading. The experimental program included local bond tests on No. 11, No. 14, and No. 18 bars and full-scale column-pile shaft specimens subjected to quasi-static cyclic lateral loading. Based on the experimental results, the study developed two complementary constitutive approaches for the steel-concrete interface. The first was a phenomenological local bond stress-slip model for bars embedded in well-confined

concrete. The monotonic response was defined using three physical parameters: the maximum bond stress, u_τ, the slip at peak bond strength, s_{peak}, and the clear spacing between adjacent ribs, R_s. The response consisted of a nonlinear ascending branch, a plateau at the maximum bond strength, a descending branch, and a residual branch. Under cyclic loading, two damage parameters were introduced to reduce the bond resistance progressively as a function of the accumulated slip history.

The second formulation was a physically based dilatant interface model developed within a multisurface plasticity framework. It represented the coupled tangential slip and radial dilation associated with the wedging action of the reinforcing-bar ribs. It allowed the evolution of the surrounding confinement to be considered in three dimensions. In addition to these constitutive models, it was derived design relationships for the column-pile connection. The minimum embedment length required to develop the tensile capacity of the longitudinal reinforcement was expressed as

$$l_e = l_d + s + c \tag{72}$$

Where, l_d, is the tensile development length specified by AASHTO LRFD, s, is the transverse separation between the column and pile reinforcement in the non-contact splice, and c is the vertical concrete cover at the top of the pile. The required transverse reinforcement was expressed as

$$A_{tr} = \frac{\pi d_{col} u_\tau s_{tr}}{2 f_{y,tr}} \tag{73}$$

where d_{col} is the diameter of the column longitudinal reinforcement, u_τ is the ultimate bond strength, s_{tr} is the longitudinal spacing of the transverse reinforcement, and $f_{y,tr}$ is its nominal yield stress. These formulations extended bond-slip modeling toward explicit representation of the interaction between slip, radial dilation, and confinement in large-diameter reinforcement. They provided a basis for translating local interface behavior into the analysis and design of column-pile connections.

Overall, these studies established a progression from energy-based damage and local hysteresis to distributed anchorage formulations and mechanically based interface models. This progression is particularly relevant to cyclic structural analysis because it shows that bond-slip is not only a relationship between bond stress and instantaneous slip, but also a history-dependent mechanism involving energy dissipation, degradation, slip reversal, friction, confinement, and the interaction between reinforcement and surrounding concrete.

For a more comprehensive review of the state of the art on the mechanisms governing stress transfer and the modeling of the bond-slip interface in RC members, the reader is referred to Murcia-Delso [94].

2.4 Research Work on Macroscopic Bond-Slip Models

Macroscopic bond-slip models seek to incorporate the structural consequences of RC interaction into nonlinear constitutive formulations without explicitly resolving the local mechanisms governing bond transfer along the reinforcement-concrete interface. Rather than modeling the spatial distribution of bond stresses, local concrete damage, rib-concrete interaction, and reinforcement slip along the anchorage length, these formulations represent their combined effects through equivalent constitutive relationships or localized deformation mechanisms. Their objective is to reproduce the influence of bond deterioration on the response of RC members, including additional deformation, stiffness degradation, strength loss, hysteretic pinching, and changes in energy dissipation under cyclic loading.

These models are particularly useful for nonlinear structural analyses in which the effects of reinforcement-concrete interaction must be considered without explicitly discretizing the bond interface or the complete reinforcement development length. By concentrating the effects of local bond deterioration into constitutive or section-level representations, they provide a computationally efficient means of incorporating bond-related deformation and hysteretic effects into fiber-based and other nonlinear structural models. The level of abstraction, however, depends on the formulation: bond-slip effects may be represented through localized deformation mechanisms associated with reinforcement anchorage or directly through the constitutive response of embedded reinforcement.

The development of these formulations reflects the need to incorporate the consequences of local bond mechanisms into structural-scale analyses without resolving their full spatial distribution. In RC, this transition involves translating the effects of local reinforcement-concrete interaction into constitutive or section-level descriptions that can reproduce its principal consequences at the member and structural levels. The following studies illustrate this approach through formulations that account for reinforcement anchorage, cyclic degradation, and the resulting modification of the nonlinear response of RC members.

2.4.1 Zhao and Sritharan (2007)

Zhao et al. [149] proposed a zero-length section element to incorporate the effects of strain penetration into fiber-based nonlinear models of RC members. Conventional beam-column formulations generally assume perfect compatibility between the longitudinal reinforcement and surrounding concrete and therefore do not explicitly represent the extension of reinforcing bars within their anchorage region. Under cyclic loading, however, inelastic strains can penetrate the anchorage, producing bar slip at the member-support interface and an associated fixed-end rotation. The element accounts for this additional deformation mechanism, allowing the contribution of reinforcement anchorage to be incorporated into the nonlinear response of RC members.

The element consists of two coincident nodes at the member-support interface. The transverse translational degrees of freedom are constrained so that the deformation represented by the element is associated with reinforcement slip rather than transverse relative displacement. The section is discretized using concrete and reinforcing-steel fibers. The concrete fibers provide the compressive contact response between the adjacent members, whereas the reinforcing-steel fibers are assigned a constitutive relationship directly relating bar stress to slip, σ_s-s, instead of the conventional steel

stress-strain relationship. By assigning a unit analytical length to the section, the section deformation can be directly related to the rotation produced by reinforcement slip at the interface. This formulation allows the anchorage response to be incorporated into a fiber-based beam-column model without explicitly discretizing the reinforcement development length.

The constitutive relationship proposed by Zhao et al. defines the slip at yielding, s_y, as

$$s_y = 2.54\left[\frac{d_b}{8437}\frac{f_y}{\sqrt{f_c'}}(2\alpha+1)\right]^{1/\alpha} + 0.34 \tag{74}$$

Where, d_b is the nominal bar diameter, f_y is the nominal yield stress of the reinforcement, f_c' is the concrete compressive strength, and α is the exponent associated with the local bond relationship. The formulation adopts $\alpha = 0.4$, consistent with the CEB-FIP Model Code 1990 formulation.

For the monotonic response, the initial branch is assumed to be linear up to yielding,

$$\sigma_s = Ks \tag{75}$$

where the initial stiffness is defined as

$$K = \frac{f_y}{s_y} \tag{76}$$

Beyond yielding, the response is represented by a modified Menegotto-Pinto-type relationship:

$$\sigma_s = \tilde{\sigma}\left(f_u - f_y\right) + f_y \tag{77}$$

with,

$$\tilde{\sigma} = \frac{\dfrac{\tilde{s}}{\mu - \tilde{s}}}{\left[\left(\dfrac{1}{\mu b}\right)^{R_e} + \left(\dfrac{\tilde{s}}{\mu - \tilde{s}}\right)^{R_e}\right]^{1/R_e}} \tag{78}$$

Where

$$\tilde{s} = \frac{s - s_y}{s_y}, \mu = \frac{s_u - s_y}{s_y} \tag{79}$$

Here, s_u and f_u are the slip and bar stress at the ultimate point, b controls the hardening slope relative to the initial stiffness, and R_e controls the curvature of the transition toward the ultimate response. In this study, the authors adopted $R_e = 1.01$ to obtain a smooth transition in the vicinity of the ultimate response.

The formulation was also extended to cyclic loading through explicit unloading and reloading rules. During unloading, the response follows a straight line with the initial stiffness K until the stress reaches zero at a residual slip, r_{svg}. Upon load reversal, the reloading path is defined relative to the previously attained maximum or minimum response. The normalized reloading stress is expressed as

$$\sigma^* = \frac{\frac{s^*}{s_{uy} - s^*}}{\left[\left(\frac{1}{s_{uy}}\right)^{R_c} + \left(\frac{s^*}{s_{uy} - s^*}\right)^{R_c}\right]^{1/R_c}} \tag{80}$$

Where

$$s^* = \frac{s - r_{svg}}{s_y'} \tag{81}$$

s_y' represents the recovered elastic slip, and R_c controls the curvature of the reloading branch. The reloading stress is subsequently scaled according to the previously attained maximum or minimum response.

The significance of this formulation lies in its treatment of reinforcement anchorage as a localized nonlinear interface mechanism within an otherwise conventional fiber-based member model. Rather than explicitly modeling the complete bond-slip distribution along the development length, the bar stress-slip relationship condenses the effects of anchorage deformation into a zero-length section. It introduces the resulting fixed-end rotation directly into the structural response. The formulation is particularly useful in detailed nonlinear analyses of RC members and connections where reinforcement slip and anchorage deformation need to be distinguished from the flexural deformation of the member itself.

2.4.2 Rashid, James, and Dunham (2013)

Rashid et. al. [112] developed an advanced constitutive framework within the ANACAP-U software system [4] to simulate the nonlinear response of RC structures, with particular emphasis on the cyclic stress-strain behavior of reinforcing steel and its interaction with cracked concrete through bond-slip. Their work extended earlier ANATECH formulations to reproduce stiffness degradation, pinching explicitly, and strength loss observed in reinforced members subjected to seismic-type loading.

The constitutive relation adopted in ANACAP-U for reinforcing steel is expressed as:

$$\sigma_s = \phi(\varepsilon_c)\, \sigma_{s,0}(\varepsilon_s) \tag{82}$$

Where, $\sigma_{s,0}$ is the intrinsic elasto-plastic stress of the steel bar, and $\phi(\varepsilon_c)$, a yield-strength reduction factor that evolves with the dilatational strain of the surrounding concrete. As concrete cracks and

dilates, ϕ decreases, thereby reducing both the apparent yield stress and the stiffness of the embedded steel.

Under monotonic conditions, reinforcing steel is idealized by a conventional elastoplastic stress-strain curve defined by the initial modulus (E_0), yield strength (σ_y), and a strain-hardening branch. Under cyclic loading, however, the steel response becomes asymmetric due to progressive slip at the steel-concrete interface. This interfacial degradation introduces additional recoverable deformation ($\Delta\varepsilon_u$) and reduces the unloading-reloading stiffness. Consequently, the stress-strain loops narrow with each reversal, forming the characteristic pinched hysteresis observed experimentally in RC members.

Progressive bond-slip at the steel-concrete interface leads to reduced unloading and reloading stiffness, asymmetrical hysteresis, and the development of pinched loops-a phenomenon illustrated in Figure 6.

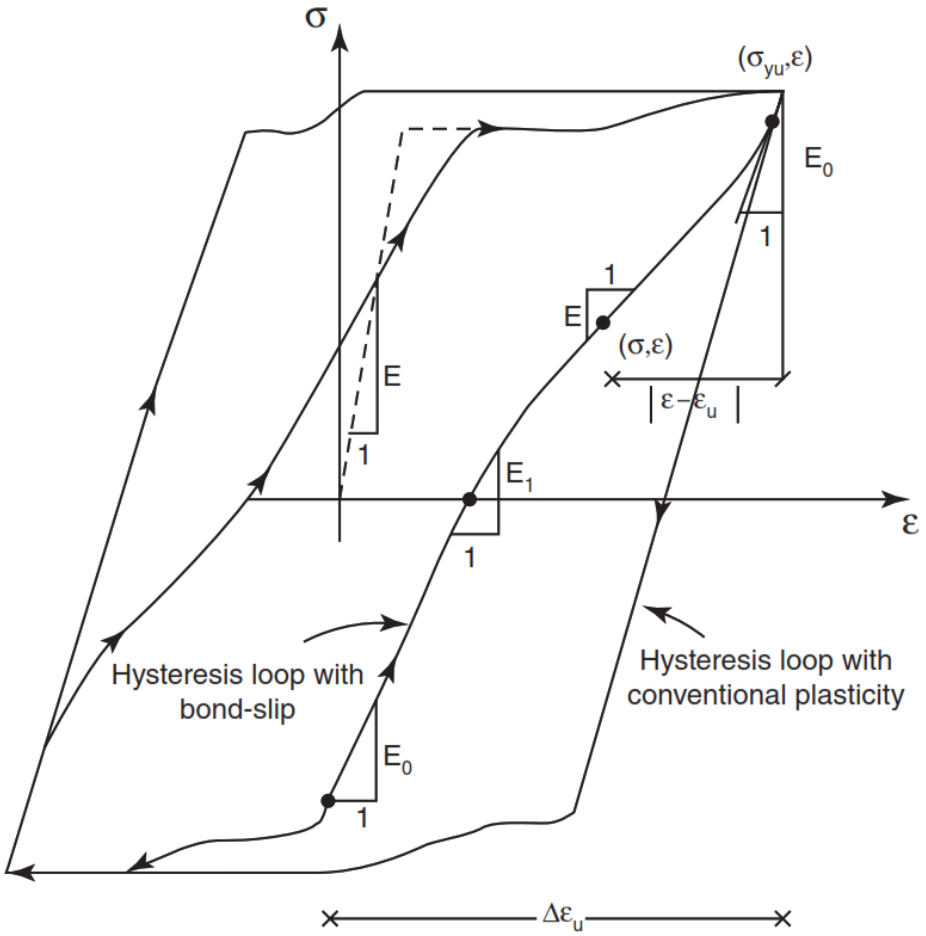


Figure 6. Rebar yield strength factor and pinched hysteresis loop [112].

The external loop corresponds to the idealized elastoplastic response, while the inner loop shows pronounced pinching, a lower slope, and vertical stress degradation due to bond loss. The horizontal

widening $(\varepsilon - \varepsilon_u)$ reflects the cumulative slip between the bar and the cracked concrete, quantifying the loss of energy-dissipation capacity with repeated cycles.

The cyclic stress-strain response exhibits three essential features:

(1) Stiffness reduction during unloading and reloading due to interface compliance,
(2) Progressive loop narrowing reflecting diminished energy dissipation, and
(3) Gradual strength loss caused by bond deterioration.

These mechanisms reproduce the experimentally observed transition from wide, stable loops to highly pinched, low-energy cycles as interface damage advances.

Constitutively, the observed pinching originates not from changes in the intrinsic plasticity of steel but from the coupling between the steel and the damaged concrete matrix. The formulation maintains continuity and differentiability in the stress-strain relation; hysteresis arises naturally through the evolving bond-slip law. This micro-mechanically consistent approach eliminates empirical reloading rules and provides a direct physical explanation for stiffness and strength degradation.

Consequently, ANACAP-U accurately simulates the progressive reduction in stiffness and energy-dissipation capacity of reinforcing steel under cyclic loading, providing a unified constitutive basis for nonlinear time-history analysis of RC structures under seismic and impact loading. By linking the steel response to concrete dilatation and interfacial slip, Rashid et al. established a physically grounded representation of pinching behavior that bridges material mechanics and structural-scale performance.

2.5 Synthesis and Identified Gaps

Existing constitutive models for reinforcing steel exhibit a clear fragmentation between monotonic rate-dependent formulations and cyclic models developed under quasi-static assumptions. Monotonic approaches incorporate strain-rate effects through empirical factors or viscoplastic frameworks, but are not formulated to reproduce hysteretic response under load reversals. In contrast, cyclic constitutive models capture key features such as the Bauschinger effect, cyclic hardening, stiffness degradation, and energy dissipation, yet do not explicitly account for strain-rate dependence.

At the structural level, experimental evidence confirms that reinforcing steel in RC members under seismic loading experiences highly transient and localized strain rates, particularly in plastic hinge regions. However, these kinematic observations have not been consistently translated into constitutive formulations that modify stress response under cyclic loading. As a result, current modeling strategies rely largely on quasi-static assumptions that may underestimate stress amplification and alter the predicted hysteretic response when strain-rate effects become significant.

Additionally, bond-slip mechanisms at the steel-concrete interface introduce additional deformation, pinching, stiffness degradation, strength deterioration, and changes in energy

dissipation that cannot be captured by the reinforcing-steel constitutive law alone. Microscopic and mechanistic bond-slip models have been developed to represent the local mechanisms governing force transfer between reinforcement and concrete, including rib bearing and wedging, friction, concrete damage, confinement, and slip reversal. Although these formulations provide a more detailed representation of the interface behavior, their level of local resolution can make their direct incorporation into structural-scale nonlinear analyses computationally demanding. Macroscopic approaches, in contrast, condense the effects of bond deterioration into localized interface, section-level, or constitutive formulations, allowing their influence on the structural response to be represented without explicitly discretizing the complete anchorage or development length. However, these approaches generally treat bond-related degradation independently from the strain-rate-dependent cyclic response of reinforcing steel.

These limitations define a clear gap: the absence of a unified constitutive framework for RC structural analysis that simultaneously accounts for strain-rate-dependent strengthening of reinforcing steel, cyclic hysteretic behavior, and bond-slip-induced pinching and degradation within a computationally tractable formulation. Such a framework should retain the essential history dependence of cyclic steel response while incorporating the effects of reinforcement–concrete interaction at the structural level, rather than treating rate dependence and bond-slip as independent modifications. This gap motivates the developments presented in the subsequent chapters.

3 Characterization of the Strain Rates in Steel Reinforcement

Predicting the seismic performance of RC structures exhibiting pronounced nonlinear behavior under strong-intensity earthquakes remains one of the most complex and enduring challenges in structural engineering. Despite substantial advances in analytical and numerical modeling capabilities since the 1960s, accurately simulating inelastic response under dynamic loading remains limited by uncertainties in material characterization, modeling assumptions, and the inherent complexity of ground motion. The most recent analytical models [54], [87], and [117] incorporated increasingly sophisticated constitutive laws, refined finite element formulations, and enhanced computational strategies. Nonetheless, these developments are still predominantly implemented within rate-independent material models for RC materials, particularly reinforcing steel.

In conventional structural modeling practice, constitutive laws for reinforcing bars are commonly formulated as rate-independent plasticity models. Consequently, damping and energy dissipation associated with strain-rate effects are typically represented indirectly through empirical damping models. While this approach may suffice for certain applications, it obscures the direct influence of strain-rate sensitivity on the stress-strain behavior of reinforcing steel, especially under the extreme loading rates characteristic of severe seismic events. Empirical damping adjustments, although calibrated to reproduce global response measures, do not explicitly reflect the physical mechanisms governing rate-dependent yielding, hardening, or post-yield softening.

Excluding explicit strain-rate effects is not merely a theoretical issue; it can significantly affect the accuracy of predicted structural performance. Extensive monotonic testing on reinforcing steel has shown that yield strength, ultimate strength, and sometimes ductility depend on the loading rate. Although monotonic test data are abundant, reversed cyclic tests capturing the combined influence of strain rate and cyclic degradation remain limited. Nevertheless, the available evidence from both monotonic and cyclic testing indicates that strain-rate sensitivity is a non-negligible factor, particularly when reinforcing bars undergo large inelastic deformations within plastic hinge regions.

Under seismic loading, the interaction among structural dynamics, material nonlinearity, and strain-rate effects becomes especially critical. Strong ground motions characterized by rapid acceleration pulses, high-frequency content, and complex displacement histories can generate transient strain rates in reinforcing steel far exceeding those encountered in quasi-static or low-rate laboratory testing. In plastic hinge regions, where inelastic curvature demands concentrate, reinforcing bars may experience strain rates that modify the yield plateau, shift the onset of strain hardening, and influence local buckling behavior. These localized effects can alter the global strength, stiffness, and energy dissipation capacity.

Despite decades of research on the nonlinear seismic response, comprehensive field or laboratory measurements of the actual strain rates in reinforcing bars during full-scale seismic events remain scarce. Existing studies have focused primarily on global force-displacement response, curvature distributions, and damage patterns, with limited emphasis on direct, high-resolution strain measurements in critical regions. This knowledge gap is significant, as accurate quantification is

essential for developing and calibrating rate-dependent constitutive models that can reliably predict behavior under seismic loading.

Incorporating rate dependence into constitutive models for reinforcing steel could enhance seismic performance predictions at both local and global scales. Locally, strain-rate effects influence yield strength, hardening, and ductility, thereby affecting curvature distribution and plastic hinge rotation capacity. Globally, these local changes can modify the structure's dynamic characteristics, influencing stiffness degradation, residual drift, and collapse capacity. Moreover, rate-dependent constitutive models could strengthen performance-based earthquake engineering (PBEE) frameworks by providing more realistic input for nonlinear dynamic analyses across a wide range of seismic intensities and frequency contents.

The present study represents an initial step toward this objective. Quantifying the strain rates in full-scale RC components subjected to realistic earthquake loading provides a unique dataset for developing next-generation material models for reinforcing steel. While the current focus lies on measuring and characterizing strain-rate demands, the broader research agenda involves integrating these empirical observations into plasticity formulations that capture the observed rate effects, validating them against experimental data, and evaluating their influence on seismic performance through nonlinear dynamic analysis.

The experimental findings presented here underscore the need to reassess the long-standing assumption of rate independence in the modeling of reinforcing steel for seismic applications. As computational capabilities and experimental techniques continue to advance, the field is increasingly well-positioned to capture the intricate interplay among loading rate, material response, and structural dynamics. Bridging the gap between empirical observation and analytical representation is essential to achieve the high-fidelity seismic performance predictions required and to design resilient RC structures in high seismic zones.

This chapter characterizes the strain rates experienced by longitudinal steel reinforcement in RC elements under realistic seismic loading. Section 3.1 compares reversed cyclic axial tests conducted at low and high loading rates, relating global cyclic response to localized yielding through strain-gauge measurements and digital image correlation. In Section 3.2, two full-scale specimens tested on the Large High-Performance Outdoor Shake Table (a seven-story wall-building slice and a single-column bridge bent) are described with respect to instrumentation, reinforcement detailing, and applied ground motions. Section 3.3 examines the reversed cyclic stress-strain response of reinforcing bars, identifying elastic behavior, the Lüders plateau, and work hardening. Section 3.4 develops a first-principles framework to estimate average strain rates from curvature distributions within the Direct Displacement-Based Assessment methodology, with applications to the wall-building and bridge column specimens. The distinction between average and instantaneous strain rates is established in Section 3.5, where the dimensionless κ-ratio is defined and expressed as the product of three factors associated with Lüders band propagation, higher-mode dynamic effects, and waveform characteristics. Representative strain time histories for both specimens are presented in Section 3.6. Section 3.7 defines three complementary period measures used in the analysis: initial, predominant, and effective. Section 0 outlines the signal-processing workflow, including Arias-intensity-based truncation, two-stage Butterworth filtering to isolate all-modes and lower-mode signals, temporal realignment via normalized cross-correlation, and frequency-domain

spectral differentiation to obtain strain-rate signals. Peak strain rates are characterized in Section 3.9, distinguishing between the Lüders plateau and work-hardening regimes, and evaluating the κ-ratio and its components: κ_L, κ_H, composite κ statistics, and κ_W. Section 3.10 summarizes the principal findings and their implications for rate-dependent constitutive modeling of reinforcing steel under seismic loading.

3.1 Influence of Loading Rate

To better illustrate the influence of loading rate on the mechanical response of reinforcing steel, the discussion begins by comparing two reversed cyclic axial tests conducted at different loading rates: one rapid and one slow. This approach allows direct examination of the material's rate-dependent features. By combining localized strain-gauge measurements with full-field strain data obtained via digital image correlation (DIC) [34], the study links the global cyclic response to the underlying mechanisms of localized yielding, Lüders plateau propagation, and subsequent work hardening. This dual perspective- macroscopic and microscopic- provides a more complete understanding of how loading rate alters the steel's mechanical behavior.

Such insight is particularly relevant for RC structures subjected to seismic actions. In the plastic hinge zones that form during strong ground motions, strain rates in reinforcing steel can vary significantly, directly influencing both strength and ductility. These rate-induced changes alter the apparent yield point, modify hardening behavior, and affect the overall energy dissipation capacity, all of which are central to the nonlinear dynamic performance of structural members. Recognizing and quantifying these effects is therefore critical for refining constitutive formulations and improving predictive accuracy under realistic earthquake demands.

To bridge experimental observations with engineering applications, this work integrates structural mechanics principles with dynamic response parameters, establishing a rigorous framework for interpreting experimentally recorded histories and refining constitutive models that incorporate rate sensitivity. This framework supports incorporating measured rate-dependent behavior into analytical models used for performance-based seismic assessment.

The experimental basis of this study derives from two full-scale RC specimens tested on the National Science Foundation-funded single-axis Large High-Performance Outdoor Shake Table (LHPOST) under the George B. Brown Jr. Network for Earthquake Engineering Simulation (NEES) program, at the University of California, San Diego [116]. In both specimens, strain gauges on longitudinal bars in the plastic hinge regions captured inelastic deformation histories under seismic-type loading. From these measurements, the authors computed strain rates, compared them across loading conditions, and systematically characterized their influence on the steel's mechanical performance. By integrating these results with the conceptual approach presented later, the study provides both direct experimental evidence and a transferable methodology for addressing rate effects in seismic engineering practice.

3.2 Description of Specimens

The experimental program involved two full-scale RC specimens, each representing critical structural components commonly used in seismic-resistant construction. The first specimen consisted of a vertical segment of a 7-story wall-building slice, intended to capture the interaction

between vertical elements and floor diaphragms under multi-story loading conditions. The second specimen was an RC bridge pier, configured to emulate the seismic response of a single-support bridge bent. Both specimens were constructed in accordance with contemporary design codes and detailing practices, with particular attention to forming well-defined plastic hinge regions capable of accommodating strong earthquake-induced demands.

Dynamic testing was conducted on the LHPOST shake table. This facility enabled the application of realistic, full-scale earthquake ground motions, allowing direct observation and measurement of nonlinear seismic behavior, including local strain accumulation, plastic hinge development, and overall member response. Despite differences in geometry, reinforcement detailing, and loading configuration, both specimens exhibited characteristic dynamic responses that reflect how structural layout and input-motion properties influence strain-rate demands, energy dissipation, and post-yield behavior, ultimately governing seismic performance.

3.2.1 7-Story Building Slice

A 19.2 m tall, seven-story RC building slice, hereafter referred to as the specimen, was meticulously designed, constructed, and experimentally tested at the LHPOST during the 2006-2007 experimental campaign [99]. The specimen represented a full-height segment of a prototype building and was intended to replicate the primary seismic load-resisting elements under realistic boundary conditions. The specimen's total weight, excluding its massive RC foundation, was 20.45 MN.

The main structural component, a rectangular bearing wall (shown as the web wall in Figure 7), was 3660 mm in length. Its thickness varied along the height: 203 mm at the first and top levels, and 152 mm in the intermediate stories. The wall was oriented east-west, which corresponded to the LHPOST system's horizontal excitation axis.

Each story featured a 3660 mm wide by 7900 mm long by 203 mm thick RC slab spanning from the wall and supported at the slab edges by 102 mm diameter, grout-filled, high-strength steel pipe gravity columns. Additional lateral and torsional stability was provided by a segmental pier and flange wall oriented north-south, as depicted in Figure 7.

The experimental program consisted of two phases. In Phase I, the isolated web wall, as shown in Figure 7, acted as the sole lateral load-resisting system for the building slice [97]. In Phase II [98], the web and flange walls were joined by casting concrete into the vertical gap between them, forming a T-section wall with enhanced stiffness and strength. This thesis focuses exclusively on the strain-rate data from Phase I, thereby isolating the influence of the single web wall under dynamic excitation. Figure 8 illustrates the reinforcement layout at the base of the bearing wall, the region where localized plasticity and inelastic deformations were observed during the test.

The east and west boundary elements incorporated 8#5 longitudinal bars each, with the east end extended to form a boundary element reinforced with 4#4 bars. #3 resistance-welded steel grids provided boundary element confinement in accordance with ICC-ES ESR-2352 [60]. Except for these confinement grids, all reinforcement complied with ASTM A615 Grade 60 specifications [7]. The #5 longitudinal bars exhibited a yield strength of f_y=454 MPa, a tensile-to-yield strength ratio

of 1.54, a strain at the onset of work hardening of 0.8%, and a uniform tensile strain capacity of 11.2%, indicating a ductile steel behavior suitable for seismic applications.



Figure 7. Southwest view of the 7-story wall-building test specimen (photo by Dr. José Restrepo).

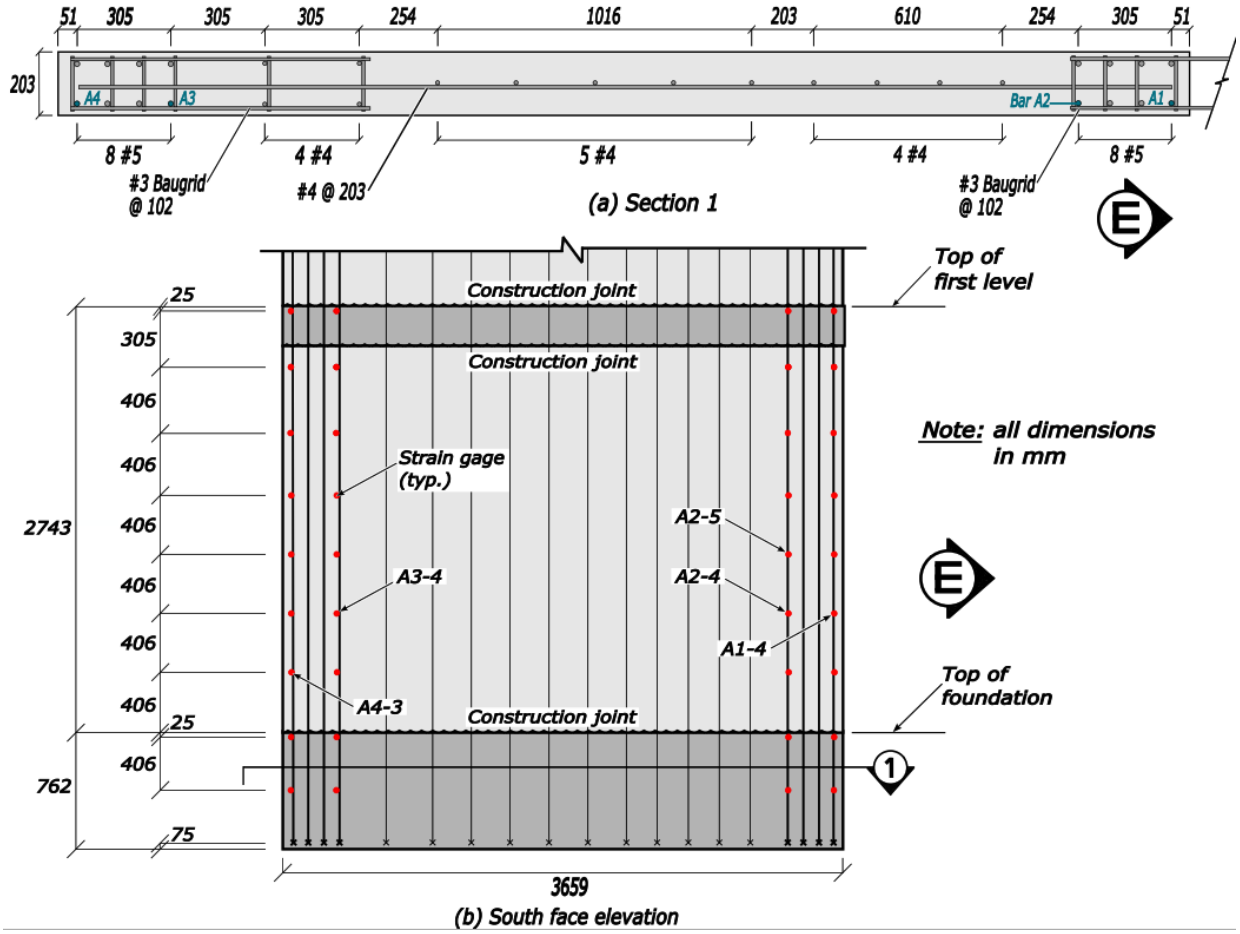


Figure 8. Longitudinal and transverse reinforcement layout for the wall-building test specimen.

A single curtain of #4 bars provided longitudinal and transverse reinforcement across the wall's web. To capture localized strain demand, the two #5 bars within each boundary element (see bars A1-A4 in Figure 8) were instrumented with strain gauges positioned at critical locations along their length. Of these, gauges A1-4, A2-4, A2-5, A3-4, and A4-3 remained fully functional and provided continuous data throughout the entire test program.

The specimen was subjected to four progressively intensified single-horizontal-axis ground motions (EQ1-EQ4), each representing historical Southern California earthquake records scaled to hazard levels with up to a 10% probability of exceedance in 50 years [96]. These motions were carefully selected to encompass a range of frequency contents, amplitudes, and near-fault effects. Figure 9 presents the pseudo-acceleration response spectra for elastic response at 5% damping for EQ1-EQ4, as reproduced in LHPOST.

The lowest-intensity motion, EQ1, corresponded to the longitudinal component of the Mw 6.6 1971 San Fernando earthquake, recorded at the Van Nuys Station (VNUY). EQ2 and EQ3 represented medium-intensity excitations with similar spectral ordinates in the 0.6-1.9 s range, although EQ3 exhibited significantly larger ordinates in the short-period range (0.1-0.4 s). Specifically, EQ2 was the transverse component of the 1971 San Fernando earthquake (VNUY), while EQ3 was the

longitudinal component of the Mw 6.7 1994 Northridge earthquake recorded at the WHOX station. The most severe excitation, EQ4, was the 360° component from the 1994 Northridge earthquake recorded at the Sylmar Olive View Medical Station, characterized by a pronounced velocity pulse typical of near-fault ground motions. Strain demands exceeding 1% were observed in the longitudinal reinforcement during EQ2-EQ4.

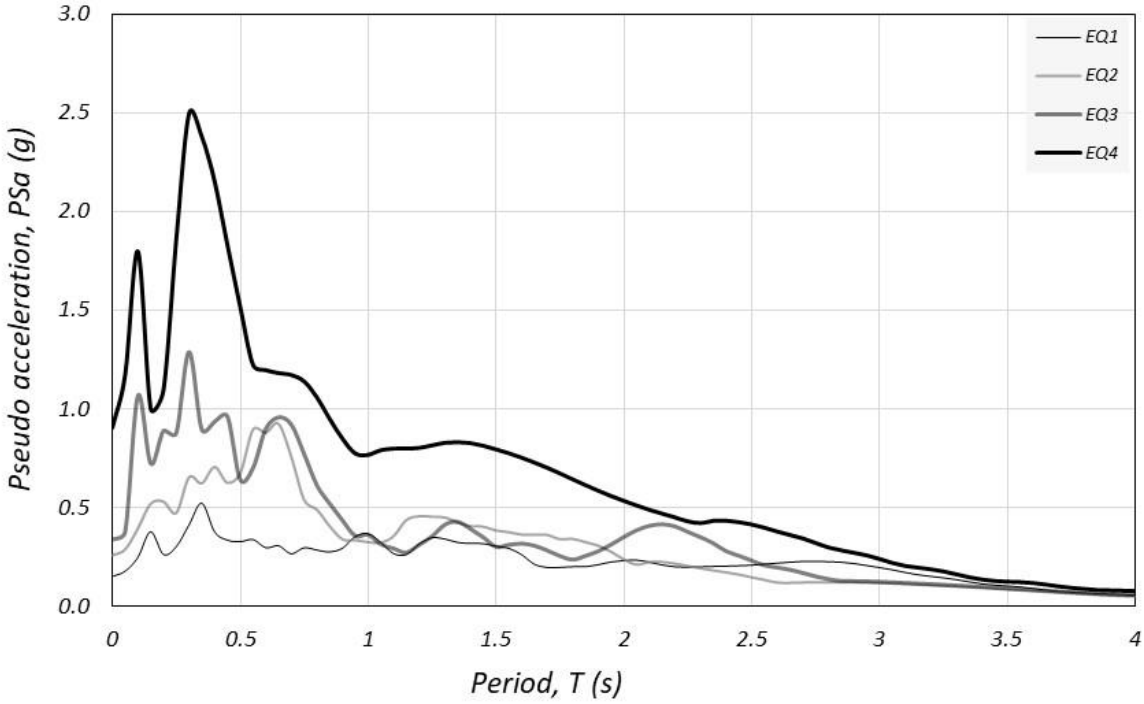


Figure 9. Pseudo-acceleration response spectra (5% damping) of input ground motions for the wall-building specimen.

Ambient vibration testing before EQ1 identified the specimen's first two east-west translational modes with initial periods T_{o1}=0.52 s and T_{o2}=0.095 s [91], corresponding to modal mass participation ratios of 69% and 18%, respectively. During EQ1, the specimen achieved a peak lateral displacement of 50 mm at the roof, corresponding to a drift ratio of 0.28%, and a peak tensile strain in the longitudinal reinforcement of 0.61%. The first and second predominant periods were T_{p1}=0.67 s (T_{p1}/T_{o1}=1.29) and to T_{p2}=0.099 s (T_{p2}/T_{o2}=1.04), respectively. For EQ2 and EQ3, peak lateral displacements were 140 mm and 160 mm, corresponding drift ratios of 0.75% and 0.83%, and the reinforcement tensile strains reached 1.73% and 1.78%, respectively. The predominant periods for EQ2 were T_{p1}=0.98 s (T_{p1}/T_{o1}=1.88) and T_{p2}=0.11 s (T_{p2}/T_{o2}=1.16), while for EQ3 they were T_{p1}=0.99 s (T_{p1}/T_{o1}=1.91) and T_{p2}=0.18 s (T_{p2}/T_{o2}=1.86). Under the extreme excitation of EQ4, the specimen reached a peak displacement of 400 mm (roof drift ratio of 2.06%), and the maximum tensile strain in the longitudinal reinforcement increased to 2.85%. Damage at the wall base included localized spalling of the concrete cover and degradation of a lap splice above the first story (Figure 10). The fundamental periods are further elongated to T_{p1}=1.5 s (T_{p1}/T_{o1}=2.89) and T_{p2}=0.2 s (T_{p2}/T_{o2}=2.07), consistent with substantial stiffness degradation and permanent damage accumulation.



a) Overall view (Note: open cracks have been digitally enhanced)

b) Close-up view of the wall's southwest corner

Figure 10. View of the south face of the first floor of the wall-building specimen at maximum displacement during test EQ4 (video-sourced images by J. Restrepo).

3.2.2 Single-Column Bridge Bent

In 2008, an RC bridge column specimen with a circular cross-section measuring 1,219 mm in diameter and a total height of 7,315 mm was constructed and tested to collapse at the LHPOST [124]. The test program was designed in accordance with the *Bridge Design Specifications* [25] and the *Caltrans Seismic Design Criteria* [26], with the explicit objective of inducing a predominantly flexural response under seismic excitation. The design avoided premature shear failures and ensured that plastic deformations would localize at the intended plastic hinge region near the column base. Figure 11 provides a southwest view of the specimen before testing.

An inertial block weighing 2.32 MN was cast integrally at the top of the column. It served as both a concentrated mass for dynamic excitation and a constant axial load source. The center of mass was positioned precisely at the full column height (7315 mm from the base), ensuring consistent axial force application and realistically simulating the superstructure weight in a bridge configuration. The block's dimensions and mass were proportioned so that the column's dynamic characteristics would closely replicate those of single-bent bridge piers in service.

The column's reinforcement arrangement and overall geometry are depicted in Figure 12. The longitudinal reinforcement consisted of 18 #11 (35.8 mm diameter) bars, uniformly distributed around the perimeter. The confinement reinforcement consisted of double #5 (15.9 mm diameter) hoops spaced on-center at 152 mm, providing sufficient lateral restraint to the core concrete and preventing premature buckling of the longitudinal bars during cyclic loading. All reinforcement was ASTM A706 Grade 60 [8], selected for its ductility and weldability. The #11 bars had a measured yield strength of f_y= 519 MPa, a tensile-to-yield strength ratio of 1.36, a strain at the onset of work hardening of 1.1%, and a uniform strain at the tensile point of 12.2%.

The seismic testing program consisted of 10 single-horizontal-axis earthquake simulations (EQ1-EQ10) using input ground motions recorded during 4 historical Mw 6.9 earthquakes. Three of these motions were recorded during the 1989 Loma Prieta earthquake at the Agnew State Hospital,

Corralitos, and LGPC stations. The fourth motion corresponded to the 1995 Kobe earthquake recorded at the Takatori station [124]. Figure 13 presents the pseudo-acceleration response spectra for the first five records (EQ1-EQ5) at 5% viscous damping, as reproduced on the LHPOST.



Figure 11. Southwest view of the bridge column specimen (photo by Dr. José Restrepo).

Of the ten available earthquake records, this dissertation discusses only EQ2-EQ5 in detail. In EQ6, several strain gauges installed within the column's plastic hinge region were lost, compromising data reliability. During EQ7, a reduction in the bond between the longitudinal reinforcement and the surrounding concrete became evident, and signs of potential bar buckling were observed. By EQ8, longitudinal bars began to fracture, and concrete core crushing was visible. Finally, in EQ9 and EQ10, approximately two-thirds of the longitudinal bars fractured, resulting in partial specimen collapse. Due to this progressive loss of instrumentation and structural integrity, records beyond EQ5 were excluded.

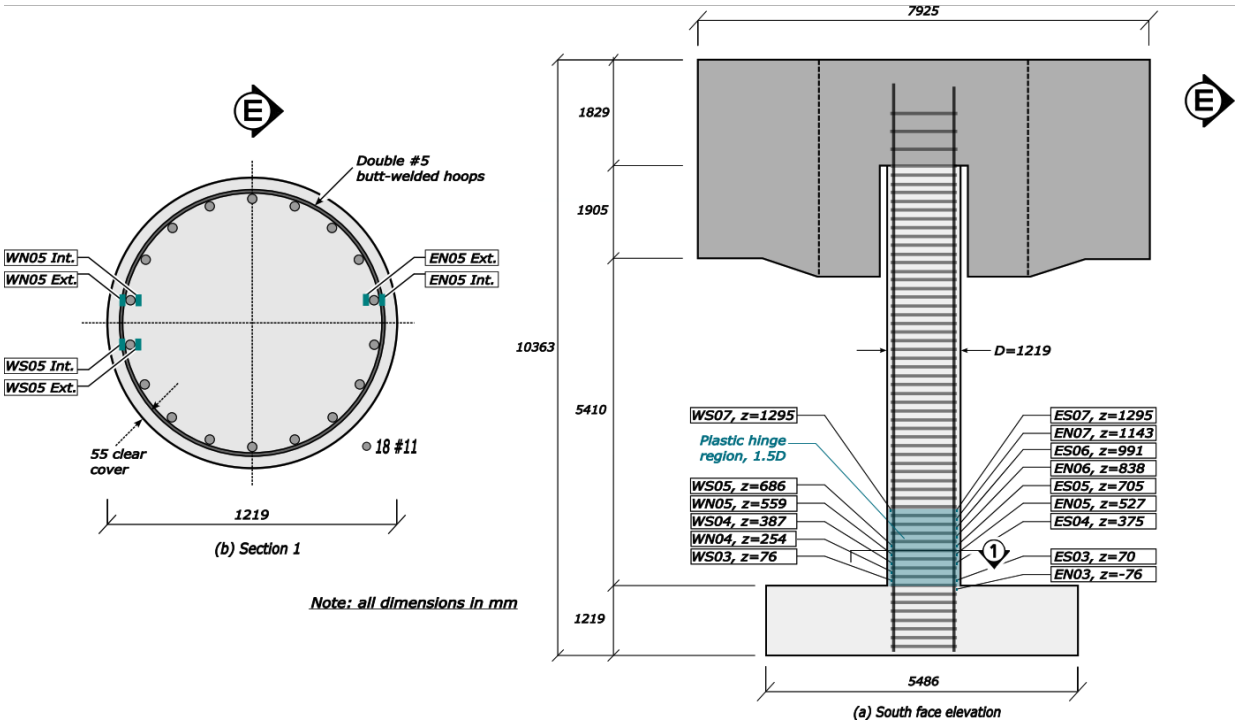


Figure 12. Longitudinal and transverse reinforcement layout for the bridge column specimen.

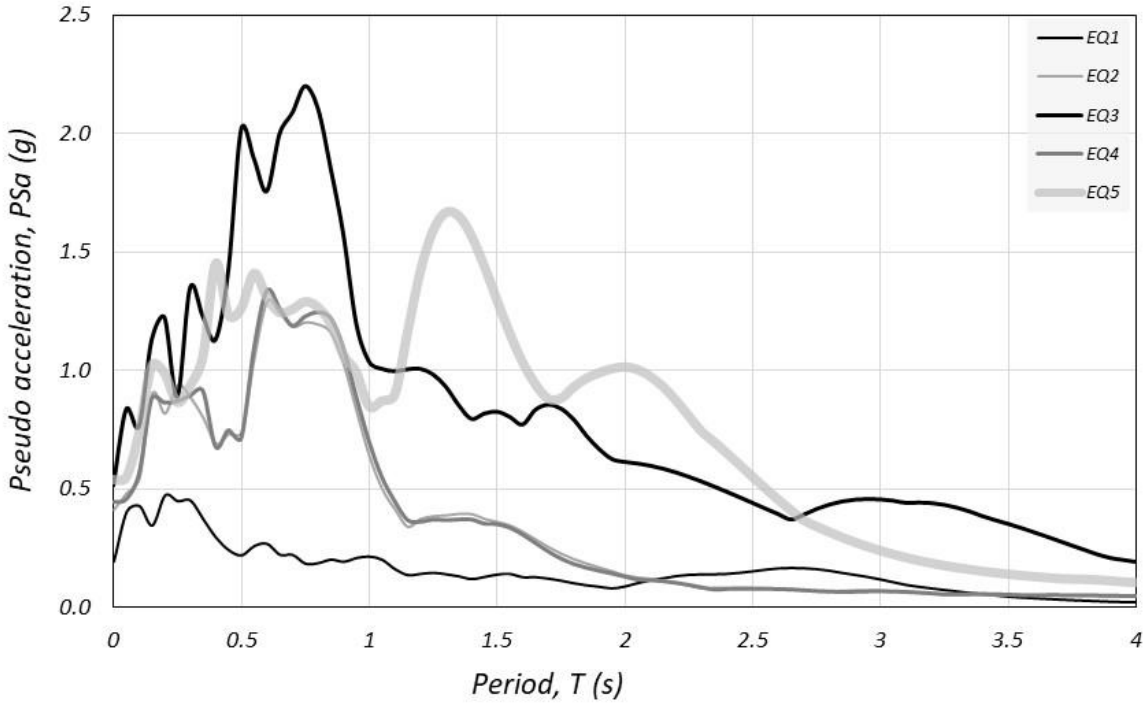


Figure 13. Pseudo-acceleration response spectra (5% damping) of input ground motions for the bridge column specimen.

Before dynamic testing, ambient vibration measurements established the column's initial dynamic properties. The first two east-west translational modes had initial periods T_{o1}=0.88 s and T_{o2}=0.17 s, with corresponding modal participating mass ratios of 98% and 2%, indicating that the fundamental mode dominated the seismic response.

In test EQ1, light cracking was observed, but the reinforcing steel remained elastic. The presence of distributed microcracks was sufficient to increase the fundamental period to T_{p1}=1.15 s or T_{p1}/T_{o1}=1.31, and the second mode to T_{p2}=0.18 s or T_{p2}/T_{o2}=1.06. In EQ2, the peak lateral displacement at the center of mass of the inertial block relative to the column base reached 133 mm, corresponding to a drift ratio of 1.82%. The maximum tensile strain recorded in the longitudinal reinforcement was 1.32%, indicating localized yielding at the plastic hinge. Residual crack widths increased compared to EQ1. The identified predominant periods were T_{p1}=1.35 s (T_{p1}/T_{o1}=1.53) and T_{p2}=0.21 s (T_{p2}/T_{o2}=1.24).

Test EQ3 simulated the design-level earthquake for the specimen. Peak lateral displacement reached 361 mm (drift ratio of 4.93%), and the column exhibited incipient crushing of the concrete cover at the compression face, along with widespread yielding of longitudinal reinforcement. The fundamental period elongated to T_{p1}=2.65 s (T_{p1}/T_{o1}=3.01), while the second mode reached T_{p2}=0.24 s (T_{p2}/T_{o2}=1.42). Test EQ4, intended to represent an aftershock, resulted in a smaller maximum displacement of 170 mm (2.33% drift ratio) but continued to accumulate damage in previously cracked and spalled regions. Peak tensile strain was 1.44%. Periods elongated further to T_{p1}=1.7 s (T_{p1}/T_{o1}=1.93) and T_{p2}=0.26 s (T_{p2}/T_{o2}=1.52).

The most demanding motion, EQ5, produced a lateral displacement of 569 mm (7.78% drift ratio) and a peak longitudinal bar strain of 4.66%, accompanied by extensive spalling above the column base. The periods reached T_{p1}=3.15 s (T_{p1}/T_{o1}=3.58) and T_{p2}=0.27 s (T_{p2}/T_{o2}=1.59). Beyond EQ5, progressive damage compromised instrumentation: in EQ6, many gauges in the plastic hinge region failed; by EQ8, several longitudinal bars had fractured; and by EQ10, approximately two-thirds of the longitudinal bars had failed, leading to the complete collapse of the column against the safety catching frame.

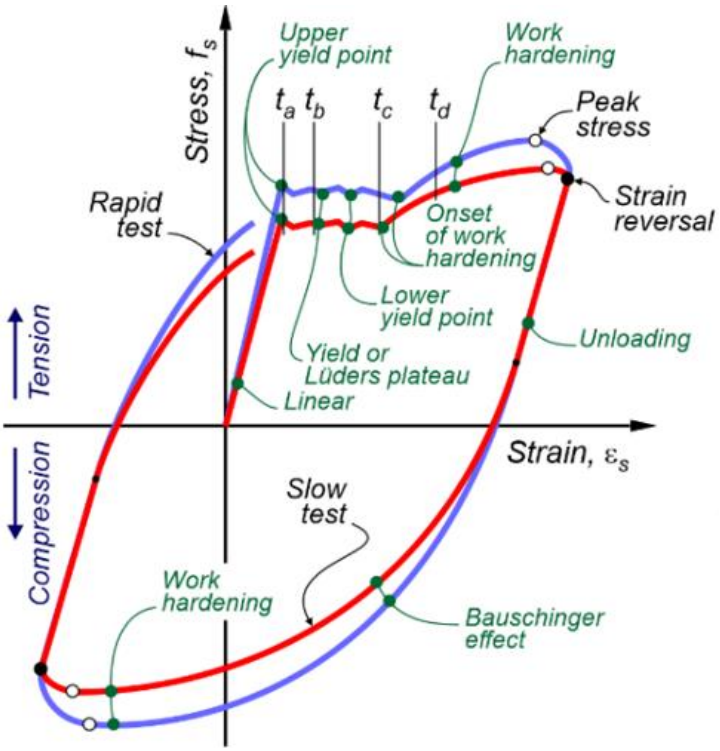
3.3 Reinforcing Bar Reversed Cyclic Stress-Strain Response

Figure 14a presents a schematic comparison of the reversed cyclic axial stress-axial strain response from two identical reinforcing bar tests: one performed at a high loading rate (purple line) and the other at a low loading rate (red line), both initiated in tension. Axial strains were measured using a miniature electrical foil strain gauge affixed at the bar's mid-height, positioned between two adjacent lugs.

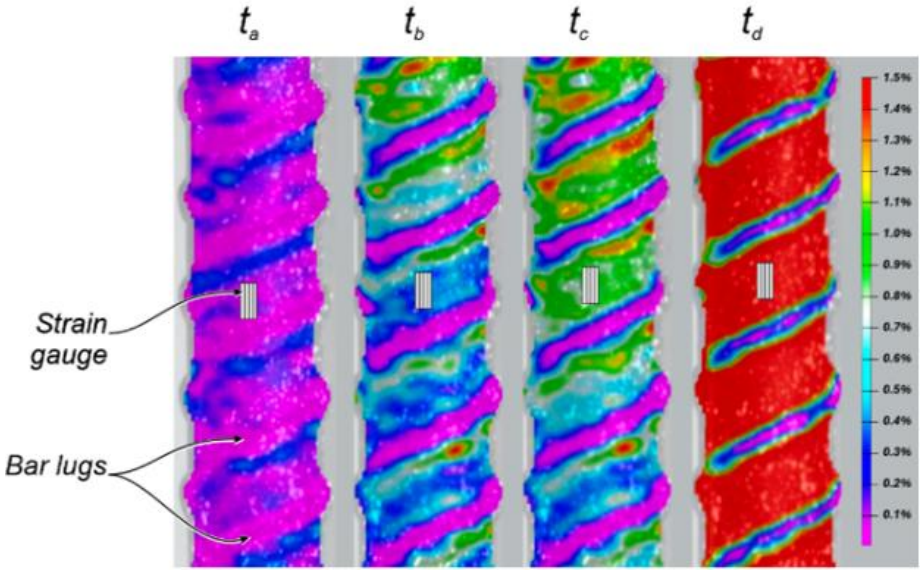
Before any load reversal, the stress-strain response can be divided into three characteristic regions:

1) A linear elastic phase governed by a nominal Young's modulus, terminating at the upper yield point (or simply the yield point if no upper yield point is present);
2) A yield plateau, commonly referred to as the Piobert-Lüders or simply Lüders plateau, during which stress remains approximately constant, and a lower yield point often emerges; and
3) The onset of work hardening, marking the conclusion of the yield plateau.

A qualitative comparison of the two tests underscores the influence of loading rate: faster loading rates extend the yield plateau [114]. The viscoplastic (rate-dependent) nature of reinforcing steel is most pronounced near load reversals, where the maximum stress does not coincide with the reversal strain, which occurs when the strain rate reaches zero.



a) Stress-strain response



b) Bar axial strain visualization at different times

Figure 14. Stress-strain response in a reinforcing bar.

Two distinct phases preceded the return to work hardening at higher compressive stresses. The first is a linear unloading segment, nearly identical for both tests, with a modulus smaller than the initial Young's modulus [43]. The second is a nonlinear behavior associated with the Bauschinger effect. This effect, first documented by Johann Bauschinger in 1886 [11], describes the reduction in yield strength observed when a metallic material undergoes reverse plastic deformation following initial loading in the opposite direction. It is more pronounced for the rapid test.

Figure 14b depicts the full axial strain field of one specimen at four selected instants during the test, capturing the transition from yield initiation to the work-hardening regime (as correlated with Figure 14a). These strain fields were obtained using DIC techniques [34], which provide a global view of strain distribution not possible with localized measurements from a single mid-height strain gauge.

The onset of localized yielding is first observed at the roots of the lugs, where manufacturing processes influence the complex local geometry and stress state; specifically, the interaction between the rolling dies and the rolling direction, which produces a phenomenon analogous to the so-called wiping effect (see time t_a in Figure 14b). The rolling direction induces anisotropy in the microstructure and mechanical properties of steel [103]. At the same time, the concept of wiping dies in metal forming illustrates how tooling contact can constrain material flow and induce localized surface smearing or displacement [95], [130]. Although no direct study on the combined effect of reinforcing bars is available, these observations provide a conceptual basis for interpreting how manufacturing processes influence strain localization.

At time t_b, corresponding to the Lüders plateau, the strain field between the lugs is distinctly nonuniform: in the upper section of the bar, strains range from 1.0 % to 1.2 %, while at mid-height (where the strain gauge is located), strains remain between 0.4 % and 0.5 %. By time t_c, near the end of the Lüders plateau, the strain field remains heterogeneous, confirming that yielding at this stage propagates progressively along the bar.

Yield propagation during the Lüders plateau significantly influences measured strain rates, which this research examines in detail later. Piobert first reported this phenomenon in 1842 [102], and Lüders reported it in 1860 [78], noting fine, matte lines on prismatic steel specimens. These so-called Lüders bands are now recognized as the macroscopic manifestation of underlying dislocation dynamics during plastic flow [90], reflecting the propagation of localized plastic deformation through the material.

Recent studies provide additional insights into this behavior. Liu et al. [76] showed that the Lüders strain rate and dislocation multiplication rate are critical microstructural parameters controlling band formation in medium-Mn steels. Qiu et al. [108] demonstrated, using digital image correlation, that in hot-rolled steel the onset of plastic bands coincides with the macroscopic yield plateau and governs subsequent plastic flow. In ferrite-pearlite steels, Qiu et al. [110] reported that band nucleation occurs at a stress below the upper yield point. Although most of these investigations have focused on flat or plate geometries, the present observations confirm that the phenomenon is equally relevant in reinforcing bars. In these materials, the manufacturing-induced anisotropy and the microstructural state inherited from rolling play a decisive role in the initiation and evolution of Lüders bands, governing localized plastic deformation and the progressive

propagation of yielding along the bar. Consistently, Lüders bands have been documented in reinforcing steel bars, where strain discontinuities nucleate at single locations and propagate along the bar axis under nearly constant load [72].

Once the Lüders band front has fully propagated along the gauge length, the material transitions from localized yielding to more uniform plastic deformation. Initially, the band produces highly localized and heterogeneous strains, but as it travels along the bar, more material yields and the heterogeneity diminishes. After propagation completes, the bar enters a regime of nearly uniform plastic deformation, with subsequent loading governed by strain hardening rather than localized yielding. Experimental observations in fine-grained TWIP and TRIP steels indicate that, once the Lüders band has traversed the entire specimen, typically at strains beyond approximately 0.028, the strain field becomes nearly homogeneous, marking the onset of uniform plastic flow [64]. In reinforcing steel bars, the region ahead of the band yields locally as it propagates. Meanwhile, the area behind deforms more steadily, consistent with the influence of microstructural state and manufacturing-induced anisotropy on both the initiation and evolution of Lüders bands [72]. These findings confirm that the propagation mechanism governs the transient heterogeneity in the strain field and that microstructural and processing characteristics critically affect the development of Lüders bands.

The present observations at the time t_d, where the strain distribution between lugs becomes uniform, confirms that the propagation phenomenon characteristic of the Lüders plateau has ceased in this region.

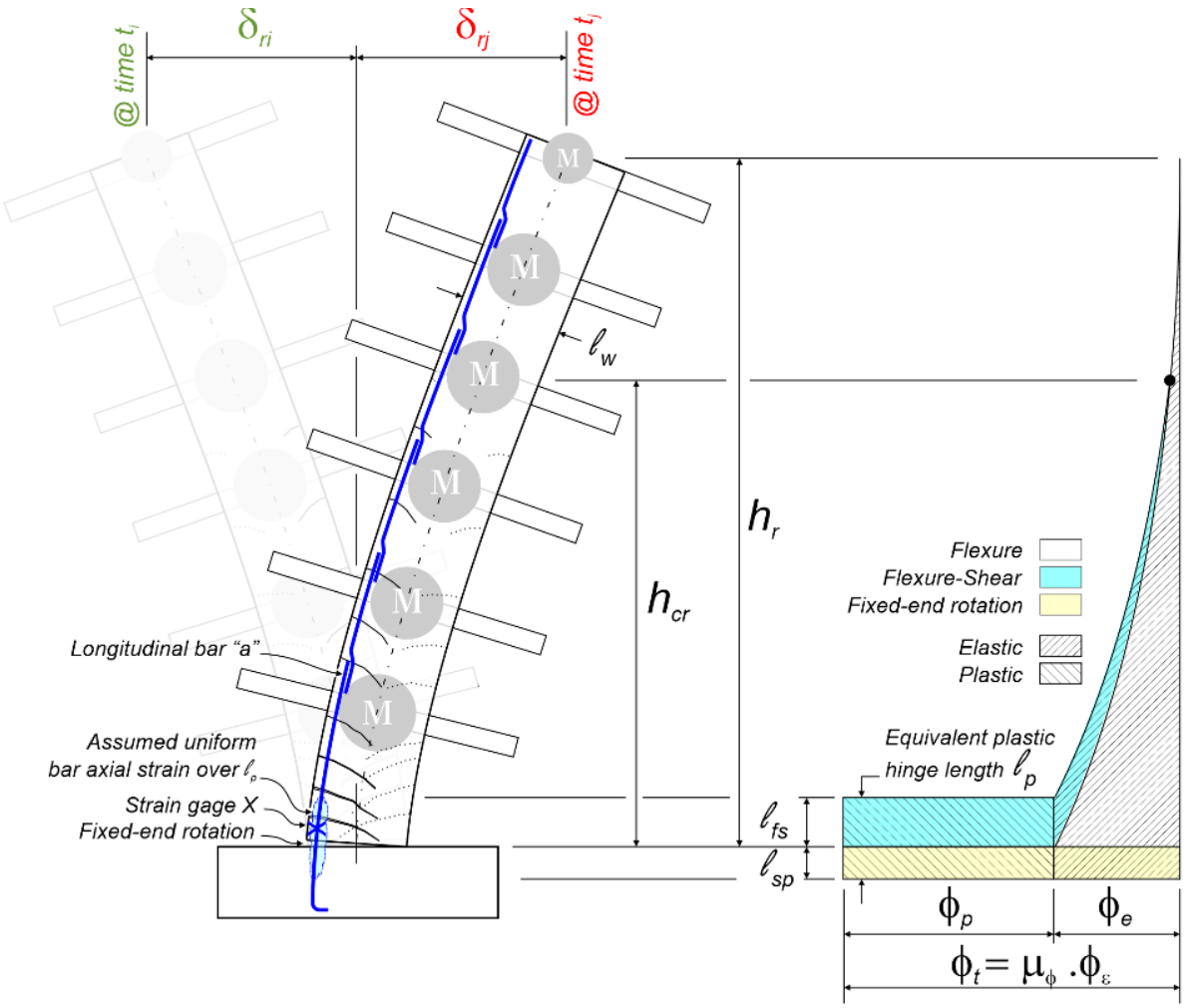
3.4 Evaluation of Bar Strain Rates Using First Principles

Strain rates in a bar within the plastic hinge of an RC structural element can be approximated using first principles. Figure 15 schematically depicts a laterally displaced structural wall at two distinct times, t_i and t_j, within its response history to an earthquake excitation. The structural wall is assumed to be part of a building system, which undergoes significant nonlinear deformation at its base due to the formation of a plastic hinge. Within this context, the longitudinal reinforcing bar labeled “a” (blue line) is instrumented with a strain gauge near the wall base to capture axial strain histories. The figure highlights this bar and the strain-measurement location, underscoring the importance of this critical zone where plasticity localizes.

At time t_i, the wall’s response clearly indicates the development of a plastic hinge at the base, characterized by substantial inelastic curvature demands. Figure 15b shows the idealized curvature profile along the wall height, illustrating how curvature concentrates near the base and diminishes toward the roof level. The overall roof displacement reflects contributions from several deformation modes: (1) pure flexure, generating a smooth curvature gradient; (2) flexure-shear interaction, which introduces abrupt curvature changes associated with diagonal cracking and shear deformations; and (3) fixed-end rotations resulting from slip phenomena at the bar-concrete interface near the foundation, represented as curvature penetration into the footing.

To model the plastic hinge accurately, the concept of an equivalent plastic hinge length, denoted as l_p, is introduced. This length represents the segment along the wall base over which the reinforcing bar strain is approximately uniform. The plastic hinge length is comprised of two components: the

strain penetration length, l_{sp} which accounts for the bar's slip into the foundation, and the flexure-shear spread length l_{fs}, capturing the extension of plasticity due to combined flexural and shear effects. Accurately estimating these lengths is essential for characterizing strain gradients and strain rates within the reinforcing bar, which, in turn, dictate the local material response.



a) Laterally deformed structural element at times t_i and t_j

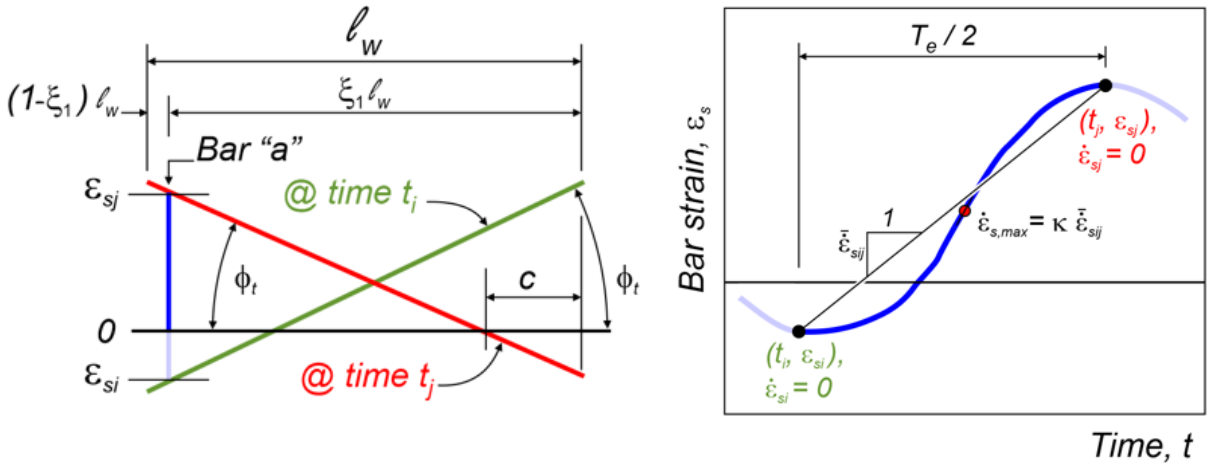
b) Element's idealized curvature profile at time t_j

Figure 15. Schematic representation of a laterally deformed structural wall responding to earthquake input.

The curvature at the wall base, ϕ_t, is the summation of an elastic component ϕ_e and a plastic component ϕ_p. The total curvature is conveniently expressed in terms of the curvature ductility factor, μ_ϕ, relating plastic deformation to the elastic curvature as:

$$\phi_t = \phi_e + \phi_p = \mu_\phi \phi_e \tag{83}$$

Figure 16a presents an idealized strain profile for bar "a" at the elevation corresponding to the strain gauge position. At time t_i, the bar is subjected to a compressive strain ε_{si}, reflecting the local curvature and plastic hinge rotation. Later, at the time t_j, the same location experiences a tensile strain ε_{sj}, as the loading direction reverses, a condition representative of cyclic demands induced by seismic excitation. At these instants, the strain rate $(d\varepsilon/dt)$ is zero, indicating the points of strain reversal where the deformation changes sign. These turning points delimit half of an effective strain cycle, which can be used to quantify the cyclic deformation amplitude in the reinforcing bar. As loading continues, the alternating sequence of such cycles progressively accumulates plastic strain. It induces stiffness degradation, providing a direct link between local strain histories and the member's macroscopic cyclic response.



a) Equivalent plastic hinge strain profile b) Strain gage X on a bar "a" strain history

Figure 16. Idealized strain profile at the wall elevation at times t_i and t_j.

Figure 16b plots the strain time history of bar "a" between t_i and t_j, representing one-half of the bar's cyclic strain period, denoted as T_e. This interval defines the temporal window over which both average and peak strain rates are determined, providing essential information for characterizing the rate-dependent response of the material. Accurate estimation of these strain rates is critical for calibrating constitutive models and capturing the dynamic behavior of reinforcing steel under cyclic loading.

In wall-type building systems akin to those depicted in Figure 15, the maximum roof displacement δ_{rj} can be approximated through displacement-based frameworks. Among these, the Direct Displacement-Based Assessment (DDBA) methodology proposed by Priestley et al. [106] is widely recognized. This approach estimates inelastic deformation demands by linking structural displacement capacities to equivalent plastic hinge lengths and material ductility parameters.

The maximum roof displacement δ_{rj}, at the time t_j is functionally related to the curvature distribution along the wall height, moment-area properties of the cross-section, and section overstrength factors. This relation captures the contributions of elastic and plastic curvatures, as well as geometric and material nonlinearities, within the plastic hinge. Precise quantification of δ_{rj} is necessary to accurately estimate bar strain amplitudes and, subsequently, strain rates.

The maximum roof displacement δ_{rj}, at the time t_j is the sum of the elastic, δ_e, and plastic, δ_p, displacements as follows:

$$\delta_{rj} = \delta_e + \delta_p \tag{84}$$

The resulting elastic displacement, δ_e, can be expressed as the sum of three components: (1) the flexure contribution, $\delta_{e,F}$ (2) flexure-shear contribution, $\delta_{e,FV}$; and (3) the fixed-end rotation contribution, $\delta_{e,sp}$, which are determined by applying the second-moment area theorem to the idealized curvature profile (Figure 15).

$$\delta_e = \Omega_{ws}\left[\delta_{e,F} + \delta_{e,FV} + \delta_{e,sp}\right] \tag{85}$$

where,

$$\begin{aligned} \delta_{e,F} &= \nu\phi_e {h_r}^2 \qquad\qquad \nu \approx \left({}^4/_3 + n\right)/(3+4n) \\ \delta_{e,FV} &= \frac{l_{fs}\phi_e}{h_{cr} - l_{fs}}\left\{\frac{h_{cr}}{2}\left(h_r - \frac{1}{3}h_{cr}\right) - \frac{l_{fs}}{2}\left(h_r - \frac{1}{3}l_{fs}\right)\right\} \\ \delta_{e,sp} &= \phi_e l_{sp}\left(h_r + \frac{1}{2}l_{sp}\right) \end{aligned} \tag{86}$$

where n, the number of levels, and Ω_{ws}, the overstrength factor to reflect contributions from material variability, supplementary reinforcement, and structural redundancy that are not captured in the nominal design.

The elastic curvature, ϕ_e, can be approximated using the relationship provided by Priestley [105].

$$\phi_e = \lambda\frac{\varepsilon_y}{l_w} \tag{87}$$

Where λ is referred to as the cross-section coefficient. Hence,

$$\delta_e = \Omega_{ws}\psi_e\phi_e \tag{88}$$

Where, ψ_e is a second-moment area coefficient corresponding to the elastic portion of the curvature diagram, given by

$$\psi_e = \left[\nu {h_r}^2 + \frac{l_{fs}}{h_{cr} - l_{fs}}\left\{\frac{h_{cr}}{2}\left(h_r - \frac{1}{3}h_{cr}\right) - \frac{l_{fs}}{2}\left(h_r - \frac{1}{3}l_{fs}\right)\right\} + l_{sp}\left(h_r + \frac{1}{2}l_{sp}\right)\right] \tag{89}$$

If $h_{cr} \approx h_r$ and $h_r \gg l_{sp}$, the coefficient can be greatly simplified with minimal loss of accuracy,

$$\psi_e \approx \left[\nu {h_r}^2 + \frac{1}{h_r/l_{fs} - 1}\left\{\frac{{h_r}^2}{3} - \frac{l_{fs}}{2}\left(h_r - \frac{1}{3}l_{fs}\right)\right\} + l_{sp}h_r\right] \tag{90}$$

The resulting plastic displacement, δ_p, can be expressed as the sum of two components: strain penetration into the footing, $\delta_{p,sp}$, and the spread of plasticity caused by flexure-shear interaction within the wall, $\delta_{p,FV}$.

$$\delta_p = \delta_{p,sp} + \delta_{p,FV} \tag{91}$$

Where,

$$\begin{aligned} \delta_{p,sp} &= \phi_p l_{sp}\left(h_r + \frac{1}{2}l_{sp}\right) \\ \delta_{p,FV} &= \phi_p l_{fs}\left(h_r - \frac{l_{fs}}{2}\right) \end{aligned} \tag{92}$$

Hence,

$$\delta_p = \psi_p \phi_p \tag{93}$$

where, ψ_p, is a second-moment area coefficient corresponding to the plastic portion of the curvature diagram, given by

$$\psi_p = \left[l_{sp}\left(h_r + \frac{1}{2}l_{sp}\right) + l_{fs}\left(h_r - \frac{l_{fs}}{2}\right)\right] \tag{94}$$

In a simplified form,

$$\psi_p \approx \left[l_{sp}h_r + l_{fs}\left(h_r - \frac{l_{fs}}{2}\right)\right] \tag{95}$$

The coefficients ψ_e and ψ_p are the second-moment area coefficients.

Therefore, the maximum roof displacement δ_{rj} at the time t_j, is given by

$$\delta_{rj} = \psi_e \Omega_{ws} \phi_e + \psi_p \phi_p \tag{96}$$

With reference to Figure 16a, the strain, ε_{sj}, in the bar "a" at the time, t_j, is given by

$$\varepsilon_{sj} = (\xi_1 l_w - c)\phi_t \tag{97}$$

Assuming now that at the time, t_i, the lateral displacement, δ_{ri}, and the curvature distribution are identical to those at the time, t_j, (a crude assumption),

$$\varepsilon_{si} = -(c - (1 - \xi_1) l_w)\phi_t \tag{98}$$

The average strain rate, $\bar{\dot{\varepsilon}}_{sij}$, in the interval $(t_j - t_i)$, see Figure 16b, is defined by

$$\bar{\dot{\varepsilon}}_{sij} = \frac{2\left(\varepsilon_{sj} - \varepsilon_{si}\right)}{T_e} = \frac{2\phi_t l_w (2\xi_1 - 1)}{T_e} \tag{99}$$

Following the description of the experimental setup, instrumentation layout, and seismic input records applied to both specimens described in Section 3.2, the analysis proceeds to quantify average strain rates attained at the maximum theoretical displacement for each specimen-ground motion considered, obtained by applying the DDBA procedure [106] in combination with (84)-(99). Using this methodology, the calculated maximum strain rates for the two specimens analyzed in this study were 4.8% and 7.5%, respectively.

3.4.1 Average Strain Rates for the Wall-Building Specimen

In this subsection, all parameters required for the computation of the average strain rates measured for the wall-building specimen under the input ground motions EQ2-EQ4 are presented.

Table 1 lists the corresponding seismic weights and heights.

Table 1. Seismic Weights (*) and Corresponding Heights.

Level	h_i (m)	W_i (kN)
7	19.1	234.7
6	16.4	291.2
5	13.6	284.1
4	10.9	284.1
3	8.1	284.4
2	5.4	284.9
1	2.6	309.8
0	0	72.6

(*) Does not include the foundation. Refer to Figure 15a for the location of the lumped seismic weights and [96] for more details.

Using these values of h_i and W_i, the modal effective height, $h_{e,i}$ and the contribution factor Γ_1^*, for the first mode of vibration, are calculated as

$$h_{e,i} = \frac{\sum_{i=1}^{n} W_i \phi_{1,i}\, h_i}{\sum_{i=1}^{n} W_i \phi_{1,i}} = 14.5\ m \qquad \Gamma_1^* = \left[\frac{\sum_{i=1}^{n} W_i \phi_{1,i}}{\sum_{i=1}^{n} W_i \left(\phi_{1,i}\right)^2}\right] \phi_{1,n} = 1.46$$

The bar strain penetration length l_{sp} and the flexure-shear plastic length l_{fs} are, respectively.

$$l_{sp} = 6d_{bl} = 0.096\ m$$

$$l_{fs} = K_{sp}.h_{e,i} + 0.1l_w = 1.53\ m \text{ and } K_{sp} = min\left[0.08, 0.2\left({f_{su}}/{f_y} - 1\right)\right]$$

The elastic and plastic second-moment area coefficients are, respectively.

$$\psi_e = 109\ m^2 \text{ and } \psi_p = 30\ m^2$$

The dimensionless curvature for this specimen is $\phi_e.l_w$=0.00455, with a cross-section coefficient λ=2. The equivalent displacement of linear single-degree-of-freedom oscillators is given by

$$\delta_{r,e} = \frac{\delta_{rj}}{\Gamma_1^*} \tag{100}$$

The corresponding equivalent viscous damping, ξ_{eq}, and the damping correction factor, R_ξ, are given by Priestley [106].

$$\xi_{eq} = 0.05 + 0.0444\left(\frac{\mu - 1}{\mu\pi}\right) \qquad R_\xi = \left(\frac{0.10}{0.05 + \xi_{eq}}\right)^{0.5} \tag{101}$$

Table 2 summarizes the average strain rates obtained for the wall-building specimen under input ground motions EQ2-EQ4.

Table 2. Average strain rates at the maximum theoretical displacement - Wall-building specimen.

Test	$T_p\ (s)$	$\delta_{rj}\ (m)$	ξ (%)	Ω_{ws}	$\phi_p.L_w$	$\phi_t.L_w$	$\bar{\bar{\varepsilon}}_{sij}\ (1/s)$
EQ2	1.01	0.164	7.4	1	0.00341	0.00796	0.015
EQ3*	0.89	0.129	5	-	-	-	-
EQ4	1.32	0.388	14.2	1.15	0.02835	0.03290	0.048

(*) The DDBA approach gives an elastic response.

3.4.2 Average Strain Rates for the Bridge Column Specimen

In this subsection, all parameters required for the computation of the average strain rates measured for the bridge column specimen under the input ground motions EQ2-EQ5 are presented.

For this case, the contribution factor equals unity. The bar strain penetration length, l_{sp}, and the flexure-shear plastic length, l_{fs}, are, respectively.

$$l_{sp} = 6d_{bl} = 0.216\ m$$

$$l_{fs} = K_{sp}.L + 0.1D = 0.65\ m$$

The elastic and plastic second-moment area coefficients are, respectively.

$$\psi_e = 21\ m^2 \text{ and } \psi_p = 6\ m^2$$

The geometric and section properties are $\phi_e.D$=0.00608, λ=2.25.

The corresponding equivalent viscous damping is the same as that used for the wall-building specimen and the damping correction factor [106].

$$R_\xi = \left(\frac{0.07}{0.02 + \xi_{eq}}\right)^{0.5} \tag{102}$$

Table 3 summarizes the average strain rates obtained for the wall-building specimen under input ground motions EQ2-EQ5.

Table 3. Average strain rates at the maximum theoretical displacement - Cridge column test.

Test	$T_p\ (s)$	$\delta_{rj}\ (m)$	ξ (%)	Ω_{ws}	$\phi_p.D$	$\phi_t.D$	$\bar{\dot{\varepsilon}}_{sij}\ (1/s)$
EQ2	1.15	0.114	6.2	1	0.00199	0.00807	0.012
EQ3	2.00	0.387	15.3	1	0.05632	0.06240	0.054
EQ4	1.74	0.167	10.3	1.1	0.01042	0.01649	0.016
EQ5	2.45	0.636	16.8	1.25	0.10087	0.10695	0.075

3.5 Instantaneous and Average Strain Rates

The average strain rate can be defined, based on fundamental elasticity principles, as the ratio of the total strain increment to the corresponding time interval, or, equivalently, in terms of the total curvature and the geometry of the structural element. The conceptual formulation in Section 3.4 estimates the section's overall kinematic response during a loading cycle. It serves as a reference for subsequent evaluation of local strain-rate variations. However, the average strain rate inherently smooths over rapid local fluctuations and does not capture transient or high-frequency phenomena. Specifically, it cannot resolve sudden strain peaks and reversals associated with local plasticity, such as local material yielding, nucleation and propagation of Lüders bands, hardening onset, or high-frequency strain fluctuations during dynamic or cyclic loading.

To address the limitations of the average strain rate, the instantaneous strain rate ($\dot{\varepsilon}_{sij,max}$) will be introduced. Unlike the average rate, which integrates the strain response over a finite time interval, the instantaneous strain rate provides a continuous, differentiable description of strain evolution at any point, rather than a discrete approximation as in the time-domain approach. In this study, the instantaneous rate is obtained by spectral differentiation in the frequency domain rather than as a simple temporal derivative. By analyzing the strain signal in the frequency domain, it is possible to resolve these high-frequency components with greater precision, thereby enhancing the characterization of the transient phenomena that govern inelastic deformation in reinforcing steel under cyclic or seismic actions. Integrating these perspectives establishes a comprehensive framework for analyzing the nonlinear cyclic response of reinforcing bars, connecting global deformation with the local mechanisms that govern material behavior and energy dissipation,

thereby enabling more precise modeling of rate-dependent behavior under cyclic or seismic actions.

To integrate the average and instantaneous strain rates into a unified description, a dimensionless parameter, κ, will be introduced, defined as the ratio of the instantaneous to the average strain rate at a given point in time; hereafter referred to as the strain rate κ-ratio, or simply the κ-ratio.

$$\kappa = {\dot{\varepsilon}_{sij,max}}\Big/{\bar{\dot{\varepsilon}}_{sij}} \tag{103}$$

The κ-ratio will provide a quantitative measure of local strain concentration and temporal variation, reflecting the combined effects of Lüders band propagation, higher-frequency response components, and the shape of the structural response waveform. In other words, the κ-ratio can be conceptually decomposed into three multiplicative factors: (1) k_L-ratio, representing the macroscopic manifestation of dislocation dynamics under stress (the speed of propagation of Lüders bands when strains are within the Lüders plateau), (2) k_H-ratio, capturing the contribution of "higher" vibration modes, and (3) k_W-ratio, accounting for the influence of the strain history waveform.

$$\kappa = k_L . k_H . k_W \tag{104}$$

This function will serve as a baseline case to: (1) compare average and instantaneous strain rates, the latter obtained through differentiation; (2) contrast the idealized harmonic response with experimental signals exhibiting Lüders band propagation and higher modes; and (3) assess the influence of the waveform on the κ-ratio. To illustrate the calculation of this ratio, both the average and instantaneous strain rates are shown over one half-cycle of a harmonic strain-time history, represented by $\varepsilon(t) = \varepsilon_0 \sin(t)$, where ε_0 is the strain amplitude in Figure 17.

The average strain rate (shown in green) corresponds to the slope of the secant line connecting the endpoints of the half-cycle. In contrast, the instantaneous strain rate (shown in blue) corresponds to the tangent at a specific point and captures the local rate of change in strain. The lower plot in Figure 20 shows the time derivative of the harmonic strain, representing the instantaneous strain rate over the same time interval. The figure illustrates the basic distinction between the two measures for harmonic loading: the instantaneous rate varies continuously over the cycle, whereas the average rate equals the net change in strain divided by the half-cycle duration.

Lüders bands do not develop under harmonic excitation because the material undergoes rapid, reversible deformation, without sufficient time for band nucleation or sustained propagation. These bands may develop under cyclic loading only when the strain amplitude and rate allow a stable passage through the yield plateau, conditions that are not met in a purely harmonic response, where plastic excursions are brief and periodically reversed. Therefore, for a harmonic strain function, k_L=1.

A purely harmonic loading excites a single frequency; the contribution of higher modes is negligible. Therefore, the factor k_H, which accounts for the influence of higher-frequency response components, can be assumed equal to 1 under harmonic excitation.

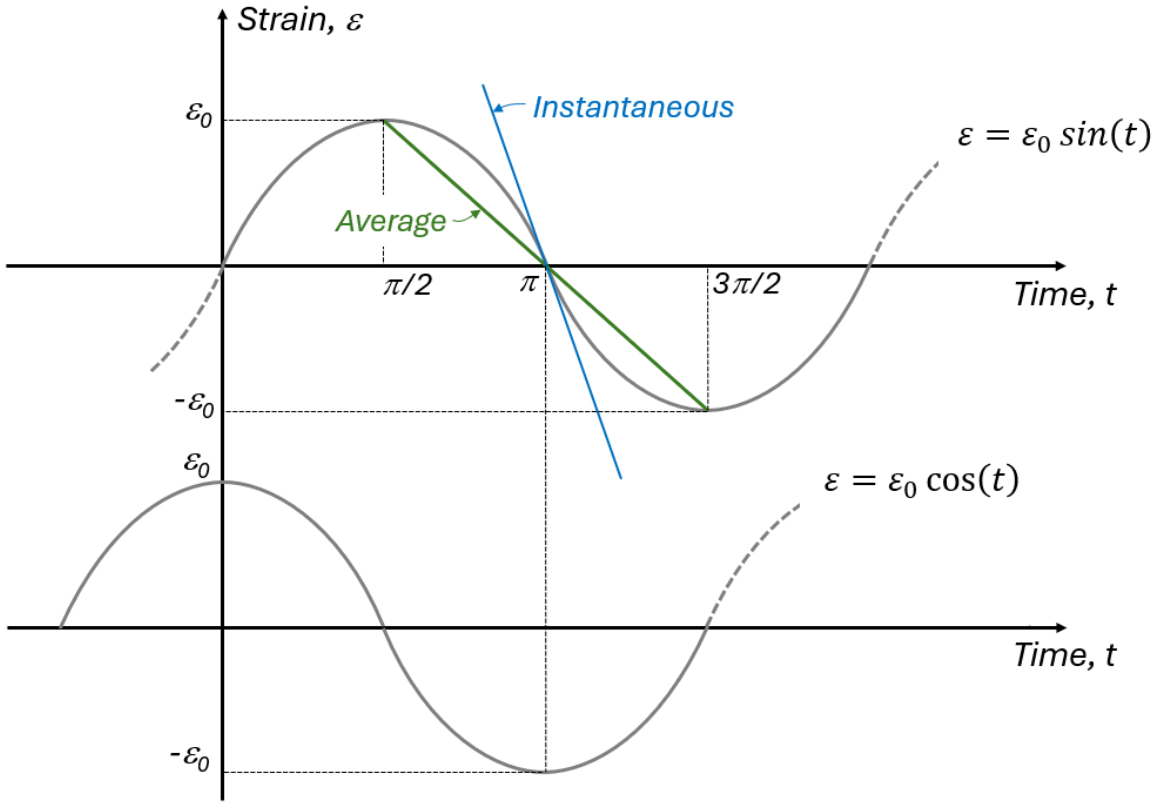


Figure 17. Harmonic strain-time history.

Purely harmonic loading excites a single, well-defined frequency, rendering the contributions from higher-order modes effectively negligible. Consequently, the factor k_H, introduced to quantify the amplification effects associated with higher-frequency components, can be rigorously taken as unity under harmonic excitation. This assumption simplifies the analytical evaluation of the system response, isolates the fundamental-mode behavior, and provides a direct reference for comparing idealized and observed strain histories.

The average strain rate is calculated as

$$\bar{\dot{\varepsilon}}_{sij} = \frac{2\left(\varepsilon_{sj} - \varepsilon_{si}\right)}{T_e} = \frac{2[\varepsilon_0 - (-\varepsilon_0)]}{2\pi} = \frac{2\varepsilon_0}{\pi}$$

The peak instantaneous strain rate corresponds to the amplitude of the strain history:

$$\dot{\varepsilon}_{sij,max} = -\varepsilon_0$$

Accordingly, the κ-ratio is as follows:

$$\kappa = \left| \frac{-\varepsilon_0}{2\varepsilon_0/\pi} \right| = \frac{\pi}{2} \tag{105}$$

Thus, for a harmonic strain history, the waveform effect factor k_W, equals

$$k_W = \frac{\pi}{2} \cong 1.57 \tag{106}$$

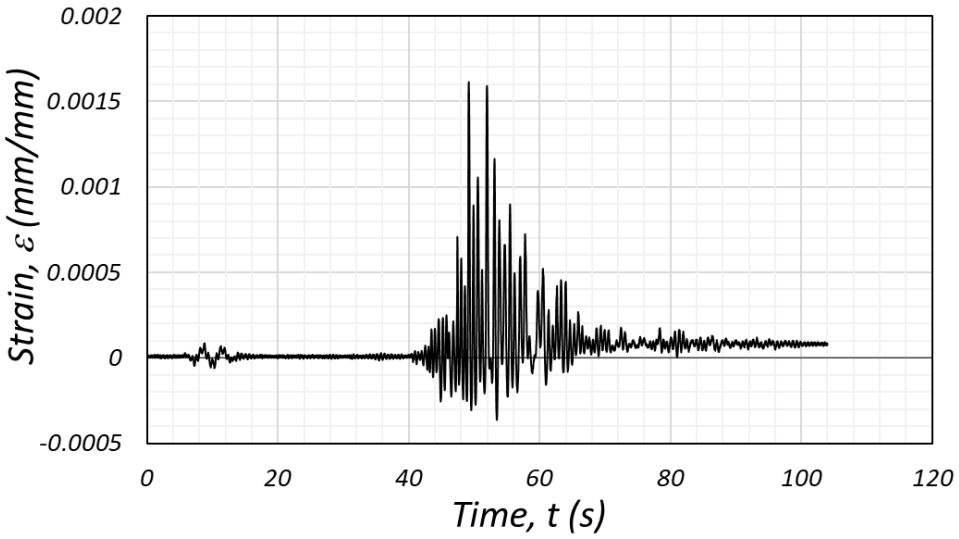
This value serves as a reference for subsequent κ-ratio calculations based on the strain signals from the tests described earlier, providing a benchmark for assessing how waveform characteristics influence the experimental responses.

3.6 Strain Signals

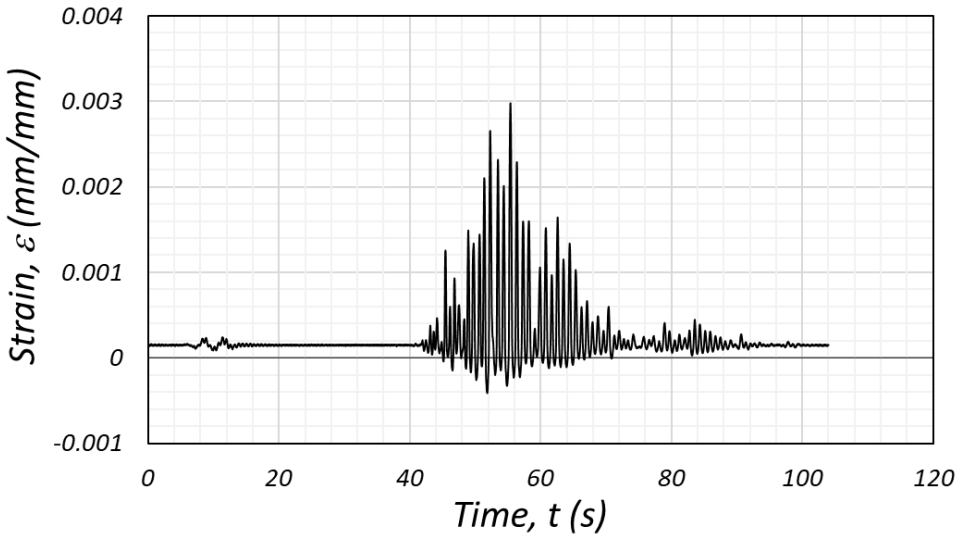
Strain signals from the longitudinal reinforcement in the plastic hinge regions were recorded during seismic-type excitations. Both specimens experienced inelastic deformations, leaving residual strains. Figures 18 and 19 present representative strain time histories from selected gauges, illustrating variations in strain amplitude, phase, and cyclic behavior across different ground motions.

The recorded signals exhibit nonstationary behavior, with amplitudes and frequency content evolving in response to the transients in the input motions. Peaks are irregularly spaced and vary in magnitude from cycle to cycle, reflecting progressive stiffness degradation and energy dissipation associated with inelastic behavior. This response is consistent with a viscous-type attenuation pattern, in which amplitudes generally decrease over successive cycles, though not strictly monotonically.

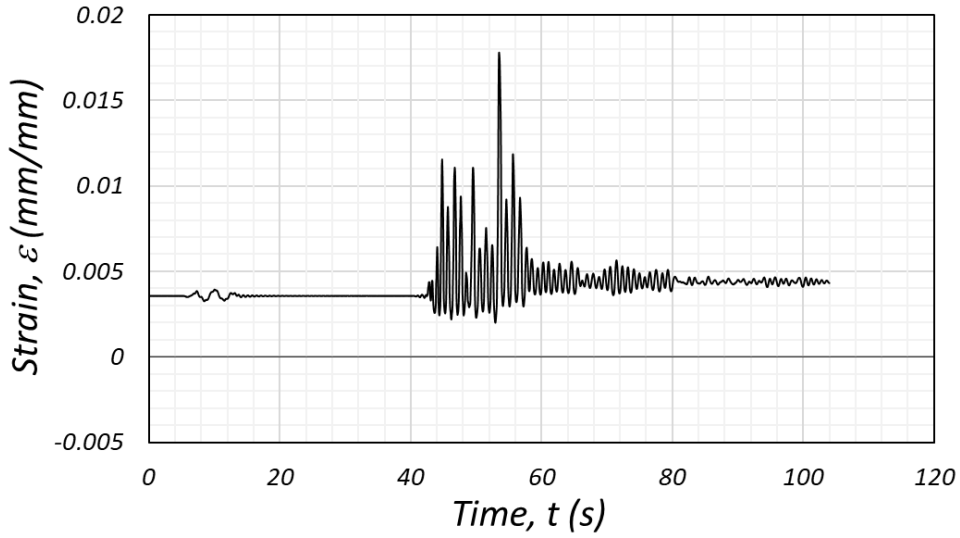
Furthermore, the phase differences observed between gauges reveal localized variations in deformation demand within the plastic hinge regions, indicating a non-uniform strain distribution along the reinforcement. The continuous variation in peak spacing implies that the effective cycle period is not constant throughout the response. Consequently, the assumption of a single dominant period, commonly used in simplified or linearized analyses, does not suit these signals.



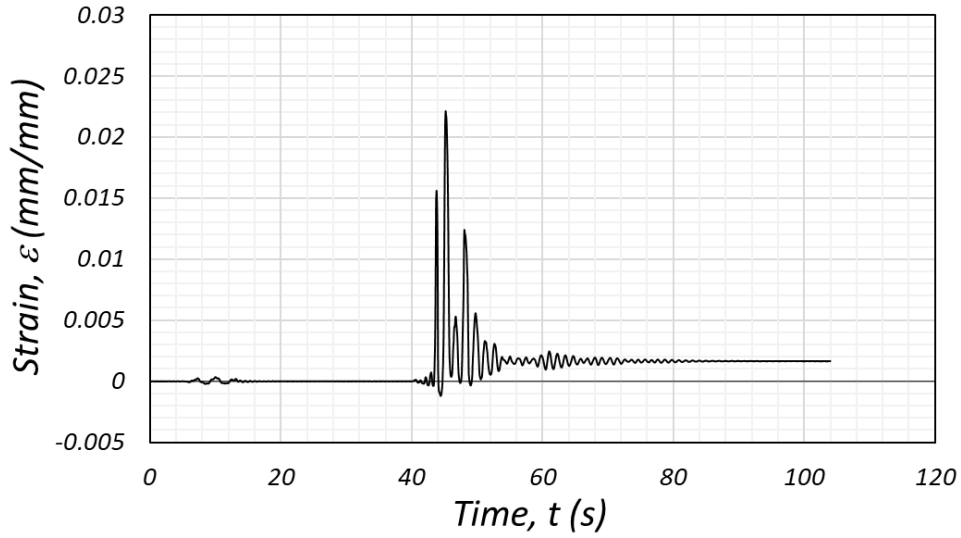
a) EQ1-A1_4.



b) EQ2-A2_4.

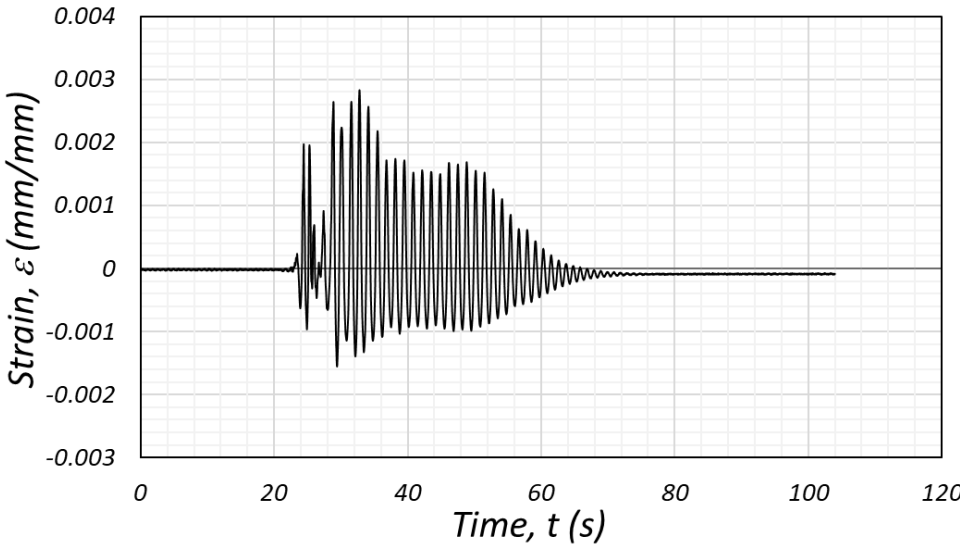


c) EQ3-A4_3.

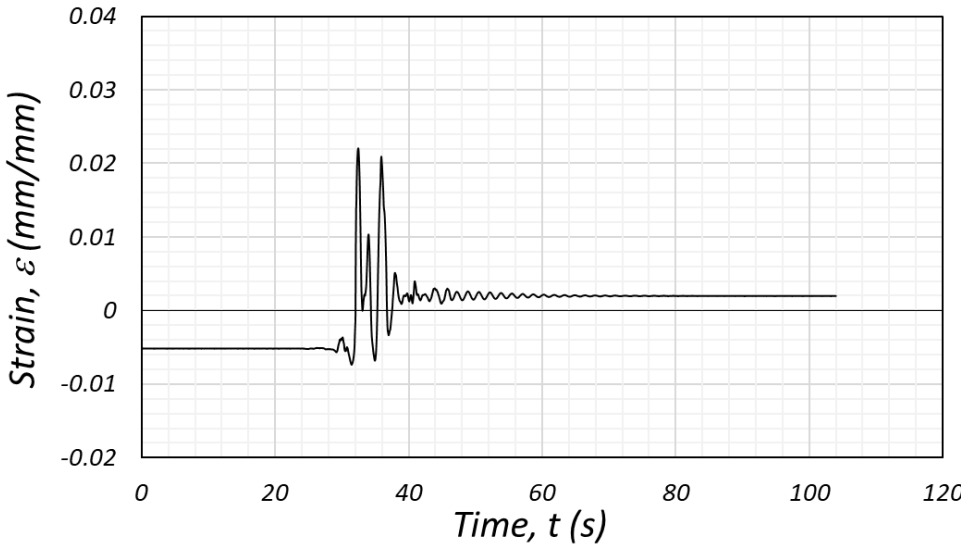


d) EQ4-A3_4.

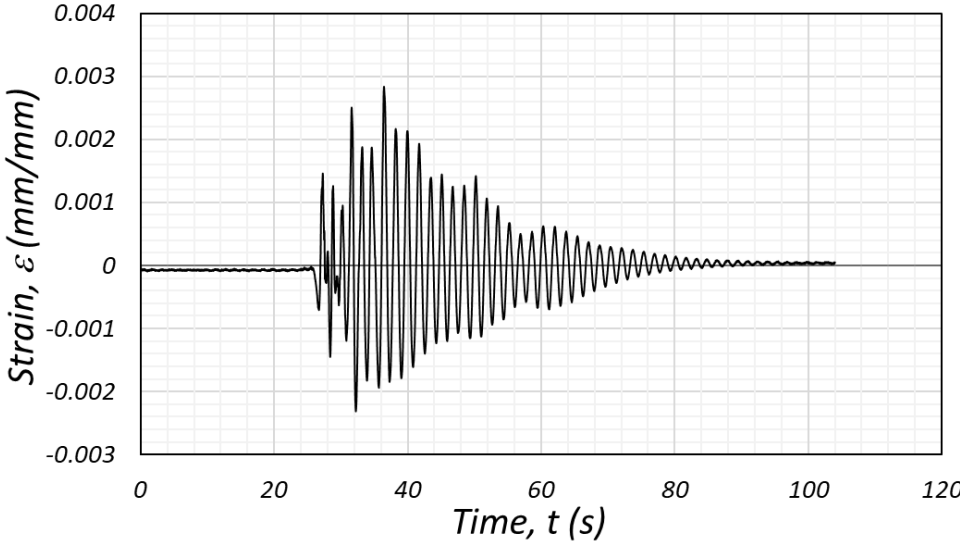
Figure 18. Strain-time signals - Wall-building specimen.



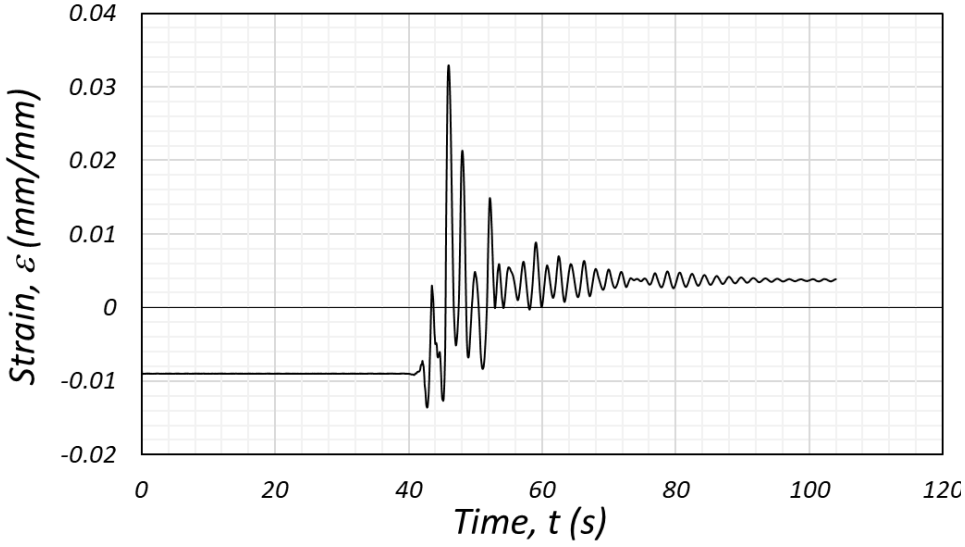
a) EQ2-ES03.



b) EQ3-EN05.



c) EQ4-WN04.



d) EQ5-WS03.

Figure 19. Strain-time signals - Bridge column specimen.

3.7 Period Definitions

In linear structural dynamics, a system's set of natural periods is uniquely determined by its stiffness and mass properties and remains constant unless these properties change. RC systems, however, deviate from this linear ideal due to their inherent nonlinearity, which manifests almost immediately upon loading. This nonlinearity arises primarily from cracking, which may occur at very low stress levels, even before service loads are applied, due to restrained shrinkage, early-age thermal effects, or localized stress concentrations. Once cracking develops, the effective stiffness decreases, resulting in longer natural periods. As a result, a single fixed period cannot accurately capture the structural response over the entire loading history. To address this, three complementary definitions of periods are adopted in this study, capturing different aspects of the dynamic behavior of the test specimens under seismic excitations.

3.7.1 Initial Periods, T_o

Initial periods are obtained through ambient vibration testing conducted before applying any seismic or dynamic loading to the specimen. These periods are closely approximated by linear elastic models developed with transformed section properties, measured Young's modulus and Poisson's ratio for the concrete, and a realistic representation of the actual mass distribution. For clarity, T_{o1} and T_{o2} in this study correspond to the initial periods of the first and second translational modes, respectively. Because they are derived from undamaged specimens, these periods serve as a baseline for evaluating stiffness degradation throughout the testing program. Table 4 summarizes the measured values for both specimens.

Table 4. Initial periods for the first two translational modes

Specimen	$T_{o1}\ (s)$	$T_{o2}\ (s)$
Wall-building	0.52	0.095
Bridge column	0.88	0.17

3.7.2 Predominant Periods, T_p

Predominant periods provide a fundamental indicator of a structure's dynamic properties when subjected to actual earthquake excitations. These periods reflect not only intrinsic modal characteristics but also progressive changes induced by nonlinear material response. These periods are strongly amplitude-dependent: higher levels of seismic shaking systematically lengthen the periods as damage, cracking, and inelastic deformations accumulate within the structure. Such elongation directly reflects stiffness degradation, particularly in RC members, where cracking, bond deterioration, and yielding progressively reduce effective lateral stiffness. At more advanced damage stages, additional mechanisms such as bar buckling and fracture further accelerate stiffness loss, leading to pronounced increases in the fundamental period. These effects are most significant in the plastic hinge regions.

In this study, the predominant periods associated with the "first" and "second" translational modes, denoted as T_{p1} and T_{p2} were rigorously extracted from the measured shake-table responses. This identification relied on a combined transfer-function and spectral-ratio approach, ensuring reliable detection of resonance peaks across a broad frequency range. To improve the accuracy of these estimates, additional time-domain optimization techniques [77] were employed, thereby capturing subtle shifts in the predominant periods as the specimens progressed through progressive damage.

The resulting values for all input ground motions applied to the wall-building and bridge-column specimens are reported in Tables 5 and 6.

Table 5. Predominant periods for the first two translational modes
Wall-building specimen.

	Mode 1		Mode 2	
Test	$f_{p1}\ (Hz)$	$T_{p1}\ (s)$	$f_{p2}\ (Hz)$	$T_{p2}\ (s)$
EQ1	1.495	0.669	10.101	0.099
EQ2	1.024	0.977	9.091	0.11
EQ3	1.007	0.993	5.650	0.177
EQ4	0.666	1.502	5.076	0.197

Table 6. Predominant periods for the first two translational modes
Bridge column test.

	Mode 1		Mode 2	
Test	$f_{p1}\ (Hz)$	$T_{p1}\ (s)$	$f_{p2}\ (Hz)$	$T_{p2}\ (s)$
EQ1	0.869	1.151	5.650	0.177
EQ2	0.741	1.350	4.673	0.214
EQ3	0.378	2.647	4.132	0.242
EQ4	0.588	1.701	3.876	0.258
EQ5	0.317	3.150	3.745	0.267
EQ6	0.388	2.580	4.132	0.242
EQ7	0.323	3.098	3.745	0.267
EQ8	0.325	3.075	3.704	0.270

These tables systematically record how the predominant periods evolve across successive excitations, offering insight into the relationships among input intensity, stiffness degradation, and modal characteristics. While this discussion focuses on EQ2 to EQ4 for the wall-building specimen and EQ2 to EQ5 for the bridge column specimen, the tables include the full results to provide a comprehensive view of period-elongation trends across all test runs. The results confirm a clear, progressive lengthening of the fundamental period, consistent with the gradual loss of tension stiffening as cracks developed and propagated within the concrete. This behavior corresponds to the well-documented reduction in secant stiffness, which became more pronounced at higher input amplitudes. In contrast, the second longitudinal mode remained nearly constant throughout the tests, with mean values of 0.136 s for the wall-building specimen and 0.234 s for the bridge-column specimen. The relative stability of this mode indicates that higher-order responses are less sensitive to cracking and local damage processes, as their deformation pattern involves smaller global displacements and lower demands on flexural stiffness. This distinction between the first and second modes highlights the different mechanisms controlling stiffness degradation and further confirms that the first translational mode primarily governs period elongation.

Figures 20 and 21 illustrate the evolution of the first two longitudinal vibration periods for both tests, respectively, for all input ground motions applied to the specimens.

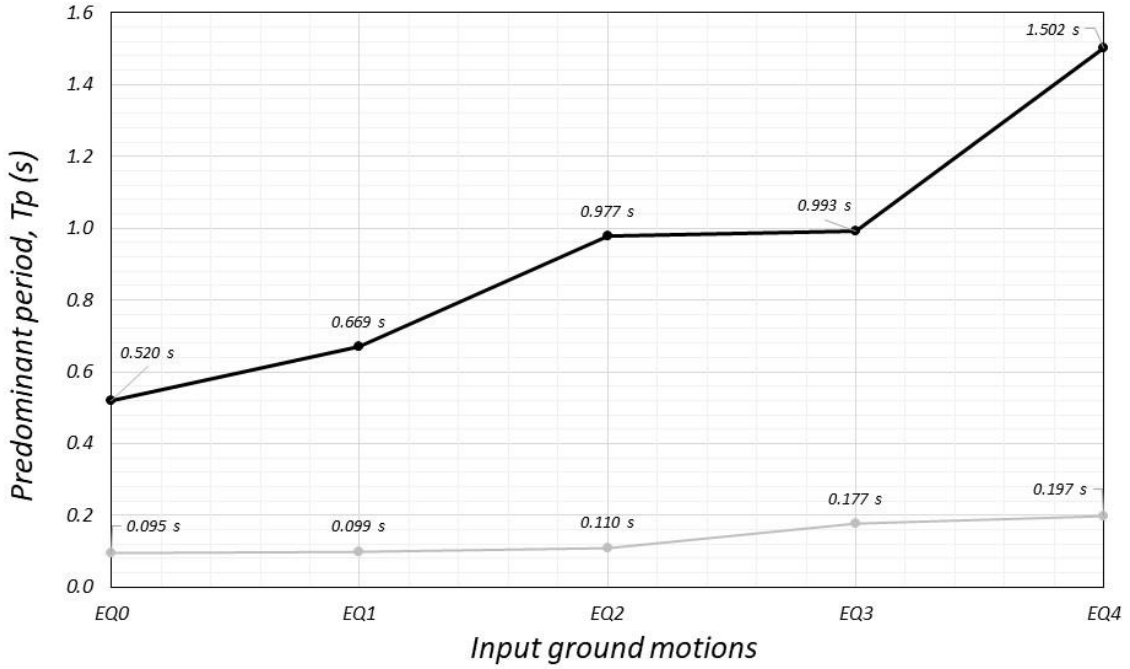


Figure 20. Variation of the First and second mode periods with shaking intensity - Wall-building specimen.

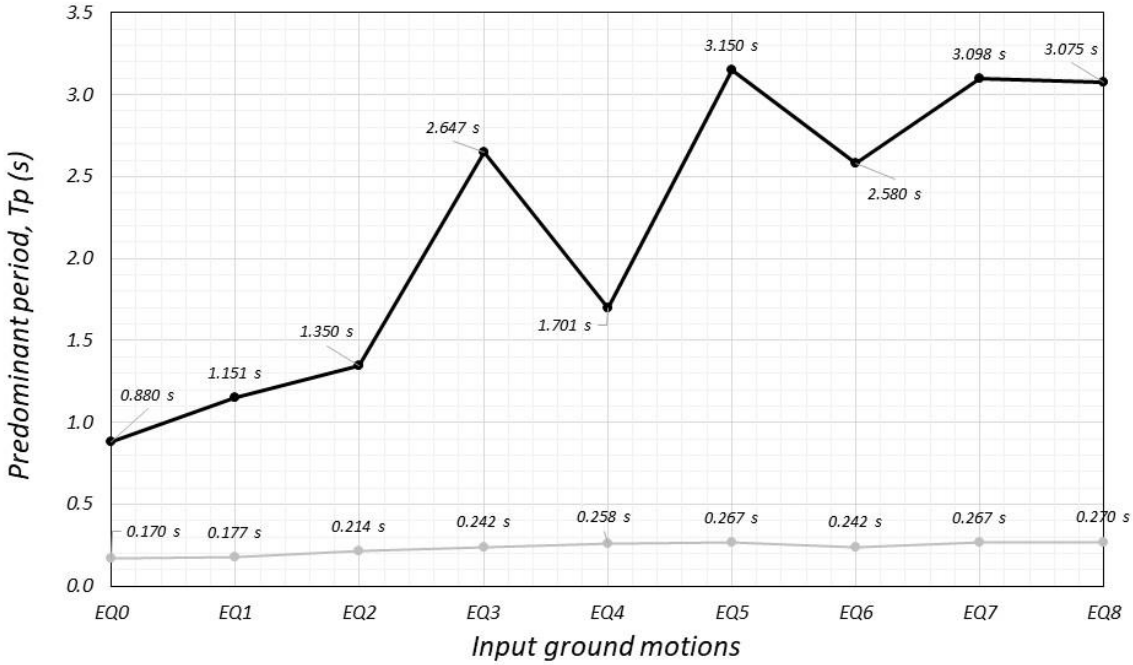


Figure 21. Variation of the First and second mode periods with shaking intensity - Bridge column specimen.

These figures provide a systematic record of how the predominant periods evolve across successive excitations, offering insight into the relationships among input intensity, stiffness degradation, and modal characteristics. At the start of the first earthquake simulation, both tests were subjected to long-duration ambient vibration tests and to long-duration low-amplitude 0.5-25 Hz band-clipped white noise (WN) tests with root-mean-square (RMS) amplitudes of 2%, 3%, and 5% g. The initial motion, with an RMS amplitude of 0.03 g, verified instrumentation and ensured quality control. The same five-minute white-noise motion was repeated immediately before testing and again between successive earthquake simulations to monitor changes in fundamental periods and mode shapes resulting from damage accumulation [56].

The predominant periods in the EQ2 and EQ3 simulations of the wall-building specimen are nearly identical, likely because these tests exhibited limited nonlinear response [96]. In contrast, simulations EQ4 and EQ6 in the bridge-column specimen do not show the expected period elongation. EQ4 was designed to simulate an aftershock following the EQ3 event and produce an essentially elastic response, whereas EQ6 represents a repetition of EQ3, causing no further damage beyond that produced in the preceding test [124].

The evolution of predominant structural periods was evaluated as a function of peak ground velocity (PGV) [32], a widely recognized, reliable indicator of seismic intensity and potential structural damage. Westergaard [141] initially proposed evaluating seismic intensity in terms of maximum ground velocity rather than acceleration, arguing that velocity better reflects the kinetic energy imparted to a structure and its corresponding demand. Building on this concept, Yamazaki and Murao [143] developed fragility curves for Japanese buildings based on observed damage from the 1995 Kobe earthquake, demonstrating that PGV is a key predictor of structural vulnerability and highlighting its dependence on building type and construction era.

Empirical studies further confirmed the correlation between PGV and deformation demands. Akkar and Özen [2] analyzed single-degree-of-freedom (SDOF) oscillators using nonlinear response-history analyses. They showed that PGV consistently predicts deformation demands more accurately than peak ground acceleration (PGA), especially for short-period systems. Bommer and Alarcón [17] reinforced these findings, showing that PGV correlates more reliably with structural damage, macroseismic intensity, and energy input by capturing both the velocity content and cumulative effects of ground motion. Wu et al. [142] extended this understanding to real earthquake data from the 2011 Tōhoku earthquake, showing that building damage ratios correlate more strongly with velocity-based indices, particularly PGV, than with acceleration-based indices, providing lower variability and greater predictive stability.

Taken together, these studies establish a robust, empirically supported link between PGV and structural damage. The evidence consistently shows that period elongation and stiffness degradation in RC systems are closely related to PGV, validating its use as a quantitative measure of nonlinear dynamic response and linking observed damage to both global deformation and local material effects in RC structures. The observations made in this study are consistent with these trends. As illustrated in Figure 22, the period ratio T_{p1}/T_{o1} increases systematically with PGV for both the wall-building specimen (EQ1-EQ4) and the bridge-column specimen (EQ1-EQ5).

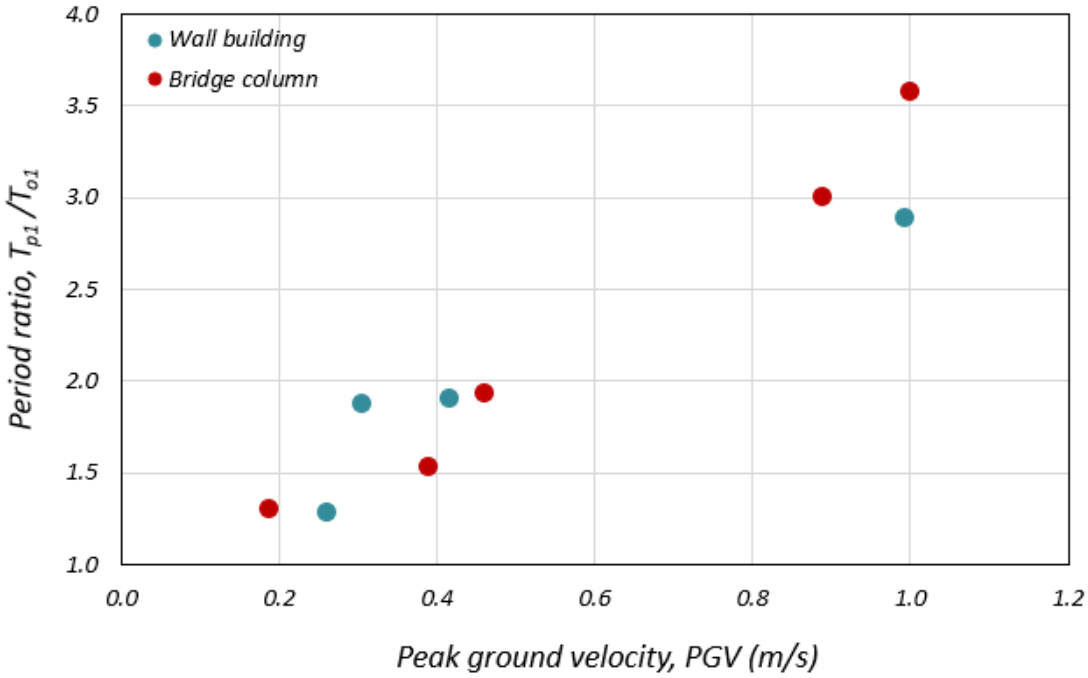


Figure 22. Period ratio T_{p1}/T_{o1} versus PGV for the test specimens.

This trend confirms that higher PGV levels lead to more pronounced stiffness degradation and corresponding elongation of the fundamental period. Notably, the correlation between PGV and period elongation is nearly identical for the two specimens despite their markedly different dynamic characteristics, highlighting the robustness and generality of PGV as a predictor of nonlinear response in distinct RC structural systems. This consistency across specimens underscores that PGV effectively captures energy transfer from ground motion to structural elements, reflecting both global deformation patterns and localized inelastic mechanisms such as cracking, bond slip, and reinforcement yielding. Consequently, period elongation can be interpreted as a direct manifestation of accumulated damage, with PGV serving as a unifying parameter to quantify structural vulnerability and to compare nonlinear dynamic behavior across different RC configurations.

3.7.3 Effective Periods, T_e

Effective periods, T_e, are the time intervals between successive peaks in a signal. They are obtained from peak-to-peak bar strain measurements and capture localized cyclic deformation and inelastic excursions in plastic hinge zones. Multiple periods can be extracted from a single record, reflecting variations across loading phases. Figure 23 shows the strain response from gauge A2_5 in the wall-building specimen during EQ3. Similarly, Figure 24 shows the strain response recorded by gauge WS08 in the bridge-column specimen during EQ5. The upper plots in both figures show the full strain history, while the lower plots zoom into 8-second and 10-second windows around some of the highest strain demands, showing consecutive peaks with peak-to-peak times of 0.93 s to 1.14 s and 1.36 s to 2.28 s, respectively, for both specimens.

Strain amplitudes exceed yielding, reflecting the combined influence of global motion and localized nonlinear mechanisms within the plastic hinge. Early peaks grow progressively as the specimens enter deeper inelastic deformation, then partially attenuate as energy dissipates through hysteresis. The irregular spacing and varying amplitudes indicate that the system does not behave as a linear oscillator with a fixed period and that the interaction between global seismic excitation and localized inelastic effects strongly governs the cyclic response. To quantify these variations, only periods equal to or greater than the initial fundamental period, T_{o1}, will be considered, filtering out transient fluctuations and high-frequency artifacts that do not contribute to the nonlinear response. The maximum effective period, $T_{e,max}$, corresponds to the largest temporal separation between peaks and is associated with cycles exhibiting the most pronounced inelastic deformation and stiffness degradation, representing the maximum elongation of the response beyond T_{o1}. Table 7 presents the maximum effective periods obtained from the strain measurements of both specimens, each subjected to its selected seismic simulation, highlighting differences in their dynamic responses.

Table 7. Maximum effective periods for both tests.

Test	Wall-building	Column bridge
EQ2	1.19	1.94
EQ3	1.29	2.57
EQ4	1.80	2.34
EQ5	-	3.08

Analysis of the results shows that, for the wall-building specimen, the mean maximum effective period is $T_{e,max}$=1.425 s with a standard deviation of 0.328 s. For the bridge-column specimen, $T_{e,max}$=1.237 s and 0.475 s. These statistics indicate that the bridge-column system exhibits both higher effective periods and greater variability, reflecting its increased flexibility and the more pronounced influence of localized nonlinear mechanisms.

Considering both specimens together, the mean maximum effective period-to-predominant period ratio of $T_{e,max}/T_{p1}$ is 1.21 with a sample standard deviation of 0.182, showing that localized inelastic effects can increase effective periods by approximately 21% above the fundamental period. These findings confirm that the effective period is not constant during seismic excitation but evolves as inelastic deformations accumulate. Overall, Table 7 shows that accounting for effective periods provides a more realistic characterization of the structural response under seismic loading, capturing the combined effects of global dynamics and localized nonlinear mechanisms that a single fundamental period alone cannot.

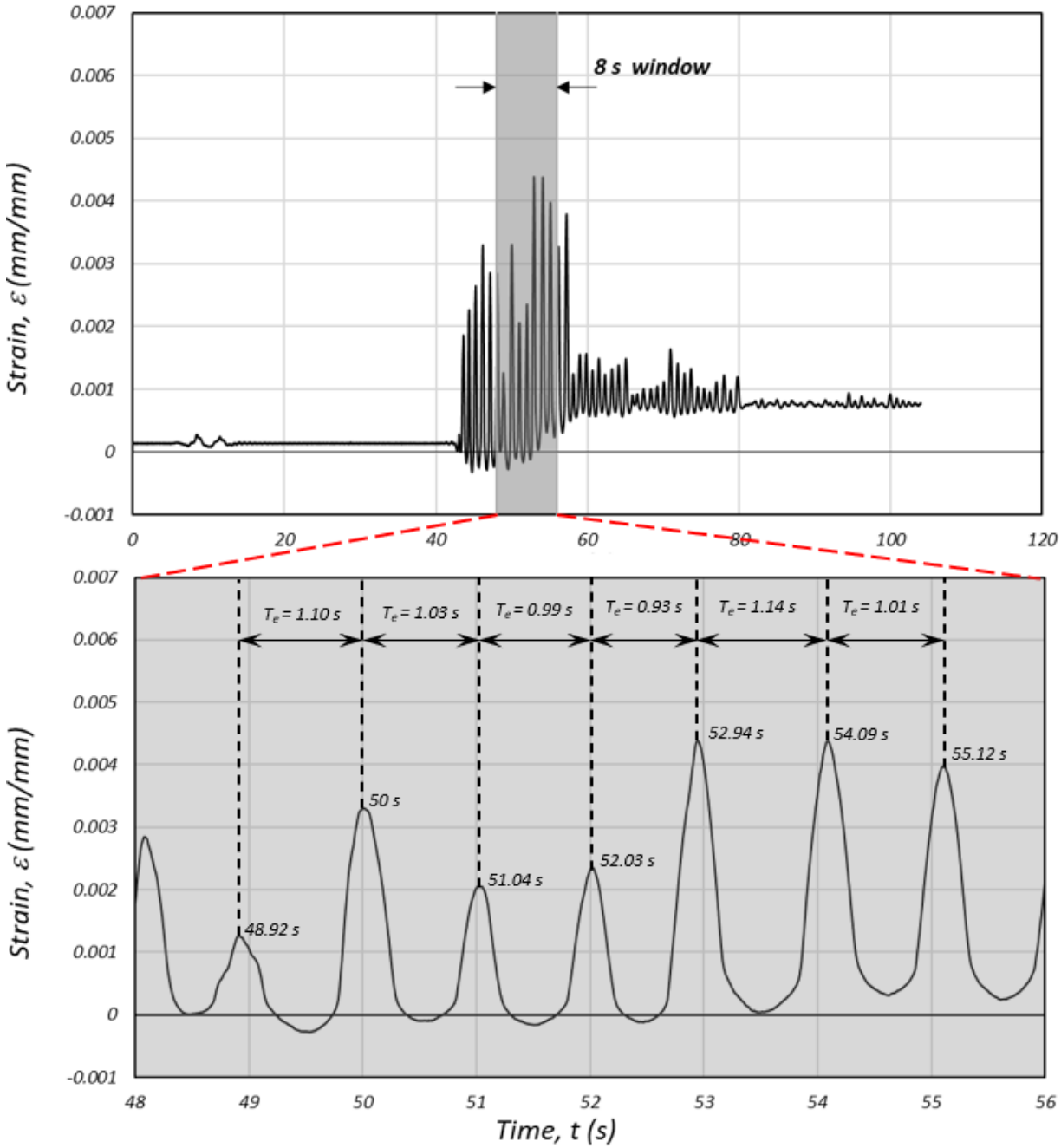


Figure 23. Variable effective periods from the strain gauge A2_5 Wall-building specimen.

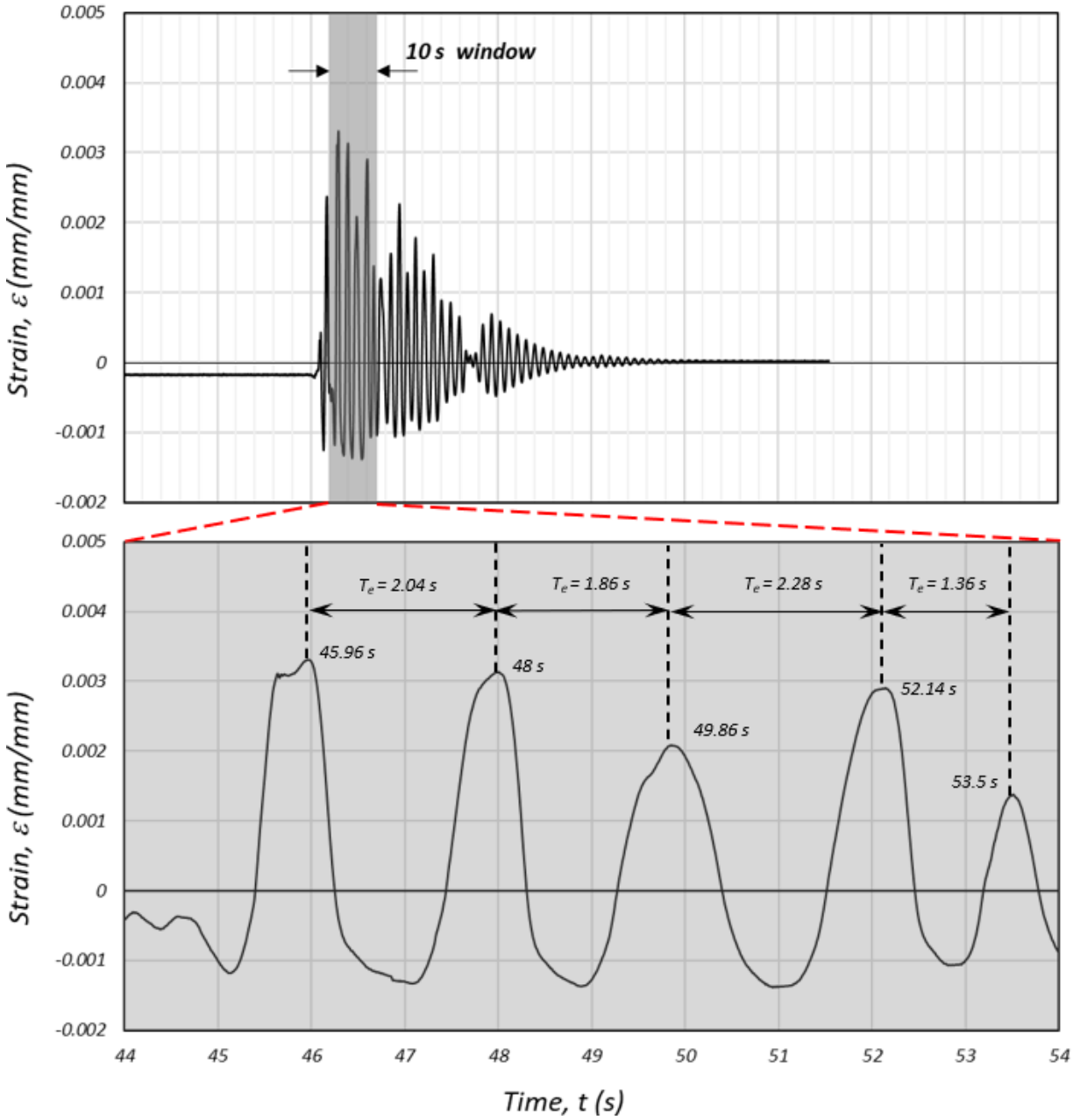


Figure 24. Variable effective periods from the strain gauge WS8 Bridge-column specimen.

3.8 Signal Processing Workflow

This section describes the methodology for processing raw strain signals and calculating peak strain rates from a selected set of gauges located in the plastic hinge regions of the specimens. Only gauges that remained operational during the strongest and most structurally significant shaking events were considered, as these provided the most representative measurements of inelastic demand under severe seismic loading.

The strain signals were acquired using a 16-bit data acquisition system, whose high resolution ensured that even rapid, small-magnitude variations in the strain histories could be captured without significant quantization errors. This precision was particularly critical because localized plastic deformations in reinforcing bars can produce abrupt strain-rate spikes that lower-resolution systems would severely underestimate. Before digitization, the raw analog signals were conditioned to reduce contamination from spurious frequencies and measurement noise. A 100 Hz fourth-order low-pass Butterworth filter was applied to suppress high-frequency components while preserving the structural response. The Butterworth filter was chosen for its flat passband, which minimizes distortion and maintains the amplitudes of relevant structural frequencies. After digitization, the signals were further refined using a 60 Hz narrowband notch filter to remove electromagnetic interference from the mains power supply. By targeting this specific frequency while leaving surrounding content essentially unaltered, the notch filter substantially improved the signal-to-noise ratio of the processed data.

The LHPOST operator provided the complete set of conditioned measurements from the filtering and digitization chain as the official “raw” data package. Here, “raw” indicates that while pre-filtering had removed obvious noise sources, the signals had not undergone higher-level post-processing. This dataset therefore represents the most direct, minimally processed record of the strain gauge outputs, from which subsequent post-processing and analytical procedures quantified strain histories and extracted peak strain-rate demands associated with seismic loading in the plastic hinge regions.

3.8.1 Signal Truncation

Raw strain gauge time-history records were first truncated to the interval defined by the 5%-95% range of the Arias Intensity [5], ensuring that subsequent analyses focused on the portion of the response corresponding to the most significant seismic energy input. Establishing these temporal bounds required computing the cumulative Arias Intensity at both the ground level and the location of maximum structural response, since these points represent the input and the transmission of seismic energy through the structural system, respectively. The ground-level record characterizes the original energy imparted by the incoming ground motion, whereas the upper-level response captures the dynamic amplification and redistribution within the structure. For the wall specimen, the maximum structural response was recorded at the seventh story, whereas for the bridge column specimen, it occurred at the center of mass.

The procedure began with the acceleration histories, which were first resampled onto a uniformly spaced time grid to eliminate minor irregularities in the original sampling intervals that could otherwise introduce numerical errors during integration. This resampling step ensured that all subsequent numerical operations used a consistent temporal discretization, maintaining the accuracy of the cumulative Arias Intensity calculation. Once the acceleration records were aligned

on this uniform grid, each time series was squared and incrementally integrated over time to obtain the cumulative Arias Intensity.

The shape of this cumulative curve provides insight into the temporal distribution of seismic energy input, distinguishing periods of intense shaking from intervals of relatively low seismic activity. To enable comparison across ground motions of different magnitudes, durations, and frequency characteristics, these cumulative curves were normalized to their maximum values, providing a consistent reference framework for identifying the 5% and 95% Arias Intensity thresholds**.** These bounds exclude the low-energy tails at the beginning and end of the records while retaining the dominant phase of seismic demand.

For each specimen, four earthquake records were considered, yielding sixteen temporal bounds corresponding to the 5% and 95% Arias Intensity times. To obtain a common analysis window across all cases, the lower bound was defined as the maximum of the four 5% times, while the upper bound was defined as the minimum of the four 95% times. The resulting interval therefore represents the portion of the records that consistently encompasses the predominant phase of seismic energy input across all specimens.

Tables 8 and 9 summarize the analysis windows for the wall-building and bridge-column specimens, respectively, considering the ground motion and the corresponding structural reference point: the roof level for the wall-building specimen and the center of mass of the loading block for the bridge-column specimen.

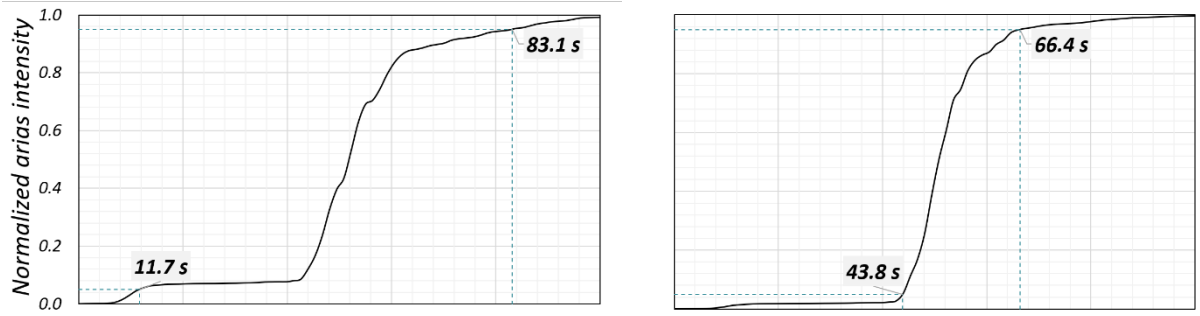
Table 8. Arias intensity bounds for the wall-building specimen.

Ground			**Roof level**		
Test	$t_{min}\ (s)$	$t_{max}\ (s)$	**Test**	$t_{min}\ (\mathbf{s})$	$t_{max}\ (s)$
EQ1	11.7	83.1	**EQ1**	43.8	66.4
EQ2	45	56	**EQ2**	45.8	66.1
EQ3	43.7	53.7	**EQ3**	44.1	64.2
EQ4	43.3	48.1	**EQ4**	43.3	51.3

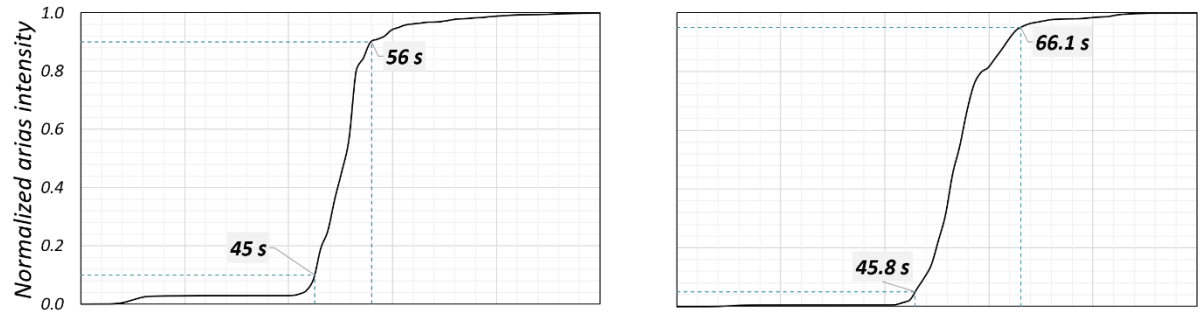
Table 9. Arias intensity bounds for the bridge column specimen.

Ground			**Block's center of mass**		
Test	$t_{min}\ (s)$	$t_{max}\ (s)$	**Test**	$t_{min}\ (\mathbf{s})$	$t_{max}\ (s)$
EQ2	13	40.8	**EQ2**	24.1	94.3
EQ3	18.2	29.5	**EQ3**	24.5	109.5
EQ4	13.1	33.5	**EQ4**	12.2	107.9
EQ5	13.4	31.7	**EQ5**	33.1	66.6

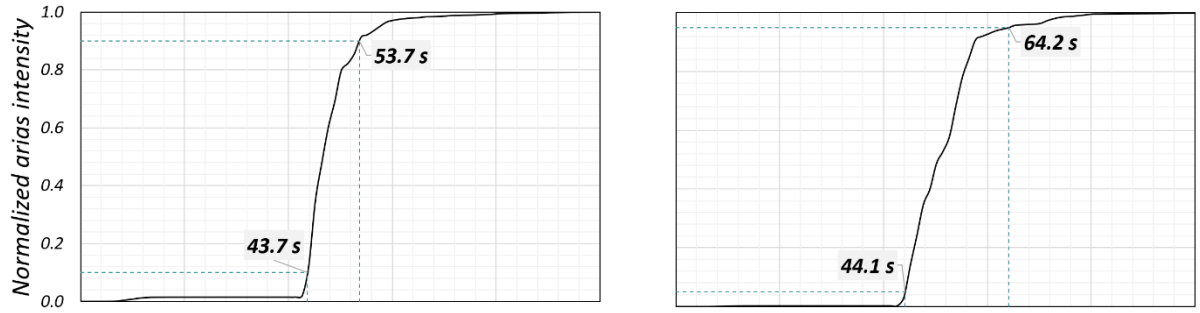
Figure 25 presents the cumulative Arias Intensities for the wall-building specimen evaluated at the seventh floor and at ground level. In contrast, Figure 26 shows the corresponding cumulative intensities for the bridge-column specimen at the center of mass and at ground level.



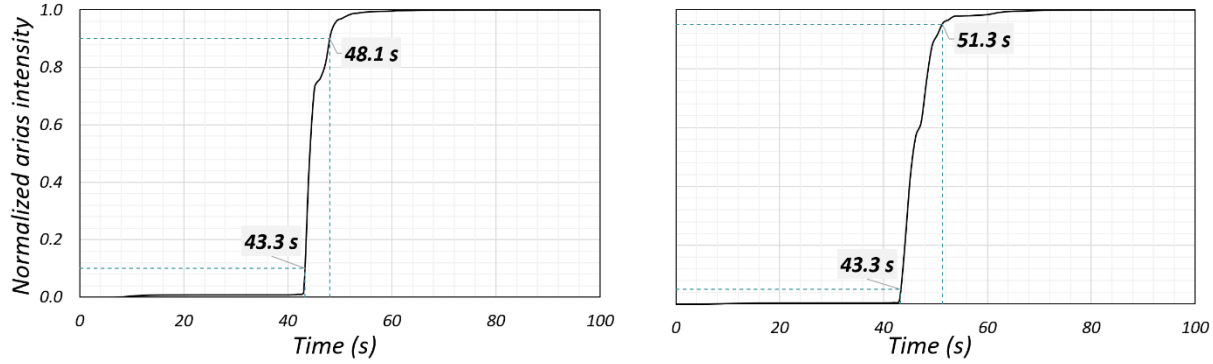
a) EQ1 simulation.



b) EQ2 simulation.



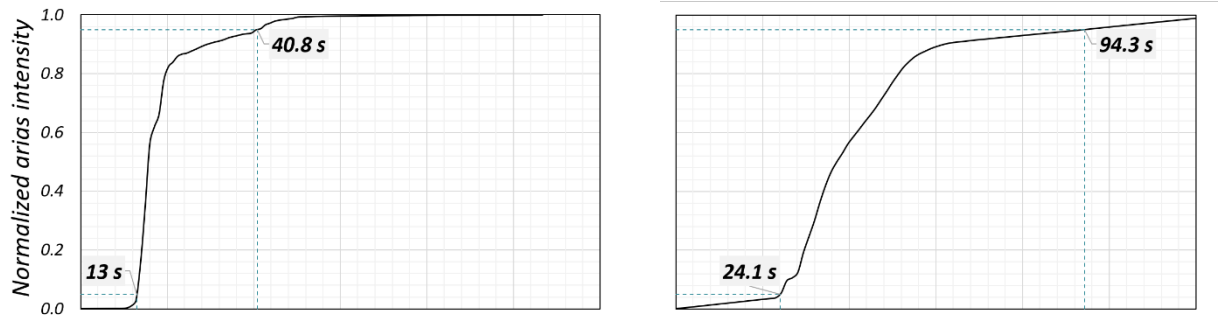
c) EQ3 simulation.



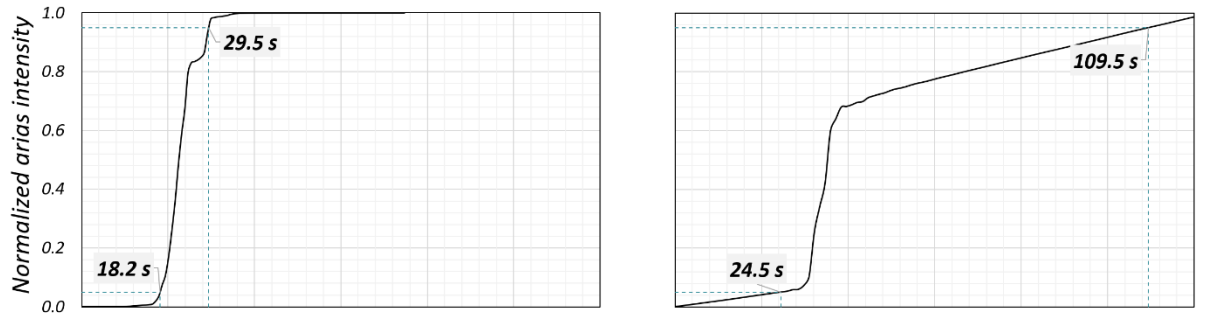
d) EQ4 simulation.

Ground level. Seventh floor.

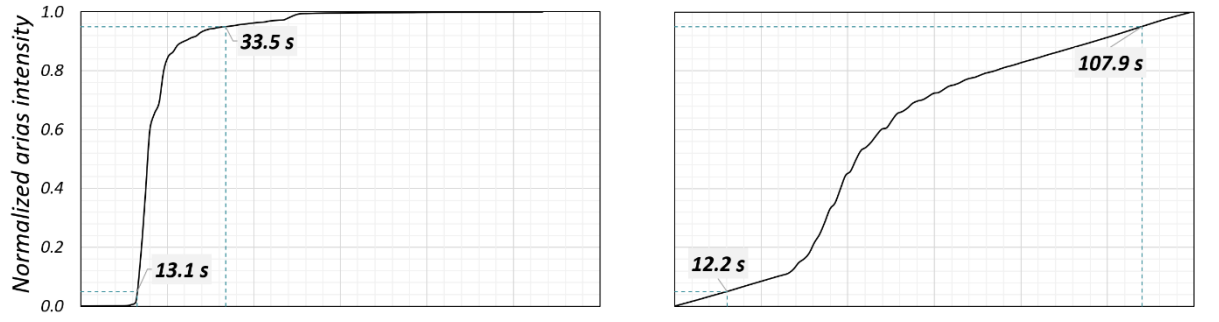
Figure 25. Cumulative Arias Intensity for the wall-building specimen.



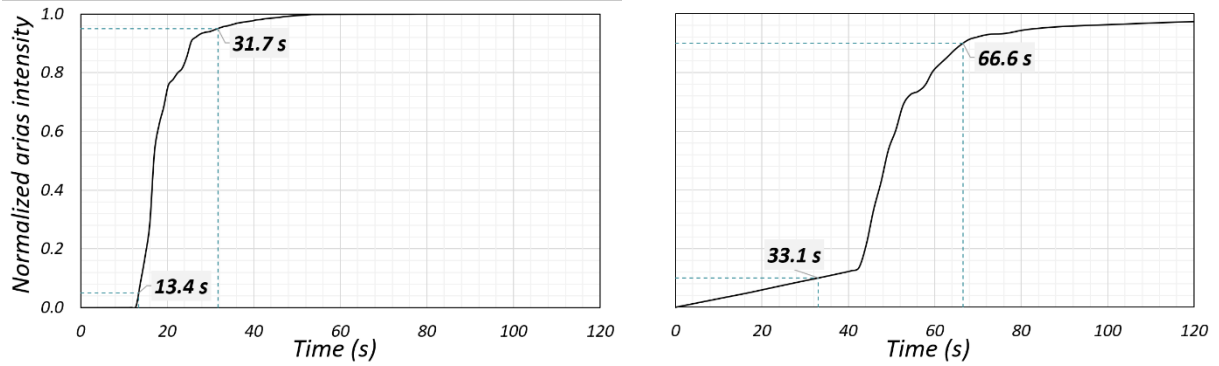
a) EQ2 simulation.



b) EQ3 simulation.



c) EQ4 simulation.



d) EQ5 simulation.

Ground level. Center of mass.

Figure 26. Cumulative Arias Intensity for the bridge column specimen.

3.8.2 Signal Filtering

After truncation, the strain histories were further processed to derive two distinct datasets designed to isolate different components of the structural response for detailed analysis. The first dataset, referred to as the *All Modes* (AM) signal, was intended to preserve the full frequency content associated with all significant response modes of the specimens. This AM signal was processed using a fourth-order low-pass Butterworth filter, which provided smooth attenuation of frequency components beyond the selected cutoff while maintaining the integrity of the modal contributions within the retained range. The cutoff frequency was set at 2.5 times the frequency of the second translational mode (f_2) obtained from ambient vibration testing. The first and second modes capture the majority of the system's dominant dynamic behavior, and the selected cutoff ensures that these modes are fully retained. In contrast, higher-order modes (third, fourth, and higher) are effectively excluded, as their contributions to the overall response are negligible.

At the same time, keeping the cutoff well below the Nyquist frequency (half the data-acquisition sampling rate) prevents aliasing, in which unresolved high-frequency components can appear as lower-frequency artifacts. Frequencies above the cutoff, typically associated with localized high-frequency vibrations, are effectively attenuated. This configuration represents a practical balance: a lower cutoff ($<2f_2$) would risk excluding minor but potentially relevant higher-mode contributions, whereas a higher cutoff ($>3f_2$) could admit noise, compromising the fidelity of the digitized strain records. Consequently, the selected $2.5f_2$ cutoff provides a technically justified empirical value, ensuring that the AM signal accurately reflects the physical behavior of the specimens without distorting or losing critical modal information.

Table 10 summarizes the periods and frequencies for the second translational mode obtained from the ambient vibration tests.

Table 10. Second initial mode periods and frequencies.

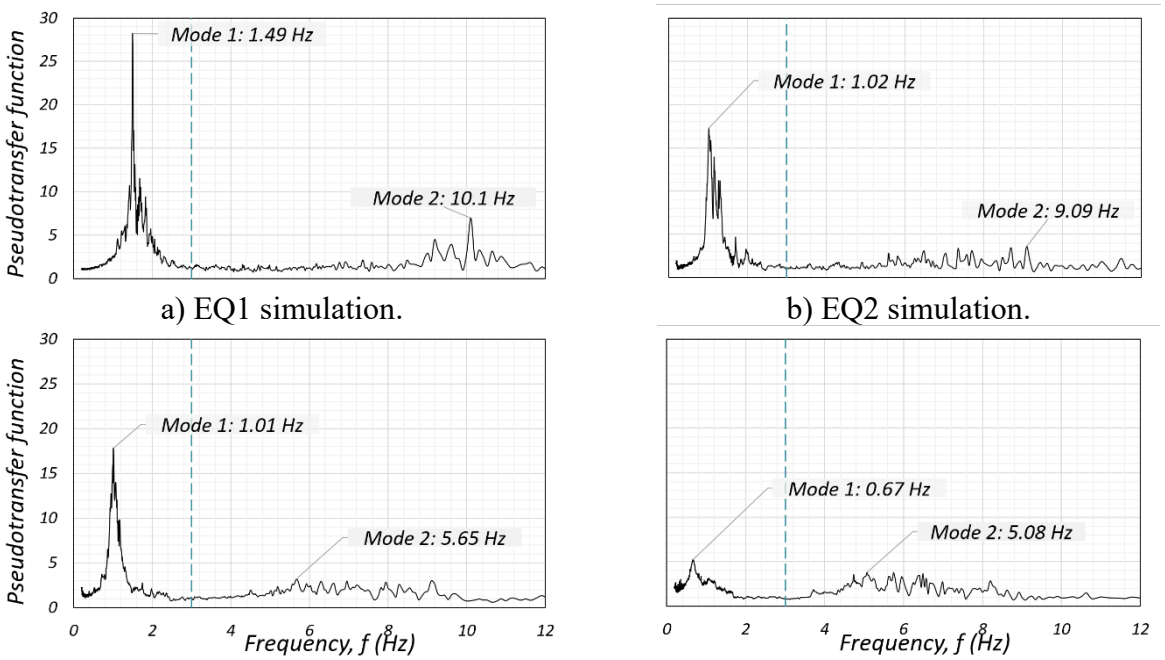
Specimen	T_{o2} (s)	f_{o2} (Hz)
Wall-building	0.095	10.5
Bridge column	0.17	5.9

Based on these values, the cutoff frequencies for the fourth-order low-pass Butterworth filter were set at 26.3 Hz for the wall-building specimen and 14.7 Hz for the bridge-column specimen, ensuring the first and second translational modes are fully captured while higher-order modes are effectively excluded.

The second dataset, referred to as the *Lower Mode* (LM) signal, was obtained using a fourth-order low-pass Butterworth filter with cutoff frequencies of 3 Hz (0.333 s) for the wall-building specimen and 2 Hz (0.5 s) for the bridge-column specimen. These frequencies were selected to suppress higher-mode contributions while preserving the fundamental mode, enabling evaluation of strain-rate demands associated with the primary structural vibration. The cutoff frequencies were established from pseudo-transfer functions calculated as the ratio of the Fourier transforms of the response and excitation signals: the seventh-story-to-base ratio for the wall specimen and the center-of-mass-to-base ratio for the bridge column. These functions were obtained from the same

acceleration records used to establish the temporal bounds and were used to identify the fundamental and higher-frequency components of each specimen.

Figure 27 presents the pseudo-transfer functions for the wall-building specimen. The first peak near 1 Hz corresponds to the fundamental mode, whereas higher-frequency peaks between 5 and 10 Hz correspond to the second mode and local vibrations. The vertical dashed line at 3 Hz marks the applied cutoff, showing that the selected frequency preserves the fundamental mode while attenuating higher-frequency contributions. Thus, the resulting LM signal represents the specimen's primary dynamic response for the subsequent strain-rate analysis.



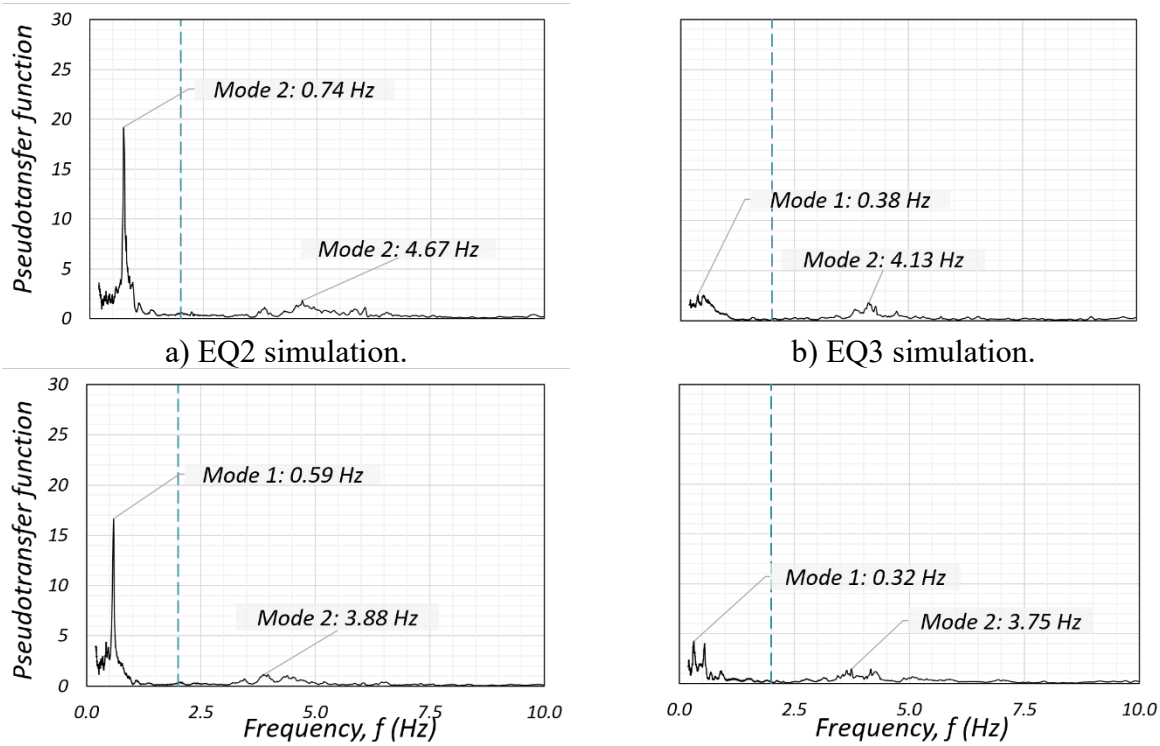
a) EQ1 simulation. b) EQ2 simulation.

c) EQ3 simulation. d) EQ4 simulation.

Figure 27. Pseudo-transfer functions for the wall-building specimen (3 Hz cutoff).

Similarly, Figure 28 presents the pseudo-transfer functions for the bridge column specimen. The first peak near 0.7 Hz corresponds to the fundamental mode, while higher-frequency peaks between 3.5 and 5 Hz indicate the second mode of vibration. The vertical line at 2 Hz marks the applied cutoff frequency, showing that the selected filter preserves the fundamental mode while attenuating higher-frequency components. The resulting LM signal therefore represents the specimen's primary dynamic response. In contrast, the combined AM and LM signals allow the subsequent analysis to distinguish global deformation demands from local strain-rate effects associated with higher-mode excitation.

Figure 29 presents the measured strain signal from gauge A4_3 for the wall-building specimen, illustrating the progressive effect of the two filtering stages.



a) EQ2 simulation. b) EQ3 simulation.

EQ4 simulation. EQ5 simulation.

Figure 28. Pseudo-transfer functions for the bridge-column specimen (2 Hz cutoff).

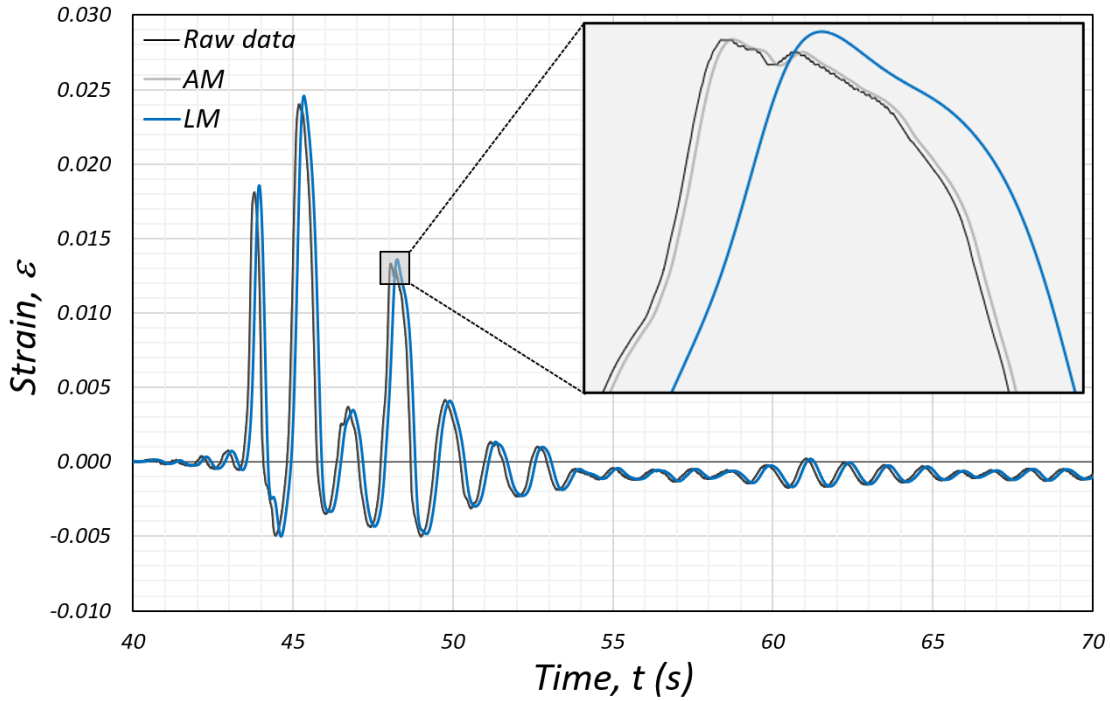


Figure 29. Sequential filtering stages for the strain gauge A4_3 subjected to EQ4 Wall-building specimen.

The inset highlights a representative peak to clarify local behavior. The black curve shows the raw data, where high-frequency fluctuations mask the underlying cyclic pulses. The gray curve corresponds to the first filtering stage, which removes most high-frequency content but leaves residual irregularities near the peak. The blue curve represents the second filtering stage, which further suppresses high-frequency contributions and produces a smoother, monotonic peak evolution.

Figure 30 shows the strain signal from gauge WS05 for the bridge-column specimen, processed through the same two-stage filtering. The transition from raw to first- and second-stage filtered signals exhibits the same pattern as the first specimen. These figures demonstrate that each filtering stage incrementally attenuates spurious high-frequency components, yielding strain histories with peak shapes, amplitudes, and temporal evolution that more accurately reflect the physically admissible response of the specimens. Additionally, delays were introduced in each filtering phase.

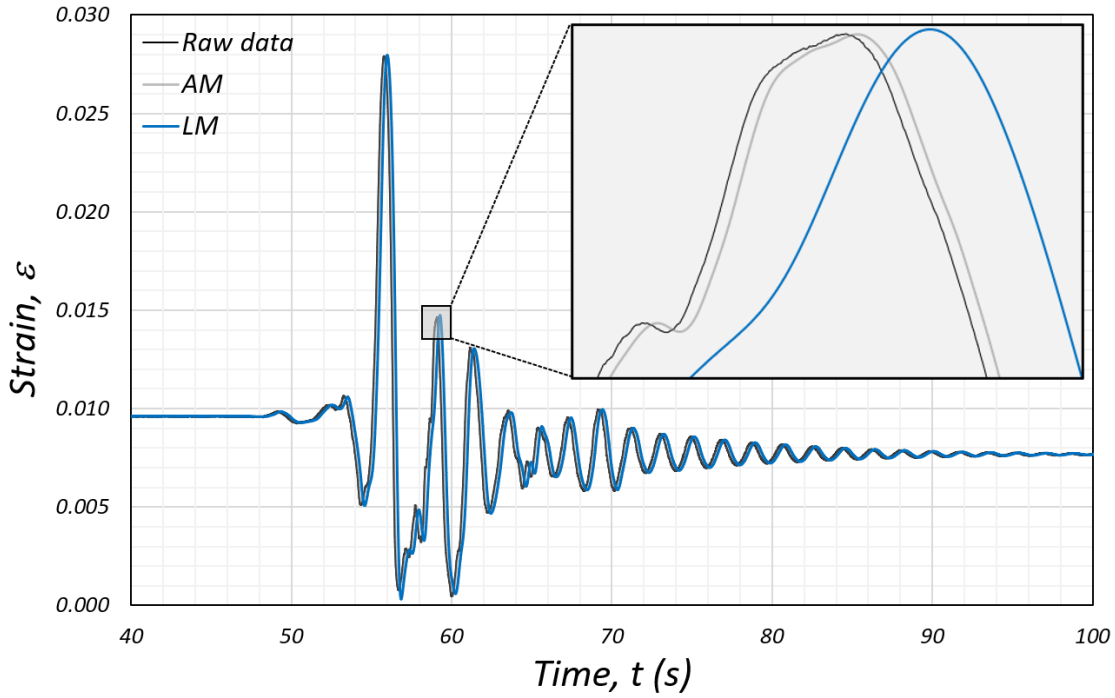


Figure 30. Sequential filtering stages for the strain gauge WS05 subjected to EQ6 Bridge column specimen.

3.8.3 Signal realignment

Butterworth filters inherently introduce frequency-dependent phase delays, as each spectral component of the input signal experiences both amplitude modification (attenuation beyond the cutoff) and a frequency-dependent temporal delay. In structural response signals, which can be viewed as the superposition of multiple harmonic components, this effect shifts peaks, troughs, and transitions in time, potentially distorting the temporal alignment between filtered signals processed with different cutoff frequencies. In the present study, the *AM* and *LM* datasets were filtered with distinct cutoff frequencies (Section 3.8.2), yielding distinct phase-shift patterns for each dataset. Without correction, these discrepancies could prevent accurate temporal correspondence between

key response events, such as strain peaks or inflection points, biasing comparisons of strain histories across the two datasets.

To mitigate this misalignment, normalized cross-correlation was employed to identify the optimal temporal shift between each pair of filtered signals. The cross-correlation function, $r(d)$, quantifies the dissimilarity between two discrete time series as a function of lag d, evaluating how well one signal matches the other when shifted by d steps. The lag that maximizes $r(d)$ corresponds to the displacement that best synchronizes key features between the AM and LM signals, thereby ensuring that comparisons are not affected by phase shifts introduced by filtering.

$$r(d) = \frac{\sum_{i=1}^{N}[\{AM(i) - mA\} * \{LM(i-d) - mL\}]}{\sqrt{\sum_{i=1}^{N}\{AM(i) - mA\}^2}\sqrt{\sum_{i=1}^{N}\{LM(i-d) - mL\}^2}} \tag{107}$$

Where N is the number of samples, $AM(i)$ and $LM(i)$ are the filtered strain values at time step i, and mA and mL denote the mean values of each signal. The numerator represents the covariance between the two signals at a given lag d, and the denominator normalizes this covariance by their standard deviations, constraining $r(d)$ between -1 and 1. Zero-padding was applied when $i - d$ extended beyond the vector limits, ensuring consistent series length and avoiding indexing errors. The integer lag corresponding to the highest correlation is

$$d_0 = argmax\, r(d) \tag{108}$$

This lag yields the discrete temporal shift that maximizes similarity. Because this estimate is limited by the sampling interval Δt, it was refined to sub-sample precision through local parabolic interpolation around d_0. Considering the discrete correlation values $\{r(d_0 - 1),\ r(d_0), r(d_0 + 1)\}$, the interpolated lag is

$$\hat{d} = d_0 + \frac{r(d_0 - 1) - r(d_0 + 1)}{2[r(d_0 - 1) - 2\, r(d_0) + r(d_0 + 1)]} \tag{109}$$

And the corresponding temporal correction is

$$\tau = \hat{d}\, \Delta t \tag{110}$$

Where Δt is the sampling interval, the aligned LM signal is then obtained as a discrete shift:

$$LM_{aligned}(i) = LM\left(i - \hat{d}\right) \tag{111}$$

Or for non-integer lags, through continuous interpolation:

$$LM_{aligned}(t) = interp[LM(t - \tau)] \quad (112)$$

This interpolation estimates signal values at intermediate times between samples, enabling precise temporal alignment without altering amplitude or spectral content. This approach ensures that strain-rate calculations reflect the true physical response rather than artifacts introduced by filtering. The maximum correlation coefficient $r_{max} = r(d_0)$ provides a quantitative measure of alignment quality, with values near 1 indicating excellent correspondence. To explicitly quantify the residual temporal misalignment at each instant, a continuous phase shift function can be defined:

$$\delta(t) = AM(t) - LM_{aligned}(t) \quad (113)$$

This function measures the instantaneous temporal offset between signals after realignment. Across intervals of maximum strain demand in both the wall-building and bridge-column specimens, $\delta(t)$ remains close to zero, confirming that the cross-correlation procedure effectively eliminates phase distortions while preserving amplitude and spectral content. Cross-correlation realignment therefore guarantees temporal synchronization at sub-sample accuracy while preserving amplitude and spectral content, allowing direct comparison of AM and LM datasets without introducing artificial phase distortions. The maximum correlation coefficient $r_{max} = r(d_0)$ provides an overall quantitative measure of alignment quality, with values near unity indicating excellent correspondence.

Figure 31 presents the strain histories recorded by gauge A2-5 in the wall-building specimen under excitation EQ4. The AM and LM signals were temporally realigned using cross-correlation to correct phase shifts introduced by Butterworth filtering. The 7-second window captures the interval of maximum strain demand. After realignment, peaks, troughs, and inflection points align consistently across the signals. Minor amplitude variations remain, attributable to differences in the frequency content of the filtered datasets rather than temporal misalignment. The alignment confirms that the procedure accurately preserves the timing of key strain events, allowing reliable examination of local deformation patterns in the plastic hinge region.

Figure 32 shows strain histories from gauge WS05 in the bridge-column specimen under the same excitation. The 8-second window corresponds to the peak strain-demand interval. Following cross-correlation realignment, the AM and LM signals exhibit precise temporal correspondence of peaks, troughs, and inflection points. As in the wall specimen, remaining amplitude discrepancies reflect spectral differences, not phase errors. The aligned signals provide a consistent representation of the strain evolution, supporting a detailed assessment of inelastic deformation and response within the column's plastic hinge region.

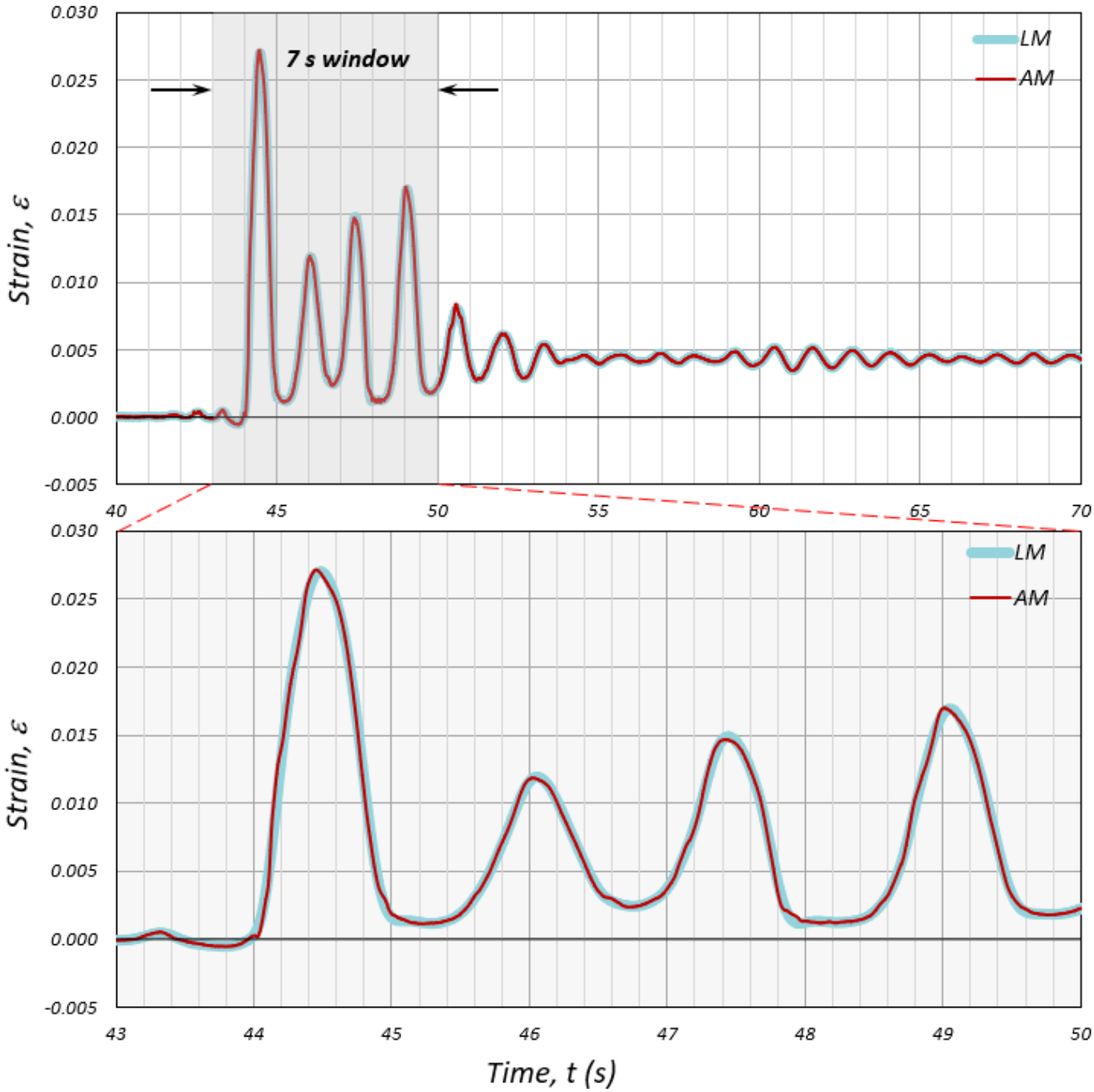


Figure 31. *AM* and *LM* strain signals for the wall-building strain gauge A2-5 under EQ4.

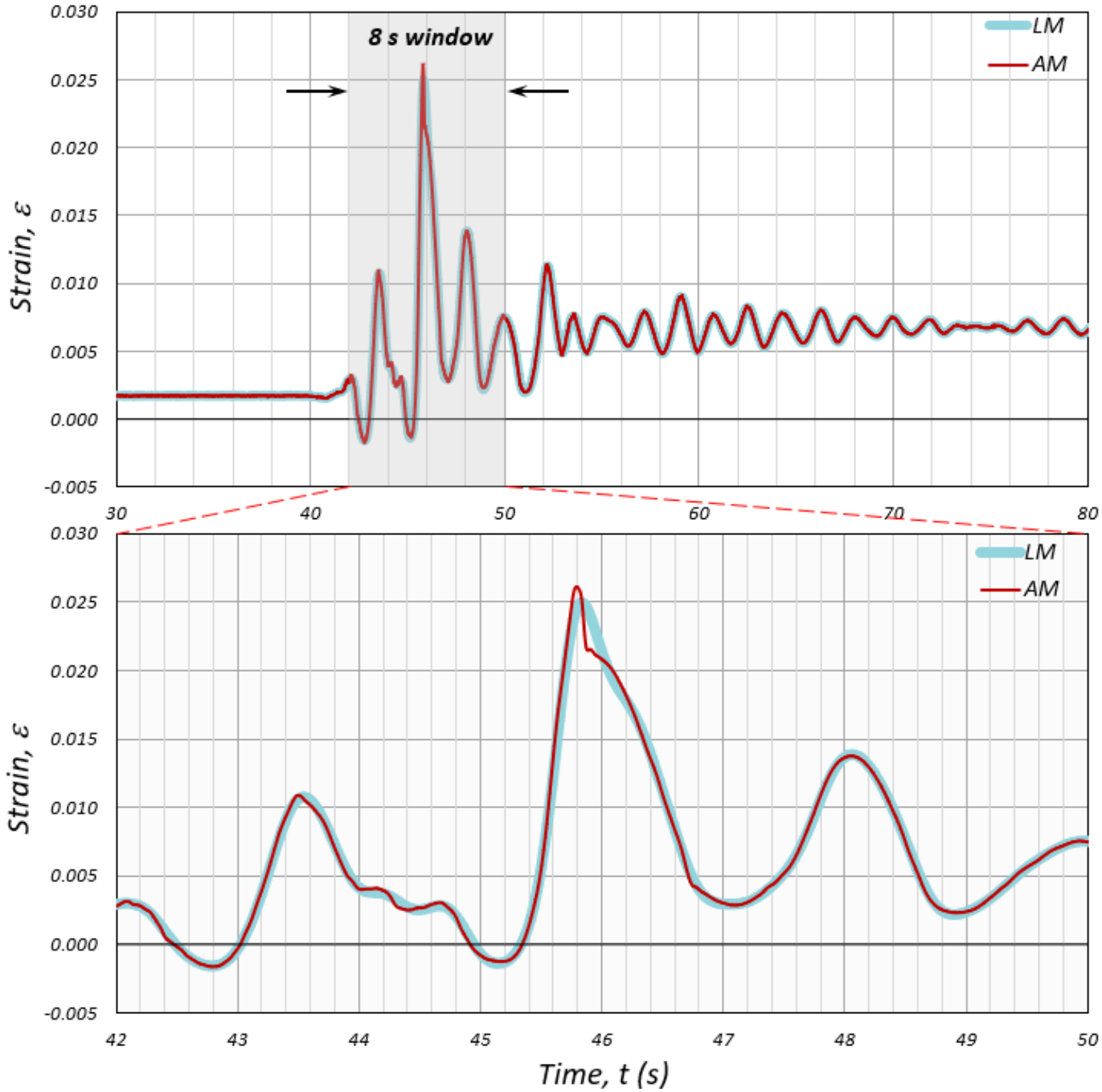


Figure 32. *AM* and *LM* strain signals for the bridge column strain gauge WS under EQ5.

3.8.4 Strain Rate Signals

Time-domain finite-difference methods, applied directly to discrete experimental signals, tend to amplify measurement noise, exaggerate local gradients, and introduce spurious oscillations, compromising the reliability of histories, as was stated by Fornberg [51] and Savitzky & Golay [122]. To overcome these limitations, the strain rate signals are computed via spectral differentiation in the frequency domain, which provides mathematically exact derivatives while preserving the spectral content of the original signals.

Strain rates are obtained by taking the first derivative of the strain time histories $\varepsilon(t)$ in the frequency domain. The signal is decomposed into a weighted sum of harmonic components of the form, $e^{j\omega t}$, where ω is the angular frequency, each of which is smooth and differentiable. Because each spectral component is smooth and differentiable at every point, the resulting strain-rate signal, $\dot{\varepsilon}(t)$, is also continuous, even though the original strain measurements are discrete. This representation captures instantaneous strain variations without the spurious oscillations or noise amplification inherent to finite-difference derivatives, providing an accurate depiction of transient and high-rate phenomena in reinforcing steel under cyclic or seismic loading.

To formalize this procedure, the measured strain signal is first expressed in the frequency domain via the Fourier transform $F(j\omega)$. This representation provides a continuous description of the signal in terms of its harmonic content, expressed as

$$F(j\omega) = \mathcal{F}\{\varepsilon(t)\} = \int_{-\infty}^{\infty} \varepsilon(t)\, e^{-j\omega t} dt \tag{114}$$

In practice, the strain signal is discrete, so this continuous transform $F(j\omega)$ is approximated computationally using the Fast Fourier Transform (FFT). The FFT decomposes the discrete signal into a finite set of harmonic components, preserving the spectral content and enabling efficient numerical computation. Once the FFT of the discrete signal is obtained, the zero-frequency component is shifted to the center of the array. This "zero shift" arranges the negative and positive frequencies symmetrically around zero, ensuring proper alignment of the frequency indices and allowing direct correspondence with the algebraic properties of the continuous Fourier transform. The complex frequencies $j\omega$ are then assigned according to this centered arrangement, providing the correct mapping for further frequency-domain manipulations.

Strain rate signals are then obtained in the frequency domain by differentiating $F(j\omega)$.

$$\mathcal{F}\{\dot{\varepsilon}(t)\} = \mathcal{F}\left\{\frac{d\varepsilon(t)}{dt}\right\} = \int_{-\infty}^{\infty} \frac{d\varepsilon(t)}{dt} e^{-j\omega t} dt \tag{115}$$

The integral is evaluated by applying integration by parts, followed by the change of variables $u = e^{-j\omega t}$ and $dv = d\varepsilon(t)/dt$, which yields

$$\int_{-\infty}^{\infty} \frac{d\varepsilon(t)}{dt} e^{-j\omega t} dt = \left[\varepsilon(t) e^{-j\omega t}\right]_{-\infty}^{\infty} - \int_{-\infty}^{\infty} \varepsilon(t) \frac{d}{dt}\left(e^{-j\omega t}\right) dt$$

Under the physical assumption that $\varepsilon(t) \to 0$ as $t \to \pm\infty$, the boundary term vanishes, and the expression reduces to

$$\begin{aligned} \int_{-\infty}^{\infty} \varepsilon(t) \frac{d\varepsilon(t)}{dt} e^{-j\omega t} dt &= -\int_{-\infty}^{\infty} \varepsilon(t) \frac{d}{dt}\left(e^{-j\omega t}\right) dt \\ &= -\int_{-\infty}^{\infty} \varepsilon(t)(-j\omega) e^{-j\omega t} dt \\ &= j\omega \int_{-\infty}^{\infty} \varepsilon(t) e^{-j\omega t} dt \end{aligned}$$

Therefore,

$$\mathcal{F}\{\dot{\varepsilon}(t)\} = \mathcal{F}\left\{\frac{d\varepsilon(t)}{dt}\right\} = j\omega\, F(j\omega) \tag{116}$$

The strain-rate spectrum is obtained by multiplying each spectral component of the shifted Fourier transform by its corresponding complex frequency $j\omega$. The spectrum is then rearranged into the standard FFT order to maintain consistency with the inverse transform. Through successive applications, higher-order derivatives are computed algebraically [133], leading to

$$\mathcal{F}\left\{\frac{d^n \varepsilon(t)}{dt^n}\right\} = (j\omega)^n\, F(j\omega) \tag{117}$$

In the frequency domain, the n-th derivative corresponds to multiplying each harmonic component by $(j\omega)^n$, reflecting the derivative order. The continuous strain-rate history in the time domain, $\dot{\varepsilon}(t)$, is finally recovered via the Inverse Fast Fourier Transform (IFFT):

$$\dot{\varepsilon}(t) = \mathcal{F}^{-1}\{F(j\omega)\} \tag{118}$$

This procedure ensures mathematically exact differentiation in the frequency domain, limited only by discretization and sampling.

By preserving the signal's harmonic content, FFT-based differentiation avoids the instabilities inherent to finite-difference schemes. Since strain histories in RC structures under seismic loading often include high-frequency components from cracking, bond slip, and localized concentrations, this approach effectively suppresses noise while capturing meaningful strain-rate trends. Figures 33 and 34 show representative strain and strain-rate time windows for the *AM* and *LM* signals of both specimens.

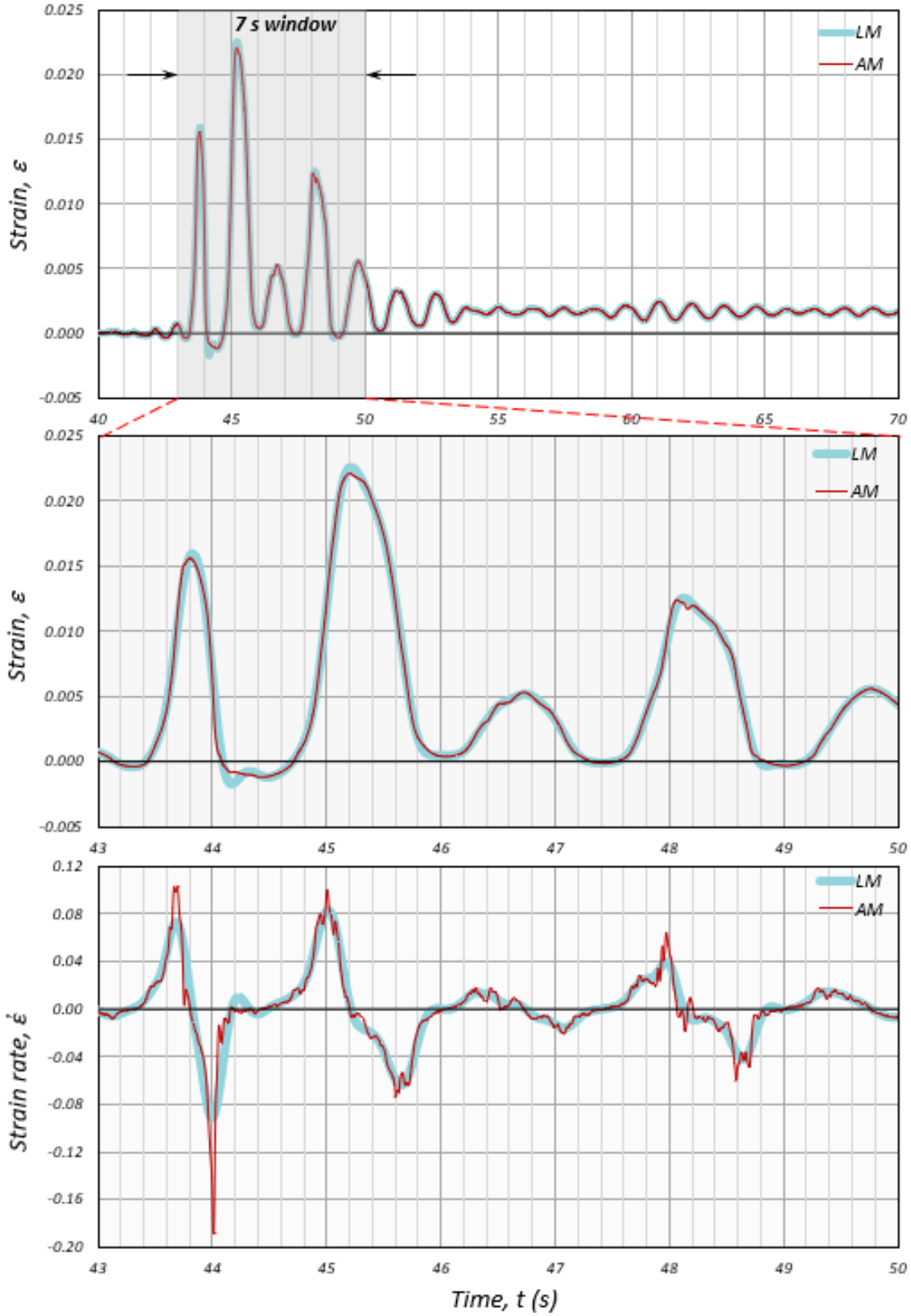


Figure 33. Strain and strain-rate time histories for the wall-building strain gauge A3-4 from EQ4.

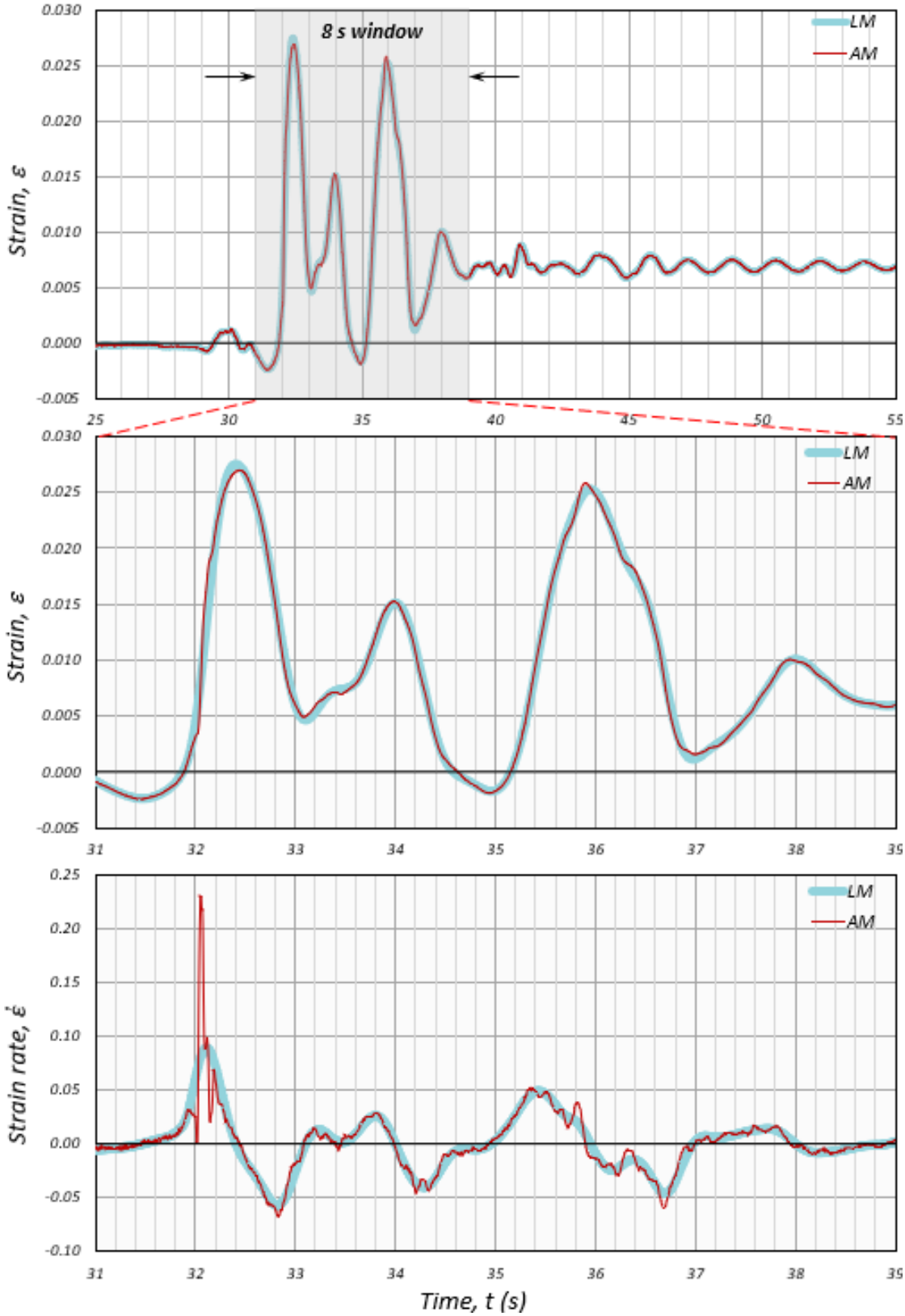


Figure 34. Strain and strain-rate time histories for the bridge column strain gauge EN5 from EQ3.

The derivative relationship is evident: strain maxima and minima coincide with zero crossings of the corresponding strain-rate traces. In contrast, intervals of steepest strain variation produce positive or negative peaks in the strain-rate response. This direct correspondence confirms that FFT-based differentiation accurately reflects the dynamic evolution of localized strains, showing that the observed strain-rate peaks are physically meaningful rather than numerical artifacts.

It can be qualitatively observed that strain-rate peaks in the AM signals are consistently higher than those in the LM counterparts. This difference indicates that the additional dynamic content in the AM records, arising from higher vibration modes, amplifies instantaneous strain rates. While LM signals capture the fundamental response, AM signals include higher-frequency components activated by localized cracking, reinforcement slip, and other nonlinear mechanisms. These higher modes increase the amplitude of strain-rate peaks and alter the timing and localization of extreme values, thereby changing the rate of damage accumulation. The comparison between AM and LM records demonstrates that higher-mode participation, often neglected in simplified analyses, can substantially influence strain-rate histories, with direct implications for assessing RC elements under seismic loading.

3.9 Strain Rate Characterization

Using the Fourier-based differentiation procedure described above, strain-rate signals were computed for all measured strain histories from the selected strain gauges, providing a continuous, physically reliable representation of instantaneous strain evolution. For subsequent analysis, attention was focused on the peak values of these derivatives, which represent the maximum rates of deformation in the reinforcing steel. To focus the analysis on intervals that are both structurally meaningful and materially significant, a subset of these AM and LM signal windows was retained based on two rigorous criteria.

First, the effective period, T_e, associated with each chosen interval, was required to be equal to or greater than the initial first-mode period, $T_{o1} \leq T_e$. This selection ensured that the retained intervals reflected the global dynamic behavior of the specimens, consistent with their fundamental vibration characteristics, rather than isolated high-frequency fluctuations that could distort the physical interpretation of the strain-rate histories. Second, the strain excursion within each interval, defined as the difference between maximum and minimum strain, was required to exceed twice the yield strain of the longitudinal reinforcement, determined from standard monotonic tension tests. This condition guaranteed that the intervals involved substantial inelastic deformation sufficient to activate the nonlinear mechanisms of interest. The experimentally determined yield strains were 0.27% for the wall-building specimen and 0.23% for the bridge column specimen. By applying these criteria simultaneously, the selected intervals maintained both structural relevance in terms of modal participation and a clear connection to the steel's material nonlinearity, providing a consistent foundation for subsequent strain-rate evaluation.

The variation of the peak strain rates with respect to the effective-to-initial period ratio, T_e/T_{o1}, was analyzed for all retained intervals in both experimental programs. Figures 35 and 36 present these results for the wall-building and the bridge column specimens, respectively.

Each data point represents the maximum strain rate recorded at a specific gauge location, obtained through the Fourier-based differentiation procedure. In both figures, the size and darkness of the dots vary systematically with the amplitude of the ground-motion input, providing a straightforward visual indicator of excitation intensity.

In the wall-building specimen (Figure 35), three levels of seismic input are shown: the largest, darkest markers correspond to EQ4; the intermediate-sized gray markers represent EQ3; and the smallest, lightest markers correspond to EQ2. In the bridge-column specimen (Figure 36), the intensities encompass four levels: the largest black markers denote EQ5, followed in decreasing order of size and darkness by EQ4 and EQ3. In contrast, the smallest black dots correspond to EQ2. In addition, dots highlighted with a blue ring identify the intervals where peak strain rates were attained, with the corresponding strain remaining within the Lüders plateau (i.e., the region characterized by an almost constant stress following initial yielding).

This progressive gradation not only provides a visual indicator of excitation intensity but also helps identify how strain-rate demands scale across different levels of seismic excitation in both specimens. For the first specimen, the peak strain rates observed under test conditions (EQ2, EQ3, and EQ4) are summarized as follows. Under EQ2, the Lüders phase exhibited a peak strain rate of 17.8 %, while the work-hardening phase reached 12.9 %. For EQ3, the corresponding values were 10.6% and 7.0%, respectively. Under EQ4, the Lüders region recorded a peak strain rate of 21.2%, while the work-hardening region recorded 18.1%. These results indicate a consistent trend: the Lüders bands exhibit higher strain rates than the work-hardening phase across all tested conditions, with EQ4 showing the highest values in both regions.

In contrast, the bridge specimen exhibited distinct strain-rate behavior under test conditions (EQ2, EQ3, EQ4, and EQ5). Under EQ2, the maximum strain rates were 17.7 %/s in the Lüders zone and 7.2 %/s in the work-hardening zone. For EQ3, the Lüders bands recorded a significantly higher strain rate of 43.6 %/s, while the work-hardening zone was limited to 7.8 %/s. Notably, under EQ4, no Lüders response was observed, and the work-hardening zone was limited to 2.3 %/s. Under EQ5, the Lüders phase reached 33.5 %/s, with the work-hardening zone at 15.1 %/s. The bridge specimen's response is predominantly governed by pronounced Lüders peaks under EQ3 and EQ5, reflecting significant localized deformation during these loading conditions.

Figures 35 and 36 demonstrate that the highest peak strain rates in the longitudinal bars occurred during strains within the Lüders plateau. In this region, some strain rates exceeded 10%/s, reaching peak values of 21.2%/s and 44%/s in the wall-building and in the bridge column specimens, respectively.

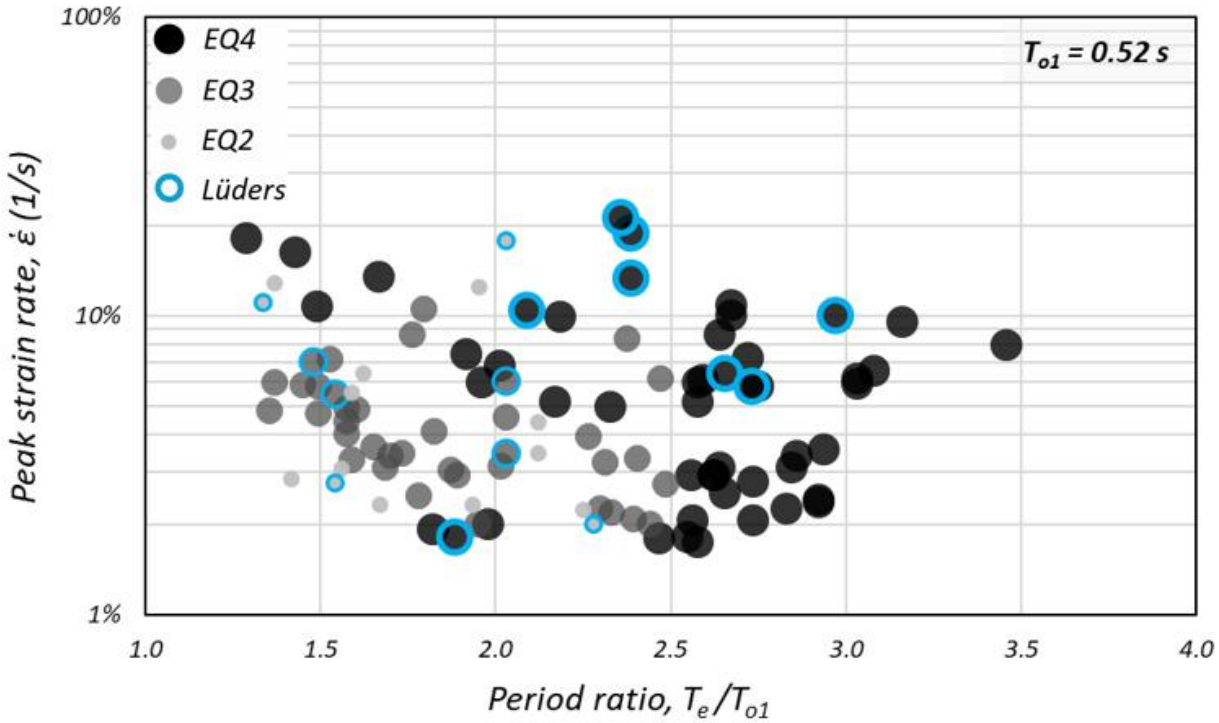


Figure 35. Peak strain rate versus effective-to-initial first mode period ratio in strain-gauged bars in the plastic hinge region of the wall-building specimen.

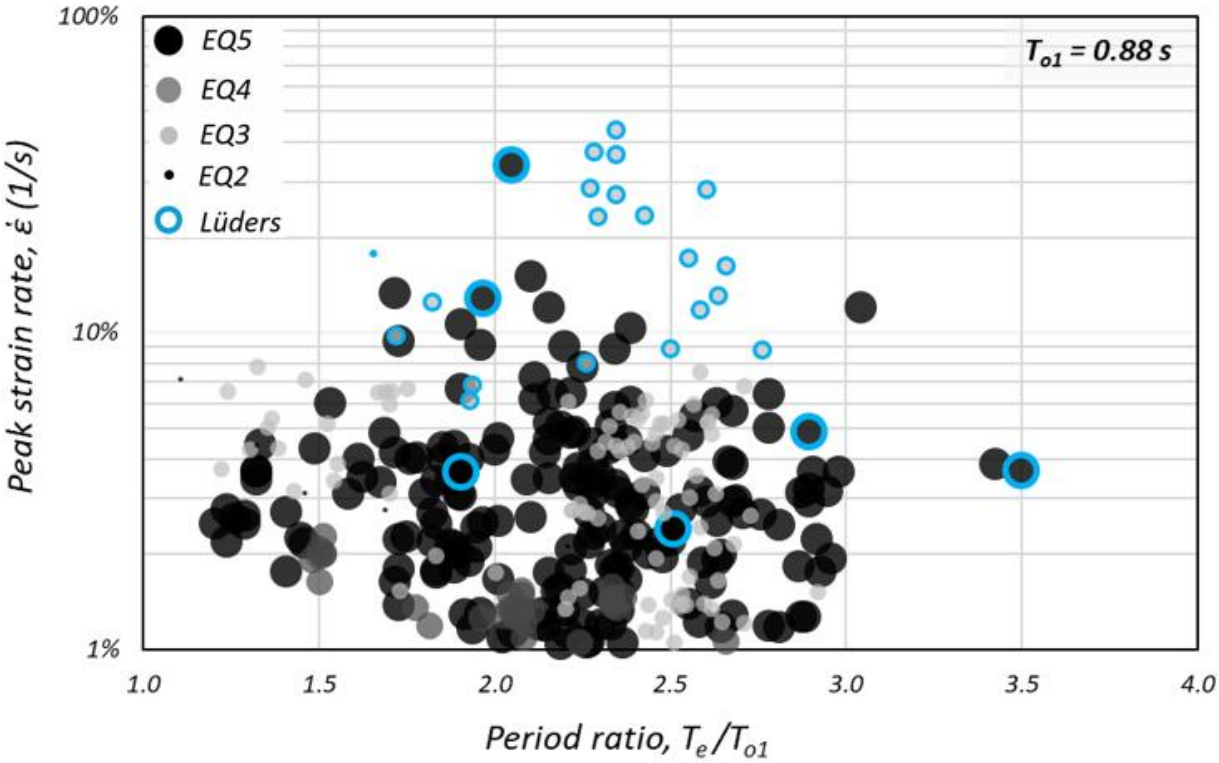


Figure 36. Peak strain rate versus effective-to-initial first mode period ratio in strain-gauged bars in the plastic hinge region of the bridge column specimen.

Such measurements are consistent with previous experimental findings on reinforcing bars [114] and [115], which reported that strain-rate amplification is particularly pronounced when plastic strains develop within the Lüders region. They are also consistent with studies investigating the explicit dependency of strain rate on loading velocity during this stage [129], in which physical equations were proposed for annealed mild steel to describe the strain-rate dependency of both the strain itself and the propagation velocity of Lüders bands, thereby providing a mechanistic explanation for the observed sensitivity in this range.

Table 11 summarizes the peak strain rates observed under test conditions. Here, peak strain rates are delineated for both the Lüders and work-hardening regions.

Table 11. Peak Strain Rates for both specimens.

	Wall-building		**Bridge column**	
Test	**Lüders**	**Hardening**	**Lüders**	**Hardening**
EQ2	17.8 %/s	12.9 %/s	17.7 %/s	7.2 %/s
EQ3	10.6 %/s	7 %/s	43.6 %/s	7.8 %/s
EQ4	21.2 %/s	18.1 %/s	(**)	2.3 %/s
EQ5	*	(*)	33.5 %/s	15.1 %/s

(*) This specimen was not subjected to the EQ5 test condition.
(**) No Lüders band response was observed.

At first glance, it is reasonable to expect strains outside the Lüders plateau during the more intense tests (e.g., EQ3, EQ4, and EQ5), as reinforcing bars in plastic hinge zones are expected to exhibit strains characteristic of the work-hardening regime. The Lüders plateau is typically more pronounced under lower-intensity or quasi-static conditions where plastic deformation initiates. In contrast, intense seismic loading subjects critical regions to elevated strain demands, driving the material response into the work-hardening region.

This direct progression to the work-hardening regime without exhibiting Lüders behavior is facilitated by the spread of plasticity away from the critical region, driven by the interplay of work hardening and flexure-shear interaction. As the material in the critical region hardens, its increased stiffness and strength cause plastic deformation to propagate into adjacent, less-strained areas. This effect is particularly significant in structural components subjected to combined flexure and shear, as in seismic loading scenarios. The resulting complex stress states redistribute plastic strains, diminishing the prominence of Lüders bands and promoting a more uniform strain distribution typical of the work-hardening regime.

Furthermore, an analysis of the experimental results, as illustrated in Figures 35 and 36, reveals no discernible correlation between the observed peak strain rates and the period ratio T_e/T_{o1}. This lack of correlation suggests that the strain rate response is primarily influenced by local material behavior and the loading intensity, rather than global dynamic parameters such as the period ratio. This observation underscores the importance of considering localized deformation mechanisms, such as Lüders band formation, when evaluating the seismic performance of structural components.

Tables 12 and 13 compare the average strain rates, computed using the approach described in Section 3.4 for the maximum lateral displacement predicted by the DDBA procedure, with the 95th percentile of peak strain rates derived from strain gauge data, as presented in Figures 35 and 36. These comparisons encompass both the wall-building and bridge-column specimens, with strain rates reported for the Lüders plateau and work-hardening regions.

Table 12. Comparison of experimental peak strain rates to the average by DDBA
Wall-building specimen.

	DDBA	**95th percentile**	
	(99)	**Lüders**	**Hardening**
EQ2	1.5 %/s	16.8 %/s	12.7 %/s
EQ3	(*)	(**)	8.5 %/s
EQ4	4.9 %/s	20.4 %/s	13.3 %/s

(*): The DDBA procedure does not predict an inelastic response
(**): Only six points of output are insufficient for an analysis

Table 13. Comparison of experimental peak strain rates to the average by DDBA
Bridge column specimen.

	DDBA	**95th percentile**	
	(99)	**Lüders**	**Hardening**
EQ2	1.2 %/s	17.7 %/s	6.3 %/s
EQ3	5.4 %/s	38.9 %/s	6.8 %/s
EQ4	1.6 %/s	(***)	2 %/s
EQ5	7.5 %/s	28.3 %/s	8.7 %/s

(***): No output data occurred

The 95th percentile was selected as a representative measure of peak strain rates to exclude outliers, ensuring a robust characterization of maximum strain response. As anticipated, the peak strain rates in both the Lüders plateau and the work-hardening regions exceed those predicted by the DDBA approach, highlighting its conservatism relative to the experimental data.

These computed values are noticeably lower than the maximum strain rates recorded directly during the experimental tests. This divergence underscores a key limitation of DDBA estimation: its reduced ability to capture localized, transient deformation peaks that occur during highly nonlinear response phases. Such differences are not merely numerical deviations; they imply that, under certain dynamic loading scenarios, the real structural demand can exceed the analytical predictions, potentially affecting performance assessments and safety margins. In practical terms, this highlights the need to interpret DDBA-based results cautiously, particularly when these values inform design decisions or calibrate numerical models simulating inelastic structural behavior under seismic excitation.

3.9.1 Ratio of peak to average strain rate: κ-ratio

Next, evaluate the κ-ratio directly from the experimental strain histories.

The κ-ratio, introduced in Section 3.5, is evaluated for the AM and LM signal intervals and quantifies the temporal and spatial variability of strain-rate response under seismic loading. The interpretation extends beyond the idealized harmonic case, providing a quantitative description of strain-rate variability in experimentally observed deformation patterns.

3.9.1.1 Effect of Dynamic Dislocations in the Lüders Plateau: κ_L-ratio

The Lüders plateau is a distinctive phase in the tensile stress-strain response of certain polycrystalline metals, characterized by a nominally constant stress after an abrupt drop from the upper to the lower yield point. This plateau arises from localized plastic deformation, in which strain accumulates without a corresponding increase in applied stress, reflecting inhomogeneous yielding.

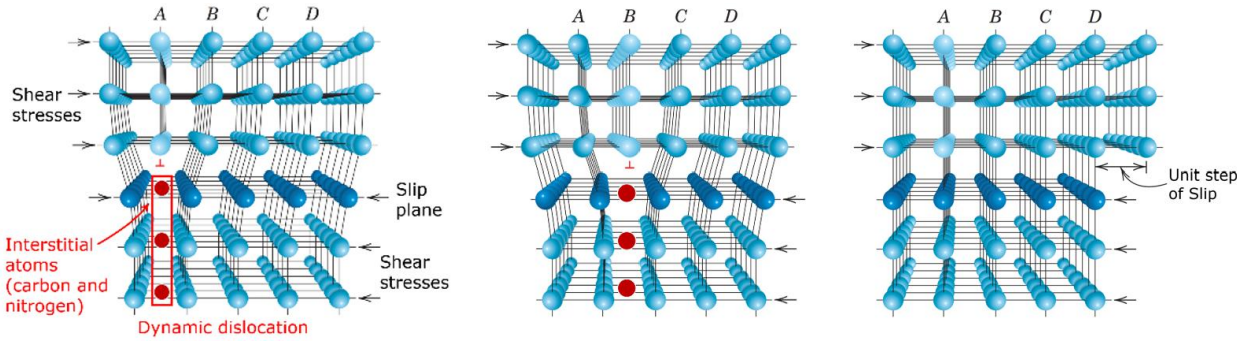
Macroscopically, the phenomenon manifests through the nucleation and propagation of Lüders bands, localized zones of intense shear deformation that typically initiate at sites of elevated stress concentration, such as the lugs of a tensile specimen. These bands propagate axially along the specimen at a velocity that scales with the imposed strain rate, progressively deforming the material until the entire section has yielded. At this juncture, the plateau terminates, and the material transitions to homogeneous work hardening, marking the onset of uniform plastic deformation. The extent of the plateau is quantified by the Lüders strain, which encapsulates the cumulative inhomogeneous deformation and depends on microstructural attributes [136].

At the microscopic level, the formation and propagation of Lüders bands are governed by dislocation dynamics; dislocations are line defects within the crystal lattice that facilitate plastic slip, and the lattice is composed of atoms (e.g., iron in steel) that form the ordered crystalline structure. Figure 37 illustrates a schematic of dislocation dynamics in a crystal lattice during Lüders band formation. In the undeformed state, dislocations are immobilized by interstitial solute atoms, primarily carbon or nitrogen, which migrate to form Cottrell atmospheres [39] (see column A of the crystalline structure in Figure 37a). These atmospheres arise from elastic interactions between solute atoms and dislocation strain fields, creating a pinning effect that significantly increases the stress required for dislocation breakaway and corresponds to the upper yield point observed in the stress-strain curve.

Figure 37b illustrates the onset of plastic deformation, in which the enclosed lattice atoms begin shifting and realigning along the failure plane as the dislocation mobilizes. When the applied stress exceeds the critical threshold, dislocations unpin abruptly, initiating an avalanche-like process of multiplication and gliding. This rapid dislocation motion at the advancing front of a Lüders band drives the band's propagation and sustains the "constant-stress" plateau. The unpinned dislocations multiply swiftly, producing localized strain rates that far exceed the globally imposed strain rate. The high velocity of these mobile dislocations outpaces the diffusion kinetics of interstitial solutes, preventing immediate repinning and enabling sustained plastic flow within the band.

Figure 37c shows the fully propagated state, where the dynamic dislocation has traversed the lattice, leaving a trail of plastic deformation, and shear stresses have aligned the lattice along the failure plane. The enclosed lattice atoms are now stabilized in their new positions after significant

displacement. The Cottrell atmosphere is fully redistributed, reflecting sustained plastic flow within the Lüders band and maintaining the "constant-stress plateau" until the entire gauge section yields.



a. Initial state with interstitial atoms forming Cottrell atmospheres to pin potential dislocations.

b. Onset of a dynamic dislocation under shear stresses.

c. Fully propagated state with stabilized plastic deformation.

Figure 37. Evolution of Dislocation Dynamics During Lüders Band Propagation. Modified from [27].

The mechanical behavior of polycrystalline metals in tension is strongly influenced by the applied strain rate, which controls the rate of plastic deformation and the emergence of localized yielding mechanisms, such as Lüders bands. When the imposed rate is low, dislocation multiplication, solute drag, and the formation of Cottrell atmospheres proceed with sufficient time to stabilize the discontinuous yielding front, allowing Lüders bands to initiate and propagate over an extended plateau. When the imposed rate increases, dislocation flux rises, solute atmospheres cannot reform as quickly, and the Lüders front advances faster, leading to a shorter plateau and a modified yielding regime [136]. These behaviors reflect interactions among rate sensitivity, dynamic strain aging, and dislocation transport.

A useful parameter to characterize this process is κ_L, which represents the propagation rate of the Lüders band. Although this is often assumed to be primarily material-controlled, the evidence here indicates a geometric contribution. Figures 35 and 36 show that the 35-mm bars used in the bridge-column specimen reached peak strain rates more than twice those of the 16-mm bars from the wall-building specimen when the deformation remained within the Lüders region. This observation suggests a geometric contribution to the Lüders-band propagation rate. However, the two bar diameters were tested in different structural configurations, under different loading histories, and with different gauge lengths. The available data therefore do not permit isolation of the diameter effect from these confounding variables, and the quantitative relationship between bar size and the Lüders-band propagation rate remains unresolved. The following discussion offers a plausible physical interpretation of the observed differences, intended to guide future experimental campaigns rather than to constitute a validated finding of this study.

Table 14 lists the minimum, maximum, and average strain rates recorded within the Lüders plateau for all specimens, providing a consolidated quantitative basis for comparing the geometric effects on localized strain-rate behavior.

Table 14. Peak strain rates in the Lüders plateau region.

	Wall-building	**Bridge column**
Average	9 %/s	17.2 %/s
Minimum	1.8 %/s	2.4 %/s
Maximum	21.2 %/s	43.6 %/s

Figure 38 shows the distribution of peak strain rates measured during the Lüders plateau for both bar geometries. The histogram for the 35-mm bars shifts toward higher rates: frequencies increase in the 0.05-0.10 s^{-1} interval, peak in the 0.10-0.20 s^{-1} range, and remain non-zero up to 0.25 s^{-1}. The 16-mm bars, by contrast, display a tighter distribution, concentrated between 0.05 and 0.15 s^{-1}, with an abrupt decline above that interval.

The divergence of both distributions demonstrates that bar diameter affects the local strain-rate response associated with Lüders propagation. Larger diameters produce a broader, higher-level strain-rate range, while smaller diameters confine the activity to a narrower, lower-level interval.

Both histograms intersect near 0.10 s^{-1}, where the two bars have comparable frequencies. This convergence reflects the minimum strain rate required to sustain stable Lüders-band propagation, which is primarily governed by the initial release of solute atmospheres and the activation of mobile dislocations. At this threshold, the deformation kinetics are controlled by fundamental dislocation-solute interactions and remain largely independent of specimen diameter. Beyond this point, the influence of bar size becomes dominant, producing the right-shifted and broadened distribution observed in the 35-mm bars.

This behavior follows directly from the material volume that must deform cohesively as the Lüders front moves. Propagation through a larger diameter requires activating more grains simultaneously, generating greater plastic deformation per unit time inside the band, even when the externally imposed loading rate is identical. As a result, larger bars experience higher internal strain rates, a broader range of peak-rate occurrences, and a faster transition out of the Lüders plateau. The narrower distribution of the smaller bars indicates that their limited cross-sections constrain the deformation zone, reducing the rate of plastic strain accumulation.

Cai et al. [24] demonstrated that Lüders-band propagation in Al-based alloys depends on specimen thickness: thinner geometries develop higher local strains and higher local strain rates because the same localized slip is confined to a smaller deformation volume, even though the band propagates more slowly. These values correspond to measurements taken inside the narrow Lüders front, where deformation is concentrated.

In the present work, the reported peak strain rates correspond to the specimen scale during the Lüders plateau. These global values indicate the rate at which the entire bar accumulates plastic deformation as the band advances. A larger diameter requires a greater internal dislocation flux to

maintain compatibility across a larger deformation volume, producing higher global peak strain rates even if the local strain within the band front is lower than in a thin specimen.

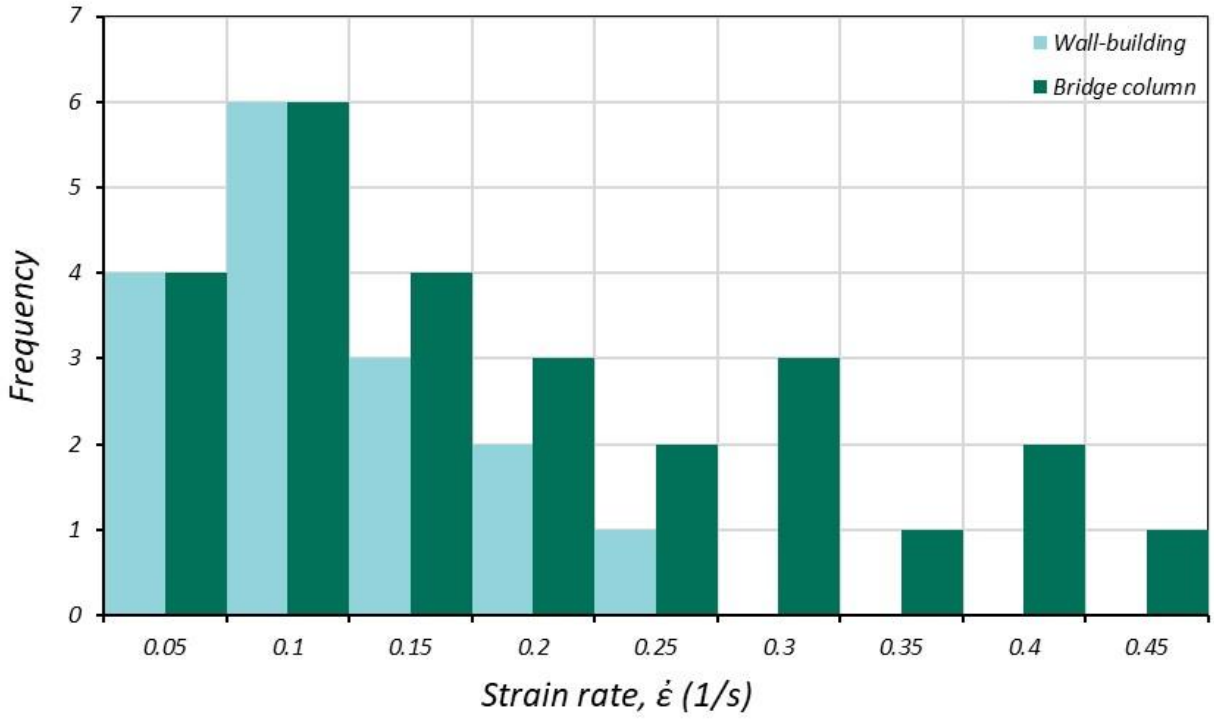


Figure 38. Histogram of strain rate distribution in the Lüders plateau for wall-building and bridge column specimens.

Both behaviors are consistent: thin specimens exhibit higher local strain and strain rate at the band front, while thick specimens require a higher global strain rate to transmit the same localized front through a larger material volume. The difference arises from the measurement scale, not from a contradiction in mechanics. Transmission electron microscopy observations by Wang et al. [138] further demonstrate that the accelerated multiplication and glide of mobile dislocations control the rapid plastic-strain buildup within Lüders bands. When the deformation front spans a larger cross-section, the number of activated dislocation sources increases, producing higher local strain rates and reducing the duration of the plateau.

Qui et al. [109] identified heterogeneous local strain and strain-rate patterns in tempered martensite, showing that multiple microstructural regions may concentrate deformation simultaneously. When the affected volume increases, as in larger bars, the aggregated contributions of many such regions elevate the overall strain rate during Lüders propagation. This observation is consistent with the higher peak rates observed in the 35-mm bars. High imposed strain rates can also shift Lüders propagation from a smooth to a discrete mode due to interactions with dynamic strain aging [42]. The elevated peak rates in the larger bars replicate this condition even at nominally similar global loading rates, because the larger deformation volume intensifies internal rate sensitivity. This connection is supported by the findings of Van der Heijde and Samad [135], who documented

increased Lüders-band propagation velocities in larger AISI 1524 steel specimens. The present data indicate that the same geometric dependence may influence κ_L in reinforcing steels.

Because peak strain rates within the Lüders plateau are governed by dislocation-controlled kinetics, the present measurements cannot isolate geometric influences with the precision required to quantify size effects. The dataset is insufficient to determine how bar diameter or the interaction between diameter and strain-gauge length affects the global strain rate demanded by Lüders-band propagation. These dependencies remain unresolved and require dedicated experimentation to establish their contribution to size-dependent behavior in reinforcing steels.

Furthermore, continuum-level nonlinear structural models cannot reproduce the dislocation processes that control the onset, velocity, and decay of Lüders-band propagation. More critically, the bar overstrength relevant to structural applications is governed by the stresses developed after the Lüders region, in the work-hardening regime where deformation becomes spatially uniform. Capturing these mechanisms would require crystal-plasticity finite-element simulations that resolve individual slip-system activity and the evolution of dislocation structures. Consequently, no attempt is made here to calibrate the κ_L-ratio, and its quantitative dependence on specimen size and strain rate remains outside the scope of the current framework.

In the work-hardening region, where Lüders mechanisms cease and deformation spreads uniformly, κ_L-ratio is taken as unity, consistent with a regime in which the material response no longer depends on the propagation of a localized front but on conventional isotropic plasticity.

3.9.1.2 Effect of "Higher" Modes of Response: κ_H-ratio

The AM signal preserves the full modal content of the measured response, whereas the LM signal filters the record to the first vibration mode. The κ_H-ratio, defined as the ratio of AM-derived to LM-derived peak strain rates computed exclusively for intervals beyond the Lüders plateau, quantifies the contribution of "higher-order" modal content to the strain-rate demand under nonlinear excitation. Restricting the calculation to the work-hardening regime avoids contamination by transient localization and ensures that κ_H-ratio reflects modal dynamics rather than material-specific banding. The term "higher" is enclosed in quotes to reflect that, during strong-intensity shaking, specimens often transition into the plastic range, disrupting the conventional modal hierarchy by altering the structure's stiffness and damping characteristics. This shift complicates the traditional assumptions of linear modal analysis, as plastic deformation introduces nonlinear effects that can amplify higher-mode contributions. Consequently, comparing AM and LM signals provides valuable insights into how these "higher" modes affect the structural response, particularly under extreme loading conditions.

Figures 39 and 40 present the κ_H-ratio as a function of the period ratio T_e/T_{o1} for the wall-building and bridge-column specimens, focusing exclusively on strains in the work-hardening regime beyond the Lüders plateau to isolate the dynamic influence of higher-order modes and avoid contamination from Lüders band propagation.

In the wall-building specimen, κ_H-ratio exhibits a clear increase with T_e/T_{o1}, indicating that higher-order vibration modes actively contribute measurably to strain-rate amplification once the response

enters the post-plateau region. This correlation highlights the interplay between global dynamic characteristics and localized strain accumulation, demonstrating that modal participation significantly shapes the temporal evolution of plastic deformation. The pronounced sensitivity observed in this specimen aligns with the expected second-mode participation in a seven-story system with distributed mass and height-dependent flexibility. Activation of this mode introduces additional curvature and strain-rate variability along the height, which becomes more apparent in the work-hardening regime beyond the Lüders plateau.

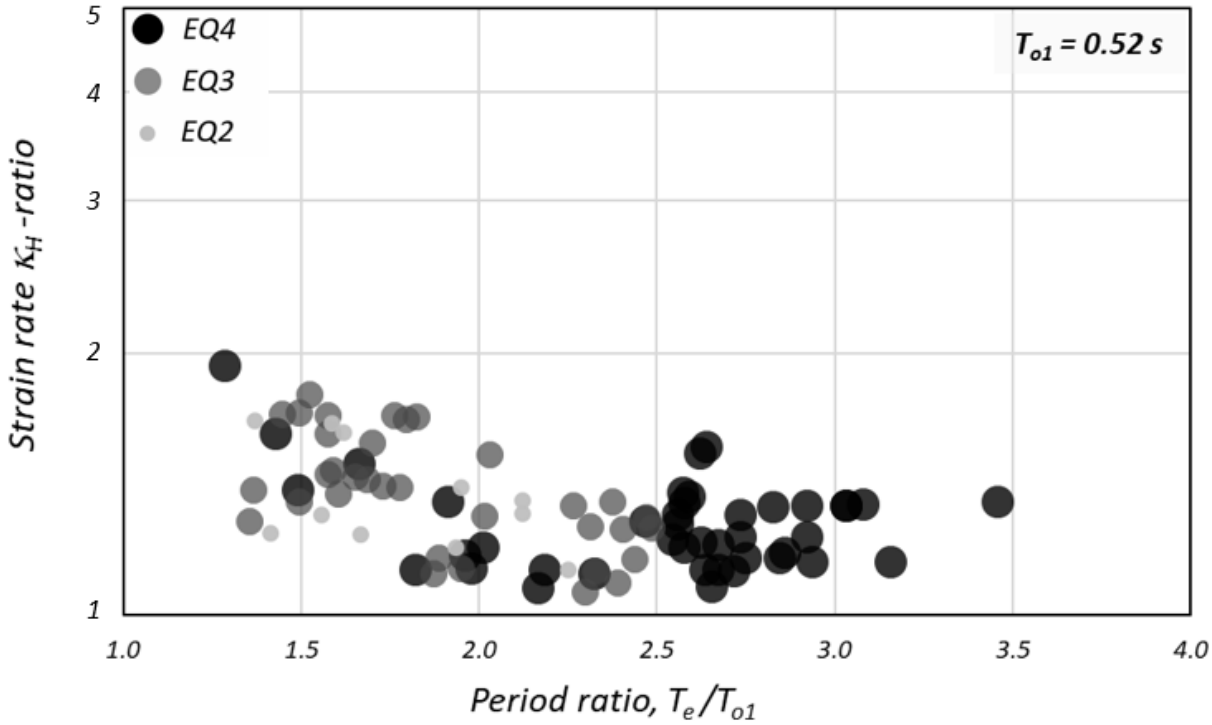


Figure 39. κ_H-ratio variation versus effective-to-initial first mode period for the wall-building specimen.

By contrast, the bridge-column specimen shows no systematic relationship between κ_H-ratio and T_e/T_{o1}. Its geometry and more compact mass distribution, which approximate a single-degree-of-freedom response, restrict participation of higher modes and confine the dynamic behavior primarily to the fundamental mode. Under these conditions, local strain-rate histories are predominantly governed by section-level curvature demands and reinforcement detailing, thereby limiting the influence of higher-mode dynamics.

These findings indicate that the influence of higher-order modes on strain-rate evolution within the hardening range depends on specimen geometry, stiffness distribution, and reinforcement detailing, rather than being uniformly present across structural configurations. They also show that strain-rate effects under seismic loading must be interpreted with respect to each specimen's dynamic characteristics. The κ_H-ratio results demonstrate that higher-mode participation can modify localized strain-rate histories in systems with significant modal interaction. In contrast, in other

systems, the effect is minimal, reinforcing the need to evaluate rate-dependent mechanisms in seismic design on a configuration-specific basis.

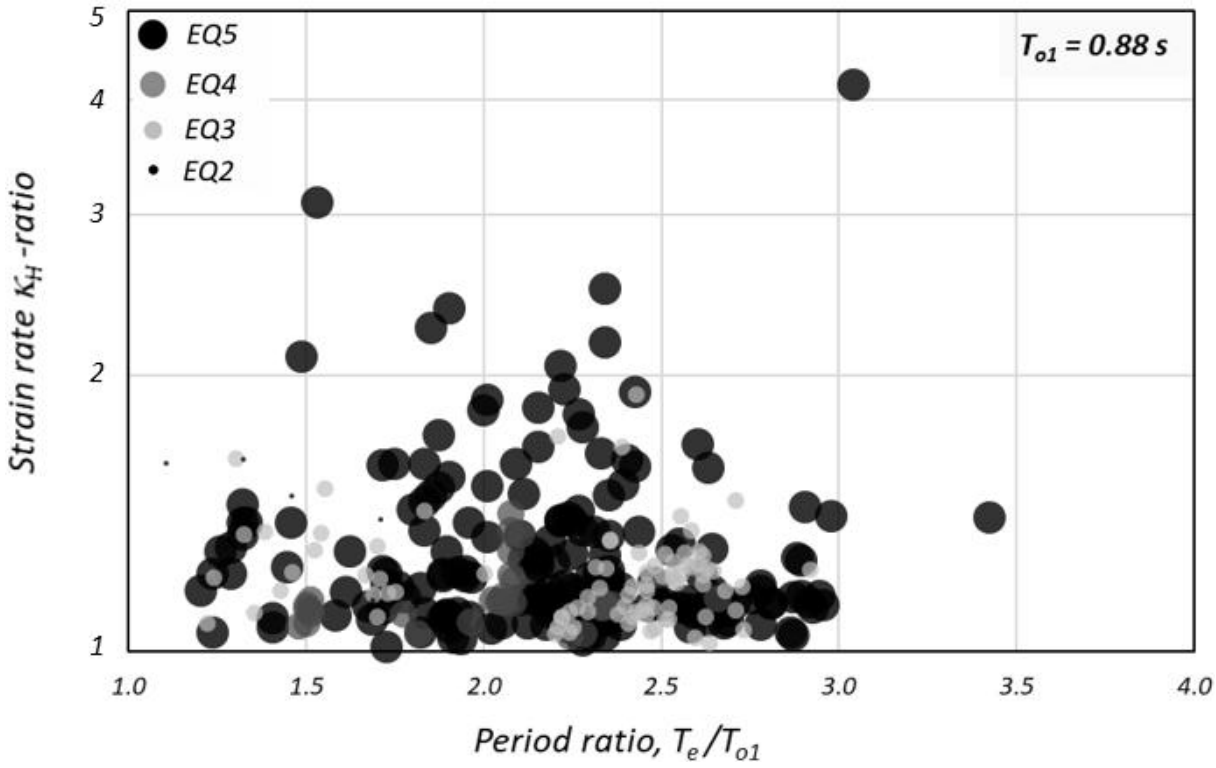


Figure 40. κ_H-ratio variation versus effective-to-initial first mode period for the wall-building specimen.

To interrogate these differences more deeply, time-frequency analyses were conducted using Short-Time Fourier Transform-based spectrograms on both AM and LM strain-rate signals, evaluated over the same post-Lüders intervals used for the κ_H-ratio computations (see Figures 41 and 42). For illustration, strain signals from gauges A1_4 in the EQ4 simulation and EN07 in the EQ3 simulation were selected for the respective specimens. These spectrograms directly visualize frequency-content evolution under nonlinear structural response and allow assessment of whether higher-mode activity is present and energetically significant.

Subtracting LM from AM removes, to first order, the shared narrowband contribution of the dominant mode, revealing residual energy in higher frequencies or broadband regions caused by localized nonlinearities. This residual energy reliably indicates sustained higher-mode participation during the nonlinear response, as it is unaffected by fundamental-frequency variations or curvature-induced amplitude modulation confined to the fundamental band. The amplitude and temporal coherence of the AM-LM field directly measure higher-order mode activity, its transience or persistence, and whether its activation aligns with specific phases of material hardening.

This decomposition is necessary for interpreting κ_H-ratio trends. An observed increase in κ_H-ratio cannot be attributed to higher-mode effects unless the strain-rate signal exhibits demonstrable

spectral energy outside the fundamental band. The AM-LM field supplies that evidence by separating true higher-mode content from the dominant-mode background. Conversely, when κ_H-ratio remains insensitive to T_e/T_{o1}. The absence of coherent energy in the AM-LM field confirms that the response is effectively single-mode and that strain-rate amplification arises from section-level curvature demands rather than modal interactions. The AM-LM separation thus provides the required diagnostic link between time-frequency characteristics and rate-dependent strain evolution in the hardening regime.

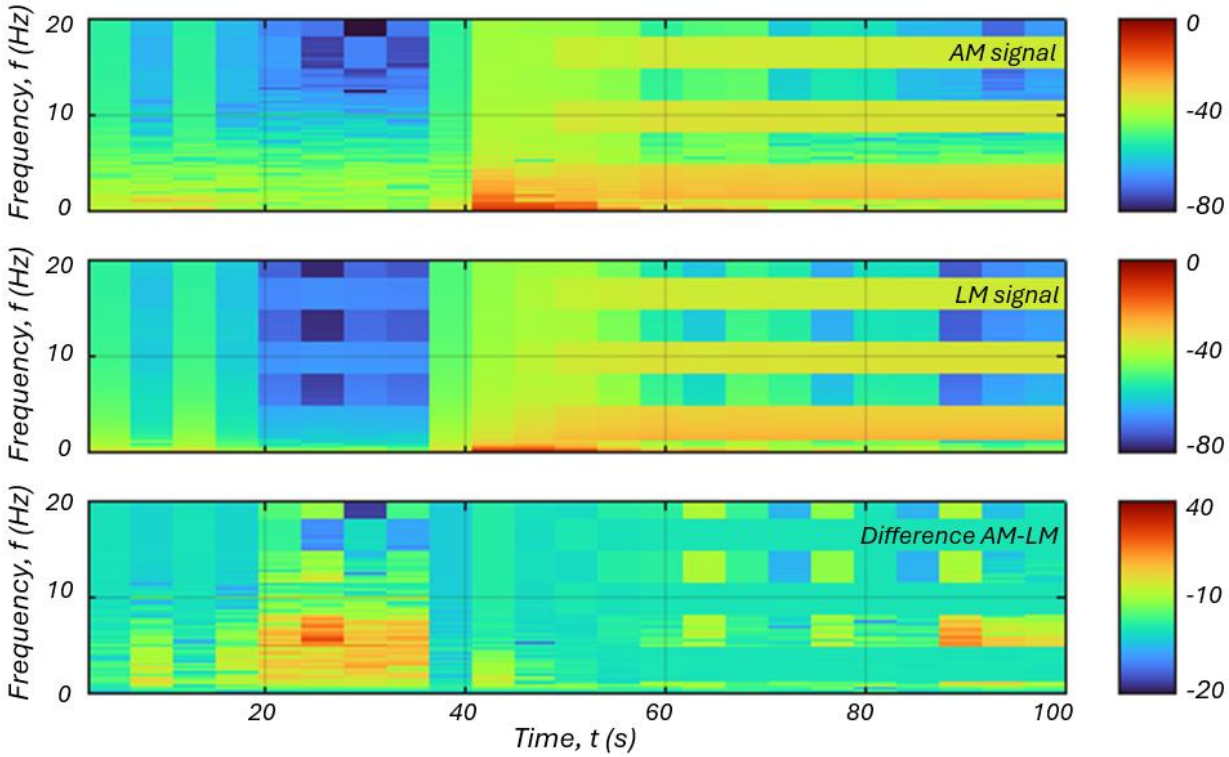


Figure 41. STFT Spectrograms for the strain gauge A1_4 under EQ4 Wall-building specimen.

The vertical arrangement in each panel set follows the convention: the top panel shows the AM signal, the middle panel shows the LM signal, and the bottom panel shows the AM-LM difference. Color intensity encodes spectral amplitude: in the AM and LM panels, warmer colors (yellow-red) indicate higher energy levels, and cooler colors (green-blue) indicate lower energy levels; in the AM-LM difference panels, the color map is centered around zero, with positive deviations in red, negative deviations in blue, and near-zero differences in green, highlighting the spectral contributions not captured by the fundamental mode.

For the wall specimen, the AM spectrogram (top panel) reshows a dominant energy concentration in the fundamental-frequency band (~5-10 Hz), with intermittent bursts at higher frequencies (~15-20 Hz), reflecting both the primary-mode response and minor contributions from higher modes. The LM spectrogram (middle panel) primarily contains fundamental-mode content, with attenuated high-frequency energy. The difference field (bottom panel) highlights residual energy in the 10-20 Hz range, indicating sustained higher-mode activity not accounted for by the fundamental mode

alone. The persistence of positive and negative excursions in the $AM\text{-}LM$ field correlates temporally with post-Lüders strain intervals, suggesting that higher-mode activation aligns with phases of material hardening.

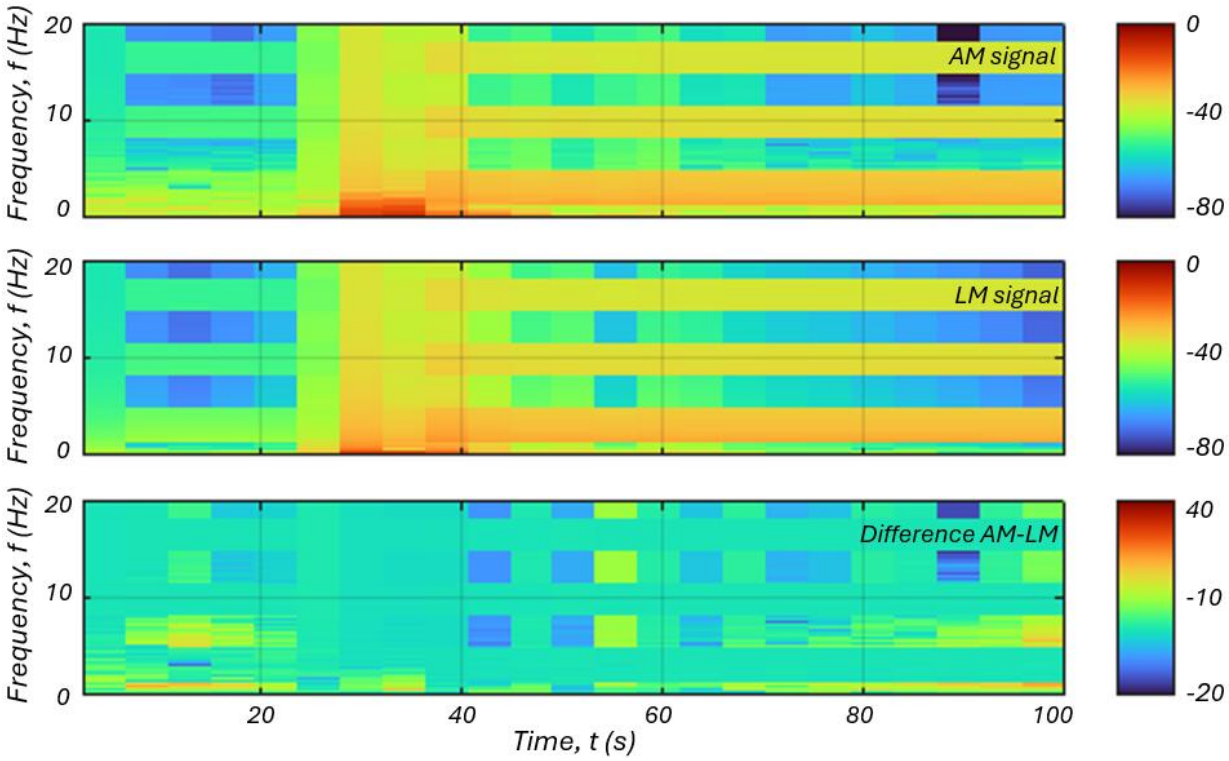


Figure 42. STFT Spectrograms for the strain gauge EN07 under EQ3 Bridge column specimen.

The AM and LM spectrograms for the bridge-column specimen exhibit an almost complete overlap across the entire time-frequency domain. The only meaningful deviation appears as a localized red region, confined to a short time window and centered within the 0-2 Hz band. This isolated high-energy patch reflects spectral content present in the general response (AM) but absent from the fundamental-mode projection (LM). Its narrow extent and limited intensity indicate that higher-mode activity in the column is intermittent and weak rather than sustained.

The absence of broader warm-colored regions in the difference field shows that the column's response remains overwhelmingly dominated by the fundamental mode, with upper modes contributing only marginal corrections during brief intervals associated with localized nonlinear behavior. In contrast, the wall specimen develops persistent, energetically dense higher-mode signatures and shows greater sensitivity to higher-order deformation patterns. Overall, the column specimen exhibits a predominantly first-mode-controlled response with minimal and short-lived second-mode involvement. In contrast, the wall specimen displays a substantially stronger and more coherent activation of higher modes under nonlinear strain-hardening conditions.

In both specimens, the $AM\text{-}LM$ difference fields directly indicate higher-mode involvement. The warm-colored regions in the different panels identify frequencies where the structure exhibits energy not accounted for by the fundamental mode. In contrast, the green regions indicate frequencies dominated by the primary mode with minimal higher-mode influence. These observations confirm that, under post-Lüders nonlinear response, higher-mode contributions are both energetically significant and temporally correlated with specific stages of strain hardening. Notably, the wall specimen exhibits consistently higher residual energy and stronger temporal coherence in the approximately 0-20 Hz band than the column, indicating a more pronounced activation of the second mode. This asymmetry underscores that the strain-rate response is strongly conditioned by each specimen's structural dynamics (specifically its stiffness distribution, geometric configuration, mass layout, and reinforcement detailing), which govern how much nonlinear curvature demand projects onto higher-order modal shapes.

Figure 43 presents the probability density function (PDF) and cumulative distribution function (CDF) of the κ_H-ratio associated with strain-rate intervals recorded in the work-hardening range, for the wall-building specimen.

The PDF displays a single dominant peak within a narrow interval, followed by a rapid decline toward the upper tail, indicating limited dispersion and a strong concentration of κ_H-ratio amplification around the most frequent values. The shape of the curve is consistent with a right-skewed distribution with minimal probability mass beyond $\kappa_H \approx 1.8$, reflecting the restricted variability observed in this specimen.

The CDF shows close agreement between the empirical data and the fitted lognormal model across most of the domain. Both curves rise steeply over the main interval of observed κ_H-ratios, confirming that a large proportion of the data is clustered within a relatively small range. Minor deviations appear only near the upper tail, where scatter increases and the empirical curve departs slightly from the theoretical trend. The combined PDF-CDF behavior demonstrates that the wall-building specimen exhibits a comparatively uniform strain-rate response, with the bulk of κ_H values concentrated near the mode, with limited influence from extreme events.

Figure 44 presents the PDF and CDF of the κ_H-ratio obtained from the strain-rate segments in the work-hardening zone of the bridge column specimen. The PDF reveals a compact distribution: almost all realizations fall within a narrow band centered near $\kappa_H \approx 1.3$, and the density decreases abruptly as κ_H increases. The overall shape shows a pronounced right skew, driven by the concentration of observations in the modal zone and the rapid decline toward the higher κ_H-values, exhibiting minimal probability.

The CDF compares the empirical accumulation of κ_H to the theoretical model. Both curves exhibit a steep ascent across the main interval of occurrence and approach unity within a moderate κ_H-range, confirming that the data are fairly clustered. The central region shows relatively close correspondence between empirical and theoretical behavior, while minor separation becomes visible near the upper tail, where the empirical curve levels off earlier. This combined response indicates that the κ_H-ratio for this specimen is tightly bound, dominated by moderate amplification levels, and only marginally affected by infrequent high κ_H events.

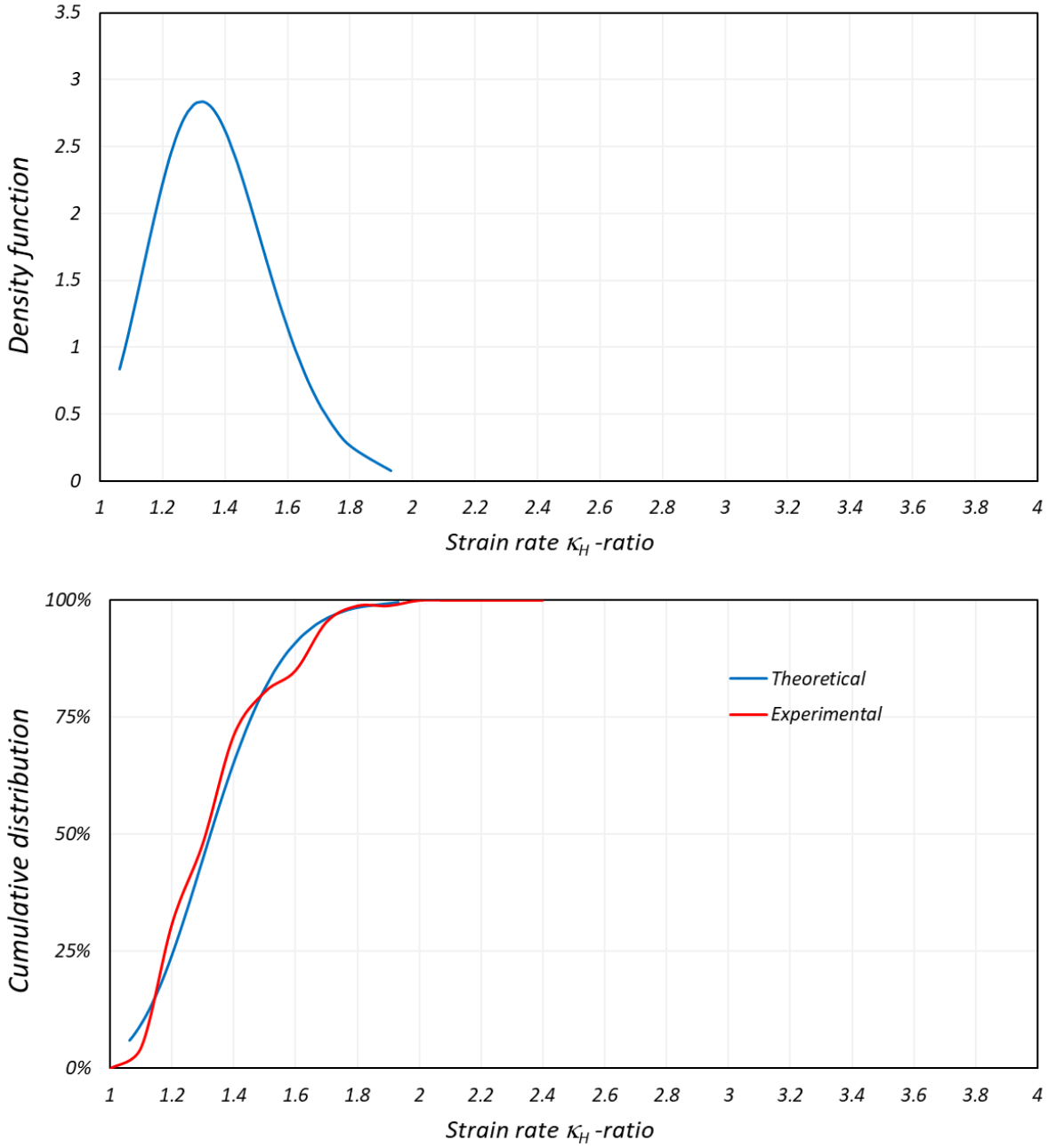


Figure 43. κ_H-ratio PDF and CDF for the wall-building specimen.

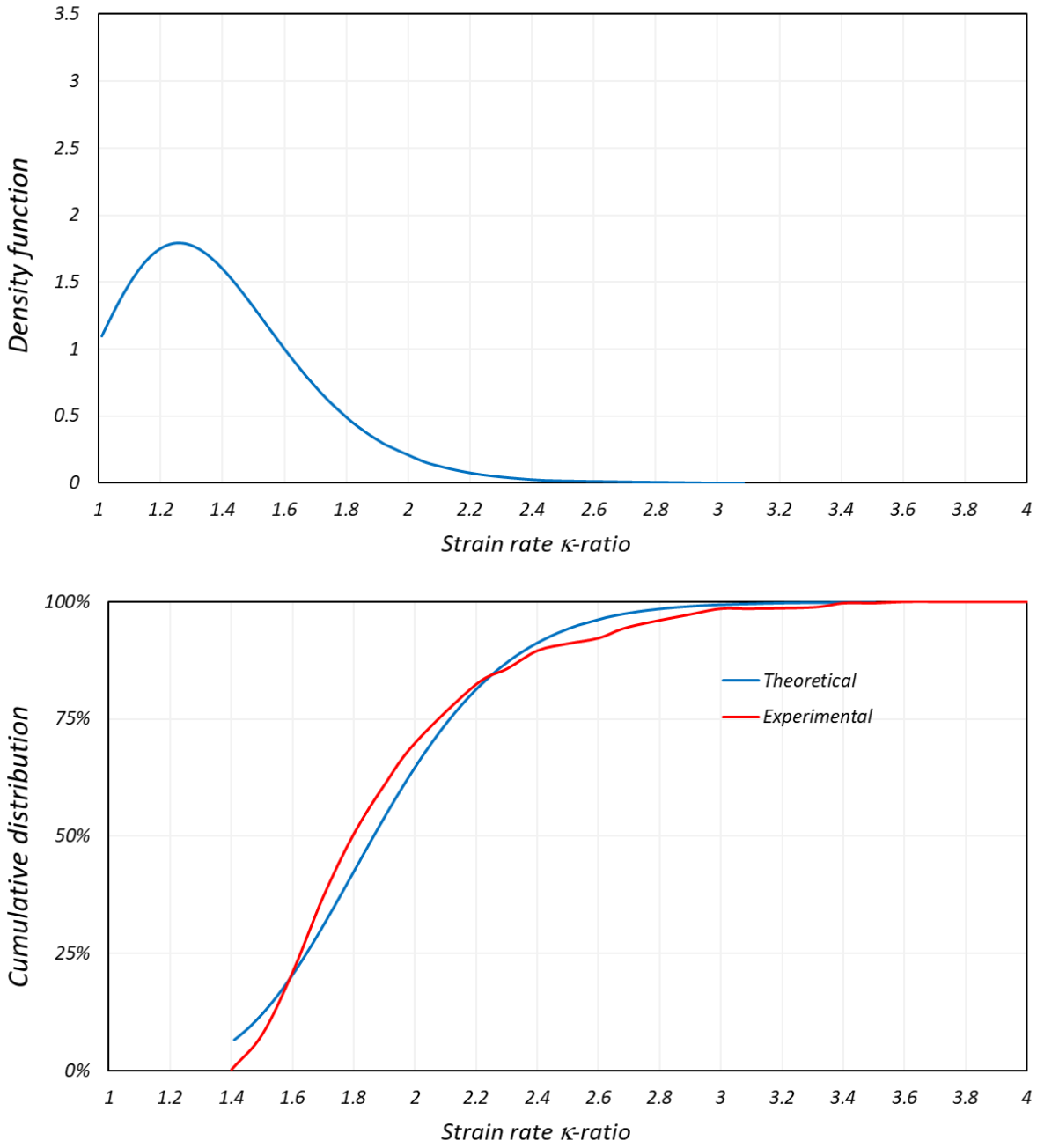


Figure 44. κ_H-ratio PDF and CDF for the bridge column specimen.

Figure 45 presents the cumulative frequency of the κ_H-ratio values derived from the datasets shown in Figures 39 and 40. For the wall-building specimen, the first, second (median), and third quartiles are 1.17, 1.31, and 1.43, respectively, while the corresponding quartiles for the bridge-column specimen are 1.11, 1.18, and 1.33. The similarity of these quartile ranges indicates that the central tendency and dispersion of κ_H-ratio values are broadly comparable between both structural systems. The very high κ_H-ratio exceeding 2 observed in the bridge-column specimen (Figure 40) populate only the extreme upper tail of the cumulative distribution (Figure 45) and may represent outliers introduced by the signal-processing procedure rather than genuine physical response.

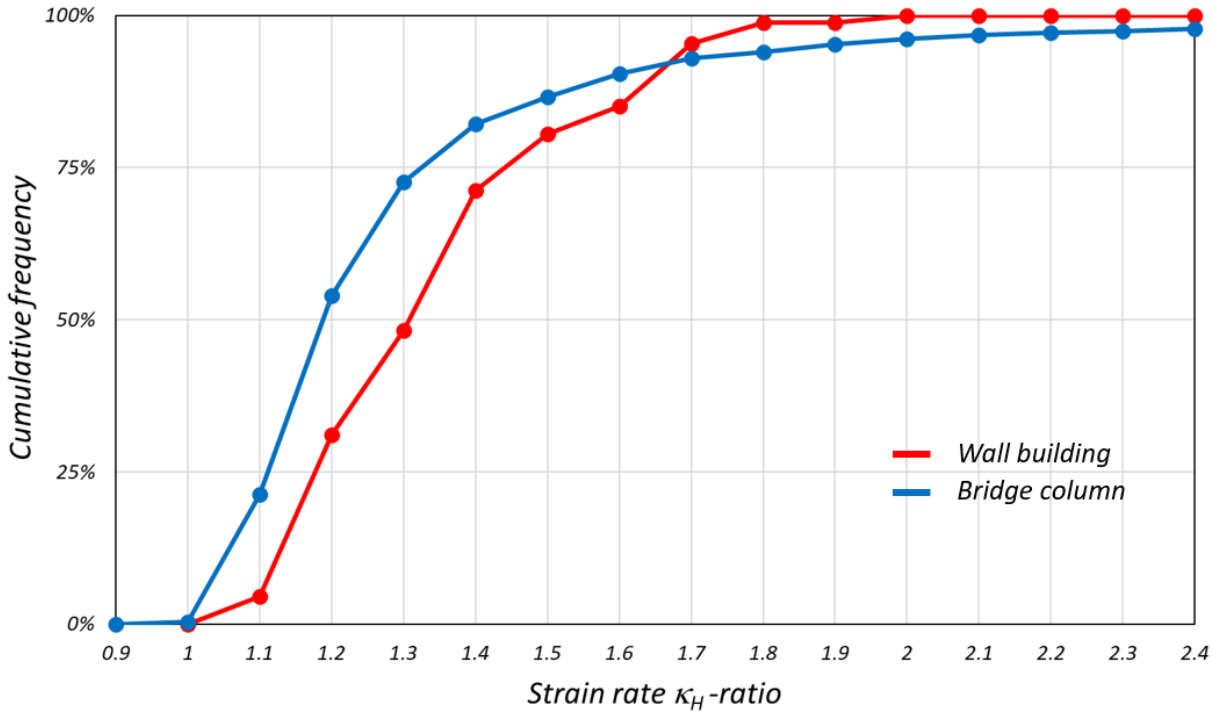


Figure 45. Cumulative frequency of the κ_H-ratio for both specimens.

The statistical characteristics of κ_H-ratio in the work-hardening regime are summarized in Table 15 for both specimens, reporting the first, second, and third quartiles. When the data are fitted to a lognormal model, the κ_H-ratios exhibit a characteristic mean-standard-deviation pair of (0.28, 0.14) and (0.23, 0.22).

Table 15. κ_H-ratio statistics in the work-hardening regime.

	Wall-building	**Bridge column**
1st quartile	1.17	1.11
2nd quartile	1.31	1.18
3rd quartile	1.43	1.33
Log. mean	0.28	0.23
Log. deviation	0.14	0.22

3.9.1.3 Ratio of peak to average strain rate: κ-ratio

Strain-rate fluctuations were quantified using the peak-to-average strain-rate ratio, referred to as the strain-rate κ-ratio, (simply κ-ratio), computed over each selected interval of the strain-rate time-history signals. Figures 46 and 47 show the κ-ratio plotted against the period ratio T_e/T_{o1} for the wall-building and bridge-column specimens, respectively.

The color and size indicate the strain intensity level. Larger and darker markers correspond to intervals with higher local strain intensity, while smaller and lighter markers indicate lower local strain intensity. The dominant cloud of black and gray points, corresponding to strain intervals outside the Lüders plateau, and the subset of points enclosed by the blue ring represent the intervals associated with Lüders-band behavior.

In Figure 46, the scatter plot reveals two clearly differentiated behaviors. The points belonging to the Lüders plateau form a compact cluster that occupies a relatively narrow range of κ-values. Their marker intensities (visible through color saturation and point size) are mostly moderate, indicating that these intervals are associated with limited strain-rate amplification during Lüders band propagation. Outside this region, the work-hardening points dominate the right-hand portion of the plot. They appear in significantly greater numbers and exhibit a broader range of intensities, including some high-amplitude events. The vertical scatter also increases markedly beyond the blue ring, indicating that thet κ-ratio becomes more variable after the bar exits the Lüders plateau and enters a curvature-driven hardening regime. Although κ shows only a weak dependence on T_e/T_{o1}, the distribution of points confirms that strain-rate amplification in this specimen is governed primarily by localized transient mechanisms, with the work-hardening phases exhibiting greater variability and a wider intensity range than the compact, low-amplitude Lüders intervals.

Figure 47 displays the same structural partition but with substantially greater dispersion.

The Lüders intervals lie in a narrow band of κ-values , at levels visibly higher than those observed for the work-hardening ones, forming a compact cloud with very limited horizontal spread. The work-hardening intervals produce a much wider, more dispersed cloud that extends across the right-hand portion of the figure. The points populate a broader domain of κ-values, although the marker intensities remain in the low-to-moderate range. This pattern indicates that once the bar exits the Lüders plateau, the κ-ratio becomes sensitive to local fluctuations induced by curvature development, cyclic hardening, and transient strain-rate variations. The absence of strong-amplitude markers and the predominance of moderate intensities suggest that, although the response becomes more variable, the underlying strain-rate amplification remains bounded.

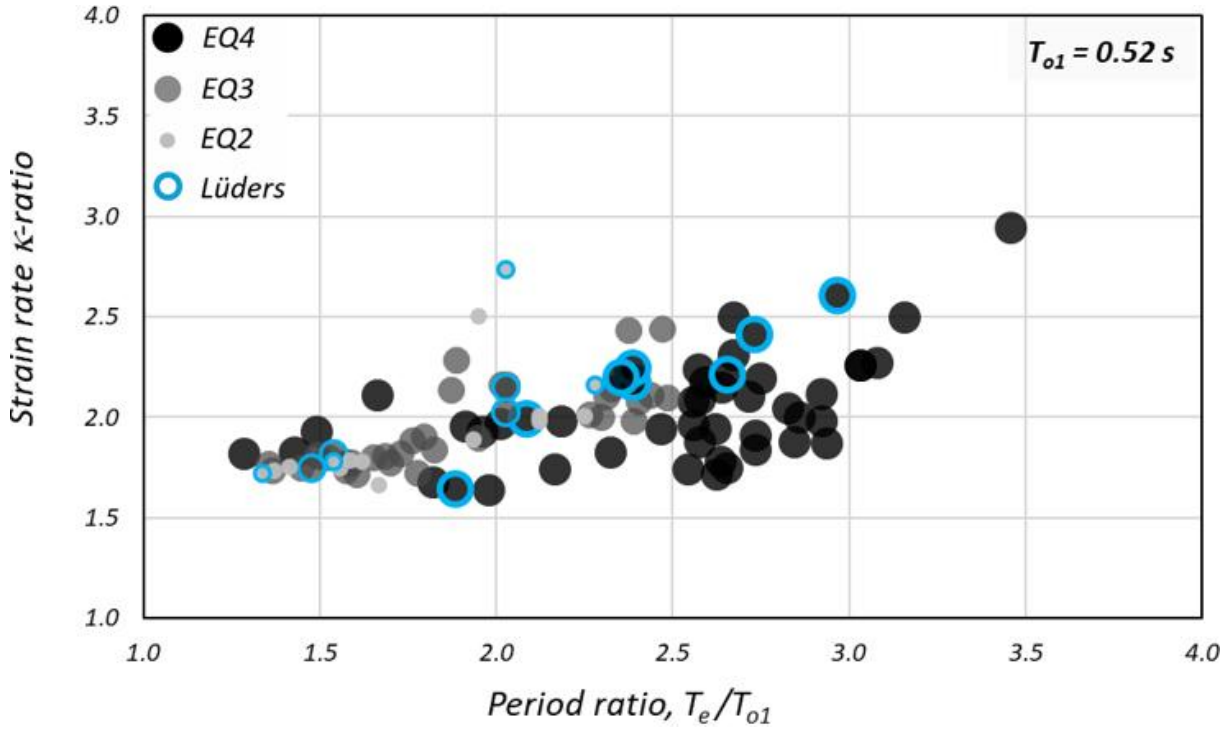


Figure 46. κ-ratio variation versus effective-to-initial first mode period ratio for the wall-building specimen.

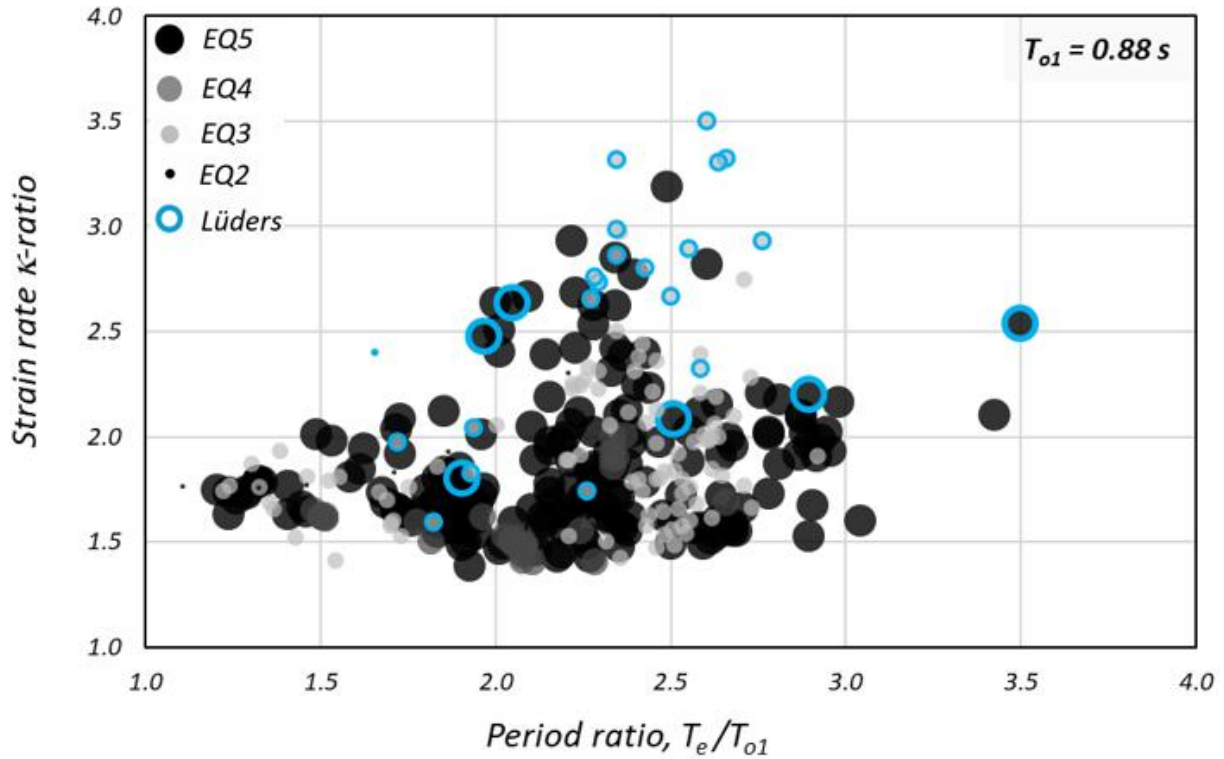


Figure 47. κ_H-ratio variation versus effective-to-initial first mode period for the bridge column specimen.

The statistical characteristics of κ-ratio in each deformation regime are summarized in Table 16 for both specimens. Each table reports the first, second, and third quartiles. Additionally, when fitted to a lognormal model, the κ-ratios associated with all data exhibit mean-standard-deviation pairs of (0.67, 0.11) and (0.60, 0.16) for the two specimens, respectively.

Table 16. κ-ratio statistics in the work-hardening and Lüders regimes.

	Wall-building		**Bridge column**	
	Lüders	**Work-hardening**	**Lüders**	**Work-hardening**
1st quartile	1.79	1.78	2.26	1.62
2nd quartile	2.16	1.93	2.73	1.77
3rd quartile	2.23	2.10	2.96	2.01
Log. mean	0.73	0.67	0.95	0.60
Log. deviation	0.15	0.11	0.22	0.16

Figure 48 presents the PDF and CDF of the κ-ratio for the wall-building specimen, constructed from the full dataset, including strain-rate intervals from both the Lüders plateau and the work-hardening region. The resulting distribution exhibits a relatively concentrated peak and a faster decay in the upper tail, consistent with the narrower dispersion observed in this specimen. The cumulative curve closely follows the fitted lognormal model across most of the domain, deviating only near the upper tail, where scatter becomes more noticeable. These characteristics reflect a more uniform strain-rate response once the bar enters the hardening regime, even when including Lüders-related intervals.

Figure 49 shows the probability density and cumulative distribution functions of the κ-ratio for the bridge-column specimen, also obtained from the complete dataset encompassing both Lüders-plateau and work-hardening intervals. In this case, the distribution displays a flatter peak and a longer, more dispersed upper tail, indicating greater variability in the strain-rate amplification. The cumulative curve departs from the lognormal fit earlier and more visibly than in the wall specimen, particularly in the high-κ range, reflecting the broader scatter associated with the column's more heterogeneous curvature demand and transient axial-flexural interactions.

Figure 50 presents the cumulative frequency distributions of κ-ratio for both specimens. Solid curves correspond to strain intervals within the work-hardening region, while dashed curves isolate intervals belonging to the Lüders plateau. For the work-hardening data, the first, second, and third quartiles of κ-ratio are 1.78, 1.93, and 2.10 for the wall specimen, and 1.62, 1.77, and 2.01 for the bridge-column specimen. These distributions are similar despite differences in structural configuration, boundary conditions, and input motion characteristics.

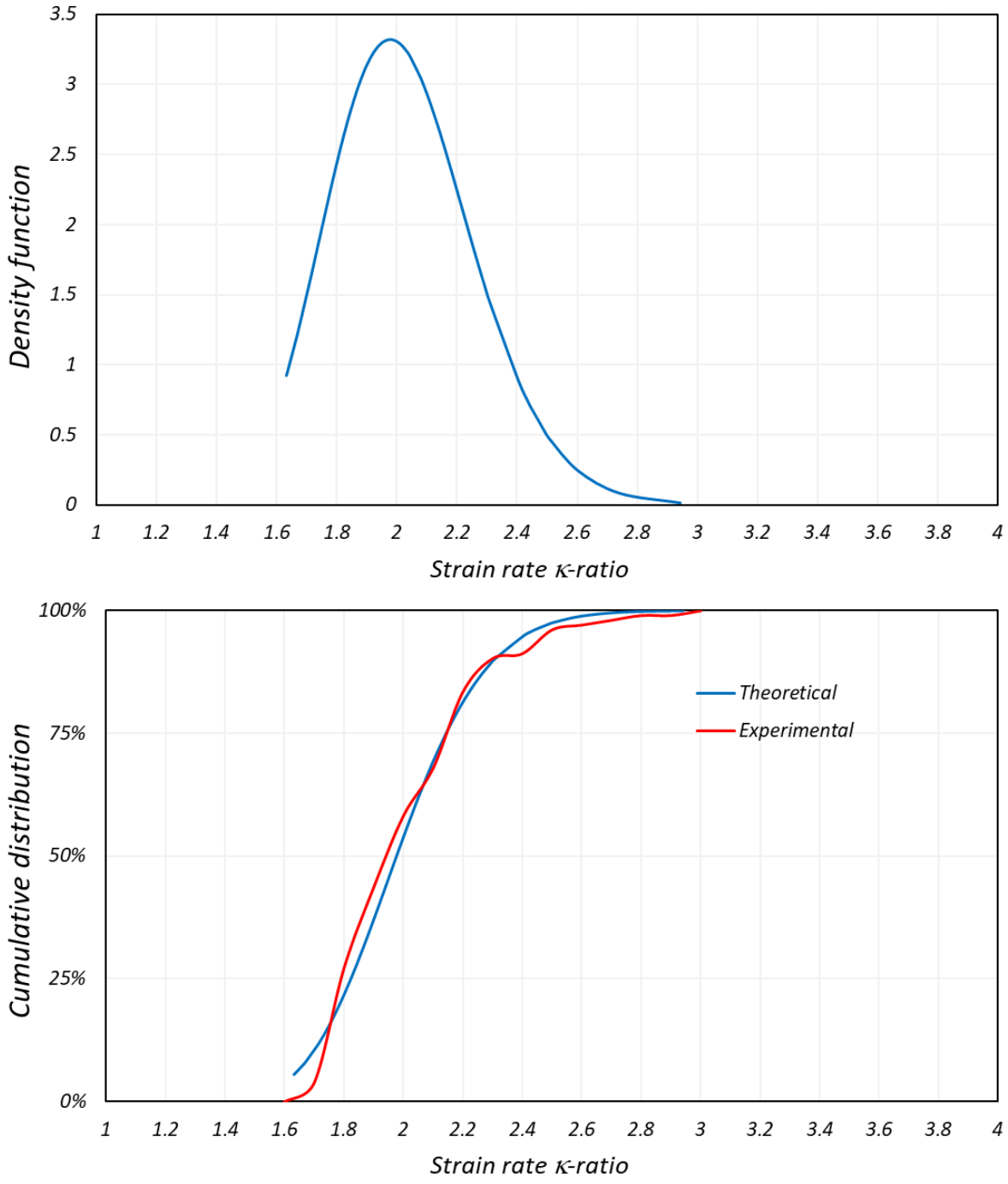


Figure 48. κ-ratio PDF and CDF for wall-building specimen.

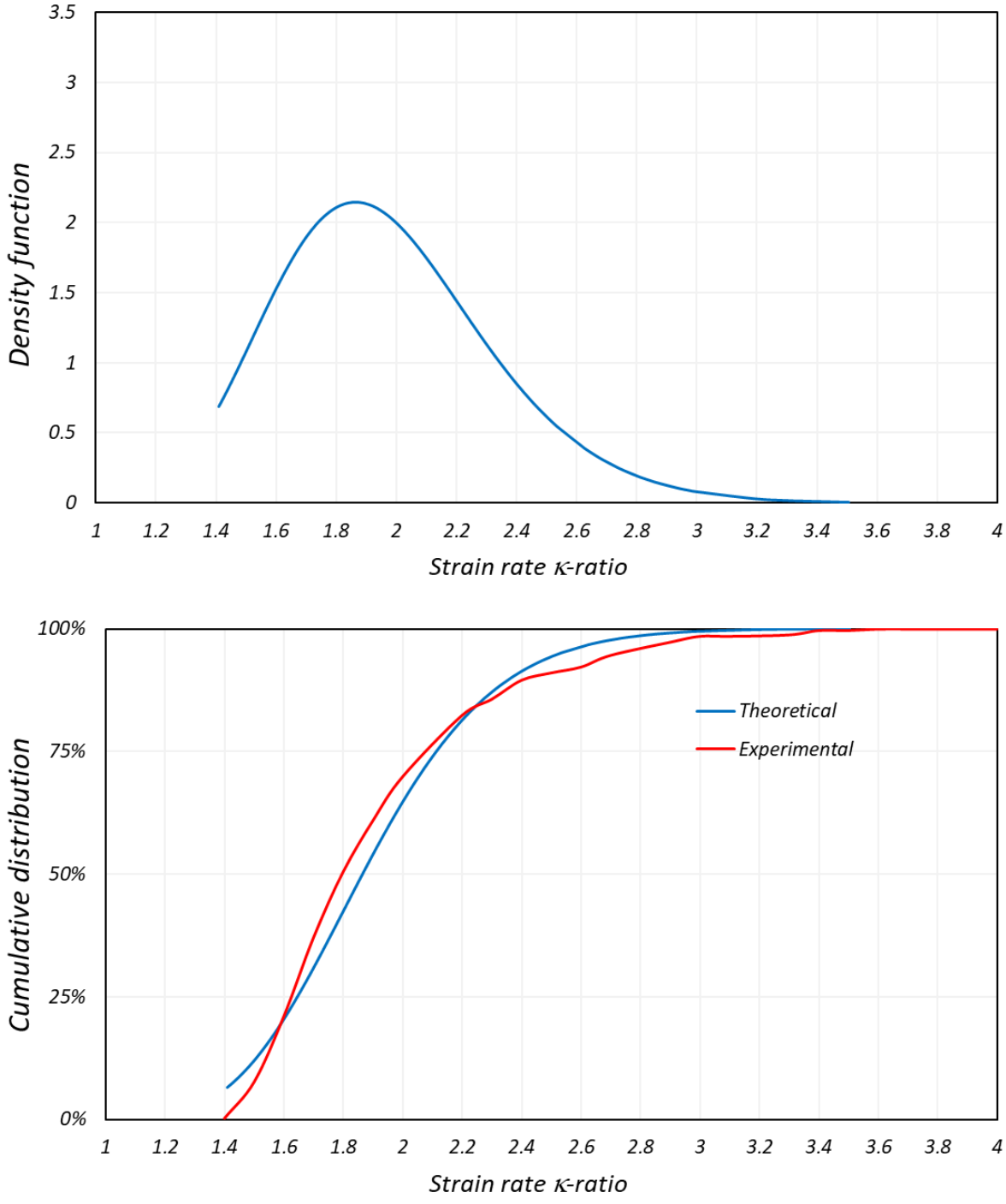


Figure 49. κ-ratio PDF and CDF for bridge column specimen.

In contrast, the κ-ratio distributions computed from Lüders-plateau intervals differ markedly between specimens. For the wall-building specimen, the first, median, and third quartiles are 1.79, 2.16, and 2.23. For the bridge-column specimen, the corresponding values increase substantially to 2.26, 2.73, and 2.96.

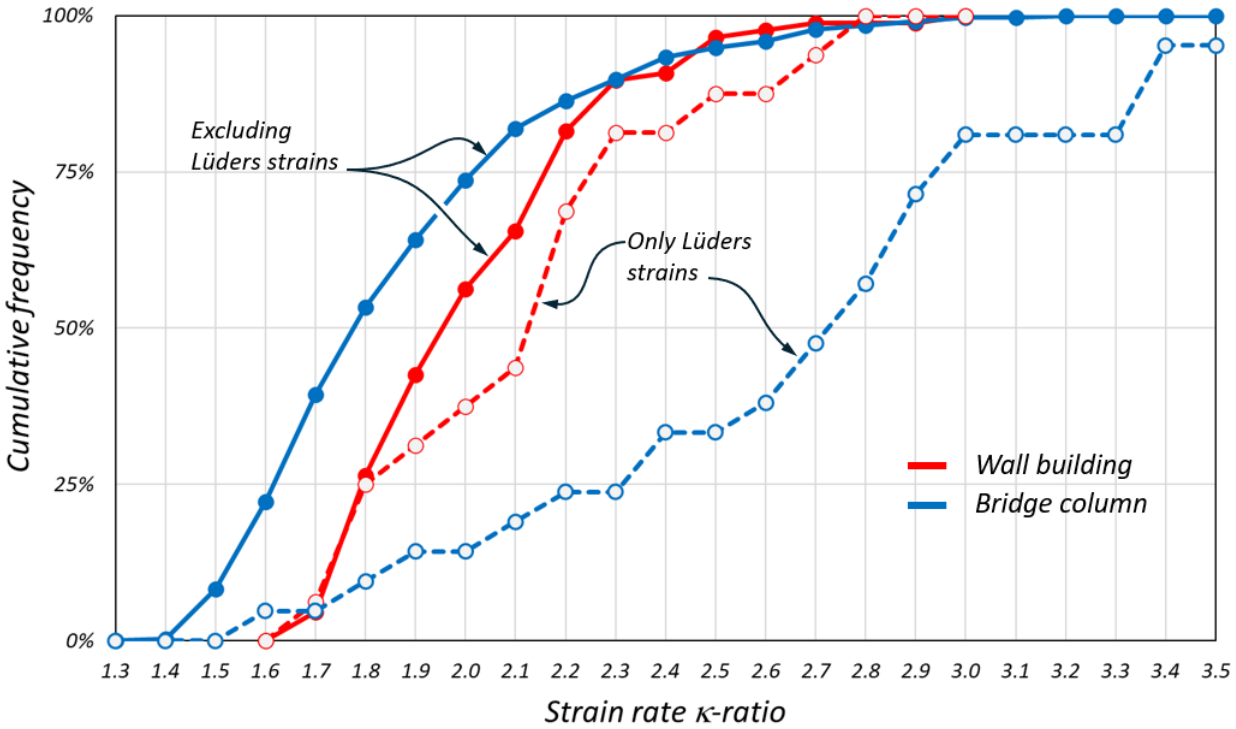


Figure 50. Cumulative frequency of the strain rate κ-ratio for both specimens.

Together, Figures 46 and 47 show that while Lüders-band intervals consistently form a compact, easily identifiable cluster with higher intensities, the work-hardening data dominate the overall strain-rate response and exhibit far greater variability in both specimens. The bridge column displays a broader and more intense pattern of strain-rate amplification than the wall, reflecting its more complex and heterogeneous local deformation mechanisms. Building on these observations, the consistency between the two specimens, despite their markedly different dispersions, suggests that the κ-ratio stabilizes within a narrow band once Lüders-related effects are excluded and strain-rate amplification governs the response in the work-hardening regime. In fact, although the median values for the wall and bridge column specimens (1.93 and 1.77, respectively) reflect distinct strain-rate environments, their combined distribution exhibits a well-defined central tendency around κ-ratio $\approx$1.85.

This convergence is not incidental: it indicates that, beyond the specimen-specific variability associated with confinement, curvature demand, and transient axial-flexural coupling, the underlying amplification mechanisms responsible for κ-ratio remain bounded within a consistent range. The lognormal characterization reinforces this interpretation by showing that the probability density concentrates near this value, even when dispersion differs across tests.

For these reasons, κ-ratio=1.85 is adopted as the representative value, as it captures the central tendency across specimens while remaining consistent with the physics of strain-rate modulation in the post-Lüders regime. Its selection, therefore, reflects not only statistical robustness but also mechanical plausibility, ensuring that subsequent modeling steps remain both conservative and experimentally grounded.

3.9.1.4 Effect of Waveform: κ_W-ratio

A detailed examination of the amplification process clarifies the origin and structure of the representative value κ-ratio ≈1.85. This value is obtained by averaging the k-ratios computed for both specimens exclusively in the uniform hardening range, after the Lüders band has fully dissipated. Once the dataset is restricted to strains beyond the Lüders strain, where plastic flow is spatially homogeneous, the measurements from both tests converge to a consistent amplification level, and their mean defines κ-ratio.

This averaged value reflects the combined effect of three sequential mechanisms. The first is associated with Lüders propagation. The Lüders-related ratio κ_L-ratio is not calibrated within this framework. Dislocation-level processes drive the onset, speed, and fading of Lüders-band propagation, which continuum plasticity models cannot reproduce. These mechanisms require crystal-plasticity simulations that explicitly resolve slip-system activation and the evolution of dislocation structures. Because such physics is outside the scope of the present modeling strategy, the dependence of κ_L on strain rate or specimen geometry is not quantified here. Once the material enters the work-hardening regime, where the Lüders front has disappeared and deformation becomes spatially uniform, the contribution associated with Lüders propagation is taken to be κ_L=1.

The second amplification mechanism, attributed to higher-mode participation, develops once the material leaves the Lüders regime and deformation becomes spatially uniform. At this stage, the response no longer behaves as a single-mode system. The rapid increase in tangent stiffness that accompanies the onset of work hardening alters the local wave speed, redistributing strain-rate demand along the bar. This redistribution activates longitudinal modes admissible in the bar geometry but suppressed during Lüders propagation, constraining the velocity field to a nearly uniform pattern.

After the front disappears, these secondary modes introduce small but measurable oscillatory components in the strain-rate records. Their amplitudes are limited by specimen geometry, boundary conditions, and the rate at which the tangent modulus evolves. Yet, they are sufficient to increase the ratio between peak and mean strain rate. This increase is what κ_H-ratio quantifies: the portion of the amplification governed by the modal structure of the deformation field. The observed value κ_H ≈1.25 is consistent with this interpretation. It corresponds to the amplification level expected when the strain-rate histories include contributions from the lowest higher longitudinal modes, whose participation remains moderate because the system never approaches resonant conditions. Its magnitude matches the experimentally measured bandwidth and amplitude envelope, indicating that higher-mode activation is systematic but bounded and contributes a stable fraction of the overall κ-ratio.

These contributions capture the geometric and kinematic features of the structural response but are largely insensitive to the temporal fine-structure of the ground motion. The remaining portion of κ-ratio originates from the temporal shape of the stress waveform itself. After isolating the Lüders propagation and the higher-mode component, the ratio κ_W-ratio is computed as:

$$\kappa_W = \frac{\kappa}{k_L . k_H} = \frac{1.85}{(1)(1.25)} = 1.48 \approx 1.50$$

Once this component is factored out, the remaining amplification, κ_W, reflects the influence of waveform sharpness: the clustering of velocity pulses and the asymmetry of strain-rate cycles.

The resulting value of $\kappa_W \approx 1.5$ closely matches the theoretical limit of $\pi/2$ expected for a pure harmonic signal, indicating that the experimentally observed waveform-driven amplification is consistent with established analytical predictions. This agreement reinforces the physical validity of adopting κ-ratio=1.85 as the representative amplification factor for modeling strain-rate effects under non-Lüders, work-hardening conditions.

3.10 Conclusions

This study systematically quantified the strain rates experienced by longitudinal reinforcement during the nonlinear inelastic response of RC elements subjected to dynamic earthquake excitations. Strain time histories were recorded from gauges embedded in plastic hinge regions of two full-scale specimens tested on the Large High-Performance Outdoor Shake Table at UC San Diego, providing direct measurements of realistic seismic behavior.

Average strain rates can be obtained from recorded time histories; however, they consistently underestimate peak values, which are statistically characterized here as the 95th percentile across the tests. This underestimation arises from the combined influence of "higher" vibration modes and the waveform characteristics of the seismic input, which amplify localized strain responses. Analytical evaluation shows that dynamic effects, including displacement-wave propagation along the reinforcement and the rapid formation and motion of Lüders bands, drive peak rates above average values.

Within the Lüders plateau, characterized by localized plastic deformation bands, peak strain rates reached approximately 22%/s in the wall-building specimen and 44%/s in the bridge column specimen. These elevated rates reflect the intrinsic propagation speed of Lüders bands, which is absent in the steel's work-hardening regime. For strains in the work-hardening domain, peak strain rates were estimated by multiplying the average rate by an empirically derived factor of 1.85, attributed to "higher" mode contributions (≈1.25) and waveform shape effects (≈1.50). Purely harmonic excitation without higher mode effects produces a theoretical peak-to-average ratio of approximately 1.57, consistent with experimental observations.

Variations in coupon size, documented in complementary studies, can influence measured peak strain rates; these effects are negligible when evaluating full-scale RC response under seismic loading, where dislocation dynamics controlling Lüders band propagation dominate. The rate-dependent behavior of reinforcing steel also implies potential reductions in empirical viscous

damping ratios commonly applied in nonlinear analyses. Incorporating strain rate sensitivity, therefore, requires development and calibration of rate-dependent constitutive models, supported by extensive reversed cyclic testing of reinforcement coupons over a wide range of strain rates.

These results enable more accurate prediction of RC seismic performance, quantify strain rate amplification in plastic hinge regions, and inform the calibration of nonlinear models that account for dynamic reinforcement behavior, ultimately supporting resilient and safe structural design under earthquake excitations.

4 Rate-Dependent Hysteretic Model for Reinforcing Steel with Bond-Slip-Induced Pinching

Chapter 3 concluded that reinforcing steel embedded in RC members subjected to seismic loading can experience highly localized, transient strain rates that significantly exceed those typically assumed in quasi-static analyses. These elevated strain rates developed primarily within plastic hinge regions, driven by localized inelastic deformation and dynamic redistribution of internal forces, with potential contributions from higher vibration modes. While the previous chapter quantified the magnitude and spatial distribution of these strain rates, the mechanical implications for the reinforcing steel stress response remained unresolved. In particular, the extent to which such rate effects modify the cyclic hardening behavior of reinforcement represents a critical gap between experimentally observed kinematics and the constitutive assumptions commonly adopted in nonlinear structural analyses. This chapter addresses that gap by explicitly linking strain-rate effects to stress increments in reinforcing steel and formalizing this relationship within a rate-dependent cyclic constitutive model.

Under seismic excitation, reinforcing steel bars experience loading histories characterized by rapid strain reversals, highly nonuniform deformation rates, and repeated excursions into the inelastic regime. Despite this, many experimental interpretations and constitutive formulations for reinforcing steel continue to rely on quasi-static assumptions, implicitly neglecting the influence of strain rate on the local stress response. Moreover, even among the relatively few models developed specifically for cyclic loading, strain-rate effects are typically not explicitly incorporated, particularly in describing hardening behavior.

From a physical standpoint, this limitation matters because the mechanical response of metallic materials depends not only on accumulated plastic deformation but also on the temporal characteristics of the imposed kinematics. Variations in deformation rate directly influence dislocation mobility, viscous resistance, and dynamic recovery processes, thereby affecting stress evolution during cyclic loading. While these effects may remain secondary under slowly varying or monotonic loading, they become more pronounced under cyclic loading with frequent strain reversals and transient rate fluctuations. In these regimes, the interactions among strain rate, deformation history, and stress evolution cannot be adequately represented by purely quasi-static descriptions, particularly in the work-hardening range, where the incremental stress response governs hysteretic behavior.

Motivated by these considerations, this chapter begins by establishing experimental evidence of strain rate sensitivity through direct examination of stress increment-strain rate relationships obtained from cyclic tests on reinforcing steel. Rather than relying on global stress-strain curves or averaged rate measures, the analysis focuses on transient stress increments associated with instantaneous strain-rate variations. These relationships are presented as stress increments versus strain-rate increments, providing a direct, physically interpretable measure of rate sensitivity during cyclic loading. To contextualize the results, the experimentally derived trends are systematically compared with pseudo-static cyclic test data reported in the literature, highlighting the extent to which conventional testing protocols may misrepresent stress amplification effects associated with rapidly varying deformation rates, particularly those reported by Malvar [80]. This selection is

deliberate: while numerous studies have addressed strain rate effects in reinforcing steel (Chapter 2), Malvar's investigation provides the only systematically tabulated cyclic database with explicit strain rate decomposition across the range from 10^{-4} s^{-1} to 10^{-1} s^{-1}, encompassing the transition from pseudo-static to dynamic response regimes.

Building on this experimental characterization, the chapter then formulates a rate-dependent cyclic constitutive model for reinforcing steel. The model is intrinsically cyclic by construction and extends classical kinematic hardening formulations by including an explicit Voigt-type viscous contribution, with the incremental stress response depending on the instantaneous strain rate. Rate sensitivity parameters are calibrated directly from experimentally derived stress increment-strain rate relationships obtained under reversed cyclic loading. Particular emphasis is placed on reproducing essential cyclic features, including tension-compression asymmetry, unloading-reloading transitions, and the progressive evolution of rate sensitivity (manifested through increasing stress increments for a given strain rate) with increasing cumulative plastic deformation, as observed in the work-hardening regime. The resulting formulation is both physically grounded and directly implementable in nonlinear numerical simulations of RC members subjected to seismic loading.

The experimental program underpinning the proposed framework relies on cyclic tests conducted on reinforcing bars with a nominal yield strength of grade 60 [7], [8], consistent with the steel grades used in structural applications. Specimens are subjected to fully reversed axial strain histories under strain-controlled conditions, with progressively increasing strain amplitudes that extend into the strain-hardening regime. Two distinct strain-rate levels are considered: 0.001 s^{-1} (low rate) and 0.02 s^{-1} (high rate), imposed through controlled strain histories. This range captures the influence of strain rate on the stress response in the strain-hardening regime under cyclic loading. High-resolution instrumentation and data-acquisition systems capture localized strain histories and corresponding stress responses with sufficient temporal resolution to resolve transient strain-rate effects. The experimental configuration, loading protocols, and measurement procedures are defined to ensure reproducibility and to provide a consistent basis for constitutive calibration.

This chapter presents the experimental characterization of the reinforcing steel and the development of the SteelDRCV constitutive model. Section 4.1 describes the testing procedure, including the reinforcing steel configuration, mechanical properties, chemical composition, and cyclic strain-loading protocols. Section 4.2 documents the experimental cyclic stress-strain response. Section 4.3 presents the experimental evidence of strain-rate sensitivity under cyclic loading, and Section 4.4 characterizes these effects using a time-window-based approach, distinguishing between the tension branch, compression branch, and undulation-resolved stress increments versus strain-rate excursions. Section 4.5 discusses the implications for constitutive modeling. Section 4.6 describes the baseline rate-independent model (SteelDRC), covering the unloading branch, strain-hardening branch, closed-form Bauschinger curve, implementation of tangent/secant/initial moduli, and its calibration and verification. Section 4.7 develops the strain-rate-dependent extension (SteelDRCV). Section 4.8 develops the quadrant-dependent bond-slip (pinching) mechanism, defining the β-factor evolution interval, λ-governed evolution, truncated evolution due to reversal, the resulting cyclic response with pinching, and structural-level strain histories. Section 4.9 presents the conclusions.

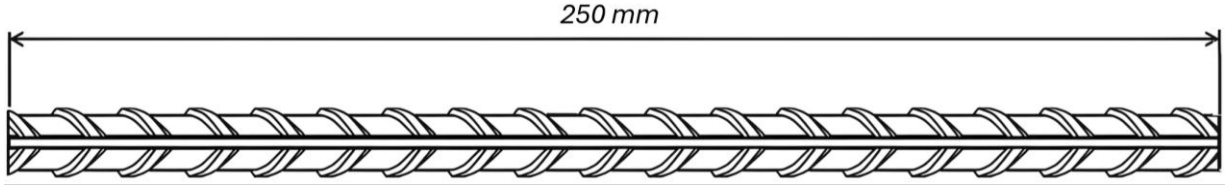
4.1 Testing Procedure

4.1.1 Reinforcing Steel Configuration

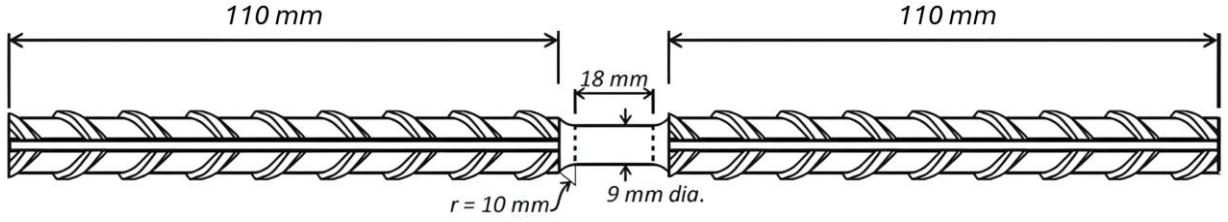
Reinforcing bar specimens representative of Grade 60 steel were selected to ensure consistency with the structural applications considered in this study. From 4.6 m-long straight #4 bars obtained from three steel mills (A, B, and C), 250 mm-long coupons were extracted and systematically grouped according to manufacturer and ASTM specification [7], [8], resulting in six distinct groups (A615-A, A615-B, A615-C, A706-A, A706-B, and A706-C) [30], each comprising six specimens, each prescribed strain-rate level (0.001 s^{-1} and 0.02 s^{-1}), ensuring direct comparison between rates while maintaining replication within each condition.

To ensure uniform stress distribution and localize deformation within a predefined region, the central portion of the coupons was machined to a constant diameter, resulting in a length-to-diameter ratio of 2. This configuration minimizes geometric nonlinearities and ensures that the measured response is governed by material behavior. Figure 51 illustrates the geometry of both unmachined and machined coupons. For the machined specimens, the reduced section and transition regions are explicitly defined, with the constant-diameter section, whose length is twice the reduced diameter, establishing the region of uniform stress and localized deformation.

To establish the baseline mechanical properties of the six rebar sets, three supplementary coupons from each group were tested under monotonic tension to failure, including two specimens in the as-received condition and one machined according to the geometry shown in Figure 51.



a) Unmachined coupons



b) Machined coupons

Figure 51. Geometry and dimensional configuration of reinforcing steel test coupons [30].

All machined coupons used for cyclic testing were instrumented with two opposed 5-mm high-yield electrical resistance strain gauges installed within the reduced section (Figure 52). This configuration measures average longitudinal strain over the gauge length and helps detect instability phenomena such as bar buckling. For monotonic tensile tests, a high-precision extensometer measured strain to accurately characterize the stress-strain response up to failure. All tests were conducted using a 500-kN MTS universal testing machine (MTS Systems, Eden Prairie,

Minnesota), Load Unit Model 318.50, at the Charles Lee Powell Structural Research Laboratories at the University of California, San Diego.



Figure 52. Application of strain gauges to machined coupons [30].

4.1.2 Mechanical Properties

Table 17 presents the mechanical properties of unmachined coupon segments extracted from the as-received reinforcing bars, serving as a pre-machining verification protocol to ensure conformance with mill certification data before specimen preparation. The 250 mm segments were tested in their original condition, maintaining the full nominal cross-sectional area of #4 bars (12.7 mm diameter), thereby providing a baseline assessment of material homogeneity and compliance with ASTM A615 and A706 specifications ([7] and [8], respectively) without the geometric stress concentrations introduced by reduced-section machining [30].

The comparison between mill certificate values and in-house tensile test results reveals systematic negative deviations across all coupon groups, with yield strength exhibiting greater disparity than tensile strength.

Table 17. Baseline mechanical properties of unmachined reinforcing bar segments for pre-machining verification (ASTM A615/A706 compliance) [30].

	Mill certificate		**In-house test (unmachined)**		**Comparison** $(f_{mill} - f_{in-house})/f_{mill}$	
Coupon	**Yield strength (MPa)**	**Tensile strength (MPa)**	**Yield strength (MPa)**	**Tensile strength (MPa)**	**Yield strength (%)**	**Tensile strength (%)**
A615-A	474	741	445	720	6.12	2.83
A706-A	492	687	440	660	10.6	3.93
A615-B	503	731	487	725	3.18	0.82
A706-B	453	631	438	626	3.31	0.79
A615-C	608	707	525	638	13.7	9.76
A706-C	492	641	414	576	15.9	10.1

A statistical parametric procedure is conducted using the paired-samples t-test [128], intended to evaluate the significance of the mean difference between mill certificate and in-house test results. The following considerations justify the adoption of this method: (1) the observations correspond to the same specimens evaluated under two distinct measurement conditions; (2) the distribution of the paired differences is approximately normal, thereby satisfying the principal assumption underlying the test; and (3) the objective of the analysis is to identify systematic bias between the two measurement conditions, rather than to assess variability between independent groups.

For both yield strength and tensile strength, the statistical hypotheses are defined such that the null hypothesis ($\mu_d = 0$), assuming no systematic difference between the mill certificate values and the in-house experimental measurements; whereas the alternative hypothesis ($\mu_d \neq 0$) indicates the presence of a systematic difference between the two datasets. The significance level α=0.05 for bilateral hypothesis testing. The paired-samples t-test for yield strength produced a test statistic of 3.68 and an associated p-value of 0.014, which falls below the predetermined significance threshold. Consequently, the null hypothesis is rejected, confirming statistically significant differences between certified and experimentally determined yield strength values. For this property, the mean overestimation is 45.5 MPa, a relative difference of 9.2% relative to the experimental mean. Similarly, the analysis of tensile strength led to a test statistic of 2.78 with a p-value of 0.038, which likewise satisfies the criterion for statistical significance at the 95% confidence level. The null hypothesis is therefore rejected for tensile strength, indicating significant differences between mill certificate values and in-house test results. The mean overestimation of 32.2 MPa corresponds to a 4.9% relative difference.

The bias direction is consistent across both mechanical properties: mill certificates report higher strength values than independent testing. This systematic deviation has important implications for structural engineering practice, as design calculations based on certified properties may incorporate non-conservative assumptions regarding material behavior. The large effect sizes were quantified using Cohen's d [36], calculated as the mean difference divided by the standard deviation of differences. The obtained values of d=1.50 for yield strength and d=1.14 for tensile strength exceed the conventional threshold of 0.80 for large effects, indicating that these discrepancies are not only statistically significant but also practically meaningful. The magnitude of the observed deviation exceeds typical material safety factors in structural design codes, suggesting a potential compromise of safety margins if uncorrected certificate values are employed.

This discrepancy is primarily attributed to differences in testing strain rates. Mill certification tests are commonly conducted at relatively high loading rates, which increase the apparent strength of steel due to strain-rate sensitivity. In contrast, the in-house tests were performed at lower strain rates, resulting in lower measured strengths. This variation is consistent with the expected rate-dependent behavior of reinforcing steel and reflects differences in testing protocols rather than material inconsistency.

The mechanical characterization of the reinforcing steel was conducted in two sequential phases to establish both baseline material properties and the response of geometrically standardized specimens for constitutive calibration. Table 18 presents the mechanical properties of unmachined 250 mm segments tested in their as-received condition, preserving the nominal bar geometry (12.7

mm diameter). These results serve as a pre-machining verification, confirming consistency with mill certification data and providing a reference for material variability across suppliers.

A706 steels exhibit a lower yield-to-tensile strength ratio range (1.39-1.50) than A615 steels (1.21-1.62), consistent with their higher ductility requirements. Measured yield strengths range from 414 MPa to 525 MPa across categories. Coupon A706-C exhibits the lowest yield strength (414 MPa) and the highest strain at the onset of strain hardening (ε_{sh}=1.40%), indicating a more gradual transition from yielding to strain hardening relative to the other categories.

Following baseline characterization, companion specimens were machined to a reduced, constant diameter over the central gauge region, with a length-to-diameter ratio of 2.0. This geometry eliminates rib-induced stress concentrations and cross-sectional variability, enforcing a uniform uniaxial stress state and localizing deformation within the gauge length. The resulting configuration isolates material behavior and is therefore adopted for cyclic testing and constitutive calibration.

Table 18. In-house test results for unmachined coupons [30].

Coupon	f_y (MPa)	ε_{sh} (%)	ε_u (%)	f_u (MPa)	f_{su}/f_y
A615-A	445	0.74	9.40	720	1.62
A706-A	440	0.82	10.6	660	1.50
A615-B	487	1.16	9.60	725	1.49
A706-B	438	1.26	11.6	626	1.43
A615-C	525	1.34	8.80	638	1.22
A706-C	414	1.40	10.6	576	1.39

Table 19 summarizes the mechanical properties of the machined specimens. Relative to unmachined coupons, yield strength increases are observed in four of the six categories, while the strain at the onset of strain hardening decreases consistently across all categories (0.37%-1.80% compared to 0.74%-1.40% in unmachined specimens), except for coupon A615-C. Similarly, ultimate tensile strength increases from 576-725 MPa in unmachined coupons to 653-839 MPa in machined specimens, accompanied by higher f_u/f_y ratios (1.22-1.62 versus 1.32-1.92).

Table 19. In-house test results for machined coupons [30].

Coupon	f_y (MPa)	ε_{sh} (%)	ε_u (%)	f_u (MPa)	f_{su}/f_y
A615-A	438	0.37	10.4	839	1.92
A706-A	475	0.42	12.1	765	1.61
A615-B	537	0.78	11.0	837	1.56
A706-B	483	0.66	14.3	724	1.50
A615-C	522	1.80	14.1	690	1.32
A706-C	430	1.26	16.2	653	1.52

These differences arise primarily from geometric standardization. In unmachined bars, stress calculations are affected by uncertainty in the effective cross-sectional area and by non-uniform

strain distribution along the ribbed profile, where deformation localizes between ribs. Machining removes these effects, resulting in a more consistent representation of the intrinsic stress-strain response. Consequently, for cyclic testing and parameter calibration, machined coupons were adopted to ensure that the measured hysteretic response is governed exclusively by material nonlinearities, without interference from geometric effects.

4.1.3 Chemical Composition

Table 20 presents the chemical composition of each steel category, as reported by the manufacturers, with specimens ordered by descending carbon content to facilitate comparison across material batches.

The chemical composition data presented in Table 20 reveal a clear demarcation between steel categories based on carbon content, ranging from 0.26% to 0.42%. This variation is not merely a classification parameter but a determinant of microstructural evolution that directly influences the magnitude of the Bauschinger effect [11] in reinforcing steels subjected to cyclic loading. As carbon content increases, the reversed stress-strain response becomes progressively smoother and more nonlinear, with reduced stiffness and less resemblance to idealized bilinear behavior, reflecting an intensified Bauschinger effect [43].

The magnitude of this effect correlates strongly with the volume fraction and morphology of pearlite, which, in turn, are governed by carbon content. Steels with higher carbon content exceeding 0.40% (A615-A and -B in the present dataset) develop microstructures with a higher pearlite fraction, in which the lamellar cementite-ferrite interfaces act as potent obstacles to dislocation motion [71].

Table 20. Chemical composition of the coupons [30].

Coupon	C (%)	Mn (%)	Cu (%)	Ni (%)	Cr (%)	V (%)	Mo (%)	P (%)	S (%)	Si (%)	CE (*) (%)
A615-A	0.42	1.13	0.23	0.11	0.18	0.005	0.023	0.009	0.036	0.20	0.64
A615-B	0.42	1.14	0.24	0.08	0.07	-	0.017	0.014	0.035	0.20	0.62
A706-B	0.28	1.21	0.30	0.09	0.13	0.023	0.02	0.006	0.025	0.18	0.51
A706-A	0.28	1.20	0.29	0.11	0.11	0.027	0.025	0.014	0.04	0.21	0.50
A706-C	0.27	1.10	0.31	0.12	0.12	0.001	0.028	0.012	0.041	0.21	0.47
A615-C	0.26	0.75	0.34	0.11	0.11	0.001	0.02	0.015	0.038	0.21	0.44

(*) CE = Carbon Equivalent. Not a chemical element; an empirical index calculated to estimate the hardenability of steel and its susceptibility to martensite formation during cooling.

Complementary studies on pearlitic steels indicate that the high density of geometrically necessary dislocations at these interfaces produces internal back-stresses, amplifying the Bauschinger effect during cyclic loading sequences [131]. Conversely, the low-carbon categories (A706-B, A706-A, A706-C, and A615-C) with carbon content between 0.26% and 0.28% exhibit predominantly proeutectoid ferrite with dispersed pearlite colonies. The reduced carbide fraction lowers both dislocation-pile-up density and internal stress-field magnitude, attenuating the Bauschinger effect and promoting a more symmetric hysteretic response under cyclic loading.

The carbon equivalence values, ranging from 0.44 to 0.64, further elucidate the hardenability and strength potential of each category. However, susceptibility to the Bauschinger effect correlates more closely with absolute carbon content than with CE, as the latter includes manganese and other alloying elements that influence hardenability but have only secondary effects on pearlite volume fraction compared with carbon. The inverse relationship between carbon and manganese observed in the low-carbon group (A706-C: 1.10% Mn; A615-C: 0.75% Mn) reflects thermomechanical processing strategies that preserve ductility while compensating for strength reduction through solid-solution hardening.

4.1.4 Cyclic Strain Loading Protocols

The machined coupons were subjected to strain-controlled cyclic loading histories defined by four protocols named SH1, SH2, SH3, and SH4. All four protocols were applied at a strain rate of 0.001 s^{-1}, while only the first two protocols (SH1 and SH2) were selected for testing at the higher strain rate of 0.02 s^{-1}. To distinguish between strain-rate levels, the protocols are denoted using the suffix "L" for low rate and "H" for high rate, resulting in the notation SHi-L (i=1-4) and SHj-H (j=1, 2), where the indices i and j identify the specific strain history. Figure 53 presents the complete set of strain histories for the 0.001 s^{-1} tests, and Figure 54 shows the corresponding high-rate protocols. Figure 53 shows the strain histories for the 0.001 s^{-1} tests, and the corresponding high-rate protocols are shown in Figure 54.

The imposed strain histories depart from conventional sawtooth or incrementally increasing protocols and instead adopt irregular, non-periodic patterns representative of experimentally observed strain demands. The four protocols include large-amplitude strain reversals, intermediate cyclic excursions, multiple unloading-reloading sequences, and asymmetric loading patterns, covering a broad range of inelastic response conditions relevant to seismic loading.

All strain data were recorded at 256 Hz, ensuring sufficient temporal resolution to capture transient effects associated with cyclic loading. The strain amplitude was limited to ±0.05 mm/mm in all tests, consistent with deformation levels expected in reinforcing bars within plastic hinge regions and within the reliable measurement range of the strain gauges. Strain history SH3 was defined as the sign-reversed counterpart of SH1, providing a basis for evaluating asymmetry in the cyclic response. The selected high strain rate (0.02 s^{-1}) matches experimentally recorded strain rates in reinforcing steel within plastic hinge regions under strong seismic excitation. In comparison, the lower rate (0.001 s^{-1}) serves as a reference condition for identifying rate-dependent deviations in the hysteretic response.

Coupons were identified using a structured labeling system following the sequence [Manufacturer]-[ASTM code]-[Specimen number]. The first character denotes the steel mill (A, B, or C), the second digit indicates the ASTM specification (6 for A615 and 7 for A706), and the final digit corresponds to the specimen number and associated strain history, as defined in Table 21. This study primarily emphasizes the response at 0.02 s^{-1} (SH1-H and SH2-H) to evaluate strain-rate effects under conditions representative of seismic demand. Accordingly, only specimens 8 and 9 in Table 21 are considered in the subsequent analysis.

Under this convention, monotonic tension tests are denoted by the label "T" and include both machined and unmachined specimens tested to failure [30]. In contrast, all numbered identifiers

correspond to cyclic loading protocols. This notation directly maps each specimen to its material classification and imposed loading history. For example, the label C68 denotes a specimen from manufacturer C, conforming to ASTM A615, and assigned specimen number 8, corresponding to strain history SH1-H under high-strain-rate conditions.

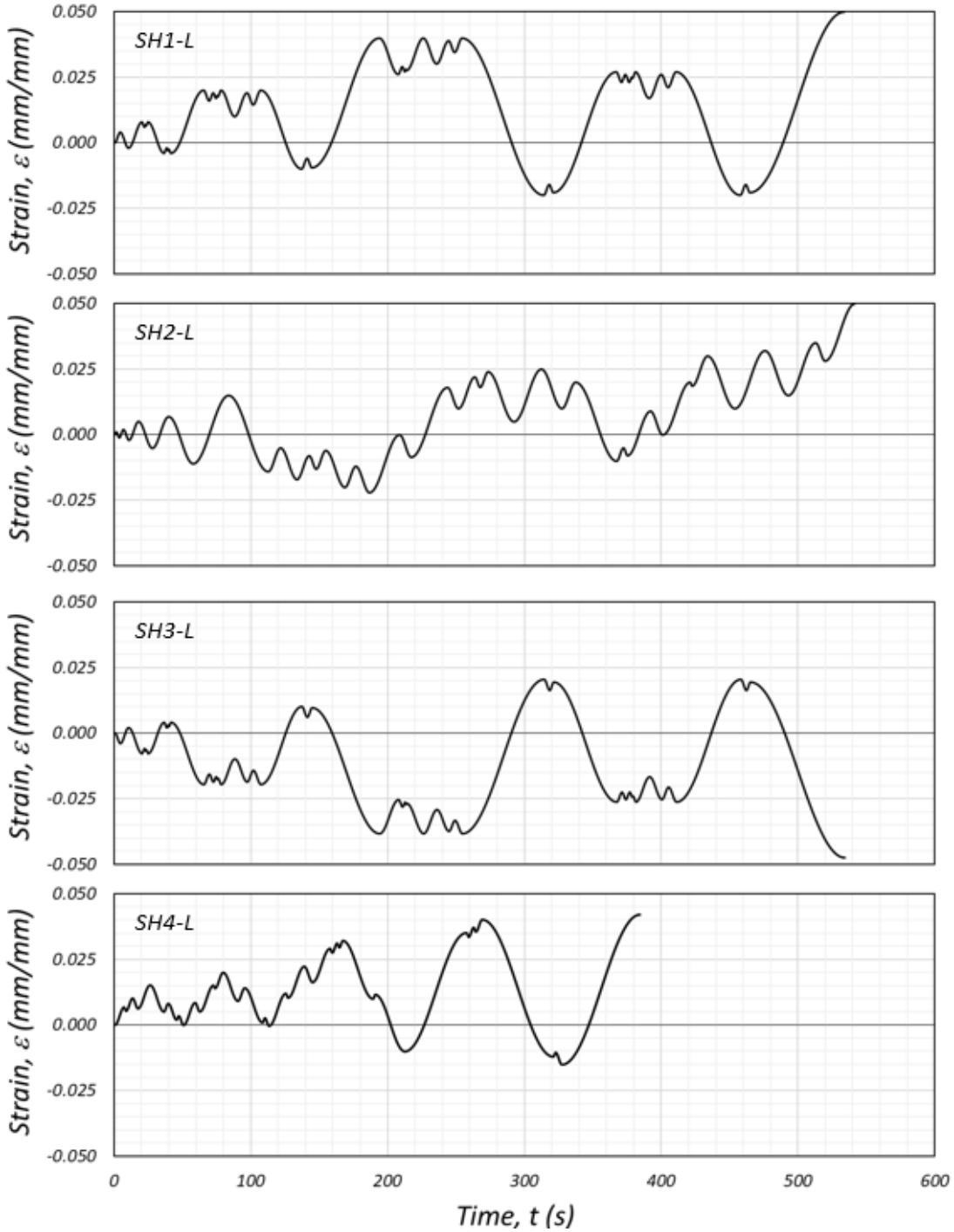


Figure 53. Cyclic loading histories at a strain rate of 0.001 s^{-1}.

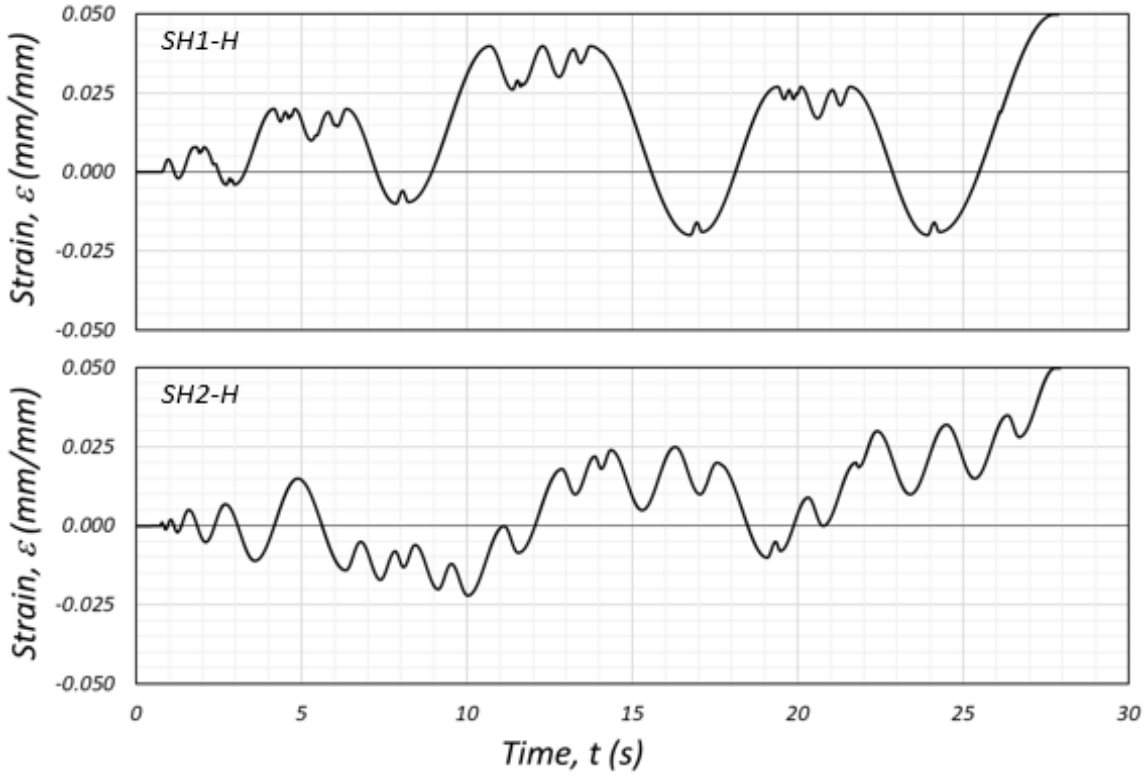


Figure 54. Cyclic loading histories at a strain rate of 0.02 s^{-1}.

Table 21. Coupon identification [30].

Strain histories	Coupons	Cross-section
T	1	Unmachined
T	2	Unmachined
T	3	Machined
SH1-L	4	Machined
SH2-L	5	Machined
SH3-L	6	Machined
SH4-L	7	Machined
SH1-H	8	Machined
SH2-H	9	Machined

4.2 Stress-Strain Cyclic Response

Figure 55 presents the stress-strain hysteretic response of machined coupons from Mill A, for both ASTM specifications, under cyclic strain histories SH1 and SH2. The eight panels correspond to specimens A64, A65, A68, A69, A74, A75, A78, and A79, representing low-rate (SH1-L and SH2-L) and high-rate (SH1-H and SH2-H) conditions, as defined in Table 21. The high-rate protocols exhibit higher peak stresses than their low-rate counterparts at comparable strain amplitudes, with stress increments of approximately 20-40 MPa discernible during strain hardening. This elevation is consistent with positive strain-rate sensitivity in the dynamic strain-aging regime characteristic of Grade 60 reinforcing steels at moderate rates.

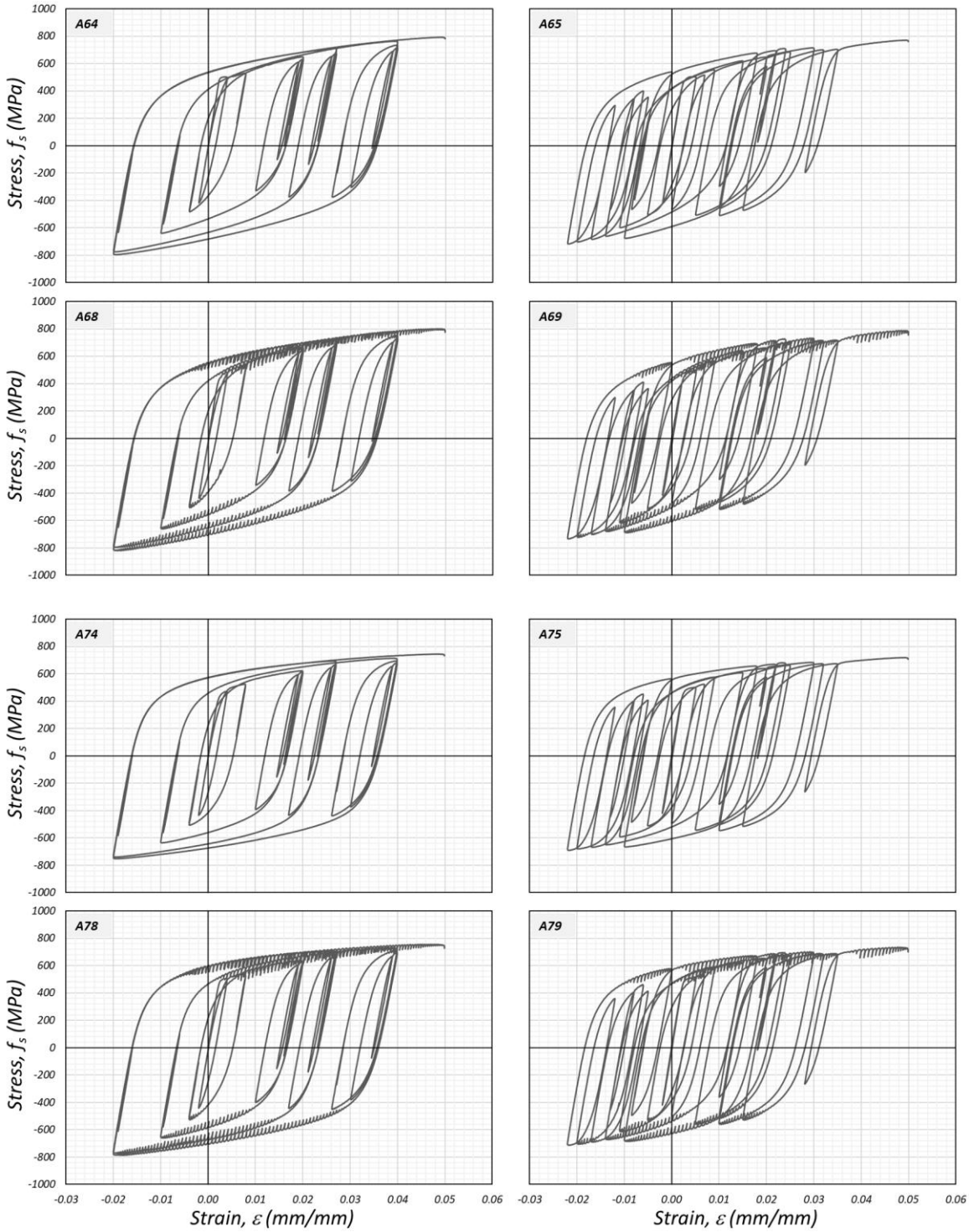


Figure 55. Cyclic stress-strain response of machined coupons from Mill A.

The hysteretic loops at 0.001 s^{-1} appear marginally narrower than those at 0.02 s^{-1}, suggesting a modest reduction in energy dissipation per cycle. However, this effect is partially masked by the stress scale. Figure 56 presents the hysteretic responses for Mill B. The same degradation,

asymmetry, rate-induced stress elevation, and absence of premature fracture observed for Mill A are also evident, indicating that strain-rate sensitivity is not manufacturing-source specific.

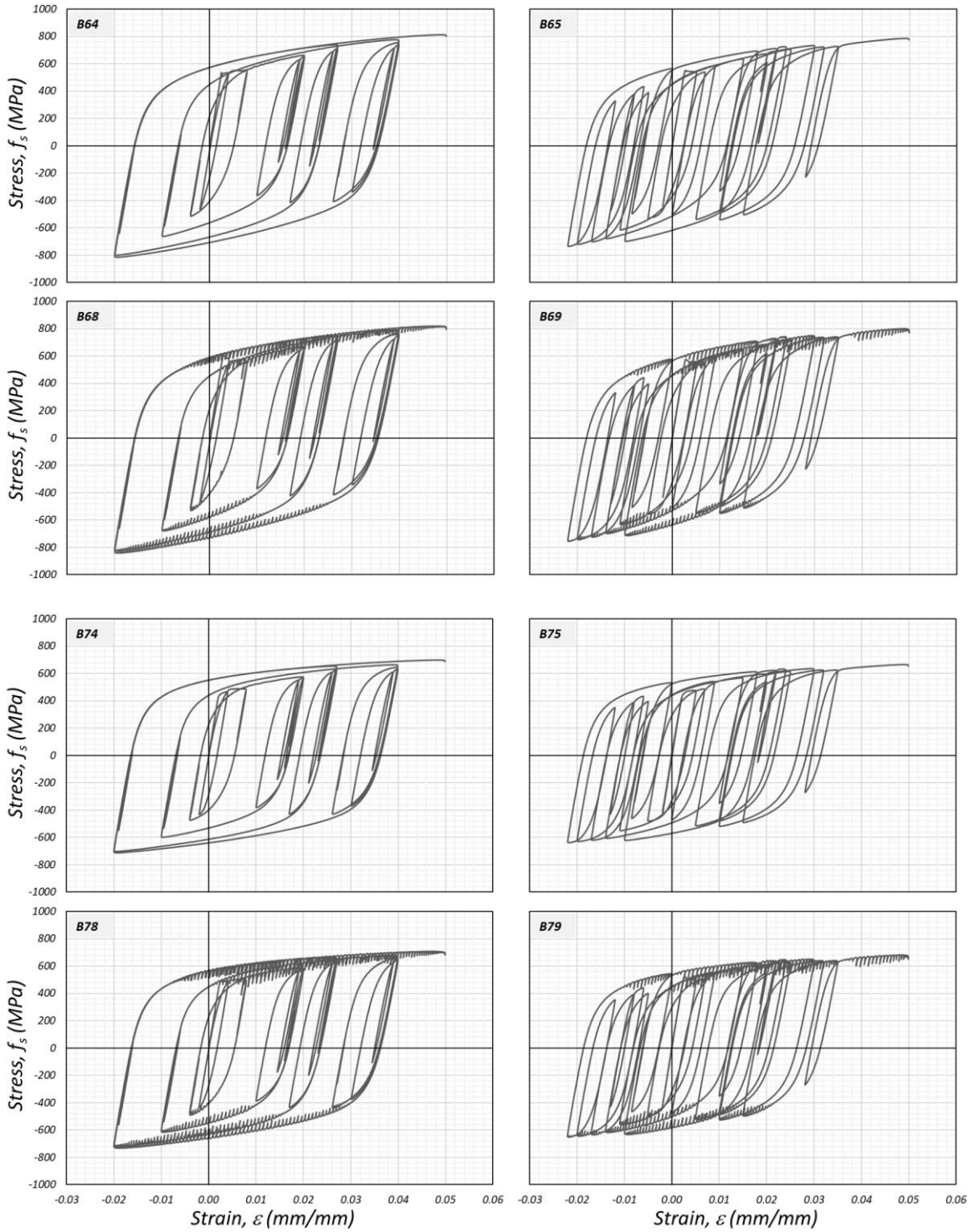


Figure 56. Cyclic stress-strain response of machined coupons from Mill B.

Figure 57 presents the hysteretic responses for Mill C. Despite the baseline strength deviations noted in Table 17 for this manufacturer, the cyclic response exhibits the same qualitative features observed in Mills A and B: stable hysteretic behavior, history-dependent asymmetry, and positive strain-rate sensitivity.

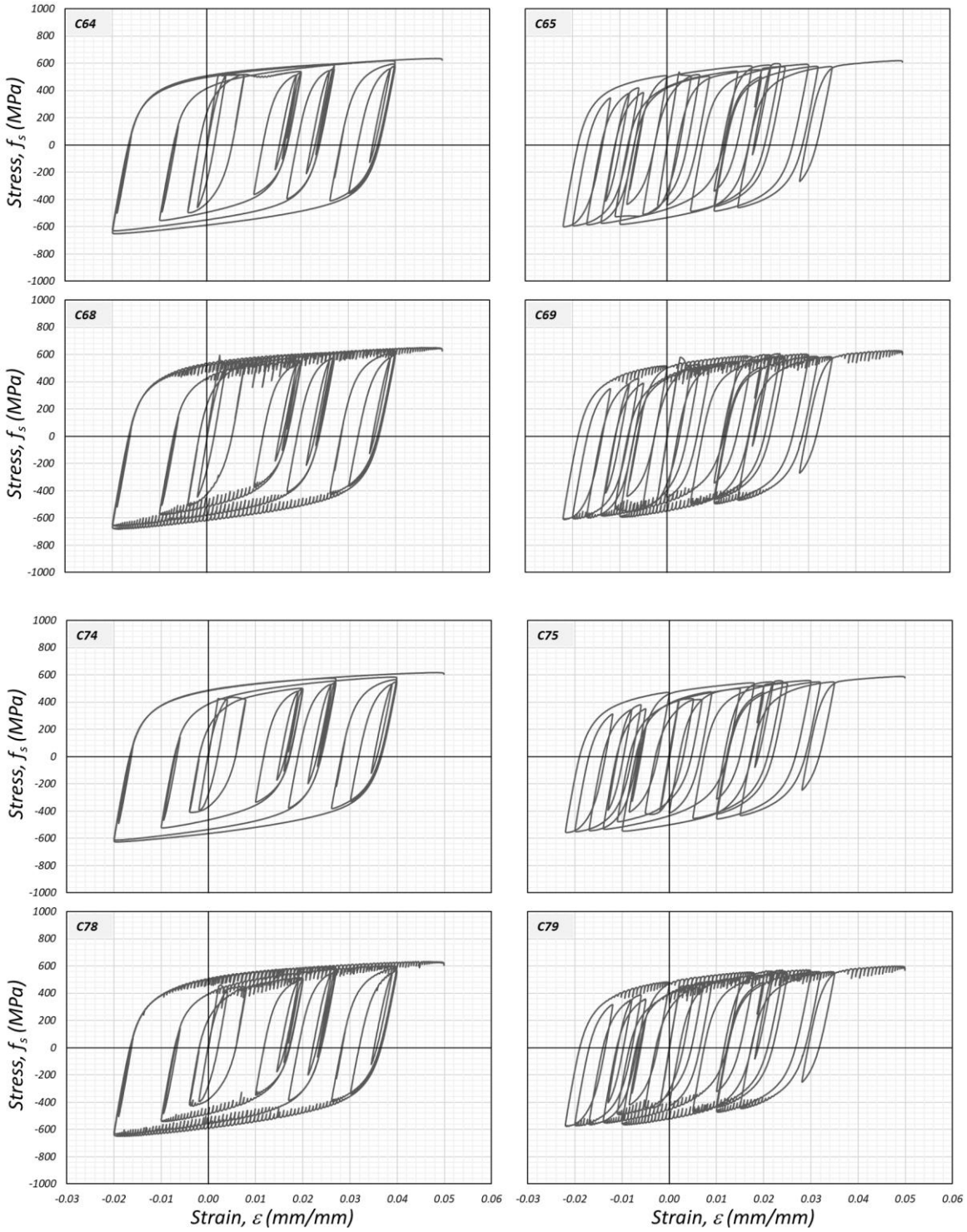


Figure 57. Cyclic stress-strain response of machined coupons from Mill C.

No premature fracture or strength degradation is observed within the imposed strain limits, indicating adequate ductility reserve for the cyclic demands considered. The consistency of response across duplicate specimens (e.g., A64/A68 and A74/A78 for SH1, A65/A69 and A75/A79 for SH2) confirms reproducibility of the testing protocol and material homogeneity within the Mill A lot. Although this study focuses on the high-rate protocols associated with specimen identifiers 8 and 9 in Table 21, it also includes the corresponding low-rate hysteretic responses for the same loading protocols to enable direct assessment of strain-rate effects.

This convergence across all three manufacturers confirms that the rate-dependent phenomena herein documented are representative of Grade 60 reinforcing steel production rather than mill-specific anomalies. This study focuses exclusively on the 12 high-rate tests, specifically specimens A68, A69, A78, A79, B68, B69, B78, B79, C68, C69, C78, and C79. Complete experimental documentation, including monotonic tension tests and supplementary cyclic protocols not considered herein, is provided in [29].

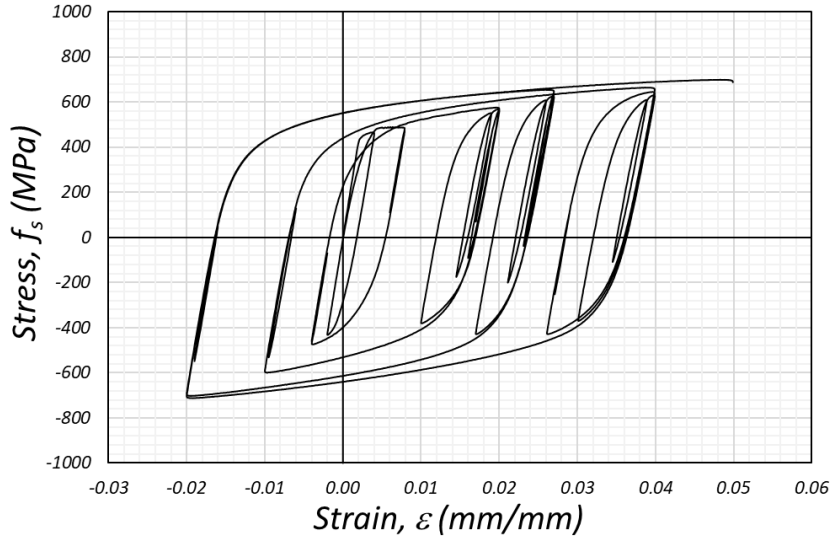
4.3 Experimental Evidence of Strain-Rate Sensitivity under Cyclic Loading

Strain-controlled cyclic tests SH1-H and SH2-H quantified strain-rate sensitivity within the plastic hardening regime. High-resolution stress-strain records (Figures 55-57), namely A68, A69, A78, A79, B68, B69, B78, B79, C68, C69, C78, and C79, show that higher strain-rate excursions develop systematic stress undulations along the hardening branches. These undulations are attributed to the hydraulic actuator reaching its flow-rate capacity at the imposed loading rate, causing the pump to stall and rebound momentarily. Figure 58 synthesizes these observations.

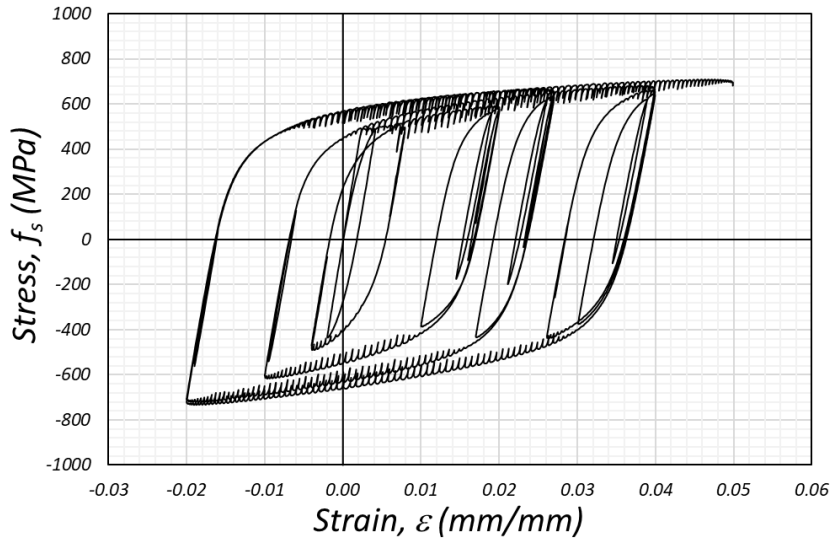
Figure 58(a) displays the full cyclic envelope obtained at the lower strain rate and serves as a mechanical reference state. The smooth, continuous hardening response confirms that the actuator operates within its flow-rate capacity at this loading rate. In contrast, Figure 58(b), recorded over the same stress and axial-strain intervals but at a higher rate, exhibits a recurring undulation pattern characterized by stress drops spaced at approximately 0.15% axial strain. These undulations are consistent with the hydraulic pump intermittently reaching its flow-rate limit and rebounding during the imposed loading history.

Figure 59 presents a high-resolution stress-strain segment at the higher strain rate, spanning seven mechanical cycles. The trace starts in the linear-elastic domain and follows successive tension-compression inversions, enabling each family of undulations to be tracked throughout the loading history.

During the Lüders-controlled elastic-plastic transition, the macroscopic stress remains nearly constant. At the same time, strain accumulates, and no repetitive-stress undulations are observed, consistent with progressive Lüders band propagation. As shown in Figure 59(b), once the Lüders band is exhausted, the material enters uniform plastic flow. Upon reloading, the first undulations emerge at stresses between approximately 380 and 515 MPa. These initial undulations define the first family, shown in red, while the preceding deformation history remains visible in gray as a mechanically frozen reference state. The early undulations are sparse, with stress-drop amplitudes of roughly 10-20 MPa, consistent with the actuator approaching its flow-rate capacity at this loading rate.



a) Stress-strain response at low rate (no undulations).



b) Stress-strain response at high rate (undulations).

Figure 58. Strain-rate sensitivity of reinforcing bars under cyclic loading.

Figure 59(c) shows an intermediate stage of cyclic plastic deformation, where a new family of undulations becomes active during compressive reloading. In contrast, earlier families remain preserved in gray. In the stress range from approximately -300 to -550 MPa, the stress-strain trajectory shows pronounced, recurrent undulations that form a coherent sequence of stress drops with amplitudes of roughly 20-30 MPa over a compressive strain interval of about 0.013 to -0.01 mm/mm.

Upon reversal into tension, Figure 59(d) shows another family of undulations becoming dominant over a broad strain range from approximately 0.0 to 0.04 mm/mm. These undulations are dense and highly regular, superimposed on a hardening envelope that rises from about 360 to 600 MPa, with individual stress drops of 20-30 MPa.

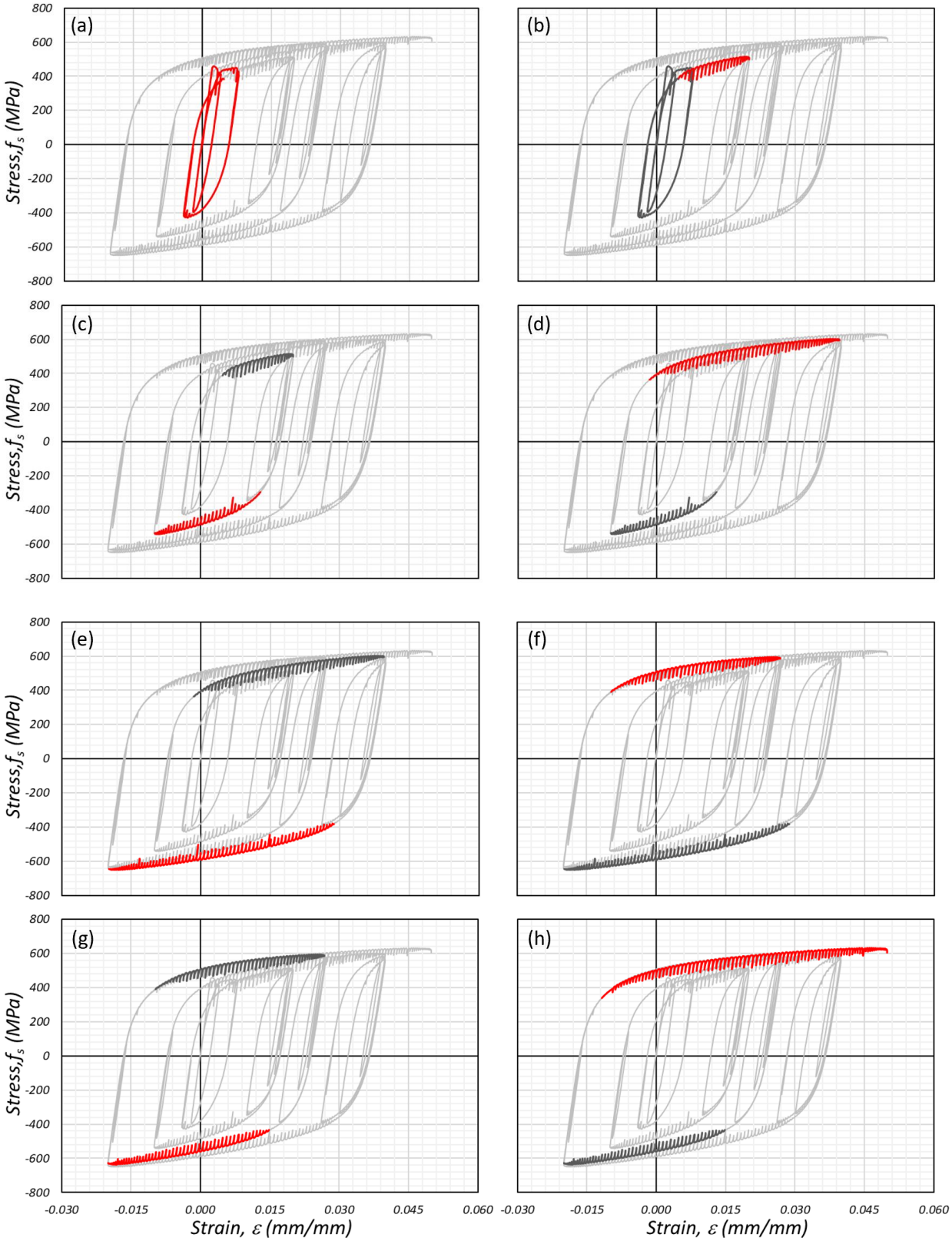


Figure 59. Evolution of actuator-induced undulation families during cyclic plastic deformation of reinforcing steel.

Further cycling activates an additional compressive family in Figure 59(e), extending to stresses near -650 MPa over strains spanning approximately 0.03 to -0.02 mm/mm. The persistence of large-amplitude undulations under reversed loading confirms that the actuator limitation manifests consistently regardless of loading direction.

At advanced tensile strains, Figure 59(f) shows the active family of undulations following a macroscopic envelope that approaches saturation near 600 MPa at about 0.026 mm/mm. The increasingly uniform spacing between successive undulations indicates a stabilized pattern within this family. Figure 59(g) shows later compressive cycles, where the active family remains visible between approximately -440 and -640 MPa. Still, the undulations become less periodic and more dispersed, with accumulated cyclic plasticity. The final stage of the sequence, shown in Figure 59(h), shows a tensile response approaching a saturation stress near 650 MPa. Concurrently, the amplitudes of the undulations progressively decrease, frequently falling below 10 MPa. The stress-strain trajectory becomes increasingly smooth as the demand on the actuator decreases near strain saturation. At the same time, all previously formed families remain mechanically imprinted in gray.

Overall, Figure 59 demonstrates that the undulation families appear in succession, each activated within a specific time window and strain range. In contrast, all previous families remain preserved as a cumulative mechanical memory of the evolving material state.

Figure 60 shows a single tension branch of the cyclic stress-strain response recorded by the extensometer during high-rate deformation. The resolution is fine enough to resolve individual undulation events. Because the extensometer integrates deformation over its gauge length, its signal reflects the instantaneous spatial average of the local strain field inside the specimen.

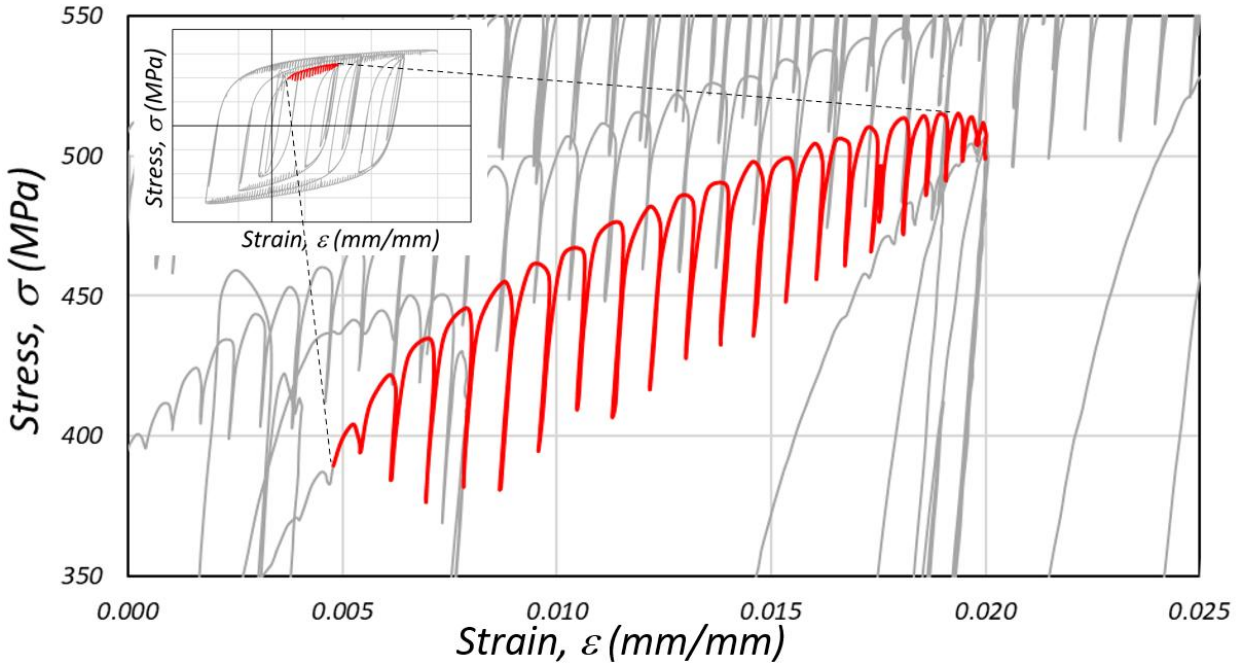


Figure 60. Extensometer-resolved undulation activity during a tensile branch of cyclic plastic deformation.

The undulations observed in Figure 60 result from the hydraulic actuator intermittently reaching its flow-rate capacity during the imposed loading history. Each stress drop corresponds to a momentary inability of the pump to sustain the demanded displacement rate, followed by a recovery as the pressure rebuilds. During unloading, the actuator demand decreases, and the stress-strain trace remains smooth. Upon reloading in the opposite direction, the undulations reappear as the actuator is again driven to its capacity. The compressive branches exhibit undulations almost symmetric to those observed in tension. Smooth portions of the curve correspond to intervals where the actuator operates within its capacity.

The cyclic loading histories imposed on reinforcing steel bars during seismic excitation are characterized not only by repeated strain reversals and progressive excursions into the inelastic regime, but also by pronounced temporal fluctuations in deformation rate. As demonstrated by the undulation activity in Figure 60, plastic flow during high-rate cyclic loading does not occur at a single, well-defined strain rate. Instead, it proceeds through a sequence of kinematically distinct states in which the actuator alternates between intervals of near-zero velocity, when the pump cannot sustain the demanded flow rate, and short bursts of rapid displacement as pressure rebuilds.

Although these fluctuations originate from the actuator's flow-rate limitation, their mechanical consequence is transient stress increments superimposed on the underlying cyclic hardening response. To quantify this effect, the next section experimentally characterizes strain-rate sensitivity by analyzing stress increments as a function of instantaneous strain-rate increments during cyclic loading. Rather than relying on nominal loading rates or global stress-strain curves, the analysis isolates transient stress changes that develop within the plastic hardening regime and are directly associated with the strain-rate excursions revealed by the undulations.

Cyclic tests are conducted under fully reversed axial strain histories imposed in strain control, with increasing strain amplitudes to ensure progressive engagement of plasticity and hardening. Different deformation-rate levels are generated by varying the imposed actuator velocity while maintaining identical strain amplitudes and reversal patterns. This design permits direct comparison of stress increments mobilized at different instantaneous strain rates under otherwise equivalent deformation states.

The resulting stress-increment-strain-rate-increments relations demonstrate that, for a given strain level within the hardening regime, higher instantaneous strain rates systematically produce larger incremental stress responses. These rate effects are not confined to initial yielding or monotonic segments but persist throughout cyclic loading, consistent with the undulations observed in Figure 60. Moreover, as cumulative plastic deformation increases with strain amplitude, stress amplification at a given strain rate becomes more pronounced, leading to wider hysteresis loops and greater energy dissipation at higher deformation demands.

Comparisons with quasi-static cyclic data reported in the literature further indicate that conventional low-rate testing protocols tend to overestimate the stress increments mobilized under rapidly varying cyclic deformation histories. Consequently, constitutive models calibrated solely from quasi-static data are prone to misrepresent the contribution of strain-rate effects to cyclic hardening, force redistribution, and hysteretic energy dissipation. Together, the undulation-resolved kinematics documented in Figure 60 and the strain-rate-dependent stress increments

quantified in the next section establish a coherent experimental foundation for the rate-dependent constitutive modeling developed in the following sections.

4.4 Time-window-based characterization of strain-rate effects

Strain-rate effects are experimentally characterized by analyzing stress increments developed during cyclic loading in the plastic hardening regime of reinforcing steel. The analysis is based on time-window-based synchronized, high-resolution measurements of stress, strain, and strain rate obtained from strain-controlled cyclic tests (Section 4.1). Although the data are recorded in the time domain, the objective is not to study temporal evolution per se, but to extract mechanically equivalent states that directly isolate the influence of instantaneous strain rate on the incremental stress response. Accordingly, all comparisons are governed by mechanical equivalence rather than by elapsed time.

4.4.1 Tension Branch

Figure 61 shows an overview of the synchronized stress, strain, and strain-rate history during tension-branch formation, which forms the basis for the window-selection procedure, and makes explicit the correspondence between stress undulations, strain evolution, and strain-rate excursions.

A time-window-based analysis isolates transient events associated with rapid changes in deformation rate caused by actuator flow-rate fluctuations. The selected windows span time intervals bounded by two consecutive extrema of the strain-rate signal. The zero crossings of each peak coincide with the momentary arrest of actuator displacement; they therefore mark physically meaningful transitions between pump-limited and freely deforming states.

By construction, the two strain-rate peaks, together with their associated zero crossings and the last one preceding each peak, enclose three successive local extrema in the strain history (three local maxima during reloading or three local minima during unloading), thereby ensuring that the selected segment spans mechanically comparable states within the same hardening regime.

Within each selected temporal segment, the analysis begins at the last zero crossing preceding the peak associated with the first local extremum in strain. This instant defines a reversal of the imposed kinematic input and a momentary condition of $\dot{\varepsilon} \approx 0$. The strain at this instant is denoted as ε_1 (-0.00609 mm/mm in Figure 61) and serves as the first reference mechanical state.

Starting from ε_1, the stress-strain trajectory is followed forward in time until the strain again reaches or exceeds ε_1. This crossing defines the first vertical reference line within the window and ensures that the response is evaluated at the same strain on the same hardening branch. The corresponding stress and strain-rate values are recorded as f_{s1} and $\dot{\varepsilon}_1$ (471 MPa and 0.06683 s^{-1}, respectively).

The second vertical reference line is defined by locating, within the descending branch of the first peak of the strain-rate peak, the instant at which the strain-rate magnitude equals $|\dot{\varepsilon}_1|$. This condition establishes a mechanically consistent pairing of deformation states with identical instantaneous strain rate but opposite acceleration directions. The associated stress and strain are

recorded as f_{s2} (501 MPa) and ε_2 (-0.00555 mm/mm), with $\dot{\varepsilon}_2 = \dot{\varepsilon}_1$. The difference between the peak strain rate $\dot{\varepsilon}_{p1}$ (0.08174 s^{-1}) and $\dot{\varepsilon}_1$ is then registered.

$$\Delta\dot{\varepsilon}_1 = \left|\dot{\varepsilon}_{p1} - \dot{\varepsilon}_1\right| = 0.01491\ s^{-1}$$

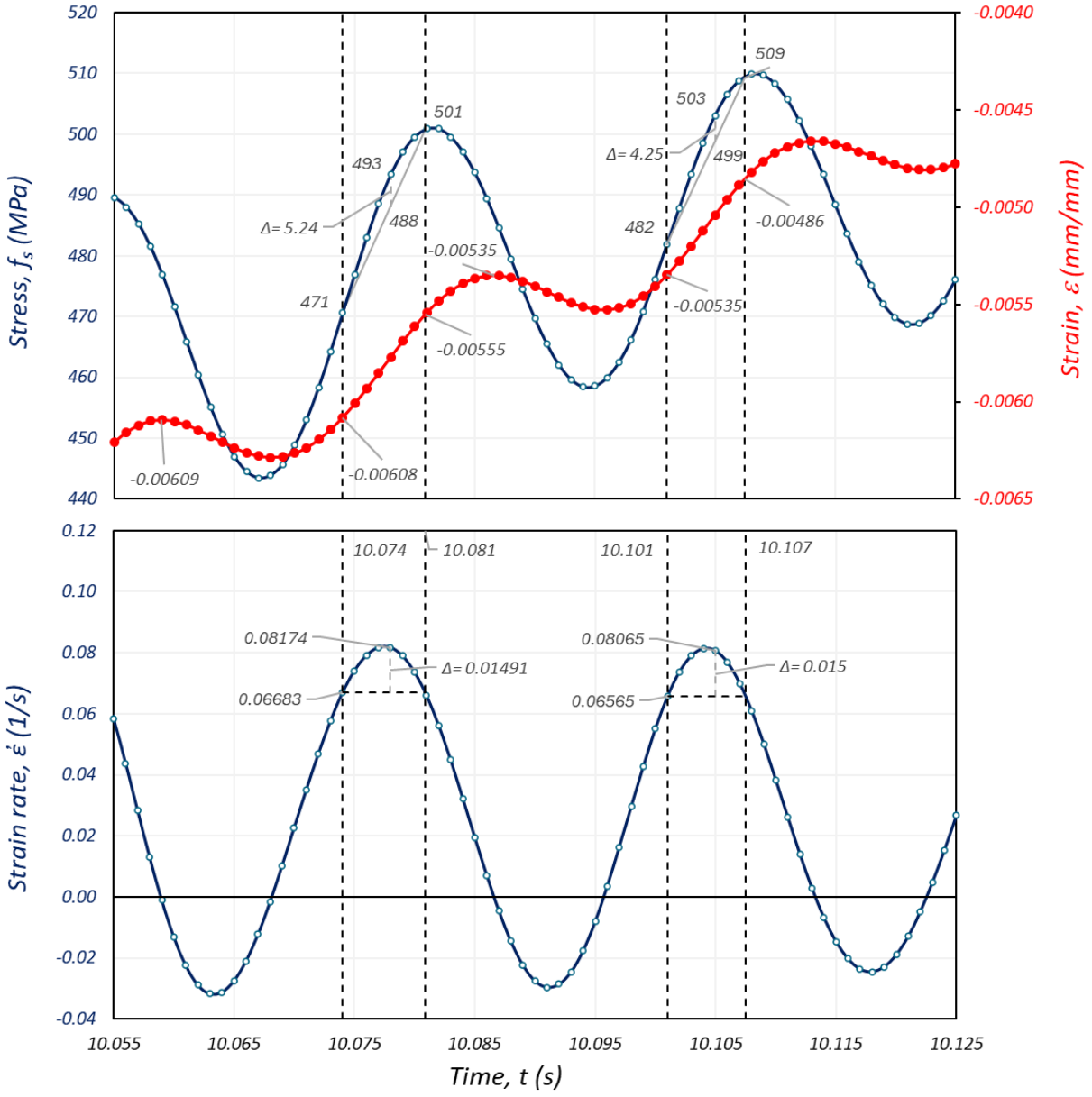


Figure 61. Tension-dominated actuator-induced rate excursions.

A straight line is then drawn connecting f_{s1} and f_{s2}. From the stress of the first strain-rate excursion f_{sp1}, corresponding to the first peak strain rate (493 MPa), a vertical projection onto this line defines an intermediate stress f_{si1} (488 MPa), which represents the stress that would have been

obtained at the same strain and hardening state without the actuator-induced strain-rate excursion. The stress increment associated with the first peak is therefore defined as

$$\Delta f_{s1} = \left| f_{sp1} - f_{si1} \right| = 5.24\ MPa$$

This construction isolates the portion of the stress response that is attributable solely to the transient increase in strain rate.

The procedure is then repeated for the second strain-rate peak within the same selected temporal window. The analysis initiates at the last zero crossing of the first peak, corresponding to the third local strain extremum (ε_3=-0.00535 mm/mm). From this reference mechanical state, the condition of equal strain on the same monotonic hardening branch is identified, recording the corresponding stress and strain-rate values f_{s3} (482 MPa) and $\dot{\varepsilon}_2$ (0.06565 s^{-1}).

On the descending branch of the second rate peak, the paired mechanical state characterized by equal strain-rate magnitude but opposite acceleration direction is located, $\dot{\varepsilon}_4 = \dot{\varepsilon}_3$, with associated f_{s4} (509 MPa) and ε_4 (-0.00486 mm/mm). The difference between the peak strain rate $\dot{\varepsilon}_{p2}$ (0.08065 s^{-1}) and the reference rate $\dot{\varepsilon}_2$ defines the increment of the second event:

$$\Delta \dot{\varepsilon}_2 = \left| \dot{\varepsilon}_{p2} - \dot{\varepsilon}_2 \right| = 0.0149\ s^{-1}$$

Through the linear interpolation between f_{s3} and f_{s4}, the vertical projection from the stress corresponding to the peak strain rate f_{sp2} determines the intermediate stress f_{si2}, allowing quantification of the stress increment attributable exclusively to the transient velocity excursion:

$$\Delta f_{s2} = \left| f_{sp2} - f_{si2} \right| = 4.25\ MPa$$

The extracted stress increments quantify the additional stress required to sustain actuator-induced surges in strain rate while the macroscopic deformation path remains continuous. Computed over approximately 0.05-s windows centered on each undulation event, those increments in stress capture the local rate sensitivity of the flow stress at an essentially fixed internal state. Because the strain accumulated within each window is negligible relative to the previously imposed plastic strain, the measured stress increase reflects a purely rate-controlled stress amplification. Accordingly, they provide a direct, physically interpretable measure of cyclic strain-rate sensitivity, kinematically linked to the localized deformation bands resolved by the extensometer.

4.4.2 Compression Branch

For compression-dominated windows, the same methodology is employed, with the temporal bounds defined by two consecutive strain-rate peaks that enclose three successive local minima in the strain history. Figure 62 presents a representative temporal window spanning 4.91 s to 4.98 s, illustrating a characteristic compression branch analysis. The analysis initiates at the last zero crossing preceding the first peak, where the imposed kinematic reversal yields a momentary condition of $\dot{\varepsilon} \approx 0$.

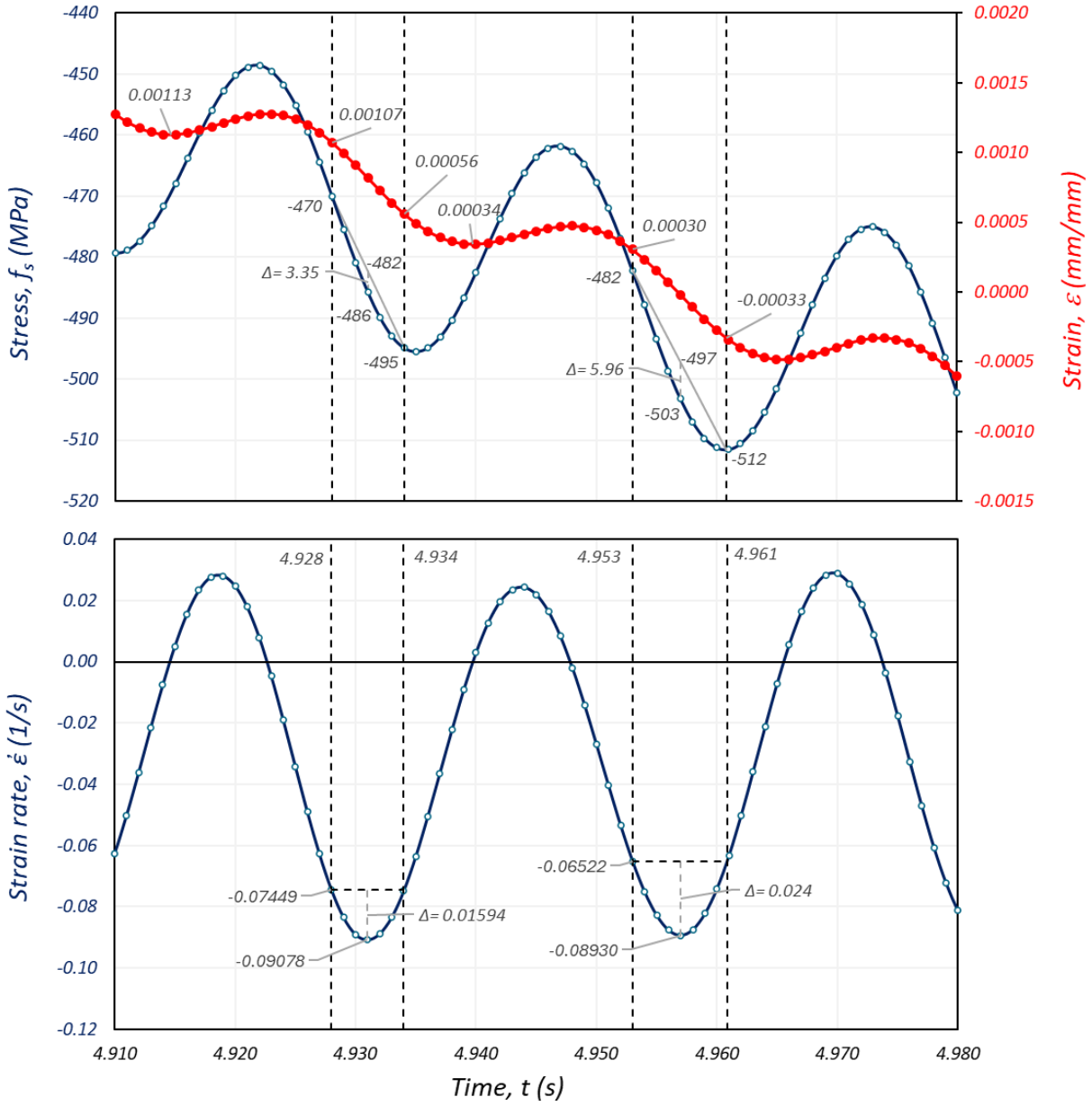


Figure 62. Compression-dominated actuator-induced rate excursions.

This reference mechanical state is denoted by its strain value, from which the stress-strain trajectory is tracked forward until the strain again reaches this value on the same monotonic hardening branch. The corresponding stress and strain rate are recorded as the first paired state. The second paired state is identified on the ascending branch of the strain-rate peak at an equal strain rate but with the opposite acceleration direction. Linear interpolation between these paired stress states enables vertical projection from the stresses corresponding to the peak strain rates to determine the intermediate stress, thereby quantifying the stress increment attributable exclusively to the transient strain-rate excursion. This same procedure is repeated for the different temporal windows of each family in tension and compression across the 12 tests described in Section 4.1.

4.4.3 Undulation-Resolved Stress Increments vs. Strain-Rate Excursions

For both A615 and A706 reinforcing steel tests, the stress increment, $|\Delta f_s|$ values obtained from undulation-resolved time windows are plotted against the corresponding strain-rate excursions, $|\Delta\dot{\varepsilon}|$, reaching values of about 20-25 MPa at $|\Delta\dot{\varepsilon}| \approx$0.10-0.12 s^{-1} (see Figures 63 and 64). The plots employ a stratification based on the hardening state: large black circles correspond to $\dot{\varepsilon}$=0, medium grey circles to $0 < \dot{\varepsilon} \leq 0.04$, and small light circles to $0.04 < \dot{\varepsilon} \leq 0.08$.

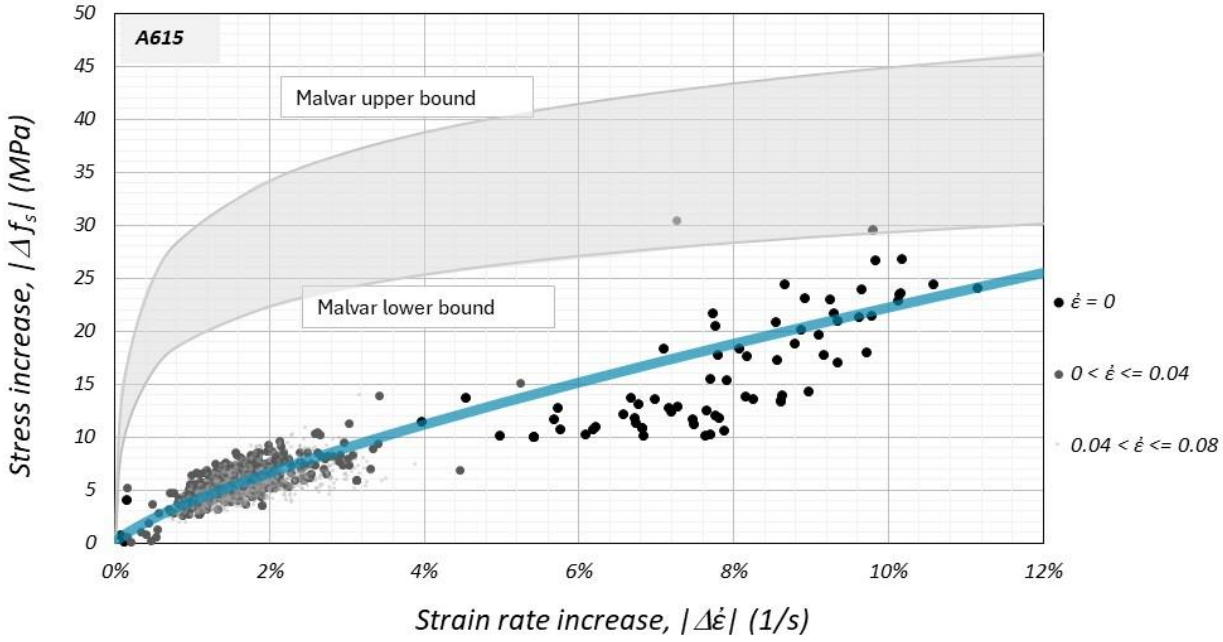


Figure 63. Rate-dependent stress increments extracted from undulation-resolved strain-rate excursions - A615 reinforcing steel.

For A615 steel, the large black points ($\dot{\varepsilon}$=0) define a tight and nearly linear trend, captured by the fitted blue line. Data obtained at nonzero background strain rates collapse onto the same trend at low $|\Delta\dot{\varepsilon}|$ and progressively scatter as $|\Delta\dot{\varepsilon}|$ increases, indicating that the background rate influences variability but does not govern the primary scaling of $|\Delta f_s|$. The Malvar lower and upper bounds [80], plotted as a shaded band, lie entirely above both the experimental points and the fitted trend across the whole domain, showing that classical monotonic-test-based dynamic increase factors (DIFs) substantially overpredict the magnitude of rate-induced stress increments under cyclic plasticity for A615 steel.

A706 steel exhibits similar structural behavior but with slightly higher rate sensitivity. The relationship between $|\Delta f_s|$ and $|\Delta\dot{\varepsilon}|$ remains approximately linear. As in A615, the black points define the cleanest trend, while data at nonzero strain rates cluster around it at small $|\Delta\dot{\varepsilon}|$ and spread at larger excursions. The Malvar shaded band again lies fully above the measured data and the fitted curve, confirming that monotonic-based DIF formulations also overestimate the effective cyclic rate strengthening of A706 steel.

The resulting pairs of strain-rate excursions $|\Delta\dot{\varepsilon}|$ and corresponding stress increments $|\Delta f_s|$, collected over virgin and progressively hardened states, were then used to fit the proposed power-law expression, so that its parameters capture the experimentally observed scaling of instantaneous stress amplification with localized strain-rate excursions during cyclic plastic deformation.

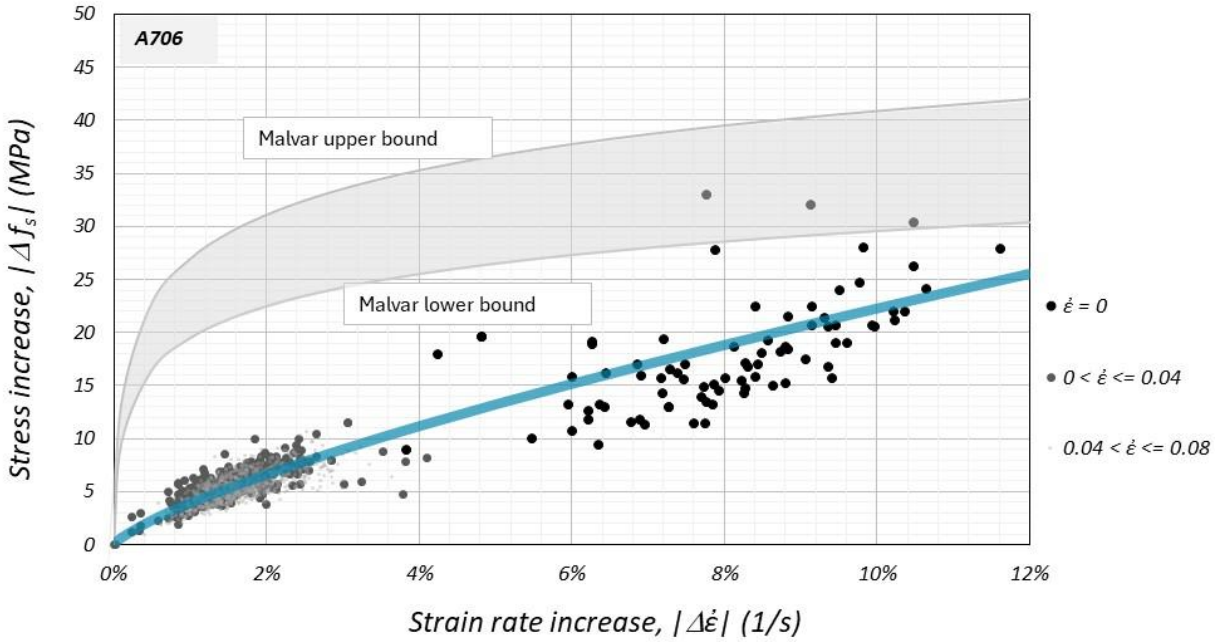


Figure 64. Rate-dependent stress increments extracted from undulation-resolved strain-rate excursions - A706 reinforcing steel.

Figures 64 and 63 demonstrate that, in reinforcing steels subjected to cyclic plastic deformation, the operative variable controlling instantaneous stress amplification is the strain-rate *excursion* $|\Delta\dot{\varepsilon}|$, not the absolute strain rate $\dot{\varepsilon}$. Both A706 and A615 show a near-linear dependence of Δf_s on $\Delta\dot{\varepsilon}$, with A706 consistently more rate-sensitive than A615. The fact that all experimental points and fitted trends lie well below the Malvar lower bound demonstrates a systematic incompatibility between monotonic dynamic increase factor formulations and the rate-dependent stress amplification observed under cyclic loading. This discrepancy shows that the cyclic plastic response of reinforcing steel cannot be represented by a fixed rate-sensitivity parameter calibrated from monotonic tests. Instead, it must be formulated in terms of localized, transient strain-rate excursions whose effects on stress depend on the evolving hardening state. Consequently, constitutive models that treat rate sensitivity as a static multiplier cannot reproduce the state-dependent stress increments generated by cyclic deformation and therefore lack physical fidelity for seismic-type loading conditions.

Following the graphical characterization in Figures 64 and 63, the experimentally extracted stress increments were quantified through the power-law relation:

$$|\Delta f_s| = k_{rate}|\Delta\dot{\varepsilon}|^{n_{rate}} \tag{119}$$

where k_{rate} is a material rate-sensitivity coefficient, and n_{rate} is a nonlinear exponent controlling how rapidly the stress increment grows with the strain-rate excursion. The best fit to the combined experimental data yields k_{rate}=125 and n_{rate}=0.75.

The sublinear exponent $n_{rate} < 1$ indicates that the rate-induced strengthening increases with $|\Delta\dot{\varepsilon}|$ but with diminishing marginal gain as the excursion magnitude becomes larger, consistent with the curvature observed in the experimental point clouds. The value of k_{rate} sets the overall scale of the response and directly reflects the intrinsic sensitivity of the plastically hardened reinforcing steel to instantaneous changes in deformation rate. Importantly, because the fitting law is expressed explicitly in terms of $|\Delta\dot{\varepsilon}|$, it captures the experimentally observed behavior that stress amplification during cyclic plasticity is governed by localized strain-rate excursions rather than by the absolute strain rate, in contrast to traditional monotonic dynamic increase-factor formulations.

4.5 Implications for Constitutive Modeling

The experimental results presented in Section 4.4 demonstrate that transient strain-rate excursions, $|\Delta\dot{\varepsilon}|$, govern the stress increments developed during cyclic plastic deformation, rather than the absolute strain rate $\dot{\varepsilon}$. This behavior is quantitatively captured by the power-law relation in (119), which links instantaneous stress amplification directly to local variations in deformation rate.

Conventional constitutive models for reinforcing steel under cyclic loading are typically formulated in terms of stress-strain relationships controlled by strain history and internal hardening variables, without explicit dependence on strain rate. By construction, such models cannot generate additional stress increments in response to a pure strain-rate excursion at fixed strain. They therefore cannot reproduce the experimentally observed rate-dependent stress amplification. This limitation is not a matter of parameter calibration but a structural deficiency of the constitutive framework.

The systematic separation between the experimental data and the monotonic-based DIF bounds further confirms that rate effects under cyclic plasticity cannot be represented through absolute-rate-based amplification laws derived from monotonic loading. Instead, the governing mechanism involves localized, transient changes in strain rate during plastic flow. Consequently, any constitutive description intended to capture the cyclic response of reinforcing steel under seismic-type loading must incorporate an explicit dependence on strain-rate excursions. This requirement motivates the extension of the baseline rate-independent constitutive model to include a rate-sensitive formulation consistent with the experimentally identified $|\Delta\dot{\varepsilon}|$-controlled mechanism.

4.6 Baseline Rate-Independent Constitutive Model

This section presents the rate-independent constitutive formulation proposed by Carreño [29], which is adopted herein as the baseline reference for modeling the cyclic response of reinforcing steel. The formulation defines a uniaxial constitutive stress-strain model, hereafter referred to as the Dodd-Restrepo-Carreño (SteelDRC) model, developed to represent cyclic material behavior better.

The SteelDRC model builds on the classical Dodd-Restrepo (DR) formulation (Section 2.2.6) and introduces refinements that enhance predictive accuracy, numerical robustness, and computational

efficiency while preserving the original monotonic backbone and maintaining a concise, physically transparent structure. Its constitutive parameters are directly associated with mechanically meaningful material properties, allowing clear interpretation in terms of observable features of reinforcing steel behavior under cyclic loading. It addresses key limitations of the original DR formulation, most notably the lack of a closed-form representation of the Bauschinger curve and the convergence difficulties commonly encountered in nonlinear finite element analyses. The SteelDRC formulation reproduces the full monotonic stress-strain response of reinforcing steel under both tensile and compressive loading, encompassing the elastic range, yield plateau, strain-hardening regime, and ultimate branch.

In addition, the model explicitly accounts for the Poisson effect, capturing the lateral contraction or expansion induced by axial straining, thereby enhancing physical realism by coupling axial and transverse deformation mechanisms. The original DR formulation expresses stress and strain in the natural (true) coordinate system to remain consistent with the specimen's instantaneous geometry during deformation. Figure 65 compares engineering and natural coordinate representations of a typical stress-strain backbone response. This figure shows that the engineering stress-strain response is markedly asymmetric between tension and compression. In contrast, the formulation in terms of natural strain and true stress yields an approximately symmetric response. As discussed in Section 2.2.6, this difference arises from the artificial asymmetry inherent in engineering measures. Accordingly, the natural coordinate system is adopted here as the baseline description for the constitutive model, providing a consistent foundation for the subsequent development of cyclic plasticity and hardening behavior.

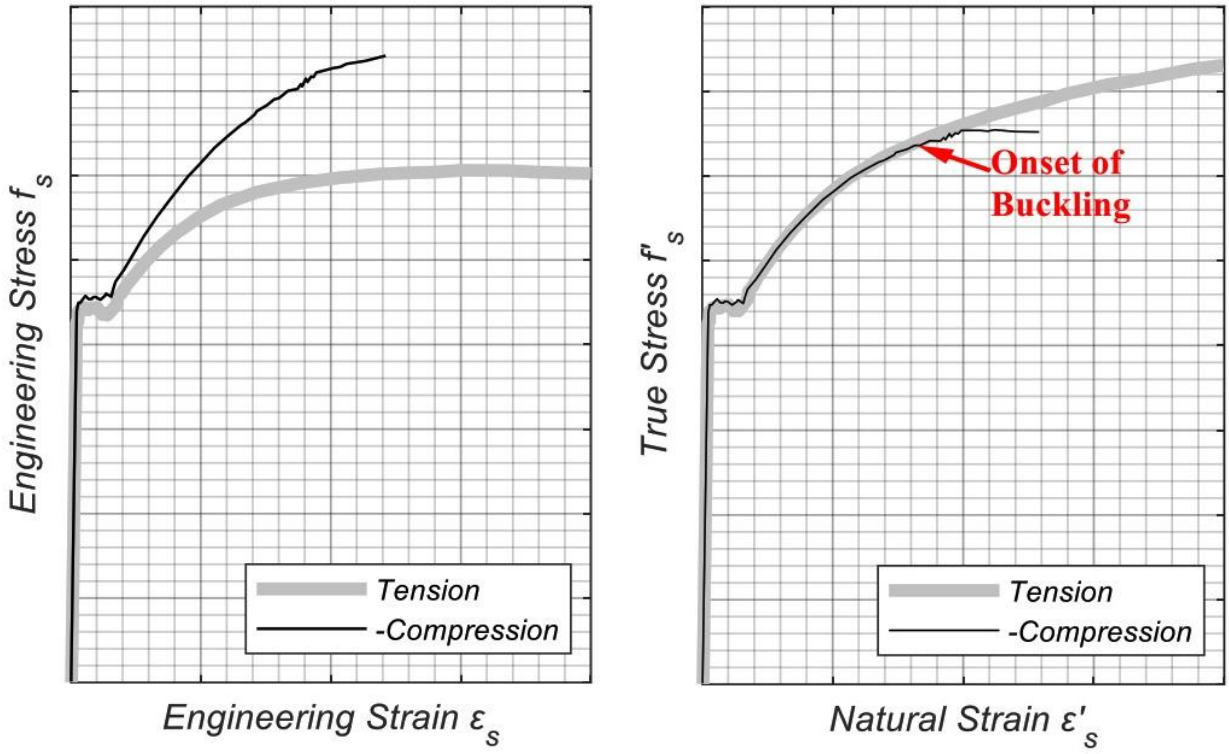


Figure 65. Stress-strain response in engineering and natural coordinates [43].

Eight fundamental parameters define the backbone curve of the original Dodd-Restrepo model: Young's modulus, E_0, yield stress, f_y, strain at the onset of strain hardening, ε_{sh}, uniform strain, ε_{su}, ultimate stress, f_{su}, an intermediate strain-stress pair $(\varepsilon_{sh,1}, f_{sh,1})$ that shapes the hardening branch, and the Bauschinger parameter, Ω_{fac}. All parameters can be directly identified from monotonic tensile coupon tests, except for Ω_{fac}, which is obtained from the area enclosed by the Bauschinger curve and reflects the steel's sensitivity to reverse loading, being strongly influenced by carbon content and microstructural characteristics. Figure 66 summarizes the parameters extracted from the monotonic backbone curve, which define the steel's elastic, yielding, and hardening characteristics under monotonic loading.

The SteelDRC model retains this backbone representation to ensure full consistency with the Dodd-Restrepo framework, preserving the original calibration of the material response under monotonic loading. The subsequent extensions therefore address cyclic behavior exclusively, without modifying the underlying monotonic formulation. In particular, these modifications affect the unloading-reloading response and transition regions, thereby enhancing the model's ability to represent cyclic stiffness evolution while maintaining the integrity of the monotonic curve. Additional mechanisms, including the pinching formulation introduced in this work, are incorporated separately and do not alter the original backbone definition.

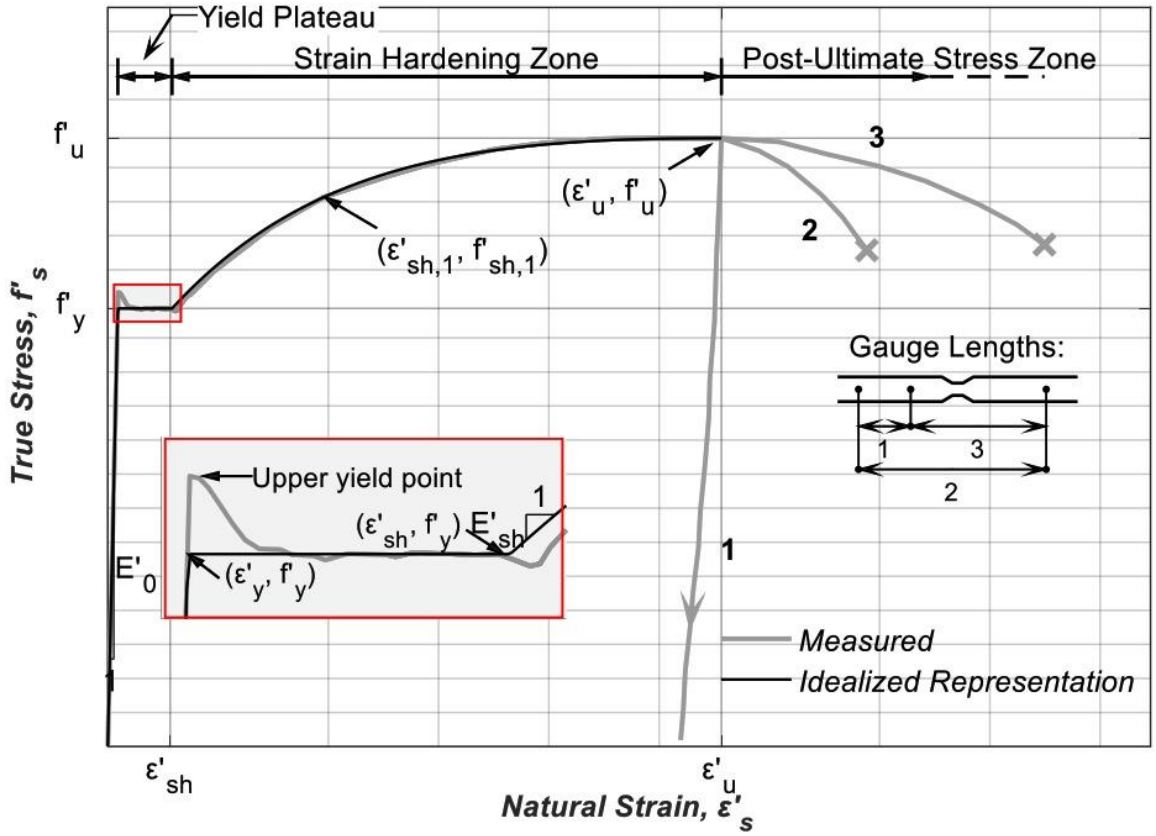


Figure 66. Backbone curve of the Dodd-Restrepo Model - Monotonic behavior [43].

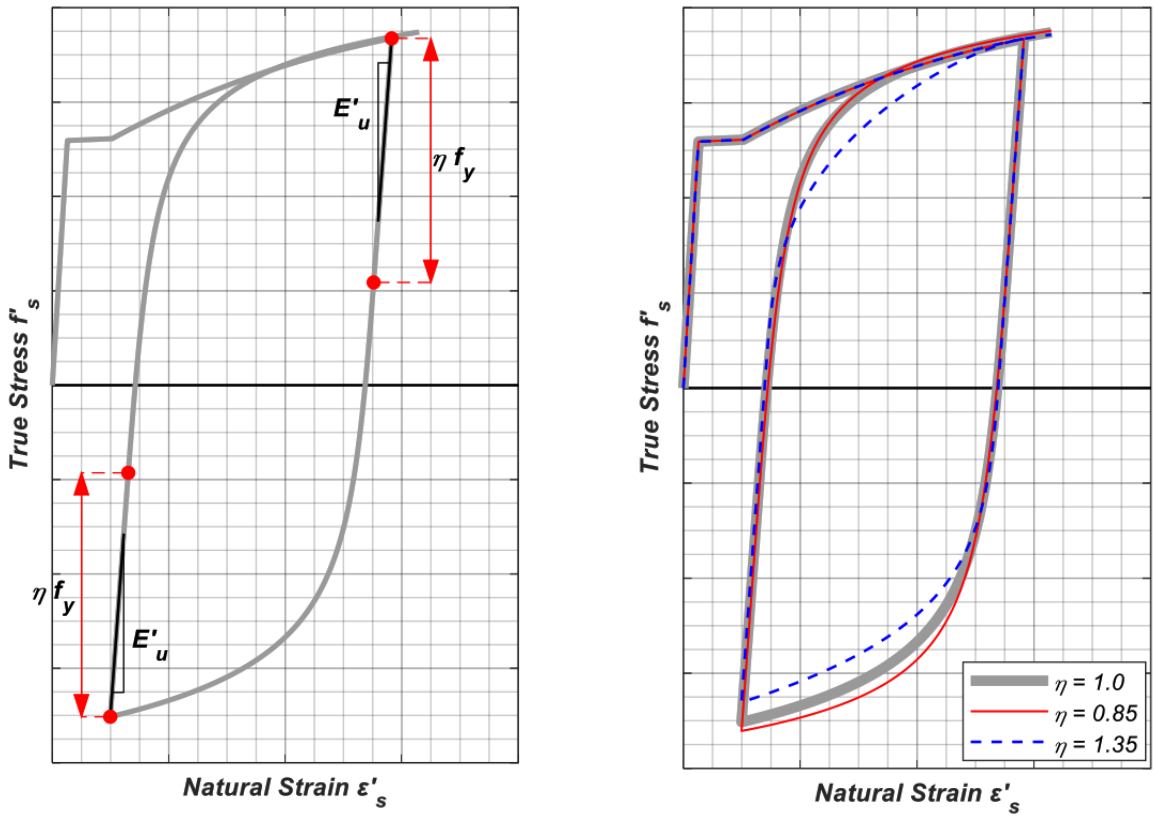
4.6.1 Extent of the Unloading Branch

An unloading-length parameter, η, is introduced to control both the slope and the effective extent of the initial linear segment of the unloading branch immediately following strain reversal. This parameter more accurately represents experimentally observed unloading-stiffness degradation. The unloading stress is given by

$$\sigma_{unload} = \eta f_y \tag{120}$$

Figure 67 shows the influence of the parameter η on the extent of the linear unloading branch following strain reversal.

The parameter η allows precise control over the steel's response during unloading, which is particularly relevant for simulations involving low-cycle fatigue or post-buckling behavior. The left panel defines ηf_y as the extent of the linear unloading branch, with constant modulus E'_u. The right panel compares responses for η=0.85 (red), η=1 (gray), and η=1.35 (blue). Lower η extends the linear unloading segment, delaying nonlinear response, while higher η shortens the linear recovery region and accelerates transition to nonlinear unloading. This parameterization enables calibration of the cyclic response independently of f_y, which remains identified from pure tension tests.



a) Definition of parameter η. b) Variation of hysteretic response for η.

Figure 67. Length of linear unloading branch [29].

4.6.2 Strain-Hardening Branch

An alternative formulation for the strain-hardening branch is provided by introducing a hardening exponent, P, which eliminates the need for an explicit intermediate point $(\varepsilon_{sh,1}, f_{sh,1})$ when detailed monotonic data are unavailable, in the current implementation, the SteelDRC model adopts the formulation proposed by Mander et al. [82] for the work-hardening branch, rather than the original approach by Dodd and Restrepo-Posada [43], while preserving the backbone curve's overall shape and enabling robust calibration with limited experimental information.

$$f_s' = f_{su} - (f_{su} - f_y)\left(\frac{\varepsilon_{su} - \varepsilon_s'}{\varepsilon_{su} - \varepsilon_{sh}}\right)^P ; \; for \;\; \varepsilon_{sh} \le \varepsilon_s' \le \varepsilon_{su} \tag{121}$$

Figure 68 illustrates the sensitivity of the strain-hardening branch to the dimensionless parameter P, which governs the curvature of the post-yield response between the strain-hardening onset (ε_{sh}, f_y) and the ultimate state (ε_{su}, f_{su}). The black curve represents the experimental monotonic test data, while the colored curves depict model predictions for P=1.0 (blue), P=3.7 (gray), and P=8.0 (red).

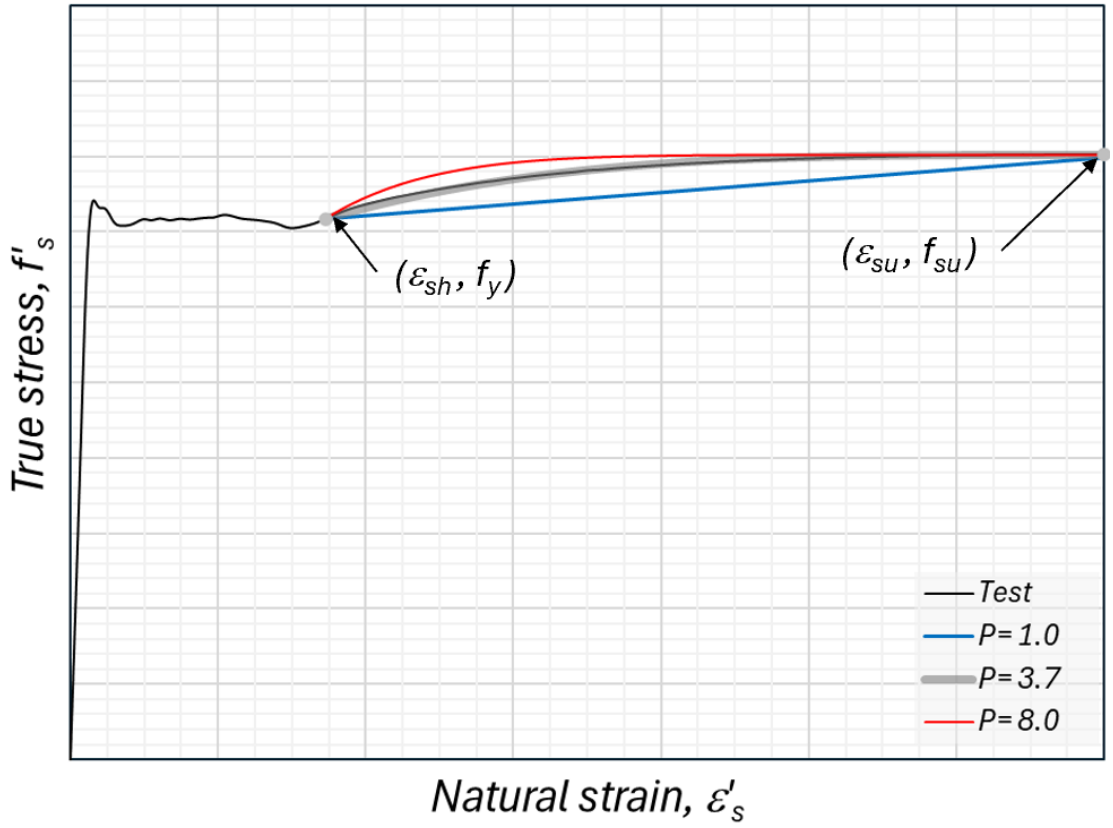


Figure 68. Sensitivity of strain-hardening response to curvature parameter P.

Lower values of P produce an almost linear hardening response with minimal curvature, systematically underestimating the stress level in the intermediate strain range and overestimating it near the ultimate strain. As P increases, the hardening curve develops progressively higher

curvature in the early post-yield region, flattening toward the ultimate state. The intermediate value P=3.7 provides a balanced approximation of the experimental trajectory, capturing the gradual transition from the last point of the yield regime to ultimate strength. The parameter P thus enables independent calibration of the hardening shape without affecting the anchor points at yield and ultimate strength, allowing optimization of the predicted monotonic response for subsequent cyclic simulations.

4.6.3 Closed-Form Bauschinger Curve

A central challenge in modeling cyclic behavior is defining a continuously differentiable curve (class C^1, [70]) that satisfies boundary conditions for strain, stress, and tangent modulus, preserves curvature, and allows control over the area under the curve. In SteelDRC, this is achieved using parametric rational Bézier curves [14], which enable fully closed-form evaluation of stress and tangent modulus while providing precise control over curve shape and smoothness. This approach replaces the original iterative DR procedure, reducing computational cost and eliminating convergence issues, while accurately representing the reverse-loading transition. Unlike other closed-form formulations, such as those based on non-uniform rational B-splines (NURBS) [67], [101], the Bézier-based implementation offers a simple yet flexible parametrization suitable for efficient nonlinear analyses.

Within this framework, the true stress, f_s', at natural strain, ε_s', along the Bauschinger curve can be computed as

$$f_s' = \frac{b_0(t^*)^T \cdot diag(f_p') \cdot w_p}{b_0(t^*)^T \cdot w_p} \tag{122}$$

The Bézier curve is defined in terms of a parametric variable, t^*, which ranges between 0 and 1, associated with the (ε_s', f_s') strain-stress point. The parametric variable, t^*, the term $diag(f_p')$, which denotes the diagonalization of the vector f_p' to a diagonal matrix, and $b_0(t)$, w_p, and f_p' are defined as follows:

$$t^* = \begin{cases} p + \sqrt[3]{r+\sqrt{\Delta}} + \sqrt[3]{r-\sqrt{\Delta}} \\ p - \frac{1}{2}.\left(\sqrt[3]{r+\sqrt{\Delta}} + \sqrt[3]{r-\sqrt{\Delta}}\right) + \frac{1}{2}i\sqrt{3}.\left(\sqrt[3]{r+\sqrt{\Delta}} - \sqrt[3]{r-\sqrt{\Delta}}\right) \\ p - \frac{1}{2}.\left(\sqrt[3]{r+\sqrt{\Delta}} + \sqrt[3]{r-\sqrt{\Delta}}\right) - \frac{1}{2}i\sqrt{3}.\left(\sqrt[3]{r+\sqrt{\Delta}} - \sqrt[3]{r-\sqrt{\Delta}}\right) \end{cases} \tag{123}$$

Vector w_p contains the weight of each characteristic (or control) point of the Bézier curve; parameters ξ_a and ξ_b define the locations of two intermediate characteristic points of the curve, whereas (ε_a', f_a', E_a') and (ε_b', f_b', E_b') define the boundary conditions at each end of the curve.

With,

$$p = -\frac{a_2}{3a_3} \qquad q = \frac{a_1}{3a_3} - p^2$$
$$r = p^3 + \frac{a_1 a_2 - 3a_0 a_3}{6a_3^2} \qquad \Delta = q^3 + r^2 \tag{124}$$

$$b_0(t^*) = \begin{bmatrix} (1-t^*)^3 \\ 3t^*(1-t^*)^2 \\ 3(t^*)^2(1-t^*) \\ (t^*)^3 \end{bmatrix} \qquad w_p = \begin{bmatrix} w_0 \\ w_1 \\ w_2 \\ w_3 \end{bmatrix} \tag{125}$$

The control-point stress vector of the Bézier curve, f_p', is defined as:

$$f_p' = \begin{bmatrix} f_a' \\ f_a' + \xi_a \cdot \dfrac{E_a'.E_b'(\varepsilon_a' - \varepsilon_b') + E_a' \cdot (f_b' - f_a')}{E_a' - E_b'} \\ f_b' + \xi_b \cdot \dfrac{E_a'.E_b'(\varepsilon_a' - \varepsilon_b') + E_b' \cdot (f_b' - f_a')}{E_a' - E_b'} \\ f_b' \end{bmatrix} \tag{126}$$

And the tangent modulus at (ε_s', f_s') can be computed as follows:

$$\frac{df_s'}{d\varepsilon_s'}(\varepsilon_s') = \frac{df_s'}{dt}\frac{dt}{d\varepsilon_s'} = \frac{df_s'}{dt}.\left(\frac{1}{\dfrac{d\varepsilon_s'}{dt}}\right) \tag{127}$$

With

$$\frac{df_s'}{d\varepsilon_s'}(\varepsilon_s') = \frac{\left(b_1^T(t^*).diag\left(f_p'\right).w_p\right)\left(b_0^T(t^*).w_p\right) - \left(b_0^T(t^*).diag\left(f_p'\right).w_p\right)\left(b_1^T(t^*).w_p\right)}{\left(b_1^T(t^*).diag\left(\varepsilon_p'\right).w_p\right)\left(b_0^T(t^*).w_p\right) - \left(b_0^T(t^*).diag\left(\varepsilon_p'\right).w_p\right)\left(b_1^T(t^*).w_p\right)} \tag{128}$$

$$b_1(t^*) = \begin{bmatrix} -3(1-t^*)^2 \\ -6t^*(1-t^*) + 3(1-t^*)^2 \\ -3(t^*)^2 + 6t^*(1-t^*) \\ 3(t^*)^2 \end{bmatrix} \qquad \varepsilon_p' = \begin{bmatrix} \varepsilon_a' \\ \varepsilon_a' + \xi_a.\dfrac{f_b' - f_a' - E_b'.(\varepsilon_b' - \varepsilon_a')}{E_a' - E_b'} \\ \varepsilon_b' + \xi_b.\dfrac{f_b' - f_a' - E_a'.(\varepsilon_b' - \varepsilon_a')}{E_a' - E_b'} \\ \varepsilon_b' \end{bmatrix}$$

The Bauschinger effect is fully characterized by six variables that govern the curve's geometry and area. Parameters ξ_a and ξ_b define the location of the intermediate control points P_1 and P_2, along the asymptotes defined by the slope at the ends of the curve, P_0 and P_3 and the intersection of the asymptotes. While the weights w_0, w_1, w_2, w_3 determine each control point's influence on the curve trajectory. Figure 69 shows improved alignment of Bézier-based predictions with experimental cyclic loops compared with the original iterative model.

The control points (ξ_a, ξ_b), and the weights w_0, w_1, w_2, w_3 are given by

$$\xi_a = \xi_b = 0.9$$

$$w_0 = 1.0 \qquad w_1 = 1.3 \qquad w_2 = 0.7 \qquad (129)$$

$$w_3 = 643e^{-100\Omega}$$

All weights are fixed except w_3, which depends on the internal state variable Ω representing the partial area under the Bauschinger curve. This dependency enables direct control of energy dissipation during reverse loading, ensuring accurate reproduction of experimental cyclic loops.

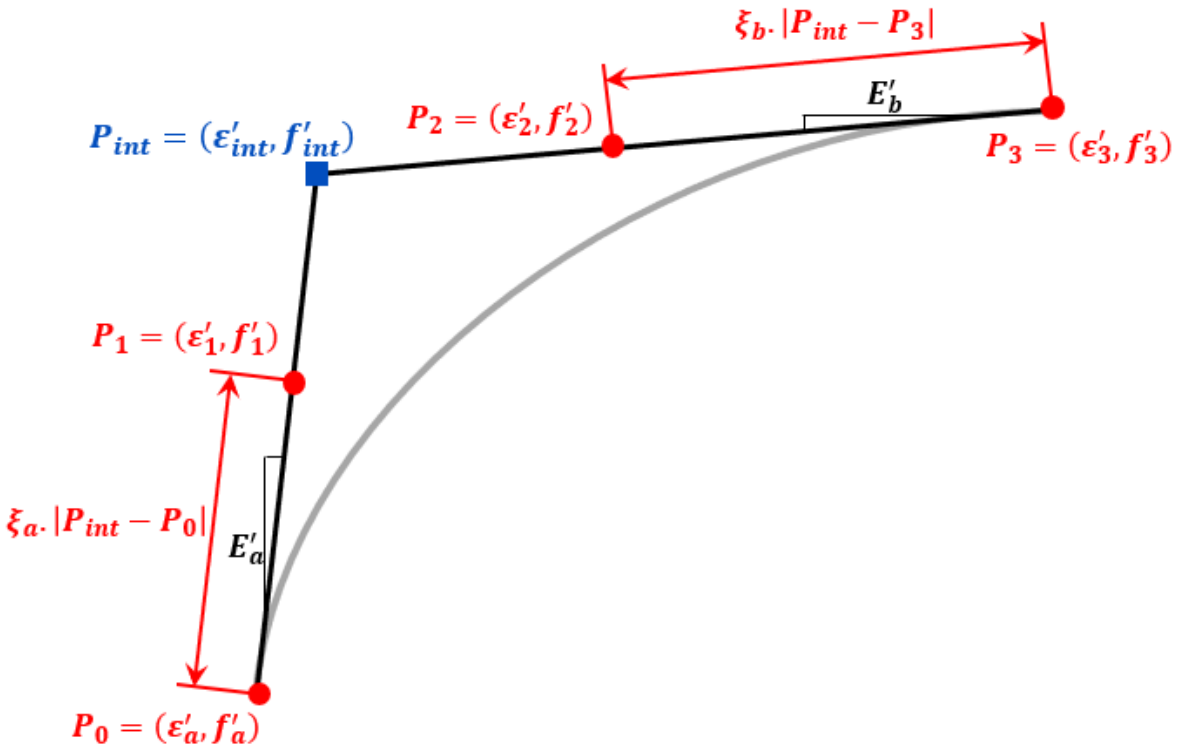


Figure 69. Bauschinger effect representation using Bézier curves [29].

The state variable Ω in the original DR model was defined after transforming and normalizing the true stress and natural strain coordinates of the Bauschinger curve, resulting in a concave function with both normalized-transformed strain, ε''_N, and normalized-transformed stress, f''_N, ranging

between 0 and 1, with infinite slope at the beginning and zero slope at the end (Section 2.2.6). The partial area under the curve, Ω, was then defined as the integral of the normalized-transformed Bauschinger curve between 0 and 0.1, as shown in Eq. (130).

$$\Omega = \int_0^{0.1} f_N''.d\varepsilon_N'' \tag{130}$$

The original DR formulation found an empirical relation to estimate the state variable Ω, based on the non-dimensional variables $\varepsilon_p'/\varepsilon_{su}'$ and f_p'/f_t', as shown in Eq. (131). The model parameter is a scale factor used to fit different steel types.

$$\Omega = \Omega_{fac}.\left[\left[0.001 + \frac{0.00108}{1.043 - \varepsilon_p'/\varepsilon_{su}'}\right]\left(\frac{f_p'}{f_t'} - 0.69\right)\frac{1}{0.18} + 0.085\right] \tag{131}$$

Where ($\varepsilon_p'/\varepsilon_{su}'$) and ($f_p'/f_t'$), are the two non-dimensional parameters: the ratio of plastic to ultimate strain and the ratio of plastic to peak stress, respectively. Ω_{fac}, which controls the shape of the Bauschinger effect in the cyclic stress-strain response, is associated with carbon content, as stated in Section 4.1.3. Figure 70 schematically illustrates the definition of the Bauschinger parameter and its influence on the shape of the reverse-loading response.

Higher values (Ω_{fac}=1, solid line) delay the onset of nonlinear behavior upon strain reversal, extending the linear elastic segment before a sharper transition to the compressive plastic branch. Lower values (Ω_{fac}=0.5, dashed line) introduce earlier curvature with a more rounded, progressively developing Bauschinger effect. Intermediate values (Ω_{fac}=0.75, thin solid line) yield a balanced transition between these extremes.

Figure 71 presents the optimal values of w_3 obtained by fitting both experimental and analytical Bauschinger curves, the latter computed with the original iterative formulation, as a function of the internal variable Ω. The regression analysis yields a coefficient of determination R^2=0.89, indicating satisfactory agreement between the predicted and experimental values.

Figure 72 compares selected experimental stress-strain responses with predictions from both the original iterative formulation and the Bézier-based SteelDRC model. For clarity, all curves were shifted to start at zero stress and zero strain, with loading oriented in the positive direction.

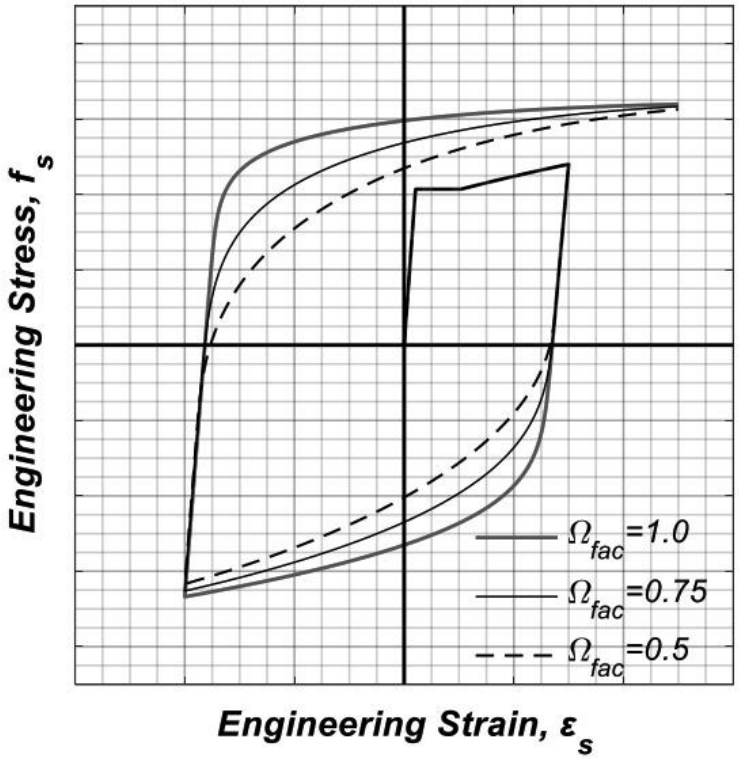


Figure 70. Shape of the Bauschinger effect [43].

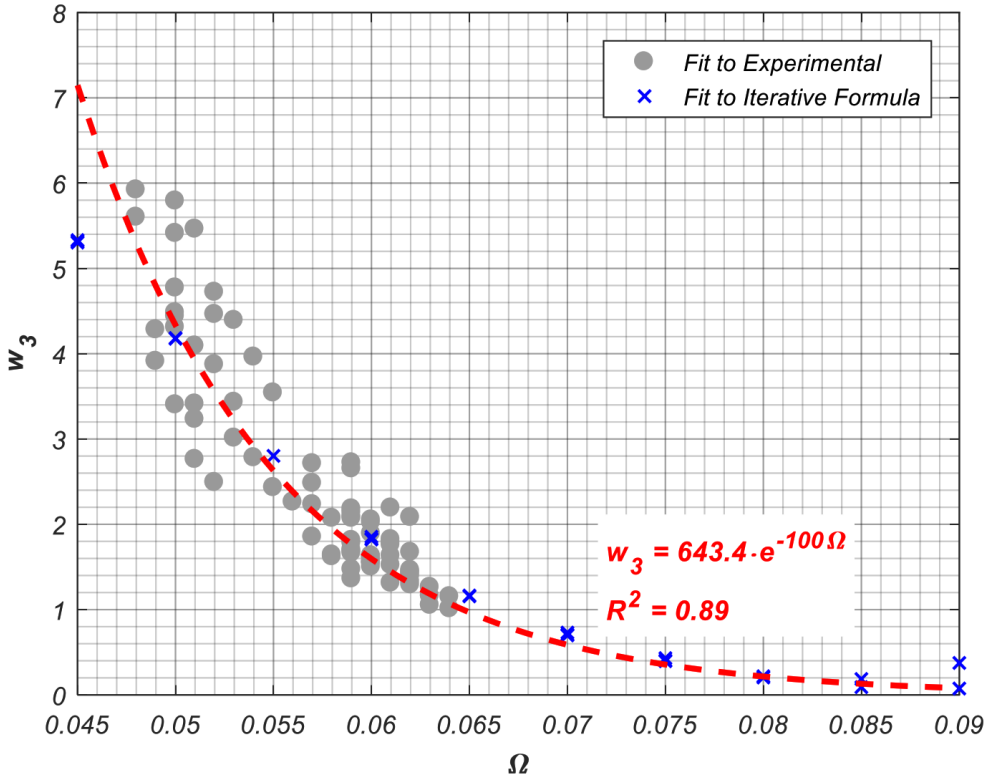


Figure 71. Regression Analysis of Bézier Curve [29].

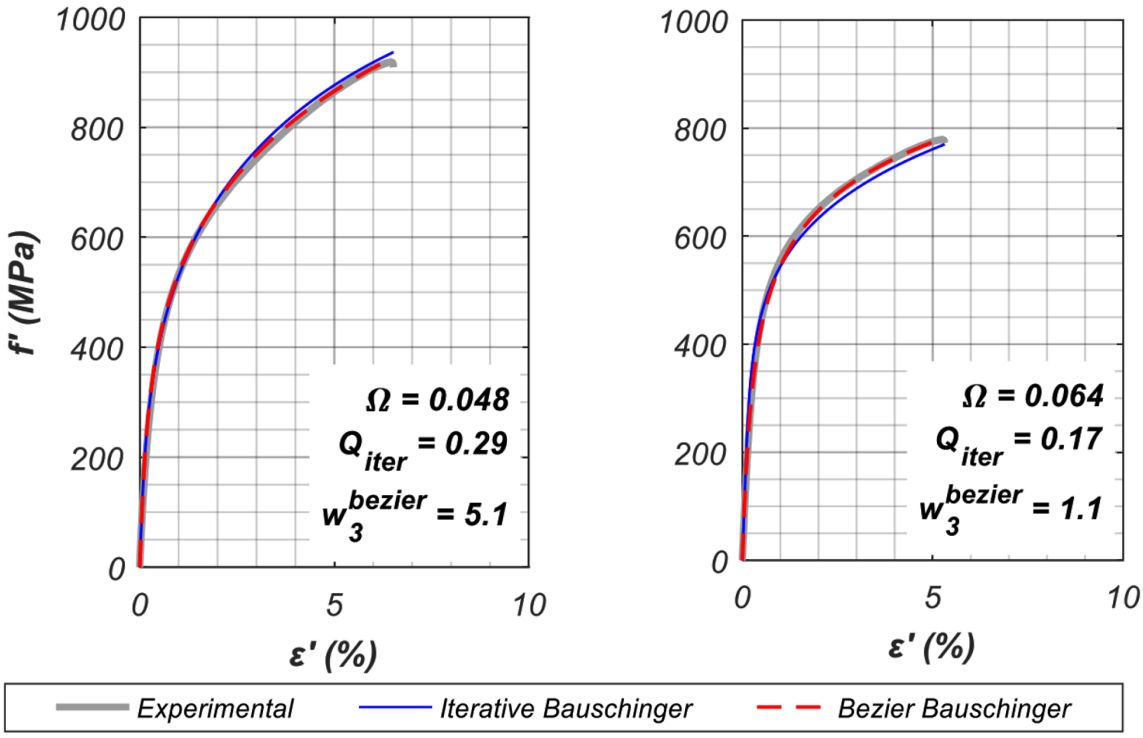


Figure 72. Sample Bauschinger curves [29].

4.6.4 Implementation of Tangent, Secant, and Initial Moduli

The SteelDRC model also provides flexibility to calculate and return the elastic modulus at each integration step during numerical simulations. While this choice does not affect the constitutive behavior, it influences the convergence characteristics of the finite element solution.

Three options are available: the tangent modulus E_T, representing the instantaneous slope of the stress-strain curve and suitable for detailed nonlinear tracking; the initial modulus E_0, corresponding to the steel's elastic stiffness during the initial loading phase, and the secant modulus E_{Sec}, defined between the current stress-strain point and the most recent reversal point as

$$E_{Sec} = \frac{f_s - f_r}{\varepsilon_s - \varepsilon_r} \tag{132}$$

The secant modulus provides a smoothed representation of stiffness along unloading-reloading paths, thereby enhancing convergence in iterative solvers. Figure 73 schematically illustrates these three stiffness options and their implementation within the SteelDRC algorithm, clarifying how each choice influences the numerical solution without altering the underlying constitutive response.

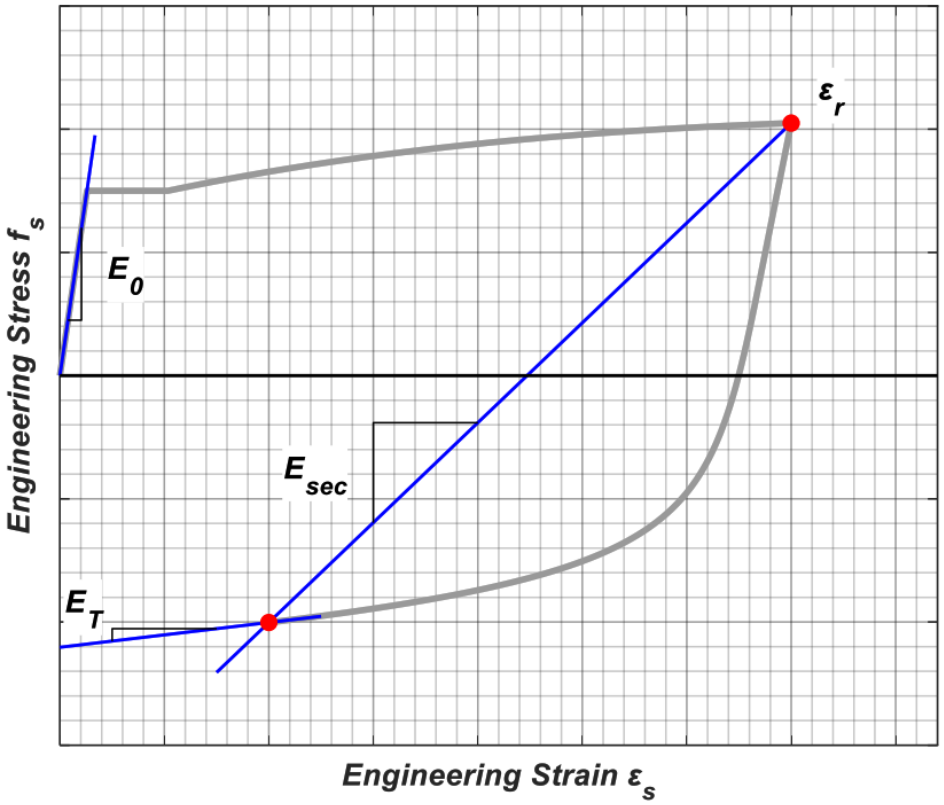


Figure 73. Different options of material modulus [29].

4.6.5 SteelDRC Model Calibration and Verification

The SteelDRC model parameters were calibrated using cyclic stress-strain data from 54 Grade 60 reinforcing steel coupons manufactured in accordance with ASTM A615 and A706. Optimal parameter sets were obtained by minimizing the relative root-mean-square error, defined as

$$error(x) = \sqrt{\frac{\sum_{i=1}^{n}\left(f_{m,i} - f_{p,i}(x)\right)^2}{\sum_{i=1}^{n} f_{m,i}^2}} x100\ [\%] \tag{133}$$

where x is the vector of SteelDRC material parameters, $x = [E_0, f_y, \varepsilon_{sh}, \varepsilon_{su}, f_{su}, P, \Omega_{fac}, \eta]$, $f_{m,i}$ is the measured stress at step i, and $f_{p,i}$ is the predicted stress.

A sensitivity analysis was conducted using the elasticity index, e_s, revealed that $\varepsilon_{sh}$and the hardening exponent Phave the lowest sensitivity, ε_{su}exhibits moderate sensitivity, and f_{su} and Ω_{fac} are the most critical, with elasticity indices reaching up to 18 for ±25% parameter variations:

$$e_s = \frac{\Delta error(x)/error(x)}{\Delta x_i/x_i} \tag{134}$$

When no test data are available, recommended parameter values for unmachined Grade 60 reinforcement are E_0=185 GPa, f_y=480 MPa, ε_{sh}=1%, ε_{su}=10%, f_{su}=728 MPa for ASTM A615 and 656 MPa for ASTM A706, P=3.7, Ω_{fac}=0.85 for A615 and 1.03 for A706, and 1.2 for both.

Verification was conducted at two levels. Independent coupon tests not included in the calibration set confirmed that SteelDRC significantly outperforms the Menegotto-Pinto model (Steel02) in predicting cyclic stress-strain responses. As shown in Figure 74, SteelDRC reduced the maximum tensile stress error from 11% to 1.3%, demonstrating the accuracy of the calibrated parameter set and the robustness of the Bézier-based formulation in reproducing experimental cyclic behavior.

Secondly, the SteelDRC model was rigorously validated through nonlinear finite-element simulations of reinforcing bars subjected to cyclic loading with inelastic buckling. This step is critical, as the interaction between bar yielding, cyclic degradation, and geometric instability presents a significant challenge for constitutive models. The numerical simulations confirmed that SteelDRC not only maintains stability during large-strain excursions but also reproduces the global force-deformation response with high fidelity. In particular, the model accurately captures the asymmetry and strength degradation that occur after strain reversals involving compressive buckling followed by tensile loading. For further details on model calibration and validation, see Carreño [29].

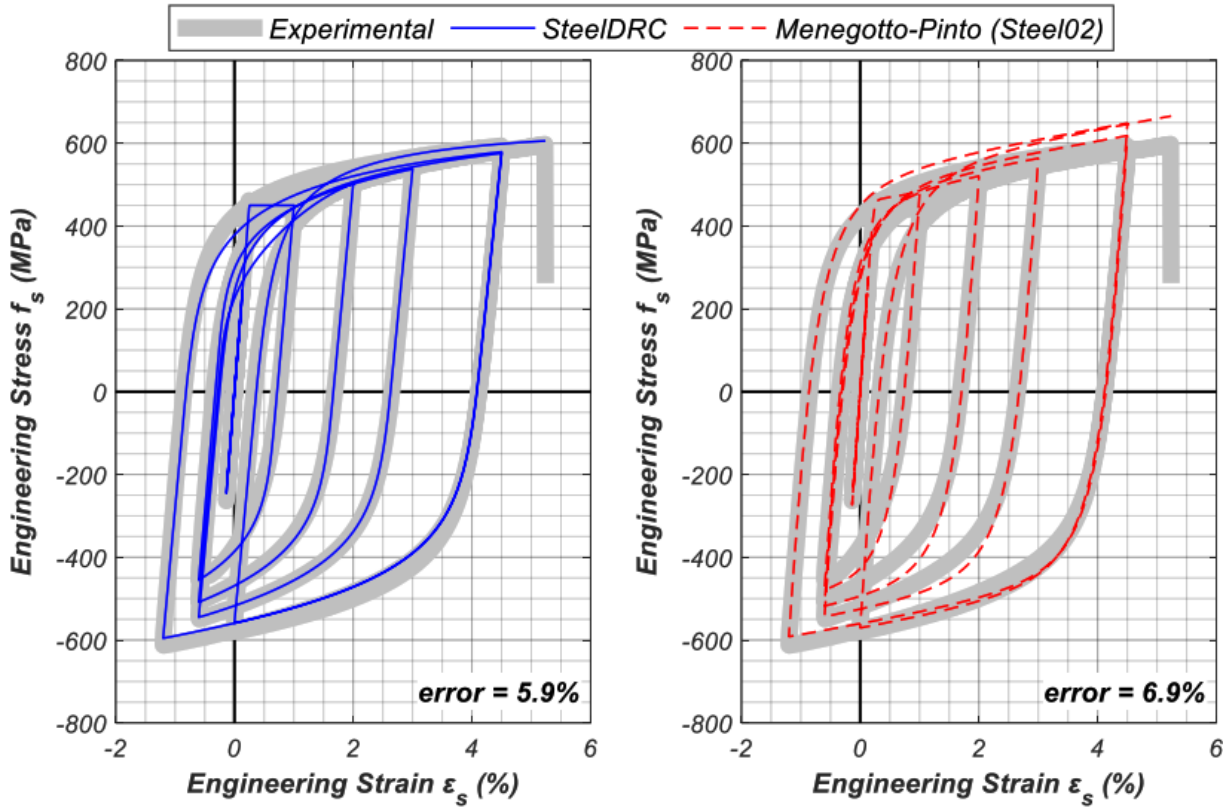


Figure 74. Comparison between the SteelDRC and Menegotto-Pinto (Steel02) constitutive models in OpenSees [29].

A key advantage of SteelDRC is its ability to avoid the spurious strain hardening commonly observed in conventional models during short strain reversals. This improvement results directly from the closed-form Bézier-based Bauschinger formulation and explicit control of unloading stiffness via η.

SteelDRC provides a rate-independent constitutive framework that reproduces the full monotonic response, captures cyclic degradation mechanisms, and ensures numerical robustness in nonlinear finite element simulations. By construction, it does not account for strain-rate effects under seismic loading, motivating a rate-dependent extension presented in the following subchapter. This section introduces the canonical formulation of SteelDRC, including the kinematic assumptions, stress decomposition, yield condition, flow rule, Bauschinger effect, and hardening laws, with all variables and parameters explicitly defined.

4.7 Strain-Rate-Dependent Extension of the SteelDRC Model

Experimental evidence consistently shows that the cyclic response of reinforcing steel under seismic-type loading depends not only on accumulated strain history but also on transient strain-rate variations during loading reversals. In particular, abrupt strain-rate excursions associated with reversal points have been observed to alter the reloading stress level, unloading stiffness, and overall hysteretic loop shape, even when the background or average strain rate remains moderate. These observations indicate that a purely rate-independent formulation, while adequate for describing quasi-static cyclic behavior, cannot fully reproduce the material response under dynamic loading conditions representative of earthquakes.

The experimental characterization presented in the preceding section demonstrates that, under cyclic plastic deformation, the dominant rate effect is not determined by the absolute strain rate but by the magnitude of localized strain-rate excursions over short time intervals. Using a time-window-based analysis that enforces mechanical equivalence (identical strain level and identical monotonic hardening branch), the extracted stress increments isolate the instantaneous contribution of strain-rate excursions at an essentially fixed internal state. This procedure establishes the strain-rate excursion magnitude, $|\Delta\dot{\varepsilon}|$, as the operative variable controlling rate-induced stress amplification during cyclic loading, independently of elapsed time or background deformation rate.

The experimental results further show that these localized stress increments scale in a systematic manner with $|\Delta\dot{\varepsilon}|$, exhibiting an approximately sublinear power-law dependence whose parameters are material-specific and weakly dependent on the hardening state. Importantly, all measured increments lie well below the bounds predicted by classical monotonic dynamic increase factor formulations, demonstrating that rate sensitivity under cyclic plasticity cannot be represented by static multiplicative scaling calibrated from monotonic tests. Instead, the cyclic rate effect manifests as a transient overstress required to sustain localized increases in deformation rate while the macroscopic deformation path remains continuous.

To incorporate these observations into the constitutive description, the SteelDRC model is extended through a strain-rate-dependent formulation that preserves the original rate-independent structure and internal-variable evolution. The extension is introduced in a manner that does not modify the monotonic backbone curve, the Bauschinger formulation, or the unloading and reloading rules

governing cyclic plasticity. Rate sensitivity is incorporated exclusively through an additive viscous overstress acting in parallel with the baseline SteelDRC response, ensuring a clear separation between rate-independent cyclic plasticity and rate-dependent dissipation mechanisms.

Figure 75 decomposes the rate-dependent stress response into hysteretic and viscous components and shows their superposition. The rheological representation consists of the original SteelDRC hysteretic element (captured by f_{shys}) in parallel with a nonlinear viscous dashpot (captured by f_{sd}). The results correspond to one half-cycle of the imposed axial strain history, illustrating the stress partition along a single loading-unloading branch. Figure 75(a) shows the hysteretic backbone and a closed loop upon reversal, preserving the yield plateau, strain hardening, and Bauschinger effect without explicit rate dependence. Figure 75(b) shows the nonlinear viscous dashpot response, representing the rate-dependent stress component over the same half-cycle.

The viscous overstress reaches approximately 50 MPa in tension, whereas in compression it remains around 20 MPa, indicating an asymmetric rate-dependent contribution along the loading-unloading branch. These values are significantly smaller than the ±750 MPa hysteretic stresses, confirming that the rate-dependent mechanism remains secondary to the equilibrium response. Moreover, because the viscous contribution follows the instantaneous strain rate without exhibiting plastic memory or hardening, it represents a purely transient, rate-controlled contribution. Figure 75(c) compares the rate-independent hysteretic response (gray line) with the superimposed response (black line), obtained by placing the hysteretic element and the nonlinear viscous dashpot in parallel.

The viscous contribution increases the peak tensile stress, widening the hysteretic loop while maintaining the yield plateau and kinematic hardening characteristics of the underlying equilibrium backbone.

Within this framework, the total uniaxial stress is decomposed as

$$f_s = f_{s_{RI}} + f_{sd} \tag{135}$$

where $f_{s_{RI}}$ denotes the rate-independent stress computed from the SteelDRC formulation, and f_{sd}, represents the viscous stress contribution associated with strain-rate effects.

Consistent with time-window-based experimental characterization in Section 4.4, the viscous overstress is formulated explicitly in terms of the magnitude of the strain-rate excursion rather than the absolute strain rate, following a nonlinear Voigt-type power law, governed by the strain rate:

$$f_{sd} = sign(\dot{\varepsilon}).k_{rate}.|\dot{\varepsilon}|^{n_{rate}} \tag{136}$$

Where f_{sd} denotes the viscous overstress, $\dot{\varepsilon}$ is the axial strain rate, n_{rate} is the strain-rate sensitivity exponent, and k_{rate} is the viscous consistency parameter.

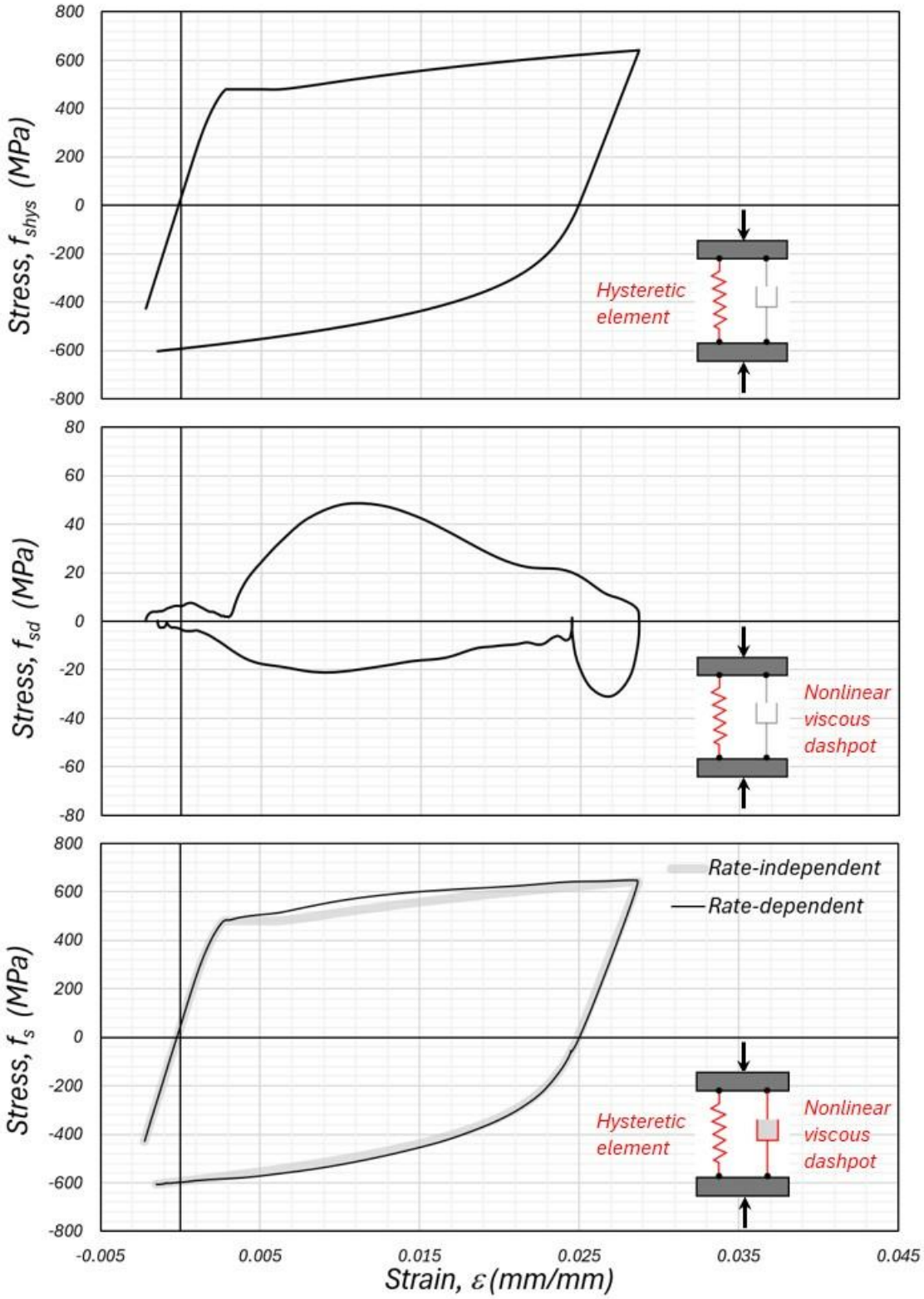


Figure 75. Decomposition of rate-dependent stress response: (a) equilibrium hysteretic component; (b) transient viscous overstress; and (c) superposition of mechanisms.

Since $\dot{\varepsilon}$ has units of s^{-1}, the term $|\dot{\varepsilon}|^{n_{rate}}$ carries units of $s^{-n_{rate}}$, and dimensional consistency requires k_{rate} to be expressed as stress multiplied by time raised to the power n_{rate}, i.e., MPa. $s^{n_{rate}}$ in the SI framework.

Based on the time-window-based experimental characterization, the parameters k_{rate}=125 MPa.s$^{0.75}$ and n_{rate}= 0.75 were identified, establishing a direct quantitative relationship between localized strain-rate excursions and the resulting stress amplification during cyclic plastic deformation. In the US customary system, this corresponds to k_{rate} ≈1.81x10^4 psi.$s^{0.75}$, while preserving temporal invariance.

To remove the implicit dependence of the consistency parameter on the strain-rate scale, the formulation can be reparameterized in terms of a prescribed reference strain rate, $\dot{\varepsilon}_{ref}$:

$$f_{sd,ref} = k_{rate}.\left|\dot{\varepsilon}_{ref}\right|^{n_{rate}} \tag{137}$$

where $f_{sd,ref}$ represents the viscous overstress predicted at the reference strain rate. The constitutive relation can then be written as

$$f_{sd} = f_{sd,ref}.\left(\left|\frac{\dot{\varepsilon}}{\dot{\varepsilon}_{ref}}\right|\right)^{n_{rate}} \tag{138}$$

Here, $\dot{\varepsilon}_{ref}$ is selected to represent the characteristic rate scale of the experimental time window, typically of the order of 10^{-2}-10^{-1} s^{-1}. This reparameterization separates the stress magnitude at the reference rate, $f_{sd,ref}$, from the exponent governing the rate dependence, n_{rate}. Consequently, the two parameters have distinct physical interpretations: $f_{sd,ref}$ controls the magnitude of the viscous overstress at the reference condition, whereas n_{rate} controls how that overstress evolves with strain rate. For illustration, taking $\dot{\varepsilon}_{ref}$=10^{-2} s^{-1} and the material-level parameters identified from the coupon tests, k_{rate}=125 MPa.s0.75 and n_{rate}=0.75, gives

$$f_{sd,ref} = 125(10^{-2})^{0.75} \approx 3.95\ MPa$$

This example illustrates that the numerical value of $f_{sd,ref}$ depends on the selected reference strain rate, whereas the underlying constitutive relation remains unchanged provided that the parameters are transformed consistently. The normalized formulation therefore provides a more transparent representation of the rate-dependent contribution, separating the viscous overstress at a specified reference rate from the exponent governing its evolution with strain rate. This representation facilitates comparison between calibration results obtained at different rate scales and provides a convenient parameterization for implementation within the SteelDRCV model in the OpenSees framework. The resulting power-law relation captures the experimentally observed increase in viscous overstress with localized strain-rate excursions and the sublinear rate dependence associated with the undulation-affected cyclic response.

The choice of a Voigt-type formulation to represent strain-rate effects is directly motivated by the experimental evidence presented in the preceding section and by fundamental considerations of cyclic plasticity under seismic-type loading. The time-window-based characterization demonstrated that rate sensitivity in reinforcing steel manifests as a transient stress amplification associated with localized strain-rate excursions. Meanwhile, the underlying plastic hardening state remains effectively unchanged. This observation indicates that the rate-dependent contribution acts in parallel with the rate-independent plastic response, rather than modifying its evolution.

From a mechanical standpoint, a Voigt-type representation consisting of a rate-independent elastoplastic element in parallel with a viscous overstress mechanism provides a natural, physically consistent description of the observed behavior. In this framework, the total stress is expressed as the superposition of an equilibrium stress governed by plasticity and a viscous overstress governed exclusively by the instantaneous strain rate. This additive structure is fully consistent with classical overstress theories for metals, in which stress amplification at high strain rates is attributed to drag-controlled dislocation motion, such as phonon or electron drag, rather than to any modification of the thermally activated yield mechanism or the hardening laws.

Since the 1960s, viscoplasticity theories have established that the rate of evolution of inelastic strain components depends on the excess stress above a static yield criterion, which generates inelastic strain rates through viscosity-type constitutive relations [68], [100], and [147]. Within this theoretical framework, extensive micromechanical and experimental investigations on aluminum, copper, and both single- and polycrystalline metals [1], [15], [16], [48], [52], and [127] have demonstrated that, as dislocation velocity approaches the shear-wave speed, additional stress components arise due to phonon and electron drag; these contributions scale with strain rate and act additively on the equilibrium stress, while leaving the yield surface and the isotropic and kinematic hardening laws unchanged. Viscous effects, therefore, represent delayed or drag-limited dislocation motion activated under rapid deformation, rather than a change in the underlying plastic flow mechanism.

Although much of the supporting experimental evidence originates from studies on low-alloy face-centered cubic metals, the governing physics is not tied to a specific lattice type or chemical composition. The drag-controlled contribution, commonly expressed through a viscous coefficient proportional to the mobile dislocation density and instantaneous dislocation velocity, reflects a generic resistance to dislocation motion at high rates. This mechanism also applies to body-centered cubic reinforcing steels. Accordingly, the Voigt-type overstress formulation adopted herein is interpreted as a macroscopic representation of rate-dependent dislocation drag, introduced in parallel with the equilibrium plastic response, without altering the yield surface or the hardening evolution of the underlying constitutive model.

Alternative rheological representations, such as Maxwell-type formulations, were not adopted because they introduce rate dependence through stress relaxation and time-dependent evolution of internal variables. Such behavior contradicts the experimental observations obtained herein, which show no evidence of stress relaxation or memory effects once strain-rate excursions subside. Instead, the stress response collapses immediately back to the rate-independent backbone when the strain rate returns to zero. A Voigt-type model intrinsically reproduces this feature, but not by series-type rheologies.

Mathematically, the Voigt formulation preserves the structure of the rate-independent SteelDRC model by leaving its internal variables, flow rule, and hardening evolution unchanged. The viscous overstress depends explicitly on the strain rate and introduces no additional evolution equations. As a result, the constitutive update remains local in time, and the rate-dependent contribution vanishes identically as the baseline SteelDRC response when $\lceil \dot{\varepsilon} \rceil \to 0$.

The Voigt nonlinear power-law form adopted for the viscous stress is consistent with experimentally observed rate sensitivity in steels under dynamic loading, where sublinear exponents are commonly reported and associated with drag-controlled dislocation motion [28], [121], and [150]. Expressing the overstress as a function of the strain-rate excursion rather than the absolute strain rate further aligns the formulation with the undulation-resolved measurements, which demonstrated that instantaneous stress amplification scales with localized changes in deformation rate at an essentially fixed hardening state.

From a numerical perspective, the Voigt-type overstress offers significant advantages for dynamic finite-element simulations. Because the viscous stress is evaluated explicitly from the strain rate and added algebraically to the rate-independent stress, the formulation does not increase the number of internal state variables. It does not introduce additional mechanisms that degrade or relax stiffness and could compromise convergence. This condition is particularly well-suited for seismic analyses of RC members, where large strain reversals, high-strain-rate excursions, and geometric nonlinearities coexist. The nonlinear Voigt-type overstress introduces strain-rate sensitivity without increasing the number of internal state variables or altering the algorithmic structure of the rate-independent SteelDRC model, requiring only the addition of two calibrated material parameters, k_f and n. The viscous stress is evaluated directly from the strain-rate excursion and added to the rate-independent stress, ensuring numerical robustness and stability in dynamic finite-element simulations of RC structures subjected to seismic loading.

In summary, adopting a nonlinear Voigt-type overstress provides a physically motivated, mathematically consistent, and numerically robust way to incorporate strain-rate effects into the SteelDRC model. It directly reflects the experimentally identified mechanism governing cyclic rate sensitivity in reinforcing steel, while preserving the integrity and interpretability of the underlying rate-independent constitutive framework.

Figure 76 presents the experimental stress-strain response (gray lines) of one of the specimens tested at a high nominal strain rate [29], together with predictions from the rate-independent (red lines) and rate-dependent (black lines) formulations. Figure 77 shows a corresponding comparison for a different specimen, exhibiting consistent trends. The rate-independent formulation again underpredicts the stress response, whereas the rate-dependent model captures the amplitude and envelope of the experimentally observed undulations across the loading cycles. The upper inset shows a magnified view of a tension-hardening branch in the strain range approximately -0.9% to -0.3%, whereas the lower inset shows a corresponding detail at strains approximately -0.1% to 0.5%.

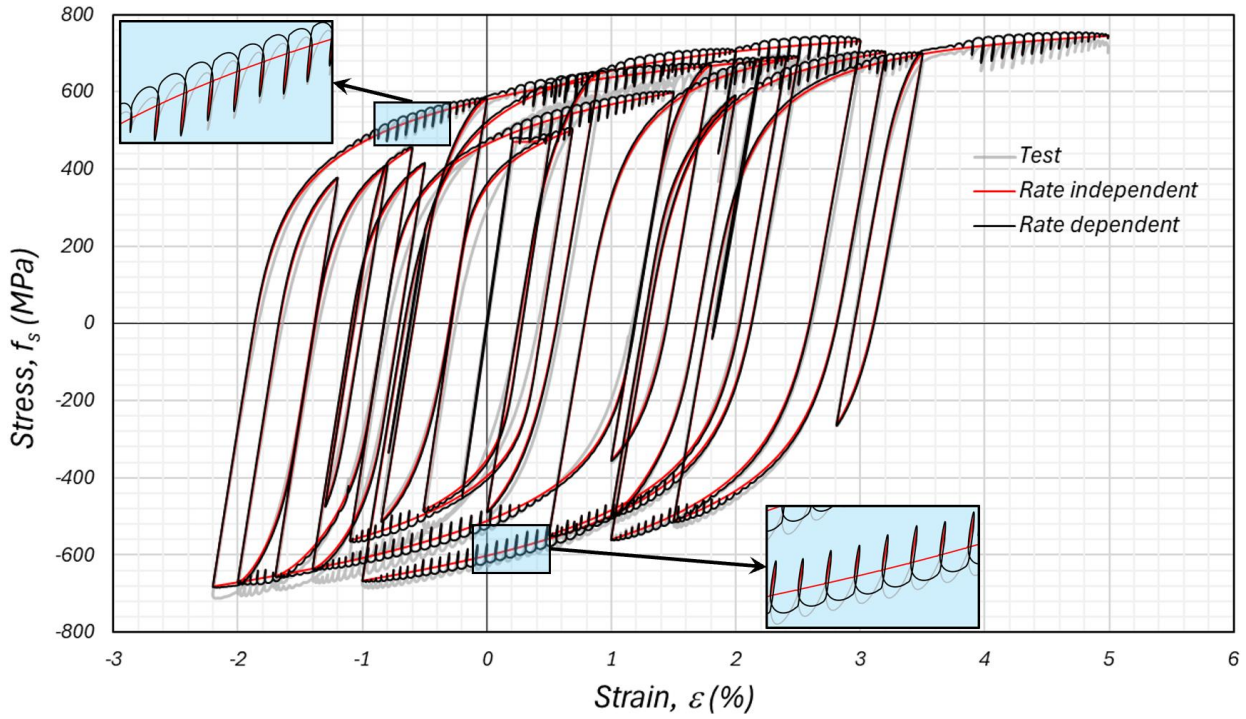


Figure 76. Experimental and SteelDRC-predicted cyclic stress-strain response with and without strain-rate dependence - A79.

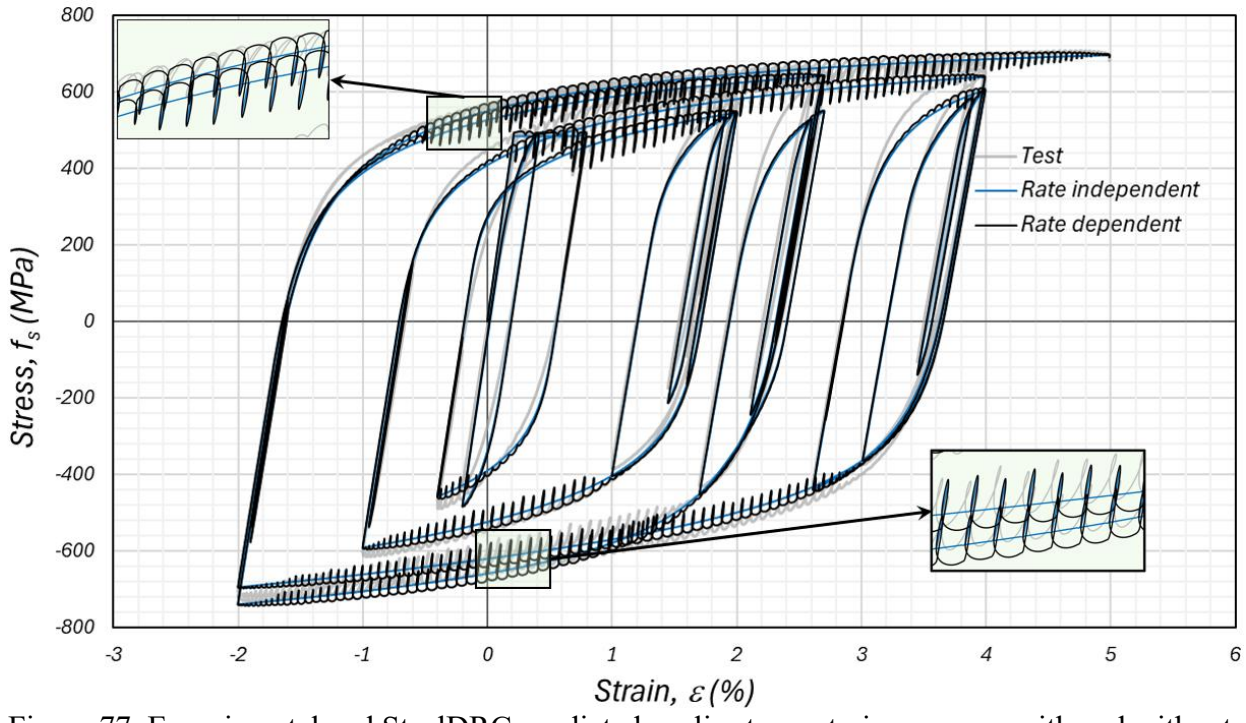


Figure 77. Experimental and SteelDRC-predicted cyclic stress-strain response with and without strain-rate dependence - B78.

The rate-independent model systematically underestimates the response and remains below the experimental stress fluctuations in both loading directions. In contrast, the rate-dependent formulation captures the envelope of the undulation-affected experimental response and reproduces the stress levels observed in the tests.

Across the examined specimens, the rate-independent formulation systematically underestimates energy dissipation per cycle, with an average difference of approximately 4% relative to the rate-dependent model.

4.8 Quadrant-Dependent Bond-Slip Mechanism

The strain-rate-dependent formulation SteelDRCV captures the viscous overstress contribution to the cyclic response of reinforcing steel under dynamic loading. The formulation assumes perfect bonding between steel and concrete, so steel strains are fully compatible with sectional deformations. This assumption neglects bond degradation and the associated accumulation of reinforcement slip. At the structural level, this mechanism manifests as pinching in cyclic force-deformation responses, characterized by reduced stiffness and diminished energy dissipation. The effect arises from the loss of kinematic compatibility at the steel-concrete interface during crack closure and reopening, where insufficient bond stresses allow localized relative displacement to accumulate over successive cycles.

To represent this effect at the structural level, phenomenological pinching parameters are introduced to reproduce the macroscopic stiffness reduction-regain phenomena associated with the collective effects of bond-slip, gradual closure of flexural diagonal cracks, and other mechanisms during cyclic loading. The formulation does not attempt to model the physical mechanisms at the steel-concrete interface. The parameters proposed herein are therefore empirical coefficients calibrated against the global hysteretic response to enable the nonlinear time history of the complex structures, rather than physical descriptors of any details of members.

This phenomenological representation is illustrated schematically in Figures 78 and 79 through the crack opening and closure cycles associated with the observed pinching response. The labels “Fixed End” and “Free End” define the kinematic reference frame. During tensile loading, cracks form and propagate, while bond stresses maintain compatibility between steel and concrete deformations and prevent significant interface slip. This condition persists during tensile unloading as long as the deformation remains tensile. Figure 78 illustrates crack closure, in which concrete shortening induces opposite steel slip, which is resisted by degraded bond stresses.

Although both concrete blocks deform, the schematic representation constrains one end, providing a unique reference for measuring interface kinematics. Within this framework, the interface slip is defined as the relative displacement between steel and concrete, resulting from the incompatibility between steel elongation and concrete deformation. This representation unambiguously identifies the direction of steel slip and the opposing bond resistance. As loading progresses beyond the tensile regime toward compression, crack closure requires the concrete to shorten to reestablish contact between the crack faces. At the same time, the steel retains residual plastic elongation. The reduced bond capacity cannot ensure compatibility, and relative displacement develops as the bar slips within the surrounding concrete, resulting in the observed stiffness reduction.

Once the cracks are closed and the response transitions into compression, steel and concrete deform compatibly, and the response follows the compressive envelope. This condition persists during unloading within the compressive regime, as long as the deformation remains compressive. As loading progresses beyond the compressive regime toward tension, crack reopening requires concrete elongation, while the steel resists extension from compression. During this transition, bond degradation permits relative displacement to develop, generating additional slip in the opposite direction, as shown in Figure 79.

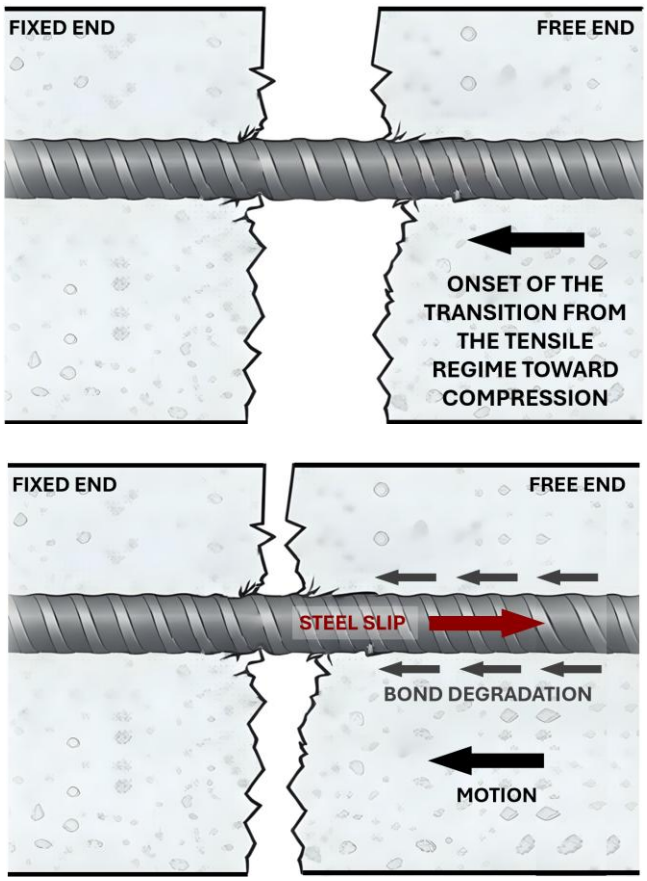


Figure 78. Steel-concrete interface kinematics - Crack closure.

The accumulation of relative displacement during intervals when slip develops at the steel-concrete interface reduces the effective stiffness, producing the characteristic pinched shape of the hysteretic response and the associated degradation of energy dissipation. The present formulation incorporates pinching through a phenomenological approach intended to capture physical mechanisms not explicitly resolved that cause stiffness degradation and hysteretic energy dissipation loss per cycle.

These mechanisms include bond-slip at the steel-concrete interface and flexure-shear interaction. These effects are represented at the material level through an effective modification of the steel stress-strain response. Under fiber-section discretization, the global element behavior is obtained by integrating individual fiber constitutive laws, and interfacial slip cannot be introduced directly without additional degrees of freedom.

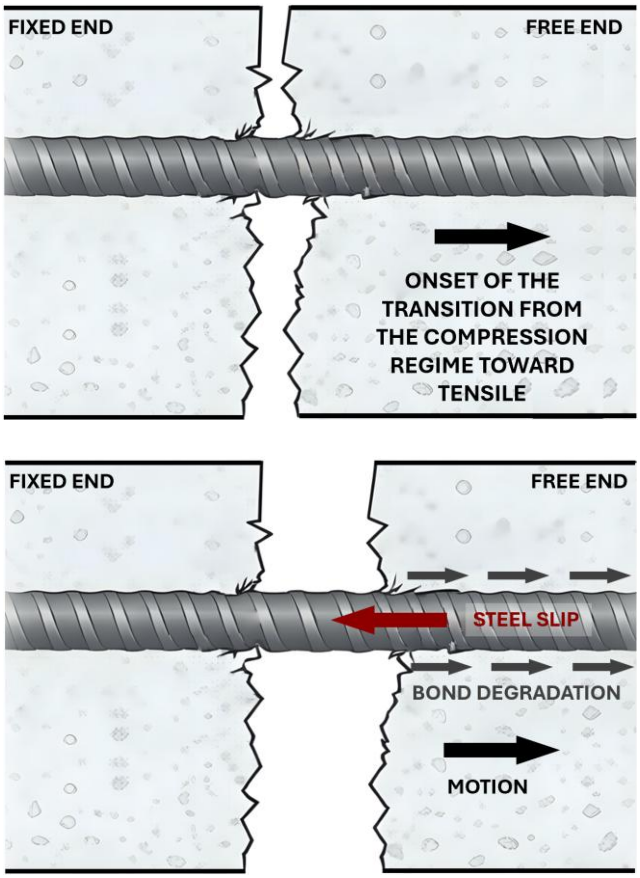


Figure 79. Steel-concrete interface kinematics - Crack opening.

4.8.1 Definition of the β-factor evolution interval

Bond-slip effects are incorporated through a dimensionless curvature factor, hereafter referred to as the β-factor, which controls the rounding of the stress-strain trajectory during relative displacement development at the steel-concrete interface, effectively reducing the local tangent stiffness and reproducing the pinched hysteretic response. The evolution of the β-factor is defined through a smooth transition function that varies between 0 and 1 over a finite strain interval.

In normalized form, the β-factor is given by

$$\beta(\xi) = [\sin(\xi)]^{n_p}$$
$$\xi = \frac{\varepsilon - \varepsilon_{s0}}{\varepsilon_{s1} - \varepsilon_{s0}} \tag{139}$$

where the exponent n_p controls the sharpness of the transition, ε is the current axial strain in the reinforcing steel, and ε_{s0} denotes the strain corresponding to f_s=0 along the current loading branch, i.e., the strain at which the stress-strain trajectory intersects the zero-stress axis. A characteristic strain length governs the interval $\varepsilon_d = \lambda|\varepsilon_0|$, where λ is a dimensionless parameter that defines the strain interval over which the modification develops relative to ε_{s0}. Accordingly, λ controls the portion of the loading branch over which the $\beta(\xi)$ evolves, with larger values extending the

modification and smaller values restricting it to a narrower strain interval. The corresponding maximum admissible terminal strain is given by $\varepsilon_{s1} = \varepsilon_{s0} \pm \varepsilon_d$, with the sign determined by the loading direction. The normalized variable $\xi \in [0, 1]$ ensures that $\beta(0)$=0 at $\varepsilon = \varepsilon_{s0}$ and $\beta(1)$=1 at $\varepsilon = \varepsilon_{s1}$.

Figure 80 illustrates the normalized $\beta(\xi)$ for different values of n_p. The curves show the evolution of $\beta(\xi)$ from 0 to 1, highlighting the influence of the exponent: lower values produce a gradual increase, whereas higher values result in a more delayed and concentrated evolution toward unity.

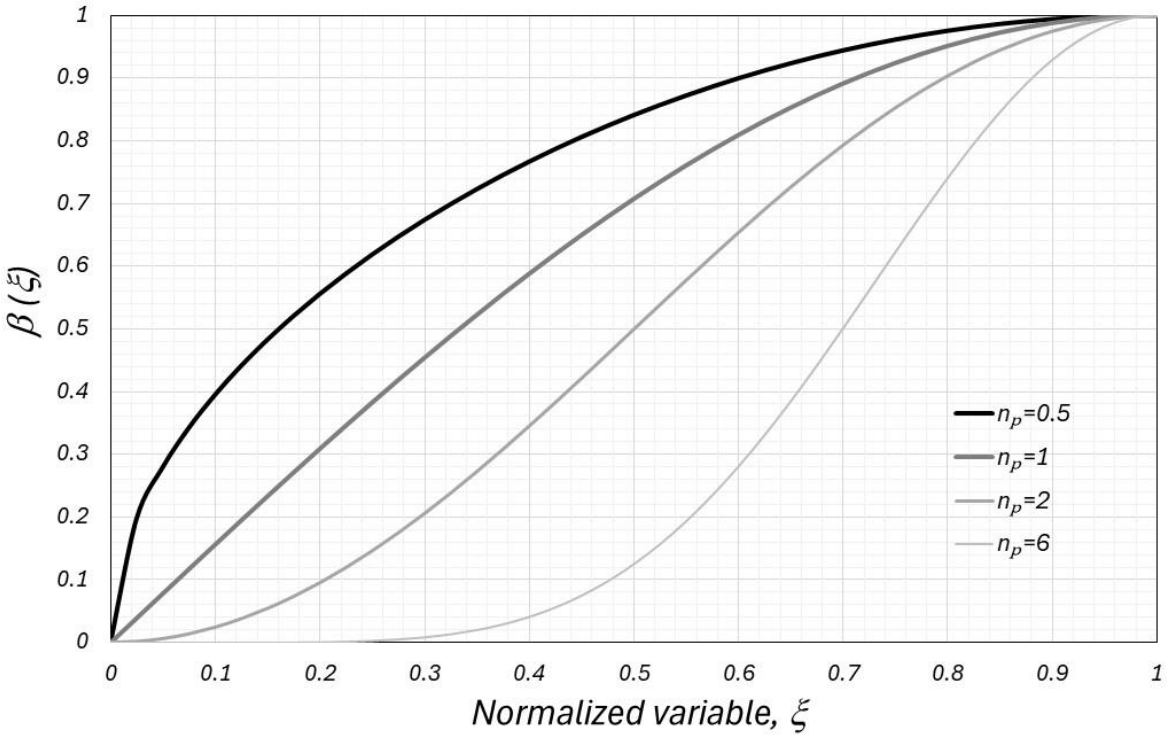


Figure 80. Function $\beta(\xi)$ for different values of the exponent n_p.

For n_p=0.5 (black curve), representing a relatively flexible boundary condition or stiffness transition, $\beta(\xi)$ exhibits a pronounced concave-down profile, reaching approximately 50% of its asymptotic value at $\xi \approx 0.15$, and approaching unity with a steep initial gradient.

For n_p=1 (dark gray curve), the function grows linearly at ξ=0 and approaches unity with zero slope at ξ=1, indicating non-delayed activation and a smooth transition to saturation. As n_p increases, the activation of $\beta(\xi)$ becomes progressively delayed, with the deviation from zero occurring at larger values of ξ and the subsequent rise toward unity becoming steeper. This effect is modest for n_p=2 and the response begins to exhibit noticeable convexity, with reduced growth rates over the initial domain followed by a more pronounced increase as ξ approaches unity. For n_p=6 (lightest gray curve), the function exhibits marked convexity and rapid growth near the terminal region. This asymptotic convergence pattern indicates that the response remains limited over most of the normalized domain and increases rapidly only as ξ approaches unity.

The effective stress, σ_{eff}, is defined as the baseline stress, σ, scaled by the dimensionless β-factor:

$$\sigma_{eff} = \beta(\xi)\,\sigma \tag{140}$$

The corresponding effective tangent stiffness, $E_{t,eff}$, required for the Newton-Raphson iteration is obtained by differentiating the modified stress with respect to the reinforcing steel strain:

$$E_{t,eff} = \frac{d\sigma_{eff}}{d\varepsilon} = \beta(\xi)E_t + \sigma\frac{d\beta(\xi)}{d\varepsilon} \tag{141}$$

where $E_t = d\sigma/d\varepsilon$ is the tangent modulus of the underlying SteelDRCV response. The first term represents the contribution of the modified baseline tangent, whereas the second term accounts for the variation of the β-factor within the transition interval.

Applying the chain rule to Eq. (139), the derivative of the β-factor with respect to strain is

$$\frac{d\beta(\xi)}{d\varepsilon} = \frac{\pi}{2}\frac{n_p}{(\varepsilon_1 - \varepsilon_0)}\sin^{n_p-1}\left(\frac{\pi}{2}\xi\right)\cos\left(\frac{\pi}{2}\xi\right) \tag{142}$$

This derivative describes the rate at which the pinching modification develops within the prescribed strain interval and therefore directly influences the effective tangent stiffness. For $n_p > 1$, the derivative approaches zero at both ends of the interval, whereas for $n_p = 1$, it remains finite at $\xi = 0$. For $0 < n_p < 1$, the derivative becomes unbounded as ξ approaches zero from within the transition interval. Thus, n_p controls not only the shape of the β-factor evolution but also the smoothness of its contribution to the tangent response.

The resulting effective tangent in Eq. (141) is provided to the Newton–Raphson solution procedure together with the modified stress. This formulation maintains consistency between the stress update and its strain derivative throughout the β-factor evolution, allowing the bond-slip-induced modification to be incorporated directly into the constitutive tangent without introducing an additional structural degree of freedom.

For computational implementation, the macroscopic stress-strain response is articulated through a rigorous quadrant-based framework. This formulation provides a systematic methodology for localizing the stiffness reduction that inherently accompanies the development of relative displacement, commonly known as bond-slip, at the steel-concrete interface.

The hysteretic domain is partitioned into four distinct operational quadrants, defined as follows:

1) First quadrant, tensile loading and unloading within the tensile regime, where deformation remains tensile and steel and concrete deform compatibly;

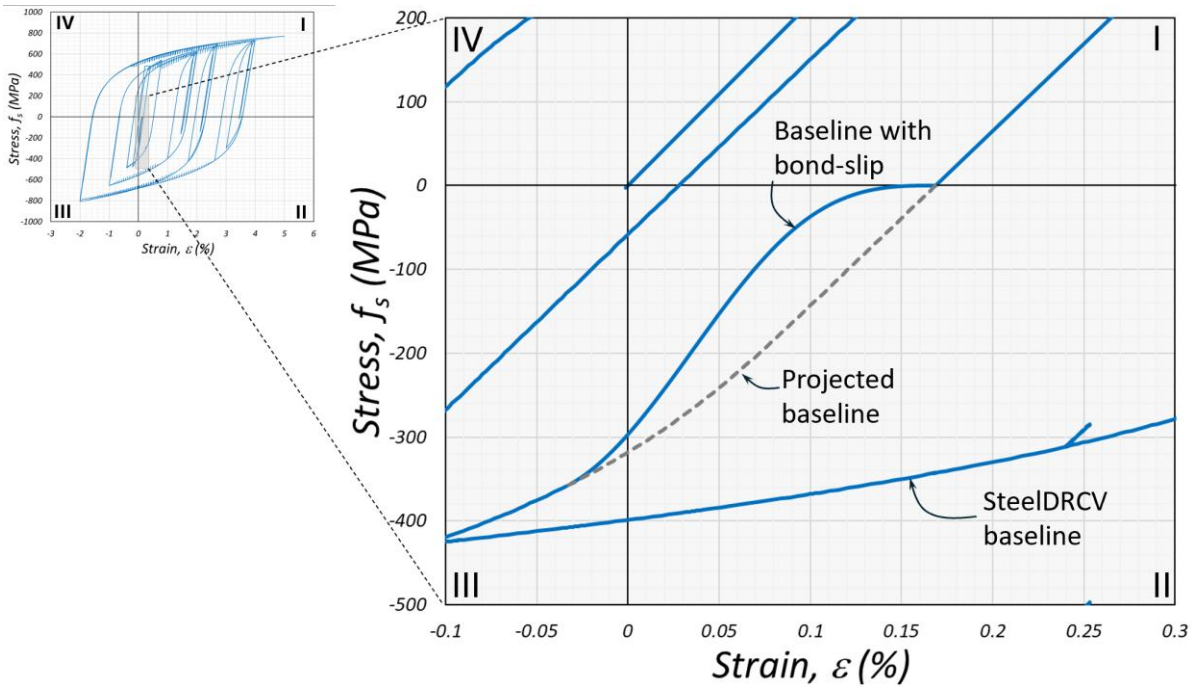
2) Second quadrant, onset of the transition from the tensile regime toward compression, during which crack closure develops, and relative displacement initiates at the steel-concrete interface;
3) Third quadrant, loading and unloading within the compressive regime, where compatibility between steel and concrete is maintained; and
4) Fourth quadrant, onset of the transition from the compressive regime toward tension, during which crack reopening develops, and relative displacement initiates at the steel-concrete interface.

Within this framework, the proposed constitutive modification is selectively activated in the second and fourth quadrants, while the remaining portions retain unmodified baseline behavior, reflecting periods of composite action. Figure 81 illustrates the effect of the designated slip function $\beta(\xi)$ on the hysteretic SteelDRCV baseline response, presenting isolated structural branches to highlight the pinching mechanism in (a) the second quadrant and (b) the fourth quadrant.

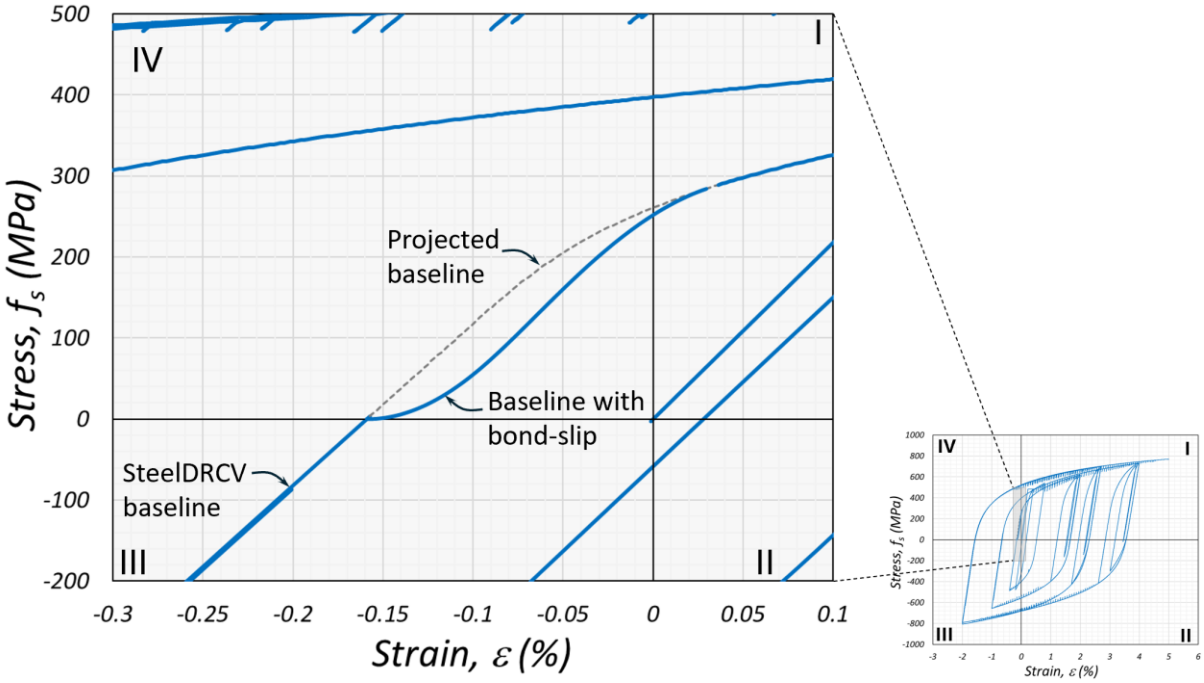
The solid blue curves, labeled 'Baseline with bond-slip,' represent the SteelDRCV response with the activated pinching module ($\beta(\xi) \neq 0$). These trajectories exhibit a pronounced, nonlinear reduction in tangent stiffness over the specific strain intervals where relative displacement accumulates at the steel-concrete interface. Conversely, the dashed gray curve, labeled 'Projected baseline,' indicates the hypothetical, uncoupled SteelDRCV response in the absence of pinching ($\beta(\xi)$=0). This curve illustrates how neglecting interfacial slip artificially overestimates the system's rigidity and its capacity for hysteretic energy dissipation.

Figure 81(a) details the modified response navigating the second quadrant during crack closure. In direct contrast, Figure 81(b) presents the homologous mechanical behavior observed within the fourth quadrant during crack reopening. In both transitional phases, the progressive stiffness reduction manifests geometrically as a smooth, rounded stress-strain trajectory governed by the continuous slip function, standing in stark contrast to the fundamentally sharper kinematic response of the unmodified baseline model.

Consequently, the pinching effect remains confined to the regions of the hysteretic envelope corresponding to active relative displacement intervals, accurately capturing the localized degradation of mechanical interlocking.



a) Second quadrant.



b) Fourth quadrant.

Figure 81. Effect of the function $\beta(\xi)$ on hysteretic response.

4.8.2 Evolution governed by λ

It is noted that the response shown in Figure 81 is obtained using a fixed value of the parameter λ for illustrative purposes, allowing the effect of $\beta(\xi)$ on the stress-strain trajectory to be isolated from variations in the extent of the modification. To examine the role of λ, its influence on the strain interval over which the $\beta(\xi)$ evolves is considered. The characteristic strain length is given

by $\varepsilon_d = \lambda|\varepsilon_{s0}|$, such that the terminal strain becomes $\varepsilon_{s1} = \varepsilon_{s0} \pm \varepsilon_d$. In this manner, λ directly controls the portion of the loading branch affected by the modification.

Figure 82 illustrates the influence of the parameter λ on the stress-strain response for representative values λ=0.5, 0.8, and 1.3, while keeping n_p constant. The curves show that increasing λ expands the strain interval over which the $\beta(\xi)$ evolves, thereby extending the region of reduced stiffness along the loading branch, whereas smaller values restrict the modification to a narrower portion of the response.

Consequently, increasing λ extends the range over which stiffness degradation develops, whereas smaller values confine the effect to a narrow interval localized around the zero-stress crossing. This scaling establishes a direct proportionality between the transition length and the reference strain $|\varepsilon_{s0}|$, ensuring consistency with the activation strain level. Phenomenologically, this flexibility enables the constitutive model to reproduce the macroscopic effects of progressive bond-slip deterioration and gradual crack closure at varying levels of accumulated damage, without resolving the underlying physical mechanisms of bond degradation, rib-concrete interaction, or confinement loss. The parameter λ controls the strain extent over which this phenomenological stiffness reduction develops, and its value is established through calibration against the observed hysteretic response rather than derived from bond-slip mechanics. Accordingly, λ governs the spatial extent of the pinching zone while preserving a fixed initiation point, thereby maintaining continuity of the response at the onset of the transition and preventing artificial distortions in the stress-strain trajectory. Preserving C^0 continuity is essential to ensure numerical stability and smooth tangent-stiffness updates during nonlinear iterative solution procedures. All cases initiate at ε_{s0}=0.1687, corresponding to the point where f_s=0. For λ=0.5, the modification terminates at ε=0.0843, remaining entirely within the second quadrant. For λ=0.8, the terminal strain reduces to ε=0.0337, approaching the quadrant boundary. For λ=1.3, the terminal strain ε=-0.0506 exceeds this boundary, indicating that the modification extends beyond the second quadrant and penetrates the third quadrant. This penetration into the negative strain domain reflects highly degraded material states, where extended compressive excursions are required to fully close residual crack widths and recover baseline stiffness.

These parametric results confirm that λ strictly governs the kinematic extent of the pinching region along the strain axis, without altering the underlying mathematical functional form of the transition.

The dashed line represents the projected baseline response, formulated in the absence of pinching phenomena. It serves as a theoretical upper bound for quantitatively assessing the magnitude of tangent-stiffness degradation. Furthermore, the integrated area enclosed between this idealized baseline and the modified transition curve provides a direct physical measure of the localized reduction in hysteretic energy dissipation capacity inherent to the pinching mechanism, accurately capturing the system's diminished damping potential. The responses shown in Figure 82 correspond to loading paths in which no reversal occurs before the strain excursion defined by λ is reached. This configuration isolates the effect of λ on the transition extent and defines the outer envelope governing the maximum admissible modification length. Scenarios involving premature reversals, which interrupt the λ evolution and generate internal hysteretic sub-cycles, are addressed separately to complete the generalized cyclic formulation.

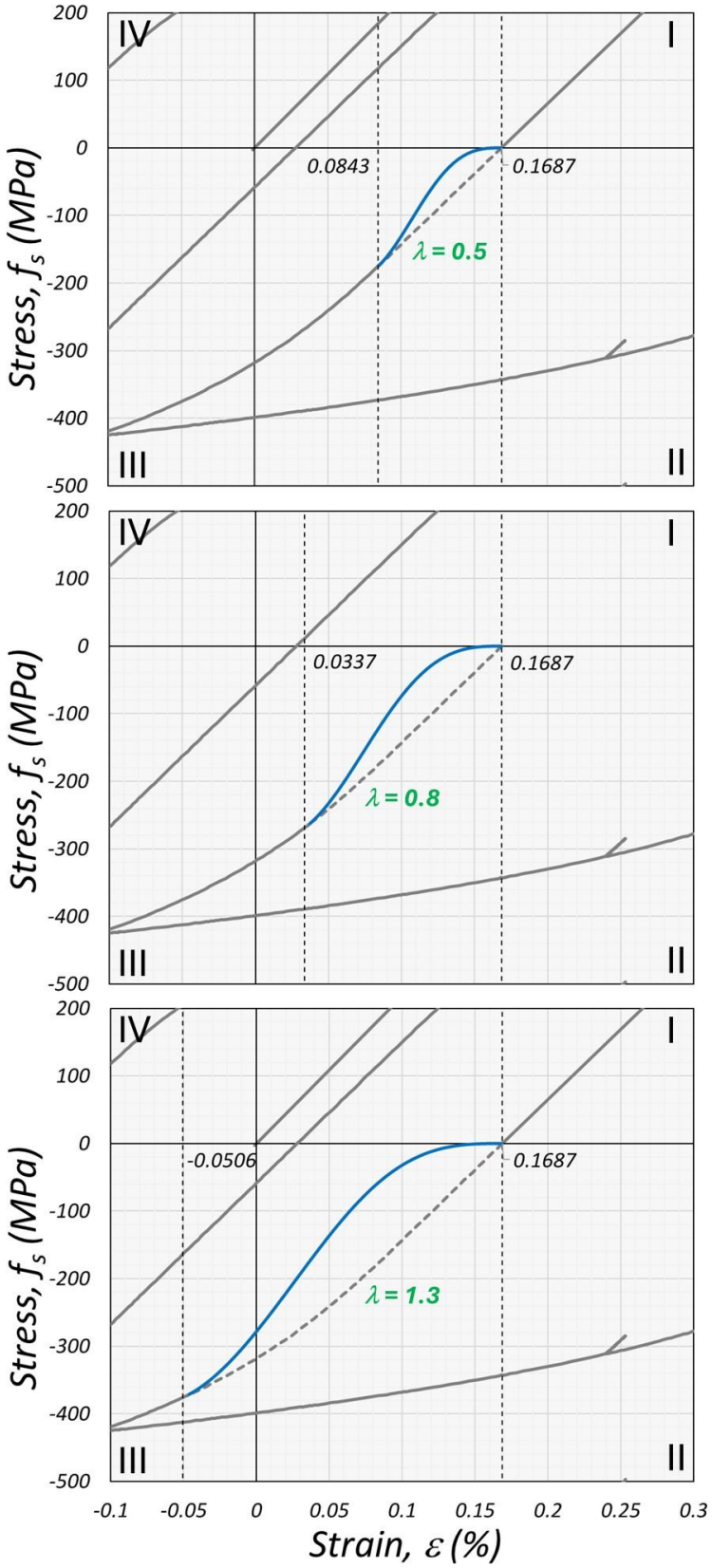


Figure 82. Influence of the parameter λ on the extent of the pinching zone.

4.8.3 Truncated evolution due to reversal

The formulation is now extended to loading paths involving reversal before completion of the strain excursion defined by λ. In such cases, the evolution of the β-factor does not reach the terminal strain ε_{s1}, and is instead interrupted at the reversal strain ε_r'.

Accordingly, the effective terminal strain is given by

$$\varepsilon_{s,end} = min(\varepsilon_{s1}, \varepsilon_r') \tag{143}$$

Figure 83 illustrates the case where load reversal occurs before completion of the strain excursion defined by λ. The solid curve shows the response with β-factor evolution truncated at the reversal strain, ε_r'=-0.141%, at which a stress of -329 MPa is attained. The dashed curve represents the projected SteelDRCV baseline in the absence of pinching (β=0); both responses are evaluated at the same reversal strain, for which the baseline reaches -561 MPa.

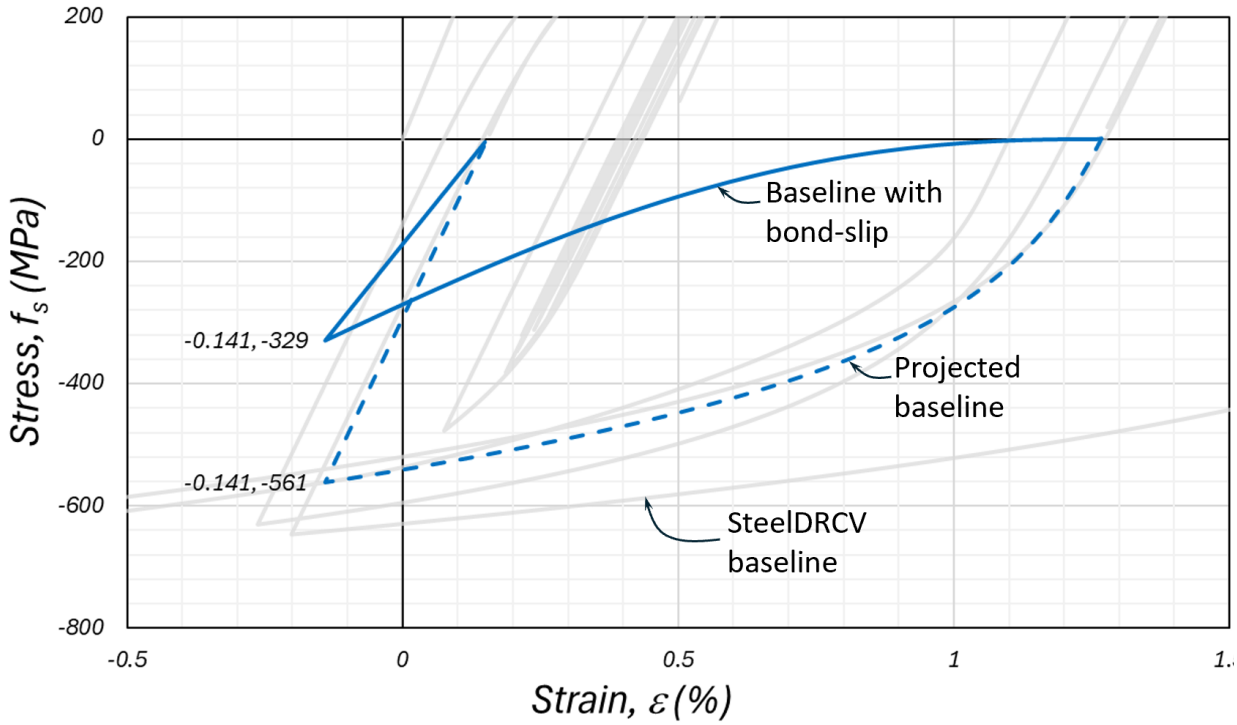


Figure 83. Effect of load reversal on the truncation of the β-factor evolution.

The difference $\Delta\sigma$=232 MPa quantifies the reduction in stress resulting from the incomplete development of the pinching mechanism at the reversal point. This behavior reflects the modification's limitation to the strain interval effectively reached along the loading path, so the stiffness reduction develops only over the portion of the transition physically attained before reversal. As a result, the extent of the pinching zone is governed not only by λbut also by the strain history. Early reversals lead to a truncated evolution of the β-factor, whereas responses approaching ε_1 progressively converge toward the fully developed case defined by the complete strain

excursion. Accordingly, the degree of stiffness reduction attained at reversal depends on the fraction of the transition interval that has been traversed. This dependency introduces a path-dependent mechanism in which the response evolves with the loading sequence, linking the degree of pinching directly to the imposed strain history without requiring additional internal variables.

4.8.4 Cyclic Stress-Strain Response with Pinching

This section presents the simulated cyclic stress-strain response of the proposed formulation under prescribed variable-amplitude strain histories. The objective is to systematically evaluate the global hysteretic behavior induced by the β-factor, with particular emphasis on tangent stiffness degradation, loop pinching, and the associated reduction in cumulative hysteretic energy dissipation relative to the uncoupled SteelDRCV baseline model.

Figures 84-86 illustrate the cyclic stress-strain response corresponding to the empirical experimental strain histories obtained from the reinforcing steel specimens previously described in Section 4.1. To illustrate and capture inherent variations in material properties, one representative test case is selected for each manufacturer: A68, B69, and C79, respectively.

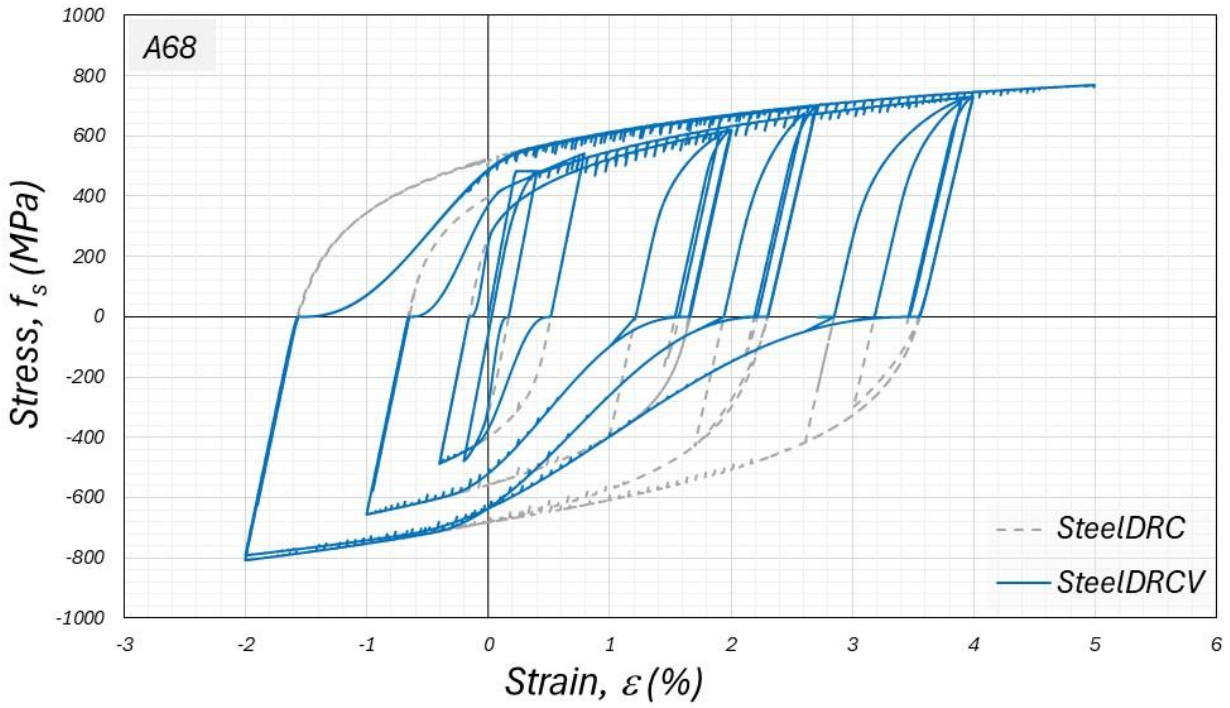


Figure 84. Comparison of cyclic stress-strain response with and without pinching - A68.

Each figure critically compares the analytical response predicted by the proposed coupled formulation with that of the idealized SteelDRC baseline, highlighting the progressive development of pinching, the associated stiffness reduction during the loading-reversal transition phases, and the resulting macroscopic decrease in energy dissipation. The stiffness reduction develops over the transition intervals, during which relative displacement evolves at the steel-concrete interface, producing a rounded stress-strain trajectory and contracting the hysteretic loops in these segments.

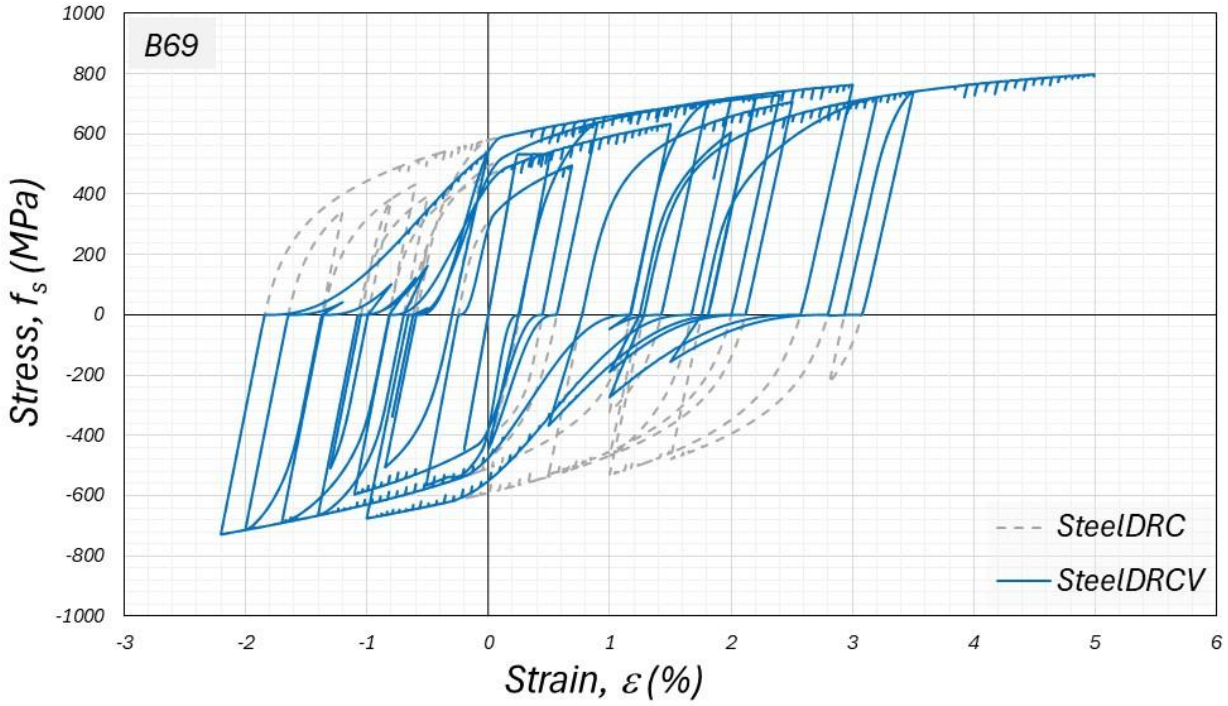


Figure 85. Comparison of cyclic stress-strain response with and without pinching - B69.

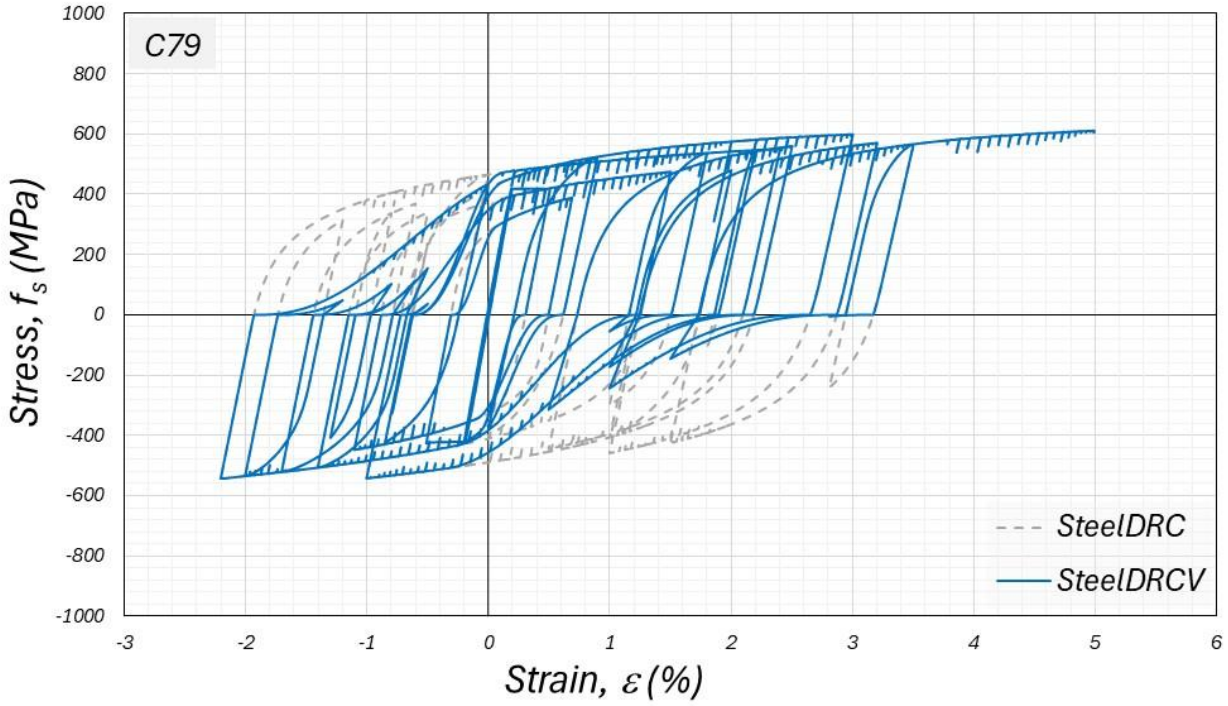


Figure 86. Comparison of cyclic stress-strain response with and without pinching - C79.

Differences in loop shape and pinching intensity reflect variations in the underlying material response. In contrast, the baseline response exhibits stable hysteretic loops with full stiffness

recovery. The reduced loop area in the modified response indicates lower energy dissipation per cycle, consistent with the physical mechanisms incorporated in the model.

4.8.5 Structural-level strain histories and material response

The experimental program included the two full-scale RC specimens, both designed to develop well-defined plastic hinge regions under seismic excitation. Dynamic tests conducted on the LHPOST shake table subjected the specimens to realistic earthquake ground motions, enabling direct observation of nonlinear behavior, including stiffness degradation, strain accumulation, and energy dissipation. While the preceding results establish the constitutive response at the material level based on reinforcing steel specimens, this section examines the implications of the proposed formulation using experimentally recorded strain histories from the full-scale tests described in Section 3.2. Although these histories originate from structural response, the comparison is performed at the material level through stress-strain relationships derived from instrumented reinforcing bars.

Figures 87 and 88 present empirically derived, representative cyclic stress-strain responses for strategically instrumented reinforcing bars embedded within the 7-story wall-building and the bridge column specimens, respectively. The recorded results correspond to local measurements from strain gauges EQ4-A4_3 (wall specimen) and EQ3-WS3 (bridge specimen), which were purposefully selected as representative cases to illustrate the complex, localized hysteretic behavior under distinct global structural demands.

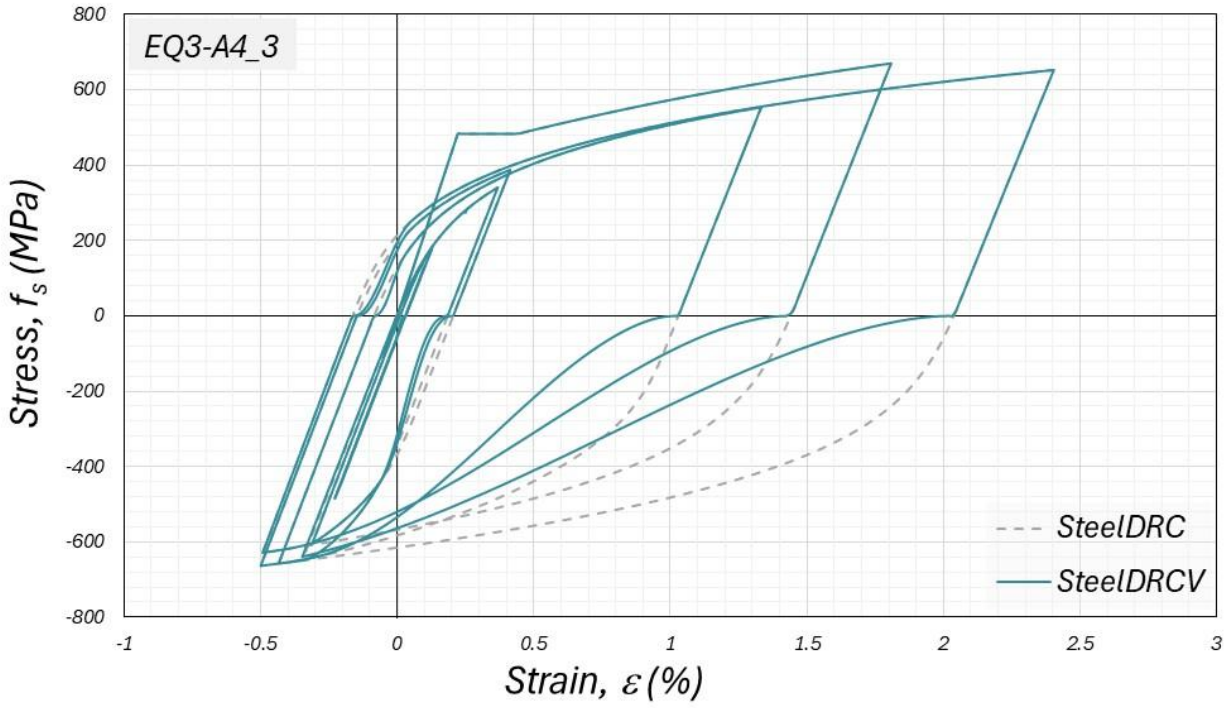


Figure 87. Comparison of simulated and measured stress-strain response of instrumented reinforcing bars - Wall-building.

The results show that the proposed formulation reproduces the cyclic stress-strain behavior under strain paths imposed by structural response, including pinching and associated stiffness degradation.

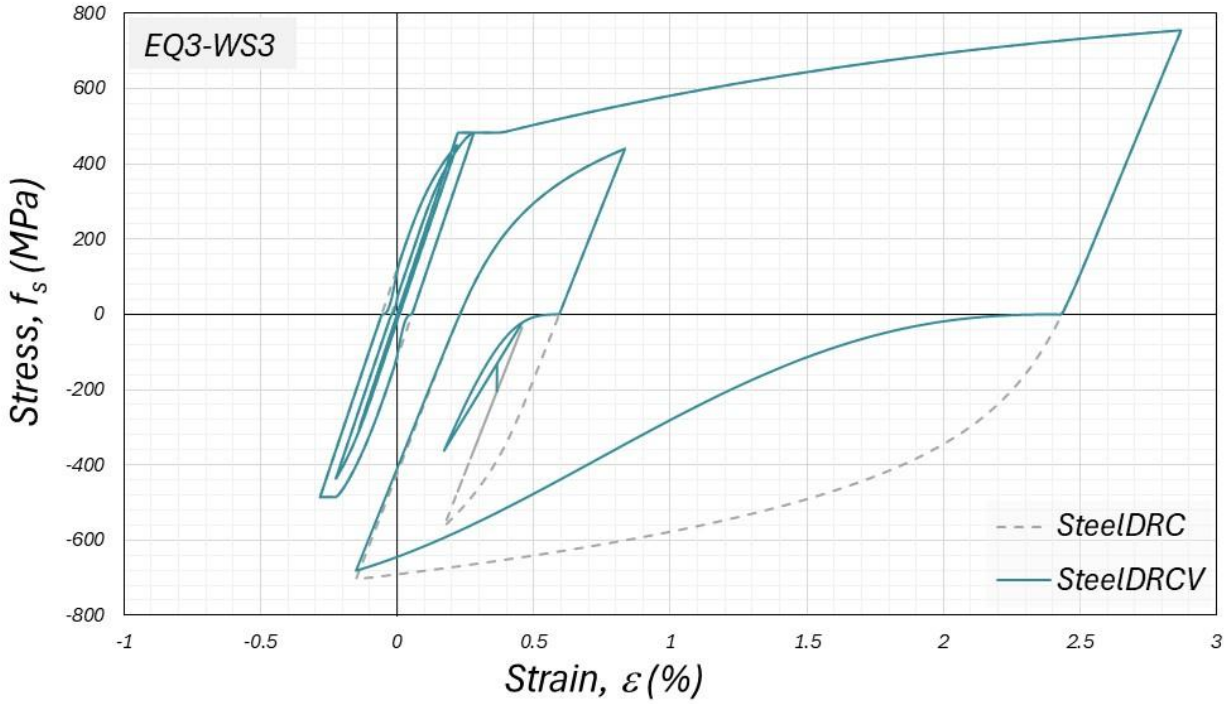


Figure 88. Comparison of simulated and measured stress-strain response of instrumented reinforcing bar - Bridge column.

Differences in loop shape and pinching intensity arise from the imposed strain histories and reflect the local response captured by the instrumentation. The comparison between the baseline SteelDRCV response (β=0) and the modified formulation ($\beta \neq 0$) highlights the influence of the β-factor on the predicted stress-strain behavior under complex, history-dependent loading conditions derived from full-scale structural response.

4.8.5.1 Parametric Study on λ and n_p

Figures 89-96 and 97-104 present a parametric study of the influence of the dimensionless bond-slip parameters λ and n_p on the cyclic stress-strain hysteretic response of SteelDRCV, with the baseline SteelDRC response shown for reference. The imposed strain histories correspond to the strain-gauge records from bridge-column specimen EQ5-EN5 (Figures 89-96) and experimental test B79 (Figures 97-104), respectively, as described previously. Both parameters varied from 0.5 to 4.0.

Across all parameter combinations, SteelDRCV and SteelDRC exhibit identical elastic unloading-reloading branches, with slopes approximately equal to the initial elastic modulus, confirming that the bond-slip formulation does not modify the elastic backbone of the parent SteelDRC model. The models differ only during inelastic reloading, where SteelDRCV develops pinching while SteelDRC retains an open hysteretic response. At low λ, SteelDRCV closely follows SteelDRC,

whereas increasing λ progressively extends the pinched region, contracts the hysteretic loops, and reduces the enclosed area, indicating stronger bond-slip effects and lower energy dissipation per cycle. For a fixed λ, increasing n_p produces increasingly flattened reloading branches near zero stress, followed by an abrupt recovery of the previously established hardened yield stress as bond engagement is partially restored.

Based on these response characteristics, the operational ranges were established as λ=0.5-2.5, with a default value of 1.5, and n_p=0.5-3.5, with a default value of 1. The upper limit of λ corresponds to the onset of excessively severe pinching. For λ>3, the reloading branches flatten into near-horizontal segments around zero stress over strain ranges exceeding 1.5%, producing responses that deviate substantially from experimentally observed behavior under conventional cyclic loading. Similarly, the upper bound of n_p=3.5 was defined by the transition observed at n_p>3, where the reloading branches exhibit an unrealistically abrupt stiffness recovery following extreme pinching, suggesting numerical instability rather than a physically representative bond-slip response.

The default values, λ=1.5 and n_p=1, were conservatively selected to provide moderate and stable pinching consistent with the expected response of deformed bar-concrete interfaces under reversed cyclic loading, while capturing the associated reduction in energy dissipation without the excessive loop contraction observed at higher parameter values.

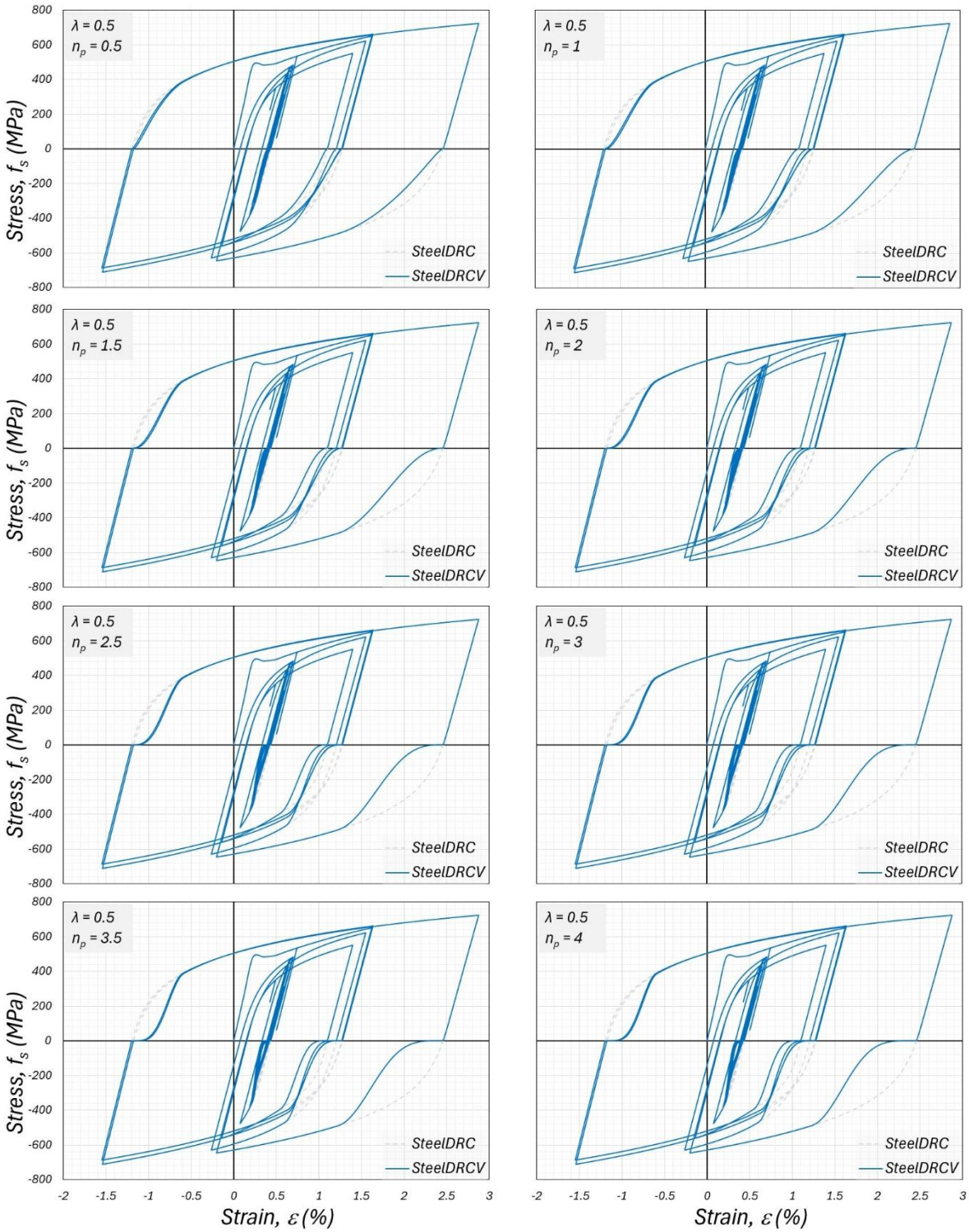


Figure 89. Cyclic stress-strain hysteretic response for λ=0.5 and varying n_p values from 0.5 to 4 - EQ5-EN5.

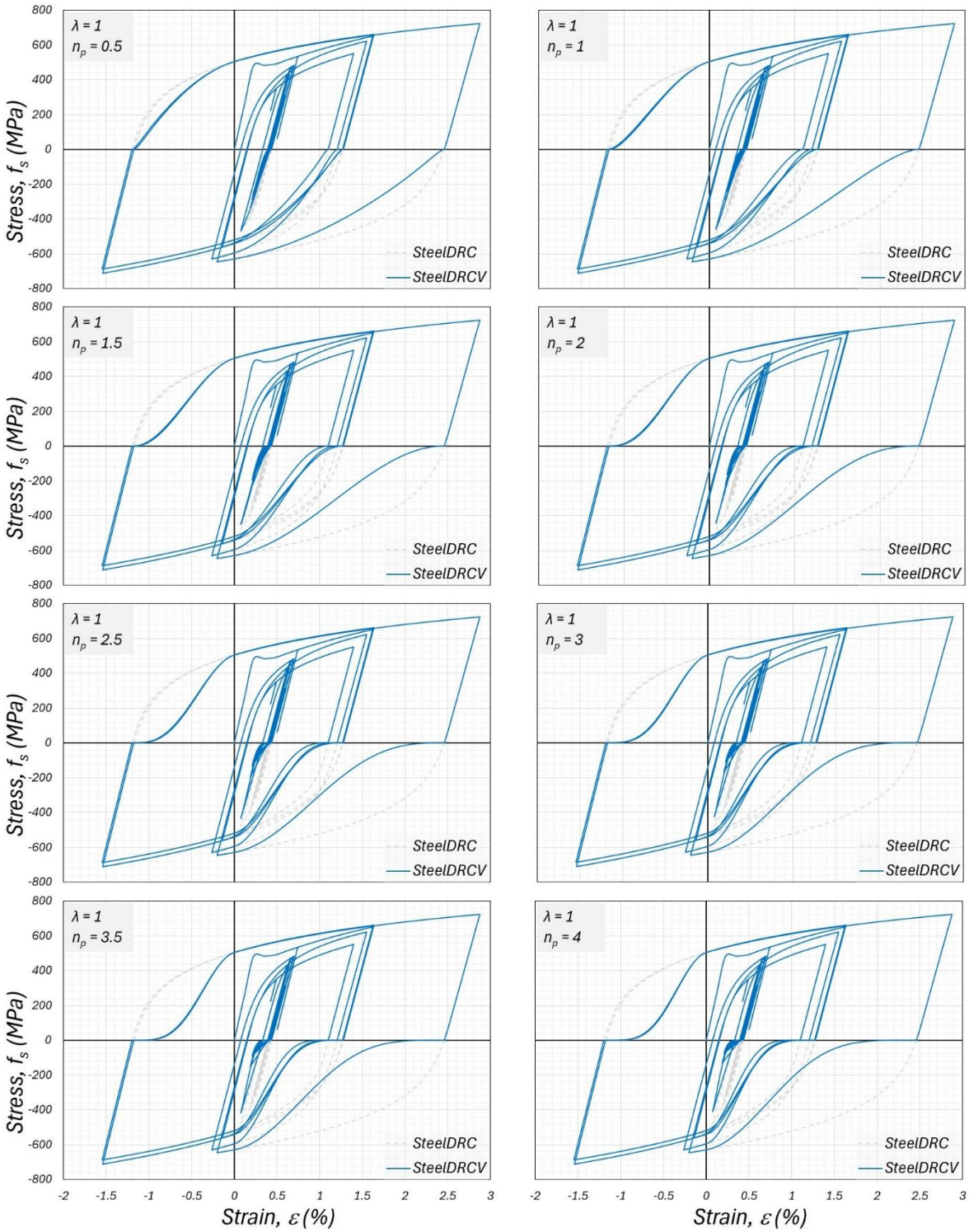


Figure 90. Cyclic stress-strain hysteretic response for λ=1 and varying n_p values from 0.5 to 4 - EQ5-EN5.

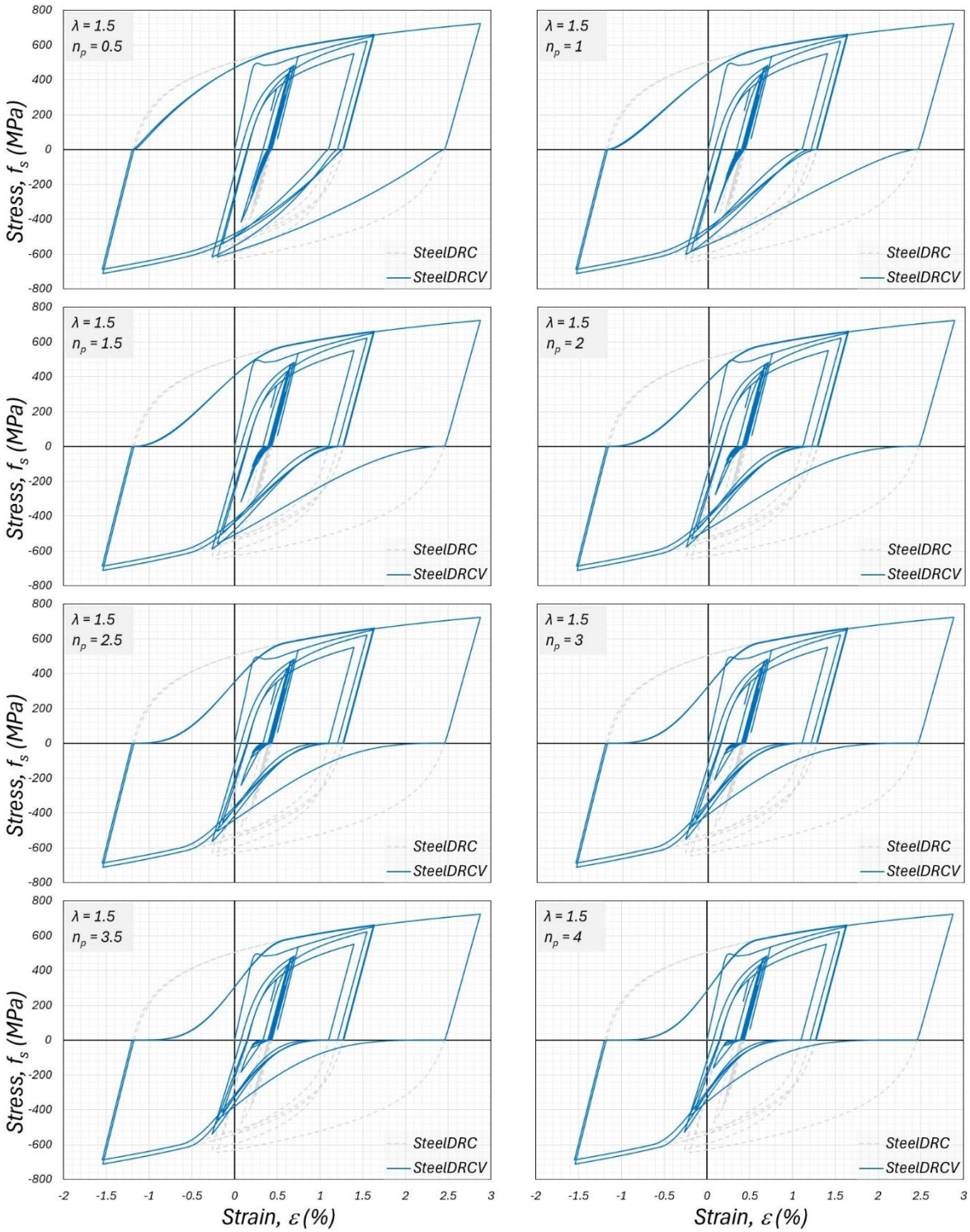


Figure 91. Cyclic stress-strain hysteretic response for λ=1.5 and varying n_p values from 0.5 to 4 - EQ5-EN5.

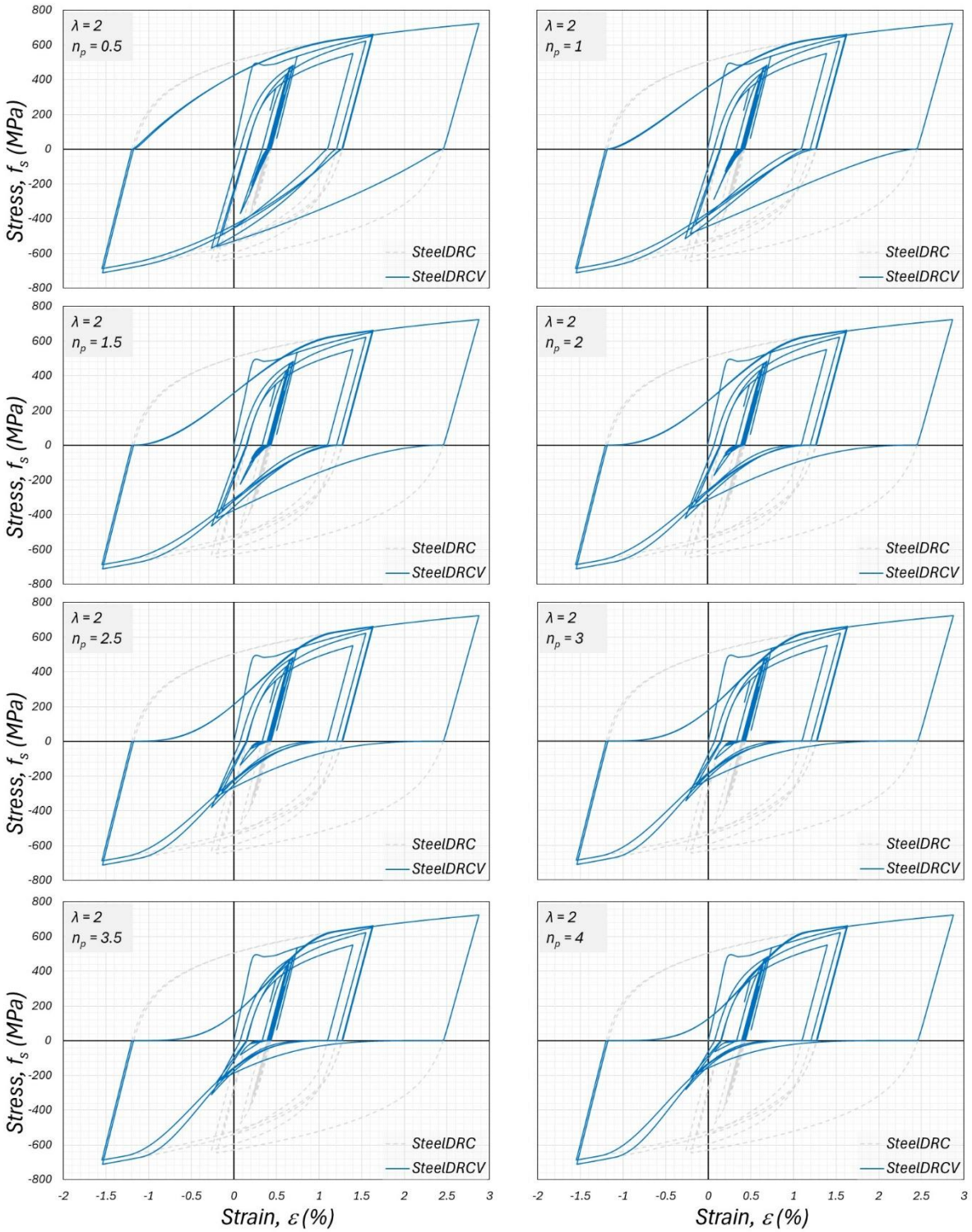


Figure 92. Cyclic stress-strain hysteretic response for λ=2 and varying n_p values from 0.5 to 4 - EQ5-EN5.

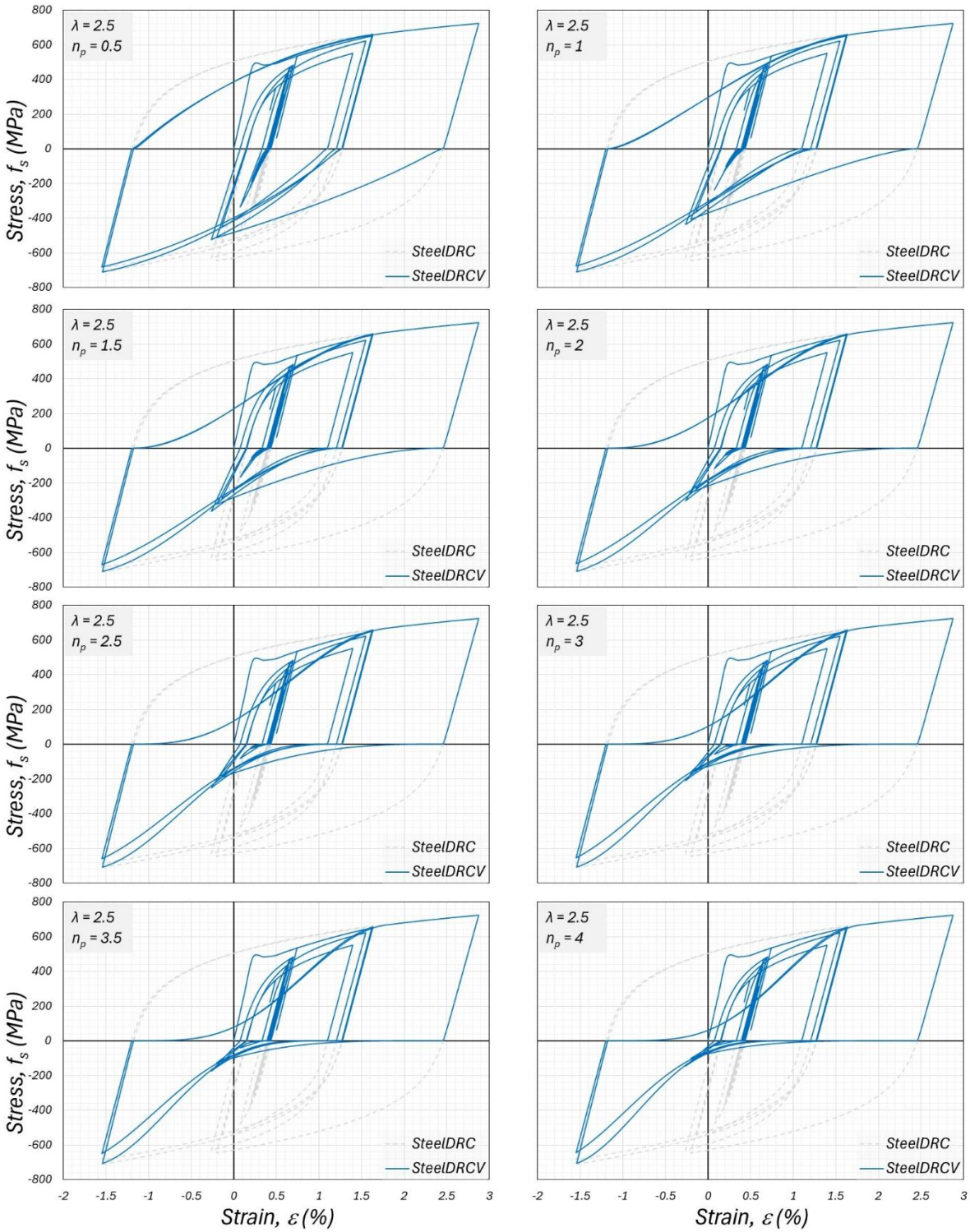


Figure 93. Cyclic stress-strain hysteretic response for λ=2.5 and varying n_p values from 0.5 to 4 - EQ5-EN5.

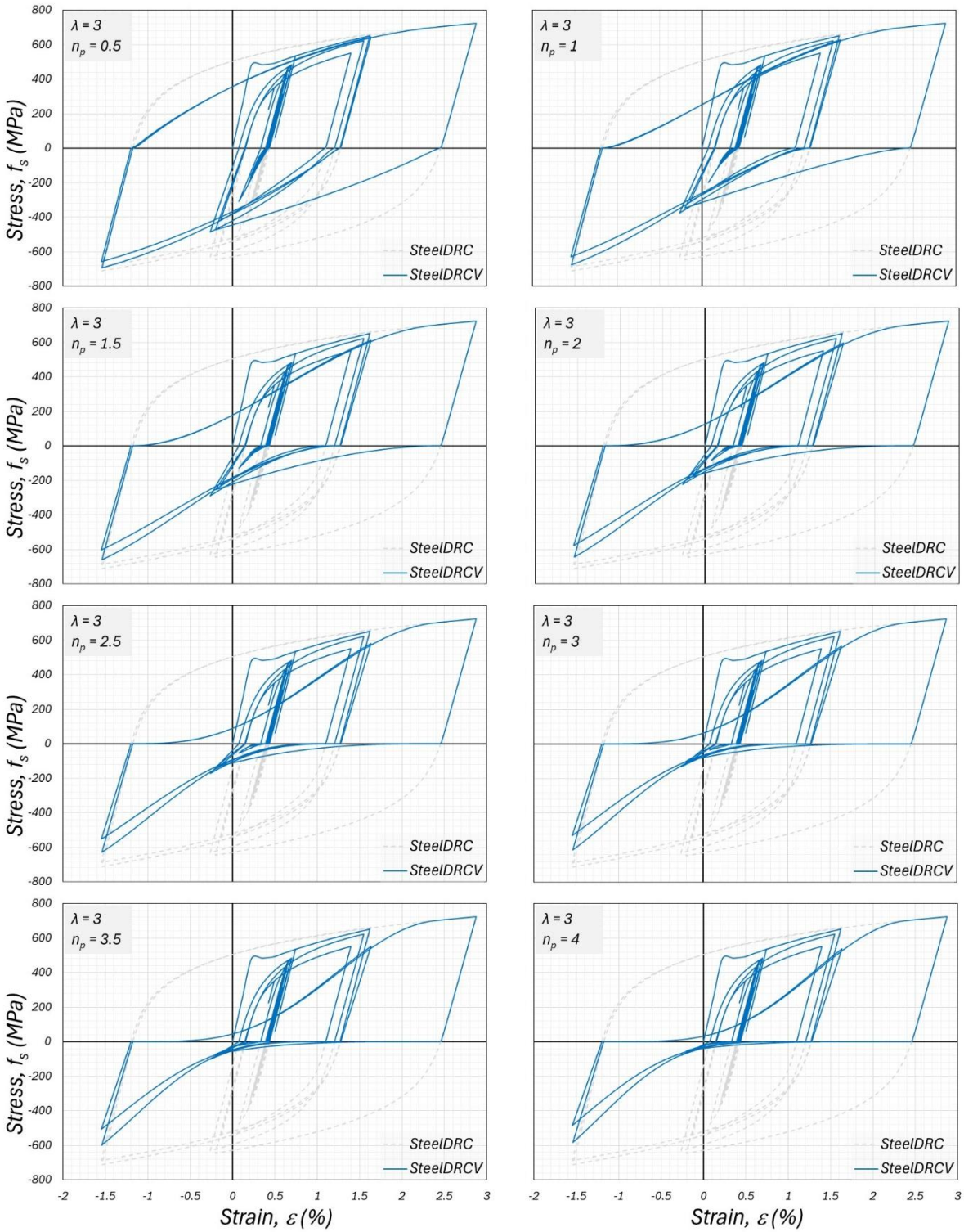


Figure 94. Cyclic stress-strain hysteretic response for λ=3 and varying n_p values from 0.5 to 4 - EQ5-EN5.

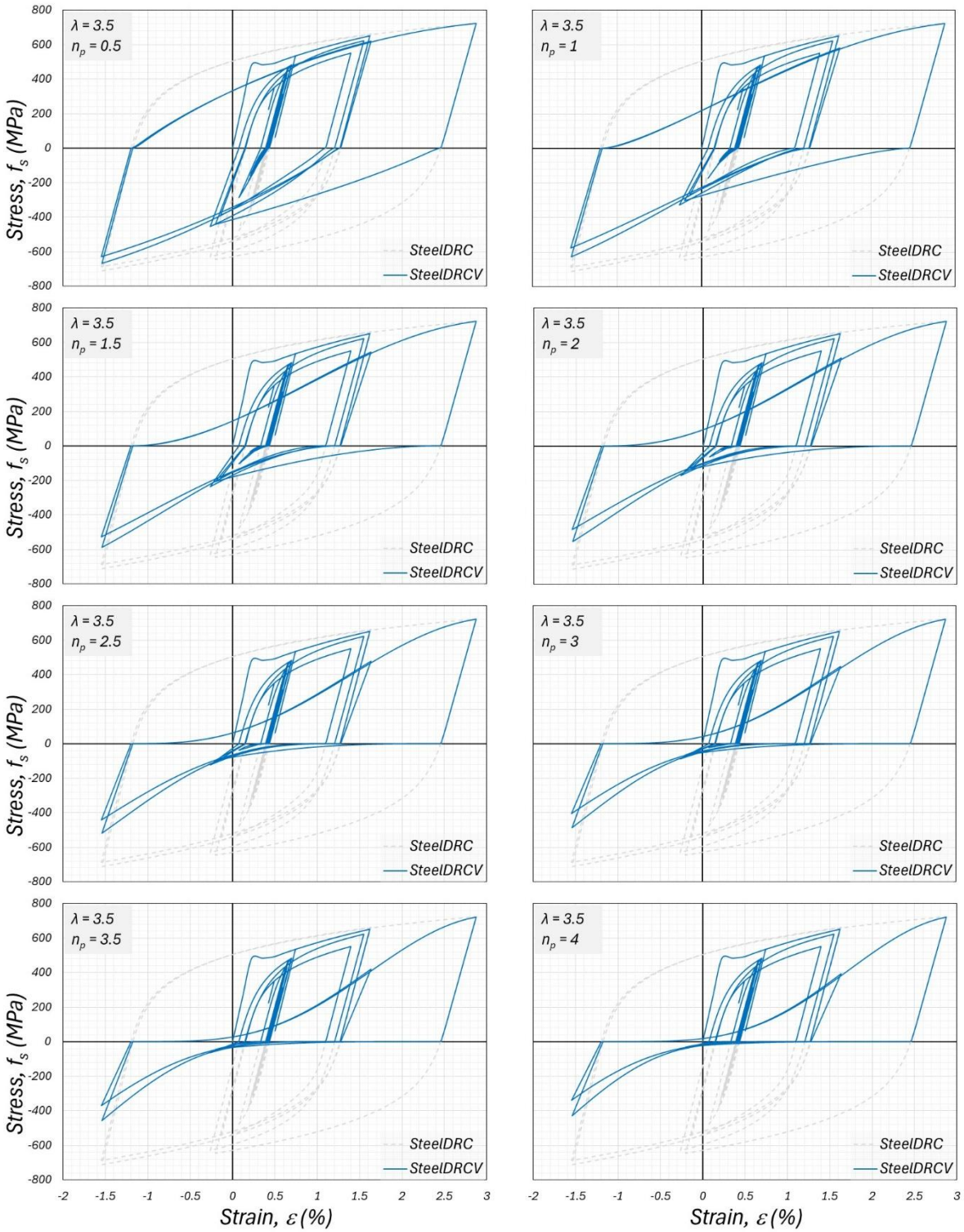


Figure 95. Cyclic stress-strain hysteretic response for λ=3.5 and varying n_p values from 0.5 to 4 - EQ5-EN5.

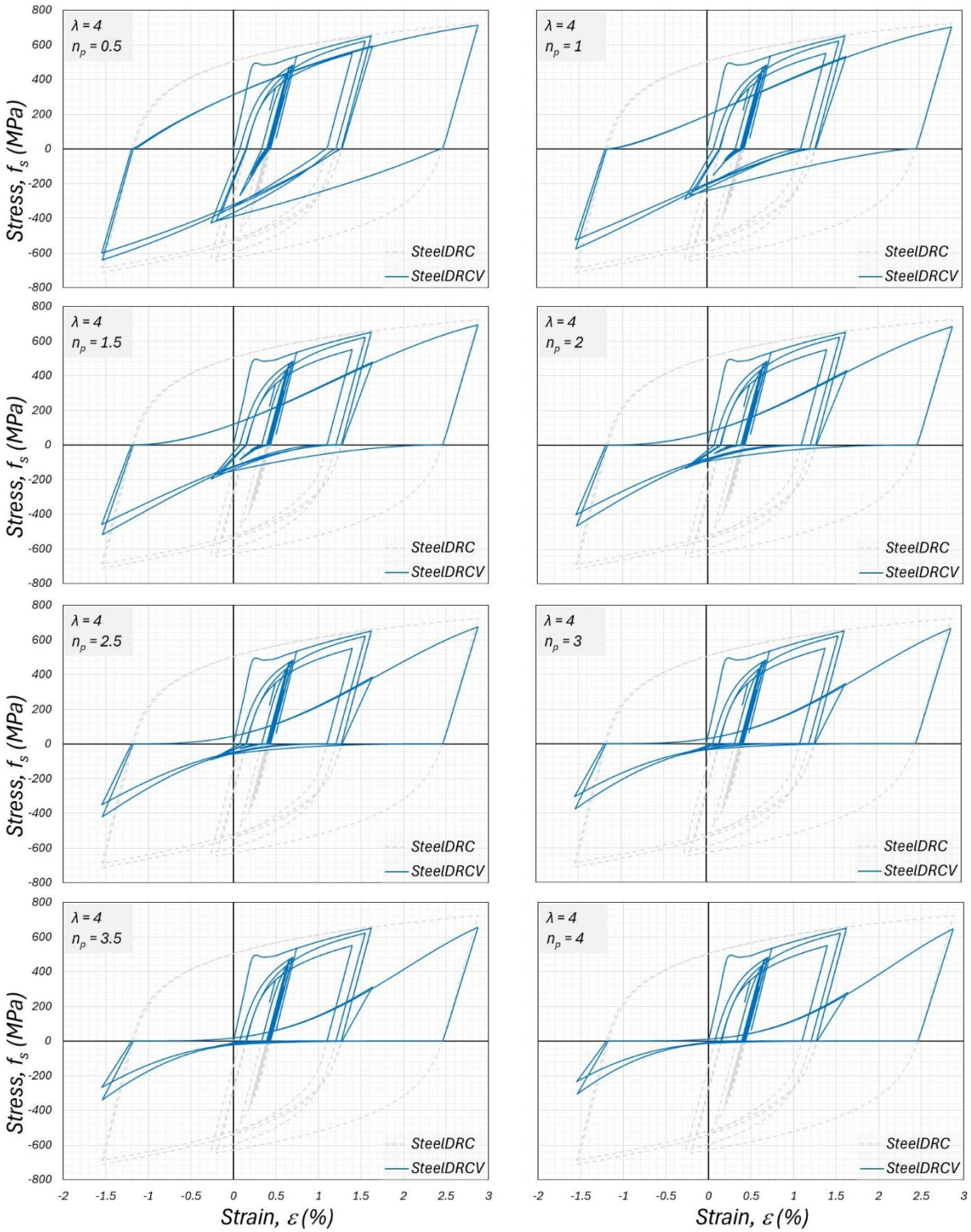


Figure 96. Cyclic stress-strain hysteretic response for λ=4 and varying n_p values from 0.5 to 4 - EQ5-EN5.

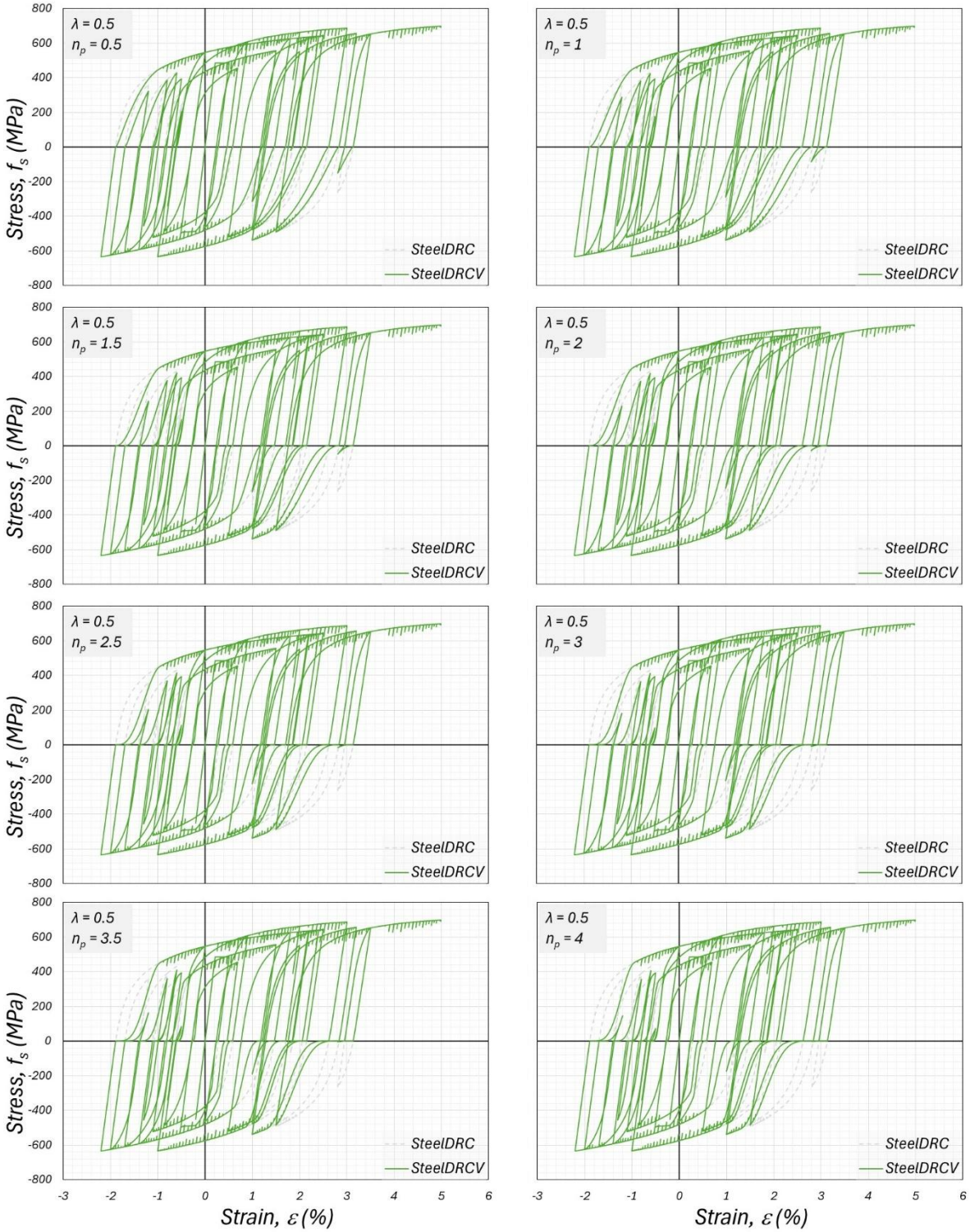


Figure 97. Cyclic stress-strain hysteretic response for λ=0.5 and varying n_p values from 0.5 to 4 - B79.

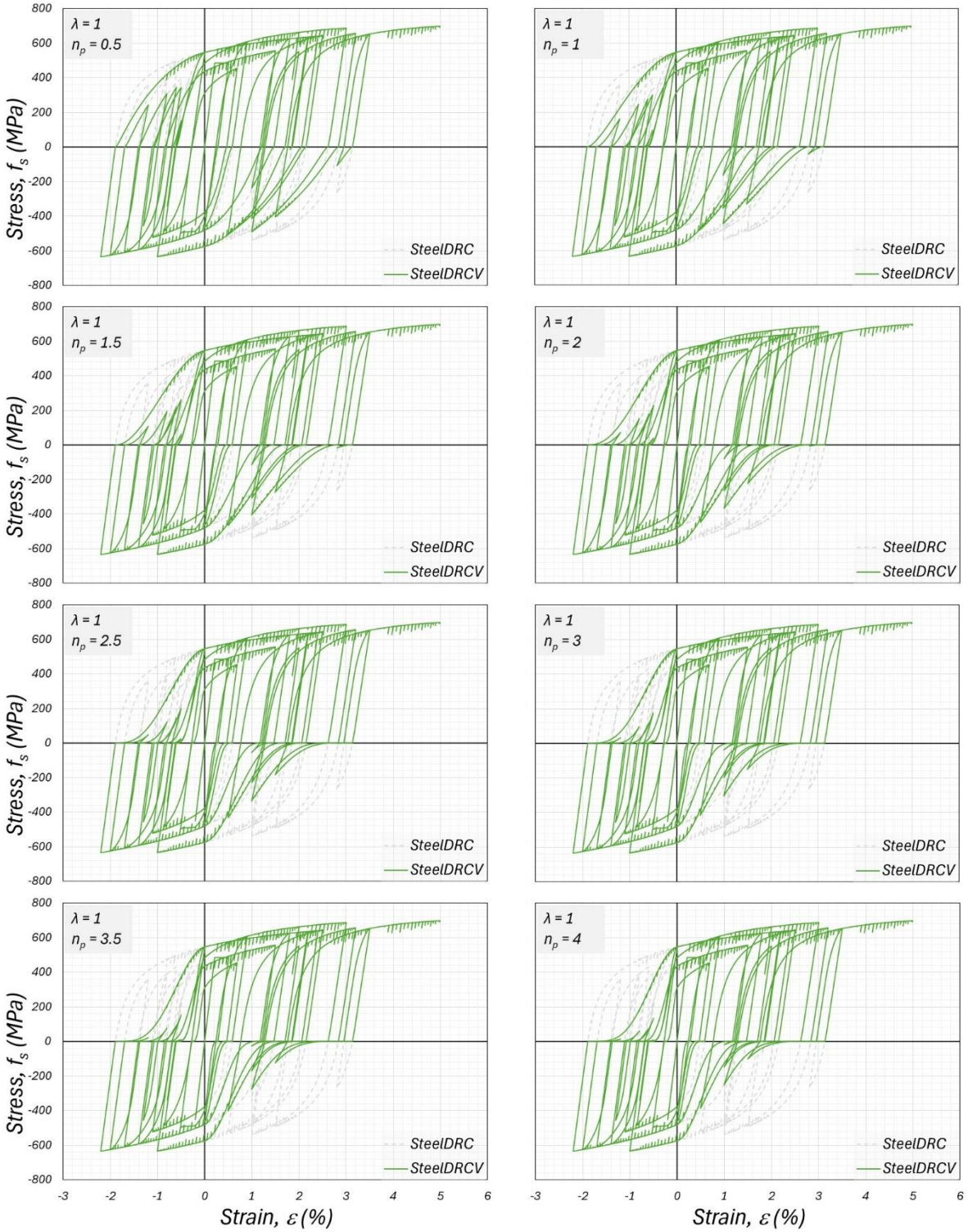


Figure 98. Cyclic stress-strain hysteretic response for λ=1 and varying n_p values from 0.5 to 4 - B79.

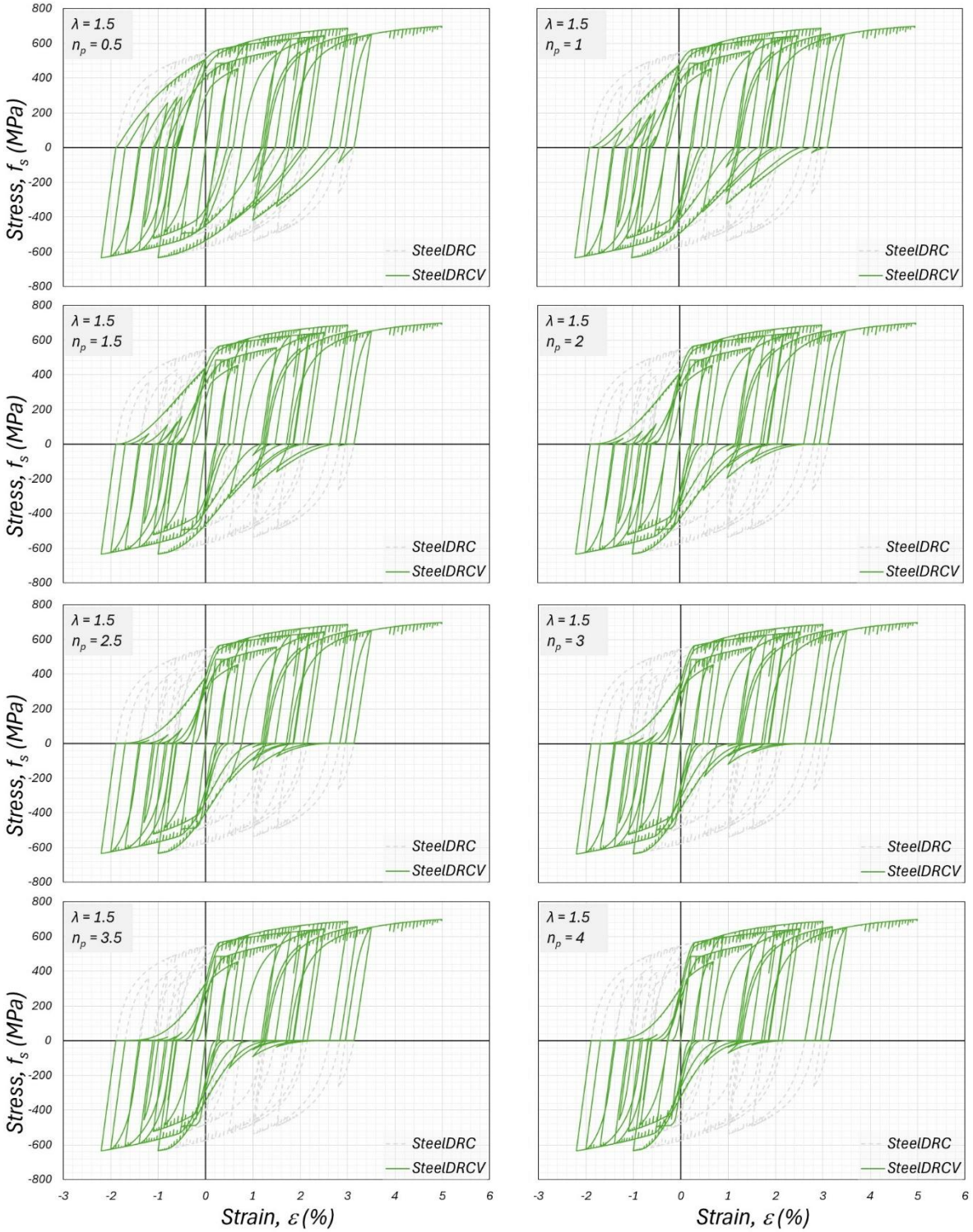


Figure 99. Cyclic stress-strain hysteretic response for λ=1.5 and varying n_p values from 0.5 to 4 - B79.

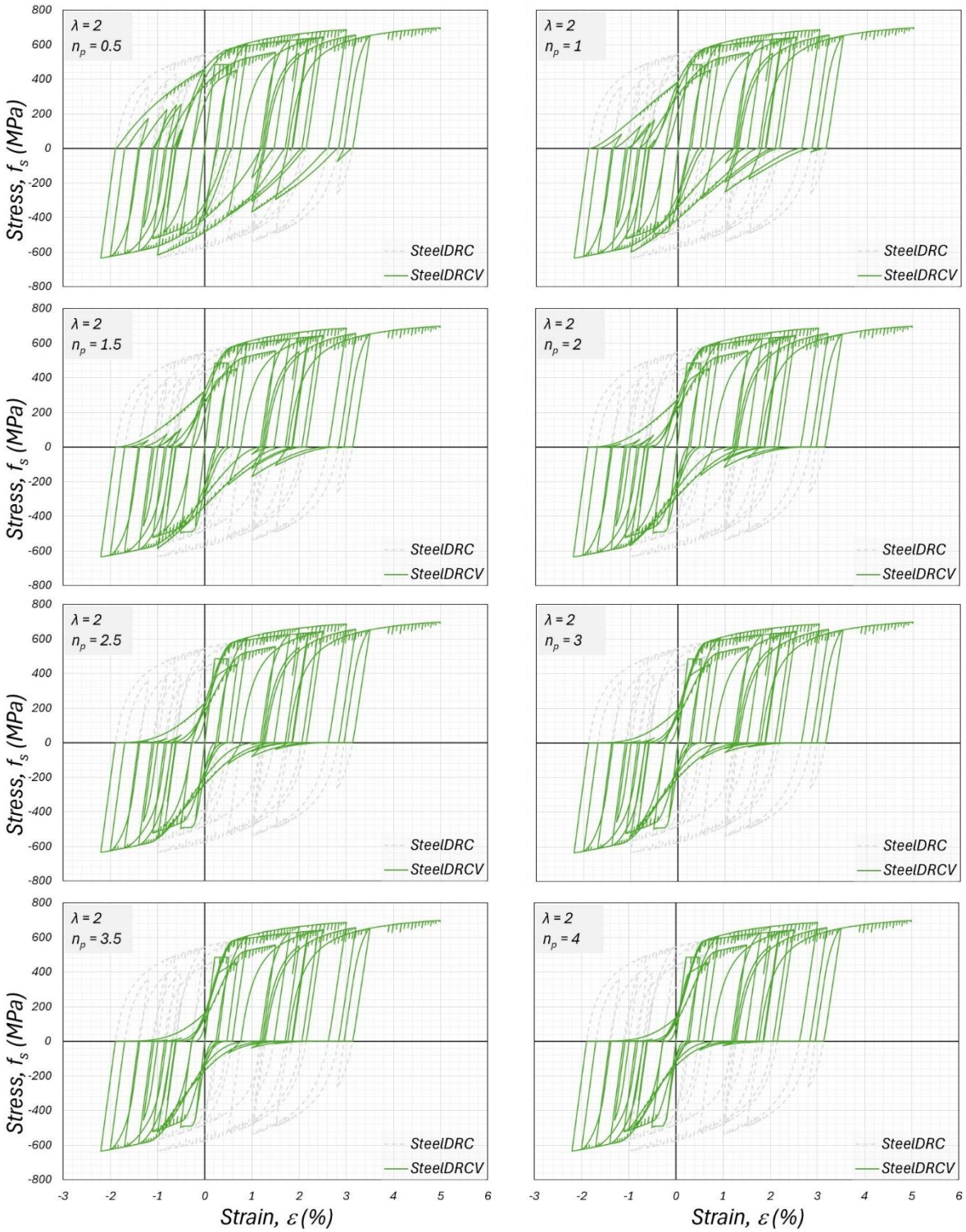


Figure 100. Cyclic stress-strain hysteretic response for λ=2 and varying n_p values from 0.5 to 4 - B79.

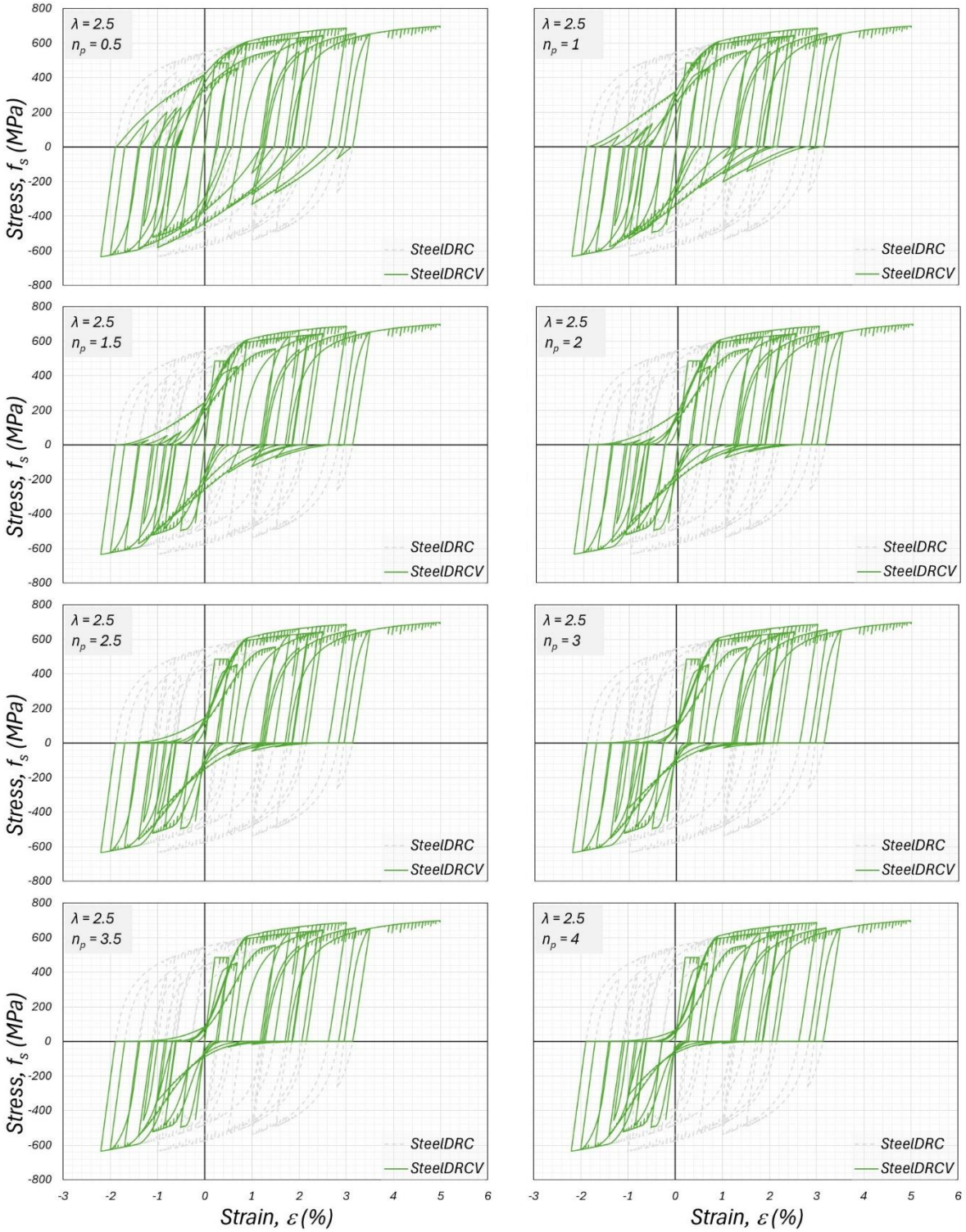


Figure 101. Cyclic stress-strain hysteretic response for λ=2.5 and varying n_p values from 0.5 to 4 - B79.

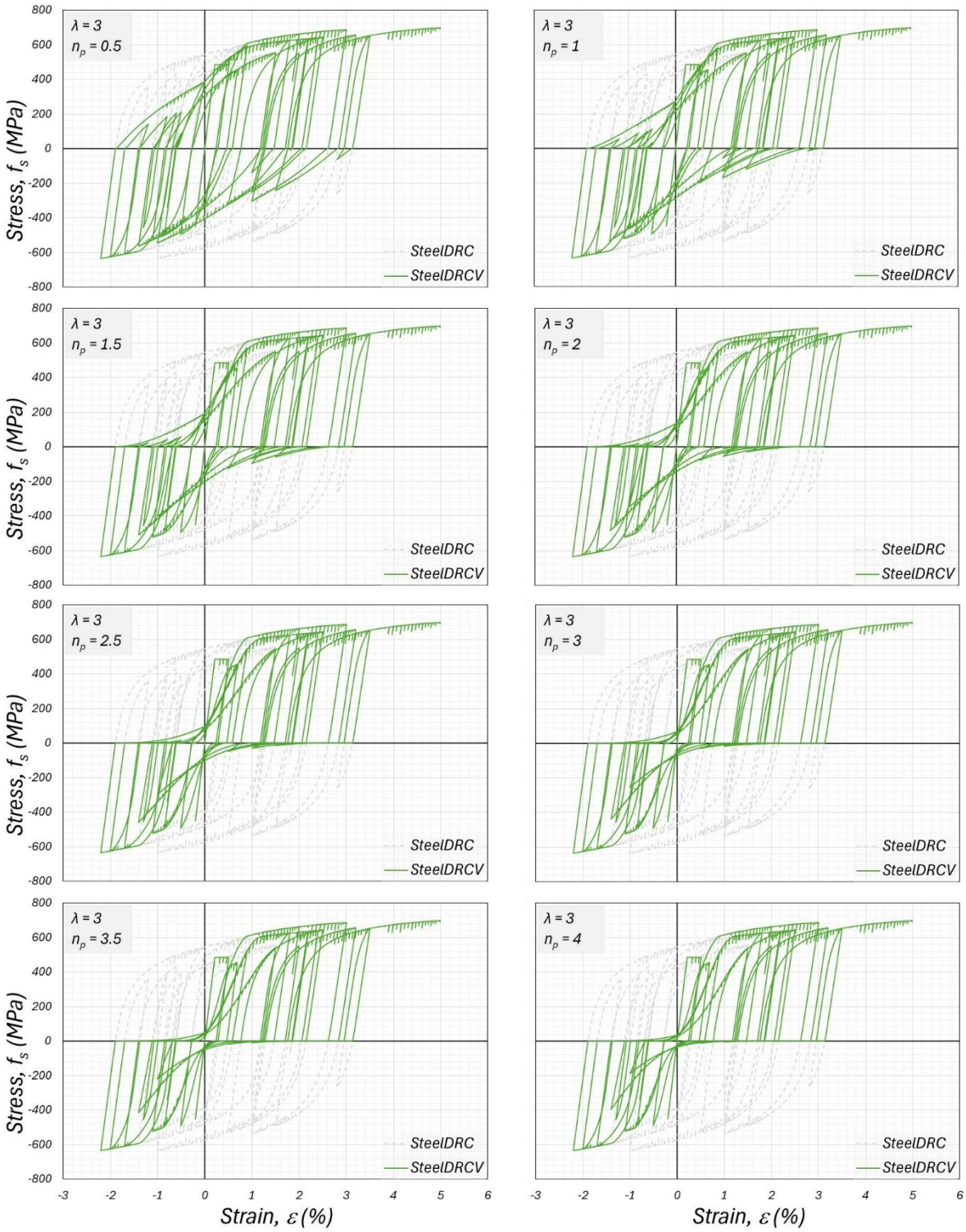


Figure 102. Cyclic stress-strain hysteretic response for λ=3 and varying n_p values from 0.5 to 4 - B79.

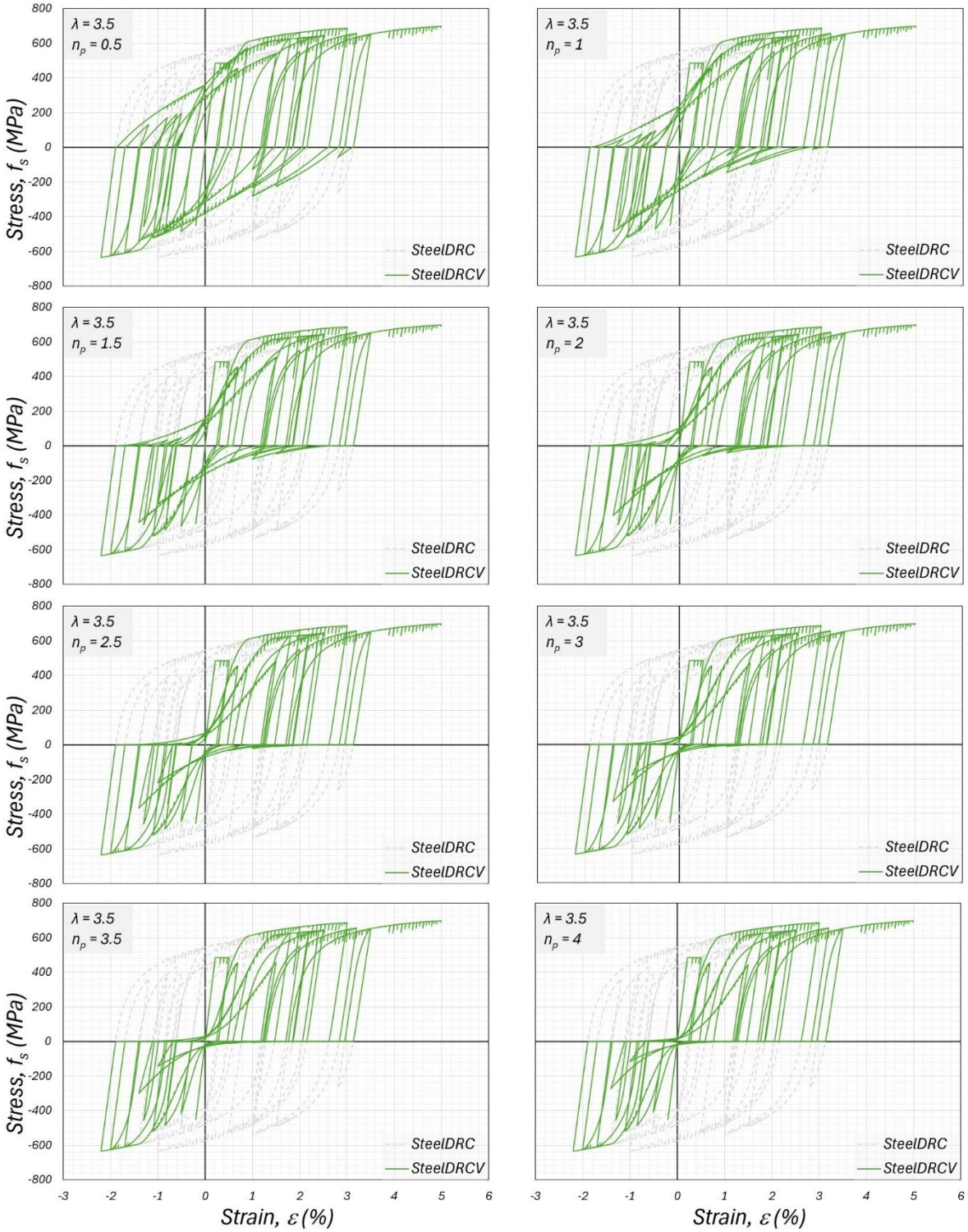


Figure 103. Cyclic stress-strain hysteretic response for λ=3.5 and varying n_p values from 0.5 to 4 - B79.

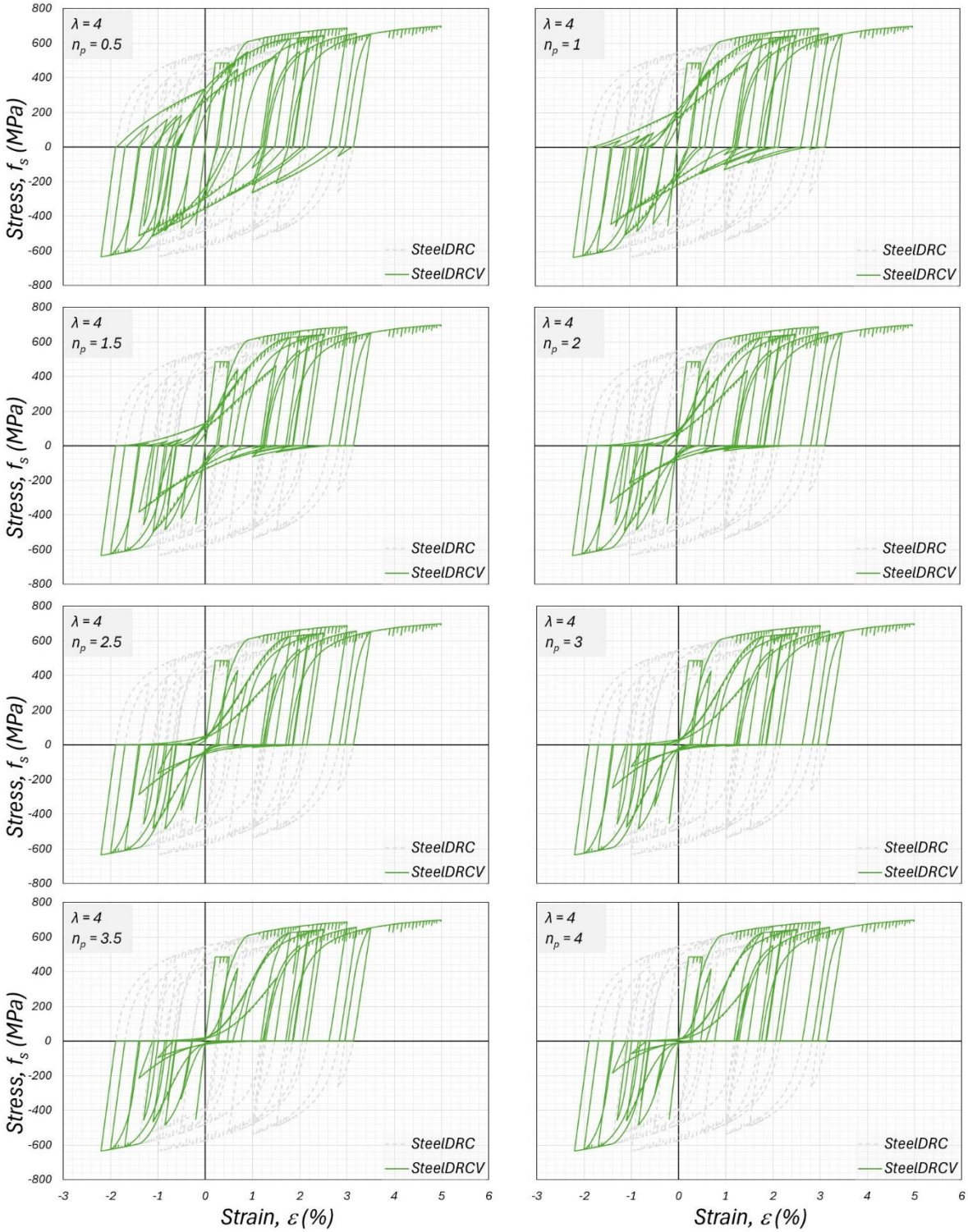


Figure 104. Cyclic stress-strain hysteretic response for λ=4 and varying n_p values from 0.5 to 4 - B79.

4.9 Conclusions

The experimental results demonstrate that Grade 60 reinforcing steel exhibits a clear positive strain-rate sensitivity under fully reversed cyclic loading in the strain-hardening regime. For comparable strain amplitudes, increasing the deformation rate from 0.001 s^{-1} to 0.02 s^{-1} produces systematic stress increments on the order of 20-40 MPa. Stress undulations were observed along the hardening branches at higher strain rates, attributed to the hydraulic actuator reaching its flow-rate capacity. These undulations are a macroscopic artifact of the testing equipment; with an actuator of unlimited capacity, the stress-strain response would remain smooth while still exhibiting the rate-dependent overstress.

A time-window-based analysis enforcing mechanical equivalence isolated the rate-dependent contribution to the stress response. The resulting stress increments scale with strain-rate excursions rather than absolute strain rate, following a sublinear power-law relationship of the form $|\Delta f_s| = k_{rate}|\Delta\dot{\varepsilon}|^{n_{rate}}$, with calibrated parameters k_{rate}=125 and n_{rate}=0.75. The experimental trends lie consistently below classical bounds derived from monotonic testing, indicating that conventional dynamic increase factors overestimate the magnitude of rate-induced strengthening under cyclic plasticity. The systematic deviation of the experimental results from the classical bounds derived from monotonic testing confirms that strain-rate effects in cyclic loading cannot be represented through multiplicative factors calibrated from monotonic conditions.

Based on these observations, a rate-dependent extension of the SteelDRC model was formulated by introducing an additive Voigt-type viscous overstress term. The resulting SteelDRCV model preserves the full rate-independent structure while incorporating a transient contribution that vanishes as the strain rate approaches zero, without modifying the internal variables or hardening evolution. Expressing the overstress in terms of strain-rate excursions directly aligns with the experimentally observed rate-dependent response. It provides a physically grounded link between strain-rate excursions and macroscopic stress amplification.

In parallel, a quadrant-dependent pinching formulation was introduced to model stiffness degradation due to bond-slip at the steel-concrete interface during the transition between tensile and compressive regimes. This mechanism is activated during the transition intervals (Quadrants II and IV). It is governed by a curvature factor whose evolution is determined by the length of the affected strain interval, and by an exponent that controls the sharpness of the transition. The formulation captures the progressive development of pinching and its truncation under premature reversals, introducing path dependency directly through the imposed strain history without requiring additional internal variables.

The quadrant-dependent pinching formulation is governed by two dimensionless parameters: λ, which controls the curvature of the stiffness degradation transition, and n_p, which regulates the sharpness of the pinching onset. Based on the parametric response characteristics observed over the ranges λ=0.5-4 and n_p=0.5-4, the operational ranges were established as λ=0-5-2.5, with a default value of 1.5, and n_p=0.5-3.5, with a default value of 1.

The default values were adopted as a modeling choice, based on engineering judgment, to produce moderate, stable pinching behavior consistent with typical deformed bar-concrete interfaces

subjected to reversed cyclic loading. This choice captures the reduction in energy dissipation associated with pinching without leading to the excessive loop contraction observed at higher parameter values. The parameter bounds were selected to maintain physically admissible hysteretic responses while avoiding computational convergence difficulties and unrealistically low energy dissipation in the structural simulations.

These results have direct implications for structural analysis and design. Using mill certificate properties, which are influenced by higher strain rates, leads to systematic strength overestimation when adopted without adjustment, potentially affecting the reliability of seismic assessments. More fundamentally, constitutive models for nonlinear RC structural analysis must incorporate both strain-rate dependence and bond-slip-induced pinching mechanisms to represent cyclic behavior accurately. The SteelDRCV formulation provides a physically consistent, computationally efficient framework for capturing rate-dependent stress amplification and stiffness degradation associated with pinched hysteresis, thereby enabling improved simulation of reinforcing steel response under seismic loading.

5 Two-Stage Calibration, Sensitivity Analysis, and Validation of the SteelDRCV Model

The preceding chapter established the constitutive formulation and material-level calibration of the SteelDRCV model through uniaxial coupon tests, incorporating both strain-rate effects and bond-slip-induced pinching. Although this calibration accurately reproduces the cyclic response of reinforcing steel, it does not by itself guarantee predictive capability at the structural level, where the global response results from the interaction among material constitutive behavior, member formulation, geometric nonlinearities, boundary conditions, damping, and loading history. Consequently, the objective of the present chapter is to assess the structural performance of a numerical model incorporating the SteelDRCV constitutive formulation by reproducing the response of the RC bridge column tested at the University of California, San Diego, described in Section 3.2.2.

The structural model is developed within the OpenSees (Open System for Earthquake Engineering Simulation; McKenna et al. [88]) framework using a concentrated-plasticity formulation. The bridge column is represented by two force-based beam-column elements connected through a common interface node. One element models the structural column, whereas the other represents the fixed-end rotation region that develops at the foundation interface due to reinforcement slip and deformation of the surrounding highly confined concrete. Both elements are discretized using circular fiber sections, with the same geometric subdivision into core and cover regions and longitudinal reinforcing steel fibers. The material assignment, however, differs between the two elements and is described in the following sections. Nonlinear flexural behavior is represented through the *HingeEndpoint* beam-integration scheme. Shear flexibility is included through elastic shear springs in the two transverse directions.

The chapter first presents the constitutive models adopted for reinforcing steel and concrete together with the calibration procedure used to identify the material parameters governing the structural response. The calibration is conducted in two successive stages. In the first stage, the experimentally measured displacement histories from the first four seismic simulations are imposed sequentially through displacement-controlled quasi-static analyses. Under prescribed displacement, the fiber strains are determined by the imposed deformation history and the adopted structural formulation; because the analysis remains quasi-static, neither inertial nor damping forces enter the equilibrium equation. The resisting moment is therefore the response quantity used to evaluate the influence of the constitutive parameters. Consequently, discrepancies between the numerical and experimental resisting moments can identify the constitutive parameters without additional inertial, damping, or strain-rate effects. This stage identifies the rate-independent constitutive parameters of concrete and reinforcing steel, including the two bond-slip pinching parameters proposed in this dissertation, and bounds the parameter space explored in the dynamic stage. In the second stage, these estimates are refined through nonlinear dynamic time-history analyses of the same four seismic simulations, in which the recorded base accelerations are applied to the numerical model. This stage identifies the Rayleigh damping coefficients and the strain-rate-dependent viscous formulation proposed in this dissertation, neither of which can be identified from the quasi-static analyses. Because the dynamic response cannot be inverted analytically and each time-history analysis is computationally expensive, this stage is formulated as a Bayesian inverse problem. The model parameters are treated as random variables, and a Gaussian process surrogate emulates the numerical simulator, enabling efficient

sampling of the joint posterior distribution. The resulting posterior distributions provide credible intervals for the identified parameters and explicitly indicate whether, and to what extent, the experimental data informed each parameter. Finally, the predictive capability of the complete calibrated model is evaluated by extending the sequence of nonlinear dynamic analyses to include the fifth seismic simulation. The recorded base acceleration from this additional simulation is applied without further modification of any model parameter, so that the fifth seismic record provides an independent assessment of the calibrated model's predictive capability.

Chapter 5 presents the two-stage calibration, sensitivity analysis, and validation of the SteelDRCV model. Section 5.1 establishes the numerical modeling framework, covering boundary conditions, fixed-end rotation, element formulation, coordinate system, solution procedure, and discretization. Section 5.2 details the material constitutive models for longitudinal reinforcement, confined and unconfined concrete, and tensile regularization. Section 5.3 outlines the calibration and validation procedure, Section 5.4 describes the experimental data used, Section 5.5 introduces the two-stage parameter identification strategy, and Section 5.6 documents parameter provenance and explored intervals. Section 5.7 presents Stage 1 (displacement-controlled cyclic calibration), including objective functions, concrete tensile and reinforcing-steel sub-stages, sensitivity of the response to identified parameters, and its outcome. Section 5.8 presents Stage 2 (Bayesian dynamic calibration), covering the inverse-problem formulation, calibration parameters and metrics, the design of experiments, the Gaussian-process surrogate and its validation, global sensitivity analysis via Sobol indices, the likelihood and error model, the TMCMC sampler and its convergence diagnostics, posterior results with prior robustness analysis, identifiability of the strain-rate mechanism, model-experiment discrepancy, closed-loop verification, held-out validation, and model-side limitations. Section 5.9 presents the model validation against the held-out seismic simulation (EQ5). The chapter concludes with an energy decomposition analysis that isolates the contributions of Rayleigh viscous damping (5.5% of input energy) and the SteelDRCV strain-rate mechanism (5.1% of hysteretic energy) to the total energy balance.

5.1 Numerical Modeling Framework

5.1.1 Boundary Conditions and Inertial Properties

The first node, located at the foundation level, was modeled as fully restrained, with all translational and rotational degrees of freedom fixed to reproduce the experimental anchorage condition. At the column top, the lateral degree of freedom corresponding to the direction of the applied excitation was left active, together with the associated in-plane rotational degree of freedom required to represent the flexural response of the cantilever. The remaining translational and rotational degrees of freedom were restrained to prevent out-of-plane deformation and enforce the planar response observed during the experiment. In the displacement-controlled analyses, the active lateral degree of freedom is prescribed according to the experimentally measured displacement history. In contrast, in the nonlinear dynamic analyses, it responds to the applied base acceleration.

A concentrated translational mass, m_t, and rotational inertia, I_r, assigned at the column-top node, represented the inertial contribution of the tributary bridge superstructure.

$$m_t = \frac{W_t}{g}, \qquad I_r = \sum m_i . d_i^2 \tag{144}$$

where g represents the gravitational acceleration, m_i, the discrete mass element, and d_i, the perpendicular distance to the rotation axis. For the present model, m_t=237 kN.s^2/m and I_r=1066 kN.m.s^2, as adopted from the experimental program to represent the inertial properties of the tributary bridge superstructure.

5.1.2 Fixed-End Rotation and Flexural Plasticity

The lateral displacement measured at the top of the flexural column model is the sum of contributions from three sources: (1) the rotation of the column relative to the footing, (2) the inelastic flexural curvature concentrated in the plastic-hinge region above the footing, and (3) the elastic flexibility of the member.

The first component is the column rotation relative to the footing, concentrated at the column-footing interface. Although the literature commonly refers to this response as *strain penetration*, this terminology is not strictly accurate. Strain penetration denotes the progressive yielding and slip of the longitudinal reinforcement along its embedment into the footing, allowing the bars to elongate over a length extending below the nominal construction joint. Interface rotation, however, also results from the opening of the base flexural crack and local deformation of the surrounding footing concrete.

Strain penetration is therefore one mechanism contributing to interface rotation, rather than the response itself. Accordingly, the term *fixed-end rotation* (FER) is adopted throughout this work to denote the total rotation of the column relative to the footing at the column-footing interface, and the element introduced below is named after the response quantity it reproduces rather than one of its contributing mechanisms. FER is one of the mechanisms that contribute to hysteretic pinching at the structural level, along with diagonal crack closure. The FER element captures the geometric consequence of this mechanism: the additional rotation at the column-footing interface. In contrast, the bond-slip-induced pinching in SteelDRCV phenomenologically reproduces the collective constitutive effect of all pinching-inducing mechanisms without modeling the physics of any individual mechanism. The two representations therefore operate at different levels (structural kinematics vs. material constitutive law) and do not represent the same phenomenon twice. To the author's knowledge, this distinction between FER as a structural kinematic response and strain penetration as one of its contributing mechanisms has not been explicitly made in the literature.

Experimental evidence from the tested column during simulation EQ2 supports this distinction, as illustrated in Figure 105. The bar-slip measurements reported during this simulation show that the extreme longitudinal bars highlighted in blue and red develop tensile pull-out of approximately 1 mm and 2 mm, respectively. Upon load reversal, however, only about 0.3-0.5 mm of this displacement is recovered as the bars are subsequently driven into compression. The mechanism is therefore markedly asymmetric and predominantly tensile, with most of the irreversible slip developing during tensile loading. Because this tensile pull-out mechanism largely governs interface rotation, the literature often refers to it as strain penetration.

Mechanically, however, the measured response cannot be attributed exclusively to reinforcement slip, as it also includes the deformation of the surrounding concrete at the interface. This observation motivates treating the interface response as a distinct deformation mechanism rather than an extension of the column's flexural plasticity. Accordingly, the constitutive formulation proposed in Section 5.2.2.2 is developed to reproduce the overall FER. At the same time, its nonlinear response is governed by the tensile behavior of the concrete assigned to the FER element.

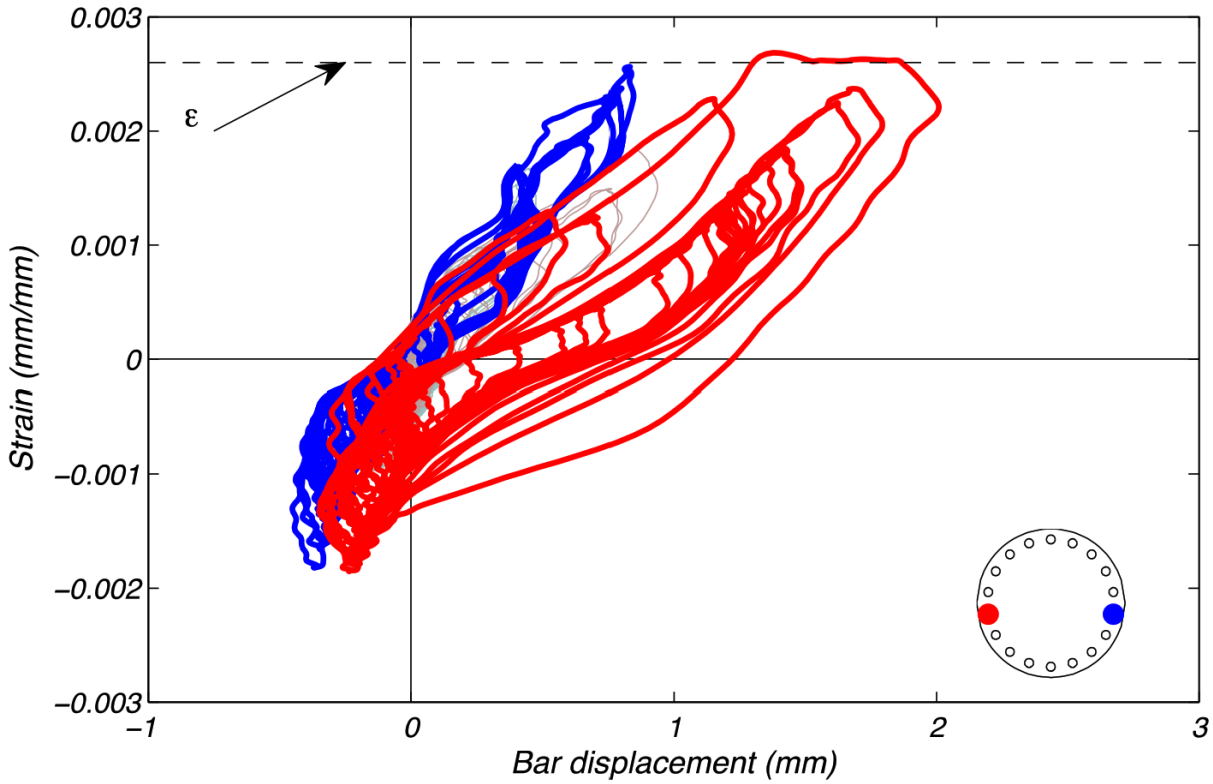


Figure 105. Bar-slip measurements during Test EQ2 [124].

5.1.3 Structural Idealization and Element Formulation

The RC bridge column tested at the LHPOST was modeled as a vertical cantilever fixed at the foundation and subjected to a constant axial compressive load representing the inertial block. The numerical idealization explicitly captures the principal structural mechanisms governing the global response: (1) flexural plasticity concentrated at the column base; (2) FER resulting from reinforcement slip and deformation of the surrounding foundation concrete; (3) geometric P-Delta effects under sustained axial load; and (4) shear flexibility of the cracked member. These mechanisms are represented within a force-based concentrated-plasticity formulation that satisfies equilibrium exactly along the member length while localizing the inelastic response through beam integration rather than mesh refinement.

The member is discretized into two force-based beam-column elements sharing a common interface node located at a reference length for fixed-end rotation, L_{sp}, defined as the length over which the tensile yielding of the longitudinal bars propagates into the footing. This length is not chosen arbitrarily; it is calculated from the column geometry and the bar size as

$$L_{sp} = \alpha(AR).D + k_a.d_{bl} \tag{145}$$

where D is the column diameter, d_{bl} is the longitudinal-bar diameter, and $AR = H/D$ is the column aspect ratio. The coefficient, k_a, accounts for the anchorage condition, taking the value 9 for columns framing into spread footings and 20 for pile shafts.

The aspect-ratio coefficient, $\alpha(AR)$, decreases from squat to slender columns, reflecting the fact that strain penetration extends over a larger fraction of the section depth when the moment gradient at the base is steeper.

$$\alpha(AR) = \begin{cases} 0.6 & AR \leq 3.17 \\ 0.6 - \left[\dfrac{0.4}{4.5 - 3.17}\right].(AR - 3.17) & 3.17 < AR < 4.5 \\ 0.2 & for\ AR \geq 4.5 \end{cases} \tag{146}$$

For the test column, L=7315 mm, D=1219 mm, d_{bl}=35.8 mm, and AR=6 ≥ 4.5, hence $\alpha(AR)$=0.2; with the column framing into a spread foundation (k_a=9),

$$L_{sp} = (0.2)(1219) + (9)(35.8) = 566\ mm$$

This value is adopted in the proposed model to define the location of the interface node. The two force-based beam-column elements are connected in series through a common interface node. The lower element models the FER that develops at the column-footing interface due to reinforcement slip and the deformation of the surrounding highly confined concrete. The upper element represents the structural column above the foundation. Figure 106 shows the resulting structural idealization and beam-integration discretization.

Lumping flexural curvature and FER into a single fiber hinge would misrepresent their relative contributions to the tip displacement, because the two mechanisms have different moment-deformation laws and localize over different lengths. The interface node does not correspond to a physical discontinuity of the specimen. However, it serves as a numerical device that separates the flexibility associated with the FER from the column's flexural flexibility, allowing both mechanisms to act in series while preserving compatibility and equilibrium. Both elements use circular fiber sections with identical geometric discretization. The FER element has a physical length of 566 mm and concentrates its nonlinear response within a fiber section located at the foundation interface. The corresponding concrete constitutive properties assigned to the fiber regions differ between the column and the FER element, as described in Section 5.2.

The structural column element employs a fiber-plastic-hinge integration region of length L_{pc}=0.8D=975 mm at both ends. The lower integration region captures the experimentally observed spread of flexural inelasticity adjacent to the foundation [124].

The upper integration region, although not intended to develop significant plasticity, allows localized cracking and limited stiffness degradation at the column-loading-block interface, where applied

lateral loading induces tensile stresses. This representation avoids artificially enforcing a fully elastic boundary at the loading interface while remaining consistent with the experimental observation that the dominant nonlinear response is concentrated at the column base. The intermediate portion of the element is assigned an effective cracked flexural stiffness ratio, EI_e/EI_g, thereby restricting the distributed nonlinear response to the prescribed hinge regions.

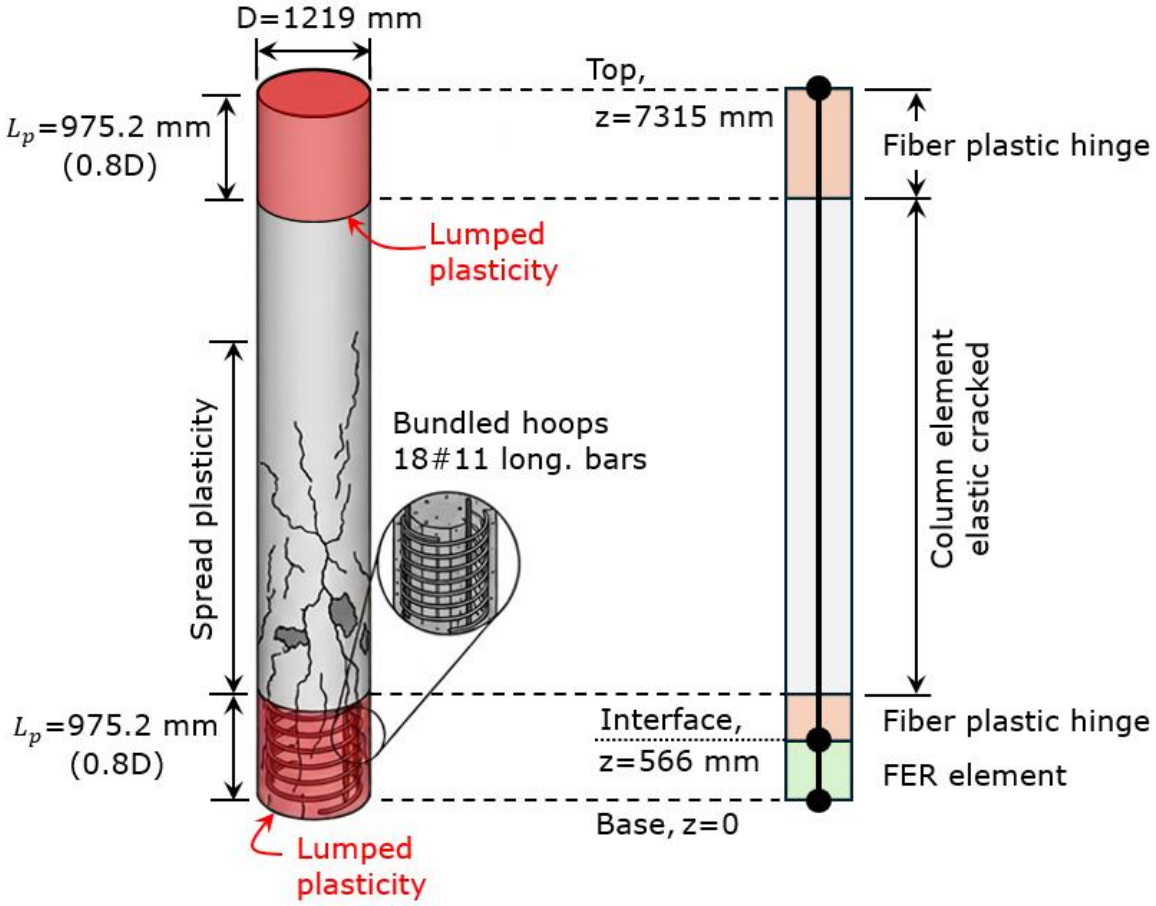


Figure 106. Structural idealization of the bridge column.

Lumping flexural curvature and FER into a single fiber hinge would misrepresent their relative contributions to the tip displacement, because the two mechanisms have different moment-deformation laws and localize over different lengths. The interface node does not correspond to a physical discontinuity of the specimen. However, it serves as a numerical device that separates the flexibility associated with the FER from the column's flexural flexibility, allowing both mechanisms to act in series while preserving compatibility and equilibrium. Both elements use circular fiber sections with identical geometric discretization. The FER element has a physical length of 566 mm and concentrates its nonlinear response within a fiber section located at the foundation interface. The corresponding concrete constitutive properties assigned to the fiber regions differ between the column and the FER element, as described in Section 5.2.

The structural column element employs a HingeEndpoint beam-integration scheme with fiber-plastic-hinge integration regions of length L_{pc}=975 mm at both ends. The lower integration region captures

the experimentally observed spread of flexural inelasticity adjacent to the foundation [124]. The upper integration region, although not intended to develop significant plasticity, allows localized cracking and limited stiffness degradation at the column-loading-block interface, where applied lateral loading induces tensile stresses. This representation avoids artificially enforcing a fully elastic boundary at the loading interface while remaining consistent with the experimental observation that the dominant nonlinear response is concentrated at the column base. The intermediate portion of the element is assigned an effective cracked flexural stiffness, EI_e/EI_g, thereby restricting the distributed nonlinear response to the prescribed hinge regions.

Shear flexibility is included through a Timoshenko-type formulation: elastic shear springs are aggregated to the fiber sections in the two transverse directions (*Section Aggregator*), with an effective shear stiffness, $G_e.A_{sh}$ obtained from an effective shear modulus (ν=0.2). The reduced effective modulus accounts, in a smeared sense, for shear cracking and the associated loss of shear stiffness in the cracked region.

The effective shear area for a solid circular section is defined as:

$$A_{sh} = K\frac{\pi D^2}{4} \tag{147}$$

where the shear coefficient K for circular sections is given by Cowper's formulation [41]:

$$K = \frac{6(1+\nu)}{7+6\nu} \tag{148}$$

The resulting *Section Aggregator* couples the nonlinear flexural response from the fiber discretization (M-ϕ) with the linear shear behavior (V-γ), enabling a realistic representation of member deformation under seismic loading.

5.1.4 Coordinate System Definition and Section Orientation

The global coordinate system for the numerical model has its origin at the column foundation node. The global Z-axis coincides with the column's longitudinal axis and points upward. The global X-axis corresponds to the direction of the imposed lateral displacement during the cyclic analysis, from east to west. The global Y-axis defines the transverse direction, completing the right-handed coordinate system. This coordinate convention establishes the reference system for defining nodal coordinates, applied loads, and structural response quantities.

For both force-based beam-column elements, the local longitudinal x-axis is defined along the line connecting the two element nodes, oriented from the base node to the node above; since both elements are stacked vertically along the column's centroidal axis, this local x-axis coincides with the previously defined global Z-axis. However, the local longitudinal axis alone is not sufficient to fully define a three-dimensional local coordinate system: an infinite number of cross-sectional axis orientations remain possible through rotation about this axis.

To resolve this ambiguity, OpenSees requires the user to specify a second, auxiliary reference vector, $v_{xz} = (0, 1, 0)$, expressed in the global coordinate system, which, together with the local x-axis, defines the local x-z plane of the element. This local y-z system defines the fiber locations of the cross-section. It therefore governs how the section's bending response is oriented relative to the global directions of imposed displacement. Figure 107. illustrates this correspondence between the global and local coordinate systems.

From this reference vector, OpenSees constructs a right-handed orthogonal local triad as follows: the local y-axis is obtained from the cross product of v_{xz} and the local x-axis,

$$y_{local} = v_{xz} \times x_{local} = (0, 1, 0) \times (0, 0, 1) = (1, 0, 0) \tag{149}$$

and the local z-axis is subsequently obtained from the cross product of the local x- and y-axes, completing the local reference frame.

$$z_{local} = x_{local} \times y_{local} = (0, 0, 1) \times (1, 0, 0) = (0, 1, 0) \tag{150}$$

The local y-axis therefore coincides with the global X-axis. In contrast, the local z-axis coincides with the global Y-axis (the transverse direction).

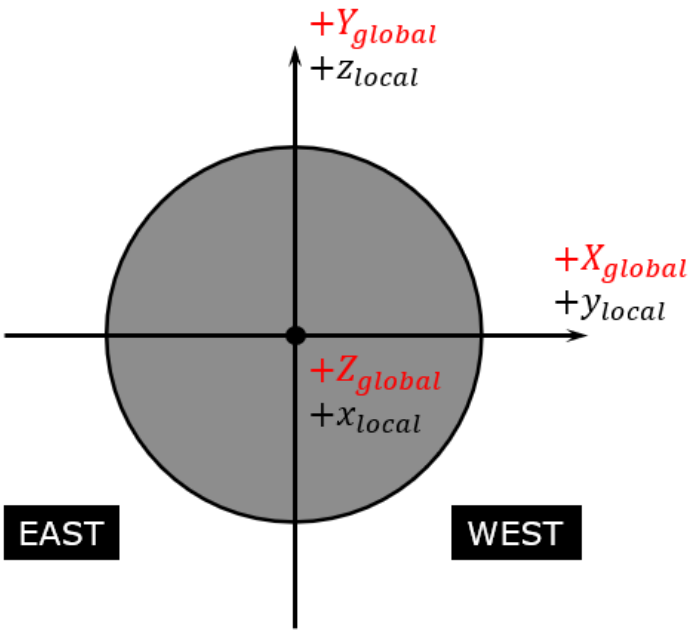


Figure 107. Coordinate system.

5.1.5 Numerical Solution Procedure

Gravity is first applied in 10 equal increments and then held constant. After establishing the gravity-loaded equilibrium configuration, the analysis proceeds according to the loading protocol adopted for the corresponding calibration or validation stage.

For both the quasi-static and nonlinear dynamic analyses, each analysis increment is initially solved using the standard Newton-Raphson algorithm under a displacement-increment convergence criterion with a tolerance of 1×10^{-6}. If convergence is not achieved, the solution strategy automatically proceeds through a sequence of increasingly robust iterative algorithms: Newton with line search, Modified Newton, Krylov-Newton, and Broyden. For the SteelDRCV constitutive model, the secant-modulus option is selected to return the element's tangent stiffness, providing a smoothed representation of the cyclic stiffness and improving the numerical conditioning of the element-level iterations.

For the quasi-static calibration analyses, failure of all iterative algorithms triggers recursive subdivision of the prescribed displacement increment until convergence is recovered or the maximum subdivision level is reached. For nonlinear dynamic analyses, if convergence cannot be achieved after exhausting the iterative solution sequence, the time step is temporarily advanced using an explicit integration step based on the Newmark formulation, along with a linear solution algorithm and very small time increments. After the explicit recovery step, the analysis automatically resumes standard implicit Newmark integration with the Newton-Raphson algorithm. This hierarchical solution strategy substantially improves numerical robustness during severe nonlinear response, particularly under load reversals associated with concrete cracking, cyclic stiffness degradation, and the pinching response introduced by the SteelDRCV constitutive model.

5.1.6 Geometric and Sectional Discretization

The column has a circular cross-section of diameter D=1219 mm with a clear cover of 51 mm. The longitudinal reinforcement consists of 18 No. 11 bars (db_l=35.8 mm, A_b=1006 mm²) arranged in a single circular layer at a pitch-circle diameter of 1049 mm. Bundled hoops of 15.9 mm diameter provide transverse reinforcement at a 152 mm pitch, which confines a core of diameter D_c=1101 mm measured to the outside of the hoops, resulting in a diameter through the centroids of the longitudinal bars of 1049 mm. Figures 108 and 109 illustrate the fiber discretization adopted for the column and FER elements.

Each fiber section comprises three regions. The confined core is meshed with 16 circumferential and 5 radial subdivisions, while the cover region, extending between the core and outer diameters, is meshed with 16 circumferential and 1 radial subdivision. The 18 longitudinal bars are represented as discrete fibers arranged in a circular layer. The column plastic-hinge section and the FER section share this geometric layout and differ only in the concrete parameters assigned to the core and cover regions, as described in Section 5.2.2.

The column plastic-hinge section and the FER section employ the same geometric fiber discretization. However, whereas the column distinguishes between confined core and unconfined cover concrete, the FER element assigns identical constitutive properties to all concrete fibers. Figure 109 illustrates the fiber discretizations adopted for the FER element.

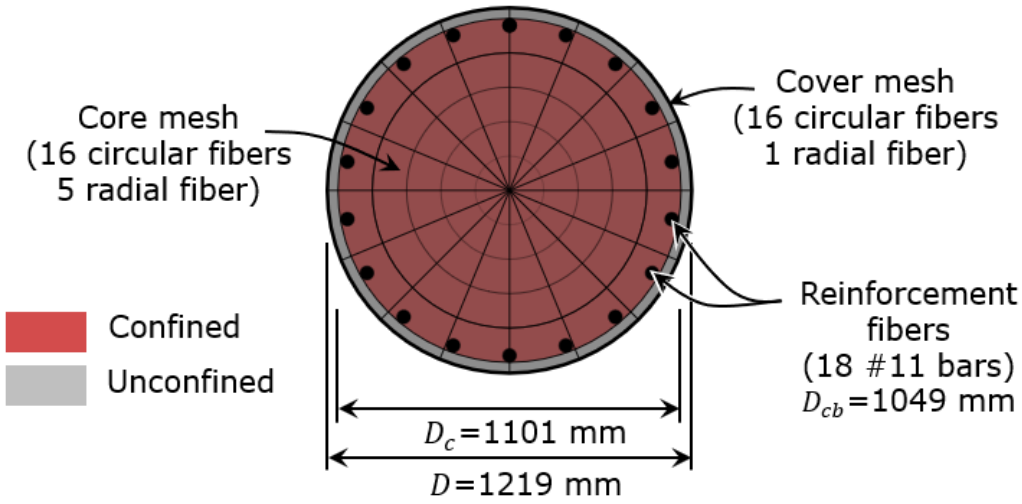


Figure 108. Circular fiber-section discretization for the column element.

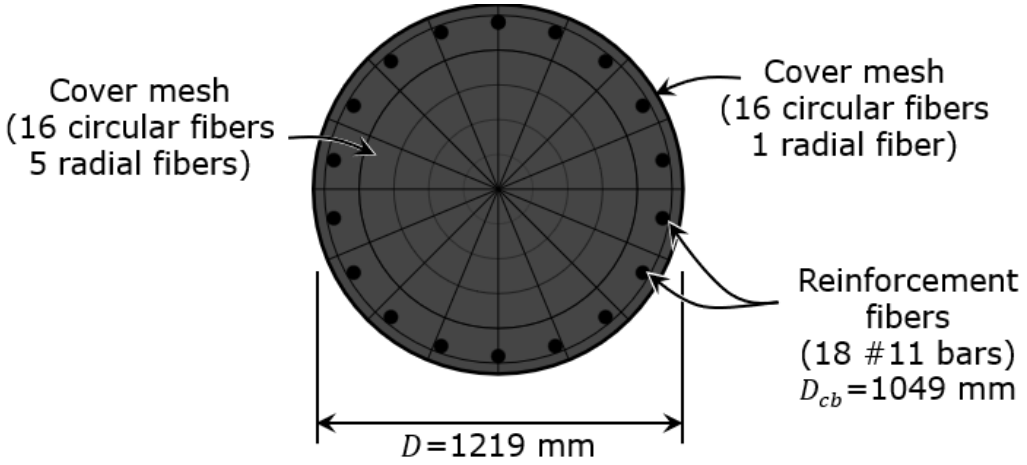


Figure 109. Circular fiber-section discretization for the FER element.

5.2 Material Constitutive Modeling

The formulation combines experimentally calibrated stress-strain relationships for reinforcing steel, unconfined concrete, and confined concrete, with confinement-dependent modifications to strength and deformation capacity based on the effectiveness of transverse reinforcement. The reinforcing-steel response accounts for the cyclic behavior, including the rate-independent backbone, unloading and Bauschinger response, strain-rate effects, and bond-slip-induced pinching. Because tensile cracking produces localized deformation that cannot be represented by a unique post-cracking stress-strain relationship independently of the adopted fiber discretization, the tensile softening response is adjusted according to the characteristic length associated with the fiber formulation. This regularization provides a consistent representation of the energy dissipated during crack opening while reducing the structural response's dependence on the adopted discretization. The resulting constitutive models are subsequently incorporated into the fiber sections of the structural elements, with the material assignment and characteristic lengths defined according to the corresponding structural regions.

5.2.1 Longitudinal reinforcement

The longitudinal bars are idealized with the SteelDRCV model developed in Chapter 4. The rate-independent backbone is defined by a modulus of elasticity E_s=196 000 MPa, the yield strength f_y=519 MPa, the onset of strain hardening at ε_{sh}=0.011, and the ultimate point (f_{su}=707 MPa, ε_u=0.122); the strain-hardening exponent P, equal to 3.67. These parameters define the monotonic backbone of the constitutive model. Under load reversals, the response is governed by the closed-form rational-Bézier Bauschinger formulation of Chapter 4, whose curvature is controlled by the Bauschinger area factor, Ω_{fac}.

The resulting monotonic constitutive response is shown in Figure 110. Table 22 lists the corresponding constitutive parameters determined from the experimental results. Beyond the conventional cyclic constitutive response, the SteelDRCV model incorporates the strain-rate- and pinching-dependent formulations proposed in this dissertation. The corresponding parameters (λ, n_p) for the quadrant-dependent bond-slip pinching and Ω_{fac} are first estimated in Stage 1 (displacement-controlled calibration, Section 5.7), where the cyclic protocol excites them directly, and then refined jointly with the strain-rate parameters (k_{rate}, n_{rate}) in Stage 2 (Bayesian dynamic calibration, Section 5.8), since the viscous mechanism is inactive under quasi-static loading.

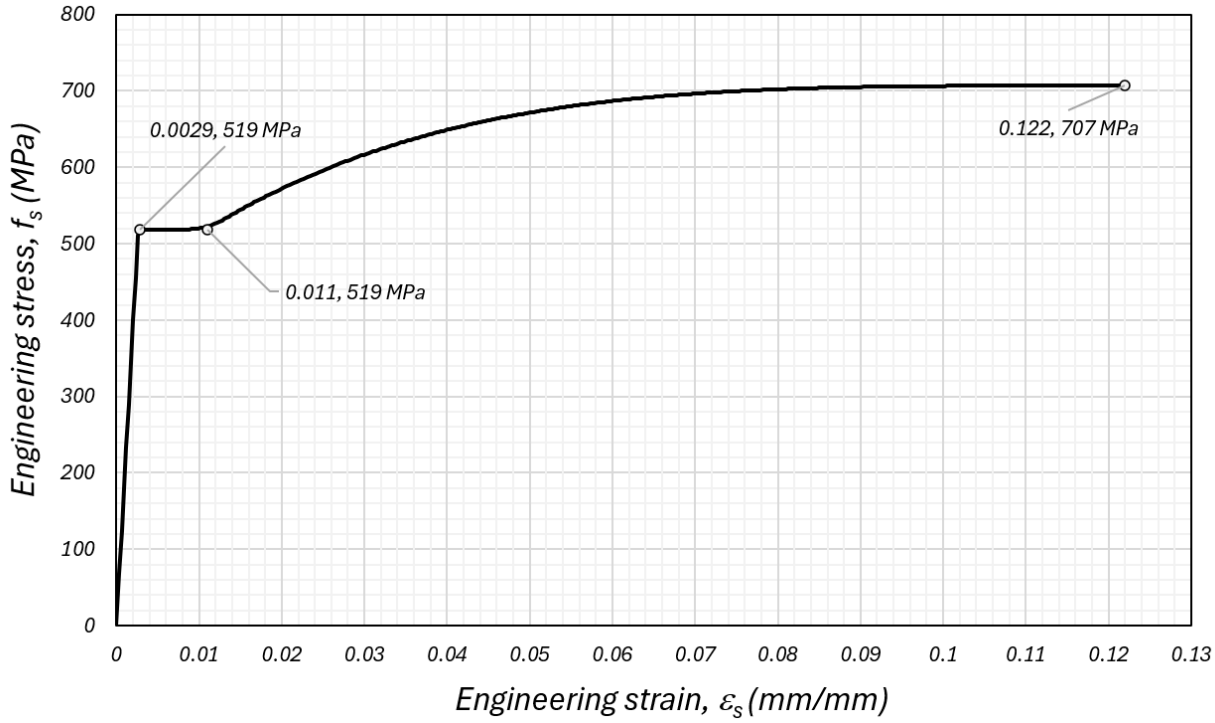


Figure 110. SteelDRCV Monotonic tensile envelope adopted for the reinforcing steel.

Table 22. SteelDRCV monotonic tensile constitutive parameters determined from the experimental results.

Thesis symbol	TCL variable	Value	Units
E_s	E_L	196000	MPa
f_y	f_{yL}	519	MPa
ε_u	ε_{uL}	0.0122	mm/mm
f_{su}	f_{uL}	707	MPa
ε_{sh}	ε_{shL}	0.011	mm/mm
P	P_L	3.67	-

NOTE: The column "TCL variable" lists the names of the variables used in the OpenSees TCL implementation of the numerical model. These names facilitate traceability between the constitutive parameters presented in this thesis and their implementation in the analysis scripts.

5.2.1.1 Unloading Modulus

Upon a load reversal from a point (ε'_r, f'_r), the initial portion of the unloading branch is essentially linear and is characterized by the unloading modulus E'_u, as reported by Restrepo-Posada [113] for a stress change of $1.0f_y$ and subsequently generalized by Carreño to a stress change of ηf_y [29]. Analysis of test data showed that E'_u decreases rapidly once yielding has occurred but stabilizes at larger strains, and that it correlates with the maximum absolute plastic strain ε'_0 accumulated over the loading history rather than with the plastic strain of the current reversal. E'_u was therefore assumed to depend on ε'_0 alone as

$$\frac{E'_u}{E'_s} = 0.82 + \frac{1}{5.55 + 1000|\varepsilon'_0|} \tag{151}$$

The influence of E'_u extends beyond the unloading-branch slope. Because the reversal strain is offset by a term proportional to f_y/E'_u, the unloading modulus also fixes the strain at which the linear branch ends and Bauschinger softening begins, as well as the origin of the shifted skeleton curve to which the response subsequently converges [113]. It therefore governs not only the slope of the unloading branch but also its extent and the position of the subsequent hysteretic response. In the present study, the formulation proposed by Restrepo-Posada is generalized through the introduction of the calibratable parameter, α_u, which controls the asymptotic unloading stiffness.

$$\frac{E'_u}{E'_s} = \alpha_u + (1 - \alpha_u)\frac{5.55}{5.55 + 1000|\varepsilon'_0|}; \quad 0.6 \le \alpha_u \le 1.0 \tag{152}$$

The decay constants 5.55 and 1000 are retained unchanged so that the degradation rate of E'_u with accumulated plastic strain remains identical to that of the original formulation, whereas only the asymptotic unloading stiffness is released as a calibration parameter. Consequently, $E'_u = E'_s$ at $\varepsilon'_0 = 0$, while $E'_u \to \alpha_u E'_s$ as ε'_0 increases. The original expression is recovered by setting α_u=0.82, whereas the limiting case α_u=1 suppresses unloading-stiffness degradation entirely and is retained

for sensitivity studies. Figure 111 illustrates how the proposed parameter α_u modifies the evolution of the normalized unloading modulus.

The formulation proposed by Restrepo-Posada remains one of the few constitutive models that explicitly relate the unloading modulus to the accumulated plastic strain. However, the asymptotic value of 0.82 reflects the experimental database used in its original calibration. Fixing this asymptote therefore embeds a dataset-specific calibration into a quantity that governs the shift strain and, consequently, the entire hysteretic response. Rather than modifying the experimentally established degradation law, the present study generalizes the formulation by replacing the fixed asymptotic value with the calibratable parameter α_u. Consequently, the asymptotic unloading stiffness is identified together with the remaining material parameters during the calibration procedure.

Figure 112 shows the influence of α_u on the unloading branch for a representative reversal point located on the strain-hardening branch (ε=0.052). The reversal point was selected solely for illustrative purposes; the qualitative effect of α_u is valid for any particular reversal strain.

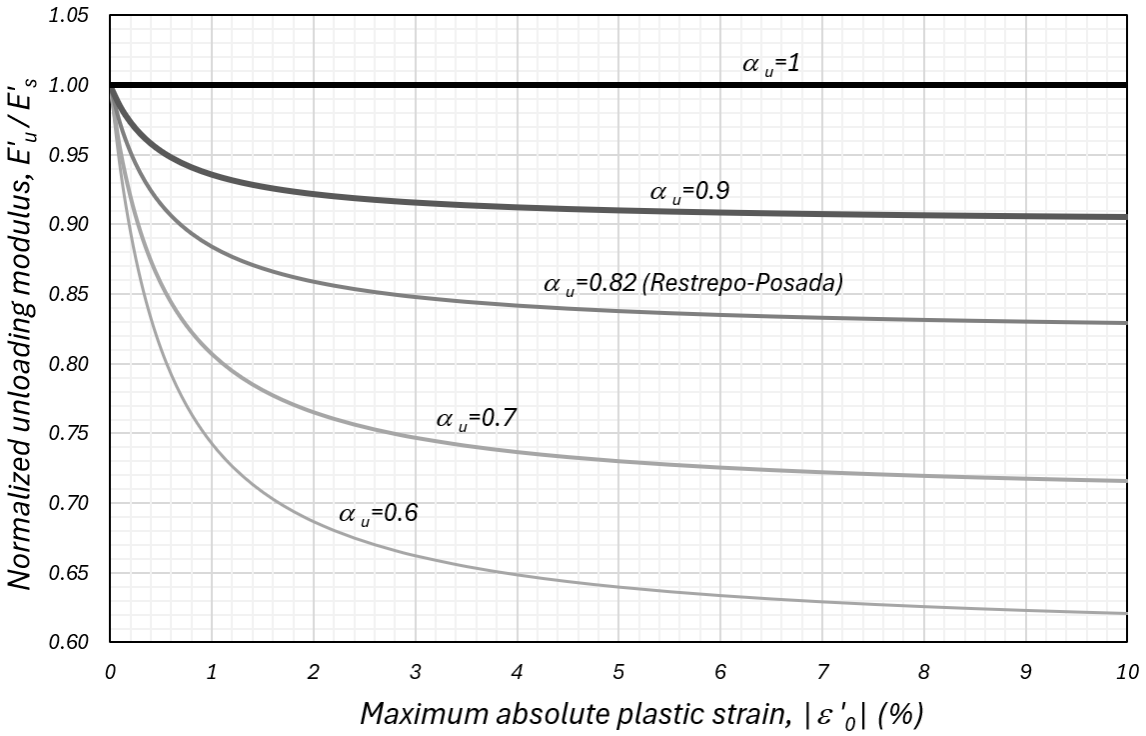


Figure 111. Normalized unloading modulus as a function of maximum absolute plastic strain for selected values of α_u.

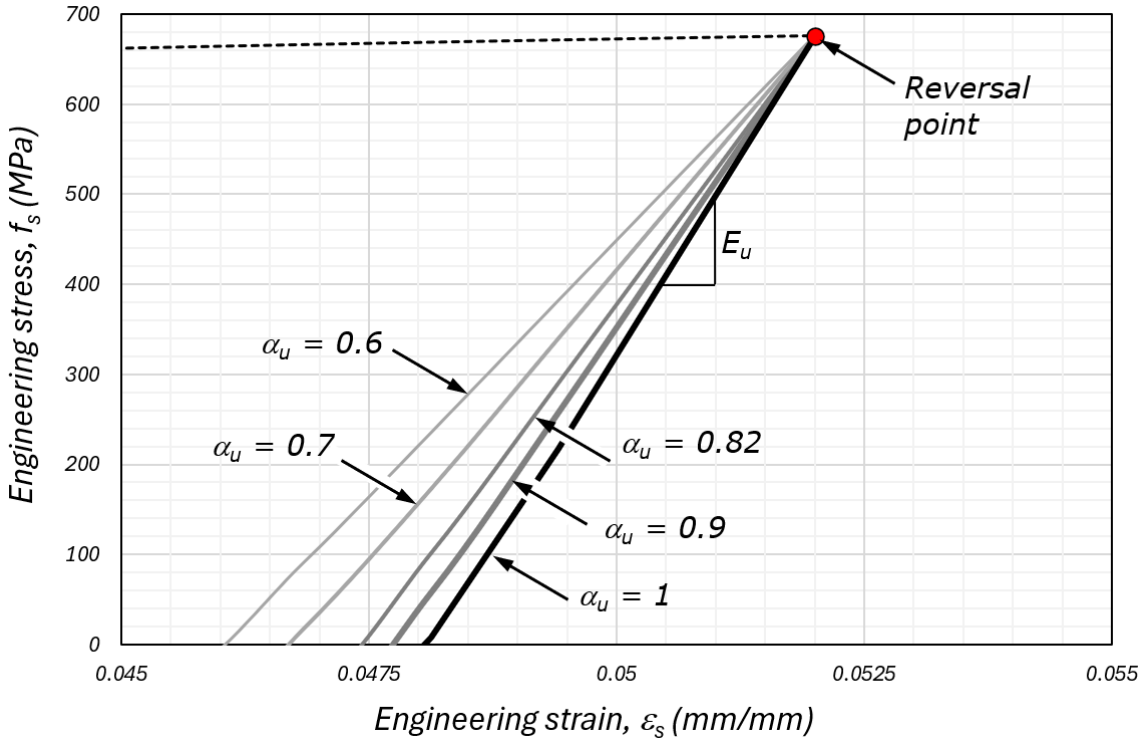


Figure 112. Influence of α_u on the unloading branch.

5.2.2 Concrete Constitutive Modeling

The ConcreteCM model by Chang & Mander [31] and Kolozvari et al. [69] represents both the cover and core concrete. This model was selected over other hysteretic formulations commonly used in uniaxial concrete models, which have limited capability to reproduce complex cyclic mechanisms such as gradual gap closure. *ConcreteCM* is a generalized, rule-based, and non-dimensional constitutive formulation that allows independent calibration of the monotonic envelope and hysteretic response for confined and unconfined concrete, including ordinary- and high-strength materials subjected to cyclic compression and tension.

The model captures continuous hysteretic response under load reversals, stiffness degradation through smooth unloading-reloading branches associated with increasing damage, and crack-closure effects. The latter are controlled through an optional gap parameter that governs the plastic stiffness during unloading from the tensile envelope and, consequently, the level of pinching in the member-level hysteretic response. The monotonic envelope follows the relation of Tsai [134], of which the Popovics [104] curve is the special case $r = n/(n-1)$. With $n = E_c(\varepsilon_c'/f_c')$, the normalized stress is:

$$\frac{f}{f_c'} = \frac{n.\varepsilon/\varepsilon_c'}{1 + \left(n - \frac{r}{r-1}\right)\left(\frac{\varepsilon}{\varepsilon_c'}\right) + \frac{(\varepsilon/\varepsilon_c')^r}{r-1}} \tag{153}$$

where the shape parameter r controls the post-peak (in compression) or post-cracking (in tension) branch, and the non-dimensional critical strains, $\varepsilon/\varepsilon_c'$, mark the point beyond which the branch is continued linearly to zero stress, in compression and in tension, respectively.

5.2.2.1 Concrete in Column Element

5.2.2.1.1 Unconfined Concrete

For the concrete cover in the column, the material parameters were defined based on the concrete properties reported by Schoettler et al. [124] from the tested column. The monotonic compressive envelope was characterized using the following parameters: a peak unconfined concrete compressive strength f_{cu}'=-42 MPa at a strain of ε_{cu}'=-0.00205 mm/mm; an initial tangent modulus E_{cU}=22900 MPa; a post-peak shape parameter r_{cU}=50, and a non-dimensional critical strain on the compression envelope x_{crnU}=2.54. The comparatively large value of r_{cU} yields the steep post-peak strength degradation characteristic of unconfined concrete following spalling. The resulting monotonic compressive envelope is shown in Figure 113. The adopted compressive constitutive parameters are summarized in Table 23.

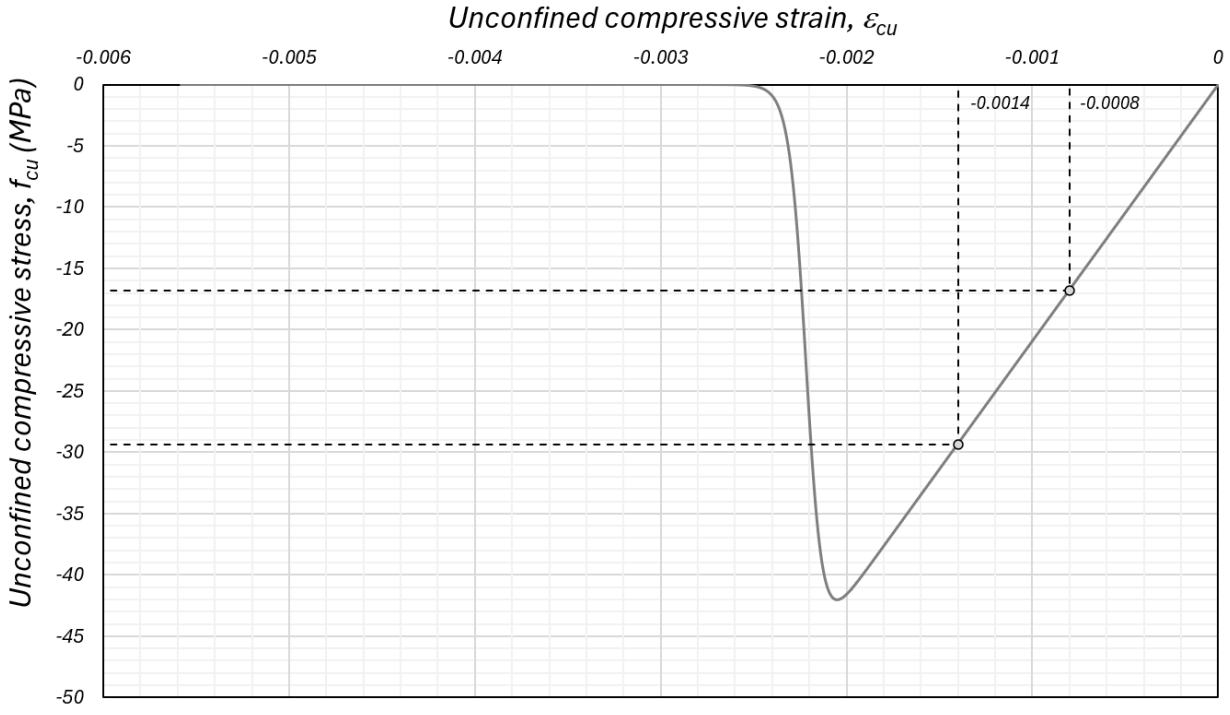


Figure 113. Monotonic compressive envelope adopted in the ConcreteCM for the unconfined cover concrete.

The modulus of elasticity of concrete is not a unique material constant because its compressive stress-strain response becomes nonlinear from the early stages of loading. It is therefore defined as a secant (chord) modulus between prescribed points on the ascending branch of the stress-strain curve. In the present study, the first reference level is taken as $0.4f_c'$ consistent with ASTM C469/C469M [6], because it lies within the quasi-linear portion of the ascending branch and provides a representative measure of the initial elastic stiffness. A second reference level, $0.7f_c'$, is introduced to characterize

stiffness in the nonlinear regime before peak stress. Although not associated with a standardized modulus determination, this level captures the stiffness degradation accompanying the transition from the near-elastic response toward compressive strength.

Table 23. ConcreteCM compressive constitutive parameters adopted for the unconfined cover concrete.

Thesis symbol	TCL variable	Value	Units
f'_{cu}	f_{pcU}	-42	MPa
ε'_{cu}	ε_{ps0cU}	-0.00205	mm/mm
E_{cU}	E_{cU}	22900	MPa
r_{cU}	r_{cU}	50	-
x_{crnU}	x_{crnU}	2.54	-

NOTE: The column "TCL variable" lists the names of the variables used in the OpenSees TCL implementation of the numerical model. These names are included to facilitate traceability between the constitutive parameters presented in this thesis and their implementation in the analysis scripts.

Since the modulus is defined as a secant rather than a tangent quantity, its value necessarily decreases as the reference stress increases from $0.4f'_c$ to $0.7f'_c$. Together, these two secant moduli provide a simple characterization of the curvature of the ascending branch: the first represents the conventional elastic modulus used in design practice, whereas the second reflects the progressive stiffness degradation as the peak compressive stress is approached.

5.2.2.1.2 Confined Concrete

The core concrete in the column is modeled using the same ConcreteCM formulation, with its compressive envelope modified to account for confinement from the transverse reinforcement. The constitutive parameters defining the confined response are obtained from confinement relationships based on the geometry and mechanical properties of the transverse reinforcement. The procedure begins by defining the effectively confined concrete region, D_s, from which the confinement ratio and the effective lateral confining pressure are subsequently determined.

$$D_c = D - 2c - d_{bt} \tag{154}$$

where c is the concrete cover measured from the outer surface of the transverse reinforcement to the external surface of the concrete (51 mm), and d_{bt} is the diameter of the transverse reinforcement (15.9 mm). Based on this geometric definition, the confinement action is quantified through the volumetric confinement ratio, which characterizes the amount of transverse reinforcement effectively engaged within the confined core:

$$\rho_s = 2.\frac{4A_{sh}}{D_c.s} \tag{155}$$

where A_{sh} (199 mm^2) denotes the area of transverse reinforcement, and s (152 mm) is the center-to-center spacing of the transverse reinforcement; the factor $4A_{sh}/(D_c.s)$ is the volumetric ratio for a circular section, and the leading factor 2 accounts for the double (bundled) hoops, which provide two equivalent transverse reinforcement layers contributing to the confinement action. However, this volumetric ratio assumes idealized, uniform confinement. The discrete arrangement of transverse reinforcement along the perimeter reduces confinement effectiveness. To account for this effect, a geometric efficiency factor has been introduced:

$$k_e = \left(1 - \frac{s_p}{2D_c}\right)^2 \tag{156}$$

where s_p denotes the clear spacing between transverse reinforcement legs, and is defined as:

$$s_p = s - db_t \tag{157}$$

The idealized lateral confinement pressure, f_{pl}, combines the volumetric contribution of the transverse reinforcement with the geometric reduction associated with its discrete distribution. The idealized confinement pressure generated by the transverse reinforcement is expressed as:

$$f_{pl} = \frac{\rho_s f_{yh}}{2} \tag{158}$$

where f_{yh} is the yield strength of the transverse reinforcement. To account for the non-uniform distribution of transverse reinforcement along the perimeter of the confined core, a geometric efficiency factor is applied to the idealized pressure, leading to the effective lateral confinement pressure:

$$f_{ple} = k_e f_{pl} \tag{159}$$

At this stage, the confinement state is fully characterized by an equivalent lateral pressure acting on the concrete core, which accounts for both the volumetric contribution of the transverse reinforcement and its geometric efficiency. This pressure is subsequently normalized with respect to the unconfined compressive strength to define a dimensionless confinement index:

$$f_{plec} = \left|\frac{f_{ple}}{f'_{cu}}\right| \tag{160}$$

This parameter governs modifications to the compressive response of concrete, leading to confinement-dependent enhancements in strength and deformation capacity, as introduced in the following constitutive relations. For the present specimen, these relations give ρ_s≈0.0095, k_e≈0.89, and f_{plec}≈0.034. In this context, the confined concrete compressive strength is defined as an enhancement of the unconfined strength as a function of the normalized confinement level:

$$f'_{cC} = f'_{cu}\left(1+4.1f_{plec}\right) \tag{161}$$

where 4.1 is the confinement coefficient of Mander, Priestley & Park [83] and the peak-strain shift is the adopted simplified form. The confinement effect is directly reflected in the increased peak compressive resistance provided by transverse reinforcement. Consistent with this strength enhancement, the strain at peak compressive stress is adjusted to reflect the delayed onset of crushing under confinement:

$$\varepsilon'_{cC} = \varepsilon'_{cu} - \frac{f_{plec}}{20} \tag{162}$$

This modification shifts the material's compressive backbone, allowing greater deformation capacity before reaching peak stress. These equations result in f'_{cC}=-47.9 MPa and ε'_{cC}=-0.00376. The confinement relationships above yield the constitutive parameters summarized in Table 24.

Table 24. ConcreteCM compressive constitutive parameters adopted for confined-core concrete.

Thesis symbol	TCL variable	Value	Units
f'_{cC}	f_{pcC1}	-47.9	MPa
ε'_{cC}	ε_{ps0C1}	-0.00376	mm/mm
E_{cC}	E_{cC1}	22900	MPa
r_{cC}	r_{cC1}	2.35	-
x_{crnC}	x_{crnC1}	11760	-

NOTE: The column "TCL variable" lists the names of the variables used in the OpenSees TCL implementation of the numerical model. These names facilitate traceability between the constitutive parameters presented in this thesis and their implementation in the analysis scripts.

Figure 114 compares the corresponding confined and unconfined compressive envelopes. The secant moduli evaluated at $0.4f'_c$ and $0.7f'_c$ were also used to verify that the confined and unconfined envelopes retain essentially the same initial stiffness. This behavior is consistent with the mechanics of confined concrete, where transverse confinement primarily modifies strength and deformation capacity after significant nonlinearity develops. The confined envelope is completed with r_{cC}=2.35 and x_{crnC}=11760, values that sustain the descending branch to the large compressive strains expected of well-confined concrete; because confinement does not enhance the tensile strength, the tensile parameters are those of the cover.

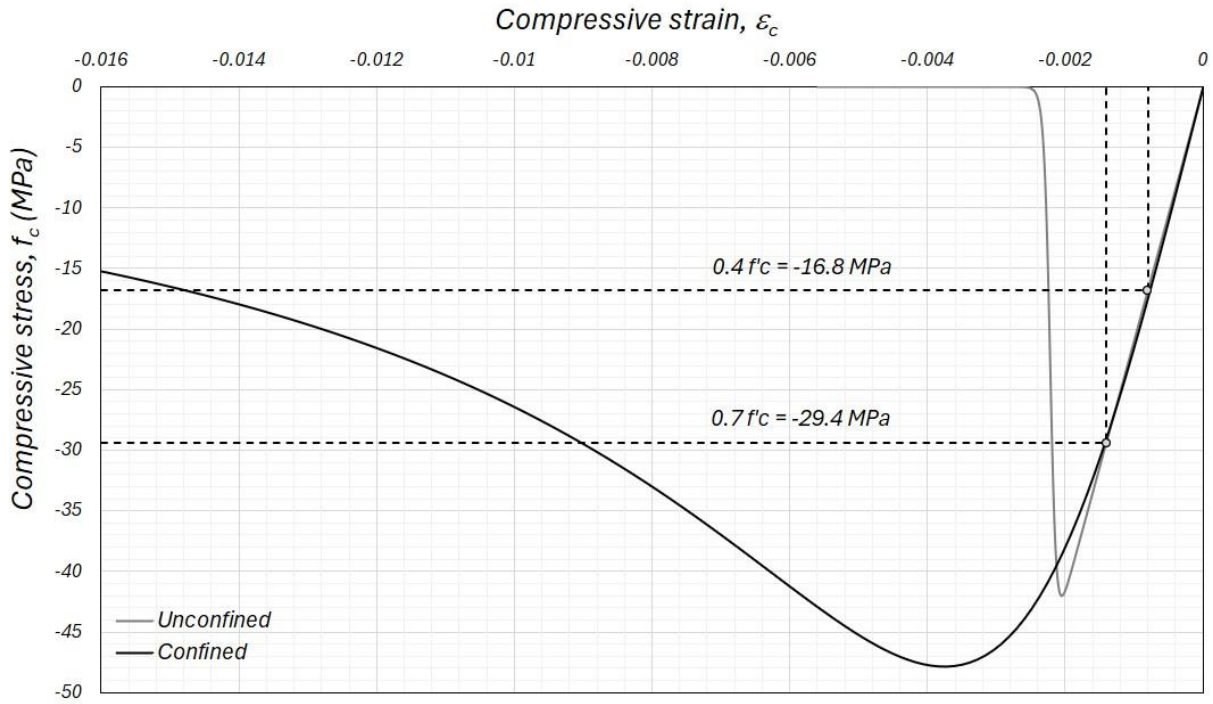


Figure 114. Monotonic compressive envelope adopted in the ConcreteCM for the confined cover concrete.

5.2.2.2 Concrete in the Fixed-End Rotation Element

The concrete assigned to the FER element differs from that adopted for the column because the two elements represent different physical conditions of the test specimen. Whereas the column develops confinement exclusively through its transverse reinforcement, the concrete surrounding the embedded base is additionally restrained by the massive RC foundation, resulting in substantially greater confinement. Accordingly, the FER element is represented using a highly confined ConcreteCM response.

The peak compressive strength and corresponding peak strain were set sufficiently high, as an ad hoc modeling choice, to keep the concrete response outside the nonlinear softening regime over the strains encountered in the analyses. This idealization is consistent with the role of the FER element, which represents the kinematic contribution of the embedded base to fixed-end rotation rather than a region in which concrete crushing and post-peak softening are expected to govern the response.

Figure 115 compares the monotonic compressive envelopes adopted for the unconfined cover concrete and the confined core concrete of the column element, as well as the highly confined concrete adopted for the FER element, illustrating the progressive increase in confinement in the numerical model.

The fiber section retains the same geometric subdivision into core and cover regions as the column, as illustrated in Figure 109. However, both regions are assigned identical ConcreteCM constitutive properties. The distinction is retained exclusively for numerical consistency with the adopted fiber-section formulation and does not represent different material properties within the FER element. Table 25 summarizes the adopted constitutive parameters.

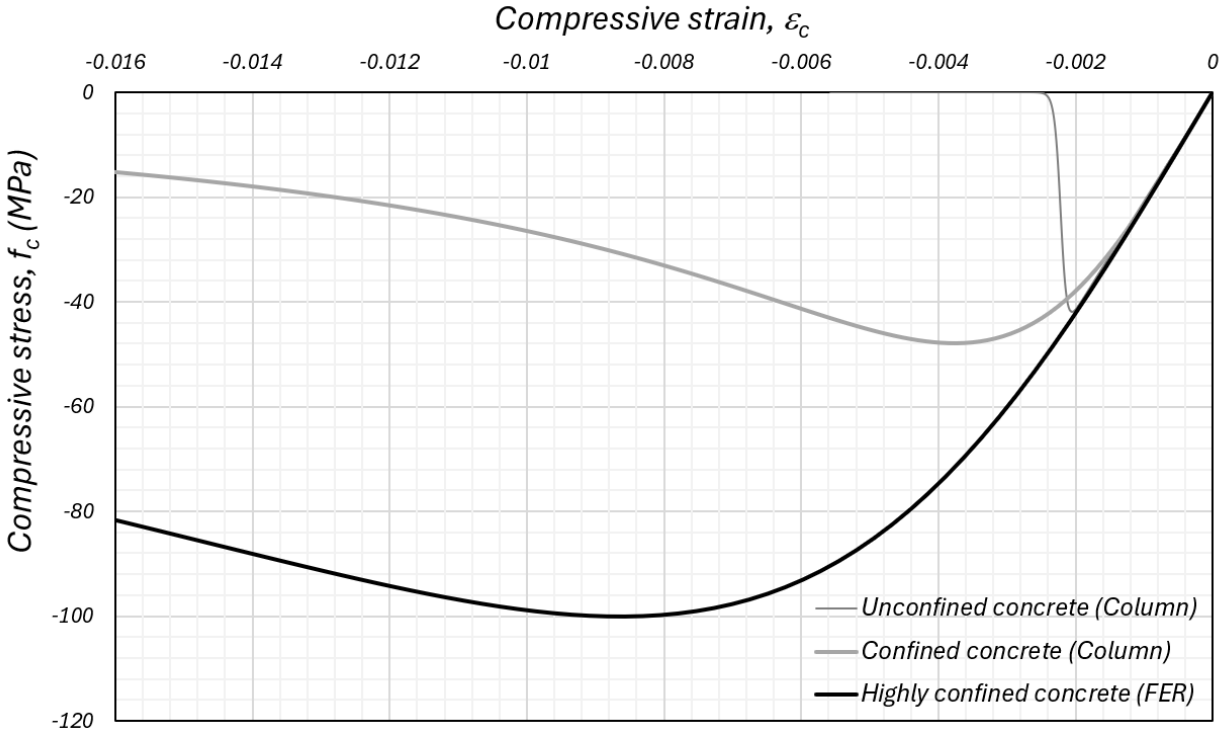


Figure 115. Monotonic compressive envelope adopted in the ConcreteCM for the FER element.

Table 25. ConcreteCM compressive constitutive parameters adopted for the FER element.

Thesis symbol	OpenSees TCL variable	Fiber region	Value	Units
f'_{cUFER}	f_{pcU_sp}	Cover	-100	MPa
ε'_{cUFER}	ε_{pcU_sp}		-0.0086	mm/mm
E_{cUFER}	E_{cU_sp}		19730	MPa
r_{cUFER}	r_{cU_sp}		2.116	-
$x_{crnUFER}$	x_{crnU_sp}		10000	-
f'_{cCFER}	f_{pcC_sp}	Core	-100	MPa
ε'_{cCFER}	ε_{pcC_sp}		-0.0086	mm/mm
E_{cCFER}	E_{cC_sp}		19730	MPa
r_{cCFER}	r_{cC_sp}		2.116	-
$x_{crnCFER}$	x_{crnC_sp}		10000	-

NOTE: The column "TCL variable" lists the names of the variables used in the OpenSees TCL implementation of the numerical model. These names are included to facilitate traceability between the constitutive parameters presented in this thesis and their implementation in the analysis scripts.

5.2.3 Tensile in Concrete

The ConcreteCM model was selected to represent the concrete response because its formulation is intended to reproduce the cyclic behavior of cracked concrete, including crack opening and closure. The mechanical response of cracked concrete is influenced by the interaction between opposing crack faces and the mechanisms governing stress transfer across the crack, including aggregate interlock [137]. These mechanisms are particularly relevant under cyclic loading, where crack opening, closure, and stiffness recovery influence the hysteretic response of RC members. The ConcreteCM formulation is therefore adopted for the concrete regions of the present structural model.

Within this formulation, the tensile response is particularly relevant because tensile cracking contributes to the deformation mechanisms governing the column-foundation interface. Experimental studies of RC bridge columns have shown that cracking and reinforcement slip at this interface contribute to FER [57] and [58]. The post-cracking tensile response therefore plays an important role in the FER element. At the numerical level, however, localization of tensile deformation makes this response dependent on the characteristic length of the fiber discretization. This dependence is addressed through the tensile-response regularization described in the following section.

The concrete tensile strength, f_t, is preliminarily established as a property governed by the unconfined compressive strength, f'_{cu}, through a logarithmic constitutive relationship that anchors the tensile capacity to the mechanical quality of the compressive matrix. The adopted expression reads:

$$f_t = 2.07\, ln\left(1 - \frac{f'_{cu}}{12.41}\right) \tag{163}$$

where f'_{cu} is expressed in MPa. This equation results in f_t=3.1 MPa. By deriving tensile strength from compressive capacity in this manner, the model ensures the tensile envelope remains physically consistent with the overall constitutive framework, providing a rational starting point for defining the post-cracking softening branch and the associated shape parameters that control stress degradation in the tensile regime. The tensile strength, f_t, characterizes the monotonic tensile envelope, reached at a tensile strain $\varepsilon_t = f_t/E_{uc}$, together with a tensile shape parameter r_t and a non-dimensional critical strain parameter x_{crpt}=10000.

The influence of r_t on the post-cracking tensile response is illustrated in Figure 116 using f_t=3.1 MPa and E_{cU}=22900 MPa, which result in a tensile cracking strain of ε_t=0.000135 mm/mm. These values are adopted solely for illustrative purposes to isolate the influence of and do not correspond to the calibrated parameters used in this dissertation.

The parameter r_t governs the shape and rate of stress degradation in the post-cracking branch. In contrast, the parameter x_{crpt} controls the extent of the tensile envelope at large tensile strains and defines the strain range over which the post-cracking response is represented. The parameters f_t and r_t are treated as calibratable constitutive parameters, whereas x_{crpt} is fixed. Higher values of r_t produce a steeper post-cracking stress degradation, resulting in a more abrupt loss of tensile stress, whereas lower values produce a more gradual softening response. The ascending branch and peak tensile strength remain unchanged, such that the effect of r_t is confined to the post-cracking branch.

Because r_t also affects the area under the post-cracking branch, it directly influences the tensile energy dissipated by the constitutive response. The parameters f_t and r_t are treated as calibratable constitutive parameters and are identified together with the remaining model parameters during the structural calibration described in Sections 5.7 and 5.8.

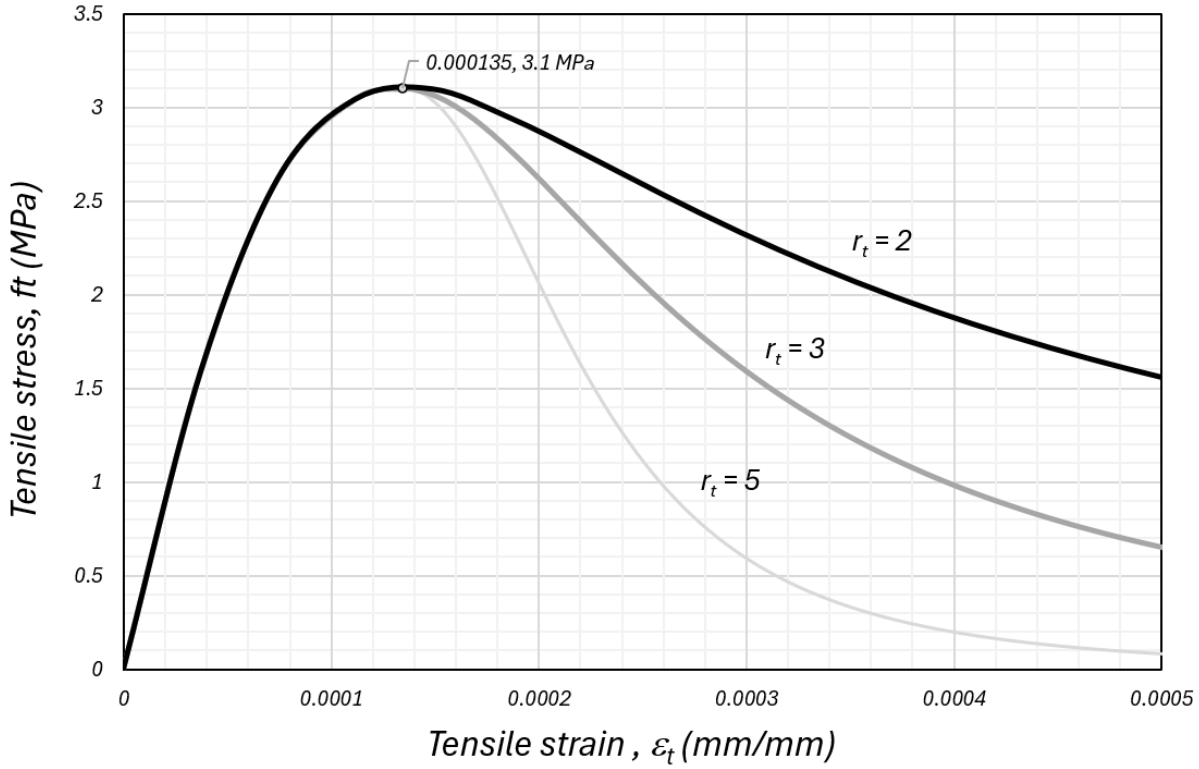


Figure 116. Influence of the tensile shape parameter r_t on the post-cracking tensile response of the ConcreteCM model.

5.2.3.1 Regularization of the Tensile Response

The tensile response of concrete requires separate consideration because tensile cracking governs the onset of damage and because the post-cracking response in a fiber-section formulation depends on the characteristic length associated with the discretization. Once cracking occurs, the tensile deformation progressively localizes within a fracture process zone, while the surrounding material unloads.

Consequently, the post-cracking stress-strain relationship cannot be defined independently of the length over which the localized crack opening is represented. Since the characteristic length controls how the localized deformation is distributed in terms of strain, the constitutive response must be linked to the energy dissipated during fracture rather than defined solely by the stress-strain relationship. This consideration is particularly relevant to the fiber sections used in the present model because the FER and structural-column regions have different characteristic lengths.

The tensile energy dissipation parameter is the tensile fracture energy, G_{ft}, defined as the energy required to create a unit area of crack surface. Consequently, the softening branch of the constitutive

response must therefore be defined so that the area under the constitutive curve, multiplied by the characteristic length, dissipates the same fracture energy regardless of the adopted discretization. Hence, the tensile fracture energy represented by the constitutive model is expressed as:

$$G_{ft} = g_{ft}.L_{ch} \tag{164}$$

where g_{ft} denotes the fracture energy dissipated per unit volume, corresponding to the area under the post-cracking branch of the constitutive response, and L_{ch} is the characteristic length associated with the fiber section and controls how localized deformation is represented in terms of fiber strain.

The influence of the tensile shape parameter and the characteristic length should be distinguished. Increasing r_t produces a steeper post-cracking stress degradation and reduces the area under the softening branch, whereas increasing L_{ch} distributes the same localized deformation over a larger strain interval.

The regularization is applied consistently to the concrete regions represented in the numerical model. The tensile strength, cracking strain, and the remaining tensile constitutive parameters are kept identical between the column and FER elements. The tensile shape parameter r_t, however, is adjusted for each element according to its characteristic length so that the corresponding post-cracking response dissipates the same tensile fracture energy, G_{ft}, despite the different fiber discretizations. Thus, the two elements represent the same underlying concrete fracture energy while allowing their equivalent stress-strain responses to account for their respective characteristic lengths.

For the FER element, this distinction matters because it represents localized deformation at the column-foundation interface. Its response results from reinforcement slip together with the opening and closing of flexural cracks surrounding the anchored bars. Under reversed cyclic loading, residual reinforcement deformation and relative slip between opposing crack faces delay re-establishing contact upon load reversal. The characteristic length assigned to the FER section therefore determines how this localized deformation is represented in terms of fiber strain, while the regularization preserves consistency in the associated energy dissipation.

Although the structural mechanisms represented by the column and FER elements differ, the regularization of the tensile constitutive response is governed exclusively by their different characteristic lengths. The column element employs the plastic-hinge characteristic length of L_{pc}= 975 mm, whereas the FER element employs the strain-penetration characteristic length L_{pFER}=566 mm. To preserve the tensile fracture energy, only the post-cracking softening branch is modified by scaling the tensile shape parameter according to

$$r_{tFER} = r_{tCOL}\frac{L_{pFER}}{L_{pc}} \tag{165}$$

The resulting tensile shape parameters, r_{tCOL} and r_{tFER}, correspond to the post-cracking softening responses assigned to the structural-column and FER fiber sections, respectively. The tensile strength and cracking strain remain unchanged because both elements represent the same concrete material.

The different values of r_t therefore account for the different characteristic lengths of the two fiber sections while preserving the same tensile fracture energy.

The tensile strength and the length-consistent tensile shape parameters, r_{tCOL} and r_{t_FER}, are subsequently held constant throughout the global constitutive-parameter identification procedure. The corresponding cracking strain is determined from the adopted tensile strength and elastic modulus and is not treated as an independent calibration parameter.

5.3 Calibration and Validation Procedure

The calibration aims to identify the constitutive parameters of the material models that best match the numerical and experimentally measured structural responses obtained during the shake-table campaign. The calibration is organized in two stages. In Stage 1, the analysis is driven by the lateral displacement history recorded experimentally at the center of mass of the loading block, which is prescribed as an input to the numerical model under quasi-static cyclic conditions. Since the displacement history is prescribed, it serves as an input to the numerical model rather than a predicted response quantity. Consequently, Stage 1 focuses on the structural response generated by the constitutive models under the experimentally recorded displacement history.

Although moment-curvature relationships are commonly used to calibrate constitutive models, the present study does not adopt curvature as the response variable. In a numerical model, curvature depends on the plastic-hinge formulation and on the associated discretization. In contrast, the experimental curvature is inferred from measurements obtained over finite gauge lengths defined by the instrumentation. Consequently, the numerical and experimental curvatures do not represent the same directly measured quantity. Under displacement control, this issue is avoided because displacement is not a response quantity to be predicted during calibration but a prescribed input, taken directly from the experimental record. The same displacement history is therefore imposed on both the numerical model and the physical specimen, providing a directly comparable basis for evaluating the corresponding structural response.

This loading strategy isolates the constitutive behavior from other sources of variability inherent to dynamic analyses. In a nonlinear time-history analysis, the structural response depends not only on the constitutive behavior of the materials but also on inertia, damping, mass distribution, numerical integration, and the characteristics of the input ground motion. Under such conditions, discrepancies between numerical and experimental responses cannot be attributed uniquely to the constitutive model. By contrast, displacement-controlled quasi-static loading eliminates inertial and damping effects, allowing the calibration to focus directly on the material constitutive response. However, the viscous mechanism of the SteelDRCV model is inactive under quasi-static loading, and the strain-rate parameters (k_{rate}, n_{rate}), among others, cannot be identified under these conditions. Their calibration requires a second stage in which the model is subjected to dynamic loading.

For each imposed displacement history, the element kinematics determine the section deformations at the numerical integration points, from which the resisting forces are computed using the constitutive relationships of the concrete and reinforcing steel fibers. The resulting structural response is then compared with the corresponding experimental response. The response is expressed in

normalized form to facilitate comparison among loading histories with different displacement amplitudes.

In Stage 1, the constitutive parameters are identified by minimizing objective functions that quantify the discrepancy between the numerical and experimental responses. Several constitutive parameters introduced in the preceding sections cannot be determined directly from the available material characterization and are therefore identified by calibrating the structural response. The parameters calibrated in this stage include the pinching, Bauschinger, and other cyclic response parameters. The Stage 1 estimates serve as prior information for Stage 2.

In Stage 2, the strain-rate parameters are calibrated jointly with the pinching, Bauschinger, Rayleigh damping, and concrete post-peak parameters using Bayesian inference via the Transitional Markov Chain Monte Carlo algorithm (TMCMC). The analyses in this stage are nonlinear dynamic time-history simulations driven by recorded base accelerations, with inertial and damping effects active and the viscous mechanism engaged. The response metrics used for inference are the peak displacement and dissipated energy of each calibration earthquake. The Bayesian framework provides not only point estimates but also posterior distributions that quantify the uncertainty in the identified parameters (Section 5.8).

The first four sequential loading histories are used for constitutive-parameter calibration in both stages, while the fifth is excluded from parameter identification. The calibrated parameters are then evaluated through a nonlinear dynamic time-history analysis under the recorded base acceleration of the fifth seismic simulation. This independent prediction provides a rigorous assessment of the calibrated model's ability to generalize beyond the training records.

5.4 Experimental Data Used for Calibration

The experimental program described in Section 3.2.2 consisted of 10 seismic simulations. However, this study considers only the first five, as progressive deterioration of the experimental instrumentation during subsequent tests led to the loss of measurements required for reliable model calibration and validation. Of these five simulations, the first four were used for constitutive-parameter calibration in both stages, while the fifth was reserved exclusively for independent validation. The four calibration records provide progressively increasing displacement demands, allowing the constitutive parameters to be identified from structural responses spanning the transition from the nearly linear regime to the highly nonlinear range. Their corresponding lateral displacement histories are shown in Figure 117. In this figure, small residual offsets are observed between consecutive seismic simulations. These very small steps are attributed to thermal dilation of the instrumentation and the reference frame, which introduces a slight zero drift in the ground motions.

In Stage 1, rather than being analyzed independently, the displacement histories are concatenated into a single continuous loading protocol and imposed sequentially without resetting the constitutive state variables between simulations. Consequently, the material state at the end of each seismic simulation serves as the initial state for the next, allowing the calibration procedure to reproduce the progressive accumulation of plastic deformation and damage. In Stage 2, the recorded base accelerations from the same four seismic simulations are used as input ground motions for the nonlinear dynamic time-history analyses from which the Bayesian inference extracts the response metrics.

The fifth seismic simulation is not used during parameter identification in either stage. Instead, the constitutive parameters identified from the two-stage calibration are kept unchanged and evaluated through a nonlinear dynamic time-history analysis under the recorded base acceleration from the fifth seismic simulation. Because this analysis includes inertial, damping, and strain-rate effects, the agreement obtained provides a rigorous assessment of the calibrated model's predictive capability beyond the training records.

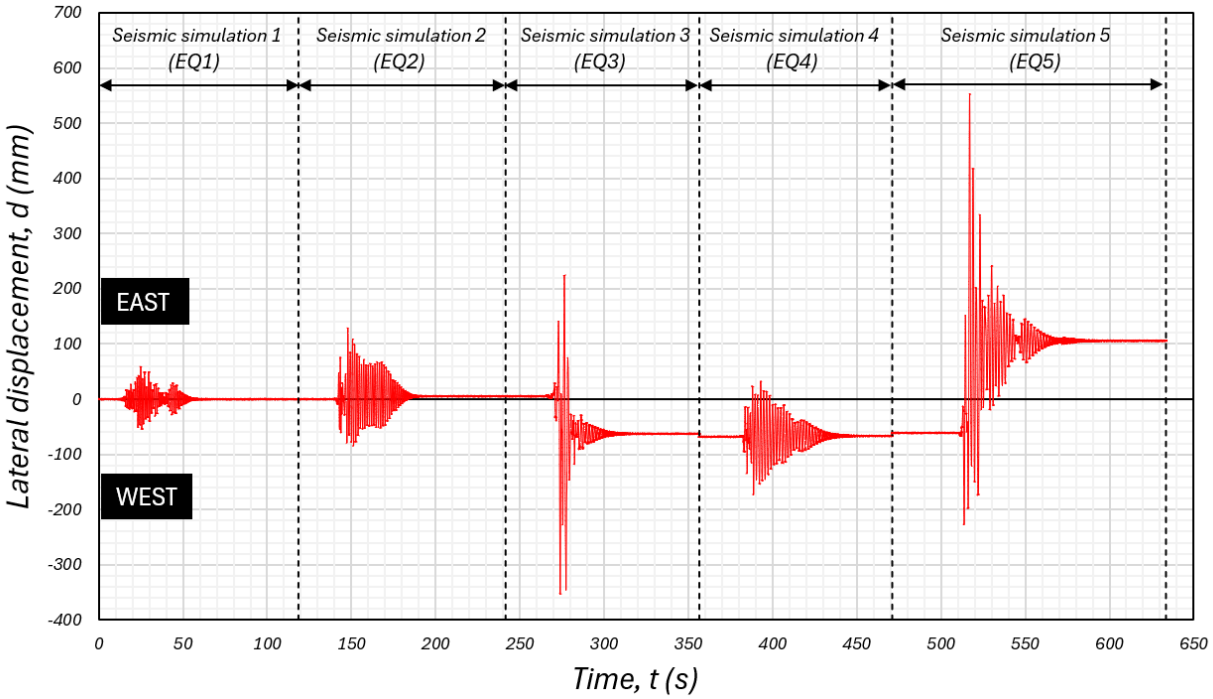


Figure 117. Lateral displacement histories of the four seismic simulations concatenated into the continuous loading protocol used for constitutive-parameter calibration.

EQ3 marks a pronounced transition toward fully developed nonlinear behavior, with drift ratios ranging from -4.9% to +3.0% and normalized moment peaks of -0.37 and +0.33, respectively. The response exhibits substantially wider hysteretic loops, pronounced stiffness degradation, and clear pinching near the origin. The grey EQ2 trace is substantially smaller than the EQ3 response, making the transition to large-deformation nonlinear behavior particularly evident. EQ4 exhibits a marked contraction of the response relative to EQ3, with drift ratios confined approximately between -1.4% and +1.4% and normalized moment values between -0.20 and +0.16, respectively. The response is predominantly linear. This simulation corresponds to the aftershock event following EQ3, and the experimental report attributes the offset to the residual deformation accumulated during the preceding test [124]. The grey EQ3 trace therefore provides a direct visual indication of the substantial reduction in response amplitude between the two consecutive simulations. EQ5 subsequently develops the most extensive nonlinear response of the sequence, extending from approximately 2.3% to +8.4% drift and reaching normalized moment peaks of -0.27 and +0.39. The response comprises multiple hysteretic loops of progressively increasing amplitude, with substantial energy dissipation and pronounced stiffness degradation. The grey trace for EQ4 is largely contained within the EQ5 response,

highlighting the sharp increase in deformation demand and nonlinear response associated with the fifth loading event.

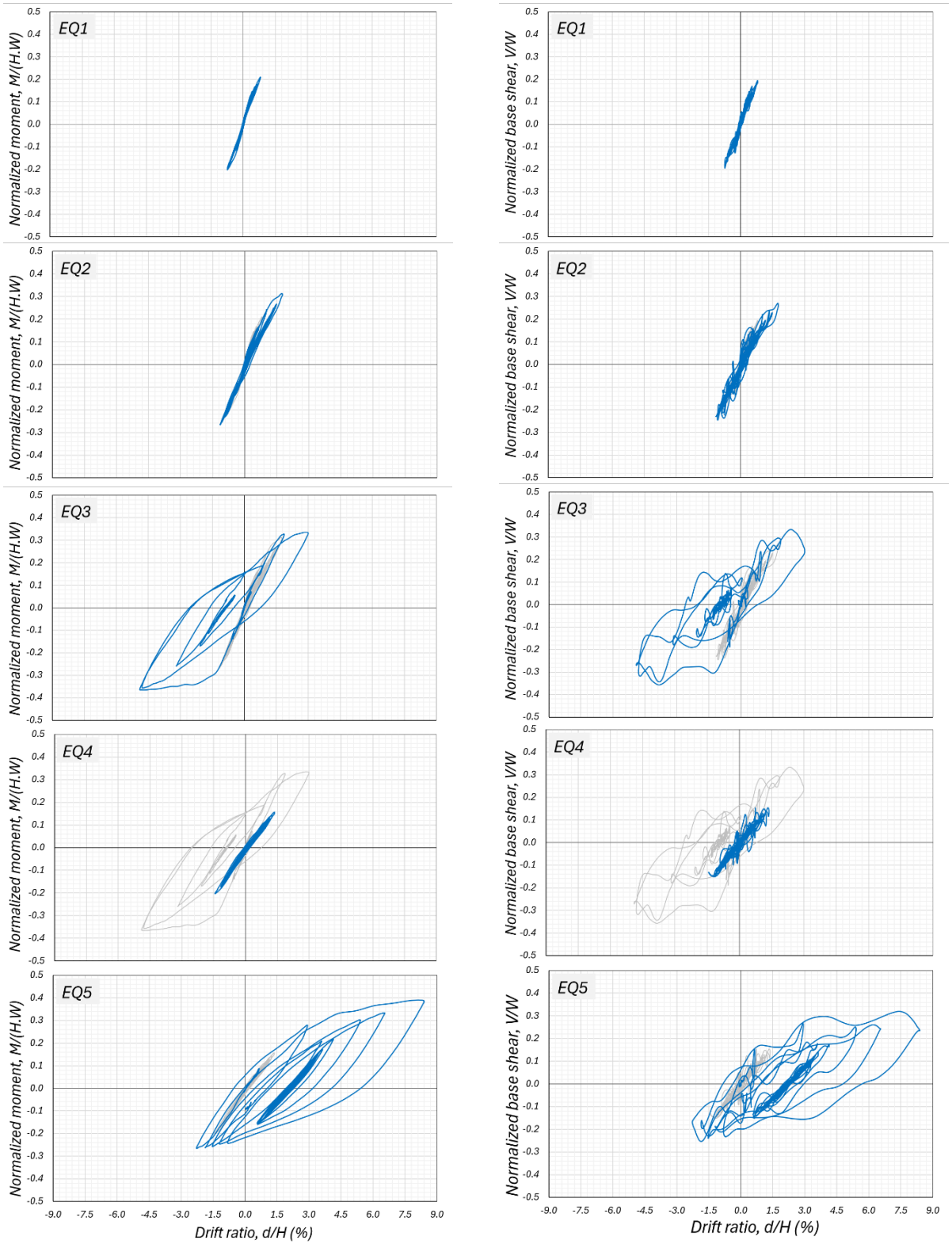
The corresponding normalized base-shear responses reported for EQ1-EQ5 show a similar variation in demand across the loading sequence, with the largest shear force occurring during EQ3, followed by a marked reduction in EQ4 and a subsequent increase in EQ5. Contributions from higher-mode response were also identified in the shear-drift response, particularly during EQ3 and EQ4 [124].

Figure 118 presents the corresponding experimental normalized moment- and normalized base shear-drift relationships from the shake-table test results. The blue curves represent the current simulation's response, whereas the grey traces show the response from the preceding simulation for direct comparison. The experimental campaign revealed a marked variation in the column response across the shake-table sequence, providing a reference for assessing the numerical response. EQ1 exhibits a predominantly linear hysteretic response, with a relatively narrow drift range extending approximately from -0.7% to +0.8% and normalized moment values between approximately -0.20 and +0.21. EQ2 shows the onset of nonlinear behavior, with the hysteretic envelope expanding to drift ratios of approximately -1.1% and +1.8% and peak normalized moments of -0.27 and +0.31, respectively. The modest but discernible opening of the hysteretic loops indicates a departure from the predominantly linear response of EQ1. The grey trace for EQ1 remains largely within the EQ2 envelope, highlighting increased deformation demand and a more pronounced hysteretic response.

The experimental and numerical responses are compared through the normalized moment-drift relationship, expressed as $M/(H.W)$ versus δ/H, where δ is the lateral displacement measured at the center of mass of the loading block, H is the column height, and W is the weight of the loading block. The numerical moment, M_N, produced by the inertial forces of the loading block about the column base, is obtained from d'Alembert's principle as:

$$M_N = m_t.a.H + I_r.\alpha_R \tag{166}$$

where a is the absolute translational acceleration at the center of mass, and α_R is the rotational acceleration. The absolute accelerations used to compute the numerical moment reflect the model's dynamic response, including the effects of the adopted damping formulation.



a) Normalized moment. b) Normalized base shear.

Figure 118. Experimental hysteretic responses vs. drift ratio for the tests.

5.5 Two-Stage Constitutive Parameter Identification

The rate-dependent cyclic constitutive framework of Chapter 4 introduces two novel mechanisms whose parameters are not directly measurable from coupon-level data and must therefore be identified against the specimen's shake-table response described in Section 3.2.2. Those two mechanisms, the quadrant-dependent bond-slip pinching, parameterized by λ and n_p, and the strain-rate-dependent viscous stress, parameterized by k_{rate} and n_{rate}, constitute the two constitutive contributions of this dissertation, and their identification is the object of the next two sections. Around them, eleven additional parameters associated with the reinforcing steel, confined and unconfined concrete, and the column's structural response are used in the calibration to complete the model description.

Identifying these fifteen parameters together from a single type of experiment is neither desirable nor possible. Some govern the shape of the hysteresis loop and are best excited by imposing displacement histories directly; others govern damping and the rate sensitivity of the response and become observable only when the column is driven by ground motion and inertial forces develop. Table 26 lists the 15 parameters, the physical mechanisms they govern, and the stage at which they are identified.

Table 26. The fifteen calibration parameters: physical role and identification stage.

Group	Symbol	Physical role	Stage
Reinforcing steel	λ	Pinching amplitude parameter	1-2
	n_p	Pinching-shape exponent	1-2
	n_{rate}	Strain-rate sensitivity exponent	2
	k_{rate}	Strain-rate sensitivity coefficient	2
	D_{fu}	Unloading-rejoining deformation parameter	1-2
	Ω_{fac}	Bauschinger-effect shape factor	1-2
	α_u	Unloading-modulus scaling parameter	2
Concrete	f_t	Tensile concrete strength	1-2
	r_t	Tensile post-cracking shape parameter	1-2
	ε'_{cc}	Confined-concrete peak strain	2
	r_c	Compressive post-peak shape parameter	2
Structural response	I_e/I_g	Effective flexural stiffness ratio	2
	G_e/G_g	Effective shear stiffness ratio	2
	ζ_1	First-mode Rayleigh damping ratio	2
	ζ_2	Second-mode Rayleigh damping ratio	2

NOTE: Reading the last column of the table therefore anticipates the division of work between the two stages that the following sections develop

The identification is therefore organized in two successive stages, each addressing the parameter group to which the corresponding experiment is sensitive. Stage 1, displacement-controlled cyclic calibration, imposes the measured lateral-displacement histories at the column top under quasi-static conditions, with the base fully restrained and without inertial or damping contributions. This stage

identifies the rate-independent parameters that shape the hysteresis loop, including the concrete tensile parameters and five reinforcing-steel cyclic parameters: λ, n_p, D_{fu}, α_u and Ω_{fac}. Stage 2, Bayesian dynamic calibration, applies the recorded base accelerations to the model with plastic hinges at both column ends and structural damping, and jointly refines the fifteen model parameters. In addition to refining the seven parameters identified in Stage 1, it identifies the strain-rate-dependent viscous parameters, the initial-stiffness parameters, the Rayleigh damping coefficients, and the confined-concrete parameters activated at larger drifts.

The two stages are physically complementary: Stage 1 resolves the hysteretic features that are identifiable under quasi-static loading, such as pinching, tension softening, and reloading, whereas Stage 2 provides access to strain-rate and damping effects activated by the shake-table motions. The variance-based sensitivity analysis confirms this complementarity, showing that several parameters are weakly identifiable from the dynamic response alone. The two-stage strategy therefore exploits the complementary information provided by quasi-static and dynamic loading to identify the full parameter set.

5.6 Parameter Provenance and Explored Intervals

The fifteen model parameters listed in Table 26 define the parameter space considered in the two-stage identification procedure. Before calibration, an initial exploration interval is assigned to each parameter. Table 27 reports the initial intervals adopted for the parameter exploration. As a general principle, the intervals are deliberately kept narrow, at a nominal value.

Table 27. Initial parameter intervals adopted for the parameter exploration.

Group	Parameter	Nominal	Explored interval
Reinforcing steel	λ	1.5	[1, 2]
	n_p	1	[0.5, 1.5]
	D_{fu}	1	[0.95, 1.05]
	Ω_{fac}	1.03	[1, 1.1]
	α_u	0.82	[0.6, 0.9]
Concrete	f_t	3.1	[2, 4.2]
	r_t	2.3	[2, 2.6]
	ε'_{cc}	-0.00376	[-0.005, -0.003]
	r_c	2.35	[1.7, 3]
Strain-rate viscous mechanism	n_{rate}	0.75	[0.2, 1.3]
	k_{rate}^{lower}	99	[47, 197]
	k_{rate}^{upper}	140	[66-266]
Structural response	I_e/I_g	0.37	[0.2, 0.85]
	G_e/G_g	0.40	[0.15, 0.65]
Structural damping	ζ_1	0.01	[0.005, 0.02]
	ζ_2	0.005	[0.002, 0.008]

These intervals are based on available material characterization, the preceding model formulation, experimental observations from the shake-table campaign, and preliminary parameter assessments described in the preceding sections. They define physically admissible regions for identification rather than arbitrary numerical bounds. Each of the fifteen calibration parameters listed in Table 26 therefore requires an interval within which its value will be sought.

Bond-slip pinching parameters (λ, n_p). Section 4.8.5.1 introduced the pinching parameters as part of the constitutive formulation, and their physically admissible bounds and default settings follow from the mechanism formulation presented there. For the present specimen, the nominal values are λ=1.5 and n_p=1, respectively. The initial parameter exploration is defined by applying absolute variations of ±0.50 to each parameter, respectively, around these nominal values.

Reinforcing-steel cyclic parameters (D_{fu}, Ω_{fac}). The unloading-rejoining deformation parameter and the Bauschinger-effect shape factor are inherited from the baseline SteelDRC formulation shown in Section 4.6. The nominal values for the present specimen are D_{fu}=1 and Ω_{fac}=1.03. The initial parameter exploration is defined by absolute variations of approximately ±0.05 around these nominal values.

Unloading-modulus scaling parameter (α_u). The unloading-modulus scaling factor introduced at the section level in Section 5.2.1.1 governs the magnitude of the unloading modulus relative to the reference steel modulus, thereby controlling the stiffness of the unloading branch of the cyclic response, and has a nominal value of 0.82. The initial parameter exploration is defined by an absolute variation of about this nominal value. The initial parameter exploration is defined as [0.6, 0.9].

Concrete tensile parameters (f_t, r_t). The tensile strength, f_t, governs the peak tensile stress of the concrete response, whereas the softening-shape parameter r_t controls the post-cracking tensile-softening branch. The nominal values are 3.1 MPa and 2.3, and the initial parameter intervals are defined by absolute variations of ±1.1 and ±0.3, respectively, about these nominal values. The nominal value adopted for f_t is obtained from the formulation presented in Section 5.2.3. For r_t, the nominal value is selected from the typical values recommended for the ConcreteCM formulation in OpenSees.

Confined-concrete parameters (ε'_{cc}, r_c). The confined-concrete shape parameter, r_c, is derived deterministically from the confined-concrete peak strain, ε'_{cc}, based on the quadratic relation established in this study from the parametric-analysis results, reproduces the coupling between the two parameters in the confined-concrete data set and avoids ill-posed joint identification.

$$r_c = 152724\ {\varepsilon'_{cc}}^2 + 1871\ \varepsilon'_{cc} + 7.22 \tag{167}$$

The nominal value of ε'_{cc}=-0.00376 is computed from the confinement formulation of Section 5.2.2.1.2 for the transverse-reinforcement configuration of the column specimen.

Strain-rate-dependent viscous mechanism (k_{rate}, n_{rate}). The nominal value of the rate exponent, n_{rate}=0.75, is taken from the coupon-level calibration of the SteelDRCV model reported in Section 4.4.3. The absolute variation is defined as ±0.55 about the nominal value.

The rate coefficient, k_{rate}, is not assigned an independent interval. For each sampled value of n_{rate}, it is constrained between two envelopes derived from the available experimental evidence. The upper bound of this interval, k_{rate}^{upper}, is defined from the quasi-static high-strain-rate stress-strain data reported by Malvar and Crawford [81]. The corresponding envelope represents the upper bound on the rate-dependent stress inferred from the experimental results, as described in Section 4.4.3 and illustrated in Figures 63 and 64.

$$k_{rate}^{upper} = 86.2\, {n_{rate}}^2 + 53.3\, n_{rate} + 51.6 \tag{168}$$

The lower envelope, k_{rate}^{lower}, is instead obtained from the coupon-level calibration performed for this dissertation and reported in Section 4.4.3, and represents the lower bound consistent with those experimental results. This construction preserves the admissible coupling between k_{rate} and n_{rate} established from the two experimental sources and prevents the joint sampling from generating combinations of the viscous parameters that are inconsistent with the available experimental evidence.

$$k_{rate}^{lower} = 75.2\, {n_{rate}}^2 + 24.2\, n_{rate} + 38.8 \tag{169}$$

Effective flexural-stiffness ratio (I_e/I_g). The effective flexural-stiffness ratio, I_e/I_g, governs the reduction of the gross-section flexural stiffness in the structural model. Its nominal value of 0.625 is determined from the empirical relation proposed by Elwood and Eberhard [47], developed from the experimental response of RC columns and accounting for the effects of axial load, longitudinal-bar diameter, and column geometry. The relation is expressed as:

$$0.2 \le \frac{I_e}{I_g} = \frac{0.45 + 2.5\left(\frac{P}{A_g f'_{cu}}\right)}{1 + 110\left(\frac{d_b}{D}\right)\left(\frac{D}{a_v}\right)} \le 1.0 \tag{170}$$

where I_e is the effective moment of inertia, I_g is the gross-section moment of inertia, P is the axial load, A_g is the gross cross-sectional area, and a_v is the shear span. For the cantilever configuration considered here, a_v corresponds to the distance between the critical section at the column base and the point of application of the lateral load, namely $a_v = L$.

For the test column, L=7315 mm, D=1219 mm, d_{bl}=35.8 mm, P_u=2320 kN, f'_{cu}=42 MPa; the resulting nominal value for the specimen is 0.37. The initial parameter exploration is defined over $I_e/I_g \in$ [0.2, 0.85].

Effective shear-stiffness ratio (G_e/G_g). The effective shear-stiffness ratio, G_e/G_g, governs the reduction of the gross-section shear stiffness in the structural model. Following Priestley et al. [106], a nominal value of 0.40 is adopted for RC columns in the moderate-to-strong seismic regime, for which diagonal shear cracking has developed but has not fully degraded the shear stiffness. The initial parameter exploration is defined over $G_e/G_g \in [0.15, 0.65]$

Rayleigh damping ratios (ζ_1 , ζ_2). The first- and second-mode damping ratios define the target modal damping used to construct the Rayleigh damping matrix. The nominal value adopted for the first-mode damping ratio is ζ_1=0.01, with an initial exploration interval of [0.005-0.02]. The second-mode damping ratio is assigned to a nominal value of ζ_1=0.005 and explored within [0.002-0.008]. These ranges provide the initial parameter space for the modal damping ratios considered in the identification.

5.7 Stage 1 - Displacement-Controlled Cyclic Calibration

Stage 1 identifies the parameters governing the rate-independent cyclic response. It comprises two successive sub-stages based on the response features resolved from the experimental loading histories. The first sub-stage uses the first two simulations (EQ1 and EQ2) to identify the concrete tensile parameters, f_t and r_t. The second uses the four calibration simulations (EQ1-EQ4) to identify the remaining four reinforcing-steel parameters considered in this stage.

The rationale for identifying the pinching parameters within this stage follows from the mechanism they represent. As established in Section 4.8, the bond-slip formulation introduces stiffness degradation during load reversal, producing pinching in the reloading branches of the cyclic response. In the SteelDRCV formulation, this effect is governed by the dimensionless parameters λ and n_p, which control the onset and evolution of the stiffness reduction in the active reloading quadrants. Because these parameters directly govern the pinched shape of the hysteretic response, their identification requires cyclic structural response. Monotonic or coupon-level material data alone cannot establish them. The displacement-controlled calibration therefore provides the appropriate basis for identifying them.

5.7.1 Objective Functions

The agreement between the numerical and experimental normalized moment-drift responses was quantified using two complementary objective functions, evaluated over the concatenated response of the imposed simulations. This formulation preserves the sequence of the loading histories and therefore accounts consistently for the progressive accumulation of plastic deformation and cyclic degradation.

The primary objective function is the relative root-mean-square error of the inertial moment, E_M, defined as the root-mean-square difference between the numerical and experimental moments, normalized by the root-mean-square of the experimental inertial moment.

$$E_M = \sqrt{\frac{\sum_{i=1}^{n}(M_N - M_E)^2}{{M_E}^2}} \times 100\% \tag{171}$$

Where M_N is the numerical moment, obtained from the inertial response of the structural model, whereas the experimental moment, M_E, corresponds to the moment determined from the measured response during the test. The metric quantifies the point-to-point deviation between the numerical and experimental responses throughout the imposed loading history and therefore captures discrepancies in both strength and stiffness. The secondary objective function is the logarithmic ratio of the cumulative hysteretic energy, E_L, defined as the natural logarithm of the ratio of the experimental to the numerical dissipated energy.

$$E_L = \ln\left(\frac{E_E}{E_N}\right) \times 100\% \tag{172}$$

where E_N and E_E are the cumulative hysteretic energies obtained from the numerical and experimental moment-drift responses, respectively. Whereas E_M is sensitive to the instantaneous ordinates of the response, E_L quantifies the cumulative energy dissipated over the hysteretic response, and is therefore sensitive to the overall fullness of the hysteresis loops. Using both objective functions prevents parameter combinations that reproduce the moment response while misrepresenting dissipated energy, or that reproduce energy dissipation while producing an inadequate moment response. A parameter combination is therefore considered satisfactory only when it provides consistent agreement under both measures.

5.7.2 First sub-stage: Concrete Tensile Parameters

The first sub-stage identified the two parameters governing the tensile response of the ConcreteCM model: the tensile strength, f_t, and the tension-softening shape parameter, r_t. Both were identified from the first seismic simulation (EQ1), whose response remains below a drift of approximately 0.008 and is dominated by crack initiation and propagation, while reinforcement yielding and bond-slip remain limited. The identified values are f_{ct}=3.1 MPa and r_t=2.3. Figure 119 compares the resulting numerical response with the experimental normalized moment-drift relationship for EQ1.

Using these identified parameters, the normalized base-moment error over the imposed history is $RRMSE_M$=8.6%. The numerical response closely follows the experimental response, reproducing the initial stiffness, the progressive softening as cracking develops, and the peak resistance at each successive amplitude. The remaining discrepancy is concentrated in the reloading branches, where the experimental loops are slightly fuller than the simulated response. These values are preliminary: they define the region subsequently explored in the dynamic stage, where both parameters are constrained against the complete set of seismic simulations.

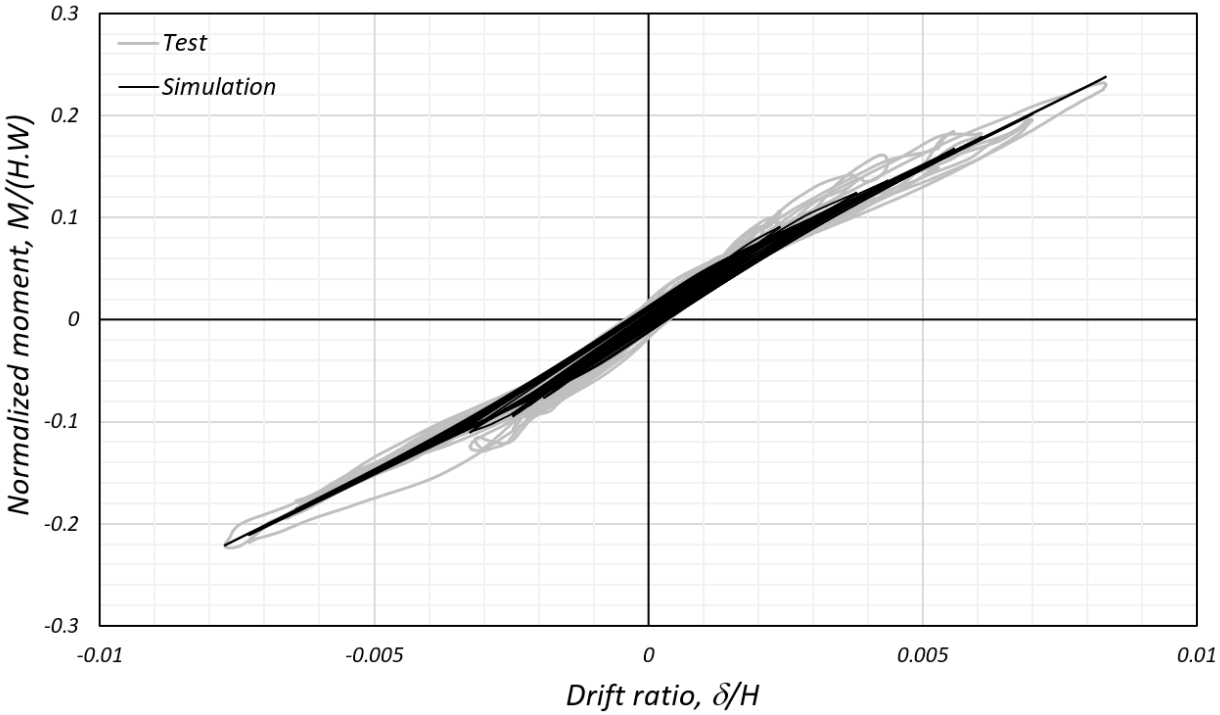


Figure 119. Numerical and experimental normalized moment-drift responses for EQ1.

5.7.3 Second Sub-stage: Reinforcing-Steel Parameters

The second sub-stage identified the reinforcing-steel and concrete parameters (listed in Table 26) through displacement-controlled cyclic analyses of the four concatenated simulations (EQ1-EQ4), spanning the nearly linear to strongly nonlinear response range. Four parameters were treated as unknowns: the pinching curvature parameter λ and the pinching exponent n_p, together with the concrete tensile parameters f_t and r_t, which were released in this sub-stage so that the tensile response could adjust to the higher demand levels reached beyond the first simulation. The unloading-rejoining deformation parameter, D_{fu}, and the Bauschinger area factor, Ω_{fac} were held at their reference values of 1.0 and 1.03, respectively. For each parameter combination, the measured displacement history was imposed on the numerical model, and the resulting inertial moment response was compared with the experimental response using the objective functions defined above. Table 28 summarizes the identified values associated with the best-performing combination.

Table 28. Reinforcing-steel cyclic parameters identified in the second sub-stage.

Group	Parameter	Identified value	Explored Interval
Reinforcing steel	λ	0.52	[0.2, 1.6]
	n_p	0.97	[0.2, 1.6]
Concrete	f_t	1.65	[0.4, 1.8]
	r_t	2.01	[1.8, 3]

The identified combination yielded an E_M=14.7% over the four concatenated simulations. The error is not uniform across the four simulations, and its distribution is informative. The error is reported in two forms. The global value is computed over the entire protocol from all converged sub-steps of the analysis. The per-simulation values are computed within the step window of each seismic simulation, defined by the segment boundaries of the concatenated protocol (EQ1: steps 3200-18000; EQ2: 31000-45000; EQ3: 58000-64000; EQ4: 83000-95000). For this purpose, each simulation is truncated at the point selected to retain the largest accumulated energy contribution within its corresponding record. The two are therefore not simple averages of one another: the global value reflects the distribution of converged sub-steps over the entire protocol, whereas each per-simulation value is computed independently within its corresponding truncated window. Table 29 reports the error per simulation. Figure 120 compares the simulated and measured normalized moment-drift responses.

Table 29. Normalized base-moment error per seismic simulation.

Simulation	$\boldsymbol{RRMSE_M}$ **(%)**
EQ1	9.0
EQ2	12.2
EQ3	16.9
EQ4	21.0
ALL	14.7

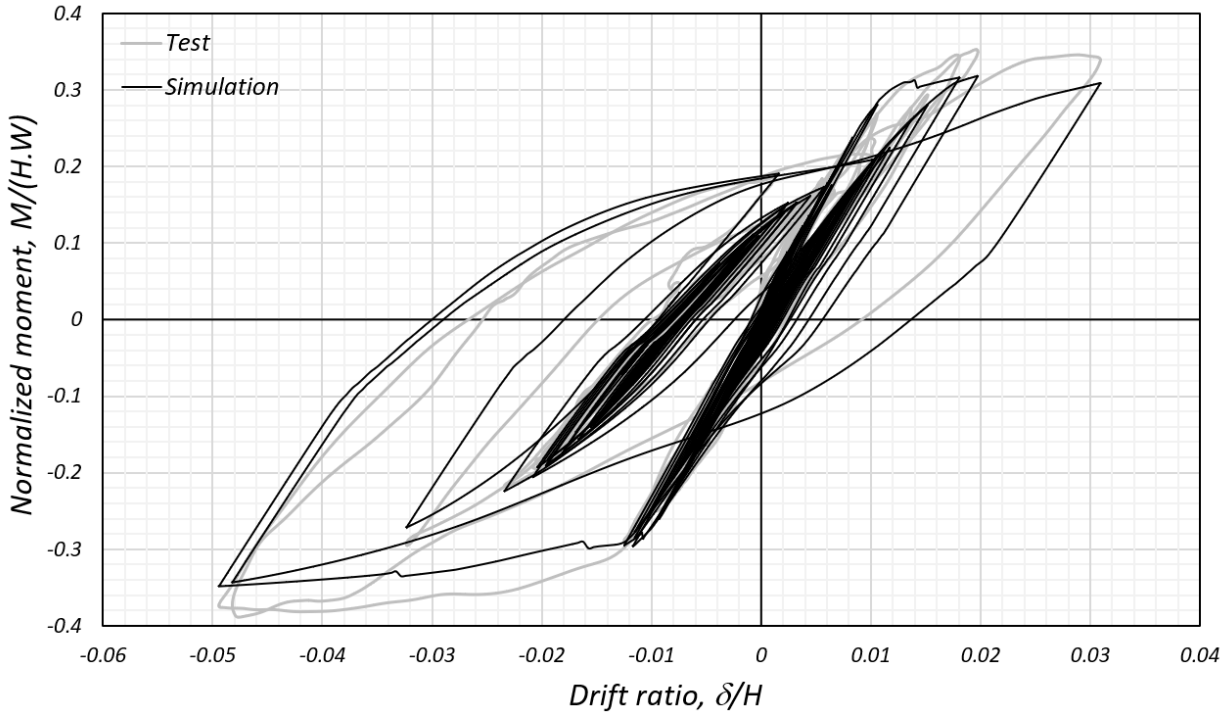


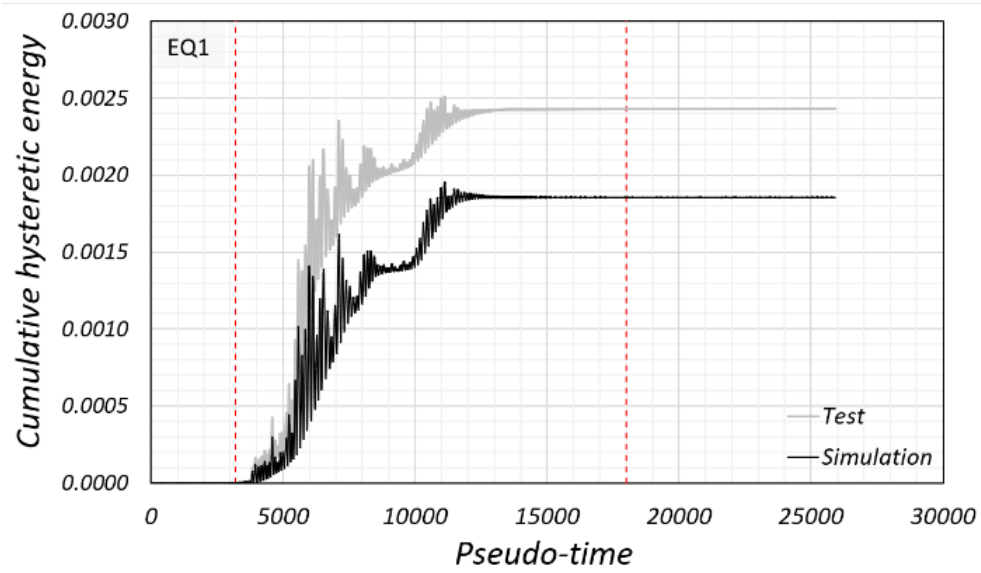
Figure 120. Simulated and measured normalized moment-drift response over the complete loading EQ1-EQ4.

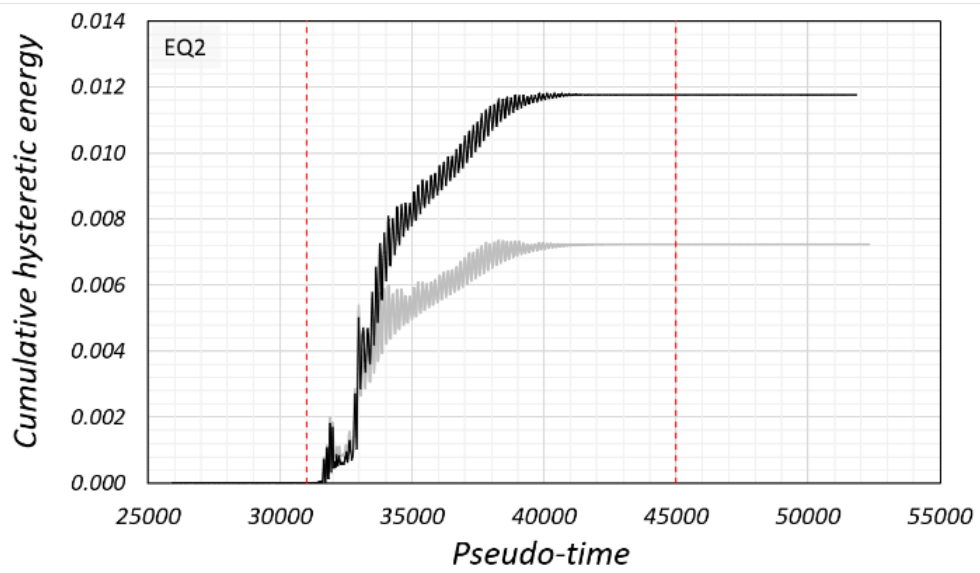
The resulting response spans a drift of -4.9% to +3.1%, encompassing the full range observed across the four simulations. The response envelope is well reproduced. The model captures the maximum moments in both directions, the response asymmetry, and the overall stiffness degradation as the protocol progresses. The discrepancy is concentrated in the interior of the response rather than in its envelope: the simulated loops are systematically wider than the measured ones.

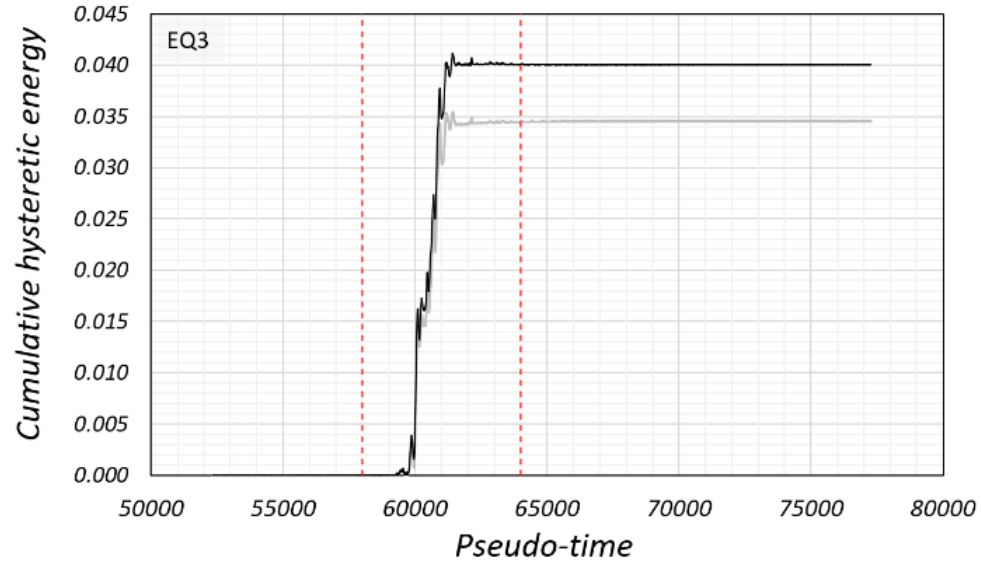
Because the concatenated response superimposes four records of increasing demand, Figure 120 alone does not make the origin of the discrepancy apparent. Figures 121 and 122 therefore decompose it by first examining the moment-drift response of each simulation separately and then comparing the energy dissipated in each.

Figure 121 compares the cumulative hysteretic energy dissipated by the model and the specimen. Unlike the moment response, which evaluates agreement at individual points in the loading history, cumulative energy integrates discrepancies over the entire record. It is therefore sensitive to systematic differences in loop shape and enclosed area that may be less apparent in a point-by-point comparison of the resisting moment.

Figure 122 presents the simulated and measured responses for each seismic simulation separately. In EQ1, the two responses are nearly indistinguishable, with an essentially linear response and close agreement in both the envelope and the narrow hysteretic loops. As the response becomes increasingly nonlinear, the differences become more apparent. In EQ2, the hysteretic loops widen, with the simulation predicting slightly larger loop widths than the measurements, particularly along the unloading branches. This discrepancy becomes more pronounced in EQ3, where the measured response develops pronounced loops over a drift range of nearly 8%. Although the simulation captures their overall shape, the enclosed area is distributed differently, indicating a different representation of the energy dissipated during the cycles. In EQ4, the loops narrow as the response becomes increasingly governed by accumulated residual drift, while the model overestimates the reloading stiffness.







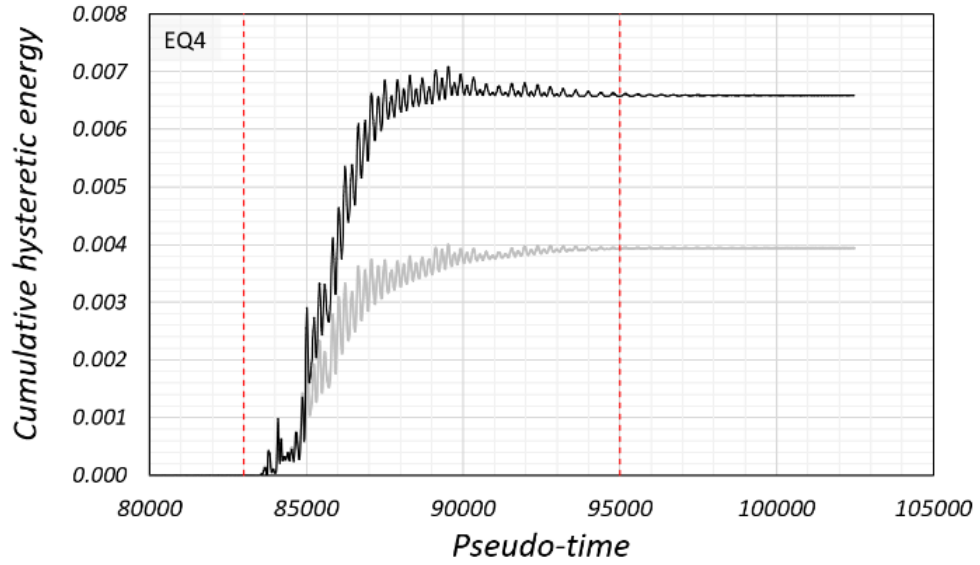


Figure 121. Cumulative hysteretic energy per seismic simulation.

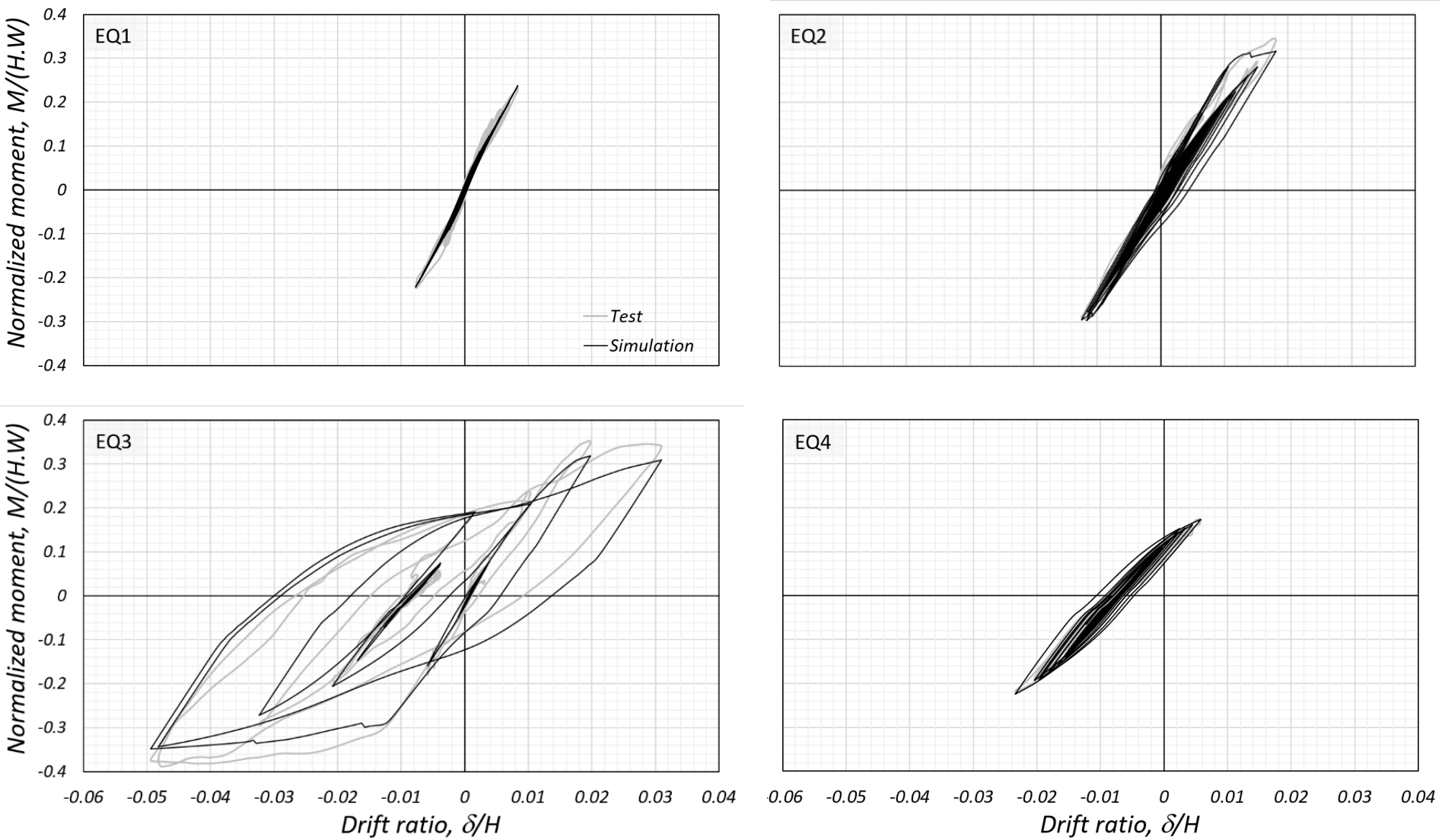


Figure 122. Normalized moment-drift response per seismic simulation.

5.7.4 Sensitivity of the Response to the Identified Parameters

Figures 123 and 124 examine the influence of the parameters on the cyclic moment response and summarize the 1110 analyses that completed the protocol across the successive designs.

Figure 123 shows the distribution of the error in the parameter space defined by the two pinching parameters λ and n_p. In panel (a), the moment error is represented by the size and grayscale of each marker, with each marker corresponding to one displacement-controlled cyclic analysis. The red diamond indicates the parameter combination that yields the minimum moment error. The lowest errors are concentrated around $\lambda \approx$0.45-0.60 and $n_p \approx$0.9-1.1, whereas the larger and lighter markers indicate progressively higher errors. The red diamond indicates the pinching parameter combination that yields the minimum moment error, as reported in Table 28.

Panel (b) shows the same parameter space in terms of the absolute logarithmic energy ratio. Its distribution differs substantially from that of the moment error: the lowest energy errors occur around $\lambda \approx$0.8-1.2 and $n_p \approx$1.2-1.5, coinciding with the region where the moment error is comparatively large. The parameter combination that minimizes the energy error (λ=0.88, n_p=1.37 (marked by a red diamond in panel (b)) reproduces the dissipated energy almost exactly but yields a moment error of 18.5%. Conversely, the combination adopted in this study (marked by a triangle in panel (b)) reduces the moment error to 14.7% at the expense of a 22.5% energy discrepancy.

The numerical values of the two metrics are not directly comparable. $RRMSE_M$ is evaluated point by point over the entire loading history and therefore penalizes local deviations throughout the response, whereas Ln_E compares a single accumulated quantity for each record and is consequently insensitive to compensating errors that cancel during integration. Thus, a given percentage in one metric does not represent the same degree of agreement as the same percentage in the other. Values of Ln_E close to zero may be obtained for parameter combinations whose individual hysteretic loops are not accurately reproduced, but whose accumulated energy dissipation matches the experimental response. In contrast, $RRMSE_M$ does not permit such compensation. This difference motivates using moment error as the primary selection criterion. At the same time, the energy ratio is reported as a complementary metric rather than combined with the index.

Figure 124 shows the marginal dependence of the moment error on each parameter. The dependence on λ is monotonic and pronounced, with the error increasing from approximately 15% at $\lambda \approx$0.5 to approximately 26% at $\lambda \approx$1.3, indicating that λ has the strongest influence on the cyclic response among the parameters considered. The dependence on n_p is comparatively weak over the range explored, with a shallow minimum near unity, while the effects of f_t and r_t are weaker still. This behavior is consistent with the tensile parameters primarily influencing the low-demand portion of the loading protocol. This hierarchy of parameter influence guided the progressive narrowing of the sampled intervals in successive designs.

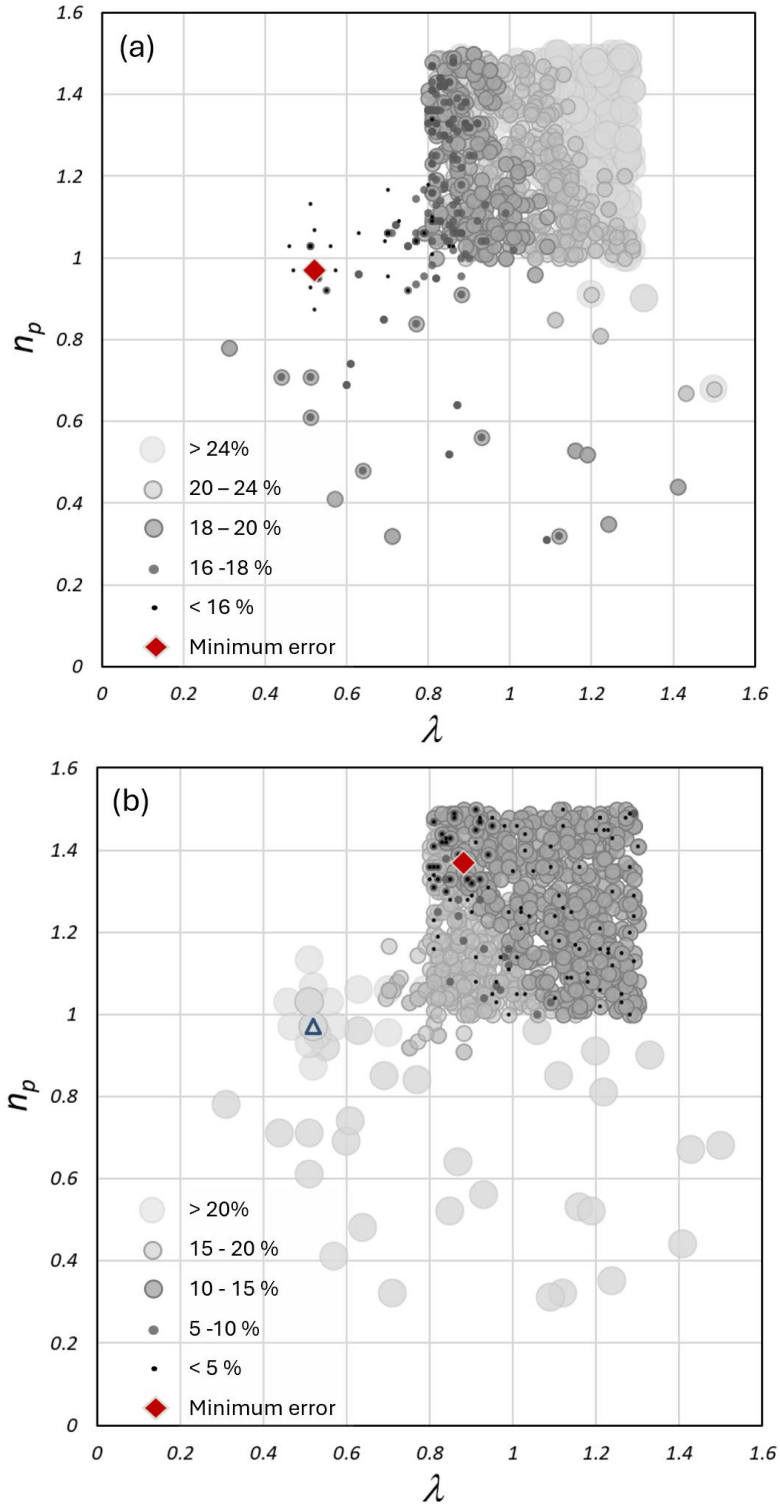


Figure 123. Distribution of the (a) moment error and (b) energy error over the plane of the pinching parameters λ and n_p.

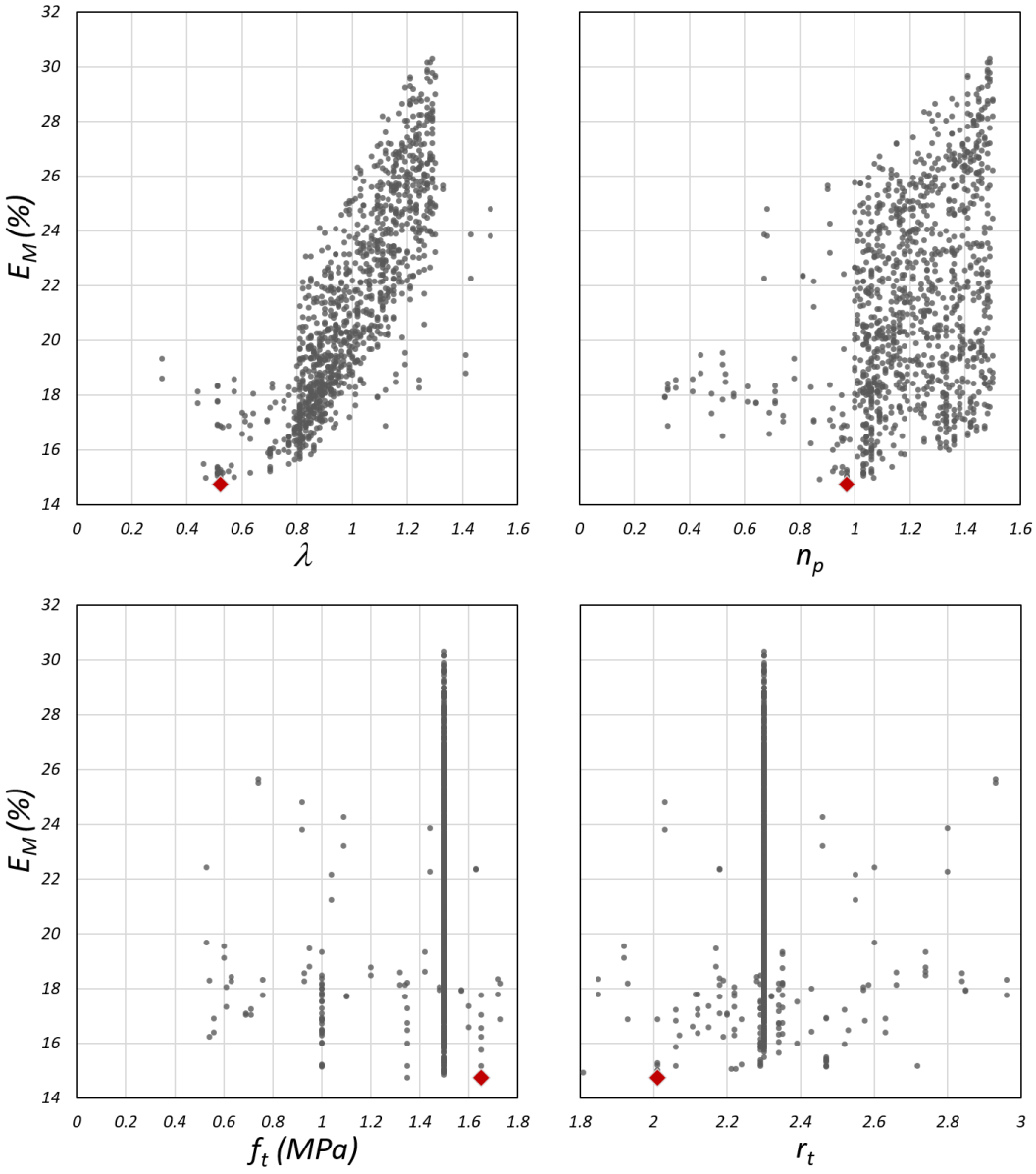


Figure 124. Dependence of the normalized base-moment error on λ, n_p, f_t and r_t.

5.7.5 Outcome of Stage 1

The error associated with the identified parameter combination increases monotonically with the imposed demand, from 9.0% in EQ1 to 21.0% in EQ4. This systematic increase reflects the progressive activation of mechanisms that a rate-independent, quasi-static idealization cannot represent. In particular, the simulations do not account for the additional resistance and energy dissipation associated with the reinforcement's strain-rate sensitivity. These effects become increasingly relevant at the higher loading velocities reached during the strong-motion simulations.

The optimal values of λ and r_t are located at the lower bounds of their respective explored intervals. In contrast, that of f_t is located at the upper bound, indicating that the true optima may lie at or beyond the limits of the parameter space considered. The pinching exponent n_p, by contrast, settles near the center of its range. Together with the release of the tensile parameters in this sub-stage and the conflict between the two objective functions discussed above, these results indicate that the values reported in Table 28 should be regarded as preliminary estimates. They therefore define the parameter-space region carried forward to Stage 2, in which all parameters are jointly re-examined against the four base-excited seismic simulations. This stage also enables, for the first time, the identification of the rate-dependent and damping parameters, which cannot be resolved from displacement-controlled simulations alone.

The conflict between the two objective functions also exposes a limitation of the identification procedure adopted in this stage. Using the moment error as the primary criterion, while reporting the energy discrepancy separately, is ultimately a judgment-based choice. Within Stage 1, there is no principled basis for determining the relative importance of the two metrics, while any weighted combination would introduce arbitrary weighting into the identification. The same limitation applies to parameters that cannot be resolved from the displacement-controlled response, for which fixed values would otherwise have to be assigned without quantifying how well the available data constrains them. Stage 2 addresses both limitations by formulating the identification as a Bayesian inverse problem. The variances of the two metric families are estimated from the a priori data, allowing the evidence to determine their relative contributions to the likelihood. In addition, each parameter is reported with a credible interval, providing an explicit measure of parameter uncertainty and of the extent to which the experimental record constrains its value.

5.8 Stage 2 - Bayesian Dynamic Calibration

The model's dynamic calibration is formulated as a Bayesian inverse problem, with the parameters governing its behavior treated as random variables. The experimental record updates their prior distributions, initially constrained by physical admissibility, into posterior distributions that reflect the data. This stage is organized into 12 numbered steps covering parameter and response-metric selection, simulation-campaign design, training and validation of a Gaussian-process surrogate, formal sensitivity analysis, likelihood construction, posterior sampling, posterior diagnostics, and final evaluation against the true simulator and a held-out motion.

The objective is not merely to obtain a single best-fit parameter set, but to establish, for each parameter, why its prior range was selected, whether the experimental data provide information about it, and what residual uncertainty remains after calibration. When the experimental response

does not sufficiently inform a parameter, this is explicitly identified, along with the calibration stage in which that parameter is instead constrained.

Figure 125 summarizes the pipeline. Steps 1 through 10 employ the Gaussian-process surrogate and are reported below, along with their final numerical results. Steps 11 and 12 employ the true finite-element simulator: step 11 verifies the surrogate predictions against the full model, and step 12 validates the calibrated model against the held-out motion EQ5.

The displacement-controlled stage of Section 5.7 identified the rate-independent constitutive parameters from the moment-drift response, but, by construction, it could not address two aspects that emerge only under dynamic loading: structural damping and the strain-rate dependence of the reinforcement. Under monotonic or slow-cyclic displacement, the viscous mechanism proposed in this dissertation remains inactive because its contribution scales with strain rate and vanishes in the quasi-static limit. Consequently, the strain-rate exponent n_{rate} and its coefficient k_{rate} are not identifiable from this stage. The same limitation applies to the Rayleigh damping ratios, whose effects cannot be inferred from a displacement-controlled analysis.

Beyond this identifiability argument, a second reason for formulating the dynamic calibration within a Bayesian framework rather than as a deterministic optimization is that the objective is not merely to obtain a single best-fitting parameter set, but to quantify how strongly the experimental data constrains each parameter. The dynamic response does not admit an analytical inverse, and each nonlinear time-history analysis is computationally expensive. A least-squares formulation provides a point estimate for each parameter. Still, it does not, by itself, provide a principled measure of the associated uncertainty or of the information gained from the experiment. The Bayesian formulation, in contrast, yields a full posterior distribution for each parameter. Its median or MAP (Maximum A Posteriori) value provides a point estimate, with the MAP corresponding to the parameter value at which the posterior density attains its maximum. The spread of the posterior distribution quantifies the remaining uncertainty. At the same time, the ratio of its width to the corresponding prior width measures how much the experimental data has reduced the uncertainty associated with each parameter.

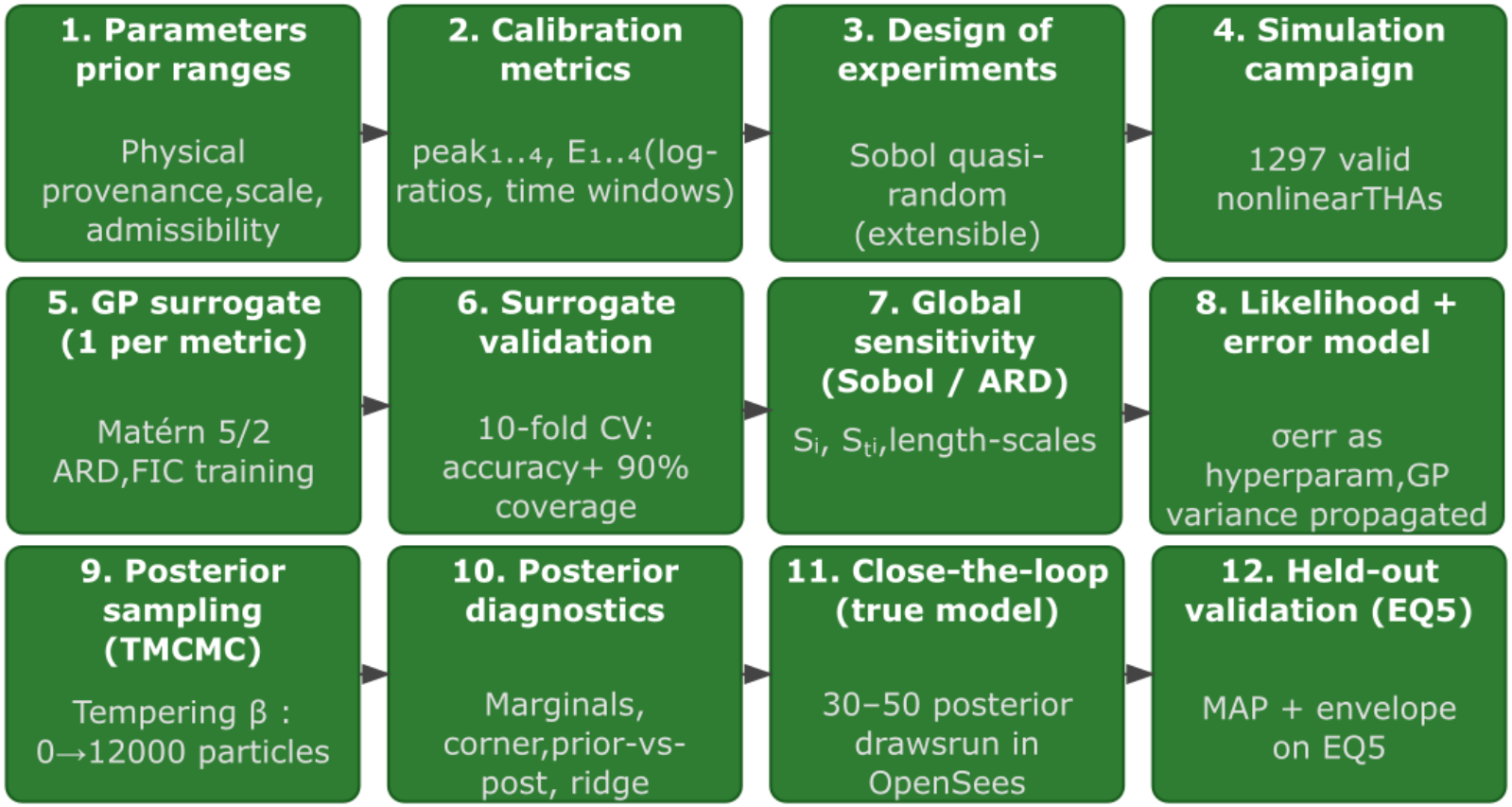


Figure 125. The twelve-step Bayesian calibration pipeline.

5.8.1 Bayesian Formulation of the Inverse Problem

Before introducing the equations, it is useful to state in words what each ingredient represents. The vector θ collects the fifteen model parameters to be identified. It is treated as a random variable, and the objective of the inversion is to characterize its probability distribution after the experimental data have been observed. The vector d^* contains the eight scalar features extracted from the experimental record: four peak-displacement log-ratios ($peak_1$ through $peak_4$) and four hysteretic-energy log-ratios (E_1 through E_4), one of each per calibration earthquake (EQ1-EQ4).

Three probability densities define the Bayesian formulation:

(1) The *prior* $p(\theta)$ represents the information available about the parameters before considering the dynamic data; in this formulation, this information is limited to their physically admissible ranges.

(2) The *likelihood* $p(d^*|\theta)$ quantifies how probable the observed discrepancy vector is for a given parameter vector θ, under the assumed statistical model for the residual error between predictions and observations.

(3) The *posterior* $p(\theta|d^*)$, which is the target of the inference, represents the updated probability distribution of the parameters after the experimental data have been observed.

Bayes' theorem relates these three densities:

$$p(\theta|d^*) = p(d^*|\theta) \dots p(\theta)/p(d^*)$$
$$p(d^*) = \int p(d^*|\theta).p(\theta)d\theta \tag{173}$$

The evidence $p(d^*)$ is a scalar normalizing constant for the posterior.

Two obstacles prevent its direct evaluation: the evidence integral is intractable in fifteen dimensions, and each likelihood evaluation requires a nonlinear time-history analysis. The first obstacle is addressed by drawing samples from the posterior using a Transitional Markov Chain Monte Carlo sampler (see Section 5.8.9), which generates the samples without requiring evaluation of $p(d^*)$ and simultaneously provides an estimate of the evidence. The second is addressed by training a Gaussian-Process surrogate (see Section 5.8.5), reducing the tens of thousands of likelihood evaluations required by the sampling procedure to inexpensive surrogate evaluations.

The prior $p(\theta)$ is taken as uniform over the admissible domain of the twelve sampled parameters. Of the fifteen constitutive parameters that define the model, two are held fixed. The second-mode Rayleigh damping ratio, ζ_2, is set to its reference value because the first mode primarily governs the column's dynamic response. The shear-stiffness reduction factor, G_e/G_g, is likewise fixed because the column is sufficiently slender so that shear deformations are negligible compared with the flexural response. Third, the confined-concrete shape parameter, r_c, is derived from ε'_{cc} through a deterministic physical relation and is therefore not sampled independently. The remaining twelve are sampled jointly. Uniformity expresses the absence of preference among admissible

combinations within the box; the box itself is not arbitrary, and its provenance is stated parameter by parameter. The two error variances entering the likelihood (one for the peak-displacement metrics and one for the dissipated-energy metrics) are treated as additional hyperparameters with weakly informative priors, allowing them to be inferred from the data rather than fixed a priori as arbitrary weighting factors (see Section 5.8.8).

5.8.2 Calibration Parameters and Physical Relations

This section corresponds to step 1 of the pipeline (Figure 125). The model-implementation sections above (Section 5.6) establish the physical meaning and constitutive role of each parameter; this section specifies that all fifteen parameters enter the Bayesian inversion and the physical constraints imposed on them. This stage jointly refines fifteen parameters: five for the reinforcing steel, four for concrete, two for the strain-rate-dependent viscous mechanism, two for the system's structural response, and two for structural damping. The corresponding classification is reproduced from Table 30 for clarity and ease of reference.

Table 30. Calibration parameters and prior bounds.

Group	Parameter	Prior range
Reinforcing steel	λ	[0.2, 1.6]
	n_p	[0.2, 1.6]
	D_{fu}	[0.95, 1.05]
	Ω_{fac}	[1.0, 1.10]
	α_u	[0.6, 0.9]
Concrete	f_t	[0.4, 1.8]
	r_t	[1.8, 3]
	ε'_{cc}	[-0.005, -0.003]
	r_c	Derived from ε'_{cc}
Strain-rate viscous mechanism	n_{rate}	[0.2, 1.3]
	k_{rate}	[50, 150]
Structural response	I_e/I_g	[0.2, 0.85]
	G_e/G_g	0.20 (fixed)
Structural damping	ζ_1	[0.005, 0.02]
	ζ_2	0.015 (fixed)

The prior bounds for the calibration parameters reflect the information available before considering the dynamic data. The pinching parameters λ, and n_p are bound by the admissible range of the bond-slip mechanism; the Unloading-rejoining deformation parameter, D_{fu}, the Bauschinger-effect shape factor, Ω_{fac}, and the unloading-modulus scaling parameter, α_u, and are bounded around their coupon-level estimates. The tensile strength, f_t, spans the range of direct-tension strengths reported for this concrete class; the softening slope, r_t, covers values consistent with the fracture energy of the section; and the confined-concrete peak strain, ε'_{cc}, is centered on the Mander confinement

estimate for the transverse-reinforcement configuration of the specimen, and the confined-concrete shape parameter, r_c, is derived deterministically from ε'_{cc}. The strain-rate sensitivity exponent, n_{rate}, spans the range observed in the high-rate tensile tests conducted in this dissertation, whereas the strain-rate sensitivity coefficient, k_{rate}, is determined through the quadratic envelopes of Section 5.2. The effective flexural stiffness ratio, I_e/I_g, the effective shear stiffness ratio, G_e/G_g, the first- and second-mode Rayleigh damping ratios, ζ_1, ζ_2 are assigned based on engineering judgment for this class of RC bridge columns.

Although the calibrated model defines fifteen parameters, only twelve are independent dimensions of the Bayesian inversion. The second-mode Rayleigh damping ratio, ζ_2, was fixed at 0.015. The displacement response of the cantilever column is dominated by the first mode, with T_1=0.927 s, whereas the second mode has T_2=0.225 s and contributes negligibly to the peak-displacement and hysteretic-energy metrics used for calibration. The effective shear-stiffness ratio, G_e/G, was likewise fixed at 0.20 because the response is predominantly flexural and the contribution of elastic shear deformation to the calibration metrics is minor for the aspect ratio considered. The posterior distribution of the compressive post-peak shape parameter, r_c, is not sampled independently but computed from ε'_{cc}at each point in the parameter space through the quadratic relation established in Section5.2.2.

The Bayesian inversion consequently operates on twelve independent parameters. The Gaussian-process surrogate, sensitivity analysis, and posterior sampling are formulated in this twelve-dimensional space, and the results reported below refer to these twelve inferred dimensions.

5.8.3 Calibration Metrics

This section corresponds to step 2 of the pipeline (Figure 125). The numerical and experimental responses are compared using scalar metrics computed separately for each seismic simulation, avoiding aggregation of responses with different physical meanings into a single index that could mask compensating errors. Two families of metrics are used, both expressed as logarithmic ratios so that a perfect match corresponds to zero and relative discrepancies are treated symmetrically. The primary family is the logarithmic ratio of the peak displacement, computed for each of the four calibration motions and denoted peak$_1$ through peak$_4$.

$$L_{n,dpeak} = \ln\left(\delta_{peak,test}/\delta_{peak,sim}\right) \tag{174}$$

The secondary family is the logarithmic ratio of the cumulative hysteretic energy, denoted E_1 through E_4.

$$L_{n,E} = \ln(E_{test}/E_{sim}) \tag{175}$$

The eight metrics therefore comprise four peak-displacement log-ratios and four hysteretic-energy log-ratios, one of each for each calibration earthquake. Peak displacement is given primary weight because it captures the response feature most sensitive to the viscous mechanism. In contrast, the energy metrics help prevent parameter combinations that reproduce the peak response while distorting the hysteretic behavior.

Both families are evaluated over complete time windows within each simulation rather than on a sample-by-sample basis. In the shake-table test, the ground-motion command sent to the actuator and the response signals recorded by the data-acquisition system do not share a common time origin: data acquisition may start before or after the actuator begins driving the table, and the resulting offset varies between seismic runs. Cross-correlation analysis of the experimental and simulated displacement histories identified a variable lag of up to approximately 3.6 s across the four motions. The window-based metrics adopted here, peak displacement and cumulative hysteretic energy computed over each seismic window, are insensitive to such a temporal shift, provided that the complete response window is retained, and therefore do not require explicit time alignment. The original ground-acceleration records, sampled at 240 Hz, are interpolated to the numerical integration time step of 1/60 s.

The calibration uses four seismic motions (EQ1-EQ4), which provide the eight calibration metrics. The fifth motion (EQ5) is excluded from the calibration and reserved exclusively for predictive validation, as described in the Held-Out Validation section.

5.8.4 Design of Experiments and Simulation Campaign

This section corresponds to Steps 3 and 4 of the pipeline shown in Figure 125. The parameter space was explored using a space-filling quasi-random Sobol sequence with Matoušek-Affine-Owen scrambling (a random linear scramble combined with a random digital shift) and a fixed seed to ensure bitwise reproducibility [59] and [86]. Sobol sequences were selected because they are extensible: additional points can be appended to an existing design without compromising its space-filling properties, which proved essential when the initial campaign was later enriched.

The simulation campaign proceeded in two stages, both spanning the twelve sampling dimensions. An initial Sobol design of 980 points covered a narrow range of the rate exponent, $n_{rate} \in [0.70, 0.78]$ 932 of these simulations converged through the complete four-earthquake protocol. A subsequent enrichment extended the rate exponent to $n_{rate} \in [0.20, 0.80]$ the range in which the viscous mechanism is physically active, and added 406 Sobol points, of which 365 converged. The combined training set therefore contains 1297 successful nonlinear dynamic analyses. Non-convergent analyses were logged and excluded from the training set rather than silently discarded.

Each analysis consists of a nonlinear time-history simulation of the column model described at the beginning of this chapter, subjected to the four concatenated ground-acceleration records (EQ1-EQ4). The simulations ran in parallel on nine cores using the OpenSees executable compiled with the Intel oneAPI toolchain; a single run took about 17 minutes. Non-convergent steps within a run were handled using an automatic sub-stepping algorithm. A run was classified as failed and excluded from the training set only when the integrator diverged or the analysis terminated because of excessive non-convergence. The complete response history of every run, including failed analyses, was archived for traceability, ensuring that no simulation was silently discarded.

5.8.5 Gaussian-Process Surrogate

This section corresponds to step 5 of the pipeline (Figure 125). Because each nonlinear time-history analysis is computationally expensive and the posterior sampler requires tens of thousands of likelihood evaluations, the simulator is replaced by a Gaussian-Process (GP) surrogate. In addition to a point prediction, the GP provides a predictive variance that increases in regions where the

training data are sparse. This uncertainty is propagated into the likelihood so that predictions in poorly explored regions receive less weight.

Formally, a GP defines a probability distribution over functions such that the values at any finite set of inputs are jointly Gaussian. It is specified by a mean function, taken here as constant, and a covariance (kernel) function $k(x, x')$ that characterizes the assumed smoothness of the response. One GP is trained for each metric (peak$_1$ to peak$_4$ and E_1 to E_4). The input parameters are mapped to the unit hypercube, and the outputs are standardized to zero mean and unit variance. An anisotropic Matérn 5/2 kernel is adopted. For two inputs separated by the scaled distance r,

$$k(r_x) = \sigma_f^2 \left(1 + \sqrt{5} r_x + \frac{5}{3} {r_x}^2\right) exp\left(-\sqrt{5} r_x\right)$$
$$ {r_x}^2 = \sum_i \frac{(x_i - x_i')^2}{\ell_i^2} \tag{176}$$

The Matérn 5/2 kernel was selected to provide sufficient smoothness while allowing the surrogate to represent the mild nonsmoothness associated with nonlinear hysteretic responses, particularly near yielding and unloading reversals. Unlike the squared-exponential kernel, which imposes infinite mean-square differentiability, the Matérn 5/2 kernel produces functions that are twice mean-square differentiable and therefore permits greater local variation in the response.

The anisotropic form of the kernel uses an independent length scale ℓ_i for each of the twelve sampling dimensions. These length scales allow the surrogate to adapt to different characteristic variation scales across the parameter space: a large ℓ_i indicates that the corresponding metric varies slowly with parameter i, and is therefore comparatively insensitive to it. The resulting length scales provide an informal indication of relative parameter sensitivity, which is subsequently assessed using the formal Sobol analysis. The signal amplitude, σ_f, sets the marginal standard deviation of the GP prior and controls the overall magnitude of the covariance, while the noise variance, σ_n^2, in Eq. (177) accounts for residual variability not represented by the latent GP function. These hyperparameters, together with the length scales, are estimated by maximizing the marginal likelihood using multiple restarts.

For a training set of N input points $X = \{x_1, \dots, x_N\}$ with corresponding responses $y = \{y_1, \dots, y_N\}$, let K_N denote the $N \times N$ covariance matrix between the training points. For a new input point x_*, let k_* denote the vector of covariances between x_* and the N training points, and let $k_{**} = k(x_*, x_*)$ denote the covariance of x_* with itself. The predictive distribution at x_* is Gaussian with mean and variance

$$\mu_*(x) = k_*^{\mathrm{T}} (K_N + \sigma_n^2 I)^{-1} y$$
$$\sigma_*^2(x) = k_{**} - k_*^{\mathrm{T}} (K_N + \sigma_n^2 I)^{-1} k_* \tag{177}$$

The predictive variance, σ_*^2, is propagated into the likelihood (see Section 5.8.8) to account for surrogate uncertainty in regions of the parameter space poorly represented by the training data.

Because exact GP training requires factorizing the $N \times N$ covariance matrix and becomes computationally demanding for approximately 1300 training points, the hyperparameters are fitted using a sparse, fully independent conditional approximation with an active subset of inducing points. The resulting surrogate provides the predictive mean and uncertainty required by the Bayesian inversion.

5.8.6 Validation of the Surrogate

This section corresponds to step 6 of the pipeline (Figure 125). The surrogate is assessed for both predictive accuracy and uncertainty calibration. Predictive accuracy measures how closely its mean predictions reproduce simulator responses, whereas uncertainty calibration assesses whether the predictive intervals appropriately represent the actual prediction errors. The latter matters because systematic underestimation of predictive uncertainty can lead to excessive confidence in the surrogate during Bayesian inversion. Both properties were assessed using ten-fold cross-validation.

The training set was divided into ten disjoint folds, and the GP was refit ten times, each time excluding one fold from the training data. Predictions for the excluded points were then compared with the corresponding simulator responses. Predictive accuracy is quantified using the cross-validated root-mean-square error normalized by the range of each metric. At the same time, uncertainty calibration is assessed from the empirical coverage of the 90% predictive interval, defined as the fraction of held-out observations contained within the corresponding predicted intervals. For a well-calibrated surrogate, this coverage should be close to 90%. The results of the ten-fold cross-validation for the four peak-displacement metrics are presented in Figure 126. Together, these figures provide a direct assessment of the surrogate accuracy and predictive-uncertainty calibration across all eight calibration metrics.

5.8.6.1 Peak-Displacement Metrics

Figure 126 shows the GP surrogates for peak displacement ($peak_1$ to $peak_4$). The predictions for $peak_1$ form a dense, narrow cloud closely aligned with the one-to-one line across the entire response range, with minimal dispersion and narrow uncertainty intervals. The quantitative measures are R^2=0.994, indicating that the surrogate reproduces 99.4% of the variance in the simulator response; a 90% predictive-interval coverage of 96.4%, indicating that the intervals contain slightly more observations than expected at the nominal level; and a normalized RMSE of 1.25%, indicating a very small prediction error relative to the response range. The coverage above the nominal level indicates mildly conservative uncertainty estimates, while the low RMSE confirms the surrogate's high predictive accuracy.

The GP surrogate for $peak_2$, compared with $peak_1$, exhibits substantially greater dispersion around the one-to-one line across the entire response range. This dispersion is particularly pronounced at low response values, where small simulator responses can yield substantially different GP predictions. The quantitative measures are R^2=0.865, indicating that the surrogate reproduces 86.5% of the variance in the simulator response; a 90% predictive-interval coverage of 87.5%, indicating that the predictive intervals contain slightly fewer observations than expected at the nominal level; and a normalized RMSE of 5.3%, indicating a prediction error of approximately 5.3% relative to the response range. The increasing width of the predictive intervals in the simulator response reflects the GP's greater uncertainty in regions where predictions are less accurate.

Although the surrogate does not meet the 5% RMSE criterion, its uncertainty estimates help limit overconfidence when propagated through the subsequent Bayesian inversion.

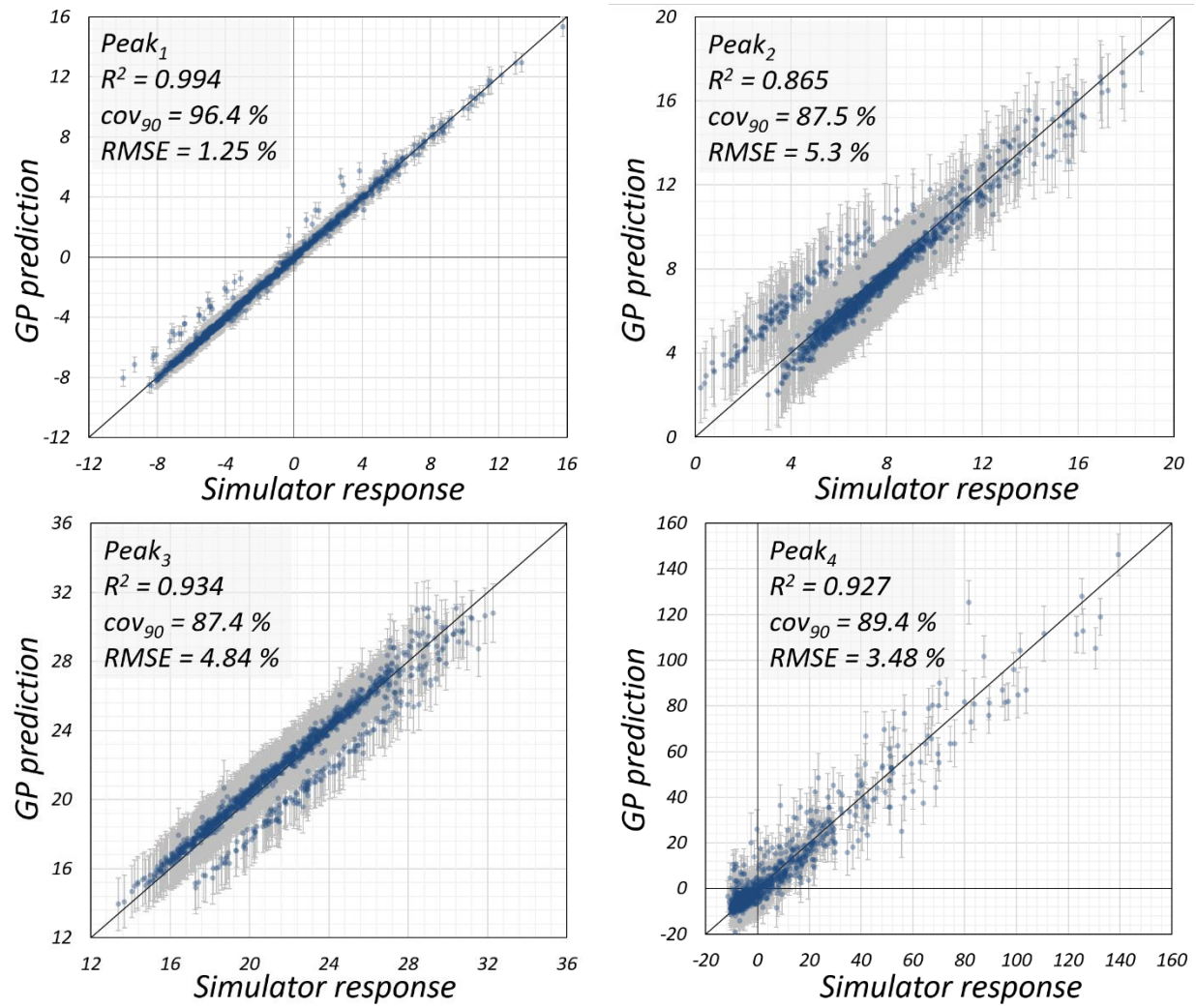


Figure 126. Ten-fold cross-validation of the peak-displacement GP surrogates.

The GP surrogate predictions for peak₃ follow a clear linear trend along the one-to-one line across the response range (12 to 36), but dispersion increases as the simulator response increases. At lower response values, the predictions remain relatively compact, whereas the spread becomes more pronounced at higher values. The widening predictive intervals and vertical uncertainty bars in this region indicate that the GP assigns greater uncertainty where predictions are more dispersed. The quantitative measures are R^2=0.934, indicating that the surrogate reproduces 93.4% of the variance in the simulator response; a 90% predictive-interval coverage of 87.4%, indicating that the intervals contain slightly fewer observations than expected at the nominal level; and a normalized RMSE of 4.84%, indicating a prediction error just below the 5% accuracy threshold. The slightly lower-than-nominal coverage indicates mild overconfidence in the uncertainty estimates, although the surrogate meets the prescribed accuracy criterion.

The GP surrogate predictions for $peak_4$ follow a one-to-one line across the broad response range from -20 to 160, but exhibit pronounced heteroscedasticity, with dispersion increasing substantially at higher simulator responses. At low responses, the predictions remain closely clustered around the one-to-one line, whereas the spread becomes progressively larger in the mid- and high-response regions.

The widening predictive intervals and uncertainty bars indicate that the GP assigns greater uncertainty where the predictions are more dispersed. The quantitative measures are R^2=0.927, indicating that the surrogate reproduces 92.7% of the variance in the simulator response; a 90% predictive-interval coverage of 89.4%, indicating that the intervals contain nearly the expected proportion of held-out observations; and a normalized RMSE of 3.48%, indicating a prediction error well below the 5% accuracy threshold. The near-nominal coverage indicates well-calibrated uncertainty estimates, while the low RMSE confirms that the surrogate meets the prescribed accuracy criterion despite the broad response range. Each panel retains the response range of its corresponding metric, allowing assessment of differences in dispersion, agreement with the one-to-one line, and predictive uncertainty without compressing the individual scales. The figure shows substantially tighter predictions for $peak_1$ than for $peak_2$-$peak_4$, along with the corresponding differences in the GP-assigned uncertainties. This joint view complements the individual validation plots by summarizing the four surrogates' relative performance.

5.8.6.2 Cumulative Hysteretic Energy Metrics

Figure 127 shows the GP surrogates for the cumulative hysteretic energy E_1-E_4. The predictions for E_1 form a dense, narrow band closely aligned with the one-to-one line across the response range from 5 to 25, with minimal dispersion and narrow predictive intervals. The quantitative measures are R^2=0.998, indicating that the surrogate reproduces 99.8% of the variance in the simulator response; a 90% predictive-interval coverage of 91.7%, indicating that the predictive intervals contain slightly more observations than expected at the nominal level; and a normalized RMSE of 0.97%, indicating a very small prediction error relative to the response range. The near-nominal coverage indicates well-calibrated, slightly conservative uncertainty estimates, while the low RMSE indicates that E_1 is the most accurately predicted metric among the eight surrogates.

For E2, predictions follow the overall trend of the one-to-one line but show substantial dispersion across the response range, making it the least accurately predicted of the eight metrics. The dispersion is particularly pronounced at higher responses, where the surrogate tends to underestimate the simulator response, although some predictions also lie above the one-to-one line. The quantitative measures are R^2=0.784, indicating that the surrogate reproduces 78.4% of the variance in the simulator response; a 90% predictive-interval coverage of 88.6%, indicating that the intervals contain slightly fewer observations than expected at the nominal level; and a normalized RMSE of 7.81%, indicating a prediction error substantially above the 5% accuracy threshold. The long uncertainty bars and broad predictive band reflect the surrogate's greater uncertainty for this metric. Although E_2 does not meet the prescribed accuracy criterion, its predictive uncertainty is retained in the Bayesian inversion to account for the surrogate's limited predictive accuracy and avoid treating its predictions as overly precise.

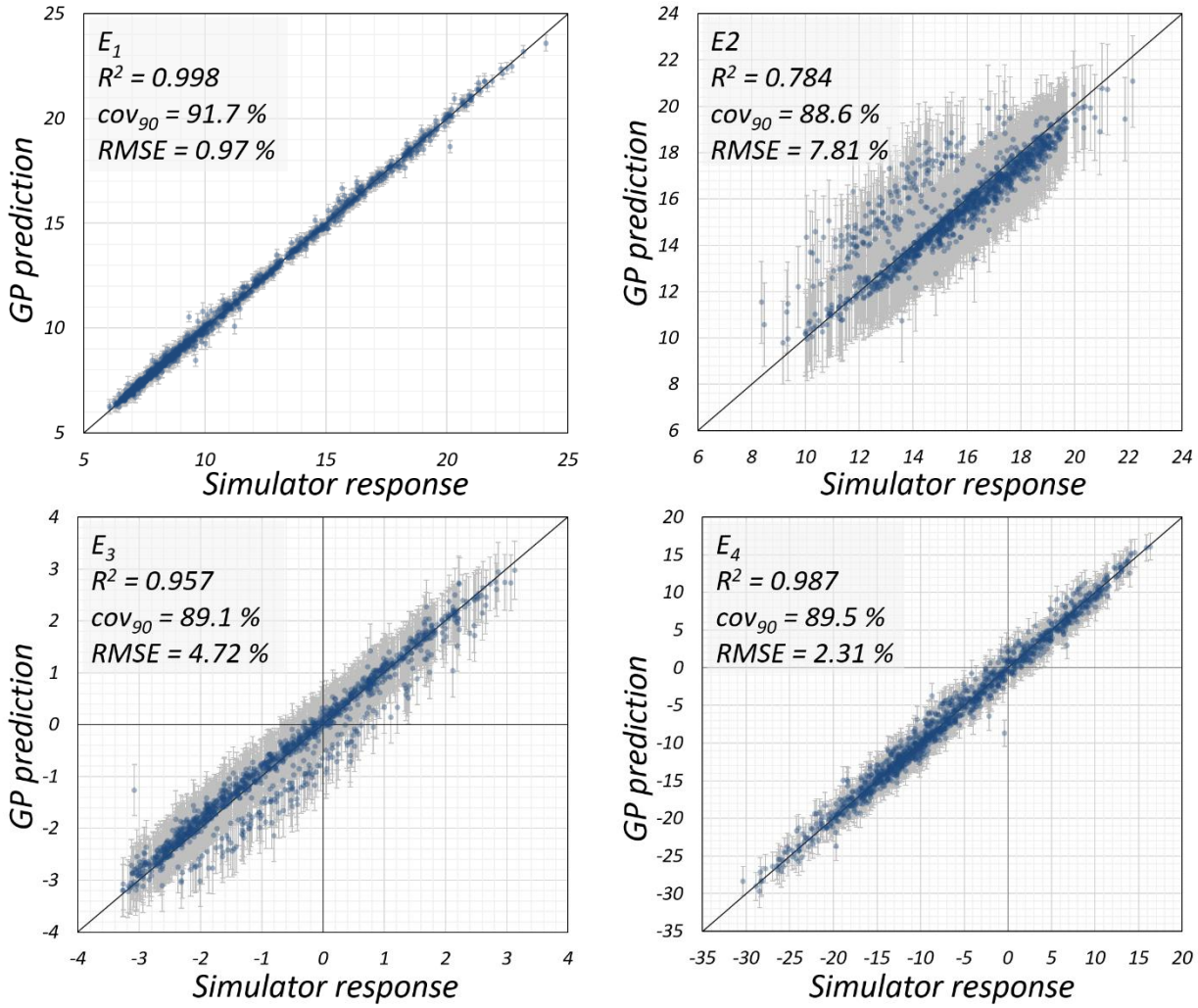


Figure 127. Ten-fold cross-validation of the cumulative hysteretic-energy GP surrogates.

The predictions for E_3 follow a clear linear trend along the one-to-one line across the response range, from -4 to 4, with greater dispersion toward the extremes than in the central region. The predictive intervals and uncertainty bars likewise widen toward the tails, indicating increased uncertainty where the surrogate predictions are less consistent. The quantitative measures are R^2=0.957, indicating that the surrogate reproduces 95.7% of the variance in the simulator response; a 90% predictive-interval coverage of 89.1%, indicating that the intervals contain nearly the expected proportion of observations at the nominal level; and a normalized RMSE of 4.72%, indicating a prediction error slightly below the 5% accuracy threshold. The near-nominal coverage indicates well-calibrated uncertainty estimates, while the RMSE confirms that the surrogate meets the prescribed accuracy criterion.

In the last GP surrogate E_4, the data form a dense, narrow cloud closely aligned with the one-to-one line across the broad response range from -35 to 20, with limited dispersion throughout the domain. The predictive intervals remain relatively narrow, widening only modestly toward the extremes, which indicates that the surrogate maintains low predictive uncertainty despite the

asymmetric response range. The quantitative measures are R^2=0.987, indicating that the surrogate reproduces 98.7% of the variance in the simulator response; a 90% predictive-interval coverage of 89.5%, indicating that the intervals contain nearly the expected proportion of observations at the nominal level; and a normalized RMSE of 2.31%, indicating a prediction error well below the 5% accuracy threshold. The near-nominal coverage indicates well-calibrated uncertainty estimates, while the low RMSE confirms the surrogate's high predictive accuracy.

Figure 127 provides a joint view of the four GP surrogates for the cumulative hysteretic energy metrics. The individual panels retain their respective response ranges, allowing assessment of differences in predictive accuracy and uncertainty without altering each metric's scale.

The surrogates for E_1 and E_4 exhibit the closest agreement with the one-to-one line, with comparatively narrow dispersion, whereas E_2 shows substantially greater scatter and wider predictive uncertainty. E_3 presents intermediate behavior, with increased dispersion toward the extremes of its response range. Overall, the joint view illustrates the variation in surrogate performance across the four-energy metrics and complements the detailed assessment provided by the individual cross-validation plots.

5.8.6.3 Overall Assessment of GP Surrogate Accuracy and Uncertainty

Table 31 summarizes the cross-validation results for the eight GP surrogates, considering both predictive accuracy and uncertainty calibration. Six of the eight surrogates: $peak_1$, $peak_3$, $peak_4$, E_1, E_3, and E_4 meet the prescribed 5% RMSE criterion. The two exceptions, $peak_2$ and E_2, exhibit RMSE values of 5.30% and 7.81%, respectively, and therefore do not meet the target accuracy.

Table 31. Summary of GP surrogate accuracy and uncertainty calibration.

GP Surrogate	$RRMSE_M$ (%)	RMSE (%)	Meets 5% criterion?	Main characteristic
$peak_1$	0.994	1.25	✓	Very high predictive accuracy
$peak_2$	0.865	5.3	✗	Largest dispersion among peak metrics
$peak_3$	0.934	4.84	✓	Good accuracy with increased uncertainty at higher responses
$peak_4$	0.927	3.48	✓	Good accuracy across a broad response range
E_1	0.998	0.97	✓	Highest predictive accuracy
E_2	0.784	7.81	✗	Lowest predictive accuracy and largest uncertainty
E_3	0.957	4.72	✓	Good accuracy with greater dispersion toward the extremes
E_4	0.987	2.31	✓	High accuracy across an asymmetric response range

Nevertheless, their relatively large predictive uncertainties are propagated through the Bayesian inversion, allowing the increased surrogate error to be reflected in the likelihood rather than treating

these predictions as overly precise. Across all eight surrogates, the observed 90% predictive-interval coverage ranges from 87.4% to 96.4%, indicating generally close agreement with the nominal coverage, although $peak_2$, $peak_3$, and E_2 exhibit slight undercoverage. Overall, the validation results indicate that the GP surrogates provide adequate predictive performance for the subsequent Bayesian inversion, with uncertainty estimates that generally remain close to the nominal coverage level.

Figure 128 shows the minimum Automatic Relevance Determination (ARD) length scale obtained for each of the twelve input parameters across the eight GP surrogate metrics. Here, sensitivity refers to how strongly the predicted response of a GP surrogate changes in response to variations in a given input parameter: length scales close to the unit-box width indicate a strong response of the metrics to that parameter, whereas length scales small relative to the unit-box width indicate that the metrics are comparatively flat in that direction. The dashed vertical line at unity represents the width of the unit hypercube used to normalize the input parameters. The parameters are ordered according to their minimum length-scale, with I_e/I_g, n_{rate}, α_u, and r_t showing the greatest sensitivity, while λ, n_p, ε'_{cc}, and Ω_{fac} exhibit substantially weaker effects. The numerical value of the minimum length scale is shown on each bar, providing a direct measure of the sensitivity's relative magnitude. This ranking provides a qualitative measure of the relative sensitivity of surrogate-predicted responses to input parameters, quantified through the variance-based analysis presented in the following section.

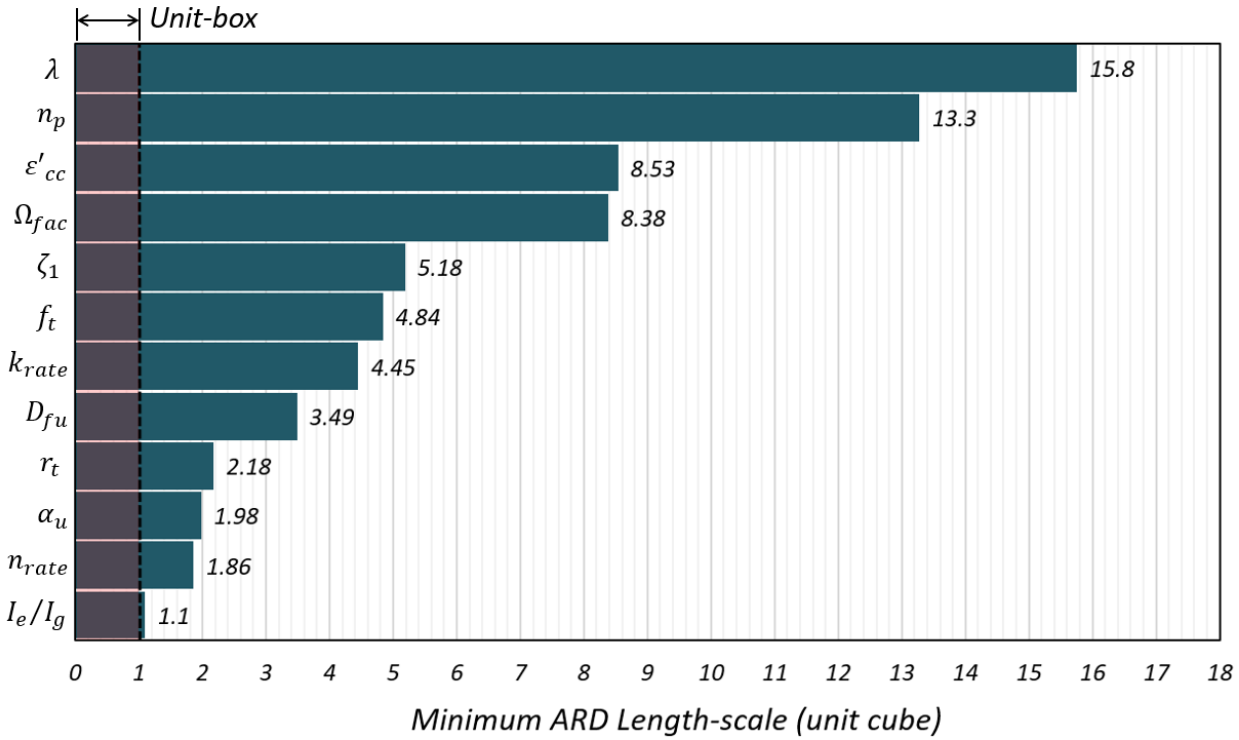


Figure 128. Minimum ARD length-scale of the twelve input parameters across the eight GP surrogates.

Moving up the scale, the intermediate-length-scale parameters k_{rate} (4.45), f_t (4.84), and ζ_1 (5.18) exert a comparatively mild influence on the surrogate metrics: their effects are present, but the corresponding responses vary gradually over the explored parameter range. The parameters Ω_{fac}(8.38) and ε'_{cc} (8.53) have length-scales roughly 8-9 times the unit-box width, indicating that their influence on the eight metrics is very weak within the explored domain. The two largest length-scales correspond to n_p (13.3) and, most notably, λ (15.8), whose length-scale is nearly sixteen times the width of the unit hypercube. Consequently, variations in λ produce negligible changes in the surrogate metrics over the explored domain.

Taken together, the ARD length-scales provide a clear qualitative hierarchy of parameter relevance, from the comparatively strongest dependence associated with I_e/I_g (1.1), n_{rate} (1.86), α_u (1.98), and r_t (2.18), the progressively weaker ones in the middle, and finally to those at the top whose influence is effectively smoothed out. The following section formally assesses this qualitative hierarchy through a variance-based sensitivity analysis.

5.8.7 Global Sensitivity Analysis via Sobol Indices

This section corresponds to step 7 of the pipeline (Figure 125). Although the ARD length-scales qualitatively rank input parameters by their influence on the surrogate metrics, they do not quantify the fraction of output variance attributable to each parameter. A formal, quantitative decomposition of the output variance was therefore performed using Sobol sensitivity indices, evaluated on the GP surrogates to keep the computational cost negligible.

For a scalar output $Y = f(\theta)$, with independently distributed input parameters θ according to the prior, the variance, $V = \mathrm{Var}(Y)$, can be decomposed into contributions from individual parameters and their interactions as

$$V = \sum_i V_i + \sum_{i<j} V_{ij} + \cdots \tag{178}$$

Where, V_i, represents the variance contribution associated with parameter i alone, V_{ij}, represents the contribution arising from the interaction between parameters i and j, and so forth. For each input parameter, two sensitivity indices are of primary interest: the first-order sensitivity index, S_i, and the total-order sensitivity index, $S_{T,i}$, [126]:

$$S_i = \frac{V_i}{V} \qquad\qquad S_{T,i} = \frac{\mathbb{E}_{\boldsymbol{\theta}_{\sim i}}\left[\mathrm{Var}_{\theta_i}(Y|\boldsymbol{\theta}_{\sim i})\right]}{V} \tag{179}$$

Here, i identifies the input parameter under consideration, θ_i denotes that parameter, and $\boldsymbol{\theta}_{\sim i}$ denotes the vector containing all input parameters except θ_i. The conditional variance $\mathrm{Var}_{\theta_i}(Y|\boldsymbol{\theta}_{\sim i})$measures the variability of the output produced by varying θ_i while holding all other parameters fixed. The expectation $\mathbb{E}_{\boldsymbol{\theta}_{\sim i}}[\cdot]$ then averages this conditional variance over the prior distributions of all remaining parameters. Thus, the numerator represents the portion of the output variance associated with variations in θ_i, including its interactions with the other input parameters.

In practical terms, if Y is the peak displacement and $\theta_i = I_e/I_g$, the numerator quantifies how much the predicted peak displacement changes when I_e/I_g is varied, averaged over all other input parameters. Dividing this quantity by the total output variance, V, expresses the result as a fraction of the overall variability of the peak displacement. Thus, $S_{T,i}$ measures the total influence of I_e/I_g on the output, including its interactions with the other input parameters.

These indices are therefore easy to interpret. A parameter with $S_{T,i} \approx 0$ has negligible influence on the output over the prescribed input domain, whereas a parameter with a large $S_{T,i}$ accounts for a substantial fraction of the output variability, either through its individual effect or through interactions with other parameters. Importantly, a large sensitivity index indicates influence on the model response, rather than parameter identifiability during calibration. Likewise, a parameter with negligible sensitivity contributes little information to the considered output within the explored domain. Because interaction effects are attributed to every parameter involved, the sum of the total-order indices generally exceeds unity. In contrast, the sum of the first-order indices equals unity for a purely additive response and is smaller than unity when interactions are present. Thus, the difference between these sums indicates the overall importance of parameter interactions [120].

The first-order index, S_i, quantifies the fraction of the output variance attributable to parameter i through its individual effect, excluding interactions with other parameters. In contrast, the total-order index, $S_{T,i}$ quantifies the fraction of output variance associated with parameter i, including its individual contribution and all interaction effects involving that parameter. Therefore, $S_{T,i} \geq S_i$, with the difference $S_{T,i} - S_i$ reflecting the contribution of interactions involving parameter i [120] and [126].

The first-order indices, $\hat{S}_i$, were estimated using the Saltelli estimator [120]:

$$\hat{S}_i = \frac{\frac{1}{N}\sum_{k=1}^{N} f\,(B_k)\left[f\left(A_B^{(i)}\right)_k - f(A_k)\right]}{\hat{V}} \tag{180}$$

The total-order indices, $\hat{S}_{T,i}$, were estimated using the Jansen estimator [62]

$$\hat{S}_{T,i} = \frac{\frac{1}{2N}\sum_{k=1}^{N}\left[f(\mathrm{A}_k) - f\left(\mathrm{A}_B^{(i)}\right)_k\right]^2}{\hat{V}} \tag{181}$$

Here, A and B are independent sample matrices, and $A_B^{(i)}$ is obtained by replacing the i-th column of A with the corresponding column of B. The index k denotes the k-th of the N sampled input combinations, and f denotes the GP surrogate. Accordingly, $f(A_k)$, $f(B_k)$, and $f\left(A_B^{(i)}\right)_k$ denote the surrogate evaluations corresponding to the k-th samples of A, B, and the hybrid matrix $A_B^{(i)}$,

respectively. N is the number of base samples, and $\hat{V}$ is the estimated variance of the surrogate output.

Here, S_i and $S_{T,i}$ denote the theoretical first- and total-order Sobol indices, respectively, whereas $\hat{S}_i$ and $\hat{S}_{T,i}$ denote their numerical estimates obtained from the finite set of surrogate evaluations using the Saltelli and Jansen estimators, respectively. The indices were estimated using the Saltelli sampling scheme. Saltelli et al. [120] recommend a base sample size of approximately N=500-1000 for this scheme. The complete model contains 15 parameters; however, two parameters (G_e/G_g and ζ_2) were held fixed, and a third, r_c, was determined from the input parameter ε'_{cc}. Consequently, the sensitivity analysis was performed over the 12-dimensional space of independent uncertain inputs rather than treating all 15 model parameters as independent variables. For d=12 independently sampled parameters, N=1000 would require $(d+2)N$ =14000 surrogate evaluations per metric. The present study adopts N=2^{13}=8192 quasi-random Sobol base samples for each of the 12 independently sampled input parameters, providing a substantially denser sampling of the input space. The next power of two, 2^{14}=16384, would double the computational cost; 2^{13} was therefore adopted as a practical compromise between sampling density and computational cost. With d=12, the adopted design required

$$(d+2)N = (12+2)(8\,192) = 114688$$

surrogate evaluations for each of the eight metrics.

The 95% confidence intervals were obtained by bootstrap resampling with 200 replicates. For each replicate, the N=8192 base samples of the Saltelli design were resampled with replacement, and the Sobol indices were recomputed, yielding an empirical distribution from which the 2.5th and 97.5th percentiles were extracted. Because the indices were evaluated on GP surrogates rather than the original simulator, each bootstrap replicate took only milliseconds, making 200 replicates computationally negligible. Table 32 reports the total-order indices for the twelve independently sampled parameters across the eight metrics.

The entries in Table 32 represent the total-order sensitivity indices, S_{T_i}, which quantify the fraction of the output variance of each metric (columns) attributable to each parameter (rows), including all interaction effects involving that parameter. Consequently, the indices may sum to more than unity when strong parameter interactions are present. Dashes denote parameters that were not included in the independent sampling for this analysis.

The variance-based decomposition quantitatively corroborates the qualitative relevance ranking suggested by the ARD length-scales in Figure 128. Parameters with the largest minimum length-scales (namely, those at the top of Figure 128, whose values exceed unity by more than an order of magnitude) exhibit negligible total-order indices ($S_{T_i} \leq 0.01$) across all eight metrics. For these parameters, the GP emulator assigns negligible sensitivity, and their variation contributes little to the surrogate response variance. Likewise, the intermediate-tier parameters identified by the ARD ranking exhibit only weak sensitivity, with Sobol indices not exceeding 0.04 for any metric.

Conversely, the parameters with the shortest length scales, closest to the unit-box width, emerge as the dominant drivers of variance. However, the peak and energy metrics differ clearly. For the peak responses ($peak_1$ through $peak_4$), the strain-rate exponent, n_{rate}, is the dominant parameter, accounting for 63% to 87% of the total variance. The first two peaks exhibit an almost identical sensitivity structure (S_T=0.87 and 0.85, respectively). The parameter k_{rate} exerts a weaker but consistent influence across the four peak metrics (S_T=0.12-0.18). The $peak_3$ and $peak_4$ also exhibit relevant sensitivity to the unloading-modulus scaling parameter, α_u, with total-order indices of 0.27 and 0.23, respectively.

Table 32. Total-order Sobol sensitivity indices for the eight GP surrogates, with bootstrap-based 95% confidence intervals.

Parameter	$peak_1$	$peak_2$	$peak_3$	$peak_4$	E_1	E_2	E_3	E_4
λ	0.00	0.00	0.00	0.01	0.00	0.00	0.00	0.00
n_p	0.00	0.00	0.00	0.01	0.00	0.00	0.00	0.00
D_{fu}	0.00	0.00	0.00	0.00	0.00	0.01	0.03	0.04
Ω_{fac}	0.00	0.00	0.00	0.01	0.00	0.00	0.01	0.01
α_u	0.00	0.00	0.27	0.23	0.00	0.00	0.62	0.37
f_t	0.00	0.00	0.00	0.00	0.01	0.01	0.00	0.00
r_t	0.01	0.04	0.00	0.00	0.03	0.23	0.02	0.00
ε'_{cc}	0.00	0.00	0.00	0.00	0.00	0.02	0.00	0.00
r_c	-	-	-	-	-	-	-	-
n_{rate}	0.87	0.85	0.63	0.76	0.52	0.12	0.30	0.56
k_{rate}	0.15	0.16	0.12	0.18	0.05	0.00	0.03	0.09
I_e/I_g	0.09	0.03	0.03	0.04	0.87	0.64	0.04	0.01
G_e/G_g	-	-	-	-	-	-	-	-
ζ_1	0.01	0.02	0.01	0.01	0.01	0.01	0.01	0.01
ζ_2	-	-	-	-	-	-	-	-

The energy metrics (E_1-E_4) reveal a markedly different sensitivity structure. The stiffness ratio, I_e/I_g, dominates E_1 (S_T=0.87) and remains the principal driver of E_2 (S_T=0.64), for which the tensile post-cracking shape parameter, r_t, also has a non-negligible secondary contribution (S_T=0.23). In contrast, E_3 constitutes a notable outlier: it is the only metric for which α_u (S_T=0.62) exceeds the contributions of both n_{rate} (S_T=0.30) and I_e/I_g (S_T=0.04), indicating that a distinct sensitivity pattern governs this energy response. The fourth energy metric, E_4, returns to a sensitivity structure more closely aligned with the peak responses, with n_{rate} (S_T=0.56) and α_u (S_T=0.37) as the primary contributors.

Overall, the variance-based analysis confirms the qualitative ARD interpretation: parameters with minimum length-scales close to the unit-box width account for most of the output variance, whereas parameters with length-scales an order of magnitude larger have negligible influence. The

main exception is r_t, whose intermediate ARD length-scale (2.18) does not preclude an appreciable contribution to E_2 (S_T=0.23). This result highlights that the ARD length-scale provides a useful measure of global smoothness but is not, by itself, sufficient to establish global sensitivity, since a parameter may exhibit relatively smooth marginal behavior while still contributing substantially to the variance of a specific response.

Figure 129 summarises the same variance-based sensitivity information in a compact form by reporting, for each parameter, the maximum total-order Sobol index, $S_{T,i}^{max}$, attained across the eight surrogate metrics. This worst-case aggregation condenses the per-metric results in Table 32 into a single hierarchy of parameter relevance. The adopted thresholds provide a practical classification of the magnitude of total-order effects: values below 0.10 indicate low influence, between 0.10 and 0.30 moderate influence, and above 0.30 a strong contribution to at least one response. This classification follows the general interpretation of Sobol indices discussed by Saltelli et al. [119].

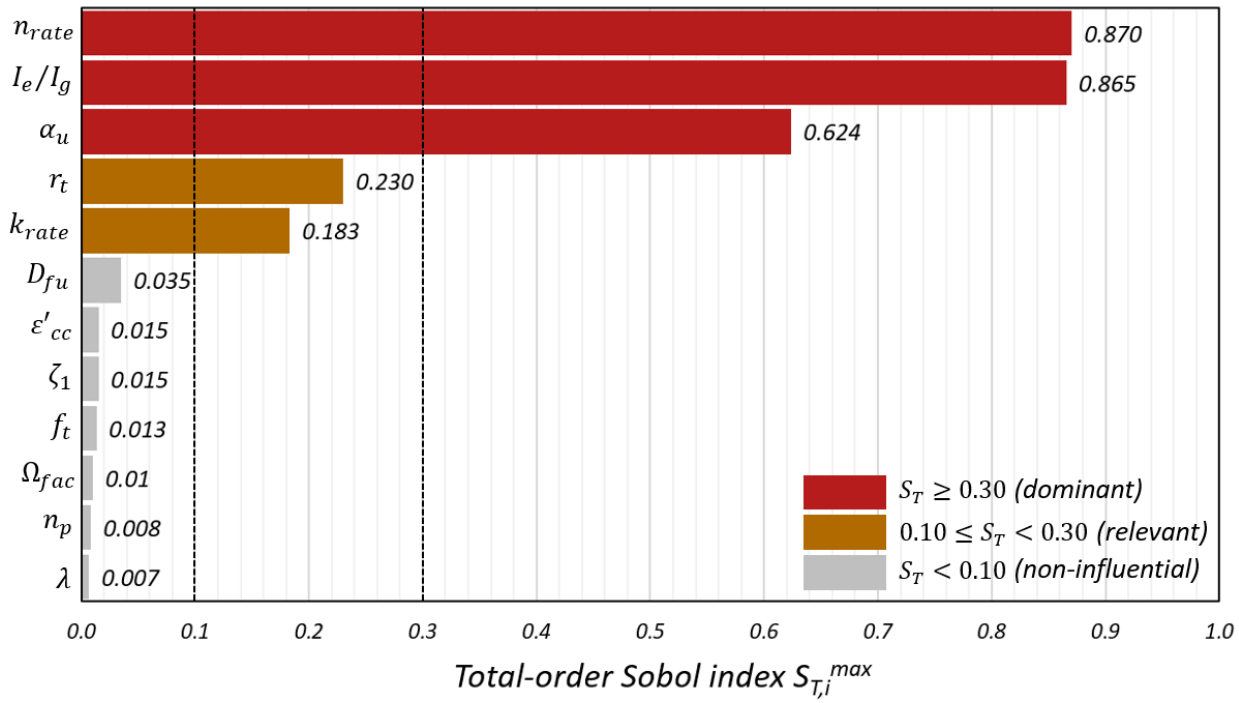


Figure 129. Total-order Sobol index $S_{T,i}^{max}$ for the twelve independently sampled parameters.

The color thresholds classify the parameters into three tiers: (1) *Dominant* parameters ($S_{T,i}^{max}$ ≥0.30, red) are the strain-rate exponent, n_{rate}, and the stiffness ratio, I_e/I_g, both with $S_{T,i}^{max}$ ≈ 0.87, followed by the unloading-modulus scaling parameter, α_u, with $S_{T,i}^{max}$=0.624. These three parameters strongly influence at least one surrogate response. (2) *Relevant* parameters (0.10≤ $S_{T,i}^{max}$ <0.30, yellow) are the tensile post-cracking shape parameter, r_t (0.23) and the strain-rate sensitivity coefficient, k_{rate} (0.183). These parameters have a moderate but non-negligible influence, with their effects concentrated on specific surrogate metrics. (3) The remaining

parameters (D_{fu}, ε'_{cc}, ζ_1, f_t, Ω_{fac}, n_p, and λ) have $S_{T,i}^{max} < 0.1$ and are therefore classified as *non-influential* within the global-sensitivity analysis.

Overall, the worst-case aggregation confirms the main finding of the per-metric decomposition: the uncertainty in the surrogate responses is concentrated in a small subset of the sampled inputs. Only five of the twelve parameters exceed the 0.10 relevance threshold, while only three reach the dominant-sensitivity range.

5.8.7.1 Physical Interpretation of the Informative Parameters

The global-sensitivity analysis identifies five informative parameters. Their sensitivity patterns directly connect the calibrated parameters to the physical mechanisms governing the dynamic response.

$n_{L,rate}$ is the dominant parameter for the peak displacements, with S_T=0.87 for peak$_1$ and S_T=0.85 for peak$_2$, and remains the leading parameter for the hysteretic energy of the motion (E$_4$, S_T=0.56). As the strain-rate exponent, it governs the amplitude of the viscous stress generated during strain-rate excursions in the reinforcement. Its strong influence on the peak responses therefore makes the dynamic data particularly informative for constraining the rate-dependent constitutive behavior of the reinforcing steel.

I_e/I_g dominates the hysteretic energy of the early motions, with S_T=0.87 for E$_1$ and S_T=0.64 for E$_2$, while having negligible influence on the peak responses and later energy metrics. This parameter controls the column's initial stiffness and, therefore, the elastic strain energy accumulated before significant cracking and yielding. As the section undergoes increasing inelastic deformation in the later motions, the initial stiffness becomes progressively less influential, which explains the observed reduction in sensitivity.

α_u governs the response of the later, stronger motions. Its influence is substantial for E$_3$ and E$_4$, and also becomes relevant for peak$_3$ and peak$_4$, whereas it is negligible for the first two motions. This parameter controls the tension-compression asymmetry of the reinforcement strength. Its influence becomes apparent in the later, stronger motions as the reinforcement experiences larger strain excursions and repeated load reversals, bringing the response into a regime where this asymmetry becomes consequential. The transition from negligible sensitivity in the early metrics to substantial sensitivity in the later ones is therefore consistent with the increasing importance of strength asymmetry as the deformation demands increase.

r_t contributes moderately to the hysteretic energy of E$_2$, with S_T=0.23, while its influence on the other metrics remains negligible. This parameter controls concrete's tensile post-cracking behavior. It therefore affects the unloading and reloading response of the section's tensile side after the first significant inelastic excursions. Its localized sensitivity to E2 indicates that this mechanism contributes to the hysteretic energy, while having little influence on the other response metrics.

k_{rate} exhibits a secondary but consistent influence on the peak responses, reaching S_T=0.18 for peak$_4$ and remaining within the range 0.12-0.16 for the other three peak metrics. As the coefficient governing the viscous stress, it acts jointly with n_{rate} to control the rate-dependent reinforcement

response. Consequently, the two parameters should not be interpreted as independently identifiable from the dynamic response. Their joint sensitivity reflects the coupled role in controlling the rate-dependent reinforcement response. This coupling limits how independently the two parameters can be identified from the dynamic data.

The remaining seven parameters have $S_{T,i} \leq 0.04$ across all eight dynamic metrics, indicating that their uncertainty contributes little to variability in the dynamic response within the adopted parameter ranges. This result does not imply that these parameters are intrinsically unidentifiable. Six of them were already constrained during Stage 1 through the moment-drift response, namely λ, n_p, f_t, D_{fu}, and Ω_{fac}, while ζ_1 is associated with damping and is addressed through a complementary analysis. The two calibration stages therefore provide complementary information: the Stage 1 response constrains parameters governing the structural response under quasi-static loading, whereas the dynamic response primarily informs the rate-dependent constitutive parameters.

5.8.7.2 Robustness of the Sensitivity Ranking to the Prior Distribution.

The Sobol indices reported in Table 32 were computed under a uniform prior over the parameter box, which assigns equal probability to all admissible parameter values. The uniform prior is the canonical choice for variance-based global sensitivity analysis because it allows the variance decomposition to characterize the model response across the entire feasible domain without assigning greater weight to any particular region [119]. However, the resulting sensitivity ranking may depend to some extent on the assumed input distribution, particularly when the model response is nonlinear or when interactions are concentrated near the boundaries of the parameter ranges. To assess the robustness of the sensitivity ranking to this assumption, the analysis was repeated using two alternative priors: a lognormal prior and a truncated normal prior, both defined over the same admissible parameter ranges.

For each parameter, the three prior specifications were defined over the same admissible interval, $[x_{lo}, x_{hi}]$so the comparison isolates the effect of probability weighting rather than changes in the feasible parameter domain. Herein, lo and hi denote the lower and upper bounds, respectively, of its admissible range. The corresponding prior distributions were defined as follows.

For the uniform prior,

$$p(x) = \frac{1}{x_{hi} - x_{lo}} \qquad x \in [x_{lo}, x_{hi}] \tag{182}$$

For the lognormal prior, the median of the underlying lognormal distribution was set to the midpoint of the admissible range. The logarithmic location and scale parameters were defined as

$$\ln \mu = \ln\left(\frac{x_{lo} + x_{hi}}{2}\right) \qquad \ln \sigma = \ln\left(\frac{x_{lo} + x_{hi}}{4}\right) \tag{183}$$

The dispersion was defined in logarithmic space so that the interval corresponding to approximately $\pm 2\sigma$ in log-space spans the prescribed parameter range. The resulting distribution was truncated to the same admissible range as the uniform distribution does. This specification produces a mildly right-skewed distribution concentrated toward the central portion of the range, while retaining the same prescribed parameter bounds.

For the truncated-normal prior, the mean was placed at the midpoint of the admissible range, and the standard deviation was selected such that the interval corresponding to $\pm 2\sigma$ spans the full range:

$$\mu = \frac{x_{lo} + x_{hi}}{2} \qquad \sigma = \frac{x_{lo} + x_{hi}}{4} \tag{184}$$

The resulting truncated normal distribution was subsequently truncated to $x \in [x_{lo}, x_{hi}]$. This prior distribution is symmetric about the midpoint and therefore concentrates probability toward the center of the admissible range without introducing the positive skew associated with the lognormal distribution.

Consequently, the three priors share identical admissible parameter ranges but provide progressively different probability weightings within those ranges: the uniform prior is flat, the lognormal prior is centrally concentrated and mildly asymmetric, and the truncated normal prior is centrally concentrated and symmetric. The sensitivity analysis was therefore repeated under these three distributions to determine whether the identified sensitivity hierarchy depends materially on the assumed prior weighting.

The sensitivity indices obtained under the two alternative priors were compared with those from the uniform-prior analysis to assess whether the sensitivity hierarchy depends on the assumed input distribution. Table 33 compares the maximum total-order Sobol index ($S_{T,max}$) across the eight metrics under both priors. Because each parameter has one S_T value per response metric, eight in total (four peak-displacement errors and four hysteretic-energy errors), the maximum across the eight metrics is reported. This criterion flags a parameter as informative whenever it influences at least one metric, rather than averaging its contribution across metrics and diluting a strong single-metric effect.

The ranking of the five informative parameters (n_{rate}, I_e/I_g, α_u, r_t, and k_{rate}) is preserved across the three prior distributions. The same three parameters exceed $S_{T,max}$=0.30, while r_t and k_{rate} remain in the second tier with $S_{T,max}$>0.10. No parameter changes its classification when the prior is changed from uniform to lognormal or truncated normal. The numerical differences in $S_{T,max}$ are modest relative to the separation between the influential and non-influential parameters.

These results demonstrate that the sensitivity ranking is robust to the assumed input distribution. Using a uniform, lognormal, or truncated normal prior over the same admissible parameter ranges yields the same hierarchy of influential parameters. Therefore, the sensitivity conclusions are not

an artifact of the uniform-prior assumption but remain consistent across the three alternative representations of the parameter distributions.

Table 33. Maximum total-order Sobol index across eight metrics: uniform vs. lognormal prior.

Parameter	$S_{T,max}$ (uniform)	$S_{T,max}$ (lognormal)	$S_{T,max}$ (truncated-normal)
n_{rate}	0.870	0.818	0.825
I_e/I_g	0.865	0.839	0.854
α_u	0.624	0.563	0.577
r_t	0.230	0.223	0.231
k_{rate}	0.183	0.164	0.143
D_{fu}	0.035	0.039	0.04
ε'_{cc}	0.015	0.023	0.023
ζ_1	0.015	0.016	0.017
f_t	0.013	0.012	0.012
Ω_{fac}	0.010	0.007	0.008
n_p	0.008	0.004	0.004
λ	0.007	0.014	0.013

5.8.8 Likelihood and Error Model

This section corresponds to Step 8 of the pipeline (Figure 125). The likelihood formalizes the requirement that the calibrated model reproduces the experimental response. For a parameter vector θ, let $\mu_i(\theta)$ and $\sigma_i(\theta)$ denote the predictive meaning and standard deviation of the GP for metric i (Eq. (177)). Since each metric is a log-ratio that vanishes for a perfect match, the residual is

$$r_i(\theta) = 0 - \mu_i(\theta) = -\mu_i(\theta) \tag{185}$$

Assuming conditionally independent Gaussian residuals, the log-likelihood is

$$\ln p\,(h|\theta) = -\frac{1}{2}\sum_i \left[\frac{r_i(\theta)^2}{v_i(\theta)} + \ln\big(2\pi v_i(\theta)\big)\right] \tag{186}$$

Here, h denotes the vector of target experimental metrics, $r_i(\theta)$ is the residual for metric i, and $v_i(\theta)$ is its total variance. The summation extends over the eight-response metrics. The first term inside the brackets measures the squared residual relative to its total variance, while the logarithmic term accounts for the normalization of the Gaussian density.

The total variance assigned to each metric combines two contributions,

$$v_i(\theta) = \sigma^2_{err,f(i)} + \sigma_i(\theta)^2 \tag{187}$$

The first term, $\sigma^2_{err,f(i)}$, represents an error variance assigned to metric family f, with one value for the peak-displacement metrics and another for the hysteretic-energy metrics. Rather than being fixed a priori as arbitrary weights, these two variances are treated as hyperparameters and estimated jointly with θ under weakly informative priors. The data therefore determine the relative weighting of the two metric families rather than imposing it externally. The second term, $\sigma_i(\theta)^2$, is the predictive variance of the GP emulator (Eq. (177)). Including this term increases the total variance in regions where the surrogate is uncertain, thereby reducing the influence of those regions on the likelihood. This propagation of emulator uncertainty prevents the inversion from assigning excessive confidence to poorly sampled regions of the parameter space, particularly when the posterior extends beyond the training data.

The estimated standard deviation errors are approximately 13.9% for the peak-displacement metrics and 11.3% for the hysteretic-energy metrics. These values are on the same order as the residual errors from the calibration campaign: the best individual analysis achieves about 7% error. In comparison, a typical good analysis is closer to 12%. This agreement indicates that the estimated error terms reflect a non-negligible model-discrepancy component rather than measurement or numerical noise alone. The Discrepancy Analysis section examines this discrepancy further, attributing the residual differences to physical features of the experimental response that the model does not reproduce.

5.8.9 Transitional Markov Chain Monte Carlo Sampler

This section corresponds to Step 9 of the pipeline (Figure 125). Direct sampling from the posterior in Eq. (173) is challenging because the posterior may be concentrated in a small, unknown region of the 15-dimensional parameter space. A Markov chain initialized arbitrarily from the prior may therefore require many iterations to reach the high-probability region. Transitional Markov Chain Monte Carlo (TMCMC) addresses this problem by constructing a sequence of intermediate distributions that progressively transform the prior into the posterior [33]. Rather than making a single transition between these two distributions, TMCMC advances a population of particles through a series of intermediate targets that differ only gradually from one another.

Formally, TMCMC tempers the likelihood through a sequence of exponents:

$$p_j(\theta) \propto p(d^*|\theta)^{\beta_j} p(\theta)$$
$$0 = \beta_0 < \beta_1 < \cdots < \beta_m = 1 \tag{188}$$

Here, β_j controls the contribution of the likelihood at stage j. Thus, $\beta_0 = 0$ corresponds to the prior, whereas $\beta_m = 1$ gives the target posterior. A population of N particles is initially sampled from the prior and progressively advanced through these intermediate distributions. At each transition from β_j to β_{j+1}, particle k receives the importance weight

$$w^{(k)} = p\left(d^*|\theta^{(k)}\right)^{\beta_{j+1}-\beta_j} \tag{189}$$

where $\theta^{(k)}$ denotes the parameter vector associated with particle k. The increment $\beta_{j+1} - \beta_j$ is selected adaptively by bisection so that the coefficient of variation of the importance weights reaches the prescribed target value of unity. This procedure keeps consecutive intermediate distributions close enough that the reweighting step remains effective.

The particles are then resampled according to their normalized weights, increasing the representation of high-probability regions while removing particles with low posterior weight. Each resampled particle is subsequently advanced through a short Metropolis random walk [55]. The proposal covariance is obtained from the weighted population covariance at the current stage and scaled to control the acceptance rate. This combination of adaptive tempering, resampling, and MCMC moves allows the particle population to progressively concentrate around the posterior high-probability region while maintaining sufficient diversity. As a by-product, the product of the mean importance weights across the transitional stages provides an estimate of the evidence, $p(d)$.

5.8.9.1 TMCMC convergence diagnostics

The number of particles in the TMCMC population, N=2000, was selected to provide sufficient resolution of the posterior marginals and pairwise correlations in the 12-dimensional parameter space while keeping the computational cost of each tempering stage manageable. Thus, the population provides the basis for resolving not only the marginal posterior distributions of these parameters but also their joint behavior and potential parameter trade-offs.

Figure 130 shows that the Bayesian calibration of the 12 model parameters proceeds in a controlled manner from prior knowledge toward knowledge updated by the observational data. The nine panels jointly show that the transition remained numerically stable while, for the three priors considered, progressively concentrating the initially broad prior distribution on combinations of the steel, concrete, viscous, and damping parameters compatible with the measured structural response.

Although the particles progressively concentrate toward combinations of the 12 parameters that are more compatible with the observations, the population does not collapse onto a small number of dominant particles. This retained diversity is physically important because the posterior is not expected to identify a unique parameter vector. Multiple combinations of calibrated steel, concrete, viscous, and damping parameters may remain compatible with the observed structural response, particularly when different physical effects can compensate for one another. The preserved particle population therefore provides sufficient representation of the posterior marginals and parameter correlations associated with this non-uniqueness.

The convergence of the three TMCMC runs was assessed using three complementary diagnostics: the adaptive tempering exponent, the Metropolis acceptance rate, and the effective sample size. These diagnostics characterize, respectively, the progression of the prior-to-posterior transition, the efficiency of the Metropolis exploration, and the preservation of particle diversity throughout the tempering sequence. Their behavior is examined separately below.

5.8.9.1.1 Tempering Exponent

The tempering schedule (Figure 130a) shows that the tempering stages are not user-prescribed but are determined automatically by the coefficient-of-variation criterion. At each stage, the increment $\Delta\beta$ is selected so that dispersion of the importance of weight remains controlled and the effective sample size after reweighting stays at approximately the prescribed level. Under the uniform prior, the algorithm reached β_7=1 in seven stages, with the first increment being particularly small, $\beta_1 \approx 0.008$, followed by progressively larger increments as the intermediate distributions approached the posterior. The very small initial value of $\beta_1 \approx 0.008$ reflects the need to introduce the observational information gradually. The observations progressively restrict the broad prior distribution to the region of the parameter space that can reproduce the measured structural response. A direct transition from the *prior* to the *posterior* could therefore produce excessive concentration of the importance weights and particle degeneracy. The seven-stage sequence progressively downweights incompatible parameter combinations while retaining sufficient representation of the viable regions. The resulting concave tempering schedule reflects the CoV criterion's adaptive response to the evolving target distribution. As the particle population becomes increasingly concentrated in regions of higher posterior probability, larger increments in β can be introduced without producing excessive weight dispersion. The final transition from $\beta_6 \approx 0.74$ to β_7=1 illustrates this behavior.

The TMCMC sampling was repeated using the lognormal prior. The sampler reaches the full posterior β=1 in only three stages, compared with seven under the uniform prior. This faster convergence is consistent with the lognormal prior concentrating probability mass near the center of each parameter range, so the initial particle population overlaps more with the region of relatively high posterior probability. Consequently, the CoV criterion permits larger tempering increments: β increases from 0.07 to 0.39 and then to 1, whereas the uniform prior requires seven smaller increments to maintain controlled importance-weight dispersion. The sampler under the truncated normal prior reaches β=1 in four stages, with β increasing from 0.065 to 0.325, 0.823, and finally 1. The intermediate stage count, between the seven stages required by the uniform prior and the three stages under the lognormal prior, is consistent with the truncated-normal prior concentrating mass symmetrically around the midpoint of each parameter range: more informative than the uniform prior but without the asymmetry of the lognormal.

5.8.9.1.2 Metropolis Acceptance

The sampler efficiency (Figure 130b) shows that the Metropolis acceptance rate remained stable at approximately 52% throughout the seven stages. This value should not be interpreted against the 23.4% asymptotic optimum commonly associated with random-walk Metropolis algorithms, because that result applies to stationary Markov chains targeting a fixed distribution under specific asymptotic assumptions. In TMCMC, the target distribution changes progressively across tempering stages, while the Gaussian proposal covariance is adaptively estimated from the evolving particle population at each stage. The approximately 52% acceptance rate therefore indicates that the proposal remained appropriately scaled throughout the prior-to-posterior transition, allowing substantial parameter movement while maintaining a high acceptance probability. Its stability across the seven stages, together with the controlled effective sample size, provides evidence of adequate sampling efficiency. The adaptive covariance proposal is particularly important in the present 12-parameter calibration because the posterior may contain

correlations arising from compensating physical effects. In particular, interactions between the steel constitutive, concrete, rate-dependent, and damping parameters may allow different parameter combinations to produce similar global structural responses. The stable acceptance rate indicates that the adaptive proposal explored such combinations as the posterior geometry evolved.

The Metropolis acceptance rate under the lognormal prior is approximately 68%, compared with 52% under the uniform prior. A higher acceptance rate indicates that a larger fraction of adaptive proposal moves are accepted during the tempering sequence. Interpret this difference alongside the effective sample size rather than against a fixed acceptance-rate target, because TMCMC samples a sequence of evolving target distributions and adapts the proposal covariance to the particle population at each stage. Despite the different number of tempering stages, the resulting posterior is essentially unchanged. The lognormal prior therefore shortens the path from the prior to the posterior without substantially altering the resulting posterior distribution. A natural concern is whether an acceptance rate of approximately 68% indicates that the proposal step size is too small, leading to inefficient exploration of the parameter space.

The Metropolis acceptance rate is approximately 67-69%, comparable to the lognormal case and again above the 52% observed under the uniform prior.

5.8.9.1.3 Effective Sample Size

The particle diversity (Figure 130c) shows that the effective sample size, N_{eff}, remains near 1000 throughout the seven stages. This behavior follows from the coefficient-of-variation criterion adopted in TMCMC. At each tempering stage, the increment $\Delta\beta$ is selected so that the coefficient of variation of the importance weights satisfies the prescribed criterion CoV=1, following Ching et al. [33].

For a population of N particles with importance weights w_i, the effective sample size is

$$N_{eff} = \frac{(\sum_{i=1}^{N} w_i)^2}{\sum_{i=1}^{N} w_i^2} \tag{190}$$

which can be written in terms of the coefficient of variation of the unnormalized weights as

$$N_{eff} \approx \frac{N}{1 + \mathrm{CoV}^2} \tag{191}$$

Therefore, with N=2000 and the criterion CoV=1,

$$N_{eff} = \frac{2000}{1 + 1^2} = 1000 = \frac{N}{2}$$

Thus, the observed N_{eff} ≈1000 is not an independently prescribed ESS target; it is the direct consequence of the adopted CoV criterion. This criterion provides a controlled balance between

the size of each tempering increment and the preservation of particle diversity. A smaller CoV threshold would require smaller increments in β a and consequently more tempering stages. In contrast, a larger threshold would permit larger increments at the expense of greater concentration of the importance weights and a reduced effective sample size.

Under the lognormal prior, the effective sample size, N_{eff}, remains at 1000 during the first two stages and increases to approximately 1059 in the final stage. Thus, the higher acceptance rate is not accompanied by a loss of particle diversity, indicating that the adaptive proposal remains appropriately scaled under the lognormal prior. This behavior provides evidence against interpreting the higher acceptance rate as a consequence of an excessively small proposal step size. During the first two stages, N_{eff}=1000, because the bisection procedure selects the tempering increment to satisfy CoV=1. In the final stage, the remaining transition from β=0.39 to β=1 is completed in a single step. Because β=1 is the prescribed final target, the tempering increment cannot be increased beyond this value even if the resulting coefficient of variation remains below the target.

The resulting CoV=0.94, therefore gives

$$N_{eff} = \frac{2000}{1 + 0.94^2} \approx 1059$$

The approximately 68% acceptance rate therefore reflects the more favorable alignment between the lognormal prior and the posterior rather than an overly conservative proposal step size.

The effective sample size remains at N_{eff}=1000 under the truncated normal prior during the first three stages; at the final stage, the transition from β=0.823 to β=1 yields CoV≈0.25, giving

$$N_{eff} \approx \frac{2000}{1 + 0.25^2} \approx 1881.$$

Taken together, the three diagnostics indicate that the three TMCMC runs provide a controlled and numerically stable transition from the prior to the posterior. The tempering trajectories differ according to the prior distribution: the uniform prior requires seven stages to reach $\beta = 1$, whereas the lognormal and truncated-normal priors require three and four stages, respectively. This difference reflects how the priors distribute probability mass over the same admissible parameter ranges. The Metropolis acceptance rates are about 52% for the uniform prior and 67-69% for the two alternative priors, indicating efficient exploration in all cases when interpreted alongside the effective sample size. The latter remains sufficiently high throughout the tempering sequences, with no evidence of severe population degeneracy. Thus, changing the prior distribution modifies the efficiency and trajectory of the TMCMC transition but does not prevent stable convergence to the posterior.

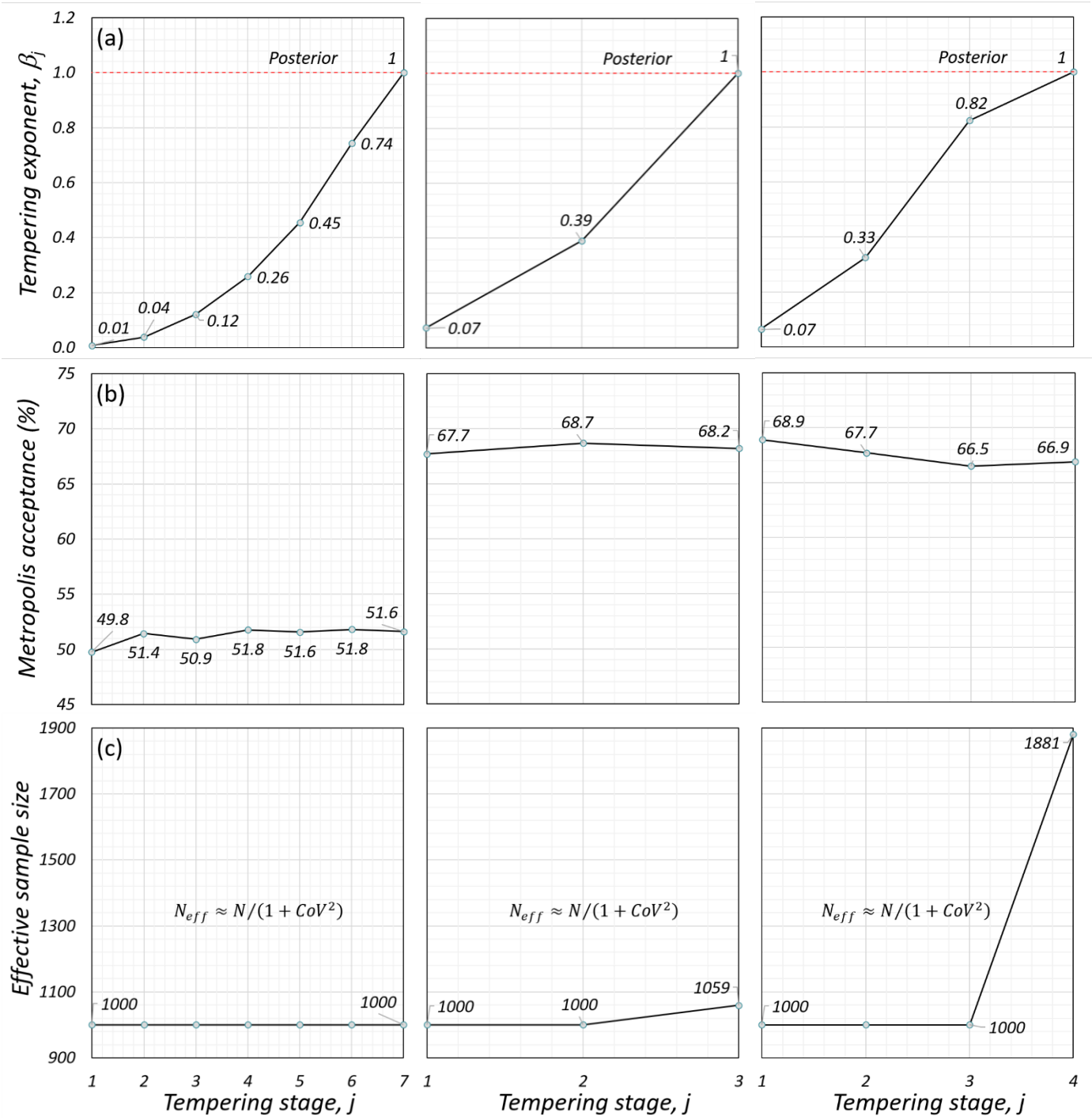


Figure 130. TMCMC convergence diagnostics during the Bayesian calibration.

5.8.10 Posterior Results

This section corresponds to Step 10 of the calibration pipeline (Figure 125). Table 34 summarizes the calibrated parameters obtained from the dynamic Bayesian analysis. The table reports fifteen model parameters in total, of which twelve are independently sampled and calibrated, two are fixed throughout the Bayesian analysis (ζ_2 and G_{eff}/G), and one, r_c is derived from the independently sampled parameter ε'_{cc}. For the 12 independently sampled parameters, four posterior statistics are reported: the maximum a posteriori (MAP) estimate, the posterior mean, the posterior standard deviation, and the 90% credible interval. The MAP corresponds to the single-joint parameter vector with the highest posterior density. It is used as the recommended point estimate for subsequent deterministic verification with the true finite-element simulator. The posterior mean, standard deviation, and credible interval characterize the marginal distribution of each independently sampled parameter and quantify the uncertainty remaining after incorporation of the dynamic observations.

The distinction between the joint MAP and the marginal posterior distributions is important. The MAP is a property of the joint 12-dimensional posterior. It does not, in general, coincide with the vector formed by independently maximizing each marginal distribution, particularly when posterior correlations are present. In this analysis, the MAP corresponds to particle 1656 of the 2000-particle TMCMC population, with a log-likelihood of -28.6, compared with a median value of -30.8 and a worst-particle value of -40.9.

The two final columns of Table 34 report the ratio of posterior width to prior width for the independently sampled parameters. This ratio directly measures how much the dynamic observations reduce uncertainty in each parameter. Values close to unity indicate that the posterior retains approximately the prior width and that the dynamic observations provide limited additional information about that parameter. In contrast, smaller values indicate greater posterior concentration and stronger data-informed updating. This interpretation is consistent with the previously presented global sensitivity analysis, which identified the parameters that most influence the dynamic response.

The posterior results show that the dynamic observations provide different levels of information for the twelve independently sampled parameters. The strongest posterior concentration occurs for the unloading-modulus scaling parameter, α_u, and for the Strain-rate sensitivity exponent, n_{rate}, whose posterior-to-prior width ratios are 0.69 and 0.68, respectively. These two parameters therefore exhibit the clearest reduction in uncertainty during the dynamic calibration. The posterior for α_u is concentrated toward the lower part of its prior range, with a MAP value of 0.632 and a 90% credible interval of [0.60, 0.74]. In contrast, n_{rate} is concentrated toward the upper part of its admissible range, with a MAP value of 0.690 and a 90% credible interval of [0.43, 0.78].

The remaining parameters show substantially weaker posterior concentration. For example, λ, n_p, D_{fu}, and ε'_{cc} retain posterior-to-prior width ratios close to unity, indicating that their uncertainty is only weakly reduced by the dynamic observations. The parameters f_t, r_t, ζ_1, k_{rate}, I_e/I_g, and Ω_{fac} exhibit relatively modest changes in posterior width. Consequently, the dynamic calibration does not identify all twelve independently sampled parameters with equal strength; rather, it provides stronger information for a subset of parameters while leaving substantial uncertainty in others.

This behavior is consistent with the inverse problem's physical nature. The measured global structural response is influenced simultaneously by the steel constitutive response, concrete properties, rate-dependent effects, and damping representation. Consequently, different parameter combinations may produce similar structural responses, allowing compensatory effects to persist in the posterior. The posterior distributions therefore provide not only updated parameter estimates but also information about the degree of identifiability achievable from the available dynamic observations.

Table 34. Posterior parameter estimates and uncertainty - Uniform prior.

Parameter	MAP	Mean	SD	90% interval	Post/prior	Informed
λ	1.106	1.097	±0.029	[1.06, 1.14]	1.00	-
n_p	0.496	0.478	±0.023	[0.44, 0.51]	0.99	-
D_{fu}	0.981	0.947	±0.029	[0.90, 0.99]	1.00	-
Ω_{fac}	1.060	1.031	±0.017	[1.005, 1.058]	0.96	
α_u	0.632	0.656	±0.040	[0.60, 0.74]	0.69	**informed**
f_t	0.796	0.858	±0.089	[0.72, 0.99]	1.03	-
r_t	1.124	1.148	±0.055	[1.06, 1.24]	0.95	-
ε'_{cc}	-0.00424	-0.00407	±0.00029	[-0.00446, -0.00357]	1.00	-
r_c	-	-	-	Derived	-	-
n_{rate}	0.690	0.635	±0.117	[0.43, 0.78]	0.68	**informed**
k_{rate}	99.6	88.0	±26.4	[52, 136]	0.95	-
I_e/I_g	0.646	0.630	±0.014	[0.605, 0.648]	0.94	-
G_e/G_g	0.2	0.2	-	Fixed	-	-
ζ_1	0.00462	0.00518	±0.00041	[0.00458, 0.00588]	0.95	-
ζ_2	0.015	0.015	-	Fixed	-	-

Table 35 evaluates the joint MAP combination against the eight calibration metrics using the Gaussian-process surrogate.

The predicted residuals range from -7.41% for $peak_1$ to +17.9 for $peak_3$, while the remaining metrics show smaller discrepancies. The root-mean-square residual across the eight metrics is 8.88%. This value is below the general surrogate error floor identified in Section 5.8.8. It indicates that the MAP lies within the range of responses supported by the adopted likelihood model. The MAP combination is therefore used as the reference parameter vector for the subsequent verification and validation with the true finite-element simulator.

Figure 131 provides a complementary visualization of the posterior results by displaying the marginal distributions within their corresponding prior bounds. The posterior marginals are constructed from the 2000 particles retained by the TMCMC algorithm. Each marginal uses 30 bins spanning its corresponding prior range.

Table 35. GP-predicted residuals at the MAP estimate - Uniform prior.

Metric	Residual at the MAP (%)	Ratio Test/Sim	σ_{err} (%)
peak₁	-7.41	0.93	10.3
peak₂	+5.29	1.05	
peak₃	+17.9	1.2	
peak₄	-4.35	0.96	
E₁	+6.81	1.07	7.65
E₂	+11.6	1.12	
E₃	-2.21	0.98	
E₄	+4.81	1.05	
RMSE (8metrics)	8.88	-	-

This combination provides sufficient resolution to visualize posterior concentration while avoiding excessive bin-to-bin sampling variability. Under a uniform distribution, the expected number of samples per bin is

$$\frac{N}{N_{bins}} = \frac{2000}{30} \approx 66.7.$$

Thus, approximately 66.7 samples per bin represents the expected histogram count if the posterior remains consistent with the uniform prior. Parameters whose posterior distributions remain approximately uniform across the prior interval show limited updating from the dynamic observations, whereas concentrated posterior distributions indicate stronger information from the data.

For visualization purposes, the parameters are evenly distributed between the two groups, with six parameters shown in each group. Figure 131a contains the six parameters primarily identified during the displacement-controlled calibration stage (λ, n_p, f_t, r_t, D_{fu}, and Ω_{fac}), whereas Figure 131b contains the six parameters accessible through the dynamic response (n_{rate}, k_{rate}, α_u, I_e/I_g, ζ_1 and ε'_{cc}). This organization allows the twelve marginal posterior distributions to be displayed with comparable visual resolution while preserving the distinction between parameters with different levels of posterior updating. This visual pattern is consistent with the posterior-to-prior width ratios reported in Table 34 and with the sensitivity results obtained from the global sensitivity analysis.

Six of the twelve marginals remain approximately uniform throughout their prior intervals, with bin counts fluctuating around the 66.7-sample reference. These include the six parameters shown in the first group (λ, n_p, f_t, r_t, D_{fu}, and Ω_{fac}), together with ε'_{cc} from the second one. The lack of pronounced posterior concentration for these parameters broadly aligns with the global sensitivity analysis, which indicates limited or metric-specific contributions to the surrogate variance. Their posterior distributions therefore remain close to the corresponding prior distributions, indicating that the dynamic observations provide limited additional information about these parameters.

Two marginals depart markedly from uniformity. The strain-rate sensitivity exponent, n_{rate}, concentrates toward the upper end of its prior range (approximately 0.69-0.77), with histogram counts increasing toward the upper tail. This concentration is consistent with its dominant sensitivity across the peak-response metrics, as reflected in its total-order Sobol indices, which are among the largest. Conversely, the unloading-modulus scaling parameter, α_u, concentrates toward the lower end of its prior range, approximately 0.60-0.66. Its posterior concentration is consistent with its substantial contribution to the energy and peak-response metrics, particularly E_3.

The remaining three dynamic parameters, k_{rate}, I_e/I_g, and ζ_1, remain comparatively broad across their prior ranges, although their posterior distributions deviate somewhat from uniformity. Their lack of pronounced one-dimensional concentration indicates that their information content is weaker or more distributed across the calibration metrics than that of n_{rate} and α_u. In particular, a parameter may have a substantial total-order Sobol index for an individual metric without producing a sharply concentrated marginal posterior when all eight responses are considered jointly. This distinction is particularly relevant for I_e/I_g, which exhibits a strong sensitivity contribution to E_1 but only a comparatively mild shift in its marginal posterior.

Overall, the posterior marginals corroborate the sensitivity hierarchy identified previously: n_{rate} and α_u exhibit the strongest updating because the dynamic observations provide the clearest information about these parameters. The remaining parameters retain substantial posterior uncertainty, indicating that their effects are either limited or insufficiently discriminated by the available response metrics.

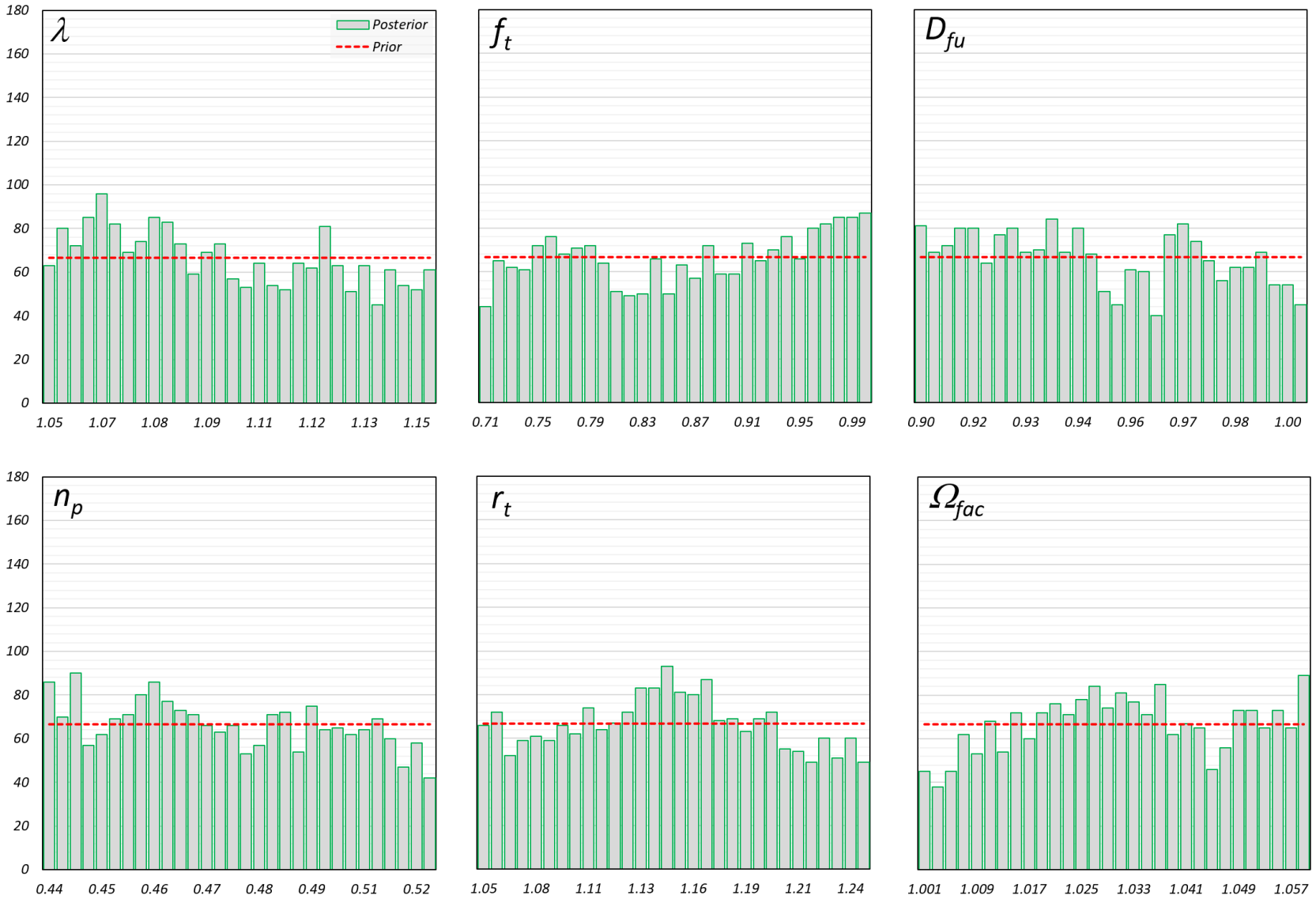


Figure 131a. Marginal posterior distributions under the uniform prior - Displacement-controlled stage parameters

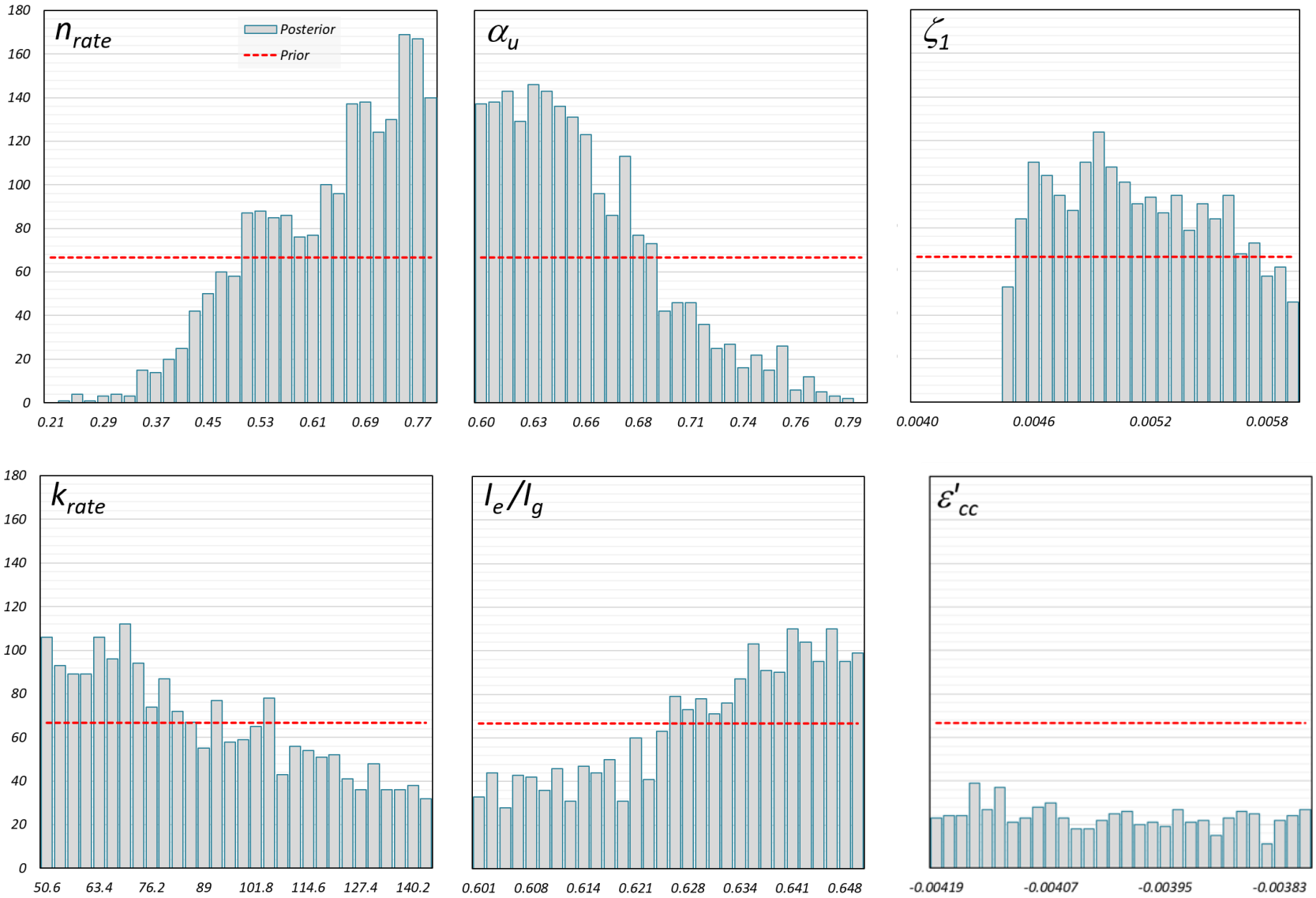


Figure 131b. Marginal posterior distributions under the uniform prior - Dynamic-response parameters

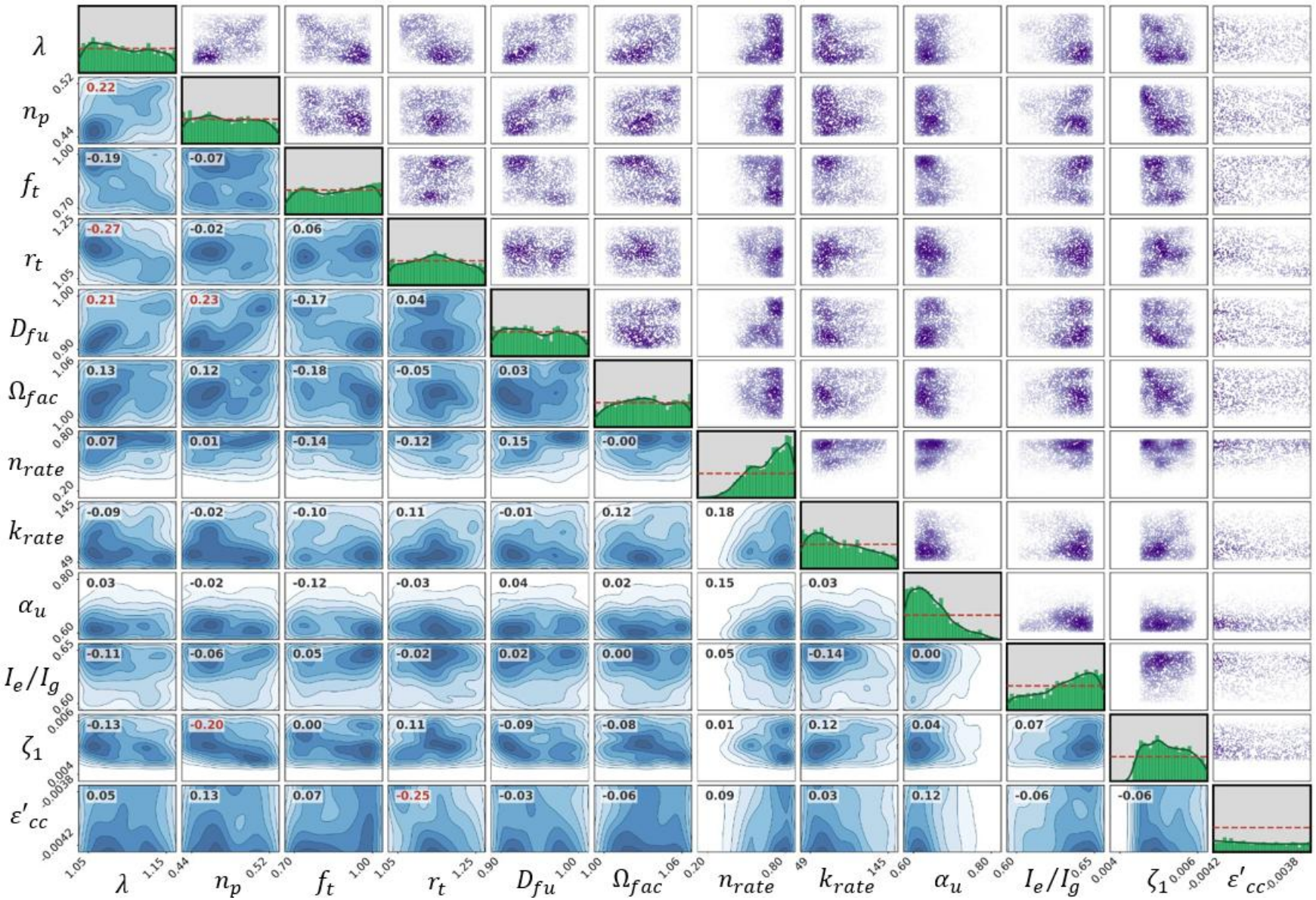


Figure 132. Corner plot of the posterior parameter distribution under the uniform prior.

5.8.10.1 Robustness of the Posterior Inference to the Prior Distribution

Table 36 shows that, under the lognormal prior, the only parameter explicitly identified as informed is n_{rate}, whose posterior width contracts to 0.79 of the prior width. However, its 90% interval, [0.428, 0.775], remains comparatively wide, indicating residual epistemic uncertainty even after calibration. The parameter α_u exhibits a more modest contraction (posterior/prior width=0.82), with its posterior mean shifted toward the lower bound (0.668), consistent with the left-skewed marginal distribution shown in Figure 133b. All displacement-stage parameters (λ, n_p, f_t, r_t, D_{fu}, and Ω_{fac}), together with the dynamic ones (k_{rate}, I_e/I_g, ε'_{cc}, and ζ_1), exhibit negligible posterior updating, consistent with the near-prior marginals shown in Figure 133a and with the global-sensitivity results, which indicate that these inputs have limited influence on the surrogate metrics.

Table 36. Posterior parameter estimates and uncertainty - Lognormal prior.

Parameter	MAP	Mean	SD	90% interval	Post/prior	Informed
λ	1.086	1.102	±0.021	[1.066, 1.137]	0.97	-
n_p	0.478	0.481	±0.017	[0.452, 0.51]	0.98	-
D_{fu}	0.954	0.948	±0.022	[0.913, 0.985]	0.98	-
Ω_{fac}	1.026	1.03	±0.013	[1.008, 1.052]	0.98	-
α_u	0.678	0.668	±0.036	[0.613, 0.732]	0.82	-
f_t	0.832	0.849	±0.066	[0.741, 0.963]	1	-
r_t	1.12	1.146	±0.044	[1.075, 1.222]	1	-
ε'_{cc}	-0.00393	-0.00403	±0.00022	[-0.00439, -0.00366]	0.99	-
r_c	-	-	-	Derived		-
n_{rate}	0.6	0.612	±0.108	[0.428, 0.775]	0.79	**informed**
k_{rate}	83.7	89.5	±20.1	[59.6, 126.3]	0.94	-
I_e/I_g	0.621	0.627	±0.011	[0.609, 0.644]	0.97	-
G_e/G_g	0.2	0.2	-	Fixed	-	-
ζ_1	0.00527	0.00522	±0.00032	[0.0047, 0.00578]	0.98	-
ζ_2	0.015	0.015	-	Fixed	-	-

Table 37 reports the GP-predicted residuals obtained by evaluating the emulator suite at the MAP estimate. The overall RMSE across the eight metrics is 11 %, reflecting emulator uncertainty, model-form inadequacy, and residual model-experiment discrepancy at the MAP parameter vector. The largest residuals occur for peak$_3$ (+20.6%, test-to-simulation ratio=1.23), E_1 (+13.6%), and E_2 (+14.5%), suggesting remaining mismatches in the higher-mode peak response and early-cycle energy dissipation. By contrast, E_3 is reproduced closely (-1.24%, ratio=0.99), while peak$_1$ (-5.64%) and E_4 (-8.64%) exhibit moderate deviations. The GP standard deviations reported for peak$_1$ (11.2%) and E_1 (10.9%) indicate that their residuals remain within approximately one surrogate standard deviation. These discrepancies are therefore commensurate with emulator uncertainty and do not, by themselves, indicate a grossly inconsistent MAP estimate.

Table 37. GP-predicted residuals at the MAP estimate - Lognormal prior.

Metric	Residual at the MAP (%)	Ratio Test/Sim	σ_{err} (%)
peak₁	-5.64	0.95	11.2
peak₂	+4.53	1.05	
peak₃	+20.6	1.23	
peak₄	+5.12	1.05	
E_1	+13.6	1.15	10.9
E_2	+14.5	1.16	
E_3	-1.24	0.99	
E_4	-8.64	0.92	
RMSE (8metrics)	11	-	-

Figure 133 shows the twelve marginal posteriors under lognormal priors for the displacement-controlled-stage parameters. The six panels compare the posterior histograms (green) with their corresponding lognormal priors (red dotted lines). For the first group, the posterior distributions remain closely aligned with the priors, with no appreciable changes in location or dispersion, consistent with the negligible posterior updating reported in Table 36 and indicating that the dynamic response provides limited information on these parameters.

The second group shows more pronounced updating. The posterior of n_{rate} shifts toward higher values, with a mode around 0.60-0.65. Although less skewed than the prior, its broad 90% interval indicates that substantial uncertainty remains. The posterior of α_u shifts toward lower values, with its mode decreasing from approximately 0.70 to 0.66; its width contracts to 0.82 of the prior width but retains a pronounced right tail. The posterior of k_{rate} remains broad and approximately unimodal, with a modest shift toward lower values around 85 and a wide 90% interval of [59.6, 126.3]. The remaining parameters exhibit little posterior updating. In particular, the limited updating of I_e/I_g, despite its high total sensitivity for E_1 (S_T=0.865), shows that response sensitivity alone does not ensure substantial posterior contraction when the prior is already compatible with the observations.

The corner plot under lognormal priors is shown in Figure 134. Compared with the uniform-prior case, the marginal distributions and joint samples are more concentrated, reflecting the stronger localization imposed by the lognormal priors. The off-diagonal panels show generally weak pairwise linear dependence, with $|r|$<0.15 for most parameter pairs. The largest correlations occur between n_{rate} and k_{rate} (+0.14) and between α_u and n_{rate} (+0.22), while the correlation between α_u and I_e/I_g is small (-0.09). Overall, the weak posterior correlations suggest that marginal updating is primarily driven by information in the dynamic response rather than by strong parameter dependence.

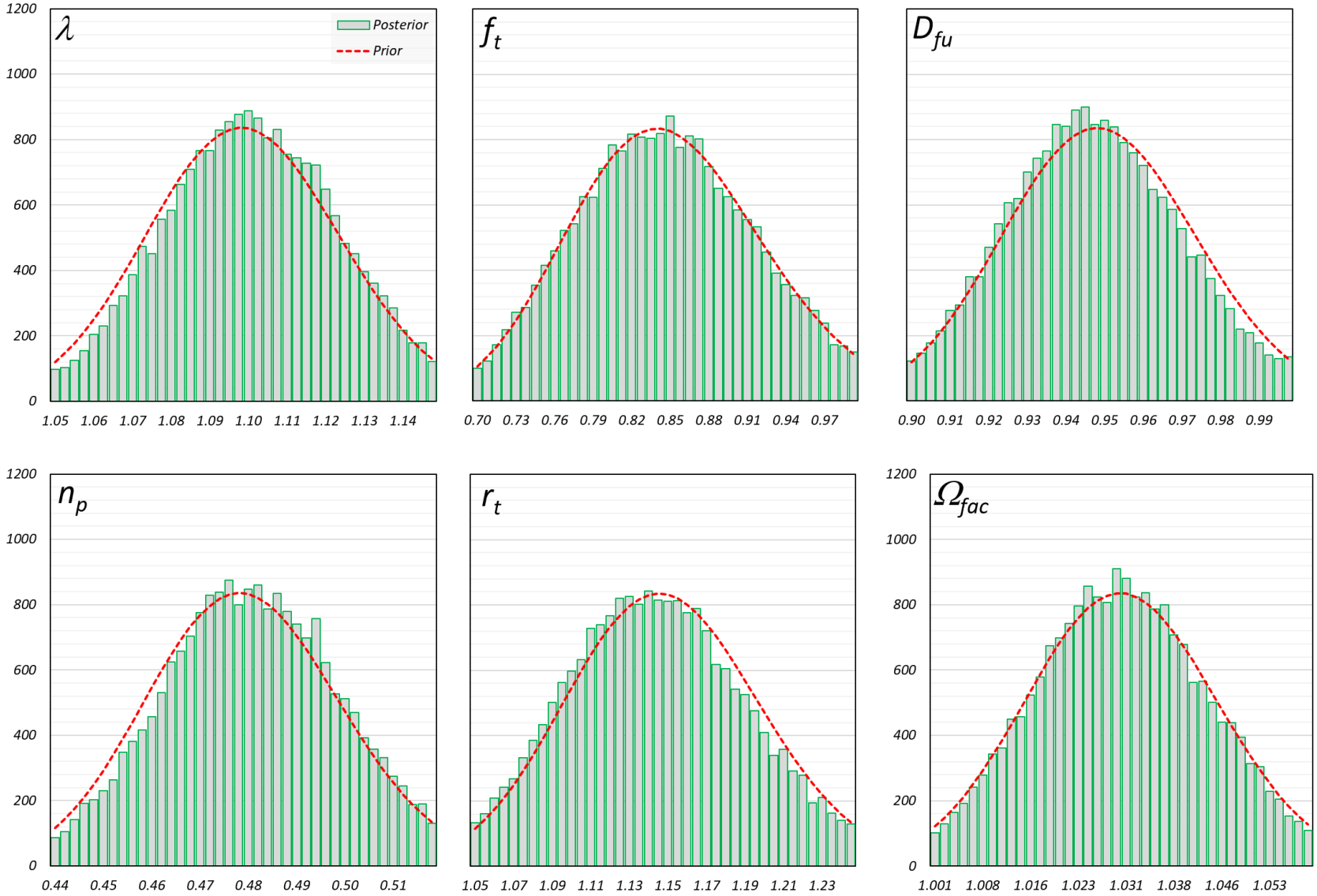


Figure 133a. Marginal posterior distributions under the lognormal prior - Displacement-controlled stage parameters.

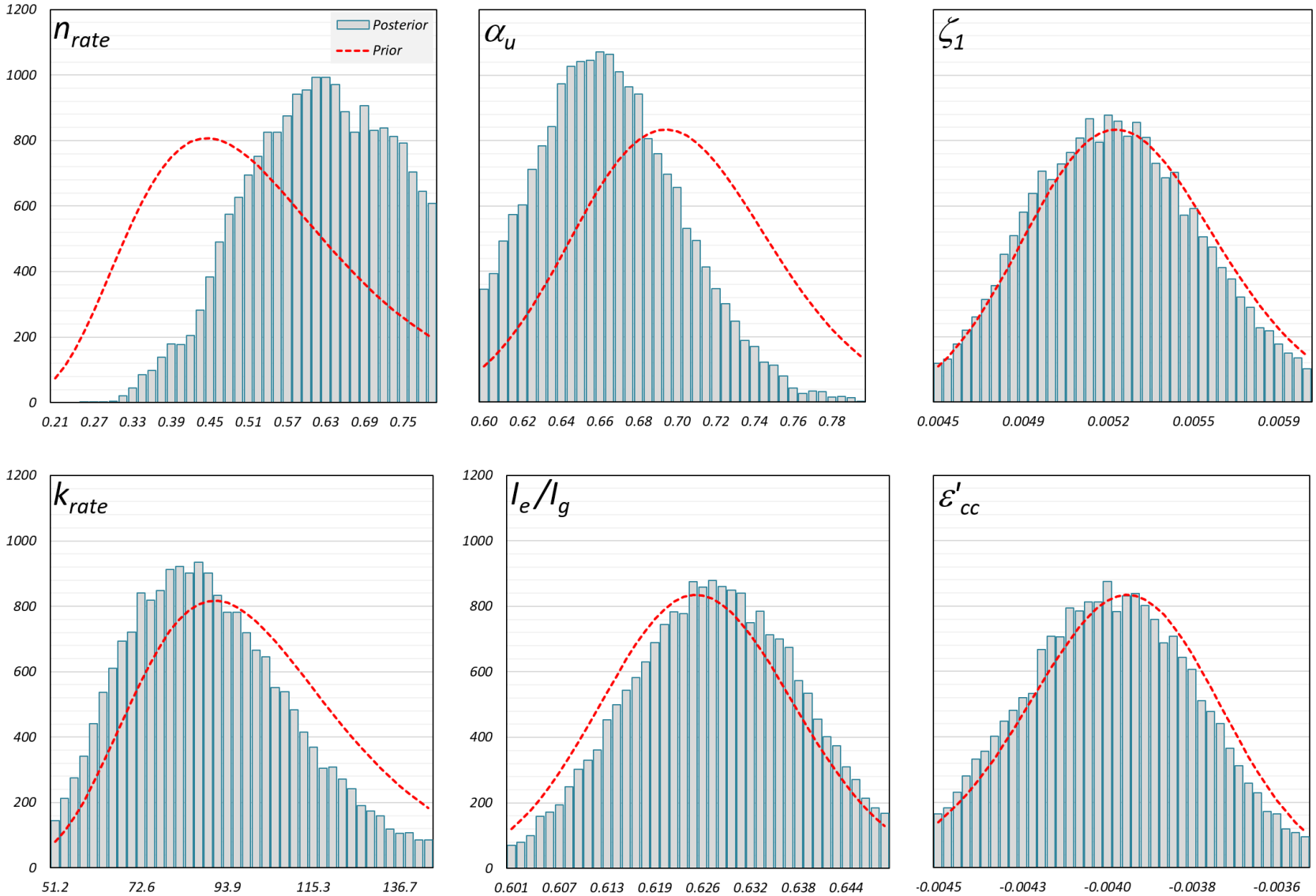


Figure 133b. Marginal posterior distributions under the lognormal prior - Dynamic-response parameters.

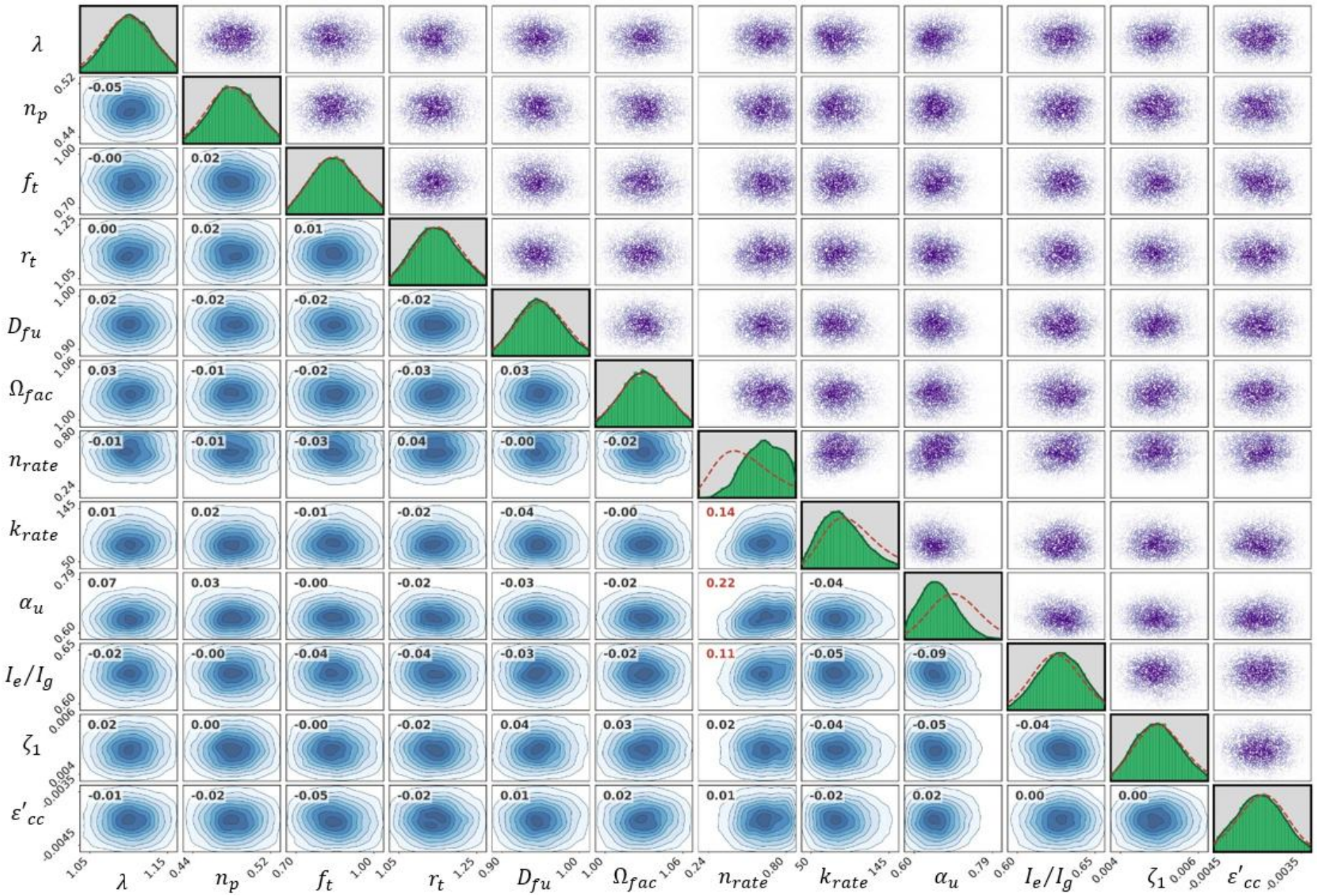


Figure 134. Corner plot of the posterior parameter distribution under the lognormal prior.

Table 38 summarizes the posterior parameter estimates obtained with the truncated normal prior. The largest differences between MAP estimates and posterior means occur for f_t, n_{rate}, and k_{rate}, consistent with the asymmetric or multimodal posterior distributions discussed below. For f_t, the MAP estimate is 0.916 compared with a posterior mean of 0.861, while for $n_{rate}$the corresponding values are 0.563 and 0.622. The largest discrepancy occurs for k_{rate}, whose MAP estimate of 72.8 is substantially lower than its posterior mean of 98.4.

Table 38. Posterior parameter estimates and uncertainty - Truncated normal prior.

Parameter	MAP	Mean	SD	90% interval	Post/prior	Informed
λ	1.094	1.106	±0.021	[1.063, 1.14]	0.94	-
n_p	0.491	0.486	±0.019	[0.454, 0.515]	1.06	-
D_{fu}	0.948	0.949	±0.019	[0.917, 0.98]	0.86	-
Ω_{fac}	1.025	1.028	±0.013	[1.008, 1.05]	1	-
α_u	0.658	0.659	±0.038	[0.607, 0.728]	0.86	-
f_t	0.916	0.861	±0.055	[0.77, 0.946]	0.84	-
r_t	1.156	1.132	±0.046	[1.06, 1.215]	1.06	-
ε'_{cc}	-0.00414	-0.00396	±0.00022	[-0.00431, -0.0036]	0.99	-
r_c	-	-	-	Derived	-	-
n_{rate}	0.563	0.622	±0.101	[0.449, 0.768]	0.77	**informed**
k_{rate}	72.8	98.4	±22.7	[62.5, 133]	1.09	-
I_e/I_g	0.625	0.629	±0.011	[0.611, 0.647]	1	-
G_e/G_g	0.2	0.2	-	Fixed	-	-
ζ_1	0.00505	0.0052	±0.00031	[0.0047, 0.00568]	0.95	-
ζ_2	0.015	0.015	-	Fixed	-	-

The post/prior ratios quantify posterior contraction relative to the corresponding prior distributions. Appreciable contraction is observed for D_{fu}, α_u, f_t, and n_{rate}, with ratios of 0.86, 0.86, 0.84, and 0.77, respectively. Thus, despite its broad and multimodal posterior, n_{rate} exhibits a 23% reduction in posterior standard deviation relative to its prior. In contrast, k_{rate} has a post/prior ratio of 1.09, indicating that its posterior standard deviation is slightly larger than that of its prior. Together with its wide 90% credible interval [62.5, 133] and substantial MAP-mean difference, this indicates weak posterior concentration and substantial residual uncertainty.

The remaining parameters exhibit limited changes in posterior dispersion, with post/prior ratios of 0.94 for λ, 1.06 for n_p, 1.00 for Ω_{fac}, 1 for I_e/I_g, 0.99 for ε'_{cc}, and 0.95 for ζ_1. These values indicate that the apparent concentration of some posterior marginals should not, by itself, be interpreted as strong data-driven identification, since posterior concentration must be assessed relative to the corresponding prior uncertainty.

Table 39 reports the residuals obtained by evaluating the GP emulator at the MAP parameter vector. The overall RMSE across the eight metrics is 10.4%. The largest discrepancy occurs for $peak_3$, with a residual of +19.5% and a test-to-simulation ratio of 1.22. Positive residuals are also observed for E_1 (+11.4%) and E_2 (+14.5%), whereas E_3 and E_4 are reproduced more closely, with residuals of -1.56% and -4.74%, respectively.

Table 39. GP-predicted residuals at the MAP estimate - Truncated-normal prior.

Metric	Residual at the MAP (%)	Ratio Test/Sim	σ_{err} (%)
$peak_1$	-6.33	0.94	11.1
$peak_2$	+5.14	1.05	
$peak_3$	+19.5	1.22	
$peak_4$	+6.95	1.07	
E_1	+11.4	1.12	9.56
E_2	+14.5	1.16	
E_3	-1.56	0.98	
E_4	-4.74	0.95	
RMSE (8metrics)	10.4	-	-

The $peak_3$ residual is the largest individual mismatch and accounts for a substantial portion of the overall RMSE. However, based on the available results, its origin cannot be attributed solely to a physical model-form inadequacy, since no GP uncertainty estimate is reported for this metric. For $peak_1$ and E_1, the reported GP standard deviations are 11.1% and 9.56%, respectively, compared with residuals of -6.33% and +11.4%. These discrepancies are therefore of the same order as the reported surrogate uncertainty. Overall, the MAP solution provides a non-uniform representation of the eight calibration metrics, with the largest remaining discrepancies concentrated in $Peak_3$, E_1, and E_2.

Figure 135a shows the posterior distributions for the displacement-controlled-stage parameters. They vary in concentration and asymmetry. The posteriors of λ, D_{fu}, and Ω_{fac} are relatively concentrated, whereas f_t and $r_t$exhibit greater asymmetry. The posterior of $n_p$shows mild bimodality, indicating that more than one region of the parameter space agrees comparably with the calibration targets.

Figure 135b shows the dynamic-response parameter posteriors. The posterior of n_{rate} remains relatively broad and multimodal, while k_{rate} exhibits the greatest dispersion and the most pronounced separation between its MAP estimate and posterior mean. In contrast, α_u, I_e/I_g, ζ_1, and ε'_{cc} show comparatively concentrated marginal distributions. These results highlight the different degrees of posterior uncertainty across the parameters under the truncated normal prior.

Finally, Figure 136 presents the joint posterior distributions. The largest Pearson correlations are observed between ζ_1 and k_{rate} (r=-0.34) and between $n_p$and f_t (r=-0.33). These correlations are moderate and indicate appreciable posterior dependence rather than strong linear coupling. The negative correlation between $n_{\mathrm{rate}}$and k_{rate} (r=-0.22), together with their broad and multimodal marginals, suggests a compensatory relationship between these dynamic parameters. Similarly, the dependence between n_p and f_t indicates partial confounding between these displacement-stage parameters. The remaining correlations are relatively weak, ranging from 0.22 to 0.24. Overall, the corner plot indicates that the posterior uncertainty is not entirely separable across parameters and that some parameter combinations provide comparable fits to the calibration targets.

The corner plot of the joint posterior is presented in Figure 136. It clarifies the dependency structure underlying the marginal behaviors. The strongest linear association is the positive correlation between k_{rate} and n_{rate} (r=+0.41), indicating a compensatory relationship between these two dynamic parameters: their effects on the model response are confounded, such that an increase in one can be offset by an increase in the other without substantially degrading the fit. A negative correlation is observed between the effective inertia ratio and the α_u factor (r=-0.34), indicating a trade-off between sectional stiffness and material strength in reproducing the observed displacements. The confined concrete strain and tensile strength also exhibit a negative correlation (r=-0.33), indicating a coupled calibration of the tension-compression envelope and suggesting that these two constitutive branches cannot be inferred independently from the available calibration data. Additional non-negligible correlations include ζ_1 with Ω_{fac} (r=-0.24) and α_u with k_{rate} (r=+0.24). In contrast, λremains essentially decorrelated from the other parameters ($|r|$<0.05), supporting its interpretation as an independently identifiable scaling factor.

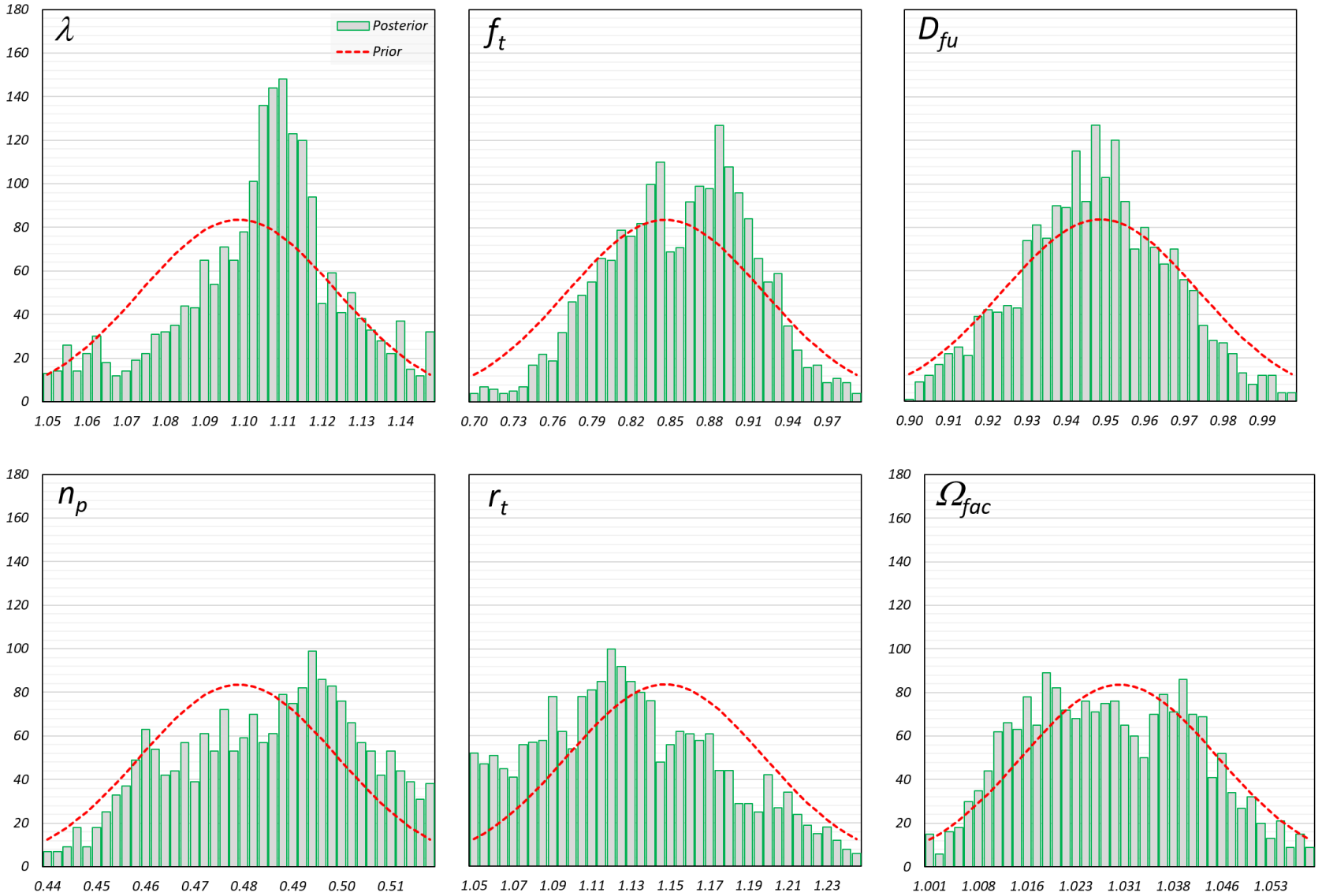


Figure 135a. Marginal posterior distributions under the truncated normal prior - Displacement-controlled stage parameters.

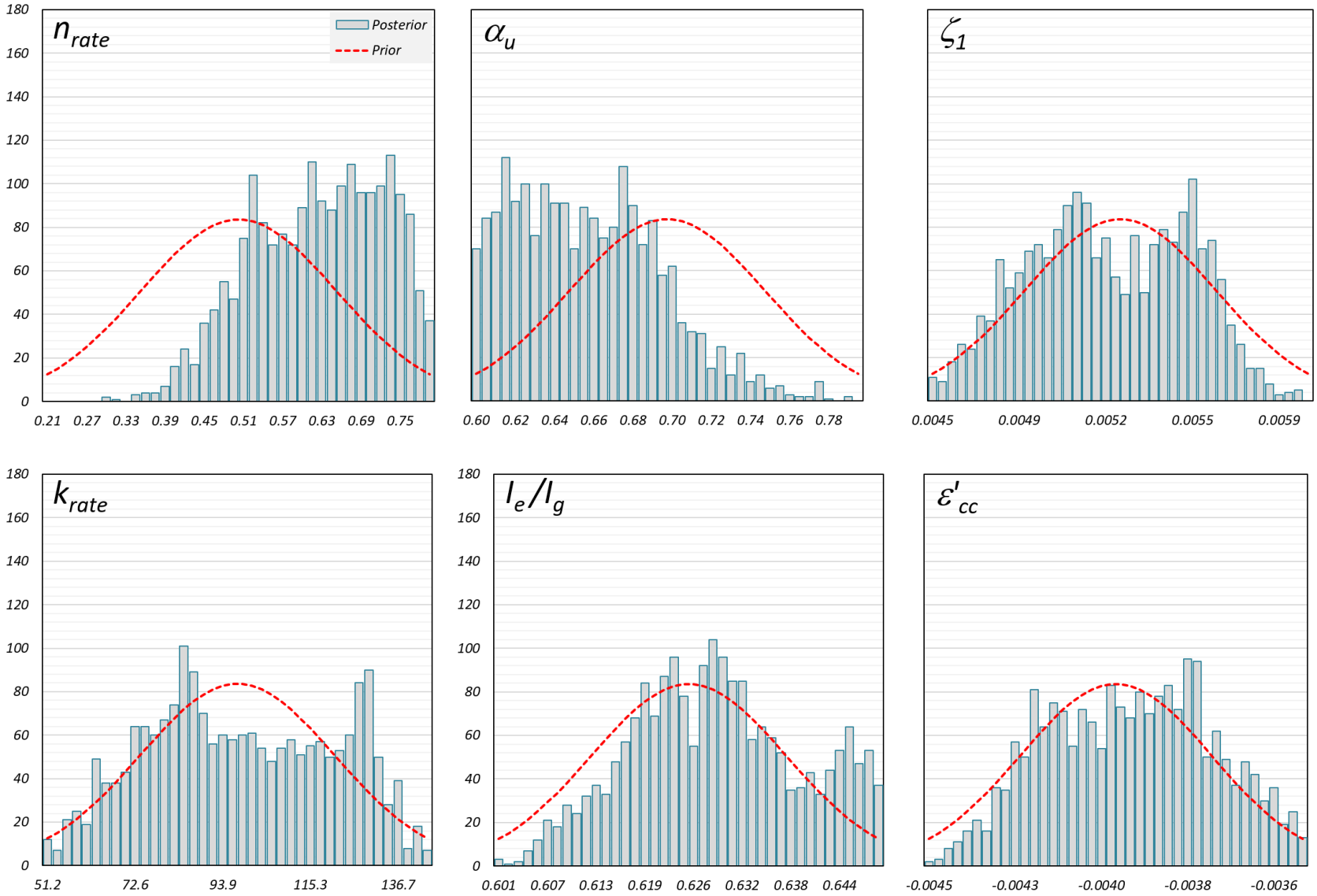


Figure 135b. Marginal posterior distributions under the truncated normal prior - Dynamic-response parameters.

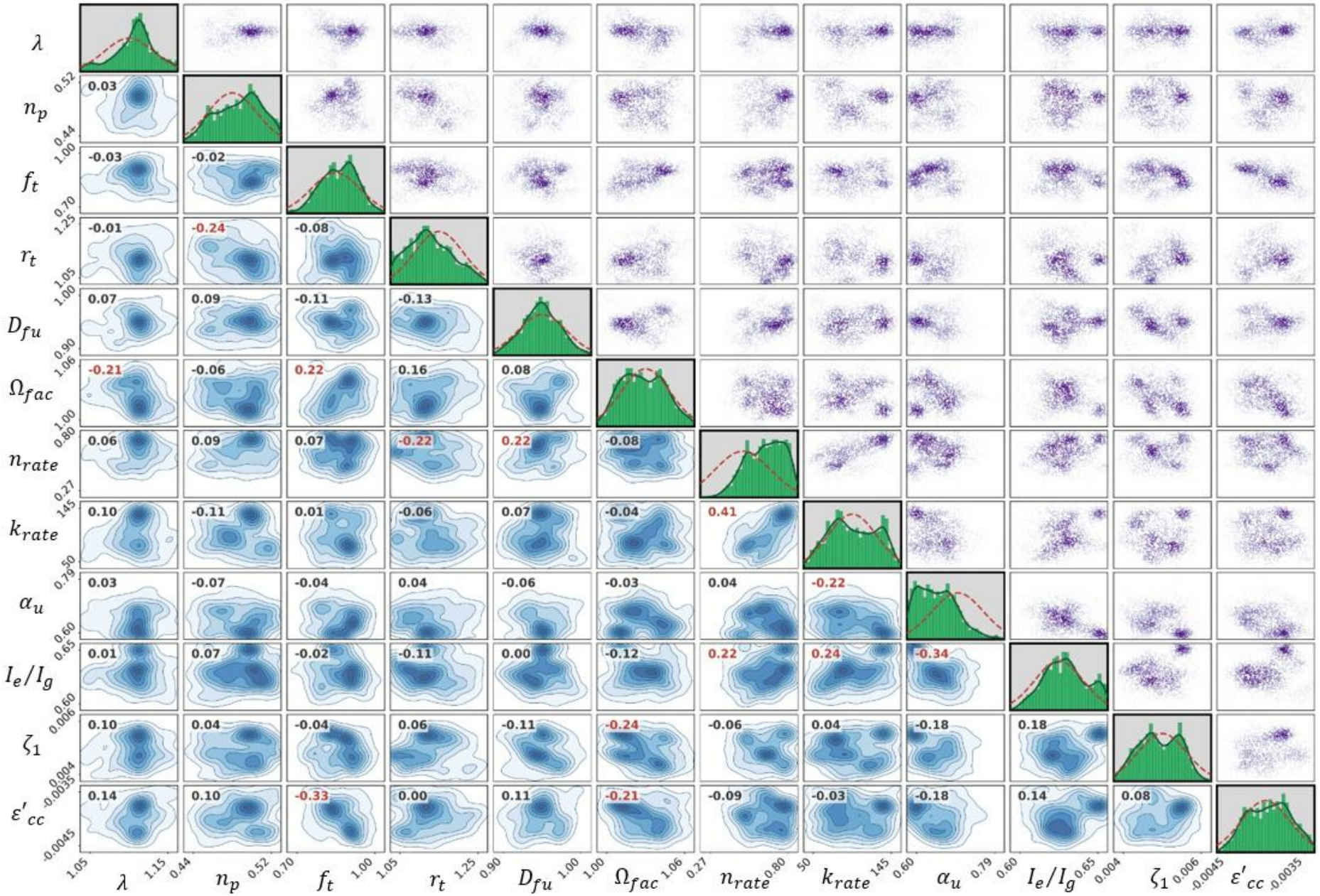


Figure 136. Corner plot of the posterior parameter distribution under the truncated normal prior.

5.8.10.2 Choice of Prior Distribution

Three alternative prior distributions were considered for Bayesian calibration: uniform, lognormal, and truncated normal. This comparison assesses the sensitivity of the posterior inference to the assumed prior shape and provides the basis for selecting a reference prior. This assessment is necessary because the prior distribution introduces assumptions not determined by the likelihood and may therefore influence posterior inference.

A uniform prior over the interval $[x_{lo}, x_{hi}]$ assigns equal prior density to all admissible parameter values. The bounds themselves are not arbitrary; they were established in Stage 1 (Section 5.6). Accordingly, the uniform prior does not represent complete prior ignorance. Rather, it expresses the assumption that the available physical knowledge is sufficient to define the admissible range but does not provide a defensible basis for assigning greater prior plausibility to one value within that range than to another. The use of a uniform prior is therefore appropriate for the present dynamic calibration because no previous experimental campaign on the same specimen provides parameter-specific prior information under the loading conditions considered here.

The lognormal and truncated normal alternatives introduce additional structure by assigning greater prior probability to values near their respective central tendencies. In the absence of independent evidence supporting such concentration within the admissible ranges, these distributions are more prescriptive than the uniform prior. Nevertheless, they provide alternative prior specifications against which the sensitivity of the Bayesian inference can be assessed. The entire TMCMC calibration was therefore repeated under both alternatives, with each distribution defined so that ±2σ in its respective space spans the same bounds, $[x_{lo}, x_{hi}]$.

The comparison of the three calibrations considers posterior contraction, MAP fit, and the resulting posterior parameter patterns. The posterior-to-prior standard deviation ratios measure how much the data reduce the uncertainty for each parameter relative to its prior distribution. Across the three prior families, n_{rate}exhibits the most consistent posterior contraction, with ratios of 0.65, 0.79, and 0.77 for the uniform, lognormal, and truncated-normal priors, respectively. Other parameters exhibit ratios close to or above unity, indicating limited posterior contraction relative to their corresponding priors. The Sobol and ARD analyses provide independent references for interpreting these results, as they characterize the GP emulator's sensitivity without involving the Bayesian prior. The agreement between the sensitivity structure and the principal posterior inferences therefore supports the conclusion that the selected prior distribution does not solely determine the calibration's dominant features.

The MAP solutions, however, show a measurable dependence on the prior specification. The uniform prior produces the lowest RMSE (8.87%), compared with 11.04% for the lognormal prior and 10.37% for the truncated-normal prior. This difference indicates that the prior shape affects the posterior mode: the uniform prior allows the MAP estimate to move freely within the admissible range, whereas the alternative priors assign greater prior weight to their respective central regions. The higher MAP residuals obtained with the lognormal and truncated-normal priors therefore indicate a greater sensitivity of the MAP solution to the imposed prior structure.

One noteworthy observation is that the truncated-normal posterior exhibits bimodality in several marginal distributions. This feature is attenuated when multiple TMCMC replicas are pooled but

remains clearly visible in an individual replica (Section 5.8.9). This multimodality suggests that the posterior landscape can depend on the adopted prior specification and should therefore be considered when assessing prior sensitivity. It does not, by itself, provide sufficient grounds to accept or reject the truncated-normal prior.

Overall, the comparison supports the uniform distribution as the reference prior for the Bayesian calibration. It introduces the least prescriptive assumption within the physically admissible parameter ranges, provides the lowest MAP RMSE among the three alternatives, and yields a principal posterior inference that is consistent with the results obtained under the lognormal and truncated-normal specifications. The alternative prior families are therefore retained as sensitivity analyses, showing that the main inferences are not solely a consequence of adopting the uniform prior. In contrast, the uniform distribution serves as the reference specification for Bayesian calibration.

5.8.10.3 Per-Parameter Synthesis of Sensitivity and Posterior Information

Table 40 synthesizes three complementary diagnostics for assessing parameter relevance in the dynamic calibration: the worst-case total-order Sobol index, the minimum ARD length-scale, and the posterior-to-prior width ratio. The first two characterize the GP emulator's sensitivity, whereas the third quantifies the degree of posterior contraction relative to the prior. Together, they distinguish parameters that are both influential and informed by the dynamic data from those that are influential but only marginally updated, and from parameters with negligible sensitivity.

In particular, n_{rate} and α_u emerge as the two parameters with the clearest evidence of posterior information, while I_e/I_g, r_t, and k_{rate} show model sensitivity but only marginal posterior contraction. The remaining free parameters exhibit negligible sensitivity and essentially no data-driven updating.

The Status column classifies each parameter into one of five categories based on the combined interpretation of the sensitivity and posterior diagnostics:

(1) Informed: the parameter exhibits high model sensitivity, indicated by a large ${S_T}^{max}$ and a small ARD $\ell_{\min}$, together with substantial posterior contraction, reflected by a Post/Prior ratio well below unity. The dynamic observations therefore provide clear evidence of parameter updating, and the calibrated value is determined primarily by the dynamic data rather than by the imposed prior bounds.

(2) Marginal: the parameter exhibits either moderate model sensitivity or moderate posterior contraction, but the evidence from the combined diagnostics is insufficient to establish clear identification. The dynamic data provide partial information, reflected in a posterior shift or mild concentration, but do not constrain the parameter sufficiently to support strong identification. Additional experimental configurations or response metrics more sensitive to this parameter could provide further information and improve its identifiability.

(3) No: the parameter exhibits low model sensitivity and a Post/Prior ratio close to unity. The dynamic response is therefore largely insensitive to parameter variations within the tested range, and the observations provide no appreciable additional information.

Table 40. Per-parameter synthesis of GP sensitivity, posterior contraction, and identification status.

Parameter	S_T^{max}	ARD l_{min}	Post/Prior	Status	Physical note
n_{rate}	**0.87**	**1.9**	**0.68**	**informed**	Strain-rate exponent; dominant on peak displacements; identifiable
I_e/I_g	**0.87**	**1.1**	0.94	**marginal**	Effective flexural stiffness ratio; dominant on E_1 and E_2; slight left-tail
α_u	**0.62**	**2.0**	**0.69**	**informed**	Unloading-modulus factor; dominant on late-motion metrics
r_t	**0.23**	**2.2**	0.95	**marginal**	Tensile post-cracking; specific footprint on E_2
k_{rate}	**0.18**	4.5	0.95	**marginal**	Strain-rate coefficient; on ridge with n_{rate}
D_{fu}	0.03	3.5	1.00	no	Unloading-rejoining; fixed by Stage 1
ε'_{cc}	0.02	8.5	1.00	no	Confined-concrete peak strain; fixed by Stage 1
ζ_1	0.02	5.2	0.95	no	First-mode Rayleigh damping ratio; small-amplitude decay elsewhere
f_t	0.01	4.8	1.03	no	Tensile concrete strength; fixed by Stage 1
Ω_{fac}	0.01	8.4	0.96	no	Bauschinger-effect shape factor; fixed by Stage 1
n_p	0.01	13.3	0.99	no	Pinching-shape exponent; fixed by Stage 1
λ	0.01	15.8	1.00	no	Pinching amplitude; fixed by Stage 1
ζ_2	-	-	-	fixed	second-mode Rayleigh damping ratio; held at reference value
G_e/G_g	-	-	-	fixed	Effective shear stiffness ratio; held at reference value
r_c	-	-	-	derived	Compressive post-peak shape parameter; derived from ε′_cc

For parameters classified as “no,” the notation “fixed by Stage 1” in the physical note does not indicate that the parameter was fixed during the Bayesian calibration. These parameters remained free in the TMCMC sampling but had already been constrained during the displacement-controlled calibration. Their posterior distributions nevertheless remain essentially unchanged from their corresponding priors, indicating that the dynamic observations provide no appreciable additional information about them within the ranges considered. Thus, the Bayesian calibration does not

overturn the Stage 1 estimates; rather, it confirms that the dynamic response considered here is not sufficiently sensitive to warrant further updating.

5.8.11 Identifiability of the Strain-Rate-Dependent Mechanism

The main finding of this stage concerns the identifiability of the strain-rate-dependent viscous mechanism. The effect of the viscous mechanism on peak displacement depends strongly on n_{rate}: a threefold change in k_{rate} alters the peak displacement by approximately 8% at n_{rate}=0.20, but by only about 0.7% at n_{rate}=0.80. Restricting the design to the upper end of the exponent range therefore confined the calibration to a region where the viscous contribution has little influence on the response, making it difficult for dynamic observations to discriminate among different parameter values.

Extending the Sobol design to n_{rate}=0.20, and thus including the region in which the viscous mechanism has appreciable influence, increased its total-order Sobol index to 0.87 for peak$_1$. The subsequent Bayesian calibration yielded a posterior concentrated approximately within [0.43,0.78], with a median of 0.66, substantially reducing the posterior probability of the low values admitted by the extended prior. Figure 137shows the posterior marginal distribution of n_{rate} over the extended prior range [0.20,0.80]. The concentration around 0.66 indicates that dynamic observations contain information about the strain-rate exponent when the experimental design space includes the region where the mechanism is active. This result supports the formulation proposed in Section 4.7 and shows that the apparent non-identifiability observed in the initial analysis was primarily associated with the restricted parameter range.

The result also has a direct implication for the calibration design. A parameter may appear non-identifiable when the sampled range lies in a region of weak model sensitivity, even though the associated physical mechanism can affect the response appreciably elsewhere in the parameter space. The design space should therefore include the range over which the mechanism produces a measurable change in the selected response metrics. In the present case, extending the range of n_{rate} was necessary to expose this sensitivity and allow the dynamic observations to constrain the parameter. The resulting posterior distribution, shown in Figure 137, provides direct evidence of this increased identifiability, with the posterior becoming concentrated within the expanded range.

As anticipated in Section 5.8.7, the pair (n_{rate}, k_{rate}) does not admit independent identification from the structural response. In Section 4.7, it was stated that the viscous overstress is a function of the axial strain rate through this pair, as:

$$f_{sd} = k_{rate}.|\dot{\varepsilon}|^{n_{rate}} \tag{192}$$

Taking logarithms gives a linear relation in $\ln k_{rate}$ and n_{rate}, such that a change in one parameter can be compensated by an appropriate change in the other along a line of constant f_{sd} at a given strain rate. The identifiable quantity is therefore not the strain-rate sensitivity coefficient, k_{rate}, alone, but the viscous stress evaluated at a reference strain rate. Figure 138 shows the posterior trade-off between n_{rate} and k_{rate} graphically. The shaded region represents the two-dimensional posterior density of the parameter pair, (n_{rate}, k_{rate}), while the red curves are isolines of the viscous overstress at the reference strain rate.

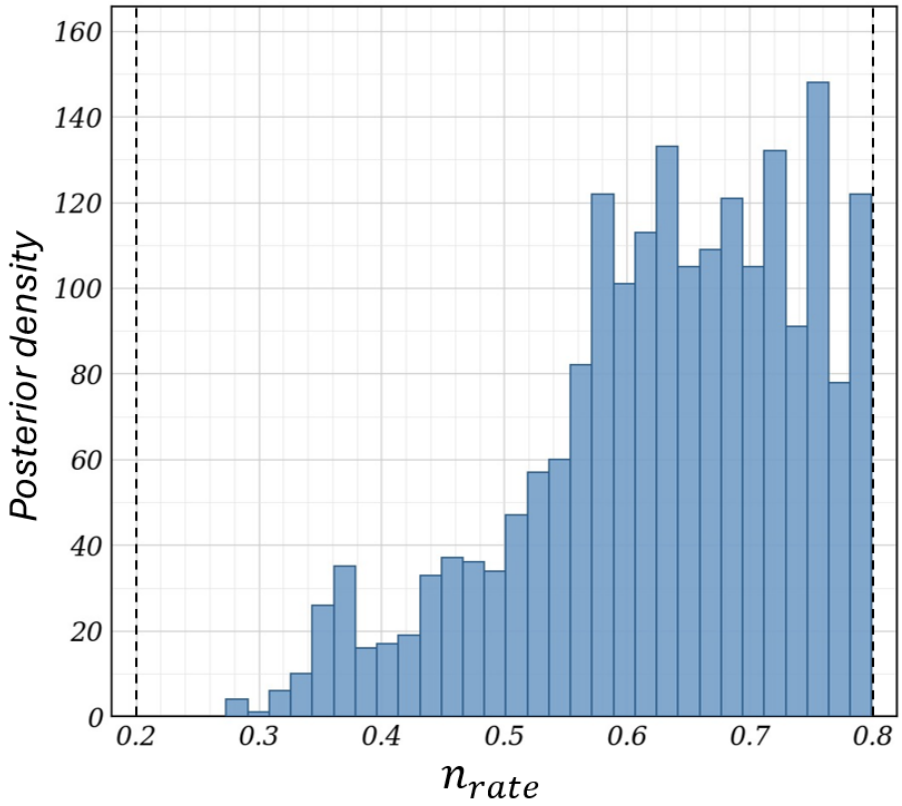


Figure 137. Posterior distribution of the strain-rate sensitivity exponent.

Each curve therefore represents all combinations of (n_{rate}, k_{rate}) that produce the same reference viscous overstress at $\dot{\varepsilon}_{ref}$. For example, the curve labeled "5" contains parameter combinations that all predict $\sigma_{v,ref}$=5 MPa, despite having different values of n_{rate} and k_{rate}. The posterior density is elongated approximately along these iso-overstress curves, indicating that the experiment primarily constrains the magnitude of the viscous overstress rather than the two constitutive parameters independently. In other words, a larger rate and a smaller consistency parameter can compensate for each other, and vice versa, while producing essentially the same viscous contribution at the strain rates relevant to the experiment.

A reference rate $\dot{\varepsilon}_{ref}$=10^{-2} s^{-1} is adopted here as a representative value within the strain-rate regime relevant to reinforcing steel during strong seismic shaking, consistent with the seismic strain-rate window of 10^{-3}-10^{0} s^{-1} established in the CEB Bulletin 187 [37] and with the dynamic increase factor calibrations of Malvar and Crawford [80]. Here, $\dot{\varepsilon}_{ref}$ instead represents the strain-rate regime relevant to the reinforcing-steel fibers in the plastic-hinge region of the column under earthquake excitation.

This observation motivates reporting the viscous stress at a reference strain rate, $f_{sd,ref}$ together with n_{rate}, rather than k_{rate} and n_{rate} alone. This parameterization more transparently represents what the experiment constrains, separating the physically interpretable stress scale from the residual trade-off between the original constitutive parameters.

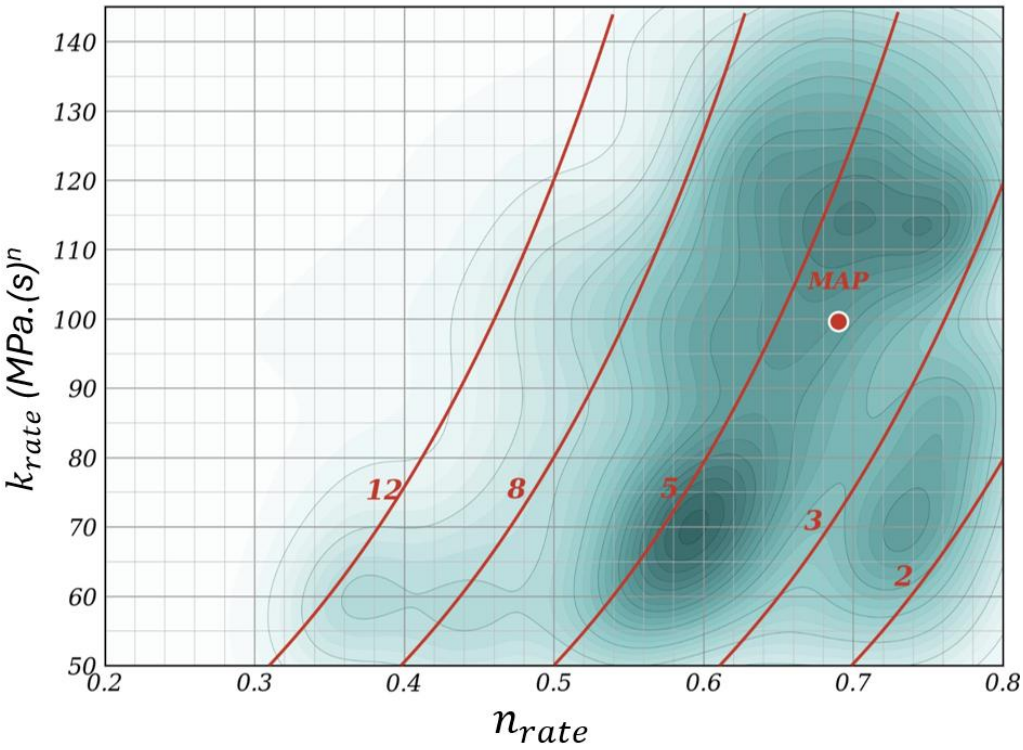


Figure 138. Joint posterior distribution of the viscous rate parameters k_{rate} and n_{rate}, with iso-overstress contours at the reference strain rate.

For the MAP estimate, $k_{rate} = 99.6$ MPa·$s^{0.69}$ and n_{rate}=0.69, the corresponding viscous overstress at the selected reference strain rate, $\dot{\varepsilon}_0$, is

$$f_{sd,ref} = 99.6(10^{-2})^{0.690} \approx 4.16\ MPa$$

Thus, the MAP solution corresponds to a viscous overstress of approximately 4.16 MPa at the reference strain rate, providing a physically interpretable stress scale for comparing the magnitude of the rate-dependent contribution across calibration results. The value k_{rate}=125 MPa·$s^{0.75}$ identified from the material-level time-window characterization in Section 4.4 lies within the prior range (50,145) adopted for the structural calibration and is of the same order of magnitude as the structural-level MAP estimate, k_{rate}=99.6 MPa·$s^{0.69}$. The difference is expected because the two estimates arise from different identification contexts: the former is obtained from isolated strain-rate excursions during quasi-static bar testing, whereas the latter reflects the full dynamic response of the column, including the interaction of viscous effects with inertia, damping, and the remaining constitutive parameters. The consistency between the two estimates supports the interpretation that the identified structural response is influenced by the same viscous mechanism observed at the material level.

5.8.12 Model-Experiment Discrepancy

The Bayesian calibration quantifies the residual model-experiment discrepancy explicitly through the two error hyperparameters, σ_{peak} and σ_{energy}, estimated in the Likelihood section. Figures 139

and 140 show the posterior predictive check for the eight calibration metrics. For each metric, the figures present the predictive density of the log-ratio obtained by sampling from the posterior and applying the emulator and error model of Eqs. (185)-(186). In the absence of model-experiment discrepancy, these distributions would be expected to concentrate around zero. Instead, the eight distributions are centered near zero but retain widths of approximately 10-15%, consistent with the inferred error hyperparameters and therefore indicative of a non-negligible discrepancy floor. Moreover, the Global Sensitivity Analysis (Section 5.8.7) shows that the sum of the total-order Sobol' sensitivity indices, $\sum S_T$, is close to one for seven of the eight metrics, indicating that the explored parameter space accounts for most of the response variance. The remaining discrepancy is therefore unlikely to be resolved through further adjustment of the calibrated parameters.

This result is substantive in itself. The Bayesian calibration identifies the response the current model formulation can reproduce and quantifies the remaining discrepancy between the model and the experiment. The two features that remain outside the training envelope also indicate where this discrepancy may originate. The higher instantaneous frequency during the quiet windows suggests limitations in representing stiffness recovery after unloading. In contrast, the larger residual displacement after EQ3 and EQ4 suggests limitations in representing the accumulation of permanent deformation. These mechanisms are therefore plausible sources of the remaining discrepancy, although the present analysis does not allow separation of their individual contributions.

In Figures 139 and 140, the peak-displacement distributions are wider (90% intervals spanning approximately 50 percentage points) than the energy distributions (approximately 40 percentage points), consistent with the larger inferred σ_{peak} relative to σ_{energy}. Zero lies within the 90% predictive interval (red dashed lines) for all eight metrics, indicating that the experimental observations are compatible with the calibrated model within the inferred discrepancy.

The text boxes in each panel report the median and the $[q_{05}, q_{95}]$ bounds. The peak-displacement metrics exhibit a progressive positive bias through the motion sequence: Peak_1 is centered at -3.1%, Peak_2 at +6.6%, and Peak_3 at +18.9%, before returning to -4.5% for Peak_4. The pronounced positive bias at Peak_3 may indicate cumulative damage mechanisms not explicitly represented in the constitutive formulation, such as progressive bond deterioration. The energy metrics (Figure 140) show a similar positive bias for the first two motions (E_1=+9.2%, E_2=+14.7%), whereas E_3 and E_4 are centered at -1.7% and 0.0%, respectively. This pattern indicates that the model tends to overestimate energy dissipation during early, lower-amplitude motions, while agreeing more closely once the column response becomes fully nonlinear.

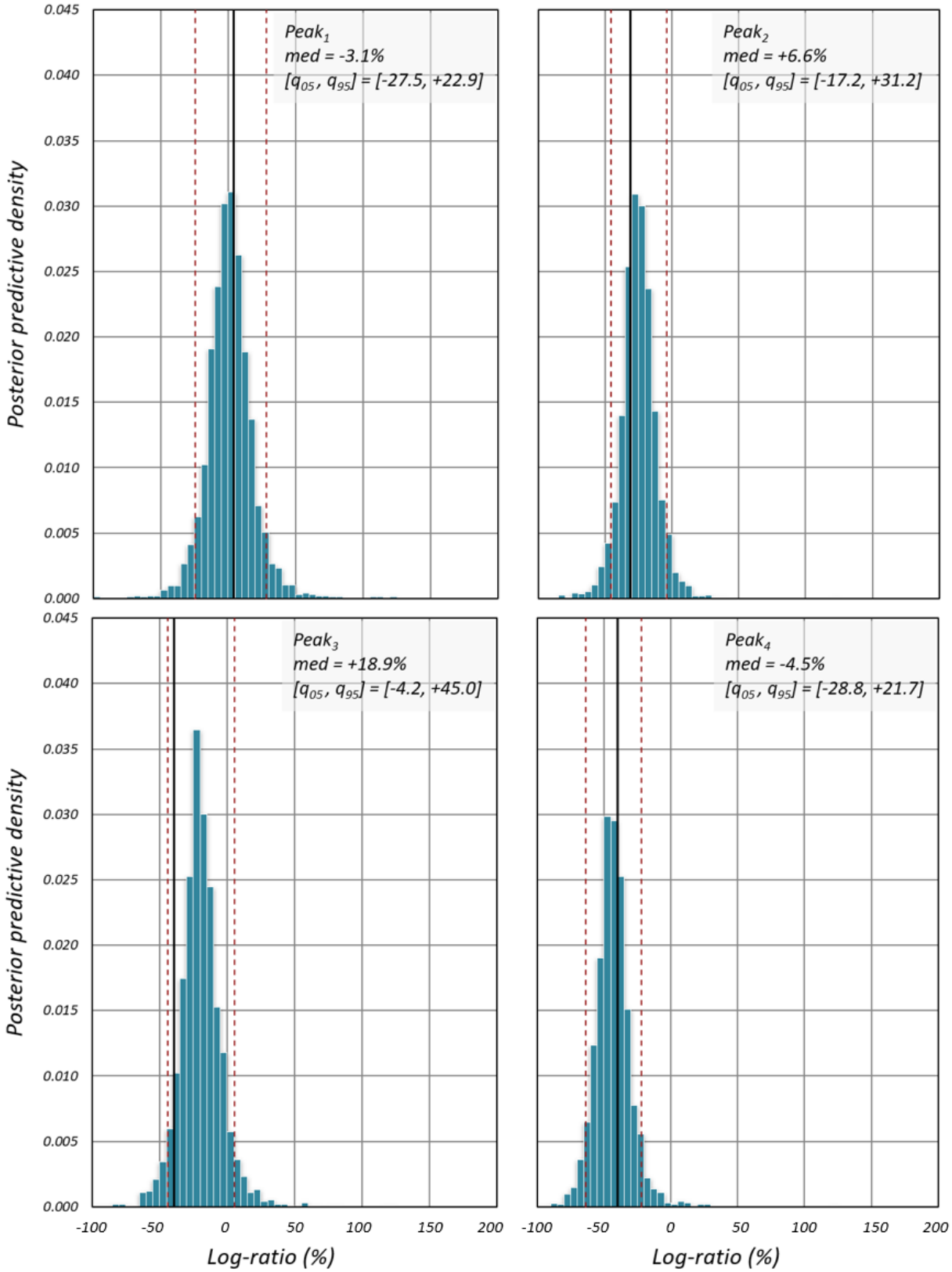


Figure 139. Posterior predictive distributions of the peak-displacement metrics.

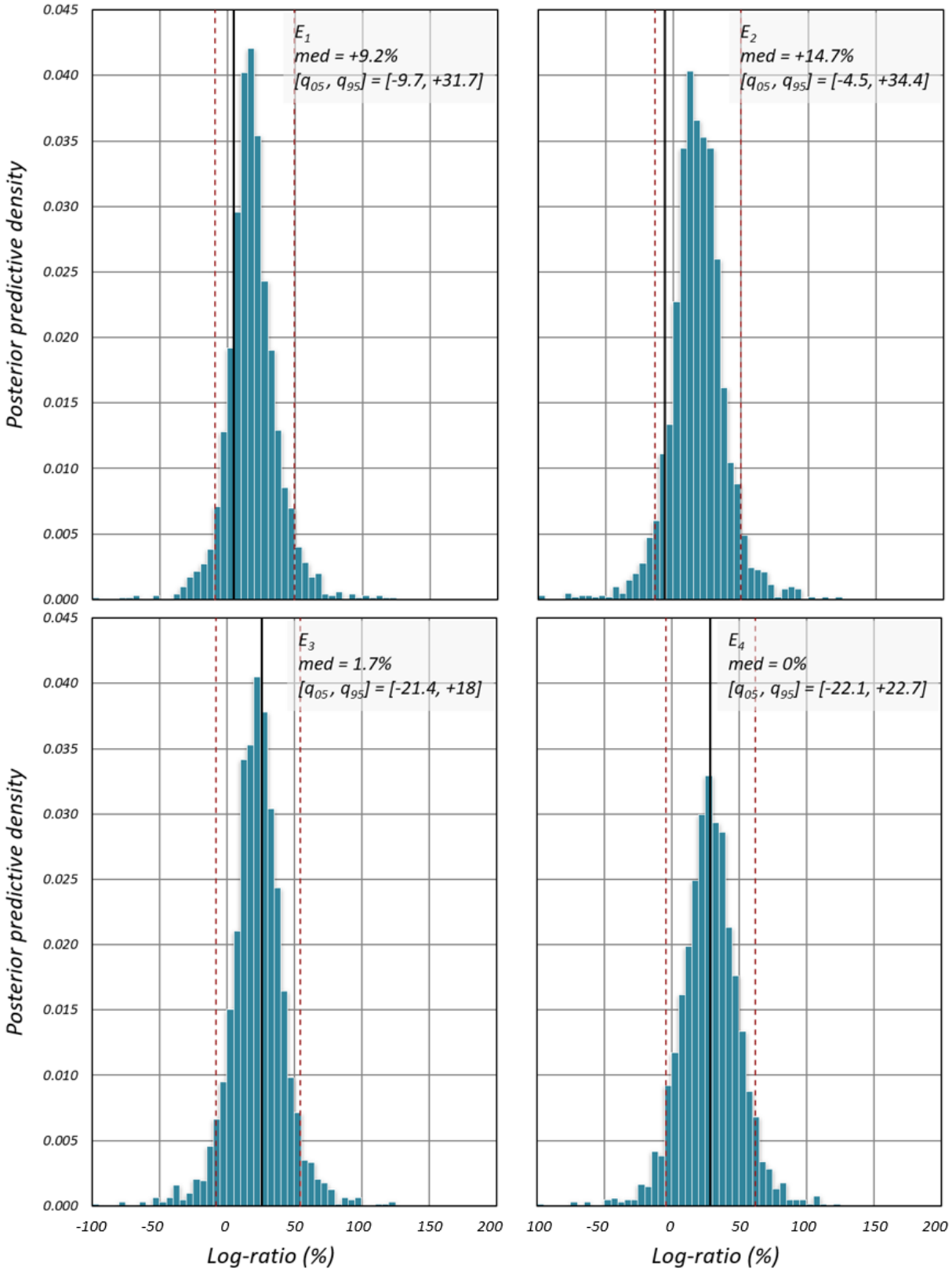


Figure 140. Posterior predictive distributions of the energy metrics.

5.8.13 Verification and Validation

5.8.13.1 Close-the-Loop Verification

This section corresponds to step 11 of the pipeline (Figure 125). Forty parameter vectors were drawn from the posterior distribution of Table 34 and run through the true OpenSees finite-element model under the four calibration motions. Of these, thirty-three completed the full protocol; the remaining seven diverged during the analysis, corresponding to parameter combinations in the tails of the posterior for which the nonlinear solver could not maintain convergence. A sample of this size is sufficient to estimate the first two moments of the GP prediction error (bias and RMSE) with a standard error below 2 percentage points and to detect systematic departures from the identity line in each of the eight metric panels.

For each of the 33 completed runs, the 8 calibration metrics were computed from the true simulator output and compared with the Gaussian Process prediction at the same point in parameter space. Figure 141 presents the comparison as eight scatter panels; the dashed line represents the identity, and the horizontal error bars span $\pm 2\sigma_{\mathrm{GP}}$. The corresponding numerical results are reported in Table 41.

Table 41. Closed-loop verification of the Gaussian-Process surrogate: RMSE, bias, and 2σ predictive coverage for the eight calibration metrics.

Metric	RMSE (%)	Bias (%)	CoV$_{2\sigma}$ (%)
peak$_1$	3.3	-3.1	8
peak$_2$	2.8	-2.6	38
peak$_3$	1	+0.1	86
peak$_4$	11.7	+3.2	78
E$_1$	3.6	+3.2	22
E$_2$	3.5	-2.9	38
E$_3$	0.5	0	86
E$_4$	6.3	-5.6	5

The surrogate's point predictions are accurate for six of the eight metrics, with root-mean-square errors of 3.3% or less and biases of 3.2% or less in absolute value. The two exceptions are Peak$_4$ (RMSE = 11.7%, bias = +3.2%) and E$_4$ (RMSE = 6.3%, bias = -5.6%), both associated with the fourth and most intense calibration motion, for which the nonlinear response is most severe and the emulator is least constrained. For Peak$_3$ and E$_3$, the surrogate is particularly accurate, with RMSE below 1.1% and negligible bias.

The surrogate's predictive uncertainty is narrower than the observed simulator-surrogate discrepancy for most metrics. For Peak$_3$ and E$_3$, the 2σ coverage reaches 86%, close to the nominal expectation, whereas for Peak$_1$, E$_1$, E$_2$, and E$_4$, the coverage falls below 40%. The underestimation of predictive uncertainty observed for these metrics indicates that the Gaussian Process underestimates it at several parameter locations, particularly for metrics associated with the more

demanding motions. This behavior is consistent with the smooth response representation imposed by the Matérn 5/2 kernel, which may not fully capture the variability of the nonlinear simulator response in regions where path dependence and numerical effects become more pronounced.

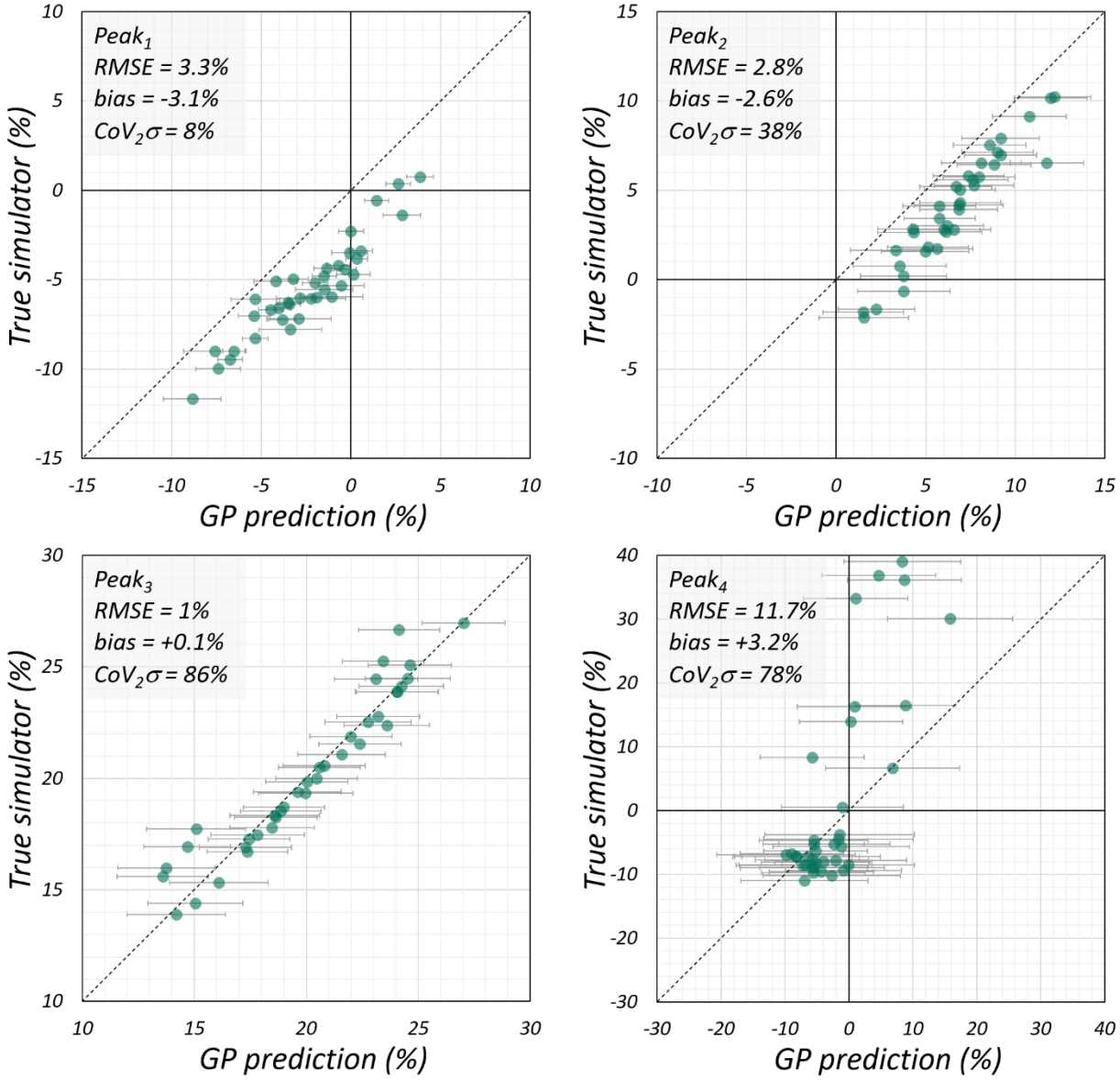


Figure 141a. Close-the-loop verification of the GP surrogate vs. the true OpenSees simulator for the peak displacements

Practically, the posterior location is supported by the close agreement between surrogate and true-simulator point predictions, particularly in the central region of the posterior. The posterior width, however, should be interpreted with greater caution, as the emulator underestimates uncertainty for several metrics. A likelihood constructed directly from the true simulator evaluations could therefore yield a broader posterior than that obtained using the Gaussian-Process surrogate.

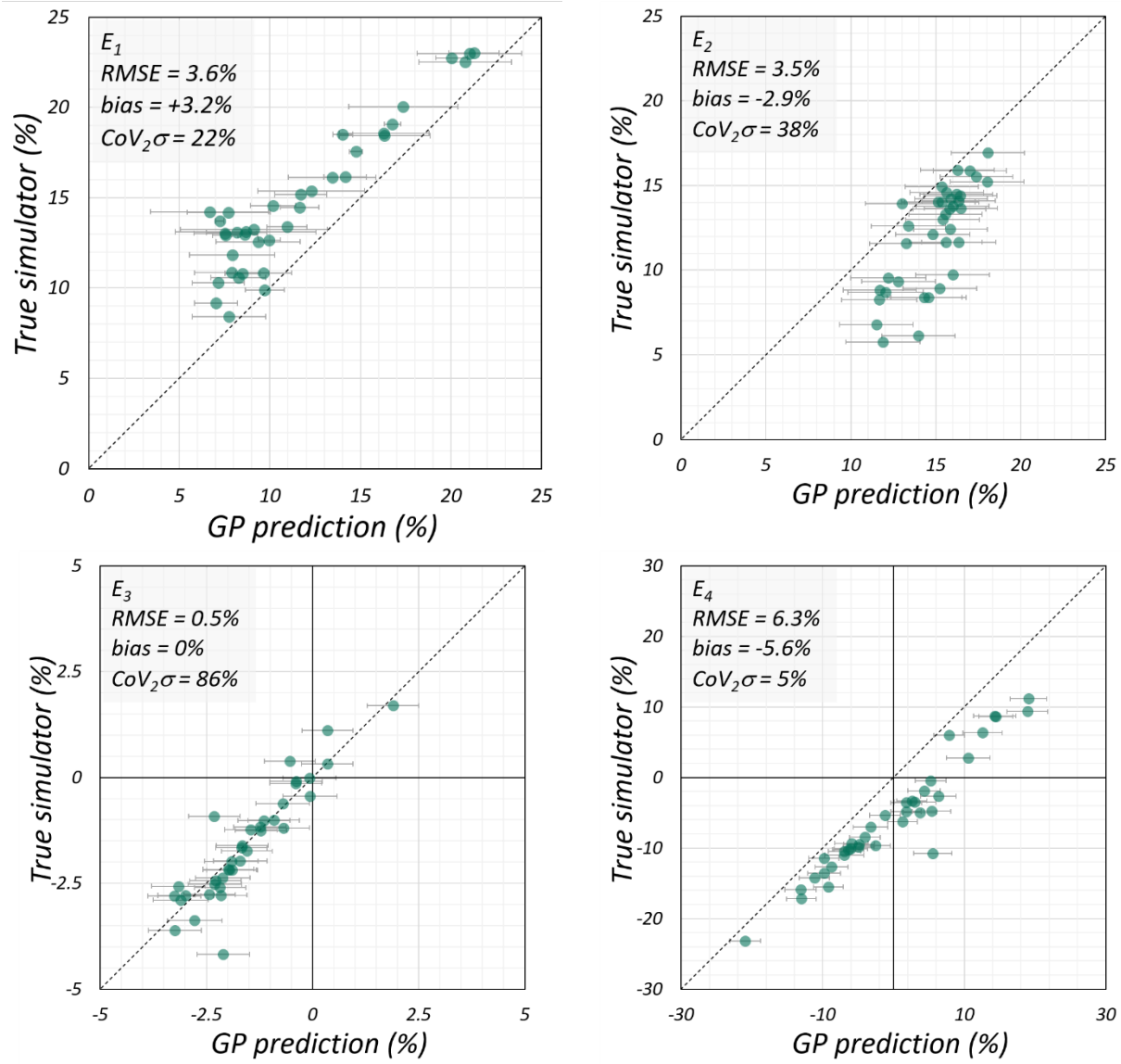


Figure 141a. Close-the-loop verification of the GP surrogate vs. the true OpenSees simulator for the peak displacements.

5.8.14 Held-Out Validation

This section corresponds to step 12 of the pipeline (Figure 125). The final step of the pipeline evaluates the calibrated model on a motion that was never used during training. The MAP parameter vector from Table 34 was evaluated using the true OpenSees simulator under the full five-earthquake protocol, and the same scalar metrics were extracted for each motion. Earthquakes EQ1-EQ4 provide an assessment of the calibrated model against the motions used for parameter identification, whereas EQ5, the most intense motion in the experimental protocol, constitutes the genuine held-out test.

For the four calibration motions, the MAP estimate reproduces the experimental peak displacements within ±14% (log-ratios of -10% for EQ1, +1% for EQ2, +13% for EQ3, and -7%

for EQ4) and the dissipated energies within ±13% (+12%, +7%, -3%, and -1%, respectively). These errors match the corresponding surrogate predictions at the MAP point, indicating that the Gaussian-process approximation does not introduce significant systematic bias in the calibrated solution location. The held-out motion EQ5 exhibits a peak-displacement log-ratio of $L_{n,dpeak}$=+15%, comparable in magnitude to the largest calibration-set error (EQ3, +13%). The energy log-ratio, however, reaches $L_{n,E}$=-16%, indicating that the model dissipates approximately 17% more energy than the experiment, an error noticeably larger than the ±13% range observed for EQ1-EQ4. Figure 142 summarizes both metrics across all five earthquakes.

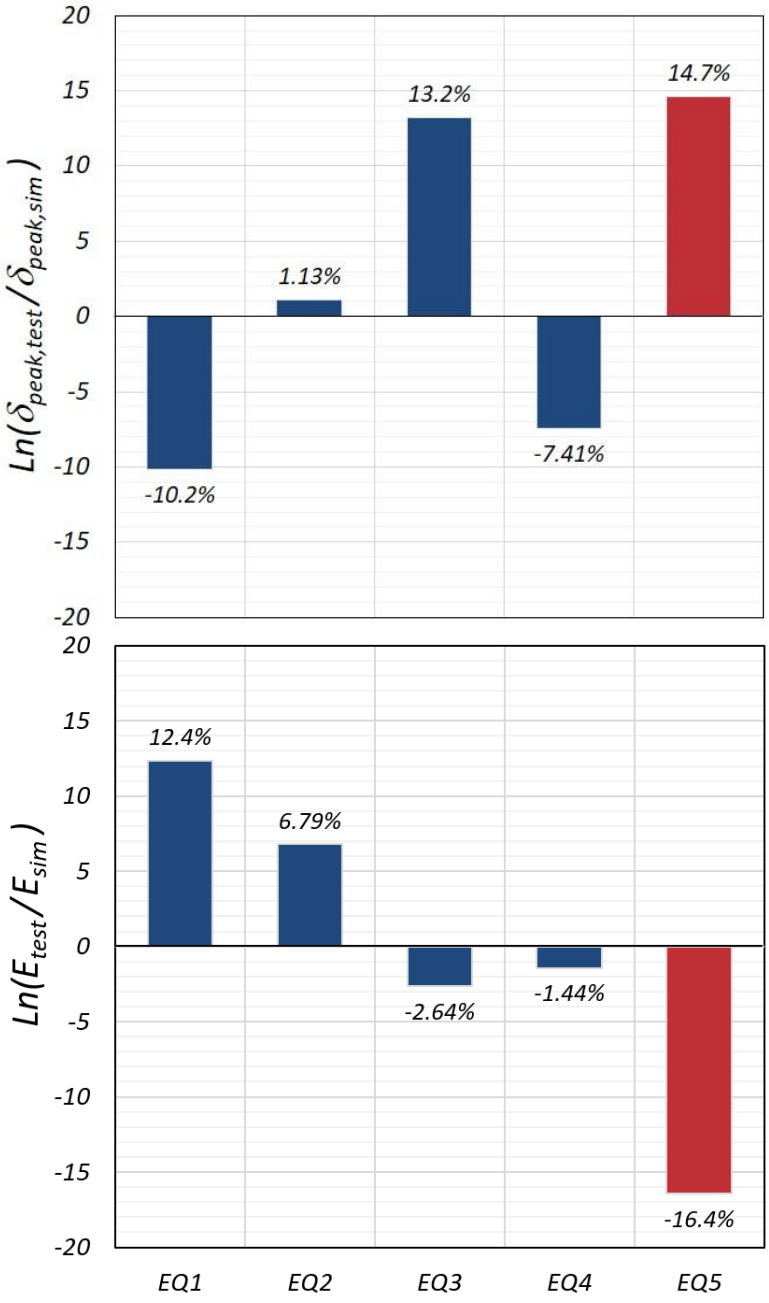


Figure 142. Held-out validation metrics.

Table 42 summarizes both metrics across all five earthquakes.

Table 42. Metrics across EQ1-EQ5 earthquakes

Simulation	$L_{n,dpeak}$ (%)	$L_{n,E}$ (%)
EQ1	-10.2	+12.4
EQ2	+1.1	+6.8
EQ3	+13.2	-2.6
EQ4	-7.4	-1.4
EQ5	+14.7	-16.4

The combination of a positive $L_{n,d_{\text{pico}}}$ and a negative $L_{n,E}$ indicates that, relative to the experiment, the model predicts smaller peak displacements while simultaneously dissipating more energy. This signature is consistent with a response that remains excessively stiff at large ductility levels: the model sustains higher forces for a given displacement, enlarging the hysteretic loop area even as displacement excursion decreases. At the demand level imposed by EQ5, mechanisms such as bar buckling, bond deterioration, and confined-core softening may contribute to stiffness and strength degradation, allowing larger displacement excursions while reducing the energy dissipated per cycle. The current formulation does not explicitly represent these effects. Calibration under EQ1-EQ4 cannot constrain such mechanisms because the corresponding demands remain within a range where the constitutive model adequately represents the response. The EQ5 results thus indicate the limit of the response range the calibration supports. Although the peak displacement remains reasonably reproduced, the energy balance begins to diverge once the demand exceeds the range covered by EQ1-EQ4.

5.8.15 Outcome

The dynamic Bayesian stage has refined the 12 independently calibrated model parameters, quantified the posterior uncertainty associated with the calibrated parameters, and established which dynamically variable parameters are informed by the experimental response. Table 43 summarizes the full evolution of the model parameters from their initial values to their posterior estimates. The principal substantive results are as follows. First, the shake-table data support the strain-rate-dependent viscous mechanism proposed in this dissertation. At the same time, the posterior dependence between the rate-sensitivity parameters indicates that their combination is better identified than either parameter individually. The dynamic response also constrains the first-mode Rayleigh damping ratio.

Second, the global sensitivity analysis shows that five parameters substantially influence the dynamic response, whereas four independently calibrated parameters have comparatively small sensitivity within the explored parameter space. The remaining three parameters were not independently calibrated: two were fixed a priori and one, r_c, was derived from the calibrated value of ε'_{cc}. These results demonstrate the complementarity of the two calibration stages: the displacement-controlled calibration first constrains the parameters governing the rate-independent

constitutive response. In contrast, the dynamic stage selectively informs the parameters whose effects are observable in the shake-table response.

Table 43. Evolution of model parameters from initial values to posterior estimates.

Group	Parameter	Initial value	Posterior estimate
Reinforcing steel	λ	1.5	1.106
	n_p	1	0.496
	D_{fu}	1	0.981
	Ω_{fac}	1.03	1.060
	α_u	0.82	0.632
Concrete	f_t	3.1	0.796
	r_t	2.3	1.124
	ε'_{cc}	-0.00376	-0.00424
	r_c	2.35	Derived
Strain-rate viscous mechanism	n_{rate}	0.75	0.69
	k_{rate}	125	99.6
Structural response	I_e/I_g	0.37	0.646
	G_e/G_g	0.4	0.2
Structural damping	ζ_1	0.01	0.00462
	ζ_2	0.005	0.015

5.8.16 Model-side Limitation

Beyond these positive results, the calibration surfaces two limitations that stem from the model rather than the identification procedure. Both must be reported honestly, because they inform the interpretation of the numerical results above and set the agenda for the future development of the constitutive framework.

The first is a missing-mechanism limitation. Two features of the experimental record fall outside the envelope of the entire almost 1300-run training campaign: the instantaneous frequency of the specimen in the quiet windows between motions is about 5.5 % higher than in any simulation, and the residual displacement after EQ3 and EQ4 is about 30 % larger than in any simulation. No combination of the fifteen parameters within their admissible ranges can reproduce those two features. The Bayesian estimation of the error hyperparameters (Section 5.8.8) quantifies this limitation as a discrepancy floor of σ_{err} ≈11-14 %; the analysis of the Global Sensitivity Analysis section (5.8.7) further shows that the total-order Sobol indices already saturate at $\Sigma S_T \approx 1$ on seven of the eight metrics, so there is no hidden variance in interaction terms that additional calibration could recover. The remaining discrepancy is therefore not readily attributable to further parameter adjustment within the current formulation. Its two most likely physical origins (given the specific features that escape the envelope) are the representation of stiffness recovery after unloading (which sets the inter-motion small-amplitude frequency) and the representation of permanent-

deformation accumulation (which sets the residual displacement). Extending the constitutive framework along these two axes is a natural continuation of this work.

5.8.16.1 Closing Statement

Steps 11 and 12 of the pipeline (Figure 125) close the calibration by evaluating the posterior against the true simulator and the held-out motion EQ5. Taken together, the identification of the two constitutive contributions developed in this dissertation, the variance-based demonstration of their complementarity across the two calibration stages, and the explicit quantification of the model's limitations constitute the substantive outcome of this chapter. The calibration therefore does more than provide fifteen parameter estimates: it shows what the experimental evidence could and could not resolve and identifies the aspects of the formulation that require further development.

5.9 Model Validation against the Held-Out Seismic Simulation (EQ5)

The two calibration stages described above have identified the 15 model parameters using the first 4 seismic simulations. The parameter values reported so far therefore reflect, directly or indirectly, the same four records used to assess fit quality. A calibration assessed only against the data that produced it cannot distinguish genuine predictive capability from a sufficiently flexible model's ability to reproduce a particular set of observations. The fifth seismic simulation, EQ5, was therefore withheld from the entire identification procedure and is used here as an independent test of the calibrated model.

Two properties make EQ5 a demanding test rather than a formality. First, it was never seen by any part of the calibration: it did not enter the displacement-controlled designs, it was not among the 1297 dynamic analyses that trained the surrogate, and it played no role in the likelihood. Second, and more importantly, EQ5 is more intense than any of the four calibration motions. The validation is therefore an extrapolation rather than an interpolation: the model must predict demand beyond the range over which it identified its parameters. This type of extrapolative validation is the more demanding of the two possible tests. A model that reproduces a motion beyond its calibration range provides stronger evidence that the calibrated formulation retains predictive capability beyond the conditions used for parameter identification. It should be noted, however, that EQ5 constitutes an extrapolation in seismic demand intensity within the same structural configuration, reinforcement grade, and element formulation used for calibration. The assessment therefore evaluates the model's predictive capability under greater seismic demand, not its generalizability across different structural typologies, cross-section geometries, reinforcement grades, or loading conditions.

Validation applies the recorded base acceleration of EQ5 to the calibrated model, holding every parameter at the MAP values reported above. No parameter is returned, no scaling factor is introduced, and the constitutive state is carried over from the end of the fourth simulation to preserve the accumulated damage history, consistent with the sequential protocol adopted throughout the identification. All fifteen parameters are held at their MAP values (Table 34); no parameter is re-tuned, and no scaling factor is introduced.

5.9.1 Quantities Compared

The comparison is deliberately not restricted to the eight scalar metrics used in the calibration. Scalar metrics were appropriate for the inversion because the response was represented by scalar quantities that a surrogate could emulate and that could be weighted in the likelihood. However, a

model can match a peak displacement while misrepresenting the path it took to reach it. The validation therefore compares the full response at two levels of increasing stringency.

The first level compares the displacement response history over the entire duration of the record. This level is the most direct measure of predictive capability and a primary engineering response quantity; it reveals not only the peak but also the response phase, the residual displacement at the end of the motion, and the amplitude of the following free-vibration decay. The second level is the hysteretic response, expressed as a normalized base moment versus drift ratio, in the same form as used in the displacement-controlled stage. This level of exposure assesses whether the model reproduces the loop shape and, therefore, whether the two constitutive contributions of this dissertation behave as intended under a demand not used for their identification. Because the bond-slip pinching parameters were identified quasi-statically and the strain-rate parameters dynamically, the hysteretic response of EQ5 tests was evaluated under seismic loading outside the conditions used for parameter identification.

5.9.2 Validation Results

Figures 143-152 present the response of the calibrated model and experimental specimen under five seismic motions, each represented by its displacement history and normalized moment-drift hysteresis. Overall, the model reproduces the measured response with reasonable fidelity, capturing the principal displacement and hysteretic characteristics across the five motions. The remaining discrepancies mainly involve local loop shape, energy dissipation, and, for the held-out EQ5 motion, displacement-response amplitude (Table 42). Agreement with the surrogate predictions at the MAP point confirms that the GP emulator adequately represents the calibrated response.

For EQ1 (Figures 143-144), the model closely follows the experimental displacement history, reproducing the timing and amplitude of the principal cycles. The normalized moment-drift response also remains in close agreement over the relatively low-drift range. For EQ2 (Figures 145-146), the larger and more sustained displacement excursions are reproduced with good fidelity, although differences in the inner cycles and hysteretic reloading branches become more evident. Under EQ3 (Figures 147-148), which produces the greatest demand among the calibration motions, the model captures the sequence and amplitude of the major displacement excursions, including the largest peaks, with a peak displacement error of +13%. The hysteretic response remains consistent with the experimental trend, although local differences in loop shape contribute to the energy discrepancy.

EQ4 (Figures 149-150) produces a comparatively different displacement history, with a more pronounced residual component; the model reproduces the principal cycles and overall response envelope, while the remaining differences are concentrated in the reloading portions of the hysteresis loops. Across EQ1-EQ4, the peak displacement errors range from -10.2% to +13.2%, while the dissipated-energy errors range from -2.6% to +12.4%. Taken together, these results indicate that the calibrated model consistently represents the displacement response and the principal characteristics of hysteretic behavior over the demand range represented by EQ1-EQ4. The agreement between these results and the surrogate predictions at the MAP point further confirms that the GP emulator adequately represents the calibrated model response at the MAP parameter combination.

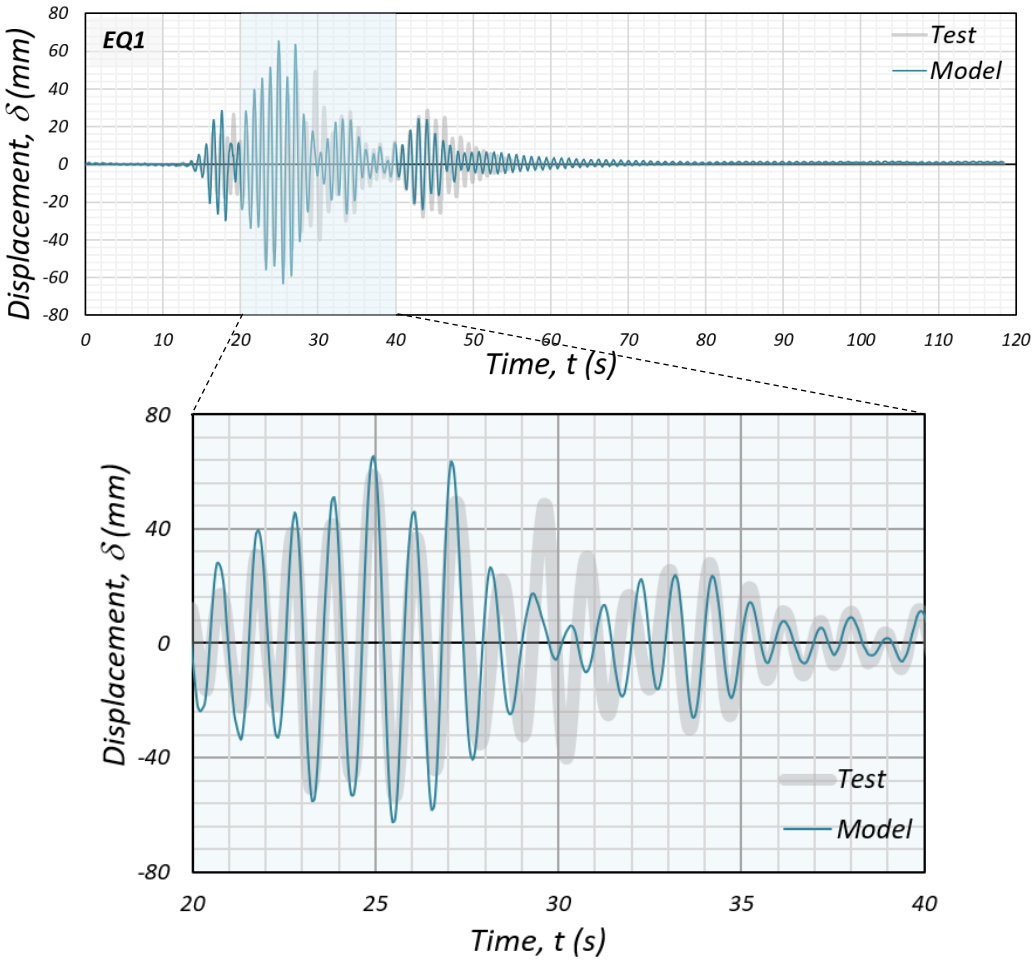


Figure 143. EQ1 displacement time history.

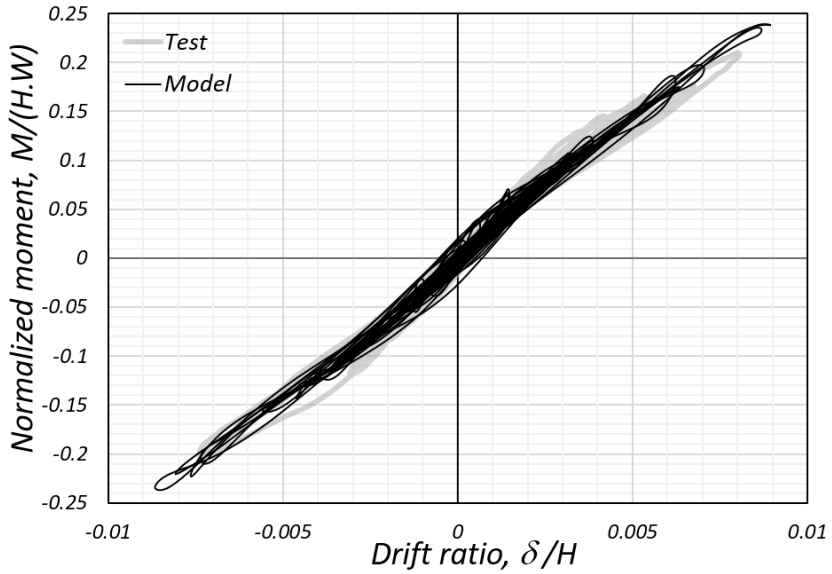


Figure 144. EQ1 normalized moment-drift hysteresis.

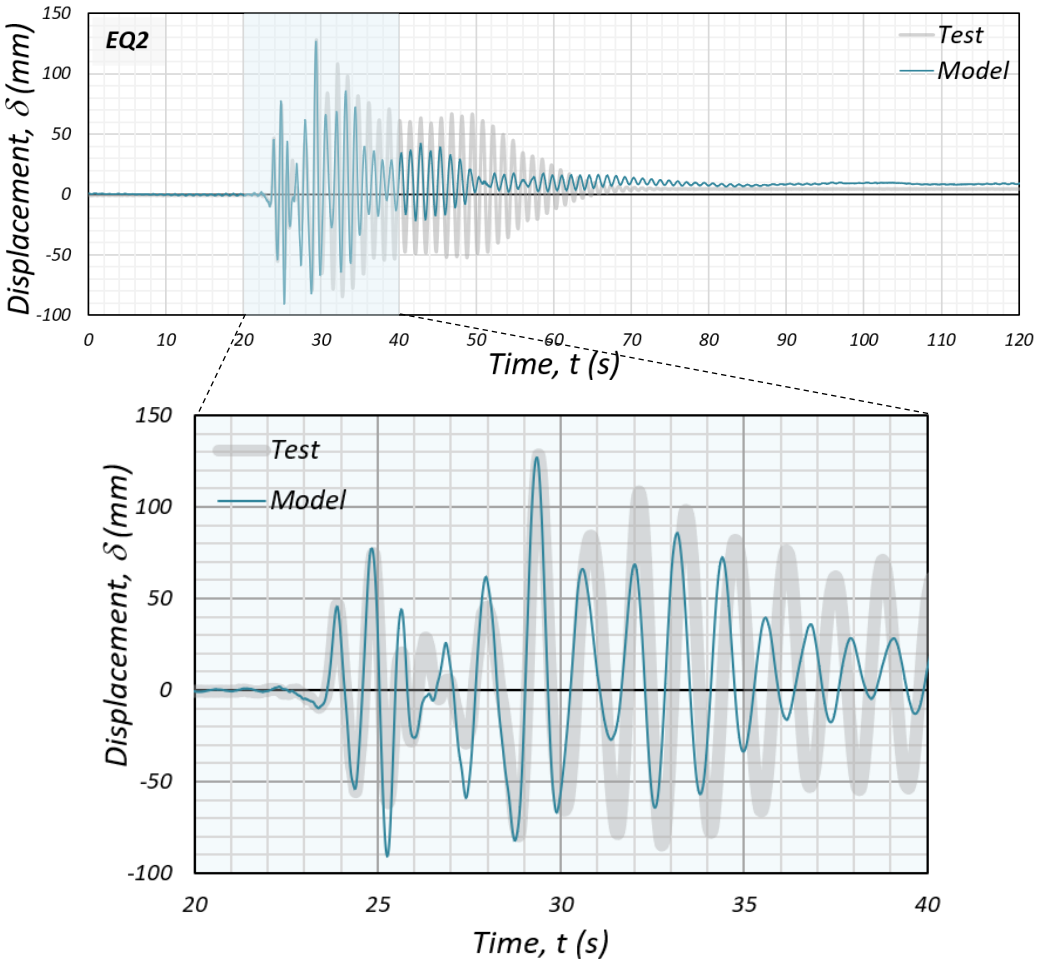


Figure 145. EQ2 displacement time history.

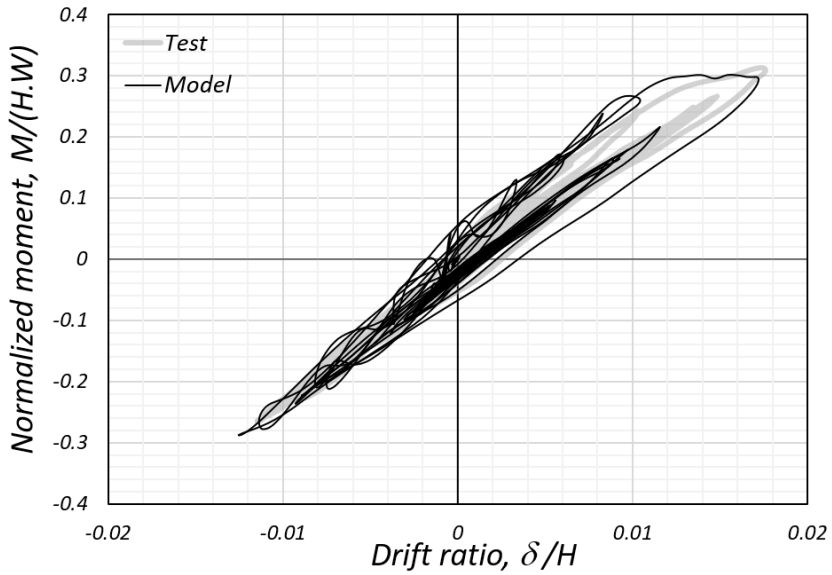


Figure 146. EQ2 normalized moment-drift hysteresis.

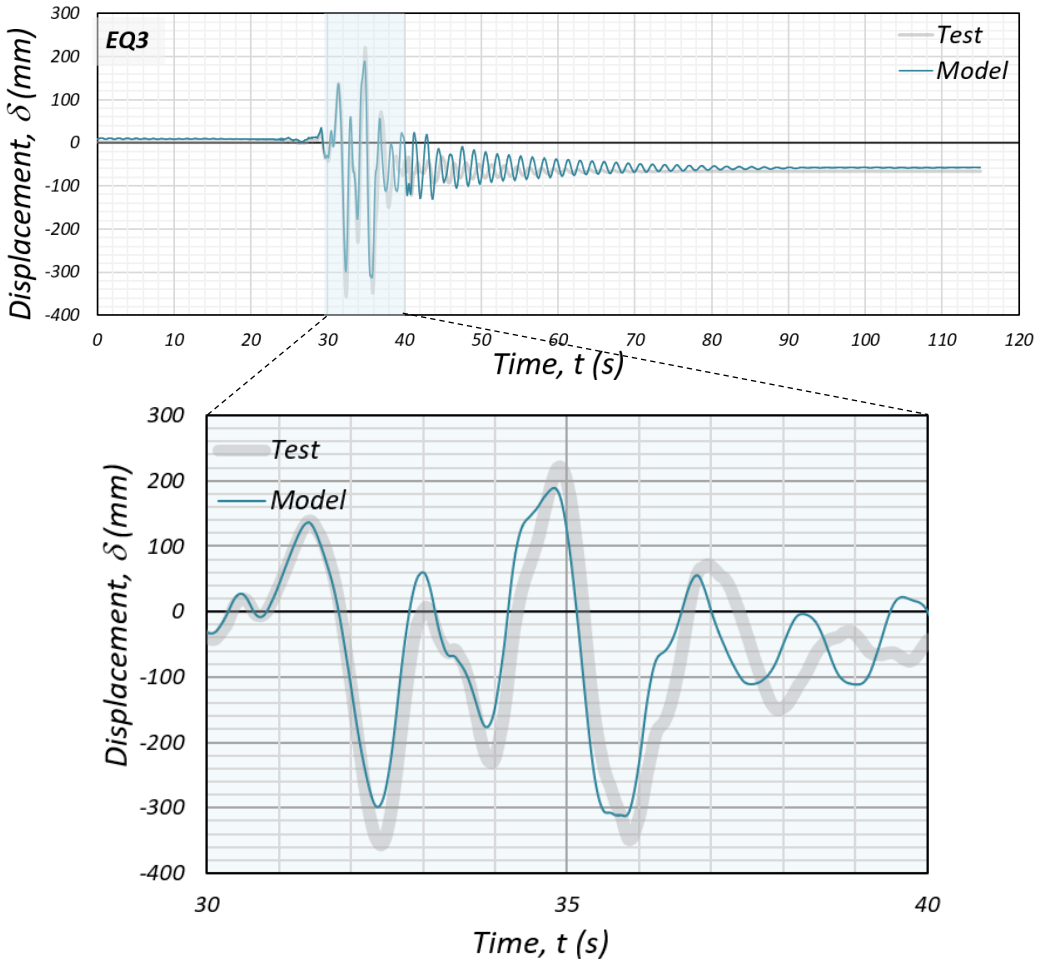


Figure 147. EQ3 displacement time history.

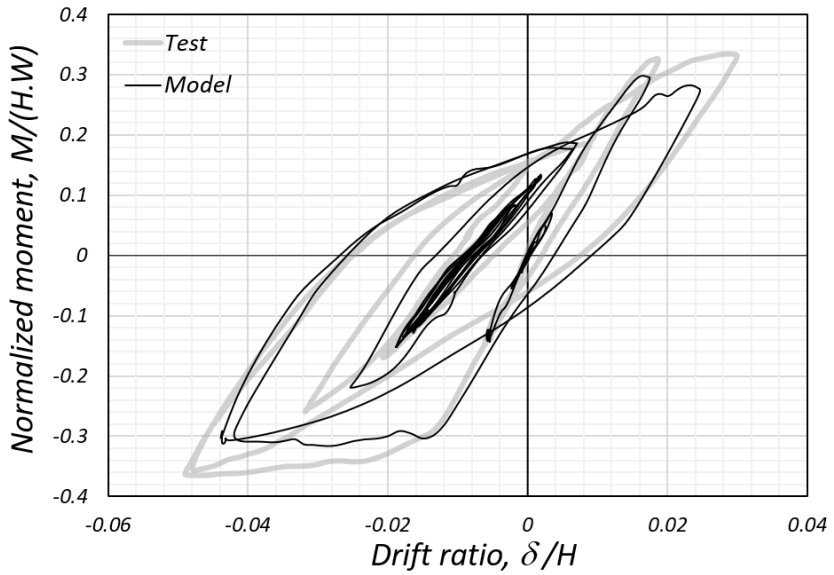


Figure 148. EQ3 normalized moment-drift hysteresis.

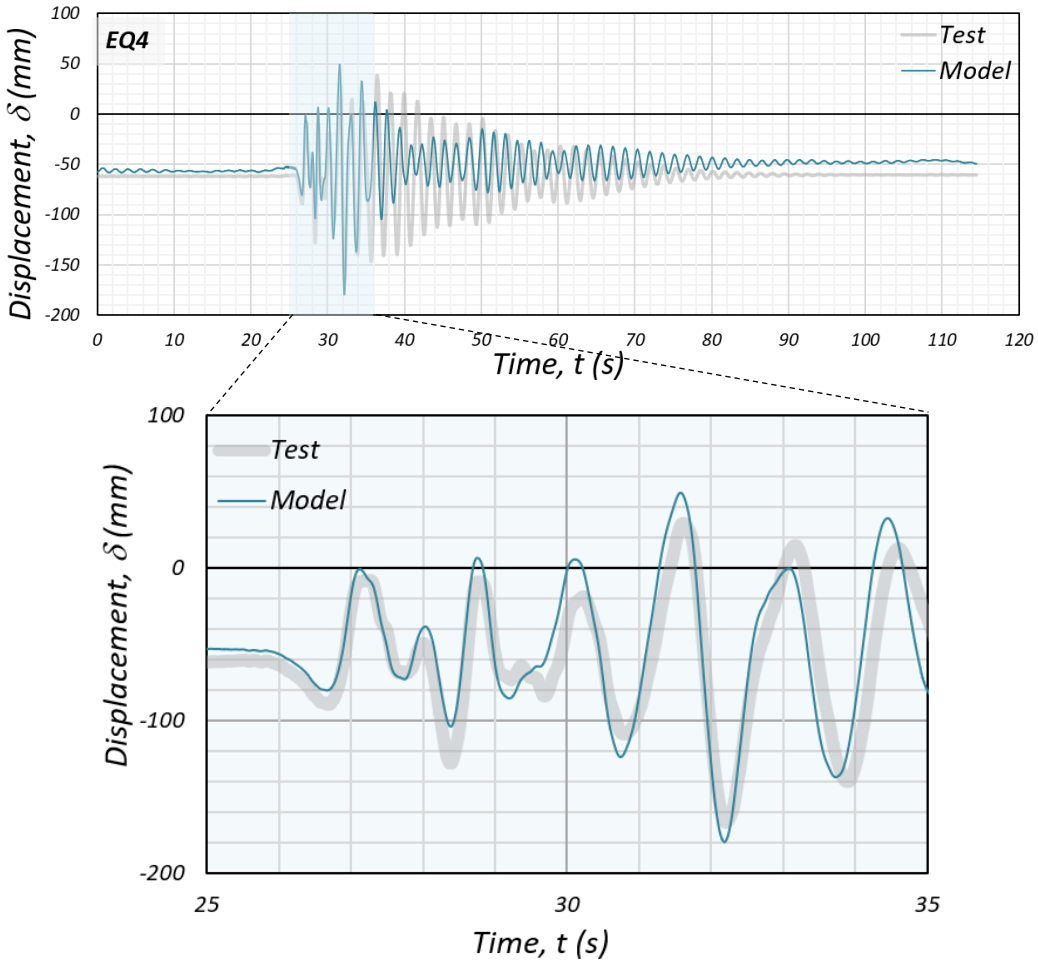


Figure 149. EQ4 displacement time history.

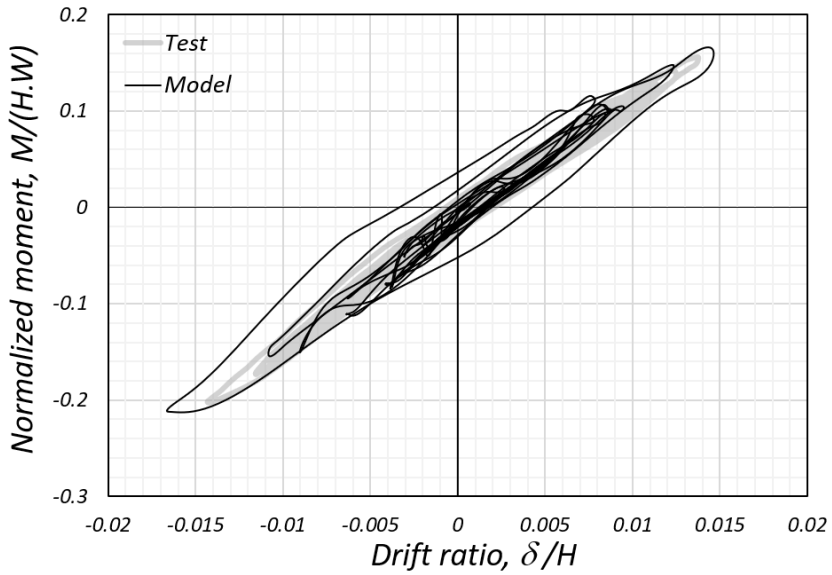


Figure 150. EQ4 normalized moment-drift hysteresis.

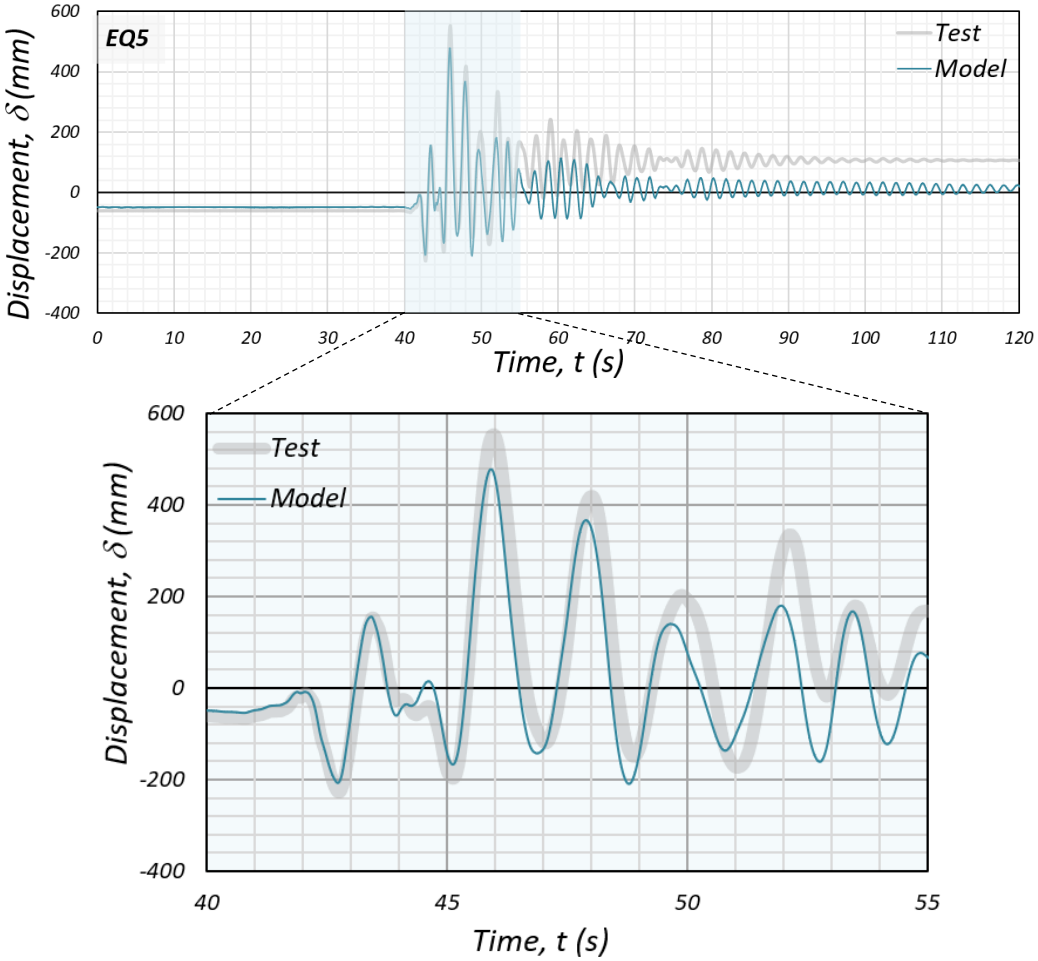


Figure 151. EQ5 displacement time history.

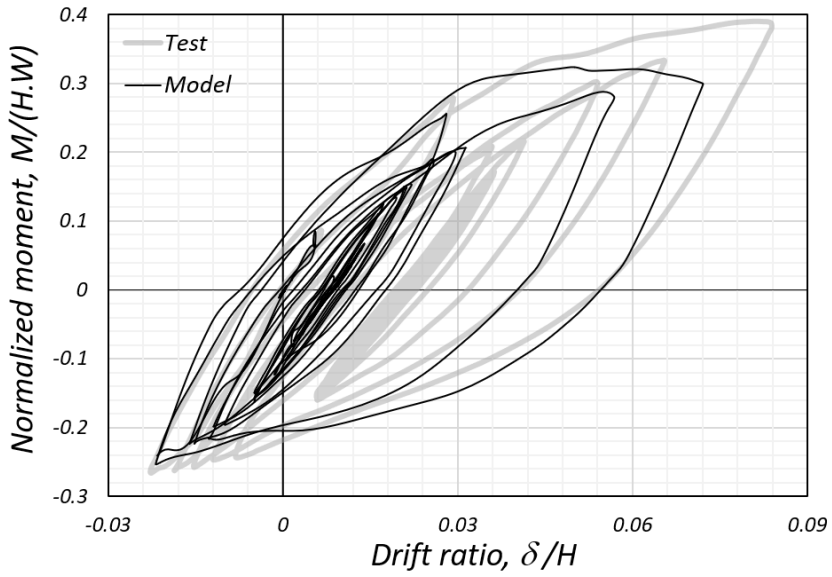


Figure 152. EQ5 normalized moment-drift hysteresis.

For the held-out motion EQ5, the model captures the phasing of the cycle train (Figure 151) but systematically underestimates the amplitude of the dominant cycles, with the experimental peak of 553 mm reduced to 478 mm in the model. The underestimation is nearly uniform along the response envelope, with no growing bias over time, suggesting a difference in global effective stiffness in the large-deformation range rather than cumulative model drift. The peak displacement error is +14.7%, comparable to the largest error observed for the calibration motions, whereas the dissipated-energy error reaches -16.4% (Table 42), indicating greater energy dissipation than measured experimentally.

The corresponding moment-drift hysteresis (Figure 152) directly reflects this discrepancy. The numerical loop reaches smaller drifts (≈0.065 versus ≈0.09 experimentally) but higher moments at comparable drift, consistent with excessive effective stiffness. Pinching is reproduced qualitatively, supporting the adequacy of the bond-slip parameters under the seismic demand; however, the larger enclosed numerical area indicates that the balance between residual stiffness and energy dissipation in the large-drift range is not well captured. The experimental loop's asymmetry, which extends further in positive drift, is also not fully reproduced, pointing to limitations in the constitutive representation of asymmetric damage mechanisms at high demand. Thus, although the calibrated model reasonably represents the global displacement demand under EQ5, its accuracy in reproducing detailed hysteretic energy dissipation deteriorates at this higher demand level. This discrepancy may reflect mechanisms such as bond deterioration and confined-core damage that the constitutive formulation does not fully capture. However, the available results do not allow isolation of their individual contributions.

5.10 Energy Decomposition Analysis

The calibrated numerical model reproduces the experimental response across the five-earthquake sequence (EQ1-EQ5) with generally good fidelity. However, the total energy input to the system during seismic excitation is not dissipated solely through material hysteresis; other mechanisms included in the model formulation also contribute. Two such contributions are examined in this section: (1) viscous damping energy associated with the Rayleigh proportional damping matrix, and (2) strain-rate-dependent energy dissipation associated with the dynamic amplification of the yield stress in the SteelDRCV reinforcing-steel model. A methodology is developed to isolate and quantify these two contributions independently, as summarized in the flowchart in Figure 153.

In all cases, the cumulative energy associated with a given base moment $M(t)$ is obtained by incremental trapezoidal integration of the equivalent base shear $V(t) = M/H$ over the top displacement history $\delta(t)$:

$$E_i = E_{i-1} + \frac{1}{2}(V_{i-1} + V_i)(\delta_{i-1} - \delta_i) \tag{193}$$

Each of the following subsections defines the specific moment $M(t)$, and hence the shear $V(t)$, entering this equation for the energy component under consideration.

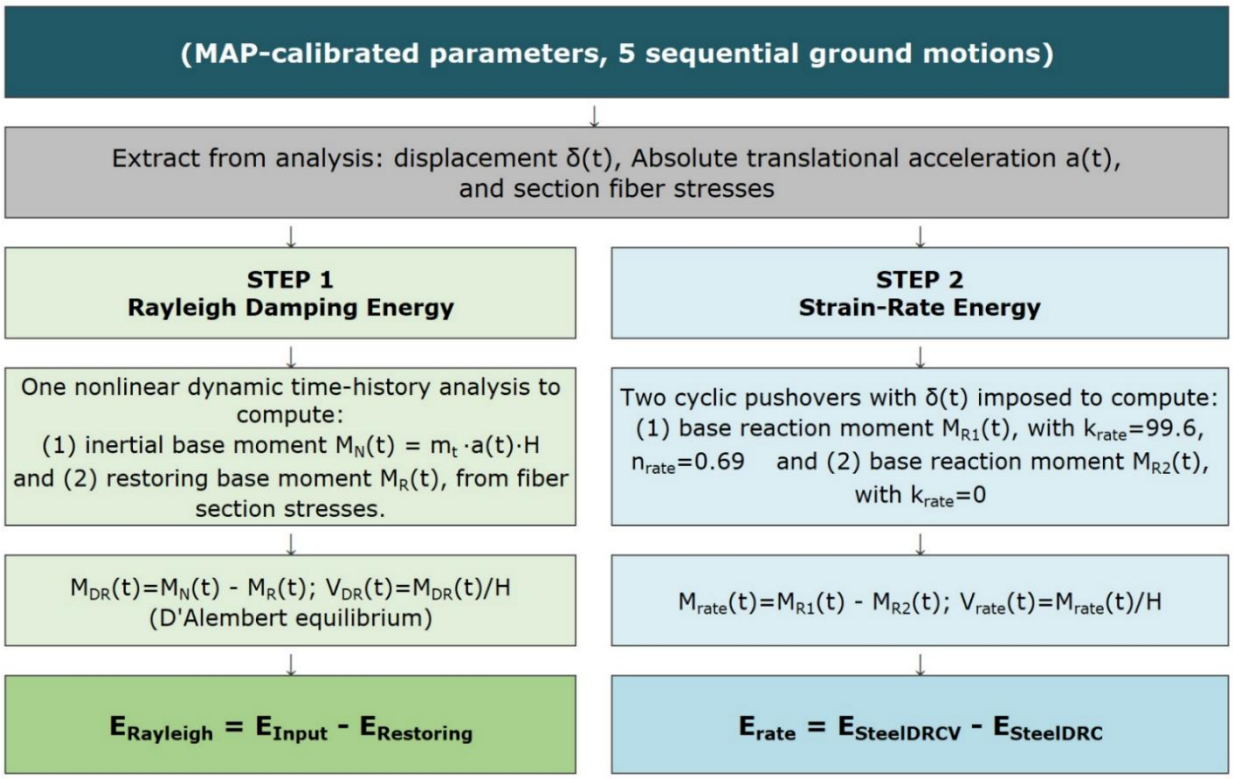


Figure 153. Energy decomposition flowchart.

5.10.1 Rayleigh Damping

The Rayleigh damping matrix adopted in the optimal model (Table 34) is constructed by using the mass-proportional coefficient α_M=0.01935; and the initial-stiffness-proportional coefficient β_{K_0}=9.316x10^{-4}. These coefficients were calculated through the Bayesian inference procedure and correspond to damping ratios of ζ_1=0.46% and ζ_2=1.5% for the first and second translational modes, respectively, with T_1=0.907 s and T_2=0.199 s.

To isolate the viscous-damping contribution, the dynamic equilibrium is evaluated at the column base by comparing the inertial base moment, $M_N(t)$, obtained from the translational mass and the total acceleration recorded at the column top according to the formulation given in Eq. (166), with the restoring base moment, $M_R(t)$, obtained from the structural response by integrating the constitutive stresses across the column fiber sections and accounting for the rotations introduced by the fixed-end rotation elements. The rotational inertia is set to zero ($I_r = 0$), thereby isolating the first-mode translational inertial response. Because the second-mode contribution is negligible in the global response of the bridge column specimen, this simplification does not significantly affect the overall energy balance.

Under D'Alembert equilibrium, the difference between these two quantities gives the residual moment associated with viscous damping, $M_D(t)$:

$$M_{DR}(t) = M_N(t) - M_R(t) \tag{194}$$

This residual corresponds to the velocity-dependent contribution introduced by the Rayleigh damping matrix, since $M_N(t)$ reflects the combined effect of the inertial, restoring, and viscous forces, whereas $M_R(t)$ contains only the deformation-dependent material restoring forces.

The Rayleigh damping contribution is obtained as

$$E_{Rayleigh} = E_{Input} - E_{Restoring} \tag{195}$$

Here, E_{Input} denotes the energy introduced into the structural system by the imposed ground-motion response. This input energy is partitioned between material hysteresis and viscous damping, with $E_{Restoring}$ representing the energy dissipated through irreversible material hysteresis in the fiber sections and $E_{Rayleigh}$ representing the energy dissipated by the velocity-proportional forces associated with the Rayleigh damping matrix.

Table 44 summarizes the energy decomposition obtained for each earthquake in the sequence, including the input energy, the hysteretic contribution, and the energy dissipated through Rayleigh damping.

Table 44. Viscous damping energy contribution for the earthquake sequence.

Simulation	E_{Input} $(kN.m)$	$E_{Restoring}$ $(kN.m)$	$E_{Rayleigh}$ $(kN.m)$	$E_{Rayleigh}/E_{Input}$ (%)
EQ1	36.8	26.5	10.3	28
EQ2	153	136	17	11.1
EQ3	574	553	21	3.66
EQ4	84	73.2	10.8	12.9
EQ5	1262	1205	57	4.52
Total	2110	1994	116	5.5

The total input energy across the five-earthquake sequence is 2110 kN·m, of which 116 kN·m (5.5%) is dissipated by Rayleigh viscous damping. The remaining 1994 kN·m is dissipated through material hysteresis in the fiber sections. The Rayleigh contribution is largest in relative terms for the low-amplitude earthquakes EQ1 and EQ4 (28% and 12.9%, respectively), for which the limited development of inelastic response results in a comparatively small hysteretic contribution. In contrast, for the high-amplitude earthquakes EQ3 and EQ5, the Rayleigh fraction decreases to 3.66% and 4.52%, respectively, while hysteretic dissipation, E_R, accounts for 96.2% and 95.5% of the corresponding input energy. This shift in the energy balance reflects the progressive dominance of material hysteresis as the response develops into the inelastic range, whereas the Rayleigh contribution remains comparatively limited.

5.10.2 Strain-Rate Dissipation Energy

The SteelDRCV constitutive model adopted in the optimal model incorporates a strain-rate-dependent amplification of the yield stress governed by the rate-sensitivity coefficient and exponent k_{rate}=99.6 and n_{rate}=0.69, respectively. These parameters were obtained through the Bayesian inference procedure and define the strain-rate-dependent response of the reinforcing steel in the optimal model.

To isolate the strain-rate energy contribution of this mechanism, the displacement history, $\delta(t)$, recorded at the top of the column during the optimal dynamic analysis (Table 34), is imposed as the loading protocol of a cyclic pushover analysis. Because the prescribed displacement history is applied with the same temporal discretization as the original dynamic analysis, its velocity history is preserved, ensuring that the strain rates experienced by the reinforcing-steel fibers remain consistent with those generated by the seismic excitation. Two analyses are then performed under otherwise identical conditions: (1) one retaining the full SteelDRCV formulation with the MAP-calibrated rate parameters, and (2) the other suppressing the strain-rate-dependent amplification by setting k_{rate}=0, while preserving all other material parameters, including those governing the monotonic envelope, Bauschinger effect, and pinching behavior. Since the two analyses differ only in the strain-rate-dependent yield-stress amplification, the difference in the resulting base reaction moments is attributable exclusively to this mechanism.

$$M_{rate} = M_{R1} - M_{R2} \tag{196}$$

Where, M_{rate} is the strain-rate moment. The strain-rate energy contribution is therefore obtained as:

$$E_{rate} = E_{SteelDRCV} - E_{SteelDRC} \tag{197}$$

where $E_{SteelDRCV}$ denotes the hysteretic energy dissipated with the strain-rate-dependent amplification active, whereas $E_{SteelDRC}$ denotes the corresponding hysteretic energy with the rate-dependent amplification suppressed. Each energy term is evaluated by incrementally integrating the corresponding base reaction moment with respect to the imposed top displacement, using the trapezoidal formulation defined in Eq. (193). Table 45 summarizes the results for each earthquake in the sequence.

The total strain-rate energy contribution is 93 kN·m, representing 5.1% of the hysteretic energy dissipated with the rate mechanism active. As with the Rayleigh component, the relative contribution is largest for the low-amplitude earthquakes EQ1 and EQ4 (19.4% and 14.3%, respectively), for which yielding cycles remain near the onset of plasticity, and the rate-dependent amplification constitutes a proportionally larger fraction of the section resistance. For the high-amplitude earthquakes EQ3 and EQ5, the rate fraction decreases to 4.5% and 4.4%, as the extensive post-yield deformations dominate the energy balance and the rate amplification becomes a comparatively minor contribution.

Table 45. Strain-rate energy contribution for the earthquake sequence.

Simulation	$E_{SteelDRCV}$ $(kN.m)$	$E_{SteelDRC}$ $(kN.m)$	E_{rate} $(kN.m)$	$E_{rate}/E_{SteelDRCV}$ (%)
EQ1	17.5	14.1	3.4	19.4
EQ2	117	108	9	7.7
EQ3	510	487	23	4.5
EQ4	58.1	49.8	8.3	14.3
EQ5	1112	1063	49	4.4
Total	1815	1722	93	5.1

5.10.3 Energy Dissipation Mechanisms and the Role of Strain-Rate Effects

The energy decomposition reveals that material hysteresis accounts for approximately 90% of the total seismic input energy, while Rayleigh damping and strain-rate effects contribute approximately 5.5% and 5.1%, respectively. The strain-rate contribution is thus of the same order of magnitude as the empirically prescribed viscous damping, demonstrating that material rate dependence provides a non-negligible contribution to energy dissipation under seismic loading. On a per-earthquake basis, the relative strain-rate contribution ranges from approximately 4% for the strongest ground motions (EQ3 and EQ5) to approximately 19% for the lower-amplitude events (EQ1 and EQ4), depending on the earthquake considered, reflecting the greater relative influence of rate-dependent amplification when the hysteretic response is less developed. These results imply that neglecting strain-rate effects in the constitutive model may cause the associated dissipation to be represented disproportionately by the remaining energy-dissipation mechanisms, particularly Rayleigh damping and material hysteresis, potentially distorting the predicted balance of dissipation mechanisms in nonlinear time-history analysis.

Figure 154 shows the cumulative normalized energy dissipation decomposed by mechanism for the five shake-table events, EQ1-EQ5. The cumulative energy dissipation exhibits a clear predominance of the hysteretic mechanism across all five records, although the relative contribution of the non-hysteretic mechanisms varies between events. The energy contributions are color-coded throughout: the blue area denotes the hysteretic energy, the green area the strain-rate-dependent dissipation, and the gray area the viscous damping energy.

EQ1 exhibits the lowest hysteretic share of the campaign and, consequently, the largest combined contribution from viscous damping and strain-rate effects, approximately 37%. This departure from the overall pattern is consistent with EQ1 exhibiting the most linear response of the campaign, with inelastic excursions accounting for only 63% of the total dissipated energy. In EQ2, the hysteretic contribution increases to approximately 83%, while the viscous damping and strain-rate contributions account for approximately 11% and 6%, respectively. Although viscous damping remains the larger of the two non-hysteretic mechanisms, their contributions differ by less than a factor of two.

EQ3 is one of the most intense records and exhibits one of the largest hysteretic contributions, together with EQ5, with approximately 92% of the dissipated energy associated with hysteretic behavior. Nevertheless, the strain-rate contribution (4.1%) slightly exceeds the viscous damping

contribution (3.8%). This behavior indicates that the relative contribution of these two non-hysteretic mechanisms may vary substantially among records, even when the overall intensity of the ground motion is high. In EQ3, these local strain rates remain sufficiently high to produce a strain-rate-dependent contribution comparable to, and slightly larger than, that associated with Rayleigh damping. For EQ4, the hysteretic contribution decreases to approximately 77%, resulting in a combined non-hysteretic contribution of approximately 23%. The strain-rate contribution reaches approximately 10%, despite not being the most severe record. This contribution is probably associated with the sustained accumulation of strain-rate-dependent dissipation over the successive inelastic excursions. The viscous damping contribution (12.9%) exceeds the strain-rate contribution by only about 31%, representing a relatively close balance between these two mechanisms among the records in which viscous damping is dominant.

In EQ5, the strain-rate contribution (3.9%) remains slightly lower than the viscous damping contribution (4.6%). Thus, although EQ5 exhibits a hysteretic contribution comparable to that of EQ3, the relative contributions of strain-rate-dependent dissipation and viscous damping differ between the two records.

The comparison across all five records, summarized in Table 46, shows that these two non-hysteretic mechanisms remain of the same order of magnitude for EQ2-EQ5. Their relative contributions differ by less than a factor of two in these four records, with strain-rate dissipation exceeding viscous damping in EQ3. In contrast, viscous damping remains slightly larger in EQ2, EQ4, and EQ5. EQ1 represents the only clear departure from this near-parity, with the viscous damping contribution (28.1%) three times the strain-rate contribution (9.2%). This behavior is consistent with the predominantly linear response observed in EQ1, which results in fewer and less pronounced inelastic excursions of the reinforcing steel and, consequently, a lower contribution from strain-rate-dependent dissipation.

Table 46. Viscous damping and strain-rate dissipation ratios.

Simulation	Viscous damping (%)	Strain-rate (%)	Ratio
EQ1	28.1	9.2	3.05
EQ2	11.2	5.96	1.87
EQ3	3.78	4.1	0.92
EQ4	12.9	9.88	1.31
EQ5	4.55	3.89	1.17

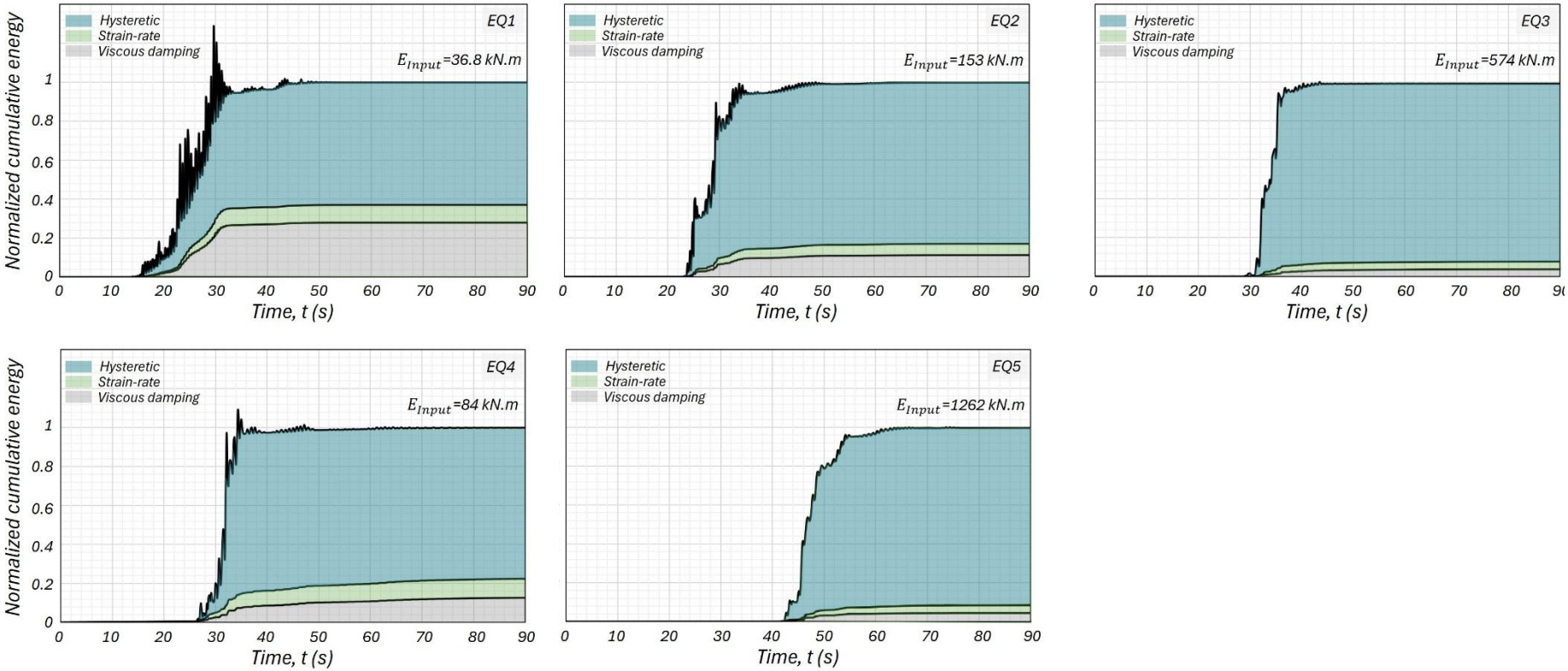
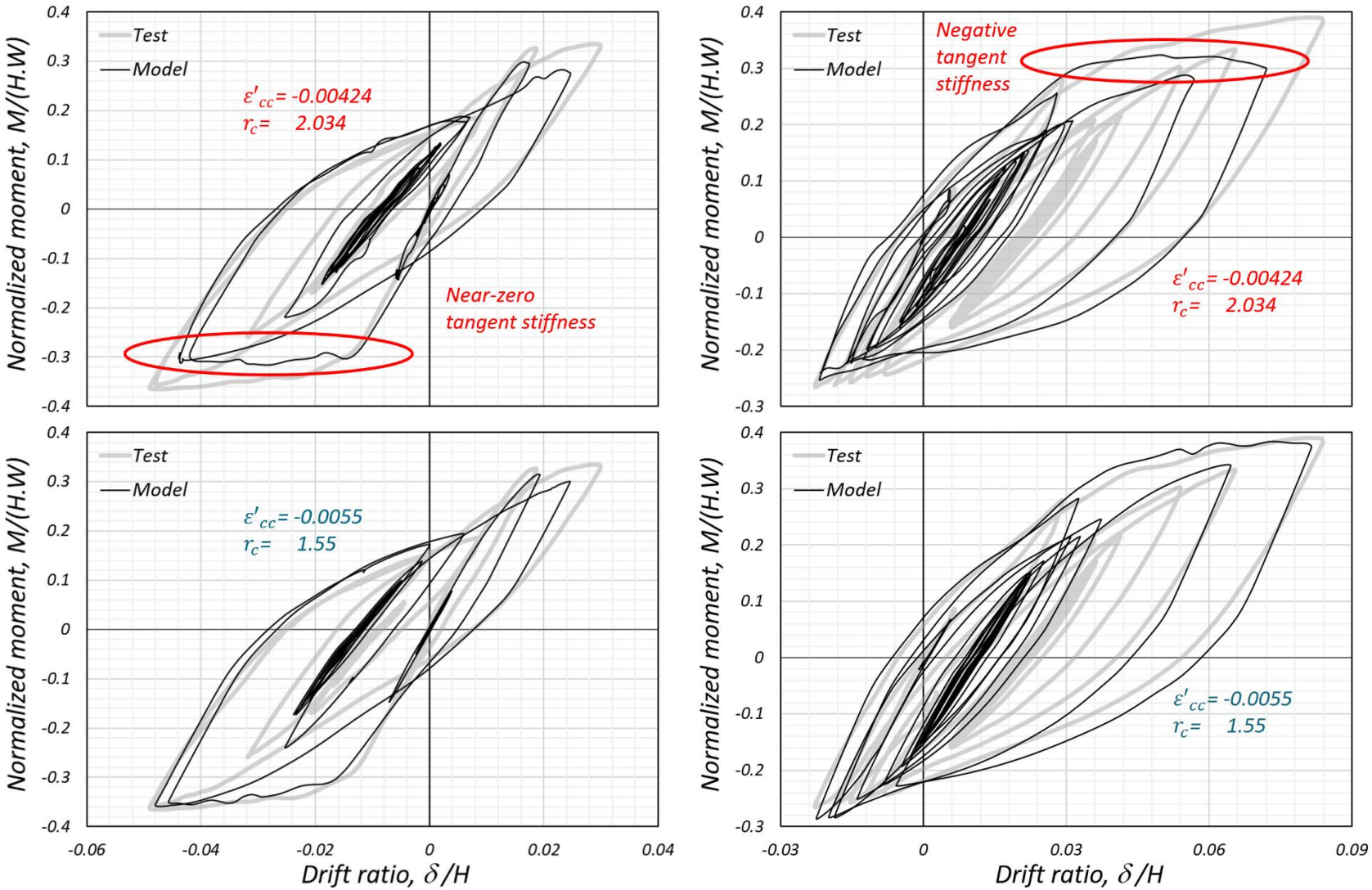


Figure 154. Cumulative normalized dissipated energy by mechanism for the five shake-table events.

5.10.4 Post-Calibration Refinement of Confined Concrete Parameters

The moment-drift hysteresis at the MAP parameter combination reveals that the model exhibits a near-zero or slightly negative tangent stiffness as peak drift is approached during EQ3 and EQ5 (Figures 148 and 152). In contrast, the test retains positive stiffness throughout this stage of the response. This behavior indicates that the confined concrete in the compression zone enters its post-peak branch prematurely, exhausting the flexural capacity of the critical section before the specimen does. In other words, with ε'_{cc}=-0.00424, the compression fibers in the plastic hinge reach their peak stress at a strain below that sustained by the specimen. Once the constitutive response enters the descending branch, the associated reduction in concrete stress decreases the sectional moment as curvature continues to increase.

A single adjustment from ε'_{cc}=-0.00424 to -0.0055 (with r_c recalculated accordingly from 2.034 to 1.55) delayed the onset of post-peak degradation and visibly improved the hysteretic loops for both EQ3 and EQ5. This improvement was achieved through a single physics-informed adjustment, guided by the observed softening pattern in the hysteresis. The fact that the Bayesian calibration converged to a different value highlights a limitation of GP-based surrogates when applied to highly nonlinear models: a smooth, stationary emulator may not adequately capture the abrupt change in response associated with the transition of the constitutive law from its ascending to descending branch. Engineering judgment therefore remains an essential complement to statistical inference when strong constitutive nonlinearities govern the model response.



a) Simulation EQ3 b) Simulation EQ5

Figure 155. Effect of confined concrete post-peak parameters on moment-drift hysteresis for EQ3 and EQ5.

6 Conclusions And Recommendations

6.1 Conclusions

This dissertation investigated the role of reinforcing-steel strain-rate effects and bond-slip-induced pinching in the nonlinear seismic response of RC structures. The research combined full-scale shake-table measurements, constitutive model development, deterministic and Bayesian calibration, and energy-based response assessment. The conclusions below address the experimental characterization of strain-rate demands, the SteelDRCV formulation, parameter identification, predictive performance, and the limitations of the resulting framework.

6.1.1 Strain-Rate Demands in Reinforcing Steel Under Seismic Loading

The experimental characterization of longitudinal reinforcement strain rates in two full-scale RC specimens tested on the Large High-Performance Outdoor Shake Table (LHPOST): a seven-story structural wall and a circular bridge column, showed that seismic strain-rate demands can substantially exceed those represented by conventional quasi-static testing. Peak strain rates reached approximately 44%/s in the Lüders plateau of the bridge column and 22%/s in the wall specimen. The measurements indicate that the rates imposed on reinforcing steel during strong seismic excitation cannot be represented adequately by nominal quasi-static loading rates.

The comparison with Direct Displacement-Based Assessment (DDBA) estimates showed a similar limitation in approaches based on average deformation rates. The measured peak strain rates were approximately 2 to 3 times larger than the corresponding analytical estimates. The difference is associated with the combined effects of strain localization, higher-mode structural vibrations, and the non-harmonic character of the measured deformation histories. The κ-ratio decomposition separated these contributions and yielded a representative post-Lüders amplification factor of approximately 1.85 for the strain-hardening regime.

The experimental results support the inclusion of strain-rate demands in constitutive modeling of reinforcing steel under seismic loading. They also show why local strain-rate demands cannot be inferred reliably from global displacement histories alone, particularly when the objective is to reproduce material response in plastic hinge regions.

6.1.2 Development and Assessment of the SteelDRCV Constitutive Model

The SteelDRCV constitutive model extends the rate-independent SteelDRC formulation by incorporating strain-rate-dependent viscous overstress and bond-slip-induced pinching. Both mechanisms were introduced within the existing cyclic plasticity framework, so the underlying formulation was retained without introducing additional structural degrees of freedom or internal state variables. The nonlinear Voigt-type viscous overstress formulation, $f_{sd} = k_{rate}|\dot{\varepsilon}|^{n_{rate}}$, introduces rate-dependent strengthening in the strain-hardening regime. Calibration against the high-strain-rate cyclic coupon tests yielded a sublinear power-law relationship, with k_{rate}=125 and n_{rate}=0.75. The associated stress increments remained below those predicted by conventional monotonic Dynamic Increase Factor relationships. Thus, monotonic DIF formulations do not necessarily represent transient cyclic strain-rate effects adequately. The continuum formulation captures the macroscopic stress amplification associated with strain-rate excursions through an additive overstress term.

Bond-slip-induced pinching was introduced through a quadrant-dependent curvature factor governed by λ and n_p. The mechanism acts during crack closure and reopening, producing the stiffness reduction and path dependence associated with bond-slip effects. Its implementation represents these effects at the macroscopic material level while retaining the computational structure of the underlying uniaxial model.

It is emphasized that the pinching formulation phenomenologically reproduces the macroscopic effect of multiple mechanisms, including fixed-end rotation, diagonal crack closure, and aggregate interlock, without explicitly resolving the physical processes at the steel-concrete interface. Accordingly, λ and n_p are empirical coefficients, not physical descriptors, and their structural-level interpretation is bounded by the calibration data from which they were identified.

The resulting formulation represents two mechanisms that are absent from the conventional rate-independent reinforcing-steel model: transient strain-rate-dependent strengthening and bond-slip-induced pinching. Their implementation in OpenSees allows both effects to be included in nonlinear structural analyses without explicit bond-slip elements or additional structural degrees of freedom.

6.1.3 Two-Stage Calibration and Parameter Identifiability

The fifteen model parameters governing the rate-independent hysteretic response, bond-slip-induced pinching, concrete tensile behavior, effective structural stiffness, unloading response, and strain-rate-dependent response were calibrated in two successive stages using the complementary information provided by quasi-static and dynamic loading. The first stage used displacement-controlled cyclic tests to determine the rate-independent parameters governing the hysteretic response, including the pinching and concrete tensile parameters. The second stage used Bayesian dynamic inference to refine the complete parameter set under earthquake excitation.

The variance-based sensitivity analysis showed that the dynamic response is controlled primarily by a limited subset of the independently sampled parameters. Peak displacement was particularly sensitive to the strain-rate exponent n_{rate}, whereas the effective flexural stiffness ratio strongly influenced hysteretic energy I_e/I_g and the unloading-modulus scaling parameter α_u. The different sensitivity patterns show that the same response measure does not provide equivalent information about all parameters. The Bayesian calibration used Transitional Markov Chain Monte Carlo sampling on Gaussian-Process surrogates trained from 1297 nonlinear time-history analyses. Rather than reducing the calibration to a single parameter set, the procedure produced posterior distributions that describe both the preferred parameter values and the remaining uncertainty.

A pronounced joint posterior ridge was obtained between n_{rate} and k_{rate}. The structural response therefore constrains the magnitude of the viscous overstress at the strain rates reached during the tests more strongly than it constrains the two rate parameters separately. The individual parameters are consequently only partially identifiable, even though the rate-dependent mechanism itself has a measurable influence on the response. This distinction is important when interpreting the posterior distributions and when transferring the calibrated parameters to other loading conditions.

The two-stage procedure follows directly from these sensitivity differences. Quasi-static loading supplies information about hysteretic features that are weakly constrained by earthquake records. At the same time, the dynamic stage provides the information needed to identify the parameters governing the rate-dependent structural response.

6.1.4 Limitations and Domain of Applicability

The conclusions of this dissertation are bounded by the experimental evidence and the constitutive assumptions adopted in the analysis.

First, the viscous overstress formulation is intended primarily for the strain-hardening regime. The localized dislocation dynamics associated with strain-rate amplification during the Lüders plateau are not explicitly resolved by the continuum formulation. The representation of this regime is therefore phenomenological rather than a direct description of the underlying microscopic process.

Second, the pinching mechanism represents the macroscopic effect of bond-slip degradation through an effective curvature reduction during load reversals. It does not explicitly resolve rib-concrete interaction, progressive bond deterioration, or confinement loss. Its validation is based on the global hysteretic response of the calibrated structural specimen and has not been extended to isolated bond-slip tests or other structural typologies.

Third, the structural calibration and validation rely on a single full-scale bridge-column specimen tested at the LHPOST facility. The held-out EQ5 simulation provides evidence of extrapolative predictive capability. Still, additional experimental data are needed to assess whether the formulation remains applicable to different structural configurations, reinforcement grades, and loading conditions.

Finally, the calibrated model does not reproduce all features of the experimental response. The higher inter-motion frequencies and the residual displacement accumulation after EQ3 and EQ4 indicate that stiffness recovery and permanent-deformation evolution remain incompletely represented. These discrepancies point to limitations in the constitutive representation rather than simply to deficiencies in parameter calibration.

6.1.5 Predictive Validation and Implications for Viscous Damping

The constitutive framework developed in this dissertation explicitly accounts for the principal sources of energy dissipation that, in conventional nonlinear analyses, remain unresolved and are implicitly absorbed by the prescribed viscous damping ratio. These sources include strain-rate-dependent strengthening of the reinforcing steel under dynamic loading, bond-slip-induced pinching during crack closure and reopening, and concrete cracking and damage mechanisms, including tensile fracture energy, crack-face interaction and aggregate interlock, and post-peak degradation of confined concrete in the plastic hinge regions. By incorporating these mechanisms directly into the constitutive formulation, the model separates their individual contributions to the structural energy balance, reducing the role of the ad hoc viscous damping term to account only for dissipation mechanisms that are not explicitly modeled.

The energy decomposition showed that the strain-rate-dependent mechanism contributes directly to the structural energy balance. Rayleigh viscous damping dissipated approximately 116 kN·m

(Table 44), corresponding to 5.5% of the total input energy. In contrast, the strain-rate-dependent mechanism contributed approximately 93 kN·m(Table 45), equivalent to 5.1% of the hysteretic energy when the rate-dependent mechanism was active. The two contributions were therefore of comparable magnitude for the analyzed response. These results illustrate that the strain-rate-dependent mechanism provides an energy contribution that is distinct from both Rayleigh damping and conventional material hysteresis. If the rate-dependent mechanism is omitted, part of its effect may consequently be absorbed by the other energy-dissipating components of the numerical model.

The MAP-calibrated formulation was evaluated against EQ5, the most intense earthquake simulation in the experimental sequence and a motion excluded from the identification procedure. The model reproduced the peak displacement with an error of approximately ±15%, which is comparable to the range obtained for the calibration motions. Since EQ5 imposed demands beyond those used during calibration, the comparison provides an assessment of the model response under loading conditions outside the identification set. It does not, however, establish general validity across structural typologies, reinforcement grades, or loading conditions.

Across EQ2-EQ5, which exhibited a clearly nonlinear response, the energy decomposition showed that the strain-rate-dependent contribution and Rayleigh viscous damping remained of the same order of magnitude (Table 46). Their combined contribution corresponded to an equivalent viscous damping ratio of approximately 0.9%. The Bayesian calibration resulted in a MAP value of ζ_1=0.46% for the first-mode Rayleigh damping ratio, indicating that approximately half of the equivalent dissipation associated with these two non-hysteretic mechanisms was provided by the explicitly modeled strain-rate-dependent response of the reinforcing steel. At the same time, the remaining portion was represented by Rayleigh damping. Thus, the calibrated viscous damping was substantially lower than the 2% ratio conventionally adopted in nonlinear analysis to account for additional sources of energy dissipation that are not explicitly modeled and cannot be directly measured.

6.1.6 Post-Calibration Refinement of Confined Concrete Parameters

The MAP-calibrated model exhibited near-zero and negative tangent stiffness at peak drifts during EQ3 and EQ5, respectively, whereas the experimental response retained positive stiffness throughout (Figure 155). The cause was identified as premature entry into the post-peak branch of the confined concrete constitutive law. With the MAP value of ε'_{cc} =-0.00424, the compression fibers reached their peak stress at a strain below that sustained by the specimen, causing their decreasing stress contribution to reduce the sectional moment as curvature increased. This behavior produced an artificial loss of tangent stiffness that was inconsistent with the experimental response.

A single post-calibration adjustment of ε'_{cc} =-0.0055, with the derived parameter $r_c$recalculated from 2.034 to 1.550, delayed the onset of post-peak degradation and eliminated the anomalous tangent-stiffness segments in both EQ3 and EQ5. The adjustment was therefore not introduced to improve a particular response metric, but to ensure that the constitutive model remained consistent with the observed physical behavior of the specimen over the range of compressive strains reached during the tests.

The fact that the GP-based Bayesian surrogate did not identify this parameter combination also highlights a limitation of surrogate-based inference for highly nonlinear structural models with

multiple interacting parameters. In the present study, the Bayesian calibration was performed using EQ1-EQ4, whereas EQ5 was retained as an independent validation motion. Consequently, the response under EQ5 provided an out-of-sample assessment of the calibrated model rather than an additional calibration target. The discrepancy observed in EQ5 indicates that a surrogate capable of representing the response over the calibration motions may have limited ability to extrapolate when a new excitation drives the structure into a nonlinear regime that is insufficiently represented in the calibration data. This limitation becomes particularly relevant when the structural response involves abrupt transitions between constitutive regimes, such as the onset of post-peak degradation of confined concrete, because these transitions may be difficult to represent accurately using a smooth, stationary emulator.

These results indicate that surrogate-based Bayesian inference may have limited extrapolation capability when applied to highly nonlinear structural systems, particularly when the validation motion activates response regimes that are not sufficiently represented in the calibration data. In the present case, the Bayesian calibration was based on EQ1-EQ4, whereas EQ5 was reserved as an independent validation motion. The inability of the surrogate-based calibration to identify a parameter set that remained fully consistent with the observed response in EQ5 indicates that good agreement within the calibration dataset does not necessarily ensure reliable predictions for a new excitation. This finding is particularly relevant when the structural response involves abrupt transitions between constitutive regimes, such as the onset of post-peak degradation in confined concrete, which may not be adequately captured by a smooth surrogate constructed from the calibration responses. Consequently, although Bayesian inference provides a rigorous framework for parameter estimation, its application to highly nonlinear structural models should be complemented by independent validation and physical examination of the resulting response. In this context, engineering judgment remains essential when the inferred parameter set produces structural behavior that is inconsistent with the experimentally observed response.

6.2 Scientific and Engineering Contributions

The principal contributions of this dissertation are as follows:

Experimental characterization of seismic strain-rate demands. Direct strain-rate measurements from full-scale RC members establish the magnitude of reinforcement strain-rate demands under realistic seismic excitation. The resulting κ-ratio decomposition provides a physical basis for separating the effects of strain localization, higher-mode response, and waveform characteristics when estimating local strain rates.

Development of the SteelDRCV constitutive model. A rate-dependent extension of SteelDRC was formulated and implemented in OpenSees. The model combines nonlinear viscous overstress with quadrant-dependent pinching, allowing strain-rate-dependent strengthening and bond-slip-induced stiffness degradation to be represented within a unified uniaxial formulation.

Two-stage Bayesian calibration methodology. A calibration framework was developed that combines deterministic quasi-static identification with Bayesian dynamic inference. The procedure links each parameter to the experimental stage that provides the relevant information while retaining posterior uncertainty and sensitivity information in the final calibration.

Quantification of material rate-dependent dissipation. The energy decomposition shows that strain-rate-dependent material dissipation is of the same order as the prescribed Rayleigh viscous damping for the analyzed structural response. The result gives a quantitative basis for treating material rate dependence as a separate contribution when interpreting seismic energy dissipation in nonlinear structural analysis.

6.3 Recommendations for Future Research

The findings of this dissertation motivate several directions for further research.

6.3.1 Additional Energy Dissipation Mechanisms

The constitutive framework developed in this work explicitly accounts for strain-rate-dependent strengthening, bond-slip-induced pinching, and post-peak degradation of confined concrete. Other energy dissipation mechanisms present in RC members under seismic loading, including longitudinal bar buckling, shear degradation in the plastic hinge region, progressive spalling of cover concrete, soil-structure interaction, and foundation radiation damping, were not modeled explicitly. Incorporating these mechanisms into the numerical formulation would further reduce the reliance on ad hoc viscous damping and provide a more complete description of the structural energy balance.

6.3.2 Improved Fixed-End Rotation Formulation

The fixed-end rotation element used in this dissertation was formulated on an ad hoc basis to reproduce the macroscopic effect of strain penetration into the anchorage zone. A more rigorous formulation that explicitly resolves the mechanics of the anchorage region, including the distribution of bond stresses along the development length, differential slip between the reinforcing bar and the surrounding concrete, and the progressive degradation of the bar-concrete interface under cyclic loading, would improve the physical basis of the model and its transferability to other structural configurations.

6.3.3 Three-Dimensional Solid Finite Element Modeling

The fiber-section beam-column formulation adopted in this work assumes plane sections remain plane and cannot resolve the three-dimensional strain field within the plastic hinge region. Validation against solid finite element models that directly resolve the spatial distribution of strains, stresses, and damage in the concrete and reinforcement would establish the limitations of the fiber-section approximation and identify the demand levels at which a continuum representation becomes necessary.

6.3.4 Extension to a Broader Range of Reinforcement Grades

The calibration and validation of SteelDRCV were based on A706 Grade 60 reinforcing steel. Future research should extend the characterization and calibration of the strain-rate and pinching parameters to a broader range of reinforcement grades, including both lower- and higher-strength steels, such as Grade 40 and Grade 80, as well as corrosion-resistant reinforcement. This extension would establish whether the proposed formulation and its parameter ranges remain applicable across a wider range of mechanical properties and strain-hardening characteristics.

6.3.5 Integration of Inelastic Buckling and Low-Cycle Fatigue

The current formulation does not explicitly represent the interaction between inelastic bar buckling and low-cycle fatigue under severe cyclic degradation. Future extensions could incorporate energy-based buckling and low-cycle fatigue criteria into the SteelDRCV fiber formulation to represent progressive reinforcement deterioration and rupture under extreme cyclic demands, thereby extending the model to degradation states preceding structural collapse.

6.3.6 Generalization Across RC Structural Typologies

The SteelDRCV formulation should be implemented and evaluated in a broader range of RC structural systems, including structural walls, beam-column joints, coupled wall systems, dual wall-frame systems, and bridge bents with different aspect ratios and transverse-confinement configurations. Applying the two-stage Bayesian calibration framework to these systems would allow the strain-rate-dependent and pinching mechanisms to be evaluated beyond the single-column configuration and would establish the extent to which the calibrated parameter ranges can be generalized across different structural typologies.

6.3.7 Integration with performance-based seismic design.

The calibrated model provides moment-curvature relationships, displacement ductility capacities, and energy dissipation estimates, including their posterior uncertainty, that can inform performance-based seismic design and assessment frameworks. Connecting the calibrated constitutive parameters with demand-capacity evaluation procedures would allow the experimental and analytical findings of this research to be transferred directly to engineering practice.

7 References

[1] Akhondzadeh, S., Sills, R. B., Bertin, N., & Cai, W. (2020). Dislocation density-based plasticity model from massive discrete dislocation dynamics database. *Journal of the Mechanics and Physics of Solids*, 145, 104152.

[2] Akkar, S. and Özen, Ö. (2005). Effect of peak ground velocity on deformation demands for SDOF systems. *Earthquake Engineering & Structural Dynamics*, 34(13), pp.1551-1571.

[3] American Concrete Institute. (2019). *ACI 318-19: Building code requirements for structural concrete. American Concrete Institute*.

[4] Anatech Corp. (2013). *ANACAP-U [Computer software]*. Anatech Corporation.

[5] Arias, A. (1970). A measure of earthquake intensity. *Seismic Design for Nuclear Power Plants*, 438-483. Massachusetts Institute of Technology.

[6] ASTM C469/C469M-14 Standard (2014). *Test Method for Static Modulus of Elasticity and Poisson's Ratio of Concrete in Compression*. ASTM International: West Conshohocken, PA, USA, 1-5.

[7] ASTM International. (2016). *ASTM A615/A615M-16 Specification for Deformed and Plain Carbon-Steel Bars for Concrete Reinforcement*. West Conshohocken, PA: ASTM International.

[8] ASTM International. (2016). *ASTM A706/A706M-16 Specification for Deformed and Plain Low-Alloy Steel Bars for Concrete Reinforcement*. West Conshohocken, PA: ASTM International.

[9] Asprone, D., Cadoni, E., & Prota, A. (2009). Tensile high strain-rate behavior of reinforcing steel from an existing bridge. *ACI Structural Journal*, 106(4), 523-530.

[10] Balan, T. A., Filippou, F. C., & Popov, E. P. (1998). Hysteretic model of ordinary and high-strength reinforcing steel. *Journal of Structural Engineering*, 124(3), 288-297.

[11] Bauschinger, J. (1886). On the change of the elastic limit and the strength of iron and steel, by drawing out, by heating and cooling, and by repetition of loading (summary). *Proceedings of the Institution of Civil Engineers*, 87, 463-484.

[12] Bayrak, O., & Sheikh, S. A. (2001). Plastic hinge analysis. *Journal of Structural Engineering*, 127(9), 1092-1100.

[13] Bertero, V. V., Mahin, S. A., & Herrera, R. A. (1978). *Seismic behavior of RC structural walls*. (Report No. UCB/EERC-78/10). Earthquake Engineering Research Center, University of California, Berkeley.

[14] Bézier, P. (1972). *Numerical control-mathematics and applications* (A. R. Forrest, Trad.). John Wiley & Sons.

[15] Blaschke, D. N. (2019). Properties of dislocation drag from phonon wind at ambient conditions. *Materials*, 12(6), 948.

[16] Blaschke, D. N., Mottola, E., & Preston, D. L. (2020). Dislocation drag from phonon wind in an isotropic crystal at large velocities. *Philosophical Magazine*, 100(5), 571-600.

[17] Bommer, J. J., & Alarcon, J. E. (2006). The prediction and use of peak ground velocity. *Journal of Earthquake Engineering*, 10(1), 1-31.

[18] British Standards Institution. (2014). *Eurocode 2: Design of concrete structures - Part 1-1: General rules and rules for buildings* (BS EN 1992-1-1:2014).

[19] Cadoni, E., Fenu, L., & Forni, D. (2012). Strain rate behaviour in tension of austenitic stainless steel used for reinforcing bars. *Construction and Building Materials*, 35, 399-407.

[20] Cadoni, E., & Forni, D. (2015). Strain rate effects on reinforcing steels in tension. *EPJ Web of Conferences* (Vol. 94, p. 01004). EDP Sciences.

[21] Cadoni, E., Dotta, M., Forni, D., & Tesio, N. (2015). High strain rate behaviour in tension of steel B500A reinforcing bar. *Materials and Structures*, 48, 1803-1813.

[22] Cadoni, E., Fontana, M., Forni, D., & Knobloch, M. (2018). High strain rates testing and constitutive modeling of B500B reinforcing steel at elevated temperatures. *The European Physical Journal Special Topics*, 227(1), 179-199.

[23] Cadoni, E., & Forni, D. (2021). Mechanical behaviour of B500A rebars: Effect of elevated temperature and high strain-rate. *Fire Safety Journal*, 122, 103321.

[24] Cai, Y. L., Yang, S. L., Fu, S. H., & Zhang, Q. C. (2016). The influence of specimen thickness on the Lüders effect of a 5456 Al-based alloy: Experimental observations. *Metals*, 6(5), 120.

[25] California Department of Transportation. (2004). *Bridge design specifications*.

[26] California Department of Transportation. (2006). *Bridge design specifications*.

[27] Callister Jr., W. D. (2000). Materials science and engineering-an introduction. *Anti-Corrosion Methods and Materials*, *47*(1).

[28] Cao, P., Li, D., Bai, S., Chen, Y., & Lu, H. (2024). Dynamic Compression and Constitutive Model in Fe-27Mn-10Al-1C Duplex Lightweight Steel. *Crystals*, 14(2), 178.

[29] Carreño Vallejos, R. (2018). *Characterization of large diameter reinforcement under large strain cyclic reversals* (Doctoral dissertation). University of California, San Diego.

[30] Carreño, R., Lotfizadeh, K. H., Conte, J. P., & Restrepo, J. I. (2020). Material model parameters for the Giuffrè-Menegotto-Pinto uniaxial steel stress-strain model. *Journal of Structural Engineering*, 146(2), 04019205.

[31] Chang, G. A., & Mander, J. B. (1994). *Seismic energy based fatigue damage analysis of bridge columns: Part I - Evaluation of seismic capacity* (Report No. NCEER-94-0006). National Center for Earthquake Engineering Research.

[32] Chen, M. C., Astroza, R., Restrepo, J. I., Conte, J. P., Hutchinson, T., & Bock, Y. (2017). Predominant period and equivalent viscous damping ratio identification for a full-scale building shake table test. *Earthquake Engineering & Structural Dynamics*, 46(14), 2459-2477.

[33] Ching, J., & Chen, Y. C. (2007). Transitional Markov chain Monte Carlo method for Bayesian model updating, model class selection, and model averaging. *Journal of Engineering Mechanics*, 133(7), 816-832.

[34] Chu, T. C., Ranson, W. F., & Sutton, M. A. (1985). Applications of digital image-correlation techniques to experimental mechanics. *Experimental Mechanics*, 25, 232-244.

[35] Ciampi, V., Eligehausen, R., Bertero, V. V., & Popov, E. P. (1982). *Analytical model for concrete anchorages of reinforcing bars under generalized excitations* (Report No. UCB/EERC-82/23). Earthquake Engineering Research Center, University of California, Berkeley.

[36] Cohen, J. (1988). *Statistical power analysis for the behavioral sciences* (2nd ed.). Lawrence Erlbaum Associates.

[37] Comité Euro-International du Béton. (1988). *Concrete structures under impact and impulsive loading* (CEB Bulletin No. 187).

[38] Comité Euro-International du Béton. (1993). *CEB-FIP Model Code 1990: Design code*. Thomas Telford.

[39] Cottrell, A. H., & Bilby, B. A. (1949). Dislocation theory of yielding and strain ageing of iron. *Proceedings of the Physical Society. Section A*, 62(1), 49-62.

[40] Cowper, G. R., & Symonds, P. S. (1957). *Strain hardening and strain rate effect in the impact loading of cantilever beams* (Report No. 28). Division of Applied Mathematics, Brown University.

[41] Cowper, G. R. (1966). The Shear Coefficient in Timoshenko's Beam Theory. *Journal of Applied Mechanics*, 33(2), 335-340

[42] Danilov, V. I., Orlova, D. V., Gorbatenko, V. V., & Danilova, L. V. (2023). Effect of temperature on the kinetics of localized plasticity autowaves in Lüders deformation. *Metals*, 13(4), 773.

[43] Dodd, L. L., & Restrepo-Posada, J. I. (1995). Model for predicting cyclic behavior of reinforcing steel. *Journal of Structural Engineering*, 121(3), 433-445.

[44] Dougherty, L. M., Cerreta, E. K., Gray III, G. T., Trujillo, C. P., Lopez, M. F., Vecchio, K. S., & Kusinski, G. J. (2009). Mechanical behavior and microstructural development of low-carbon steel and microcomposite steel reinforcement bars deformed under quasi-static and dynamic shear loading. *Metallurgical and Materials Transactions A*, 40(8), 1835-1850.

[45] Eibl, J. (1988). Concrete structures under impact and impulsive loading. In Comité Euro-International du Béton, *CEB Bulletin d'Information No. 187* (pp. 5-45).

[46] Eligehausen, R., Ciampi, V., Bertero, V. V., & Popov, E. P. (1982). Local bond stress-slip relationships of deformed bars under generalized excitations. In *Proceedings of the 7th European Conference on Earthquake Engineering* (Vol. 2, pp. 69-80). Athens, Greece.

[47] Elwood, K. J., & Eberhard, M. O. (2009). Effective Stiffness of Reinforced Concrete Columns. *ACI Structural Journal*, 106(4), 476.

[48] Fan, H., Wang, Q., El-Awady, J. A., Raabe, D., & Zaiser, M. (2021). Strain rate dependency of dislocation plasticity. *Nature communications*, 12(1), 1845

[49] Filiatrault, A., & Holleran, M. (2001). Stress-strain behavior of reinforcing steel and concrete under seismic strain rates and low temperatures. *Materials and Structures*, 34, 235-239.

[50] Filippou, F. C., Popov, E. P., & Bertero, V. V. (1983). *Effects of bond deterioration on hysteretic behavior of reinforced concrete joints* (Report No. UCB/EERC-83/19). Earthquake Engineering Research Center, University of California, Berkeley.

[51] Fornberg, B. (1988). Generation of finite difference formulas on arbitrarily spaced grids. *Mathematics of Computation*, 51(184), 699-706.

[52] Galligan, J. M., McKrell, T. J., & Robson, M. T. (2000). Dislocation drag processes. *Materials Science and Engineering: A*, 287(2), 259-264.

[53] Ghannoum, W., Saouma, V., Haussmann, G., Polkinghorne, K., Eck, M., & Kang, D. H. (2012). Experimental investigations of loading rate effects in RC columns. *Journal of Structural Engineering*, 138(8), 1032-1041.

[54] Godínez, S. E., & Restrepo, J. I. (2023). Stringer-panel model to support the seismic design and response verification of building diaphragms. *Resilient Cities and Structures*, 2(1), 46-67.

[55] Hastings, W. K. (1970). Monte Carlo sampling methods using Markov chains and their applications. *Biometrika*, *57*(1), 97-109.

[56] He, X., Moaveni, B., Conte, J. P., Restrepo, J. I., & Elgamal, A. (2006). Damage identification of a seven-Story RC shear wall building tested on the UCSD-NEES shake table. *In Proceedings of the 4th World Conference on Structural Control and Monitoring*. International Association for Structural Control and Monitoring.

[57] Hines, E. M. (2002). *Seismic Performance of Hollow Rectangular Reinforced Concrete Bridge Piers with Confined Corner Elements*. Ph.D. thesis, University of California, San Diego, San Diego, CA, USA.

[58] Hines, E. M., Restrepo, J. I., & Seible, F. (2004). Force-displacement characterization of well-confined bridge piers. *ACI Structural Journal*, 101(4), 537-548.

[59] Hong, H. S., & Hickernell, F. J. (2003). Algorithm 823: Implementing scrambled digital sequences. *ACM Transactions on Mathematical Software*, *29*(2), 95-109.

[60] ICC-ES. (2010). *Evaluation report ESR-252*. International Code Council.

[61] Ismail, M., Ikhouane, F., & Rodellar, J. (2009). The hysteresis Bouc-Wen model: A survey. *Archives of Computational Methods in Engineering*, 16, 161-188.

[62] Jansen, M. J. (1999). Analysis of variance designs for model output. *Computer Physics Communications*, 117(1-2), 35-43.

[63] Johnson, G. R., & Cook, W. H. (1983). A constitutive model and data for metals subjected to large strains, high strain rates and high temperatures. *In Proceedings of the 7th International Symposium on Ballistics* (pp. 541-547).

[64] Kang, S., Jeong, S., & Ahn, Y. S. (2021). Effect of discontinuous yielding on the strain hardening behavior of fine-grained twinning-induced plasticity steel. *Frontiers in Materials*, 8, 599534.

[65] Kent, D. C., & Park, R. (1973). Cyclic load behaviour of reinforcing steel. *Strain*, 9(3), 98-103.

[66] Khonsari, S. V., Shabani, A., England, G. L., & Shahsavar-Gargari, M. (2018). Mechanical behaviour of A-III steel rebars under monotonic loadings at seismic strain rates. *Magazine of Concrete Research*, 70(1), 42-54.

[67] Kim, S. H., & Koutromanos, I. (2016). Constitutive model for reinforcing steel under cyclic loading. *Journal of Structural Engineering*, 142(12), 04016133.

[68] Klepaczko, J. R., & Duffy, J. (1982). History effects in polycrystalline BCC metals and steel subjected to rapid changes in strain rate and temperature. *Archives of Mechanics*, *34*(4), 419-436.

[69] Kolozvari, K., Orakcal, K., & Wallace, J. W. (2015). *Shear-flexure interaction modeling for reinforced concrete structural walls and columns under reversed cyclic loading* (Report No. PEER-2015/12). Pacific Earthquake Engineering Research Center, University of California, Berkeley.

[70] Krantz, S. G. 1999. *Handbook of complex variables*. Boston: Birkhäuser.

[71] Kumar, T. J. P., Manikanta, L., Chenna Kesavulu, T., Cherukuneedi, R., & Leela Krishna, D. (2025). Effect of carbon composition on mechanical properties of steels: A comparative experimental study. *International Journal of Research Publication and Reviews*, 6(10), 5725-5731.

[72] Lemcherreq, Y., Haefliger, S., & Kaufmann, W. (2023). Discontinuous yielding in bare and embedded reinforcing bars: implications on the determination of steel and bond shear stresses from strain measurements. *Engineering Structures*, 278, 115235.

[73] Levings, J., & Sritharan, S. (2012). Effects of cold temperature and strain rate on the stress-strain behavior of ASTM A706 grade 420 (60) steel reinforcement. *Journal of materials in civil engineering*, 24(12), 1441-1449.

[74] Li, M., & Li, H. (2012). Effects of strain rate on RC structure under seismic loading. *Advances in Structural Engineering*, 15(3), 461-475.

[75] Lin, F., Dong, Y., Kuang, X., & Lu, L. (2016). Strain rate behavior in tension of reinforcing steels HPB235, HRB335, HRB400, and HRB500. *Materials*, 9(12), 1013.

[76] Liu, C., Hu, C., Wang, X., Huang, M., & Jiang, C. (2024). A new perspective on Lüders band formation in medium-Mn steels based on Lüders-strain-rate and dislocation evolution. *Materials Science and Engineering: A*, 901, 146553.

[77] Ljung, L. System Identification: Theory for the User (2nd edition). Prentice Hall: Upper Saddle River, NJ, 1999.

[78] Lüders, W. (1860). Über die Äusserung der Elasticität an stahlartigen Eisenstäben und Stahlstäben, und über eine beim Biegen solcher Stäbe beobachtete Molecularbewegung. *Dinglers Polytechnisches Journal*, 5, 18-22.

[79] Ludwik, P. (1909). *Elemente der technologischen Mechanik*. Springer.

[80] Malvar, L. J., & Crawford, J. (1998). Dynamic increase factors for steel reinforcing bars. In *Proceedings of the 28th DDESB Seminar* (pp. 1-17). Department of Defense Explosives Safety Board.

[81] Malvar, L. J. (1998). Review of static and dynamic properties of steel reinforcing bars. *Materials Journal*, 95(5), 609-616.

[82] Mander, J.B. (1983). *Seismic Design of Bridge Piers*. Ph.D. Thesis, University of Canterbury, Christchurch, New Zealand, 1983.

[83] Mander, J. B., Priestley, M. J. N., & Park, R. (1984). *Seismic design of bridge piers* (Research Report No. 84-2). Department of Civil Engineering, University of Canterbury.

[84] Massone, L. M., & Moroder, D. (2009). Buckling modeling of reinforcing bars with imperfections. *Engineering Structures*, 31(3), 758-767.

[85] Massone, L. M., Rosa, J., & Mesa, Á. (2023). Versatile hysteretic model of reinforcing steel bars with buckling. *Structures* (Vol. 47, pp. 1858-1868). Elsevier.

[86] Matoušek, J. (1998). On the L2-discrepancy for anchored boxes. *Journal of Complexity*, 14(4), 527-556.

[87] Mavros, M., Panagiotou, M., Koutromanos, I., & Restrepo, J. I. (2023). Nonlinear dynamic seismic analysis of a modern concrete core wall-building in Los Angeles using the BTM-shell methodology. *Earthquake Engineering & Structural Dynamics*, *52*(14), 4416-4441.

[88] McKenna, F., Fenves, G. L., Filippou, F. C., Mazzoni, S., Scott, M. H., Elgamal, A., & McKenzie, P. (2010). *OpenSees: Open system for earthquake engineering simulation* (Versión 2.0) [Software de computación]. University of California, Berkeley.

[89] Menegotto, M., & Pinto, P. E. (1973). Method of analysis for cyclically loaded RC plane frames including changes in geometry and non-elastic behavior of elements under combined normal force and bending. In *Proceedings of the IABSE Symposium on Resistance and Ultimate Deformability of Structures Acted on by Well-Defined Repeated Loads* (Vol. 13, pp. 15-22). International Association for Bridge and Structural Engineering.

[90] Messerschmidt, U. (2010). *Dislocation dynamics during plastic deformation* (Vol. 129). Springer Science & Business Media

[91] Moaveni, B., He, X., Conte, J. P., Restrepo, J. I., & Panagiotou, M. (2011). System identification study of a 7-story full-scale building slice tested on the UCSD-NEES shake table. *Journal of Structural Engineering*, 137(6), 705-717.

[92] Monti, G., & Nuti, C. (1990). Numerical model for steel bars under cyclic loading including post-elastic buckling. In *Proceedings of the Ninth European Conference on Earthquake Engineering* (Vol. 6, pp. 191-200).

[93] Monti, G., & Nuti, C. (1992). Nonlinear cyclic behavior of reinforcing bars including buckling. *Journal of Structural Engineering*, 118(12), 3268-3284.

[94] Murcia-Delso, J. (2013). *Bond-Slip Behavior and Development of Bridge Column Longitudinal Reinforcing Bars in Enlarged Pile Shafts* [Tesis doctoral, University of California, San Diego].

[95] Nilsson, M. (2012). *Tribology in metal working* (Doctoral dissertation, Uppsala University, Department of Engineering Sciences).

[96] Panagiotou, M. (2008). *Seismic design, testing, and analysis of RC wall-buildings* [Tesis doctoral, University of California, San Diego].

[97] Panagiotou, M., Restrepo, J. I., & Conte, J. P. (2011). Shake-table test of a full-scale 7-story building slice. Phase I: Rectangular wall. *Journal of Structural Engineerin*g, 137(6), 691-704.

[98] Panagiotou, M., Restrepo, J. I., & Conte, J. P. (2007). *Shake-table test of a 7-story full-scale RC structural wall-building slice - Phase II: T-wall section* (Structural Systems Research Project Report No. SSRP-07/08). Department of Structural Engineering, University of California, San Diego.

[99] Panagiotou, M., & Restrepo, J. I. (2011). Displacement-based method of analysis for regular reinforced-concrete wall-buildings: Application to a full-scale 7-story building slice tested at UC-San Diego. *Journal of Structural Engineering*, *137*(6), 677-690.

[100] Perzyna, P. (1966). Fundamental problems in viscoplasticity. *Advances in Applied Mechanics*, 9, 243-377.

[101] Piegl, L., & Tiller, W. (2012). *The NURBS book*. Springer Science & Business Media.

[102] Piobert, G. (1842). Expérience sur la Pénétration Des Projectiles Dans le Fer Forgé. *Mémoire De L'artillerie* 505: 1842.

[103] Pokropek, J., Kluczyński, J., Sarzyński, B., Jasik, K., Szachogłuchowicz, I., Łuszczek, J., Joska, Z., Małek, M. & Torzewski, J. (2025). The Influence of Rolling Direction and Dynamic Strengthening on the Properties of Steel. *Materials*, 18(16), 3808.

[104] Popovics, S. (1973). A numerical approach to the complete stress-strain curve of concrete. *Cement and Concrete Research*, 3(5), 583-599.

[105] Priestley, M. N. (2003). *Myths and fallacies in earthquake engineering*, revisited: The ninth Mallet-Milne lecture, 2003 (p. 119). IUSS Press.

[106] Priestley, M. J. N., Calvi, M. C., & Kowalsky, M. J. (2007). *Displacement-based seismic design of structures*. IUSS Press.

[107] Qiu, J. L., & Gong, J. X. (2019). Analytical hysteretic model for reinforcing bars. *Computers & Structures*, 214, 48-59.

[108] Qiu, H., Inoue, T., & Ueji, R. (2020). In-situ observation of Lüders band formation in hot-rolled steel via digital image correlation. *Metals*, 10(4), 530.

[109] Qiu, H., Ueji, R., Inoue, T., & Kimura, Y. (2021). Plastic instability in medium-carbon tempered martensite steel. *Materials*, 14(16), 4609.

[110] Qiu, H., Ueji, R., & Inoue, T. (2022). Yield-point phenomenon and plastic bands in ferrite-pearlite steels. *Materials*, 16(1), 195.

[111] Ramberg, W., & Osgood, W. R. (1943). *Description of stress-strain curves by three parameters* (Technical Note No. 902). National Advisory Committee for Aeronautics.

[112] Rashid, J. Y., James, R. J., & Dunham, R. S. (2014). Modeling and analysis of nuclear power plant structures using ANATECH-ANACAP software system. In T. T. C. Hsu, C.-L. Wu, & J.-L. Li (Eds.), *Infrastructure Systems for Nuclear Energy* (pp. 345-363). John Wiley & Sons.

[113] Restrepo-Posada, J. I., Park, R., & Buchanan, A. H. (1993). *Seismic behaviour of connections between precast concrete elements of moment resisting frames* (Research Report No. 93-3). Department of Civil Engineering, University of Canterbury.

[114] Restrepo-Posada, J. I., Dodd, L. L., Park, R., & Cooke, N. (1994). Variables affecting cyclic behavior of reinforcing steel. *Journal of Structural Engineering*, 120(11), 3178-3196.

[115] Restrepo, J. I., Crisafulli, F. J., & Park, R. (1999). How harmful is cold bending/straightening of reinforcing bars? *Concrete International*, 21(4), 45-48.

[116] Restrepo, J. I., Conte, J. P., Luco, J. E., Seible, F., & Van Den Einde, L. (2005). The NEES@UCSD large high-performance outdoor shake table. *In Earthquake Engineering and Soil Dynamics* (pp. 1-16). American Society of Civil Engineers.

[117] Restrepo, J. I., Conte, J. P., Dunham, R. S., Parker, D., Wiesner, J., & Dechent, P. A. C. (2017, enero). Detailed nonlinear FE pushover analysis of Alto Rio building. In *Proceedings of the 16th World Conference on Earthquake Engineering* (Artículo 4153). International Association for Earthquake Engineering.

[118] Ross, C. A., Tedesco, J. W., & Hughes, M. L. (1996). Rate effects on the behavior of RC beams. *Journal of Engineering Mechanics*, ASCE.

[119] Saltelli, A., Ratto, M., Andres, T., Campolongo, F., Cariboni, J., Gatelli, D., ... & Tarantola, S. (2008). *Global sensitivity analysis: the primer*. John Wiley & Sons.

[120] Saltelli, A., Annoni, P., Azzini, I., Campolongo, F., Ratto, M., & Tarantola, S. (2010). Variance based sensitivity analysis of model output. Design and estimator for the total sensitivity index. *Computer Physics Communications*, 181(2), 259-270.

[121] Salvado, F. C., Teixeira-Dias, F., Walley, S. M., Lea, L. J., & Cardoso, J. B. (2017). A review on the strain rate dependency of the dynamic viscoplastic response of FCC metals. *Progress in Materials Science*, 88, 186-231.

[122] Savitzky, A., & Golay, M. J. (1964). Smoothing and differentiation of data by simplified least squares procedures. *Analytical Chemistry*, 36(8), 1627-1639.

[123] Schenker, A., Anteby, I., Gal, E., Kivity, Y., Nizri, E., Sadot, O., Michaelis, R., Levintant, V., & Ben-Dor, G. (2008). Dynamic behavior of high-strength steel reinforcing bars. *Materials and Structures*, *41*(5), 899-907.

[124] Schoettler, M. J., Restrepo, J. I., Guerrini, G., Duck, D. E., & Carrea, F. (2015). *A full-scale, single-column bridge bent tested by shake-table excitation* (Report No. PEER 2015/02). Pacific Earthquake Engineering Research Center, University of California, Berkeley.

[125] Shing, P. S. B., & Mahin, S. A. (1988). Rate-of-loading effects on pseudodynamic tests. *Journal of Structural Engineering*, 114(11), 2403-2420.

[126] Sobol, I. M. (2001). Global sensitivity indices for nonlinear mathematical models and their Monte Carlo estimates. *Mathematics and Computers in Simulation*, *55*(1-3), 271-280.

[127] Stainier, L., Cuitiño, A. M., & Ortiz, M. (2002). A micromechanical model of hardening, rate sensitivity and thermal softening in bcc single crystals. *Journal of the Mechanics and Physics of Solids*, 50(7), 1511-1545.

[128] Student. (1908). *The probable error of a mean*. Biometrika, 1-25.

[129] Sun, H.B., Yoshida, F., Ohmori, M. & Ma, X. (2003). Effect of strain rate on Lüders band propagating velocity and Lüders strain for annealed mild steel under uniaxial tension. *Materials Letters*, 57(29), pp.4535-4539.

[130] Theis, H. E. (1999). *Handbook of metalforming processes*. CRC Press.

[131]Toribio, J., Kharin, V., Ayaso, F. J., Lorenzo, M., González, B., Matos, J. C., & Aguado, L. (2020). Analysis of the Bauschinger effect in cold-drawn pearlitic steels. *Metals*, 10(1), 114.

[132] Tripathi, M., & Dhakal, R. P. (2023). Constitutive model for reinforcing bars including bar buckling and low-cycle fatigue. *Engineering Structures*, 295, 116772.

[133] Trumper, D. (2014). *Introduction to frequency domain processing* [Lecture notes]. Department of Mechanical Engineering, Massachusetts Institute of Technology. MIT OpenCourseWare.

[134] Tsai, W. T. (1988). Uniaxial compressional stress-strain relation of concrete. *Journal of Structural Engineering*, 114(9), 2133-2136.

[135] Van der Heijde, J. H., & Samad, W. A. (2023). The effect of specimen thickness on the Lüders phenomena in AISI 1524 steel alloy: Experimental observations using DIC. *Experimental Mechanics*, *63*(5), 885-896.

[136] Van Rooyen, G. T., & Backofen, W. A. (1960). The effect of strain rate and temperature on the yield point behavior of mild steel. *Acta Metallurgica*, 8(9), 614-620.

[137] Walraven, J. C., & Reinhardt, H. W. (1981). Theory and experiments on the mechanical behaviour of cracks in plain and reinforced concrete subjected to shear loading. *HERON*, *26*(1A), 1-68.

[138] Wang, X. G., He, B. B., Liu, C. H., Jiang, C., & Huang, M. X. (2019). Extraordinary Lüders-strain-rate in medium Mn steels. *Materialia*, 6, 100288.

[139] Watstein, D. (1953). Effect of straining rate on the compressive strength and elastic properties of concrete. *Journal of the American Concrete Institute*, *24*(8), 729-744.

[140] Wen, Y. K. (1976). Method for random vibration of hysteretic systems. *Journal of the Engineering Mechanics Division*, 102(2), 249-263.

[141] Westergaard, H. M. (1933). Measuring earthquake intensity in pounds per square foot. *Engineering News-Record*, 504.

[142] Wu, H., Masaki, K., Irikura, K., Saguchi, K., Kurahashi, S., & Wang, X. (2012). Relationship between building damage ratios and ground motion characteristics during the 2011 Tohoku earthquake. *Journal of Natural Disaster Science*, 34(1), 59-78.

[143] Yamazaki, F., & Murao, O. (2000). Fragility curves for buildings in Japan based on experience from the 1995 Kobe earthquake. *In Proceedings of the US-Japan Workshop on the Effects of Near-Field Earthquake Shaking* (p. 85).

[144] Zeng, X., Huo, J., Wang, H., Wang, Z., & Elchalakani, M. (2020). Dynamic tensile behavior of steel HRB500E reinforcing bar at low, medium, and high strain rates. *Materials*, 13(1), 185.

[145] Zeng, X., Wang, Z., & Huo, J. (2020). Tensile behavior of 400 MPa-grade anti-earthquake hot-rolled ribbed bar (HRB400E) over a wide strain rate range. *Construction and Building Materials*, 249, 118729.

[146] Zeng, X., & Huo, J. S. (2023). Rate-dependent constitutive model of high-strength reinforcing steel HTRB600E in tension. *Construction and Building Materials*, 363, 129824.

[147] Zerilli, F. J., & Armstrong, R. W. (1987). Dislocation-mechanics-based constitutive relations for material dynamics calculations. *Journal of Applied Physics*, 61(5), 1816-1825.

[148] Zhang, H., Li, H. N., & Shang, B. (2012). Shaking table test and dynamic response analysis of RC structure. In *Proceedings of the 15th World Conference on Earthquake Engineering* (Paper No. 1756). International Association for Earthquake Engineering.

[149] Zhao, J., & Sritharan, S. (2007). Modeling of strain penetration effects in fiber-based analysis of reinforced concrete structures. *ACI Structural Journal*, *104*(2), 133-141.

[150] Zubelewicz, A., & Oliferuk, W. (2016). Mechanisms-based viscoplasticity: Theoretical approach and experimental validation for steel 304L. *Scientific Reports*, *6*(1), Article 23681.